UNCLASSIFIED

MARTIN MARIETTA ENERGY SYSTEMS LIBRARIES

3 4456 0286768 1

ORNL-2389
Physics and Mathematics
TID-4500 (13th ed.)

Cy. 4

APPLIED NUCLEAR PHYSICS DIVISION

ANNUAL PROGRESS REPORT

FOR PERIOD ENDING SEPTEMBER 1, 1957

CENTRAL RESEARCH LIBRARY
DOCUMENT COLLECTION
LIBRARY LOAN COPY
DO NOT TRANSFER TO ANOTHER PERSON
If you wish someone else to see this document, send in name with document and the library will arrange a loan.

OAK RIDGE NATIONAL LABORATORY
OPERATED BY
UNION CARBIDE NUCLEAR COMPANY
A Division of Union Carbide and Carbon Corporation
UCC
POST OFFICE BOX X • OAK RIDGE, TENNESSEE

UNCLASSIFIED

Printed in USA. Price $6.50 cents. Available from the

Office of Technical Services
U. S. Department of Commerce
Washington 25, D. C.

LEGAL NOTICE

This report was prepared as an account of Government sponsored work. Neither the United States, nor the Commission, nor any person acting on behalf of the Commission:

A. Makes any warranty or representation, express or implied, with respect to the accuracy, completeness, or usefulness of the information contained in this report, or that the use of any information, apparatus, method, or process disclosed in this report may not infringe privately owned rights; or

B. Assumes any liabilities with respect to the use of, or for damages resulting from the use of any information, apparatus, method, or process disclosed in this report.

As used in the above, "person acting on behalf of the Commission" includes any employee or contractor of the Commission to the extent that such employee or contractor prepares, handles or distributes, or provides access to, any information pursuant to his employment or contract with the Commission.

ORNL-2389 Errata

Summary

p. vi: Paragraph 1.6, line 5: delete "and uniformity of flux in the core"; substitute the word "lower" for the word "higher"

Paper 1.2

p. 16: insert minus sign before each number in Fig. 1.2.2

Paper 1.5

p. 25, col. 1, line 13: delete "on the flux"
col. 2, line 5: substitute "radial" for "axial"
col. 2, Table 1.5.1: substitute "5 x 5" for "5 x 6"

p. 26, col. 1, Table 1.5.2: substitute "6 x 4" for "6 x 6"

p. 27, Table 1.5.3: substitute "5 x 5" for "5 x 4"

p. 28, Fig. 1.5.1: change ordinate to read:

$$\text{PERCENT REDUCTION IN k, } \frac{100(k_{\text{infinite reflector}} - k)}{k_{\text{infinite reflector}}}$$

Paper 2.1

p. 37, col. 1, line 7: substitute "0.005-in." for "0.006-in."
col. 2, line 4: substitute "control-plate" for "control-rod"

p. 38, col. 2: Fourth line in tabulation should read:
"2 quarter elements each containing 74 g of uranium"

p. 44, col. 2, line 1: substitute "same" for "small"

p. 49, col. 1, line 7: substitute "eight plates' worth" for "8% plate worth"
line 9: substitute "four plates" for "a 4% plate"
Fig. 2.1.22: substitute "(msec)" for "(μsec)" in ordinate

Paper 3.1

p. 59, col. 2, last line: substitute "0.0285 g/cm^2" for "0.283 g/cm^2"

p. 65, Table 3.1.3: substitute "$(w \cdot cc^{-1} \cdot Mw^{-1})$" for "$(w \cdot cc^{-1} \cdot Mev^{-1})$"
Fig. 3.1.15: substitute "(watts/cc·Mw)" for "(watts/cc·Mev)" in ordinate

Paper 4.2

p. 84, col. 2, last equation: substitute "-C" for "C"

Paper 4.3

p. 87, col. 2, paragraph 2, line 4: substitute "(58 in.)" for "(59 in.)"

p. 88, col. 2, line 6: substitute "ORNL-CF-55-1-76" for "Sec. 8.5"

Paper 8.10

p. 164, Table 8.10.3, line 1: enclose "2.348 $\pm$ 0.09" in parentheses; insert similar parentheses in lines 2-5

Paper 8.11

p. 165, col. 1, line 12: substitute "of the angular distribution" for "in the angular distribution"

col. 2, last line: substitute "σ_{nX}" for "σ_X"

p. 168, col. 1: Replace last sentence in column with:
"From 200 kev down to zero energy the scattering cross section is listed in Table 8.11.2. Below 100 kev the values given have been calculated on the basis of assumed negative energy levels, as described below in the section on σ_γ."

col. 2, line 11: substitute "f'_L" for "$f_{L'}$"

lines 13 and 16: substitute "λ" for "λ"

Paper 8.13

p. 176, col. 2, line 10: substitute "uncorrected" for "corrected"

Paper 10.3

p. 249, col. 2, line 19: substitute "1.0 μsec" for "10 μsec"

p. 254, Fig. 10.3.5: for value of capacitor on grid of V_5 substitute "22 μμf" for "22 μf"

p. 257, col. 2, line 4: substitute "(0.75 μsec)" for "(~75 μsec)"
line 12: substitute "10 mμsec" for "10 μsec"

Paper 10.5

p. 267, line 9 in caption: substitute "10^4 sec" for "10 sec"

UNCLASSIFIED

ORNL-2389
Physics and Mathematics
TID-4500 (13th ed.)

Contract No. W-7405-eng-26

APPLIED NUCLEAR PHYSICS DIVISION ANNUAL PROGRESS REPORT

for Period Ending September 1, 1957

E. P. Blizard, Director
A. Simon, Associate Director

A. D. Callihan, Leader, Critical Experiments Facility
C. E. Clifford, Leader, Tower Shielding Facility
F. C. Maienschein, Leader, Bulk Shielding Facility
W. Zobel, Leader, Lid Tank Shielding Facility

DATE ISSUED

OCT 18 1957

OAK RIDGE NATIONAL LABORATORY
Operated by
UNION CARBIDE NUCLEAR COMPANY
A Division of Union Carbide and Carbon Corporation
Post Office Box X
Oak Ridge, Tennessee

UNCLASSIFIED

MARTIN MARIETTA ENERGY SYSTEMS LIBRARIES

3 4456 0286768 1

ORNL-2389
Physics and Mathematics
TID-4500 (13th ed.)

INTERNAL DISTRIBUTION

1. C. E. Center
2. Biology Library
3. Health Physics Library
4-6. Central Research Library
7. Reactor Experimental Engineering Library
8-27. Laboratory Records Department
28. Laboratory Records, ORNL R.C.
29. A. M. Weinberg
30. L. B. Emlet (K-25)
31. J. P. Murray (Y-12)
32. J. A. Swartout
33. E. H. Taylor
34. E. D. Shipley
35. A. H. Snell
36. W. H. Jordan
37. M. L. Nelson
38. G. E. Boyd
39. R. A. Charpie
40. S. C. Lind
41. F. L. Culler
42. A. Hollaender
43. J. H. Frye, Jr.
44. M. T. Kelley
45. R. S. Livingston
46. K. Z. Morgan
47. E. J. Murphy
48. A. S. Householder
49. C. P. Keim
50. C. S. Harrill
51. C. E. Winters
52. D. S. Billington
53. D. W. Cardwell
54. E. M. King
55. A. J. Miller
56. M. J. Skinner
57. R. R. Dickison
58. P. M. Reyling
59. G. C. Williams
60. L. S. Abbott
61. R. G. Ausmiller
62. J. L. Fowler
63-86. E. P. Blizard
87. A. D. Callihan
88. G. T. Chapman
89. C. E. Clifford
90. R. R. Coveyou
91. G. deSaussure
92. L. Dresner
93. J. K. Fox
94. L. W. Gilley
95. E. Guth
96. R. Gwin
97. K. M. Henry
98. L. B. Holland
99. E. B. Johnson
100. F. L. Keller
101. W. E. Kinney
102. M. E. LaVerne
103. T. A. Love
104-106. F. C. Maienschein
107. J. H. Marable
108. J. M. Miller
109. F. J. Muckenthaler
110. R. B. Murray
111. R. W. Peelle
112. A. B. Reynolds
113. E. G. Silver
114. A. Simon
115. J. G. Sullivan
116. D. K. Trubey
117. T. A. Welton
118. C. D. Zerby
119. W. Zobel
120. V. R. Cain
121. G. M. Estabrook
122. T. K. Fowler
123. S. H. Hanauer
124. J. Hilgeman
125. J. L. Hull
126. J. D. Kington
127. D. Magnuson
128. J. J. Manning
129. H. S. Moran
130. J. Wett
131. T. V. Blosser
132. D. W. Cady
133. D. F. Cronin
134. J. F. Ellis
135. R. M. Freestone

136. V. G. Harness
137. L. Jung
138. R. J. Kerr
139. J. J. Lynn
140. R. J. Mackin
141. S. K. Penny
142. E. R. Rohrer
143. D. Scott
144. J. T. Thomas
145. W. C. Tunnell
146. E. A. Warman
147. Francis L. Friedman (consultant)
148. Herbert Goldstein (consultant)
149. Henry Hurwitz, Jr. (consultant)
150. L. W. Nordheim (consultant)
151. Robert R. Wilson (consultant)

EXTERNAL DISTRIBUTION

152. R. F. Bacher, California Institute of Technology
153. E. Kuhn, Reactor Design Development Division, Combustion Engineering, Windsor, Connecticut
154. Division of Research and Development, AEC, ORO
155-710. Given distribution as shown in TID-4500 (13th ed.) under Physics and Mathematics category (75 copies – OTS)

TABLE OF CONTENTS AND SUMMARY

1. RESEARCH FOR LIGHT-WATER-MODERATED HETEROGENEOUS REACTORS

1.1. STUDIES OF PLATE-TYPE CONTROL DEVICES IN A POOL-TYPE REACTOR

E. B. Johnson, K. M. Henry, J. D. Kington, and A. B. Reynolds 3

Both the proposed BSR-II and the proposed TSR-II pose problems of nuclear control because of the size or shape of the cores. Therefore the possibility of using plate-type control devices rather than rod-type devices is being considered. Experimental tests of the effectiveness of single and paired plates of absorber have been performed with the aluminum core of the BSR-I. The absorber plates used in these tests consisted of stainless steel plates and boron-loaded aluminum plates which were inserted in various locations in a special fuel element. Other tests were performed with a two-dimensional mockup of the TSR-II control system. While extrapolation from the BSR-I core to either of the proposed cores is not straightforward, experimental evidence indicates that plate-type control devices will provide adequate control potential for each reactor.

1.2. COMPARISON OF THE DISTRIBUTED-POISON AND INHOUR METHODS FOR MEASURING REACTIVITY

A. B. Reynolds and E. B. Johnson 11

The reactivity effect of a uniform distribution of boron carbide (B_4C) in the core of the BSR was determined experimentally by means of the inhour equation. A thin strip of B_4C-impregnated Plexiglas was inserted into each fuel element. As each strip was removed, the reactor period caused by its removal was measured and the reactivity worth of each B_4C strip was then obtained from the inhour equation. Since the ratio of the nonleakage probability of prompt neutrons to that of delayed neutrons appears in the inhour equation, the experimental results depended on the value chosen for this ratio. Two values for this ratio were calculated. The total reactivity effect of the distributed B_4C was calculated from the change in thermal utilization. The calculated value agrees with the experimental value within 10%, which was within the experimental error.

1.3. DETERMINATION OF THE POWER OF THE TOWER SHIELDING REACTOR

F. N. Greene, C. R. Fink, and W. E. Price 18

Calorimetric experiments to determine the power of the TSF reactor were conducted weekly during March and bimonthly thereafter in order to collect sufficient data for a statistical analysis of the results. The results, when plotted with previous data taken at six-month intervals, indicate a trend toward increasing power with time. Thermal-neutron flux measurements on the center line of one fuel element during calorimetric experiments disclosed a shift in power distribution effecting an increase in total power for the element.

1.4. CALCULATION OF THE PHOTONEUTRON FLUX IN THE WATER NEAR THE BULK SHIELDING REACTOR

G. deSaussure 22

The neutron flux observed in water at distances greater than about 200 cm from the BSR is essentially entirely attributable to photoneutron production in the naturally occurring deuterium of the water. By using measured gamma-ray spectra at 267 cm, the expected photoneutron flux is calculated and found to agree with observed values within 4%.

1.5. COMPARISON OF POOL-TYPE REACTOR CRITICAL EXPERIMENTS WITH TWO-GROUP CALCULATIONS

E. G. Silver 25

Critical masses calculated with the UNIVAC Eyewash and the Oracle 3G3R codes for three BSF reactor loadings were previously reported. These values have been revised slightly, as a result of a recalculation of the effect of partial elements on the flux. A few additional calculations have also been performed with a modified 3G3R code. In addition, the applicability of the 3G3R code used as a two-group code was verified by performing calculations for several solution-type reactors which required no geometric transformations.

1.6. CALCULATION OF THE GAMMA-RAY SPECTRUM OF THE BULK SHIELDING REACTOR
G. deSaussure 29

A hand calculation has been performed of the leakage-gamma-ray spectrum above 3 Mev for the BSR. Simplifying assumptions were straight-ahead Compton scattering, neglect of more than single scatterings, ~~and uniformity of flux in the core~~. The calculated spectrum is significantly ~~higher~~ lower than the measured value in spite of the fact that the assumptions should lead to an overestimate. Further experiments and calculations are planned.

2. DESIGN FOR A UO_2–STAINLESS STEEL BULK SHIELDING REACTOR (BSR-II)

2.1. DESIGN FOR A UO_2–STAINLESS STEEL BULK SHIELDING REACTOR (BSR-II)
E. G. Silver and J. Lewin 33

A design for an alternate core for the BSR, to be known as the BSR-II, has been completed. This reactor, which will be a 15-in. cube, will be a convection-cooled, plate-type research reactor fueled with highly enriched UO_2–stainless steel cermet clad with stainless steel. Nuclear calculations and heat transfer calculations, as well as the control-system dynamics, are presented.

3. DESIGN FOR A SPHERICAL TOWER SHIELDING REACTOR (TSR-II)

3.1. DESIGN FOR A SPHERICAL TOWER SHIELDING REACTOR (TSR-II)
C. E. Clifford and L. B. Holland 53

A new reactor with a higher power and a geometry more amenable to calculations is needed at the TSF in order to extend the studies of the interactions of neutrons and gamma rays with air. In order to meet this need a new reactor, designated as the TSR-II, is being designed. It will be a 5-Mw, light-water-moderated and cooled heterogeneous reactor in a spherical geometry. The reactor will be controlled with curved plates that will move radially in a spherical water reflector region interior to the core. Nuclear calculations have been carried out both on the UNIVAC and the Oracle in order to establish the reactor dimensions, and Monte Carlo techniques have been utilized to determine the gamma-ray heating in the lead. Development work on the fuel elements and the control mechanism has shown the mechanical design to be feasible. Control experiments are being performed with the BSR for correlation with calculations of the amount of nuclear control available.

4. CRITICAL EXPERIMENTS

4.1. CRITICAL PARAMETERS OF AQUEOUS SOLUTIONS OF U^{235}
J. K. Fox and L. W. Gilley 71

The series of experiments to determine the critical parameters of aqueous solutions of UO_2F_2 highly enriched in U^{235} is continuing. Additional experiments have been performed to determine the critical parameters of unreflected and water-reflected solutions in single vessels of varying size. The effect of special reflectors on single vessels also has been determined. In addition, arrays of interacting vessels have been studied. The U^{235} enrichment of the solution used in these experiments was 93.2%.

4.2. DETERMINATION OF UNREFLECTED REACTOR PARAMETERS
R. Gwin 84

Data from a series of bare, aqueous, enriched U^{235} critical assemblies are fitted by diffusion theory by using both the "extrapolated end-point" method and the zero boundary return current, referred to as the "current" method. The just-critical conditions for all assemblies can be fitted well with one value of the buckling for each method. Measured reactor periods for off-critical dimensions are well fitted by the "current" method but are in some question for the "extrapolated end-point" method. Ages and effective delayed neutron fractions are also calculated.

4.3. CRITICAL PARAMETERS OF A PROTON-MODERATED AND PROTON-REFLECTED SLAB OF U^{235}

J. K. Fox, L. W. Gilley, and J. H. Marable 87

An attempt has been made to measure directly the minimum critical thickness of an infinitely high and infinitely wide hydrogen-reflected slab of aqueous solution of UO_2F_2 enriched to 93.2% in U^{235}. Extrapolation of the experimental results to infinite dimensions and correction for the container material yielded a value of 1.76 in. at an $H:U^{235}$ atomic ratio of 44. Oracle calculations for slabs which were critical in the experiment gave a value of k of 1.125. The calculated thickness of a slab for $k = 1$ was 1.38 in.

5. RESONANCE REACTOR PROGRAM

5.1. RESONANCE REACTOR PROGRAM

L. Dresner, S. H. Hanauer, D. W. Magnuson, and C. D. Zerby 91

A program is planned in which an unreflected, graphite-moderated critical assembly with a resonance energy spectrum (1 to 100 kev) will be constructed. The assembly will be parallelepipedal in shape and will contain uranium enriched to 93% in U^{235}. Control will be effected by withdrawing fuel from the assembly and/or by separating the two halves of the assembly. The purposes of the program include the correlation of experimental and theoretical critical masses, the measurement of radiative cross sections, and the measurement of the capture-to-fission ratio.

6. FISSION PHYSICS

6.1. ANALYSIS OF FISSION-PRODUCT GAMMA-RAY SPECTRA EXPERIMENT

W. Zobel, R. W. Peelle, T. A. Love, and G. M. Estabrook 97

The analysis of a previously conducted experiment, designed to determine the gross photon spectra due to short-lived fission products, is being refined. In particular, the fission rates in the uranium samples used in the experiment were redetermined, by using the cadmium difference technique for gold foils of the same area as the uranium samples. The necessity for flux depression corrections was eliminated by choosing the thickness of the gold foils to give approximately the same absorption as the uranium samples. A further refinement of the data analysis consists in an attempt to reduce the influence of the broadness of the instrument response on the spectra. These attempts have so far proved to be unsuccessful, but efforts are continuing.

6.2. ENERGY SPECTRUM OF PROMPT GAMMA RAYS ACCOMPANYING THE FISSION OF U^{235}

F. C. Maienschein, R. W. Peelle, and T. A. Love 99

Experiments are currently in progress at the BSF to measure the energy spectrum of prompt gamma rays accompanying U^{235} fission, by using the multiple-crystal scintillation spectrometer and a small spiral fission chamber. Coincidence circuits have been used to establish by time-of-flight that some of the observed pulses are neutron-induced. New shield configurations to protect the detectors from unwanted gamma rays or neutrons have been investigated, but not much improvement was found over the standard design. On completion of the quantitative determination of the neutron-induced background, the basic measurements will ensue.

6.3. U^{233} PROMPT-NEUTRON FISSION SPECTRUM

K. M. Henry 111

The large statistical errors of the previously reported U^{233} fission neutron spectrum were reduced by the use of a larger sample of material. The spectrum of a comparable mass of U^{235} is also reported. These "gray" samples produced a U^{233}/U^{235} yield ratio of 1.30 and a nearly identical spectrum.

6.4. COMPARISON OF THE AVERAGE NUMBER OF PROMPT NEUTRONS EMITTED IN FISSION OF U^{233}, U^{235}, Pu^{239}, AND Pu^{241}

G. deSaussure and E. G. Silver 113

The fast coincidence technique was employed to measure the relative prompt-neutron yields per fission of U^{233}, U^{235}, Pu^{239}, and Pu^{241} induced by thermal neutrons. The values obtained were $\nu^{23}/\nu^{25} = 1.02 \pm 0.01$, $\nu^{49}/\nu^{25} = 1.23 \pm 0.01$, and $\nu^{41}/\nu^{25} = 1.295 \pm 0.02$, where ν^{23}, ν^{25}, ν^{49}, and ν^{41} designate the prompt-neutron yields of U^{233}, U^{235}, Pu^{239}, and Pu^{241}, respectively.

7. REACTOR PHYSICS

7.1. TIME-DEPENDENT NEUTRON DIFFUSION MEASUREMENTS

G. deSaussure and E. G. Silver 119

An experiment is being designed to measure the diffusion properties of crystalline moderators at various temperatures by the pulsed-neutron-source method. The temperature effects will be most important in the regions in which crystalline effects cause sharp increases in the mean free paths (e.g., in Be, the increase from room temperature to ~100°K is calculated to be about a factor of 10). The equipment for the experiment is being assembled. The pulsed-neutron source is being constructed at the BSF. The detector will be a very small $Li^6I(Eu)$ scintillator similar to others in use at the Laboratory. Time analysis will be obtained by an 18-channel system. The moderating assemblies of materials to be studied will be cubes of pure material, initially graphite or beryllium, which can be heated or cooled uniformly. The preliminary results which have been obtained, by means of another source, on beryllium and graphite agree satisfactorily with published results.

8. REACTOR THEORY

8.1. SOME ANALYTICAL SOLUTIONS OF THE SLOWING-DOWN PROBLEM IN HYDROGEN

L. Dresner and A. Simon 131

Analytic solutions for the slowing-down density in the P_1, B_1, and Selengut-Goertzel approximations are given for two special problems. The first is for the case in which all cross sections are constant, with the heavy elements assumed to have infinite mass. The second is for pure, nonabsorbing hydrogen with a v^3 scattering cross section. The results are discussed.

8.2. EFFECT OF FLUCTUATIONS IN THE WIDTHS ON NEUTRON REACTION CROSS SECTIONS

L. Dresner 134

The effect of fluctuations in the widths on reaction cross sections is discussed. When the widths are distributed in chi-squared distributions, this effect can be expressed in terms of a single, infinite integral. The integral is evaluated explicitly in some simple cases. A Monte Carlo machine code for evaluating the integral in general is described.

8.3. ANALYSIS OF LOW-ENERGY NEUTRON REACTIONS IN U^{238}

L. Dresner 138

An analysis of experimental radiative capture and inelastic-scattering cross sections has been carried out with the statistical theory of reactions, appropriately modified to include fluctuations in the neutron widths. The analysis indicates that the *p*-wave strength function is slightly larger than the *s*-wave function.

8.4. EFFECT OF FLUCTUATIONS IN THE REACTION WIDTHS ON RESONANCE INTEGRALS

E. Kuhn and L. Dresner 143

An estimate of the resonance capture integral of nonfissile nuclei, previously given, has been corrected to include the effect of fluctuation in the neutron width.

8.5. *"CORN PONE" – A MULTIGROUP, MULTIREGION REACTOR CODE*
R. R. Coveyou, W. E. Kinney, and J. G. Sullivan, Jr. 145

A multigroup, multiregion reactor code known as "Corn Pone" is nearing completion. Equations resulting from a consistent P_1 approximation to the Boltzmann equation are incorporated in the code. Hydrogen slowing down is treated exactly, while a variety of approximate slowing-down kernels for the heavier elements are available.

8.6. *"MANFRED" – A "FEW"-GROUP, MULTIREGION REACTOR CODE*
J. F. Wett and R. R. Coveyou 147

A program designated as "Manfred" has been initiated to develop a "few"-group, multiregion reactor code for the Oracle. Manfred will allow the diffusion coefficient and the removal cross section to be spatially dependent. The code, by using the concept of albedos, collapses each region into a set of boundary conditions until the reactor is reduced to a core with a somewhat peculiar set of boundary conditions. Thus, in essence, the code reduces the problem to only one region, and, consequently, all the space points may be used in the core. After the flux in the core has been calculated, the fluxes in the other regions can be calculated by again making use of all the space points available.

8.7. *PROGRAM COMPILER FOR THE ORACLE*
M. E. LaVerne 151

The Compiler, which was previously reported, has been revised for use with the Oracle's new input-output equipment. A compilable version of the Compiler is being prepared.

8.8. *EFFECTIVE BOUNDARY CONDITIONS IN THE THREE-GROUP, THREE-REGION REACTOR CODE*
M. E. LaVerne 152

It has been found, in the Oracle 3G3R reactor code, that a manipulation of the boundary conditions allows the code to simulate the effects of regions outside the reactor and to do lattice calculations. Relations between shell β's and the shell transmission and reflection coefficients are shown. Shell β's for any transmission, but no reflection, are given.

8.9. *ORACLE SUBROUTINES*
J. G. Sullivan, R. R. Coveyou, J. H. Marable, M. E. LaVerne, and W. E. Kinney 156

Sentence descriptions are given of thirty-one subroutines which have been prepared for specific problems to be computed on the Oracle but are of general use to Oracle programmers.

8.10. *ESTIMATE OF THE NONLEAKAGE PROBABILITY FOR BARE AQUEOUS HOMOGENEOUS U^{235} REACTORS*
D. K. Trubey, H. S. Moran, and A. M. Weinberg 158

The slowing-down distribution, to thermal energy, of neutrons from a U^{235} fission source in an infinite water medium up to 160 cm has been determined from experimental data. The Fourier transform of this distribution and the indium resonance distribution, which are the nonleakage probabilities for bare reactors, have also been determined.

8.11. *COMPILATION OF NEUTRON CROSS SECTIONS OF NITROGEN AND OXYGEN*
H. Lustig, H. Goldstein, and M. H. Kalos 165

The best information – experimental, theoretical, and educated artistic – is being used to present, in convenient form for reactor and shielding calculations, the cross sections of nitrogen and oxygen. The data for nitrogen have been gathered and are presented. The data for oxygen are not yet complete.

8.12. *SOME RECENT CALCULATIONS OF THE AGE OF FISSION NEUTRONS IN WATER*
H. Goldstein and J. Certaine 174

The discrepancy between the theoretical value of 26.0 ± 0.5 cm^2 and the experimental value of 30.0 ± 1.0 cm^2 for the age of fission neutrons in water is investigated. New data on the angular distribution ($\bar{\mu}$) of neutrons scattered by oxygen for the energy region below 2.7 Mev are used in a revised calculation. The new value was higher by only about 0.5 cm^2. Overestimates of corrections to this quantity

above 2.7 Mev raise the calculated age to 28.0 cm^2. The effect on the age of several variations in the fission spectrum was also investigated, but no likely possibility is found to explain the basic discrepancy.

8.13. AGE OF FISSION NEUTRONS IN DIPHENYL AND IN OIL
J. H. Marable 176

The Oracle Monte Carlo neutron age code has been used to calculate the slowing down of fission neutrons past 1.45 ev in two organic compounds. The results were 47.51 $\pm$0.5 cm^2 for diphenyl ($C_{12}H_{10}$) and 22.75 $\pm$0.2 cm^2 for oil (essentially CH_2).

9. SHIELDING RESEARCH

9.1. STUDY OF A THIN LEAD-WATER SHIELD ad ASR
E. B. Johnson, K. M. Henry, and J. D. Kington 179

Configurations of shields consisting of lead, water, and boron were studied to develop an arrangement which would alter the leakage of neutrons and gamma rays from a TSR-II type of reactor in a desired way.

9.2. RADIATION ATTENUATION MEASUREMENTS IN PLAIN WATER, BORATED WATER, AND OIL MEDIA IN THE LTSF
D. W. Cady and E. A. Warman 180

The latest and best data are presented for attenuation from a fission source of fast-neutron dose, thermal–neutron flux, and gamma rays in water, borated water, and a saturated oil. The present thermal-neutron data are corrected for flux depression by the foil detectors, as well as for self-absorption and self-shielding of the detectors.

9.3. ATTENUATION OF FAST NEUTRONS FROM A FISSION SOURCE BY WATER: COMPARISON OF EXPERIMENT WITH THEORY
D. R. Otis 184

Several calculations of the attenuation kernel for the fast-neutron dose rate from an isotropic point fission source in water have been performed. One calculation based on LTSF experiments in which the old source plate (SP-1) was used did not agree with a calculation performed later with the "moments" method. At the time, the discrepancy could not be resolved, but the installation of the new source plate (SP-2) has allowed some differences to be explained. A new calculation based entirely on experimental data obtained with SP-2 has resulted in agreement with the moments-method calculation.

9.4. EFFECTIVE REMOVAL CROSS SECTION OF TUNGSTEN
J. M. Miller 187

The effective removal cross section of tungsten has been determined as 3.13 $\pm$0.25 barns on the basis of thermal-neutron flux measurements made at the LTSF beyond a 4-in.-thick sample of Hevimet (90 wt % tungsten, 6 wt % nickel, and 4 wt % copper). An earlier value of 2.51 $\pm$0.55 barns was determined from measurements beyond tungsten chips.

9.5. GAMMA-RAY AND THERMAL-NEUTRON MEASUREMENTS IN AIR AT VARIOUS DISTANCES FROM THE TOWER SHIELDING REACTOR
F. N. Watson, R. M. Davis, and W. R. Champion 188

As a part of the continuing study of the air capture, scattering, and attenuation of reactor radiations, measurements have been made of the gamma-ray dose rate and thermal-neutron flux in air at various distances from the reactor at the TSF. Throughout these measurements the reactor-detector height above the ground, their separation distance, the thickness of the reactor water shield, and the angle between the emitted reactor beam and the detector-reactor tank axis were varied. The results of the measurements are reported.

9.6. STUDY OF AIR AND GROUND SCATTERING OF FAST NEUTRONS AT THE TOWER SHIELDING FACILITY
M. J. Welch, R. M. Davis, W. J. McCool, and C. R. Fink 194

An experiment designed to study air and ground scattering of fast neutrons has been performed. A highly collimated beam of neutrons was obtained for the experiment by placing either of two air-filled

cylindrical aluminum pipes (8- and 15-in. ID) adjacent to the TSR in the reactor tank. Fast-neutron dose rate measurements were made with an unshielded detector at a distance of 64 ft from the reactor tank while both the direction of the beam and the height above the ground were varied. The measurements made as a function of altitude showed a maximum intensity at an altitude varying between 20 and 40 ft. A decrease in intensity as higher altitudes were approached resulted from a decrease in ground scattering that was larger than the small increase in air scattering.

9.7. DETERMINATION OF GAMMA-RAY DOSE RATES AND SPECTRA FROM SOIL AND CONCRETE SAMPLES AFTER IRRADIATION AT THE TOWER SHIELDING FACILITY
F. J. Muckenthaler, J. L. Hull, W. R. Champion, and V. R. Cain 209

One soil sample and concrete samples consisting of plain concrete, barytes concrete, and one sample of each containing an admixture of 1% boron were exposed for 20 hr to the TSR operating at 400 kev in order to determine how much they had been activated and which components were responsible. The dose rate at the positions of the concrete samples was 0.725 erg/g·hr·w, while that at the position of the soil sample was 0.896 erg/g·hr·w. Subsequent to irradiation the intensity of the gamma-ray dose rate from the samples was determined as a function of time after irradiation. In addition, pulse-height spectra of gamma rays from the samples were determined. For the barytes and soil samples a large part of the dose rate 4 hr after irradiation was due to a thermal (n,γ) reaction in Mn^{55}; between 24 and 100 hr after irradiation the main contribution was from the same reaction in Na^{23}. For the plain concrete samples the gamma-ray dose rate throughout the first 100 hr after irradiation was essentially due to the thermal (n,γ) reaction in Na^{23}.

9.8. SUMMARY OF MONTE CARLO CALCULATIONS OF GAMMA-RAY PENETRATIONS IN VARIOUS MULTIREGION SHIELDS WITH SLAB GEOMETRY
S. Auslender and A. T. Futterer 215

Several Monte Carlo calculations have been performed on the Oracle to determine the dose rate, energy flux, energy deposition, and, in some cases, the energy spectra in laminated shields as a function of the energy of the gamma-ray source and the angle of incidence of the gamma rays on the shield. Since it is impractical to publish all the results from these calculations in a progress report, a summary of the problems is presented along with references to the published data.

9.9. MONTE CARLO CALCULATION OF GAMMA-RAY PENETRATION OF LEAD-WATER SHIELDS
L. A. Bowman and D. K. Trubey 218

Calculations have been continued for one of the lead-water slab shield series mentioned in Sec 9.8 and extended to include additional total shield thicknesses, as well as additional initial gamma-ray energies. A total of 512 problems has now been computed in this series.

9.10. MONTE CARLO CALCULATION OF GAMMA-RAY PENETRATION OF ALUMINUM SLABS
D. K. Trubey 220

A Monte Carlo calculation of the energy spectrum and angular distribution of normally incident 0.662-Mev gamma rays which are transmitted through 3-, 6-, and 9-in.-thick aluminum slabs has been performed on the Oracle. Plots of the transmitted collided energy fraction are fitted with analytical expressions.

9.11. MONTE CARLO CALCULATION OF THE ENERGY AND ANGULAR DISTRIBUTION OF AIR-SCATTERED NEUTRONS FROM A MONOENERGETIC SOURCE
C. D. Zerby 224

A Monte Carlo calculation has been performed to determine the energy flux and angular distribution of air-scattered neutrons from a monodirectional beam at a source-detector separation distance of 64 ft. The source was assumed to be located on an absorbing sphere of diameter D_0, which was assigned the values of 0, which resulted in a point source, and 12 ft. Isotropic scattering in the center-of-mass system was taken as the scattering law. The source energies included in the calculations were 0.55, 1.2, 2, 3, and 5 Mev, and the angle of radiation emission from the source was considered to be 2, 15, 30, 60, 90, 135, and 180 deg. The problem was idealized in that the source-detector system was considered as suspended in an infinite body of air.

9.12. ANALYSIS OF MONTE CARLO CALCULATION OF AIR-SCATTERED NEUTRONS FROM A MONOENERGETIC SOURCE

J. Hilgeman, F. L. Keller, and C. D. Zerby 226

Analysis of the results of the Monte Carlo calculation of air-scattered neutrons from a 1-neutron/sec line beam leaving a source at angle θ_0 with initial energy E_0 has shown that the flux at the detector can be represented by the expression $\phi = [\Sigma_s(E_0)/4\pi g]\,[(\pi - \theta_0)/\sin\theta_0]$.

9.13. CALCULATION OF AIR-SCATTERED NEUTRON DOSE RATES AROUND A CYLINDRICALLY SYMMETRIC SOURCE

C. A. Goetz 227

An Oracle code has been written with which the results obtained in the Monte Carlo air-scattering calculation (Secs 9.11 and 9.12) can be utilized to calculate the neutron dose rate around a cylindrically symmetric source.

9.14. MONTE CARLO CALCULATION OF AIR-SCATTERED GAMMA RAYS

R. E. Lynch, W. P. Johnson, J. W. Benoit, and C. D. Zerby 228

A Monte Carlo calculation has been performed to determine the fluxes, tissue dose rates, angular distributions, and energy spectra of multiply scattered gamma rays in air at various distances from a monoenergetic, monodirectional source. The calculation included source energies of 0.6, 1, 2, 4, 7, and 12 Mev; source beam angles of 1, 15, 30, 60, 90, 135, and 180 deg; and source-detector separation distances of 5, 10, 20, 40, 65, and 100 ft.

10. RADIATION DETECTOR DEVELOPMENT

10.1. TOTAL-ABSORPTION GAMMA-RAY SPECTROSCOPY

G. T. Chapman and T. A. Love 233

A very large, cylindrical NaI(Tl) crystal, $9\frac{3}{8}$ in. high, $9\frac{3}{8}$ in. in diameter, and truncated at one end, is being tried in a gamma-ray spectrometer. A large low-pulse-height tail in the response was attributed partly to a crystal defect and partly to difficulties of containing a gamma ray within the crystal after the first one or two scatterings. Drilling a hole 2 in. deep in one end and collimating the incoming radiation into the hole reduced the tail but worsened the resolution (width at half maximum) somewhat. The three photomultiplier tubes which were used had to be carefully matched in response to obtain best resolution. Work is continuing on improving the resolution, with an arrangement of seven small matched phototubes to be tried next.

10.2. FAST-NEUTRON SPECTROMETER DEVELOPMENT

R. B. Murray and J. J. Manning 240

Further investigation of $Li^6I(Eu)$ crystals indicate that they will be suitable for measuring fission-like neutron spectra above an energy of $\sim$1.5 Mev.

10.3. PULSE-AMPLITUDE-INDEPENDENT TIMING CIRCUITS FOR DRIVING AN INTERMEDIATE-SPEED COINCIDENCE UNIT FROM THE OUTPUT OF A DOUBLE-LINE PULSE AMPLIFIER

R. W. Peelle and T. A. Love 249

Common types of coincidence circuitry for nuclear spectroscopy are reviewed briefly, and the properties of standard two-speed coincidence circuits are discussed. With the use of standard double-line-clipped linear pulse amplifiers a property of the pulse shape permits the resolving time of the usual intermediate-speed coincidence system to be materially improved. Two novel circuits are described for taking advantage of this circumstance, and performance characteristics for one circuit are given in detail.

10.4. NEW ION CHAMBERS FOR GAMMA-RAY DOSE MEASUREMENTS

J. D. Kington and R. K. Abele 260

A new, 50-cm^3 standard ion chamber has been built, in which the collection volume was made more nearly a spherical annulus than the previous standard composed of contiguous hemispherical and cylindrical annular regions. No improvement in uniformity of response with direction was observed. A 4-cm^3 ion chamber was also constructed for high-level measurements. Difficulties are being encountered in defining the collection volume. The leads may be responding also to the radiation field.

10.5. A SIMPLE TIME-TO-PULSE-HEIGHT CONVERTER FOR THE ANALYSIS OF TIME DIFFERENCES IN THE MILLIMICROSECOND RANGE
R. W. Peelle, F. C. Maienschein, and T. A. Love 263

A method is described for modifying the sweep circuit of a standard laboratory oscilloscope to form the basic unit of a time-to-pulse-height converter. Combined with a standard multichannel pulse-height analyzer and standard timing circuitry, the unit is capable of performing with time resolution as fine as 2 to 3 mμsec/channel. Measurements on drift rate indicate that it is sufficiently small for such resolution to be feasible.

10.6. DEVELOPMENT OF THE HORNYAK BUTTON AS A FAST-NEUTRON DOSIMETER
F. J. Muckenthaler 270

Additional work has been done on the Hornyak button to find the crystal and particle size and composition that would most nearly duplicate the response of a Hurst-type fast-neutron dosimeter at various neutron energies. Previous data showed responses that were similar for neutron energies above 1 Mev but unsatisfactory for lower energies. New crystals were tested in an attempt to make the low-energy response as good as the high-energy response. The majority of the data were obtained with a monoenergetic neutron flux generated by the Van de Graaff generator. A limited number of crystals were also tested in the spectrum of neutrons from the TSF reactor.

10.7. AUTOMATIC COUNT-TIME CLOCK FOR USE WITH SLOW PULSE ANALYZERS
T. A. Love, F. C. Maienschein, and R. W. Peelle 279

The variable, and relatively large, dead time per pulse of the 256-channel pulse-height analyzer designed at the Argonne National Laboratory leads to counting losses which are a function of the shape of the measured pulse-height spectrum as well as its magnitude. Hence a device was built to meet the desired requirement of measuring the total time during which the analyzer will accept pulses rather than the elapsed time.

11. SPUTTERING PRODUCED BY IONS WITH ENERGIES ABOVE 50 kev

11.1. SPUTTERING PRODUCED BY IONS WITH ENERGIES ABOVE 50 kev
D. T. Goldman and A. Simon 283

Since the range of an incident particle having an energy in the region of 50 kev or higher is much greater than the mean free path of the knock-on particles produced through Rutherford collisions, it is justifiable to treat the primary particles as if they were produced by a uniform source in depth. Subsequent displacement of additional particles is accounted for and the problem is reduced to an equivalent one-velocity diffusion problem. Anisotropy of the primary source is also considered. The sputtering ratio is found to vary approximately inversely as ln E/E, where E is the incident energy, as $\mu/(1+\mu)^2$, where μ is the ratio of the incident particle mass to the target particle mass, and as the secant of the incident angle.

Part 1

RESEARCH FOR LIGHT-WATER-MODERATED HETEROGENEOUS REACTORS

1.1. STUDIES OF PLATE-TYPE CONTROL DEVICES IN A POOL-TYPE REACTOR

E. B. Johnson J. D. Kington
K. M. Henry A. B. Reynolds

The possibility of using plate-type control devices rather than rod-type devices is being considered for several small reactors. The apparent advantages include: (1) a metallurgical bond between the cladding material and the neutron absorber (the BSR rod-type device[1] depends upon the integrity of at least one weld, which is difficult to check after fabrication); (2) a smaller cross-sectional area, which would tend to minimize the flux peak that results when a poison rod is withdrawn from the core and is not replaced with fuel; (3) a smaller mass, which can be inserted faster into the core by positive accelerators; and (4) the ability to insert a larger number of rods (possibly mechanically ganged) to achieve a greater total control of excess reactivity.

These considerations become dominant for a core of the size planned for the Bulk Shielding Reactor II (BSR-II) or the Tower Shielding Reactor II (TSR-II) (see Parts 2 and 3 of this report). For the design of the BSR-II, which is to be a stainless-steel-clad reactor, experimental tests of the effectiveness of single and paired plates of absorber have been performed with the aluminum-clad core of the present BSR. Extrapolation from the aluminum-clad to the stainless-steel-clad core is not straightforward, but it is more reliable than a direct calculation for the stainless steel case. Other tests have been performed with two-dimensional mockups of the TSR-II control system.

Reactor Loadings and Test-Plate Positions

The reactor loading employed for the exploratory work on the effectiveness of control plates consisted of 30 fuel elements in a 5 by 6 array designated as loading 57 and shown in Fig. 1.1.1. The loading had a critical mass of about 3.5 kg of U^{235} and contained an excess reactivity of 1.5%. The reactivity effects of the test control plates were determined in two positions in the reactor core: (1) near the center of the core (lattice position 25), and (2) near the edge of the core (lattice position 4). Each test plate was inserted in place of the seventh fuel plate from the concave side of a special removable plate element, and the resulting positions of the control rods at criticality were determined.

In order to extend the investigation of plate-type control rods from a nuclear standpoint, BSR loading 64 (Fig. 1.1.2) was assembled, with a water-filled test cell having the same dimensions as a single fuel element near the center of the core. For most of the tests, the test cell was located in position 24; however, for a few of the tests it was located in position 14. The regular BSR control rods were located so that the effect of their withdrawal on the test cell was minimized. In order to have available during these tests sufficient poison for complete, unequivocal shutdown under all conditions of the test cell, two guillotines (cadmium sheets) were installed on opposite sides of the core. The total control-rod worth (exclusive of the guillotines) was approximately 5% $\Delta k/k$. The guillotines were worth about

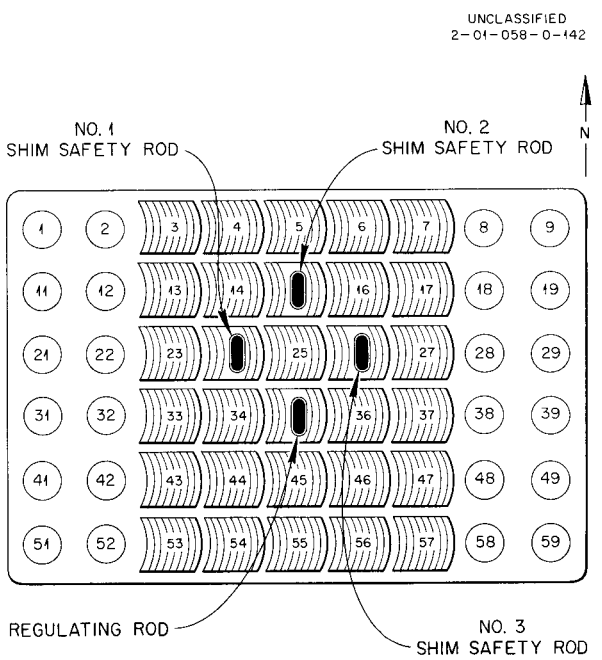

Fig. 1.1.1. BSR Loading 57.

[1]Described by R. G. Cochran *et al.*, *Reactivity Measurements with the Bulk Shielding Reactor*, ORNL-1682 (Nov. 9, 1954).

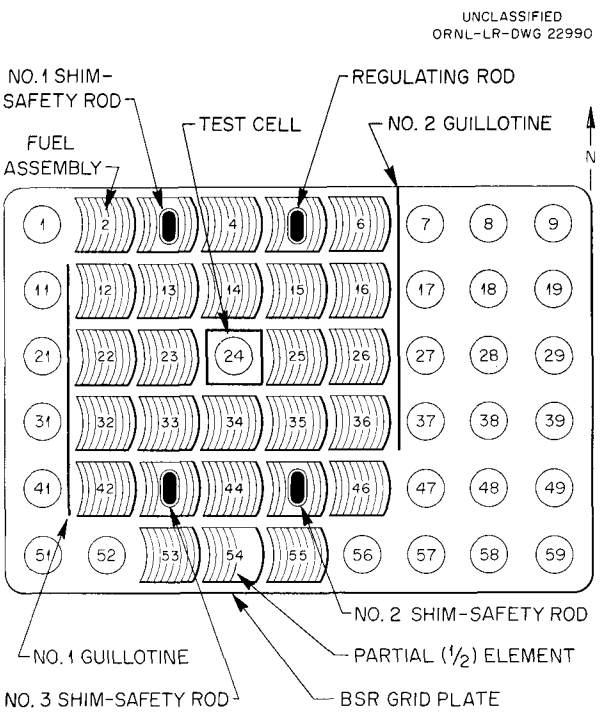

Fig. 1.1.2. BSR Loading 64.

2.5% $\Delta k/k$, giving a total of about 7.5% $\Delta k/k$ in rods.

A special fuel element which was fabricated with 12 of the 18 fuel plates removable was used in the test cell. The two outside plates and the four plates under the handle were brazed into the side plates, leaving five slots on one side of the element (the east side when in position in the reactor) and seven on the other side (the west side) available for experimentation. Throughout the experiment various poison plates were substituted for fuel plates.

The tests to aid the design of the TSR-II were performed with BSR loading 62B, which is shown in Fig. 3.1.18 of this report, where the TSR-II is described. The internal test cell consisted of a water-filled region, square in cross section, which was created by the omission of four elements (in positions 25, 26, 35, and 36) near the center of the loading. Most of the tests performed for the TSR-II are reported in Part 3 of this report, but several other tests performed in conjunction with these tests are described below. For these tests, positions 25 and 26 in the test cell were filled with dummy elements (elements containing unfueled aluminum plates). Positions 35 and 36 contained water-filled aluminum boxes formed by two unfueled plates brazed into the side plates. Boron-loaded plates could be placed in any of the 16 vacant slots in each box. The reactor loading contained approximately 5400 g of U^{235} and had an excess reactivity of 2.2% with the four dummy elements in place (no poison plates).

Description of the Test Plates

The poison plates used in these tests consisted of solid stainless steel plates and boron-loaded aluminum plates. In addition, one lead plate was used. The five stainless steel plates tested were made at the ORNL Rolling Mill of type 304L stainless steel in the shape of fuel plates. The thicknesses of the individual plates ranged from 32 to 125 mils, with the variation in thickness over each plate less than 1 mil.

The boron-loaded plates were made by compacting ~25-μ particles of boron carbide (B_4C) with aluminum powder. These compacted mixtures were then clad with 2S aluminum by hot rolling at the rolling mill. In plates containing 1, 2, 4, 8, and 16 g of natural boron, about 20 g of inert Al_2O_3 was added to the B_4C-Al powder in order to increase the density of the compacted mixtures sufficiently above that of aluminum to aid in the determination of the outline of the cores by fluoroscopic examination. The approximate dimensions (after rolling) of the boron-loaded cores in each plate are given in Table 1.1.1. The plates containing 1 through 16 g of boron were 52 mils thick. The plates containing 20 g and those with 50 g of boron were 114 mils thick. The effect on reactivity of the aluminum which jacketed the boron was determined by substituting 2S aluminum plates of thicknesses equal to those of the boron-loaded test plates.

The lead plate was formed to the dimensions of a fuel plate from 0.062-in.-thick material.

Experimental Results

Reactivity measurements were made by determining the position of the regulating rod at criticality both before and after each test plate was inserted into the core. The reactivity changes were determined from the regulating-rod calibration curve, obtained by use of the inhour equation which relates the change in reactivity ($\Delta k/k$) to the stable reactor period.

Table 1.1.1. Effect on Reactivity of Boron-loaded Plates in BSR Loading 57

Weight of Boron (g)	Plate Thickness (in.)	Length of Plate Core (in.)	Width of Plate Core (in.)	Reactivity Change (% $\Delta k/k$)			
				Lattice Position 4 (Near Edge)		Lattice Position 25 (Near Center)	
				Boron and Aluminum	Boron	Boron and Aluminum	Boron
0	0.052			−0.01	0	−0.02	0
1	0.053	22.62	2.44 ±0.03	−0.19	−0.18	−0.52	−0.49
2	0.053	22.62	2.44 ±0.03	−0.28	−0.27	−0.76	−0.74
4	0.052	22.62	2.44 ±0.03	−0.38	−0.37	−1.11	−1.09
8	0.053	22.62	2.44 ±0.03	−0.50	−0.49	−1.50	−1.48
16	0.052	22.62	2.44 ±0.03	−0.59	−0.58		
0	0.114			−0.02	0		
20	0.114	21.37	2.19 ±0.03	−0.60	−0.58		
50	0.118	21.25	2.25 ±0.03	−0.67	−0.65		
50	0.118	21.25	2.25 ±0.03	−0.69	−0.67		

Single-Plate Tests: Loading 57. – The results of the reactivity measurements for the natural-boron-loaded aluminum plates in BSR loading 57 are shown in Table 1.1.1. Values for both test-plate positions, that is, near the edge and near the center of the core, are given. For each position, values are given for the effect of the boron and the aluminum and for the effect of the boron alone. There was insufficient excess reactivity in the loading to permit the determination of the effect of any plate containing more than 8 g of boron near the center of the core. In Fig. 1.1.3 the reactivity effect due to the boron alone is plotted, for both positions, against the weight of boron.

The results of the reactivity measurements for the stainless steel plates, both near the edge and near the center of the core, are given in Table 1.1.2. The changes in reactivity resulting from the stainless steel plates are plotted in Fig. 1.1.4 for both test-plate positions, comparisons being made both between water and stainless steel and between fuel and stainless steel. Table 1.1.3 shows the effect on the reactivity of fuel and lead (compared with water) in both test locations.

Although the boron plates containing more than 8 g of boron could not be tested near the center of the core, it is noted from Fig. 1.1.3 that the ratio between the reactivity measurements for the plates containing 1 g through 8 g of boron lies between 2.76 and 3.01 for the two lattice positions (the ratio of the results for the stainless steel plates in the two positions lies between 2.77 and 2.98). Therefore the effect of the boron

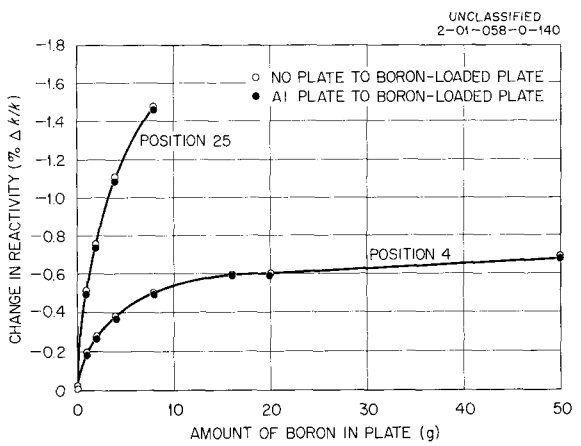

Fig. 1.1.3. Change in Reactivity Caused by Insertion of Boron-loaded Aluminum Plates in BSR Loading 57.

Table 1.1.2. Effect on Reactivity of Stainless Steel Plates in BSR Loading 57

Thickness of Plate (in.)	Reactivity Change (% $\Delta k/k$)	
	Lattice Position 4 (Near Edge)	Lattice Position 25 (Near Center)
0.032	-0.05	-0.15
0.049	-0.08	-0.22
0.077	-0.12	-0.33
0.122	-0.17	-0.46
0.125	-0.160	-0.46

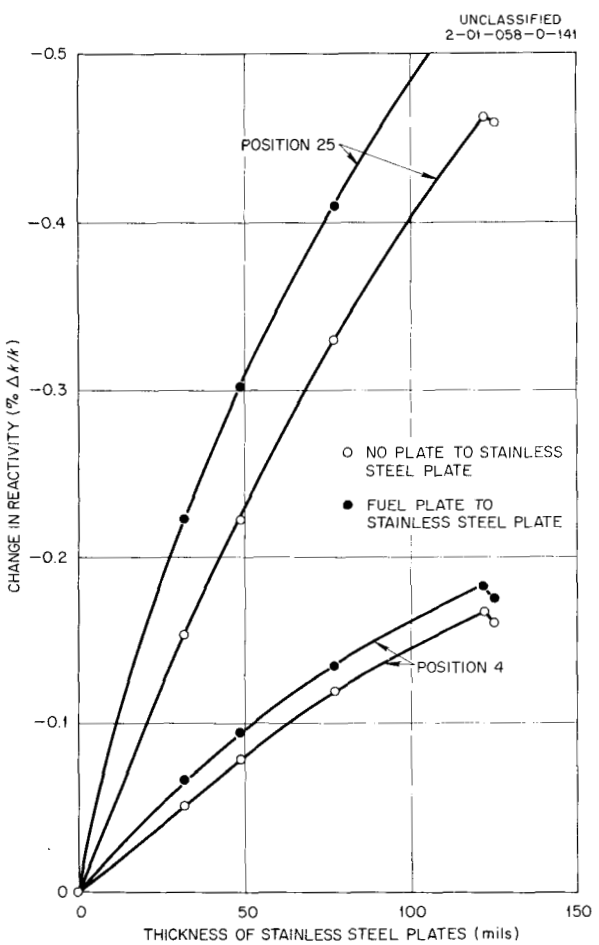

Fig. 1.1.4. Change in Reactivity Caused by Insertion of Stainless Steel Plates in BSR Loading 57.

Table 1.1.3. Effect on Reactivity of Fuel and Lead Plates Compared with Water in BSR Loading 57

Plate Designation	Thickness (in.)	Reactivity Change (% $\Delta k/k$)	
		Lattice Position 4 (Near Edge)	Lattice Position 25 (Near Center)
D535 (fuel)	0.060	+0.02	±0.08
A (fuel)	0.060	+0.02	
Lead	0.062	−0.01	−0.01

plates containing more than 8 g of natural boron can be roughly approximated for the central location by multiplying the reactivity values observed in lattice position 4 by a factor of 3.

Single-Plate Tests: Loading 64. – Figure 1.1.5 shows the net effect on reactivity of aluminum plates loaded with various amounts of natural boron compared with an aluminum plate in several slots of the test-cell element in BSR loading 64. For comparison, the data from Fig. 1.1.3 are plotted also.

Traverse with a Single Boron-loaded Plate: Loading 64. – In order to determine the relative importance of the various available slots across the test-cell fuel element (i.e., the uniformity of the flux), an aluminum plate loaded with 16 g of boron was placed successively in each available slot, and the change in reactivity from that with and without a fuel plate in the same position was determined. Since the loading contained insufficient excess reactivity to permit obtaining measurements near the center of the element with the 16-g plate, a plate loaded with 8 g of boron was used in this region. The measurements made with the 8-g plate were normalized to those made with the 16-g plate, and the results are shown in Fig. 1.1.6.

Paired-Plate Tests: Loading 64. – It has been proposed that poison plates be paired for control purposes in BSR-II, that is, that each element which will receive a control device be designed to accommodate two control plates. Therefore two plates containing the same amount of boron (2 g) were substituted for fuel plates at varying

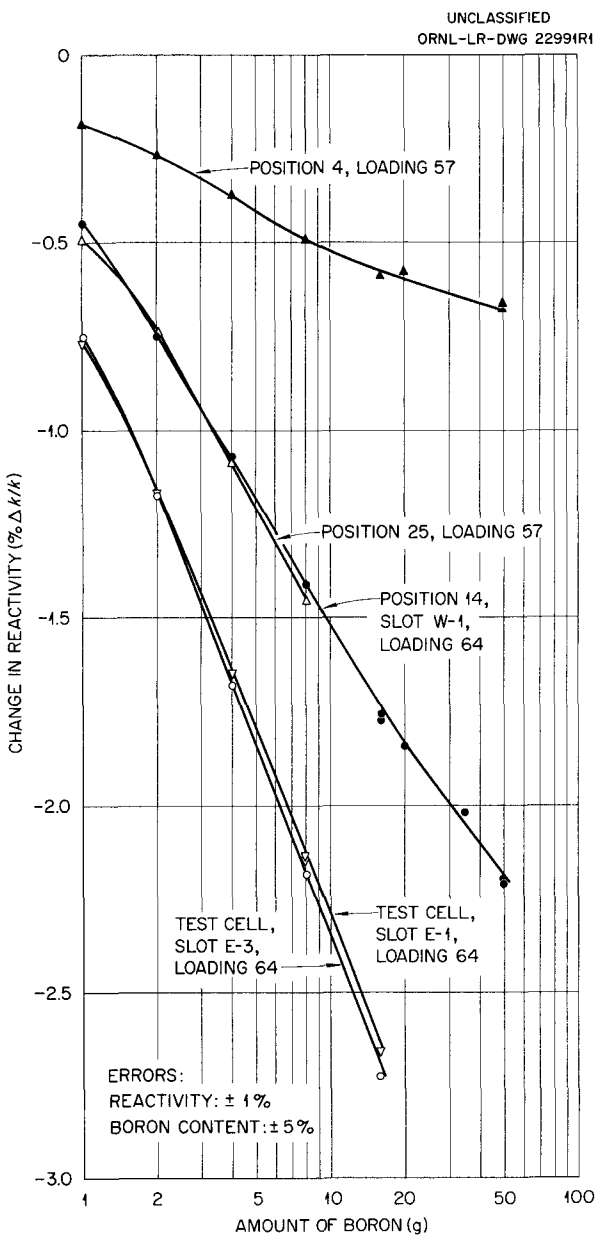

Fig. 1.1.5. Effect on Reactivity of Inserting Boron-loaded Aluminum Plates in BSR Loadings 57 and 64.

separation distances between the plates. The same experiment was performed with 125-mil-thick stainless steel plates. The results are shown in Fig. 1.1.7, where the effect of the plates is computed as the change in reactivity resulting from the substitution of the poison plates for fuel plates. The same data are replotted in Fig. 1.1.8 as the excess reactivity remaining in the core vs the distance between the two poison plates. The scatter in the points is primarily the result of the nonuniformity of the neutron flux across the test-cell element and the fact that, with four plates brazed into the side plates near the center of the element, it was necessary to move the poison plates from one side of the element to the other in order to obtain the desired separation distances. (The preferred method would allow one plate to remain fixed while the other was moved in successive slots across the element.) On the basis of these data, it would appear that a satisfactory separation distance in an aluminum-clad core for these boron-loaded plates lies between 3.5 and 6 cm, while that for the stainless steel plates is between 2.5 and 4.5 cm. The separation distance which has been tentatively chosen on mechanical grounds for the stainless-steel-clad BSR-II (see Part 2 of this report) is about 6.6 cm. According to the data obtained in the BSR aluminum core with the pair of 2-g boron-loaded aluminum plates, this separation distance will result in essentially no absorber shadowing.

Single-and-Paired-Plate Test: Loading 62B. – Several experiments were performed with the BSR to test the effectiveness of the control system proposed for the TSR-II, the results of which are included in Part 3 of this report. In conjunction with these tests, a series of tests was performed in which the effect on the reactivity of a single boron-loaded aluminum plate in a water-filled cell in the core could be determined. For this series, the test cell of BSR loading 62B was loaded as described above, and a single boron-loaded plate was placed successively in each slot of one of the water-filled boxes. The change in reactivity caused by the introduction of a plate containing 20 g of boron in position 35, as well as one containing 50 g of boron, is plotted in Fig. 1.1.9 as a function of the distance from the nearest fuel plate parallel to it.

In another series of tests, one and two boron-loaded (50-g) aluminum plates were inserted in the regular TSR-II cell (see Fig. 3.1.19) in order to investigate the shading of one plate by another. The plates were shimmed on opposite sides of the test cell to a position 1.3 in. from the nearest fuel plate. When both plates were in position, the separation distance between them was 3.4 in.

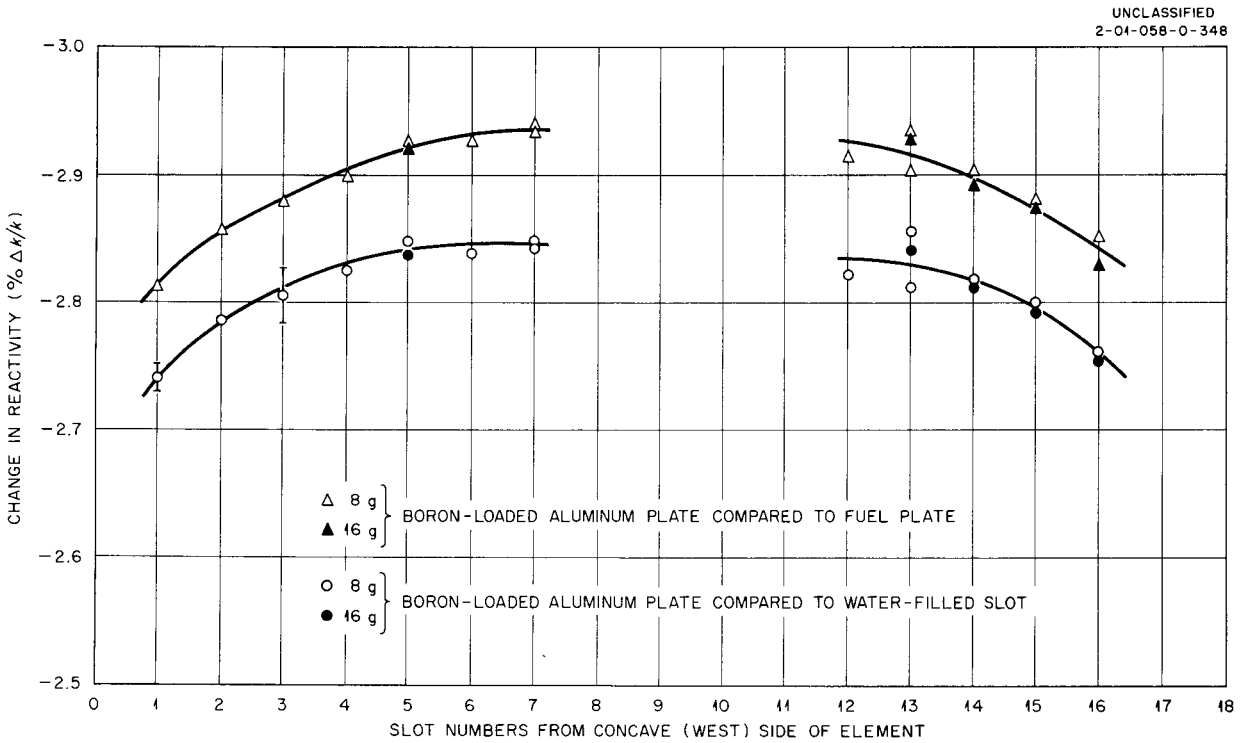

Fig. 1.1.6. Relative Importance of an Aluminum Plate Loaded with 16 g of Boron in Position 24 of BSR Loading 64.

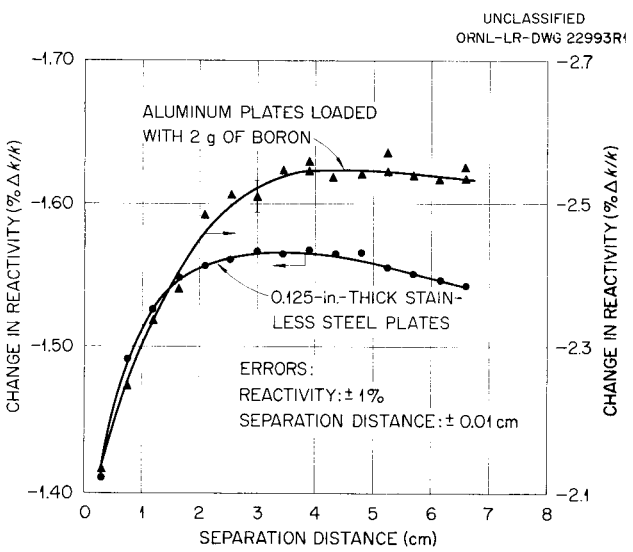

Fig. 1.1.7. Relative Effectiveness of Paired Poison Plates Compared with Fuel Plates in Position 24 of BSR Loading 64.

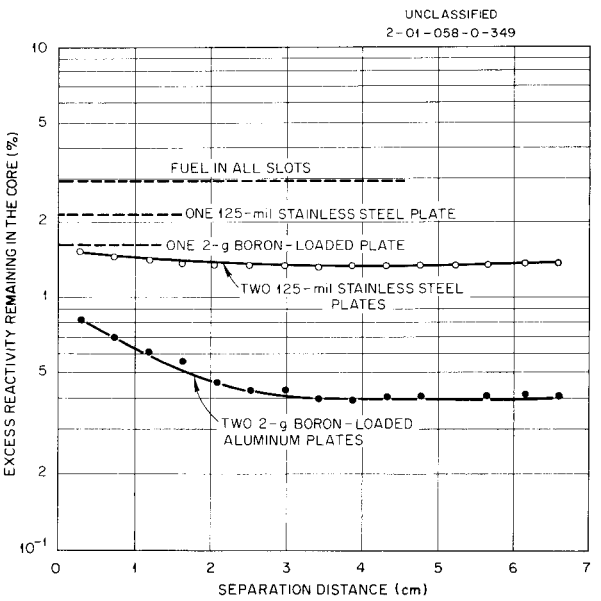

Fig. 1.1.8. Excess Reactivity Remaining in Core as the Result of Different Separation Distances Between Pairs of Poison Plates in Position 24 of BSR Loading 64.

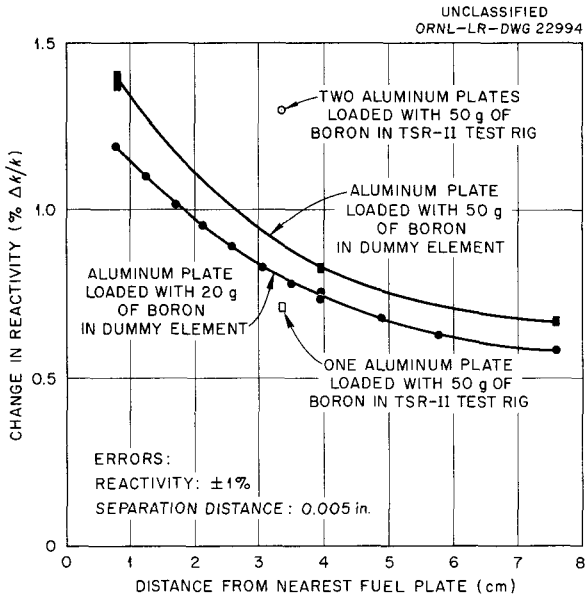

Fig. 1.1.9. Effect on Reactivity of Inserting Boron-loaded Aluminum Plates in Lattice Position 35 of BSR Loading 62B.

The results of this series of tests are also plotted in Fig. 1.1.9. For these tests the change in reactivity was determined on the basis of the reactivity when the test cell was filled with water, in which case the excess reactivity was 1.5%.

Errors

The reactivities reported for the various tests described above were determined by using the inhour equation for the calibration of the regulating rod,

$$\rho = \frac{l}{Tk_{\text{eff}}} + \sum_{i=1}^{5} \frac{\beta_i}{1 + \lambda_i T} ,$$

where the terms are as defined by Glasstone and Edlund.[2] No correction was made for the lower Fermi age for the delayed neutrons. The error in determining the stable reactor period, T, is about 5%, which will be reflected as an uncertainty of about +0.005% $\Delta k/k$. However, as analyzed in more detail in Sec 1.2 of this report, the absolute error due to the uncertainties in the knowledge of the delayed-neutron constants may be as large as 13%.

Unusually large errors must be assigned to the measurements in the portion of the experiment concerned with boron-loaded aluminum plates because of several contributing factors. Deviations in the amount or distribution of boron in supposedly identical plates resulted in different reactivity values at the same location. An arbitrary uncertainty of ±5% has been assigned to the boron concentration. Uncertainty in reactivity values has been indicated on the pertinent figures as ±0.01, which is considered as the maximum cumulative error in this quantity based on the reliability of the determination of the stable reactor period for application of the inhour equation and of the positions of the control rods at criticality. The actual error is probably about half of this.

The removable fuel plates used in the test-cell element in the same experiment were handled as if they were completely interchangeable in all respects. It was discovered toward the end of the experiment that one of the fuel plates was not positioned properly. Therefore a 1% error in reactivity has been assigned to the pertinent data.

For the portion of the experiment concerned with the TSR-II control-system mockup, the experimental reactivity errors are small, being most dependent on the influence of the condition of the test cell on the calibration of the regulating rod. The magnitude is of the order of ±1% of the value of the reactivity. The design of the TSR-II test rig (see Part 3 of this report) was such that fairly large errors could be made in the actual average distance of movement of the plates as indicated by the twist angle. However, because of the consistent movement of the plates from the position closest to the fuel to the position farthest away (in order to avoid hysteresis), the uncertainty in average plate movement was of the order of ±0.05 cm.

It is recognized that the presence and positions (amount of withdrawal) of control rods in a reactor influence the worth of all the rods (the shading of one rod by another). However, it

[2] S. Glasstone and M. C. Edlund, *The Elements of Nuclear Reactor Theory*, p 301, Van Nostrand, New York, 1952.

has been assumed that errors due to the perturbation of the flux when rods are moved to achieve criticality with the various test conditions are approximately compensated for in the calibration curves of the respective rods. It will be recalled that in order to obtain the rod calibration curves it is necessary to change the positions of the other rods so that, in practice, each calibration curve reflects the results of shading by the other rods in the core.[3]

[3] E. B. Johnson, K. M. Henry, and J. D. Flynn, *The Reactivity Effect of an Air Tank Against One Face of the Bulk Shielding Reactor*, ORNL-2179 (March 27, 1957).

1.2. COMPARISON OF THE DISTRIBUTED-POISON AND INHOUR METHODS FOR MEASURING REACTIVITY

A. B. Reynolds E. B. Johnson

Two methods which can be used to measure changes in reactivity are the "inhour method" and the "distributed-poison method." With the inhour method, the stable reactor period caused by a reactor perturbation is measured, and the change in reactivity is related to this period by means of the inhour equation. With the distributed-poison method, sufficient neutron-absorbing material is uniformly placed in or removed from the reactor core to offset the perturbation, and the change in thermal utilization is related to the reactivity. The purpose of the present investigation is to compare the two methods.

In the Bulk Shielding Reactor (BSR), reactivity effects have always been measured by using the inhour method for water-reflected cores. The control rods have been calibrated from the inhour equation, and the effects of perturbations have been determined from accompanying changes in rod positions at criticality. The interpretation of the results of this method of reactivity measurement is sometimes difficult. This is particularly true in cases involving large reactivity effects where a major change in rod position results in a very different reactor from that before the change. Furthermore, the worth of a rod might change appreciably during the course of reactivity measurements which are accompanied by relatively large changes in the flux distribution.

In view of the above uncertainties, the use of the distributed-poison method for measuring reactivity in the BSR is being investigated. Although the ideal way to introduce the distributed poison would be as a solution of the poison in the water moderator of the BSR, dissolving the poison is not presently feasible. Therefore it is necessary to insert the poison in solid form in the water channels between the fuel plates. The poison being used in the present investigation is natural boron in the form of a fine boron carbide (B_4C) powder (100% passed through a No. 325 sieve; average particle size 25 μ) which has been embedded in Plexiglas. It was claimed by the vendor that the B_4C-impregnated Plexiglas contained, on the average, 0.56% B_4C by weight. However, some variation exists in the B_4C content, and the extent of this variation has not yet been sufficiently determined. The B_4C Plexiglas was cut into $23\frac{5}{8}$-in.-long strips, the exact height of the core. The strips were $\frac{3}{4}$ in. wide and $\frac{1}{16}$ in. thick. The average weight of the strips was 23.66 g. During the experiments one such strip was inserted into each complete fuel element. (Strips could not be inserted into the control-rod elements.)

Boron was chosen for the poison for several reasons. First, since it is a $1/v$ absorber with relatively little resonance absorption, its effect on the thermal utilization and the reactivity can be easily calculated. Second, since boron has a high cross section, sufficient poison can be added to the reactor without changing the aluminum-to-hydrogen ratio enough to affect the age. Third, dispersing the finely powdered B_4C in Plexiglas provides a very convenient method for loading and unloading the poison uniformly in a reactor core which is 17 ft below the surface of the water.

A water-reflected 4 × 9 fuel-element loading with 2 corner elements missing was used for the experiments, 4 of the 34 elements being control-rod elements. The loading is shown in Fig. 1.2.1, in which the rod positions and the positions of three partial elements are indicated.

Calculated Value of the Reactivity of the Distributed Poison

The criticality constant, C, is

$$C = \eta f \epsilon p P \quad , \tag{1}$$

where

η = number of neutrons emitted per neutron absorbed in the fuel,

f = thermal utilization,

ϵ = fast-fission factor,

p = resonance escape probability,

P = nonleakage probability.

The three quantities η, ϵ, and p remain unchanged when either the poison strips or the control rods are moved. Therefore the differential of Eq. 1 is

$$dC = \frac{\partial C}{\partial f}\, df + \frac{\partial C}{\partial P}\, dP \quad . \tag{2}$$

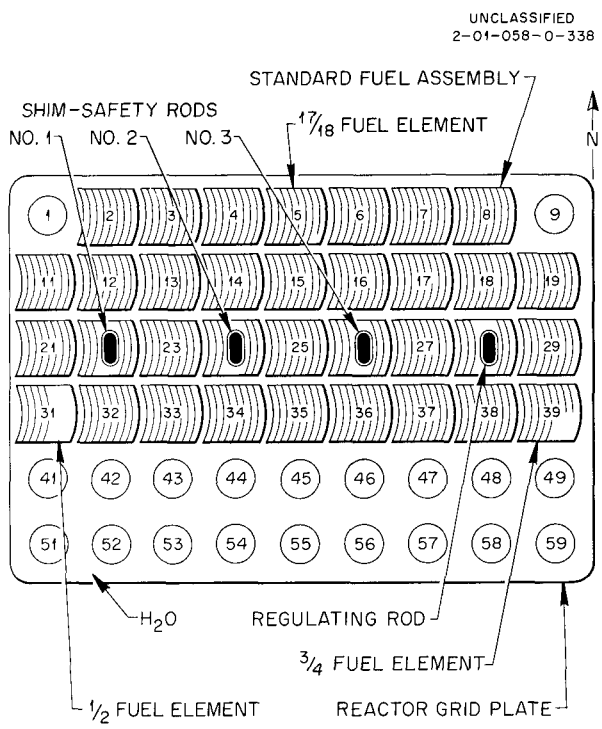

Fig. 1.2.1. BSR Loading 65.

Dividing Eq. 2 by Eq. 1 gives

$$\frac{dC}{C} = \frac{df}{f} + \frac{dP}{P} , \tag{3}$$

where dC/C represents a differential change in reactivity. For small changes in C, Eq. 3 can be approximated by

$$\frac{\Delta C}{C} = \frac{\Delta f}{f} + \frac{\Delta P}{P} . \tag{4}$$

The change in leakage accompanying the removal of poison uniformly from the reactor core is small compared with the change in thermal utilization, and, as a first approximation, the leakage term in Eq. 4 is neglected. The core of the BSR is assumed to be homogeneous even though the existence of water wells in control elements and the existence of partially inserted control rods introduce significant heterogeneity. The assumption of homogeneity within the fuel element is considered to be adequate, since the average thermal flux in a fuel plate is only about 1% less than the average thermal flux in the adjacent water channels. The flux depression in the poison strips is roughly the same as in the fuel plates, although it is evident that the importance of the position in which a strip is located in a fuel element is not exactly equal to the average importance of the element. Nevertheless, with the assumption that the core is homogeneous, the thermal utilization may be written as $\Sigma(\text{fuel})/\Sigma_a$, where $\Sigma(\text{fuel})$ is the absorption cross section in the fuel and remains constant, and Σ_a is the total absorption cross section in the homogenized core. Incorporating the above assumptions, Eqs. 3 and 4 can now be written as

$$\frac{\Delta C}{C} = - \frac{\Delta \Sigma_a}{\Sigma_a} , \tag{5}$$

where $\Delta\Sigma_a$ represents the change in Σ_a effected by the addition of the poison.

The reactivity effect of the B_4C-Plexiglas strips was calculated by the use of Eq. 5, with the use of cross sections from BNL-325.[1] The value of Σ_a was first obtained as follows:

Cross section of 30 fuel elements, including the cross section of the three partial elements being weighted according to their statistical weights	8139 ± 280 cm^2
Cross section of four rod elements (with rods out)	676 ± 20
Effective cross section of control rods with B_4C-Plexiglas strips inserted (obtained from the excess reactivity of the loading)	72 ± 10
Cross section of B_4C poison (30 strips)	108 ± 5
Total	8995 ± 281 cm^2

In order to compare the calculated and experimental values of the worth of the distributed poison, it is necessary to assume that a poison strip has been inserted into *each of the 34 elements*, that is, into the rod elements as well as into the complete elements. The rod elements are in positions of relatively high importance, and, if experimental values were not assumed for the reactivity effects of poison strips in the rod elements, the experimental value for the reactivity

[1] D. J. Hughes and J. A. Harvey, *Neutron Cross Sections*, BNL-325 (July 1, 1955).

worth of all strips would obviously be lower than the value calculated with the assumption of uniformly distributed poison.

Since some variation exists in the B_4C content of different strips, an attempt is being made to determine directly an average cross section for the poison strips, and hence the value of $\Delta\Sigma_a$, with the pile oscillator at the ORNL Graphite Reactor. From preliminary pile-oscillator data, an average cross section for the B_4C alone in the B_4C-Plexiglas is indicated to be 0.155 ± 0.008 cm^2 per gram of B_4C-Plexiglas. From this value the B_4C cross section in 34 strips of B_4C-Plexiglas is 125 ± 6 cm^2. Since the absorption cross section of the displaced water is slightly greater than that of the added Plexiglas, the difference (1.8 cm^2) is subtracted from the B_4C cross section. Therefore the change in absorption cross section, $\Delta\Sigma_a$, for the addition of 34 strips is 123 ± 6 cm^2.

A second value of $\Delta\Sigma_a$ has been calculated by assuming that the B_4C-Plexiglas contains 0.56 wt % B_4C, as specified by the vendor. A self-shielding factor of 0.93 was calculated with the use of a relation given by Hurwitz and Zweifel[2] for which the B_4C particles were assumed to be spheres with diameters equal to the average particle size of 25 μ. This second value of $\Delta\Sigma_a$ is 120 cm^2. Substituting these values in Eq. 5 gives

$$\frac{\Delta C}{C} = -1.37 \pm 0.11\% \ , \quad \text{for } \Delta\Sigma_a = 123 \pm 6 \text{ cm}^2 \ ,$$

$$\frac{\Delta C}{C} = -1.34\% \ , \quad \text{for } \Delta\Sigma_a = 120 \text{ cm}^2 \ .$$

Application of the Inhour Equation

Since the inhour method was used to measure experimentally the reactivity effect of the poison, it is necessary to analyze the inhour equation as it applies to the BSR.

The inhour equation can be written with no major approximations as

$$\frac{\Delta C}{C} = \frac{l}{CT} + \gamma \sum_i \frac{\beta_i}{1 + \lambda_i T} \ , \tag{6}$$

where γ is the ratio of the average nonleakage probability during moderation of delayed neutrons to that during moderation of prompt neutrons. Since the value of the first term on the right-hand side of Eq. 6 is much less than that of the second term for periods measured during the present experiment, and since $\gamma \cong 1$, the inhour equation can be written as

$$\frac{\Delta C}{\gamma C} = \frac{l}{CT} + \sum_i \frac{\beta_i}{1 + \lambda_i T} \ . \tag{7}$$

Two approximations have been considered for the nonleakage probabilities, P_f:

1. A value for a bare reactor obtained by use of a crude approximation for the slowing-down kernel in water is

$$P_f = \frac{1}{(3\tau B^2)^{1/2}} \tan^{-1} (3\tau B^2)^{1/2} \quad \text{(ref 3)}.$$

2. The value for a bare reactor used in the two-group approximation is

$$P_f = (1 + \tau B^2)^{-1} \ .$$

An approximate value of B^2 can be obtained by converting a reflected reactor (such as the BSR) to an equivalent bare reactor by use of the reflector savings, δ (see ref 4). Hence,

$$B^2 = \left(\frac{\pi}{x + 2\delta}\right)^2 + \left(\frac{\pi}{y + 2\delta}\right)^2 + \left(\frac{\pi}{z + 2\delta}\right)^2 \ ,$$

where

x, y, z = dimensions of the reflected core,

$\delta = (D_c/D_r)\, M_r$,

D_c = diffusion length in core = 1.32 cm,

D_r = diffusion length in reflector = 1.191 cm,

M_r = migration length in reflector = 6.40 cm.

For the loading used in the present experiment, $B^2 = 0.0082$ cm^{-2}.

---

[2] H. Hurwitz, Jr., and P. F. Zweifel, *Nuclear Sci. and Eng.* 1, 438–440 (1956).

[3] A. M. Weinberg and E. P. Wigner, *Preliminary Draft, Theory of Neutron Chain Reactions*, ORNL CF-56-11-43, vol II, chap. 13 (Nov. 27, 1956).

[4] *Ibid.*, chap. 15.

The values of the age τ for delayed and prompt neutrons in a water-aluminum lattice were obtained from Dismuke and Arnette.[5] The age used for prompt neutrons, averaged over the fission spectrum, was 62.5 cm^2. The age used for the delayed neutrons, for which a weighted average energy of 0.43 Mev was calculated from the data of Batchelor and Hyder,[6] was 25.3 cm^2. The above values of τ are for an aluminum-to-water ratio of 0.7.

With the above values for τ and B^2, the following values for γ were obtained:

$$\text{Approximation 1: } \gamma = \frac{0.8466}{0.7194} = 1.18 \ .$$

$$\text{Approximation 2: } \gamma = \frac{0.8282}{0.6612} = 1.25 \ .$$

The delayed-neutron yields and half lives used in the inhour equation were the data reported by Keepin and Wimett.[7] Use of the older data of Hughes *et al.*[8] would yield reactivity values about 7% higher than the experimental values reported here.

Experimental Measurement of the Reactivity of the Distributed Poison

The reactor loading used in the present experiment is shown in Fig. 1.2.1. The excess reactivity of the loading without poison is ~1.8%. The regulating rod was calibrated from the inhour equation, and No. 1 and No. 2 shim-safety rods were calibrated from the regulating rod. For the distributed-poison measurements a single strip of B_4C-Plexiglas poison was placed in each element other than the rod elements; therefore a total of 30 strips was inserted.

In order to measure the reactivity worth of the poison, two sequences for poison removal were followed. In the first sequence, each strip was withdrawn individually from the critical reactor; the stable reactor period was determined; and the strip was then reinserted before the next strip was withdrawn. In the second sequence, when a strip was withdrawn, it remained out of the core while the remaining strips were being withdrawn. The order of removal of the strips during this second sequence was based on keeping the strips remaining in the core as uniformly distributed as possible at all times. The worths of all strips during each sequence were totaled to give two values for the total worth of the poison. Another value for the worth of each strip during the second sequence was obtained from the regulating-rod calibration. Since the worth of the regulating rod was different for the cases of poison inserted and poison out of the core, the value of $\Delta C/C$ for each strip was obtained by an assumed linear extrapolation between the rod calibration curves with poison in and with poison out. Because of this necessary extrapolation, less confidence is placed in the measurements of $\Delta C/C$ from the regulating-rod calibration than in the measurement directly from the reactor period.

The results of these measurements of poison worth are given in Table 1.2.1 and Fig. 1.2.2. The reproduction of the total reactivity values for the three measurements appears to be quite good, even though it is realized that the results of the two sequences should, theoretically, not be in exact agreement. Two principal sources of random error were present. First, although each strip was reinserted between sequences into its same water channel, the strip was free to move sidewise in the element, and this displacement would have caused a change in effectiveness. Second, random error, as well as a possible biased error, can occur in reading the slope of the fission-chamber response on the Brown recorder from which the period was determined. These random errors present in the measurement of $\Delta C/C$ for each strip are estimated to be no greater than ±5%. Thus the random experimental error for the sum of the values of $\Delta C/C$ for all 30 strips is

$$\left[\sum_{i=1}^{30} (\text{error})_i^2 \right]^{1/2} ,$$

or ±1%. The error in the inhour equation introduced by the errors listed by Keepin and

[5] N. M. Dismuke and M. R. Arnette, *Age to Thermal Energy (0.025 ev) of Fission Neutrons in H_2O-Al Mixtures*, Mon P-219 (Dec. 23, 1946).

[6] R. Batchelor and H. R. McK. Hyder, *J. Nuclear Energy* 3, 7 (1956).

[7] G. R. Keepin and T. F. Wimett, *Proc. Intern. Conf. Peaceful Uses Atomic Energy, Geneva, 1955* 4, 162 (1956).

[8] D. J. Hughes *et al.*, *Phys. Rev.* 73, 111 (1948).

Wimett[7] for their values of delayed-neutron constants is ±12%. This value of ±12% was obtained by rewriting the relation

$$\sum_i \frac{\beta_i}{1 + \lambda_i T}$$

appearing in the inhour equation as

$$\beta \sum_i \frac{a_i/a}{1 + \lambda_i T} ,$$

where β is the total fraction of delayed neutrons

Table 1.2.1. Experimentally Determined Values of $\Delta C/\gamma C$ for Individual Poison Strips

Lattice Position*	$\Delta C/\gamma C$ (%)		
	Sequence 1, Obtained Directly from Period	Sequence 2	
		Obtained Directly from Period	Obtained from Regulating-Rod Calibration
5	−0.044	−0.047	−0.043
33	−0.023	−0.024	−0.023
37	−0.034	−0.026	−0.027
21	−0.008	−0.007	−0.009
17	−0.048	−0.050	−0.050
13	−0.035	−0.036	−0.037
29	−0.012	−0.012	−0.012
25	−0.056	−0.059	−0.056
2	−0.009	−0.010	−0.010
35	−0.040	−0.039	−0.040
8	−0.017	−0.022	−0.022
31	−0.004	−0.003	−0.003
16	−0.062	−0.065	−0.063
39	−0.006	−0.006	−0.006
14	−0.050	−0.051	−0.052
3	−0.026	−0.025	−0.026
36	−0.031	−0.038	−0.036
7	−0.036	−0.035	−0.034
34	−0.040	−0.032	−0.032
11	−0.007	−0.006	−0.007
27	−0.042	−0.048	−0.049
19	−0.013	−0.014	−0.013
23	−0.039	−0.035	−0.034
15	−0.064	−0.067	−0.066
32	−0.010	−0.007	−0.007
6	−0.038	−0.048	−0.046
38	−0.017	−0.020	−0.020
4	−0.030	−0.031	−0.030
12	−0.025	−0.016	−0.016
18	−0.030	−0.031	−0.030
Total	−0.896	−0.910	−0.899

*Listed in order of removal during second sequence.

UNCLASSIFIED
2-01-058-0-339

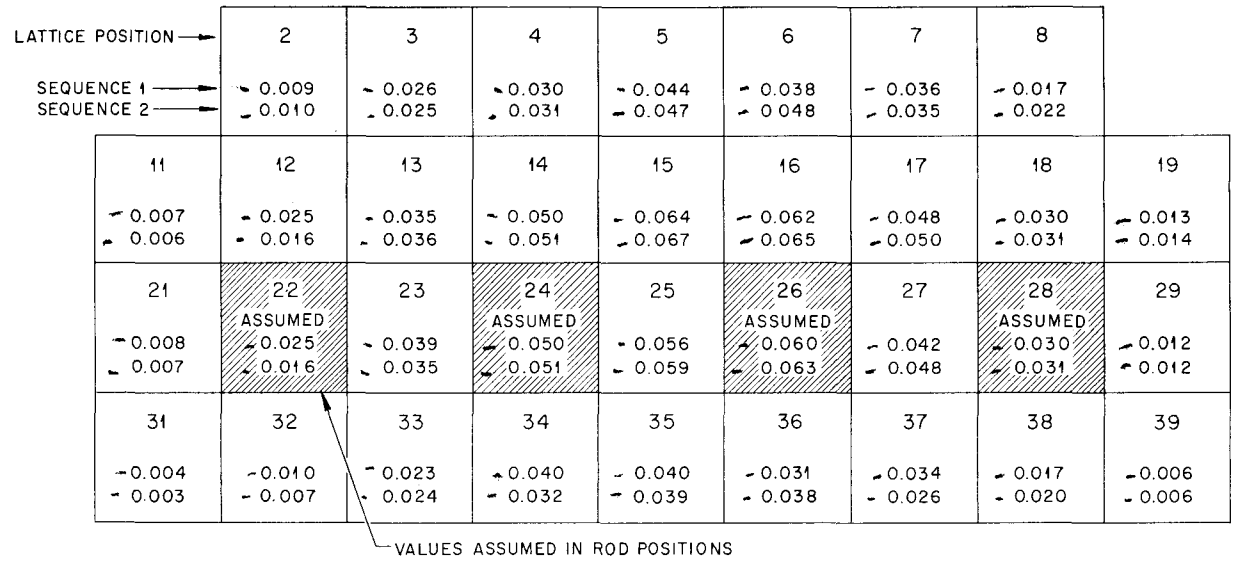

Fig. 1.2.2. Values of $\Delta C/\gamma C$ (%) in Each Lattice Position. In sequence 1, each strip was withdrawn individually from the critical reactor, the stable reactor period was determined, and the strip was then reinserted before the next strip was withdrawn. In sequence 2 each strip remained out of the core after being withdrawn.

and a_i/a is the fraction of delayed neutrons present in the ith group. The error given by Keepin and Wimett for β is ±4%. The error in

$$\sum_i \frac{a_i/a}{1 + \lambda_i T},$$

assuming errors only in a_i/a and λ_i, is ±8%. The total experimental error for the present investigation is reported as the sum of the above errors, or ±13%.

The necessity for assuming values of $\Delta C/\gamma C$ for poison strips, had they been inserted in the rod elements, was discussed above where the calculation of $\Delta\Sigma_a$ was explained. The values of $\Delta C/\gamma C$ assumed for the strips, had they been inserted into the rod elements, are given in Table 1.2.2 and Fig. 1.2.2. It is necessary to add these values to the experimental values given in Table 1.2.1 in order to obtain the total worth of the poison.

A further attempt to measure the worth of the poison was made from the position of the regulating rod and the shim-safety rods before and after the poison was inserted. The shim-safety rods had been calibrated with the poison out by comparison with the regulating rod, but they were not calibrated with the poison inserted. Because this calibration with the poison inserted was not available and because the effect of shadowing between various control rods introduces considerable uncertainty, values for total worth of the poison measured in this manner are unreliable. The two values obtained by this method for $\Delta C/\gamma C$ for the 30 strips actually inserted were −0.84% and −0.81% (cf. total values from Table 1.2.1).

Table 1.2.2. Assumed Values of $\Delta C/\gamma C$ for Hypothetical Strips Located in the Rod Elements

Rod Position	$\Delta C/\gamma C$ (%)	
	Sequence 1	Sequence 2
22 (No. 1 rod)	−0.025	−0.016
24 (No. 2 rod)	−0.050	−0.051
26 (No. 3 rod)	−0.060	−0.063
28 (regulating rod)	−0.030	−0.031
Total	−0.165	−0.161

During the first sequence, when the poison strips were being replaced after each period measurement,

the shim-safety rods remained in fixed positions. During the second sequence the rods were gradually inserted to maintain criticality. The No. 1 shim-safety rod was inserted from a position 0.23 of the way into the core at the beginning of the second sequence to 0.48 of the way at the end; the No. 2 rod was inserted from a position 0.24 of the way in to 0.37 of the way in; and the No. 3 rod position remained unchanged (out of the core). The insertion of rods Nos. 1 and 2 should be accompanied by a decrease of the flux in the vicinity of these rods and an increase elsewhere. It is of interest to observe the accompanying decrease in effectiveness of the poison strips surrounding the No. 1 rod (i.e., in lattice positions 12, 21, 23, and 32), as may be seen from Fig. 1.2.2, and the accompanying increased effectiveness of the strips in the half of the core containing rod No. 3 and the regulating rod.

Comparison of Theory with Experiment

The calculated and experimental results for $\Delta C/C$ are listed in Table 1.2.3. The agreement between experiment and theory appears to be good, the maximum difference being less than 10%, which is well within the experimental error. Continued effort will be made to investigate the numerous approximations and assumptions made. Nothing can be done at present, however, to reduce the $\pm 12\%$ error resulting from the delayed-neutron constants used in the inhour equation, which constitutes the largest single error in the use of the inhour method for measuring reactivity.

Table 1.2.3. Comparison of Calculated and Experimentally Determined Values of $\Delta C/C$

Method of Determination	$\Delta C/C$ (%)
Calculated	
From preliminary pile-oscillator cross-section data	-1.36 ± 0.11
From assumption that B_4C-Plexiglas contained 0.56% B_4C	-1.33
Experimental	
Sequence 1, assuming $\gamma = 1.18$	-1.25 ± 0.16
Sequence 1, assuming $\gamma = 1.25$	-1.32 ± 0.17
Sequence 2, assuming $\gamma = 1.18$	-1.26 ± 0.16
Sequence 2, assuming $\gamma = 1.25$	-1.34 ± 0.17

1.3. DETERMINATION OF THE POWER OF THE TOWER SHIELDING REACTOR

F. N. Greene[1] C. R. Fink[1]
W. E. Price[2]

The power of the Tower Shielding Facility Reactor (TSR) is one of the variables in every shielding experiment, since the actual power for a specified nominal power is known to change with time. Thus interpretation of test data on a dose-per-watt basis, taken over any appreciable time span, must include an evaluation of this variation in the power. In the past, calorimetric power determinations have been made at about six-month intervals, and the results obtained have varied as much as 24%. Also, there has been an indication that the power was gradually increasing with time. In order to collect sufficient data for a statistical analysis of the error and to determine possible trends, additional heat-power experiments were conducted weekly during the month of March 1957 and bimonthly thereafter.

Experimental Technique

The reactor power was determined by measuring the heat output in a simple calorimetric experiment. In order to provide a less variable environment for the apparatus during the run, the reactor tank was placed in the pool, and the pool was drained to a level below the tank. The tank was filled with a predetermined weight of moderator water, and a propeller-type agitator was placed in the water to provide stirring action in order to maintain a uniform temperature of the water throughout the tank. Earlier experiments indicated that this amount of agitation was sufficient.[3] Measurements of the water level in the reactor tank before and after the power run, together with thermal-expansion calculations for both the water and the tank, showed that the amount of water lost by evaporation was negligible.

Five type J(IC) iron-constantan thermocouples mounted on a vertical rod about 3 ft from the reactor were placed in the reactor tank at various depths, and temperature readings were taken with a potentiometer and a galvanometer. Prior to the reactor startup, the agitator was operated until thermocouple readings indicated that a state of temperature equilibrium existed in the tank. The reactor was then brought to operating power (400 kw, nominal power) within a short period so that the heat input during this period would be negligible. Thermocouple readings were taken at 10-min intervals for exactly 2 hr, after which time the reactor was shut off. The readings were continued for 2 hr in order to obtain a cooling curve. Ambient air temperatures were recorded at ½-hr intervals.

Method of Calculation

The masses of the tank, reactor, and water which absorbed the heat generated by the operating reactor were known. Therefore it was possible to determine the power of the reactor from the rate of temperature rise in the system during operation if appropriate corrections were made for cooling.

The temperature data were used in two ways in order to obtain the heat generation of the reactor. In the first method, measurements made with each of the five thermocouples were plotted as a function of time, and the plots were fitted with straight lines. The slope of each straight line was considered to be the rate of temperature increase of the system as indicated by that thermocouple, and from this the heat generation rate was obtained by using the heat capacity of the water, the reactor, and the structure. In the second method, the final heat content of the system was obtained from the near-equilibrium temperature measured after reactor shutdown. At the time of shutdown the temperature of the system continued to increase for a short period, although at a slower rate, before it began to fall steadily. This resulted from the fact that the temperature of the reactor proper was higher than that of the surrounding water at shutdown. In this second method of calculation a straight-line extrapolation of the cooling curve was made back to the time at shutdown in order to obtain a corrected temperature at shutdown. The difference between the initial temperature and the corrected final temperature was then considered to be the temperature increase in the system.

---

[1]On assignment from Glenn L. Martin Co.

[2]On assignment from Pratt & Whitney Aircraft.

[3]L. B. Holland and J. L. Hull, *Phys. Semiann. Prog. Rep. Sept. 10, 1954*, ORNL-1820, p 9 (classified).

During the period of reactor operation, cooling also occurs, but this is not a large effect, the loss of heat at the maximum temperature being only 5% of that generated. An approximate correction was made to the heating rate, however, in which it was assumed that the cooling rate during the heating cycle varied linearly with the temperature difference. The corrected slope was then used to obtain the reactor power P, as shown in the following formula:

$$P\ (\text{kw}) = K\left[S_1 + \left(\frac{\frac{T_F + T_i}{2} - T_a}{T_F - T_a}\right) S_2\right],$$

where

K = number of kwhr for each degree of temperature rise
= 38.8 kwhr/°C,

S_1 = rate of temperature increase during the heating cycle, °C/hr,

S_2 = rate of temperature decrease during the cooling cycle, °C/hr,

T_F = measured water temperature at shutdown for method 1, extrapolated water temperature at shutdown for method 2, °C,

T_i = water temperature at startup, °C,

T_a = ambient air temperature, °C.

No correction was required for the heat added to the system during reactor startup and shutdown.

Results and Discussion

A summary of the results of the power determinations by both methods 1 and 2 for all five thermocouples over a period of weeks is given in Table 1.3.1. A plot of the data (Fig. 1.3.1) clearly indicates the trend toward increasing power with time. Application of statistical analysis to the results obtained from March 1 to May 10 showed

Table 1.3.1. Summary of Actual Power Determinations by Calorimetric Experiments for the TSR Operating at a Nominal Power of 400 kw

Date	Reactor Power (kw)					
	Thermocouples					
	No. 1	No. 2	No. 3	No. 4	No. 5	Av
			Method 1			
3-1-57	508.2	512.1	528.21	495.7	500.2	508.9
3-4-57	521.8	518.7	516.5	518.0	517.3	518.5
3-8-57	499.4	510.6	504.7	500.3	495.0	502.0
3-14-57	521.6	512.5	508.3	510.1	518.0	514.1
3-22-57	521.7	526.0	542.5	514.9	513.5	523.8
4-26-57	520.3	502.8	511.1	529.3	512.8	515.3
5-10-57	520.4	558.1	504.8	517.1	503.8	520.8
			Method 2			
3-1-57	497.5	498.8	501.2	498.3	500	499.2
3-4-57	527.2	521.1	514.3	514.3	505.4	516.5
3-8-57	506.5	507.2	508.0	506.5	502.8	506.2
3-14-57	510.5	518.8	511.2	512.3	511.5	512.9
3-22-57	531.7	532.6	532.0	531.1	525.4	532.2
4-26-57	527.6	530.6	524.7	531.1	525.4	527.9
5-10-57	522.8	548.5	515.5	541.3	516.7	529.0

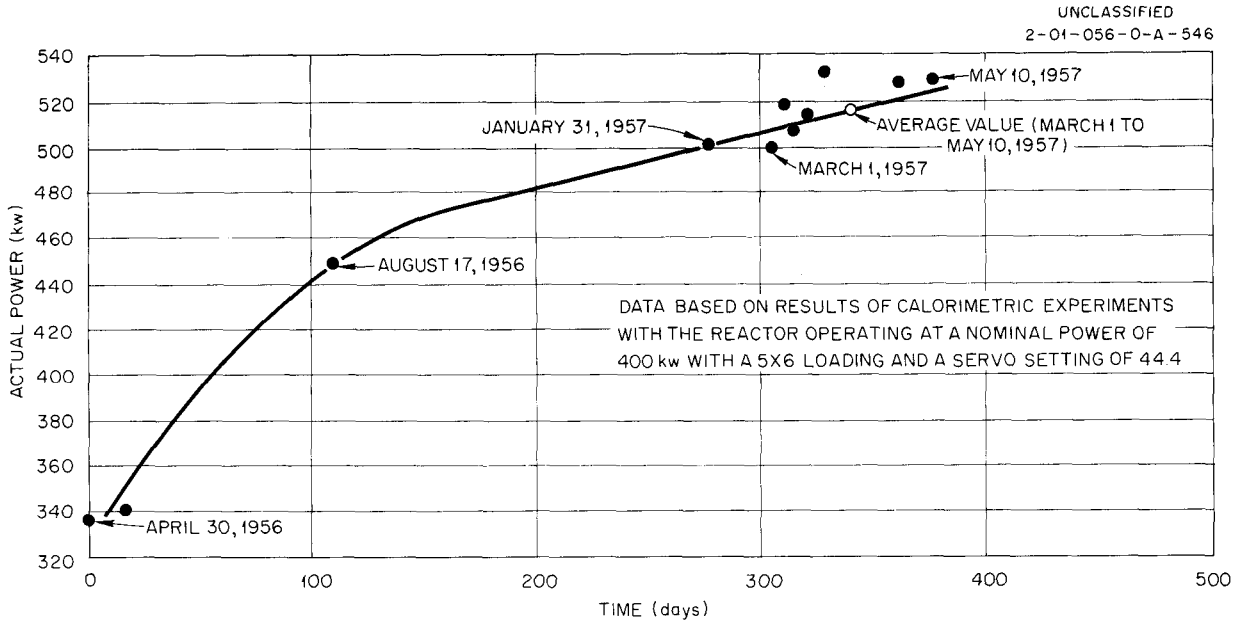

Fig. 1.3.1. Actual Power Variation of TSR from April 30, 1956, to May 10, 1957.

that all values fell within the limits of statistical variation, with a probable error of ±1.6%. Although no definite conclusions concerning the course of the trend can be made at this time, there are indications, from measurements of the thermal-neutron flux in a single fuel element, that the power distribution within the core changes with time. A re-evaluation of present experimental techniques and assumptions included in the calculations, along with a recalibration of measuring and recording devices, will be made in order to determine the sources of correctable errors.

Auxiliary Methods of Determining Power Linearity

Calorimetric experiments as a regular method of determining power linearity would be impractical because of the length of time required as well as the inherent inaccuracies associated with low power levels. As an alternative, the linearity of the TSR was determined by measuring the thermal-neutron flux at a constant distance from the reactor while varying the reactor power over the range 4 to 400 kw. The fission chamber used for these measurements was placed in the reactor tank at such a distance from the reactor as to give an adequate count rate for good statistical results at low powers and, in addition, to keep the count rate at a maximum of about 100,000 counts/min at full power. This was necessary because, at the higher count rates, an excessive error was introduced as a result of the resolution time on the chamber. The error at a count rate of 100,000 counts/min was approximately 0.67%.

The results of the fission-chamber measurements are tabulated in Table 1.3.2, along with corrected results for the higher count rates. The values shown are mean values of several measurements, and the probable errors are indicated. A plot of the count rate as a function of the nominal reactor power is given in Fig. 1.3.2.

A second experimental determination of the power linearity was made by measuring the gamma-ray dose rate in air at a distance of 64 ft from the center of the reactor tank. Since a constant water thickness, ρ, in front of the reactor could not be maintained, the resulting gamma-ray curve shown in Fig. 1.3.2 represents the total gamma-ray dose rates at each power normalized to $\rho = 15$ cm. Both these auxiliary methods show the power to be linear throughout the full range of powers.

Table 1.3.2. TSR Power Linearity Measurements with the Fission Chamber at a Constant Distance from the Reactor

Nominal Power (kw)	N, Measured Mean Count Rate* (counts/min)	N_0, Corrected Mean Count Rate* (counts/min)	Probable Error of N (counts/min)	N_0 per Nominal Watt
4	1,161	1,161	10	290 ± 3
10	2,920	2,921	16	292 ± 2
20	5,708	5,710	23	286 ± 1
40	11,548	11,557	32	289 ± 1
100	28,720	28,770	51	288 ± 1
200	57,410	57,630	72	288 ± 0
400	114,600	115,500	102	289 ± 0

*It can be shown that the ratio of the measured to the actual count rate decreases with increasing count rates according to the relationship

$$N = N_0 \left(1 - \frac{\lambda N}{60} \right) ,$$

where N is the measured number of counts per minute, N_0 is the actual (or corrected) number of counts per minute, $\lambda N/60$ is the dead-time fraction, and λ is the resolution time of the fission chamber (taken as 4 μsec for the chamber used).

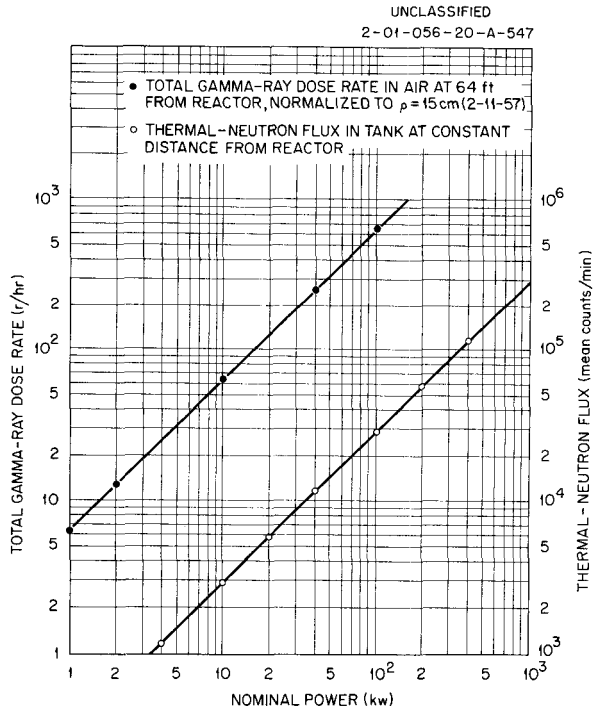

Fig. 1.3.2. Gamma-Ray Dose Rate and Thermal-Neutron Flux Measurements as a Function of the Nominal Power of the TSR.

1.4. CALCULATION OF THE PHOTONEUTRON FLUX IN THE WATER NEAR THE BULK SHIELDING REACTOR

G. deSaussure

It has been pointed out[1] that at distances larger than 200 cm from the Bulk Shielding Reactor (BSR) essentially all the neutrons in the water are photoneutrons. This assertion is borne out by the fact that beyond 200 cm the relaxation length of the thermal-neutron flux is essentially the same as that of the gamma-ray dose rate.[2]

The measurement of the gamma-ray dose rate at a distance of 267 cm from the reactor has been used to estimate the photoneutron flux at that point. This calculation and a comparison of the results with the measured thermal-neutron flux at this point are given below.

Method of Calculation

The following relation was assumed between the gamma-ray flux and the photoneutron flux at a distance r from the reactor:

$$(1) \qquad \phi(r) = d\Omega(r) \frac{\int_{E_0}^{\infty} \Gamma(E_\gamma, r)\, \Sigma_{\gamma,n}(E_\gamma)\, dE_\gamma}{\Sigma_a^{th}} ,$$

where

$\phi(r)$ = thermal-neutron flux at a distance r in centimeters from the reactor surface (neutrons·cm^{-2}·w^{-1}·sec^{-1}),

$d\Omega(r)$ = solid angle under which the reactor is seen from a point at a distance r from the face of the reactor,

$\Gamma(E_\gamma, r)$ = gamma-ray flux of energy E_γ at a distance r from the reactor face (photons·cm^{-2}·w^{-1}·sec^{-1}·Mev^{-1}·steradian^{-1}),

$\Sigma_{\gamma,n}(E_\gamma)$ = macroscopic cross section of water (cm^{-1}) for the reaction γ(D,p)n,

E_0 = threshold energy (Mev) for the reaction γ(D,p)n,

Σ_a^{th} = macroscopic absorption cross section of water for thermal neutrons.

There are two approximations implicit in Eq. 1:

1. It is assumed that the thermal-neutron flux is given by the product of the gamma-ray flux and the ratio of the cross section for photoneutron production to the cross section for absorption of neutrons. This does not account for the fact that some photoneutrons do not become thermalized at the point where they are created. However, this approximation is good, since the neutron slowing-down length in water (about 5 cm) is short compared with the gamma-ray relaxation length (about 40 cm).

2. It is assumed that the total gamma-ray flux at the distance r is equal to $d\Omega(r)$ times the flux in the forward direction, where $d\Omega(r)$ is the solid angle under which the reactor face is seen from a point at a distance r from the reactor. Actually, no data are available on the angular distribution of the gamma-ray flux far away from the reactor. But the gamma rays of interest for this calculation are those with energies larger than the threshold for photoneutron production (2.225 Mev). Such high-energy photons cannot have suffered a large-angle scattering, or their energy would have been appreciably reduced. Thus it is a good approximation to assume that the photons which will be important in photoneutron production are those which are deflected in flight very little or not at all. Thus the actual photon angular distribution, which is not known, is approximated by a distribution that is nearly uniform over those directions which intersect the reactor and is otherwise zero.

Result of the Calculation

The macroscopic cross section for the production of photoneutrons in water was calculated to be

$$(2) \qquad \Sigma_{\gamma,n}\,(\text{cm}^{-1}) = 2\mu \left(\frac{\rho}{A}\right) N\sigma = 10^{-8}\,\sigma ,$$

[1] J. M. LaRue *et al.*, *An Estimate of the Photoneutron Flux in the Water Surrounding the Bulk Shielding Facility Reactor*, ORNL CF-51-8-290 (Aug. 24, 1951).

[2] F. C. Maienschein *et al.*, *Attenuation by Water of Radiations from a Swimming Pool Type Reactor*, ORNL-1891 (Sept. 7, 1955).

where

μ = fraction of deuterium in hydrogen by natural occurrence
= 1.5×10^{-4} atom of deuterium per atom of hydrogen,[3]
ρ = density of water = 1 g/cm^3,
A = molecular weight of water
= 18 g/mole,
N = Avogadro's number = 0.602×10^{24} molecules/mole,
σ = microscopic cross section of deuterium (mb) for the (γ,n) reaction (σ is a function of the gamma-ray energy).

The solid angle $d\Omega(r)$ under which a point on the center line at a distance $r = 267$ cm from the reactor face sees the reactor face was calculated from the expression

$$(3) \qquad d\Omega(r) = \int_{\text{reactor face}} \frac{d\sigma}{\rho^2} \cos^2 \theta \ ,$$

where

ρ = distance between the point where the flux is measured and a surface element $d\sigma$ on the reactor face,
θ = angle between the center line of the reactor and the line ρ joining the surface element $d\sigma$ and the point where the flux is measured.

One of the factors $\cos\theta$ comes from the projection of the surface element $d\sigma$ on a plane perpendicular to ρ; the other comes from the fact that close to the forward direction the angular distribution of the gamma-ray flux at the surface of the reactor is expected to be proportional to $\cos\theta$.

For large values of r, $\rho \cong r$, $\cos\theta \cong 1$. Equation 3 can then be rewritten as

$$(3a) \quad d\Omega(r) = r^2 \int \frac{d\sigma}{\rho^4} \cong \frac{ab}{r^2} \left[1 - \frac{2(a^2 + b^2)}{3r^2} \right] ,$$

where

a = height of reactor face
= 62.5 cm,
b = width of reactor face
= 38 cm.

Therefore

$$d\Omega(r) = 3.17 \times 10^{-2} \ .$$

On substituting Eq. 2 into Eq. 1, the photoneutron flux becomes

$$(4) \quad \phi(r) = 2\mu \frac{\rho}{A} N \frac{d\Omega(r)}{\Sigma_a^{th}} \int_{E_0}^{\infty} \sigma(E_\gamma)\, \Gamma(E_\gamma, r)\, dE_\gamma \ ,$$

where the symbols have the same significance as above. Replacing them by their values gives

$$(4a) \qquad \phi(r = 267 \text{ cm}) = 10^{-8} \times \frac{3.167 \times 10^{-2}}{0.022} \int_{2.225 \text{ Mev}}^{\infty} \sigma(E_\gamma)\, \Gamma(E_\gamma, 267 \text{ cm})\, dE_\gamma$$

$$= 1.44 \times 10^{-8} \int_{2.225 \text{ Mev}}^{\infty} \sigma(E_\gamma)\, \Gamma(E_\gamma, 267 \text{ cm})\, dE_\gamma \ .$$

The integration in Eq. 4a can be performed graphically. With the use of values of $\Gamma(E_\gamma, 267 \text{ cm})$ from ORNL-1719[4] and values of $\sigma(E_\gamma)$ from Evans,[5] the integral is

$$\int_{2.225 \text{ Mev}}^{\infty} \sigma(E_\gamma)\, \Gamma(E_\gamma, 267 \text{ cm})\, dE_\gamma = 1.15 \times 10^3 ,$$

in appropriate units for Eq. 4a. This leads to a calculated value of the photoneutron flux of

$$\phi_{\text{calc}}(r = 267 \text{ cm}) = 1.65 \times 10^{-5} \text{ neutron}\cdot\text{w}^{-1}\cdot\text{sec}^{-1}\cdot\text{cm}^{-2} ,$$

which is to be compared with an experimental value of

$$\phi_{\text{exp}}(r = 267 \text{ cm}) = 1.58 \times 10^{-5} \text{ neutron}\cdot\text{w}^{-1}\cdot\text{sec}^{-1}\cdot\text{cm}^{-2}$$

[3] D. J. Hughes and J. A. Harvey, *Neutron Cross Sections*, BNL-325 (July 1, 1955).

[4] F. C. Maienschein, F. T. Bly, and T. A. Love, ORNL-1714, p 32 (Aug. 20, 1954) (classified).

[5] R. D. Evans, *The Atomic Nucleus*, p 335, McGraw-Hill, New York, 1955.

obtained by interpolation of values reported by Maienschein *et al.*[2]

Conclusion

The calculated value is about 4% higher than the measured value, but this discrepancy is not considered to be significant. The gamma-ray flux may be overestimated by assumption 2 discussed above, since probably not all the surface of the reactor is emitting high-energy radiation with the same intensity. On the other hand, the experimentally determined neutron flux may be in error by as much as 10%, as discussed in ORNL-1891.[2] The experimentally determined gamma-ray flux may be in error by an even larger factor, and the cross section for photoneutron production is quoted to within 14% error.

1.5. COMPARISON OF POOL-TYPE REACTOR CRITICAL EXPERIMENTS WITH TWO-GROUP CALCULATIONS

E. G. Silver

It was reported previously[1] that two reactor codes were being employed to predict the critical masses of three different fuel assemblies of the Bulk Shielding Reactor (BSR). One of the codes was the UNIVAC Eyewash 30-group code in which three spherical regions (control rod, fuel, and reflector) were used, and the other was the Oracle three-group, three-region (3G3R) code used as a two-group code. Since the publication of the earlier paper, the corrected experimental values of the critical masses have been slightly revised as a result of a recalculation of the effect of the partial elements ~~on the flux.~~ Also, a few additional calculations have now been performed with a modified 3G3R code, proposed by Nelson,[2] which circumvents the one-dimensional character of the original 3G3R code. In addition, the applicability of the two-group calculational method was verified by performing calculations for several solution-type reactors which required no geometric transformations.

The critical experiments were water-reflected loadings of the BSR in as clean a geometry as possible. The three configurations used in the experiments included (1) a 3 by 9 element array, (2) a 5 by 5 element array that contained four partial elements, and (3) a 6 by 4 element array that contained one partial element. The experimental critical masses are shown in Table 1.5.1. The third column in Table 1.5.1 shows the values of the masses after they were corrected for the presence of the partial elements and for the difference between the actual temperature of the pool water and the temperature assumed in the calculations.

The modified 3G3R code was used to recalculate the critical masses of the 5 by 5 and the 6 by 4 loadings in assumed two- and three-region cylindrical geometries. (In order to use a two-region geometry it was necessary to assume that the fuel was homogenized over the combined fuel and control-rod volumes.) For the three-region cylindrical geometry it was assumed that the three regions existed in the radial direction only; in the axial direction the core was assumed to be homogenized. In the ~~axial~~ radial direction the control rod was included under the direct control-rod volume-ratio assumption, as opposed to the "adjusted control-rod volume-ratio" assumption. (The differences between the "direct control-rod volume-ratio" and the "adjusted control-rod volume-ratio" assumptions were given in detail in the previous report.[1] Briefly, they can be described as follows: In the "direct control-rod volume-ratio" assumption the control rod is assumed to occupy the same volume fraction in the sphere or cylinder as it does in the parallelepiped. In the "adjusted control-rod volume-ratio" assumption the volume is adjusted to account for the fact that the peak-to-average flux ratio in a sphere or cylinder is different from that in a parallelepiped.)

In order to compute the critical mass by means of this modified code, a one-dimensional radial calculation is first performed, by using a first guess for the axial buckling. A value of k, the multiplication constant, is thus obtained. For the basic unreflected critical reactor, this value of k can be written as

$$k = \frac{k_\infty}{(1 + \tau B^2)(1 + L^2 B^2)}, \tag{1}$$

where

k_∞ = infinite medium multiplication constant in the core,

Table 1.5.1. Experimental Critical Masses for Various Loadings of the BSR

Loading	Critical Mass (g)	
	Actual	Corrected
6 × 4	3242 ± 10	3239 ± 11
5 × ~~6~~ 5	3246 ± 10	3189 ± 16
3 × 9	4600 to 4800	

[1] E. G. Silver, *Appl. Nuclear Phys. Ann. Rep. Sept. 10, 1956*, ORNL-2081, p 47.

[2] M. L. Nelson, *Appl. Nuclear Phys. Ann. Rep. Sept. 10, 1956*, ORNL-2081, p 115.

B^2 = buckling,
L = diffusion length for the thermal group in the core,
τ = age to thermal in the core.

Solving Eq. 1 for B^2 gives

$$B^2 = \frac{M^2}{2\tau L^2} + \frac{\sqrt{M^4 - 4\tau L^2\left(1 - \frac{k_\infty}{k}\right)}}{2\tau L^2},$$

where
M^2 = migration area in the core
$= L^2 + \tau$.

Expanding the square root in series and retaining third-order terms in $1 - k_\infty/k$ gives

$$B^2 = \frac{\left(\frac{k_\infty}{k} - 1\right)}{M^2}\left[1 - \frac{L^2\tau}{M^4}\left(\frac{k_\infty}{k} - 1\right) + 2\left(\frac{L^2\tau}{M^4}\right)^2\left(\frac{k_\infty}{k} - 1\right)^2\right].$$

The last equation is used by the code to calculate an equivalent, bare, radial buckling. This buckling is then used as input for a slab calculation in the axial direction, and the k, so calculated, is used in the same way to calculate an equivalent bare buckling in the axial direction. This process is then iterated until the k values calculated in the two directions agree to within predetermined errors. The bucklings, so calculated, are used as input to the code for both the fast and the thermal groups. In Table 1.5.2 the axial bucklings computed by this code are compared with those obtained with the 3G3R code by using the "diffusion" length and "migration" length assumptions. The critical masses calculated by this code are compared with the critical masses calculated by all the other codes in Table 1.5.3.

The modified 3G3R code is also directly applicable to a parallelepiped reactor. In this case, calculations are made in slab geometry in each of the three directions in cyclic order, and the sum of the bucklings in the other two directions is used as input at each stage. The iteration proceeds in cyclic rotation until all three directions give the

Table 1.5.2. Comparison of Axial Bucklings Calculated by Several Two-Group Methods

Assumed Geometry	Energy Group	B^2 in Axial Direction: 3G3R, Diffusion Length Assumption	3G3R, Migration Length Assumption	Modified 3G3R
5 by 5 core				
Two-region cylinder	Fast	0.00156	0.00173	0.00160
	Slow	0.00196	0.00173	0.00160
Three-region cylinder	Fast	0.00156	0.00173	0.00160
	Slow	0.00196	0.00173	0.00160
6 by ~~6~~ 4 core				
Two-region cylinder	Fast	0.00156	0.00173	0.00159
	Slow	0.00196	0.00173	0.00159
Three-region cylinder	Fast	0.00156	0.00173	0.00159
	Slow	0.00196	0.00173	0.00159

Table 1.5.3. Comparison of Calculated Critical Masses with BSR Experiments

Assumed Calculation Geometry	Number of Regions	Control-Rod Volume Ratio Assumption	Axial Buckling Assumption*	Calculation** Method	5 × 5 Loading		6 × 4 Loading	
					Calculated Critical Mass (g)	Difference from Experiment (%)	Calculated Critical Mass (g)	Difference from Experiment (%)
Sphere	2			3G3R	3164	−0.8	3183	−1.7
	3	Direct		Eyewash	3269	+2.5	3264	+0.8
	3	Direct		3G3R	3384	+6.2	3418	+6.1
	3	Adjusted		3G3R	3442	+7.9	3480	+8.2
Cylinder	2		L	3G3R	3078	−3.5	3151	−2.7
	2		M	3G3R	3162	−0.8	3227	−0.4
	2			Mod. 3G3R	3094	−3.0	3155	−2.6
	3	Direct	L	3G3R	3177	−0.4	3269	+0.9
	3	Direct	M	3G3R	3250	+1.9	3343	+3.2
	3	Adjusted	L	3G3R	3182	−0.2	3266	+0.8
	3	Adjusted	M	3G3R	3261	+2.2	3356	+3.6
	3	Direct		Mod. 3G3R	3135	−1.7	3253	+0.4
Parallelepiped	2			Mod. 3G3R	3048	−4.6	3082	−4.8

*L designates the "diffusion-length method" of calculating the axial buckling in the one-dimensional cylinder calculations; M designates the "migration-length method" of calculating the axial buckling in the one-dimensional cylinder calculations.

**3G3R is the three-group, three-region Oracle code used as a two-group code; mod. 3G3R is the iterative method proposed by M. L. Nelson for use with the 3G3R code for calculations in several dimensions.

same k value. The results of calculations using this geometry for both the 5 by 5 and the 6 by 4 core configurations are also presented in Table 1.5.3.

The values for the critical mass obtained with the modified 3G3R code are slightly lower than those resulting from the regular 3G3R code with the diffusion-length assumption, but the difference is not sufficiently clear cut to determine the better method. Therefore, the five- to eightfold increase in computing time needed with the modified method does not appear to be justified. The parallelepipedal configuration in the two-region approximation shows the error of about −4%, which is associated with the two-region approximation, as displayed in all the two-region calculations.

In order to check the applicability of the two-group calculations in a case where no geometric transformations are involved, calculations with this method were carried out for five spherical, water-reflected, solution-type, critical experiments[3] for which calculations previously have been performed[4] by the Eyewash code as well as by an earlier 30-group code known as Medusa, which does not include Goertzel-Selengut slowing down. The results of the several calculations are given in Table 1.5.4.

In calculations of this type, the assumed water reflector thickness must, of course, be as thin as is consistent with the requirement that it be effectively infinite. In order to determine the effect of varying the thickness of the water reflector, calculations were performed for the solution-type experiments having various reflector thicknesses. The results are given in Fig. 1.5.1, which shows the change in reactivity as a function of reflector thickness. A reflector thickness of 20 cm was then chosen as a usable thickness that is equivalent to an infinitely thick water reflector.

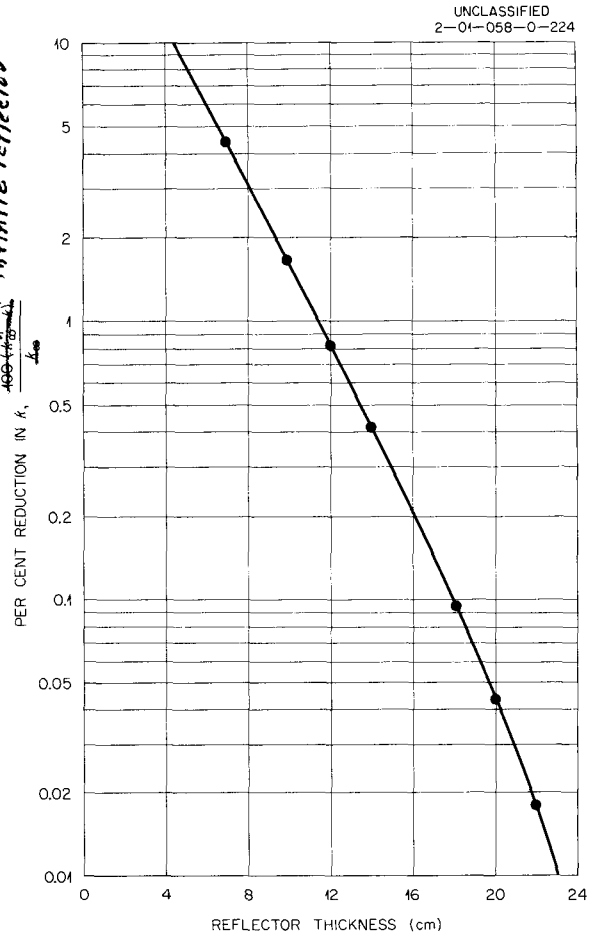

Fig. 1.5.1. Effect of the Water Reflector Thickness on the Calculated Reactivity of a Light-Water-Reflected Aqueous-Solution Reactor Having a 32-cm-dia Spherical Core.

[3]C. K. Beck *et al.*, *Critical Mass Studies. Part III*, K-343 (April 19, 1949) (classified).

[4]F. G. Prohammer, *A Comparison of One-Dimensional Critical Mass Computations with Experiments for Completely Reflected Reactors*, ORNL-2007 (March 1, 1957).

Table 1.5.4. Comparison of Values of the Multiplication Constant k Calculated by Various Methods

Reactor Radius (cm)	Reactor Temperature (°C)	k			
		Experimental	Medusa	Eyewash	3G3R
13.2	27.5	1.000	1.130	0.992	0.970
13.2	39.5	1.000	1.133	0.992	0.974
13.2	74.0	1.000	1.148	1.007	0.986
13.2	85.5	1.000	1.152	1.001	0.991
16.0	54.0	1.000		1.010	0.982

1.6. CALCULATION OF THE GAMMA-RAY SPECTRUM OF THE BULK SHIELDING REACTOR

G. deSaussure

The continued requirements for more refined shielding information necessitate that the gamma-ray spectrum of a shield-test reactor be known. The spectrum of the Bulk Shielding Reactor (BSR) was previously determined experimentally with a scintillation spectrometer,[1] and calculational attempts[2,3] have been made to estimate the gamma-ray spectrum on the surface of the reactor core over the entire energy range. An additional calculation has now been made in an attempt to determine the high-energy end of this spectrum, from 3.0 Mev up, from the known intensity and spectra of the primary gamma-ray sources inside the core.

In the high-energy portion of the spectrum the main contribution to the flux at the core surface is the uncollided flux. This can be calculated in a straightforward manner if the sources of primary gamma rays inside the core are known. In addition to the uncollided flux, the Compton-scattered flux was calculated by using two simplifying assumptions: (1) the "straight-ahead assumption," under which the energy spectrum of the scattered gamma rays is given by the correct Klein-Nishina formula, but their direction is the same as the direction of the primary gamma rays, and (2) the "one-collision assumption," under which the scattered gamma rays proceed without further absorption to the surface of the core. It is obvious that the spectrum of Compton-scattered gamma rays calculated under these assumptions will be an overestimate of the actual spectrum.

The four sources of primary gamma rays calculated were (1) the prompt fission gamma rays, (2) the capture gamma rays from aluminum, (3) the capture gamma rays from uranium, and (4) the fission-product-decay gamma rays. There are also gamma rays produced by neutron capture in water, inelastic scattering of fast neutrons, and decay of radioactive isotopes such as Al^{28}, but none of these sources contribute appreciably to the gamma radiation above 3 Mev.

In the calculation of the uncollided flux it was first assumed that the thermal-neutron flux was the same throughout the reactor core. Later, corrections were made to take into account the actual shape of the thermal-neutron flux.

For this calculation of the gamma-ray flux at the surface of the BSR it was assumed that the thermal-neutron flux was constant throughout the reactor core. This, of course, is not correct; gold-foil measurements have shown that the average value of the flux along the center line of the reactor ($\bar{\phi}_0$) is 11.23×10^{10} neutrons·cm^{-2}·sec^{-1}, while the average value of the flux throughout the core ($\bar{\phi}$) is 7.36×10^{10} neutrons·cm^{-2}·sec^{-1}. Before any comparison can be made with the experimental results, a correction must be made for the shape of the flux. In the experiment the detector collimator was pointed toward the center of the core; therefore the experimental results could be expected to indicate a greater intensity than would the calculations. In order to correct the calculations, the calculated values of the gamma-ray flux were multiplied by the ratio $\bar{\phi}_0/\bar{\phi}$.

Another correction should be made to take into account the fact that the flux distribution along the common center line of the reactor and the spectrometer collimator is not uniform. If the flux along this center line had a cosine distribution, this correction would give rise to a small decrease in the calculated flux at the surface. However, because the reactor is strongly reflected, the flux along the center line is not a cosine distribution but is more nearly uniform. Since no good data could be found on the actual shape of the flux along this center line, this correction has been assumed to be small and has been neglected altogether.

The corrected calculated gamma-ray spectrum is plotted in Fig. 1.6.1 along with the experimental spectrum and the spectrum determined in a previous calculation.[2] The two calculations give almost the same results. The similarity can be attributed to the fact that the uncollided flux used in both calculations was obtained in the same way, and the different methods of calculating

[1] F. Maienschein and T. Love, *Nucleonics* 12(5), 6–8 (1954).

[2] G. deSaussure, ORNL-2221, p 347 (Dec. 1956) (classified).

[3] W. F. Osborne and D. W. Montgomery, Babcock & Wilcox Co. (private communication).

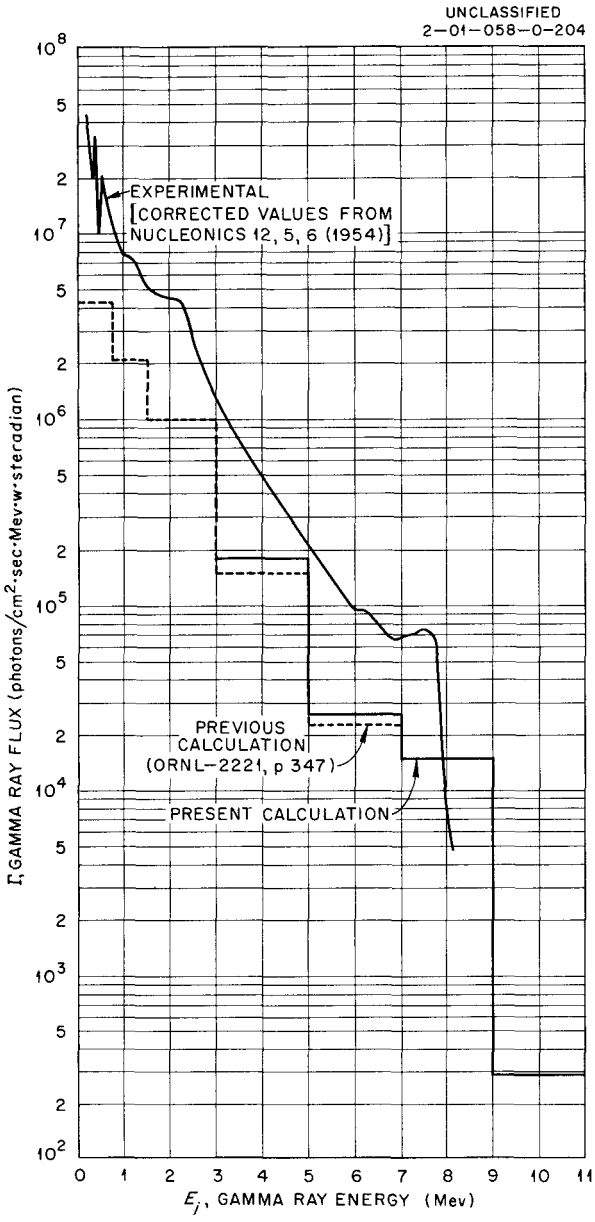

Fig. 1.6.1. Comparison of Calculated and Experimental Spectra of Gamma Rays at the Surface of the BSR.

the Compton-scattered flux had little effect on the high-energy end of the spectrum, where the Compton-scattered flux is small compared with the uncollided flux.

It should be pointed out that the experimental data in Fig. 1.6.1 have been corrected[4] since the original publication.[1] It is surprising that the calculation gave a much lower intensity for the spectrum than that measured, since all the assumptions made in the calculation were in a direction that would tend to overestimate the flux. This seems to indicate a discrepancy between the experimental data and the capture-gamma-ray spectrum of aluminum used in the calculation.[5] The error in the experimental data is uncertain, but it would appear to be less than the marked discrepancy between the experiment and the calculation. Further experimental work is planned.

The details of this calculation will be published elsewhere.[6]

[4]By F. C. Maienschein and T. A. Love, who now feel that the correction originally used for leakage through the side walls of the collimator should have been larger.

[5]B. B. Kinsey, G. A. Bartholomew, and W. H. Walker, *Phys. Rev.* 83, 519 (1951).

[6]G. deSaussure, *A Calculation of the Gamma-Ray Spectrum of the Bulk Shielding Reactor*, ORNL CF-57-7-105 (to be published).

Part 2

DESIGN FOR A UO_2–STAINLESS STEEL BULK SHIELDING REACTOR (BSR-II)

2.1. DESIGN FOR A UO_2–STAINLESS STEEL POOL-TYPE RESEARCH REACTOR (BSR-II)

E. G. Silver J. Lewin[1]

Following the development of stainless-steel-clad fuel elements for the Army Package Power Reactor (APPR), it appeared that such a fuel element might be applicable to the pool-type research reactor at the Bulk Shielding Facility (BSF). The structural material used in the present Bulk Shielding Reactor (BSR-I) is aluminum. The use of stainless steel would result in several advantages which would offset the somewhat greater critical mass and fuel inventory that would be required. Chief among these advantages would be the increased lifetime of the elements against corrosion. The estimated lifetime of an aluminum-clad fuel element is from two to four years, whereas a stainless steel element would be expected to withstand water corrosion for ten years or more. In the case of relatively low-flux research reactors, water corrosion is the limiting factor in the fuel element lifetime, and thus the increase in corrosion lifetime would be significant.

Another advantage of a stainless-steel-clad reactor would be the harder gamma-ray spectrum compared with that of the aluminum-clad core of the BSR-I. This harder spectrum is desirable for shielding measurements since most of the proposed reactors for which shielding studies are performed will have harder gamma-ray spectra than the aluminum-clad BSR-I.

A disadvantage of stainless steel would be the increased parasitic absorption cross section. However, the greater structural strength of stainless steel would allow much thinner members to be used, which would compensate to a large extent for the large absorption cross section.

For the reasons given above, a stainless-steel-clad reactor is being designed. It will be designated as the Bulk Shielding Reactor II (BSR-II) and will afford an opportunity to design a smaller core with a more symmetrical shape, which is also an advantage for shielding tests. The BSR-I is 24 in. high and, on the average, 15 to 18 in. in the other two dimensions. The new core will be cubical in shape and as small as is feasible.

[1]On assignment from The Glenn L. Martin Co.

Design Criteria

The considerations involved in the design of the fuel elements were that (1) the core should be operable in the present BSF pool, with the present control circuits and the BSR-I support structure used with the presently proposed modifications; (2) the core should be as small as possible in order to minimize the weight and size of wrap-around shield experiments and should be as symmetrical as possible in order to facilitate calculational comparisons with experiments; (3) experience gained in fabrication of stainless steel fuel elements for other reactors should be used, for example, the fabrication methods used for the APPR elements.

In accordance with these requirements, it was decided to make the core of plate-type elements with dimensions close to those used in the BSR-I, insofar as the plan view dimensions are concerned. This dictates a 3 × 3 in. fuel element and the symmetry provision suggests a 4 by 4 element array 12 in. high, or a 5 by 5 element array 15 in. high, both of which would provide cubical cores.

The fuel elements are intended to be inserted in either of two positions of rotation on a vertical axis, that is, with their plates aligned either east and west or north and south. Therefore the plates will not be curved, as they are in the BSR-I, but will be flat and perpendicular to the side plates.

In the initial design conception of the BSR-II it was planned to use four control rods like those in the BSR-I. These rods are massive structures of oblong cross section which occupy the space of nine fuel plates in the control rod elements; that is, they displace half the fuel plates in a standard BSR-I fuel element. However, the initial nuclear calculations revealed two disadvantages of such a control rod for the stainless steel design: (1) Since a spring-driven rod system must be used because of the short neutron-generation time, the heavy mass of the BSR-I control rods, which is an advantage in a gravity-dropped system, would decrease the acceleration achieved by a spring of given force; (2) the large water space left in the core by the withdrawal of the massive control rod would, as shown in Fig. 2.1.1, cause a large flux perturbation in its vicinity because of the

high absorption cross section in the core. Such a perturbation is to be avoided because the inhomogeneity it causes in the source strength would make interpretation of shielding measurements more difficult and uncertain and because it would reduce the maximum operable power of the reactor. It can be seen in Fig. 2.1.1 that the maximum flux in the fuel would occur adjacent to the control rod volume. Since it is necessary to avoid local boiling, which occurs first at the point of maximum flux, the magnitude of the maximum flux as compared with the average flux determines the maximum permissible power level. Therefore it is desirable to avoid large local flux increases, such as would accompany a large water space in the core.

The design that was adopted to circumvent these difficulties is one in which each of the four control elements carries two control plates which fit into slots on the outside of the control element. The control plates are located parallel to and outside the side plates of the control elements so that they will bear against these members, which are 0.05 in. thick, rather than against the much thinner (0.005-in.) fuel plate cladding. The two plates in each control element are given the maximum amount of separation in order to prevent them from shadowing each other.

The width of the fuel plates in a control element is reduced so that the outside dimensions of the over-all element are identical to those of standard fuel elements. Consequently, the control rods can be placed in either of the two orientations available with normal fuel elements, and a high degree of flexibility in control plate configurations is attained.

The fabricability of the elements by well-developed methods indicated a feasible side plate thickness of 50 mils and a fuel plate cladding thickness of 5 mils on each side. The thickness of the central fuel-bearing section of each plate was chosen to be 20 mils to give an over-all fuel

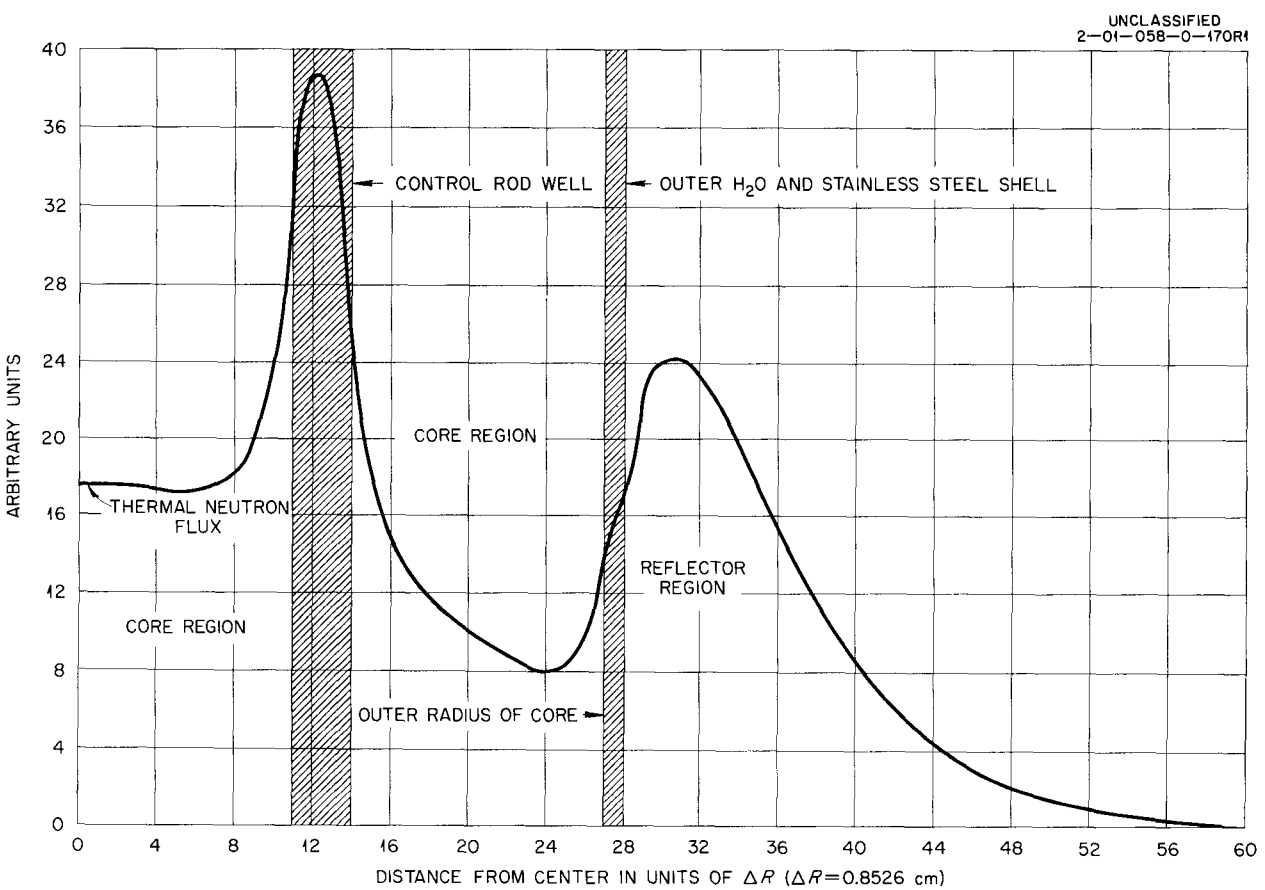

Fig. 2.1.1. Calculated Thermal-Neutron Flux in a UO_2–Stainless Steel Core Containing a 5 by 5 Element Loading and Four BSR-I Type Control Rods (Model 1).

plate thickness of 30 mils, which is dimensionally stable against warping and buckling. Each element is to contain 20 plates, a compromise between low poison (and therefore low fuel content) and high surface area, which will allow a high thermal flux and consequently a high power without local boiling.

Critical Mass Calculations

All critical mass calculations for this core were carried out by means of the 30-group, "Eyewash" code on the UNIVAC. This code calculates, in one dimension and spherical geometry, the multiplication of a system having up to nine concentric shells, each of which may contain fuel and each of which may have seven elements in it. Cross sections are contained in the code, including those for hydrogen, oxygen, U^{235}, stainless steel (type 302), and boron, the materials used in this reactor.

The stainless steel proposed for this core is type 347, whereas the type in the code is 302. Table 2.1.1 gives their analyses for comparison. They were judged to be sufficiently alike from the neutron viewpoint to be identical.

The geometric transformation from the reflected cube to the sphere was carried out by the method developed by Prohammer[2] and extended by Silver.[3]

[2]F. G. Prohammer, *A Comparison of One-Dimensional Critical Mass Computations with Experiments for Completely Reflected Reactors*, ORNL-2007 (March 1, 1956).

[3]E. G. Silver, *Appl. Nuclear Phys. Ann. Rep. Sept. 10, 1956*, ORNL-2081, p 47.

Table 2.1.1. Comparison of Composition of Types 302 and 347 Stainless Steel*

Element	Composition (%)	
	Type 302	Type 347
C	0.08–0.15	0.08 max
Mn	2.00 max	2.00 max
Si	1.00 max	1.00 max
Cr	17.00–19.00	17.00–19.00
Ni	8.00–10.00	9.00–12.00
Fe	Remainder	Remainder
Nb		10 × C min

**Stainless Steel Handbook*, pp 13, 21, Allegheny Ludlum Steel Corp., 1951.

When the method was checked against a series of critical experiments with the BSR-I, the results agreed to within 2.5% in fuel mass for the case of a 5 by 5 element core and to within 0.8% for the case of a 6 by 4 element core. This corresponds to an error in the multiplication constant of 0.81 and 0.25%, respectively. The uncertainties and errors inherent in the mathematical treatment and cross sections are of at least this magnitude or greater.

The calculations were carried out on the assumption that the core is a homogeneous distribution of the materials in it. This is justified by the dimensions of the fuel plates and claddings. Provision is made for the self-shielding in the fuel plates by multiplying the fuel absorption cross section in each group [$\bar{\sigma}_{i,r}\, N_r(25)$, where $\bar{\sigma}_{i,r}$ is a suitably averaged microscopic absorption cross section for energy group i in region r and where $N_r(25)$ is the atomic density of U^{235} in region r], by a factor, f, given by

$$f_{r,i} = 1 - LN_r(25)\,\bar{\sigma}_i \ ,$$

where

$$L = \frac{0.321 \times (\text{thickness of fuel plates})}{\text{volume fraction of fuel plates}} \ (\text{ref } 4) \ .$$

This accounts for self-shielding, but not for flux depression.

The Eyewash code treats all materials as atomic substances, disregarding chemical bond and coherence effects. This produces some errors in low-energy-transport cross sections. However, the calculations carried out for the BSR-I were not seriously affected by this assumption, which is reasonable since most of the neutron transport in highly aqueous reactors is fast transport. The slowing down in hydrogen is treated by the Goertzel-Selengut method, which yields correct energy-loss distributions but does not take into account the angular correlation.

In order to calculate the amount of fuel that can be accommodated in a given core, it is necessary to specify the maximum fuel content of the fuel material. The maximum presently feasible, yielding a material that can be readily fabricated, is a mixture of 30 wt % UO_2 and 70 wt % stainless steel. A somewhat lower UO_2 content of 25 wt %

[4]J. H. Alexander and N. D. Given, *A Machine Multigroup Calculation*, ORNL-1925, p 21 (Sept. 6, 1955).

is preferred. The total amount of fuel accommodable is proportional to the number of plates per element, the fuel region thickness, the amount of UO_2 per unit volume of fuel, and the fuel plate area in the core.

The 4 by 4 Element Core. – A calculation was carried out for a 4 by 4 element configuration (a 1-ft cube) having a maximum uranium fuel mass of 12.1 kg in a loading using 25 wt % UO_2 in the fuel material. This led to a core using fuel plates 53.6 mils thick, including the 10-mil total cladding thickness. This configuration had a multiplication constant of $k = 0.949$. Adding more fuel would mean reducing still further the water volume fraction of 0.65, which is already quite low, thus increasing the leakage and requiring much more fuel to achieve the required increase in multiplication. With 30 wt % UO_2 in the fuel material the thickness of the fuel plates would be 46.3 mils thick for 12.1 kg of uranium.

Such a reactor would have a thermal-neutron lifetime of the order of 15×10^{-6} sec, which would lead to severe control problems. The calculation showed that the reactor would be highly epithermal (see Fig. 2.1.2), with about 40% of all fissions caused by neutrons with energy greater than 0.1 ev.

For the reasons given above, this core design was discarded. It would be practical only with (1) a very fast control system and (2) a high-uranium-content fuel (at least 50 wt % UO_2 in the fuel material), which could reduce the steel volume materially, thereby increasing the moderation by increasing the core water volume.

The 5 by 5 Element Core. – A second calculation was carried out for a 5 by 5 element configuration (a 15-in. cube). Such a core has 1.6 times the volume of the 4 by 4 element configuration, thus reducing the necessary metal volume fraction considerably. As discussed above, a 20-plate fuel element with a 20-mil-thick fuel section clad with 5 mils of stainless steel on each side was decided upon for design calculations. However, a series of calculations was also carried out for the 5 by 5 element configuration, in which the number of plates per element and the

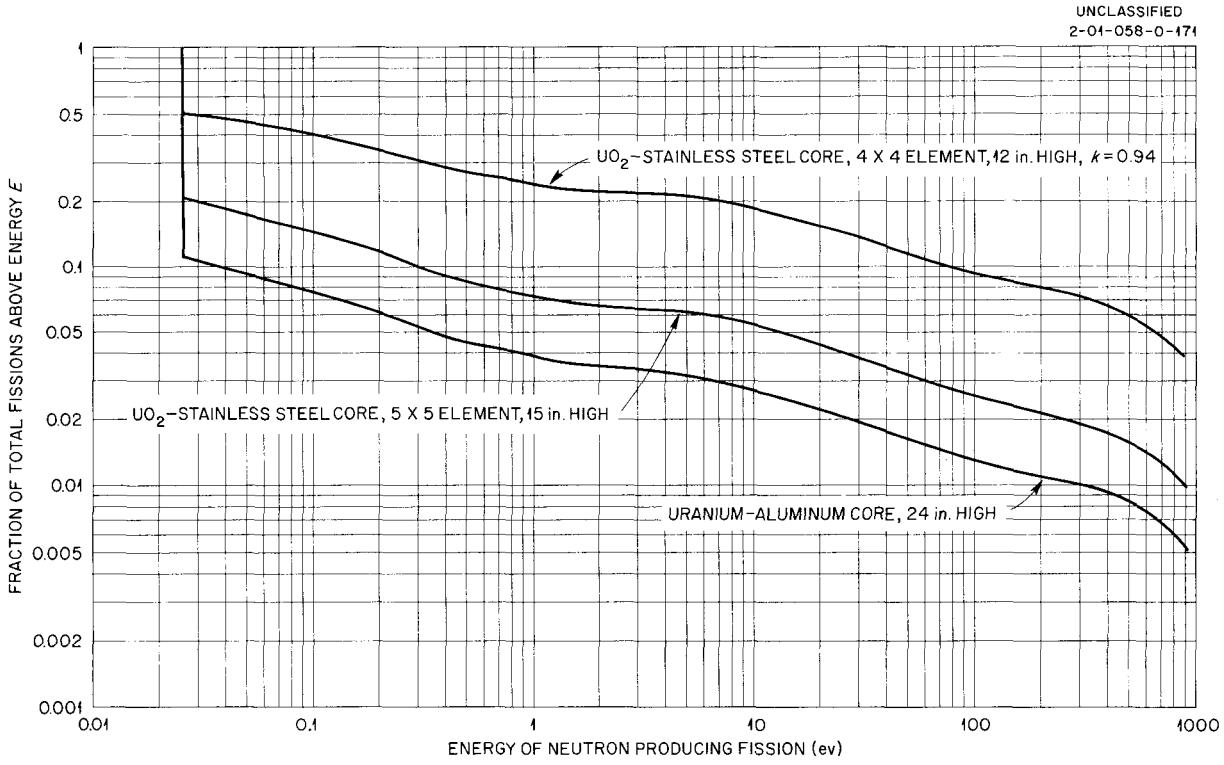

Fig. 2.1.2. Calculated Fractions of Fissions Occurring Above Energy E in Various Reactor Configurations as a Function of E.

fuel-plate thickness were used as varying parameters. In all the calculations the following design points were held fixed for all cores:

1. Each fuel element consists of a set of parallel fuel plates containing a fuel region which is 2.57 in. wide and 15.00 in. high. The fuel plates, each of which is clad with a 0.005-in. thickness of stainless steel on each side, are brazed into two side plates 0.05 in. thick and 2.991 in. wide. The width and arrangement of the fuel plates are such that the cross-sectional dimensions of the fuel element are 2.991 by 2.991 in. The core region is taken to be 15.0 in. high. Excess lengths of stainless steel on each fuel plate and side plate (see items 5 and 6 below) are taken as shell regions surrounding the core.

2. The control ~~rod~~ plate elements consist of stainless steel side plates which have the same dimensions as those in the fuel elements and of fuel plates which have the same thickness and height as those in the fuel elements but which have a reduced width. The cross-sectional dimensions of the control element, exclusive of the control-plate slots, are 2.440 by 2.991 in. The fuel region is 1.986 in. wide. The control-plate slot is provided by extensions of the side plates and a cover, as shown in Fig. 2.1.3.

UNCLASSIFIED
2-01-058-0-309

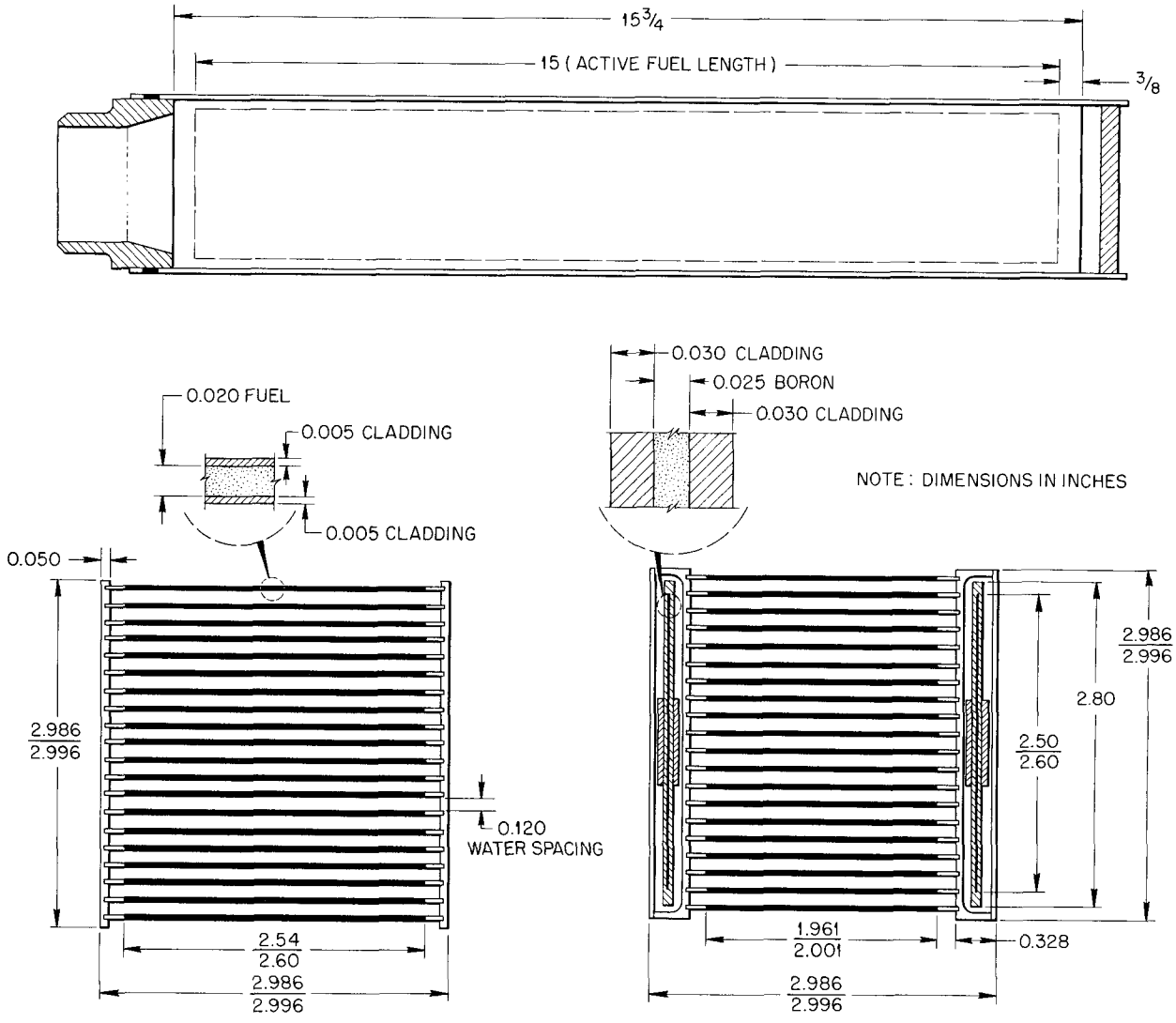

Fig. 2.1.3. Cross-Section View of Fuel and Control Plate Elements and Plan View of 15-in. Core Fuel Element of the Proposed BSR-II.

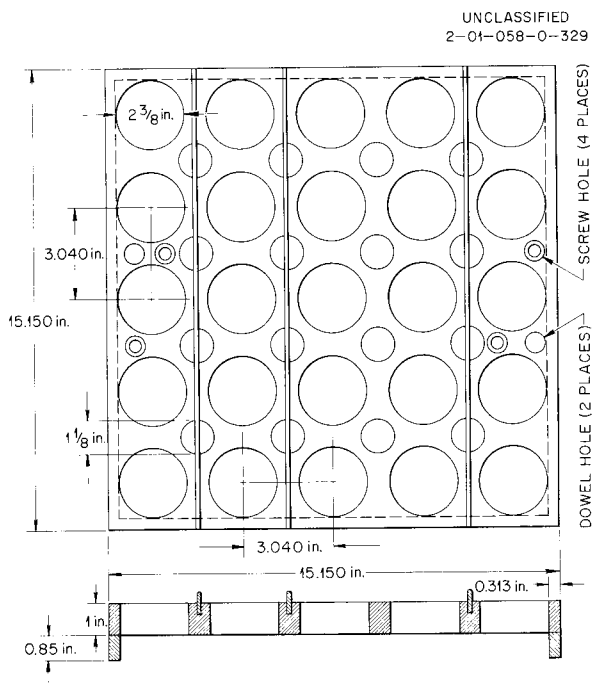

Fig. 2.1.4. Plan and Side View of Grid Plate for Proposed BSR-II.

3. The fuel and control elements are placed on a grid plate spaced in a square array 3.040 in. on the centers (Fig. 2.1.4).

4. The fuel-bearing material consists of a cermet of UO_2 and stainless steel, which is at most 25 wt % UO_2. The density is 0.92 of the theoretical density.

5. The fuel plates extend $\frac{3}{8}$ in. above and below the active core region. This material is pure stainless steel. The amount of stainless steel in this region has been included in a spherical shell Δr thick (0.871 cm). It has been adjusted in density so that the amount of steel is the same as that found in the upper and lower ends.

6. The upper stainless steel handle on the fuel elements, the lower end boxes, the 1-in. length of the control rods which normally extend into the core, and the grid plate have all been included in two further regions of thickness Δr and $2\Delta r$. The thick components and the control plate have been adjusted for self-absorption by the equations given by Bartels,[5] and the resulting equivalent amounts of homogeneously dispersed material have been spread around the core in a spherical shell.

The results of the critical-mass calculations are given in Figs. 2.1.5 and 2.1.6, which present the amount of enriched uranium (93% U^{235}) required for a cold, clean, critical core. Figure 2.1.7 shows the variation of fuel mass with multiplication for some cases of interest, from which the amount of fuel needed for an operating loading can be derived. Figure 2.1.7 shows that the mass of enriched uranium required to give a multiplication of 1.025 to the core with design dimensions is 6.53 kg. Adding 3.0% to the design multiplication to allow for errors in the calculations gives a maximum core loading of 7.15 kg of enriched uranium. A core with this much fuel in it at the design dimensions would have a "meat" (fuel region) of 17.3 wt % UO_2. Since, as mentioned above, 25 wt % is feasible, the thickness of meat could be reduced, thus reducing the critical mass. However, owing to structural considerations, the 30-mil-thick plate is considered to be a minimum, and this reduction in fuel thickness can be effected only by increasing the thickness of the cladding in order to maintain the total thickness of 30 mils. Thus, instead of 5-mil-thick cladding on a 20-mil-thick meat containing 17.3 wt % UO_2, a design has been chosen for an 8-mil-thick cladding on a 14-mil-thick meat containing 24.3 wt % UO_2. This latter design is, in the nuclear aspects, identical with the former but has the advantage of 3 mils of extra cladding on each side of a fuel plate.

In order to permit the core to be adequately adjusted in mass, the following inventory of fuel elements is proposed:

21 full fuel elements each containing 296 g of uranium	6.216 kg
4 control elements each containing 230 g of uranium	0.920 kg
8 half elements each containing 148 g of uranium	1.184 kg
2 quarter elements each containing 74 g of uranium	0.148 kg
Total inventory	8.468 kg

Judging from experience with the BSR-I, this number of partial elements should suffice for assembling a core with multiplication very close to unity.

[5] W. J. C. Bartels, *Self-Absorption of Monoenergetic Neutrons*, KAPL-336 (May 1, 1950).

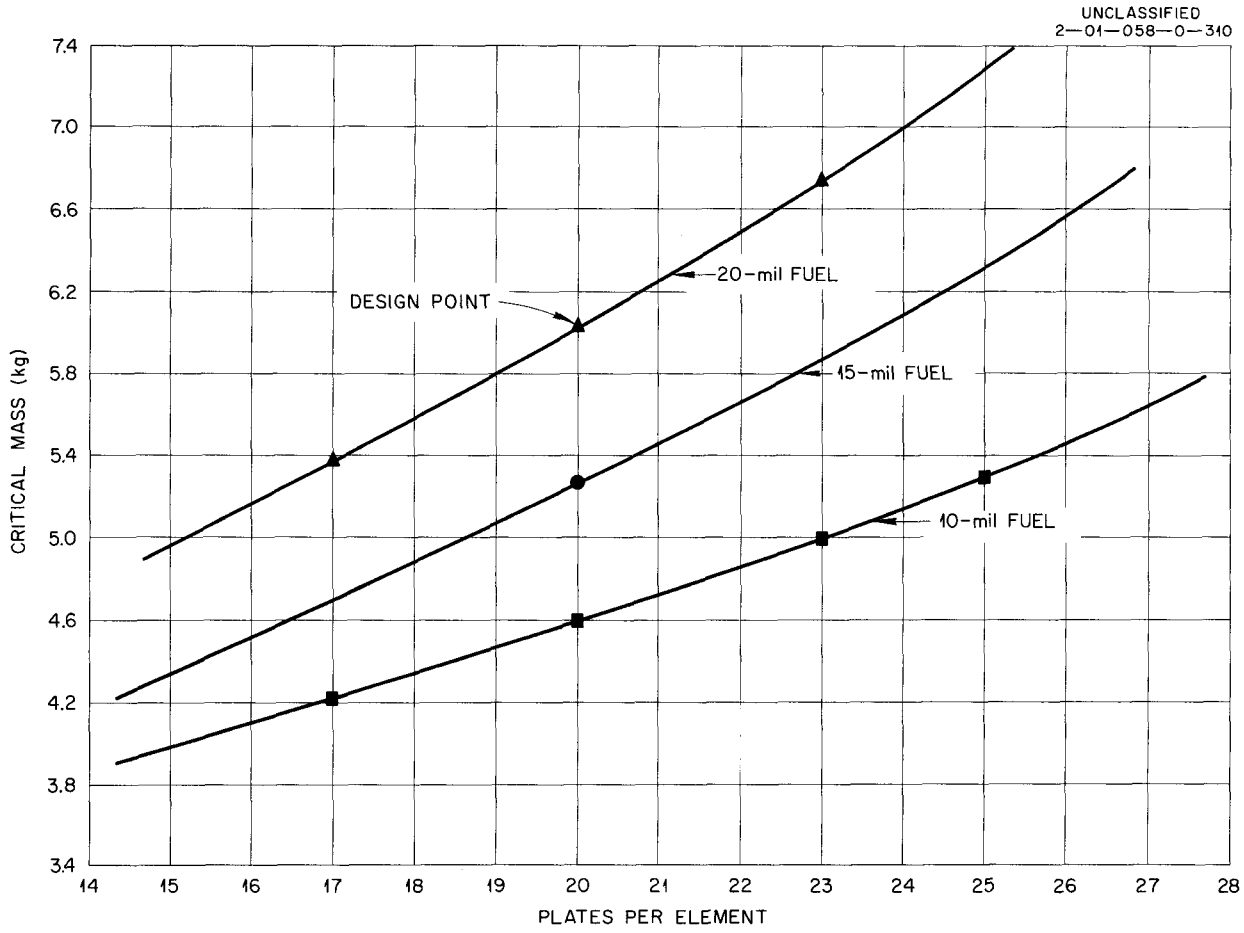

Fig. 2.1.5. Critical Mass as a Function of the Number of Plates per Element for Various Fuel Region Thicknesses of the Proposed BSR-II.

Temperature Coefficient

The temperature of the reactor core in most calculations was 66°F. In order to determine the temperature coefficient of reactivity, a calculation for the design point was also carried out for an elevated temperature of 184°F, which indicated that the net temperature coefficient is -3.5×10^{-5} $(\Delta k/k)/°C$. This result is in agreement with experimental results obtained for the APPR, where a coefficient of -2 to $-5 \times 10^{-5}/°C$ was found at room temperature for a core with very similar nuclear characteristics. It is of interest here that the over-all negative temperature coefficient is comprised of a negative coefficient of $-13.1 \times 10^{-5}/°C$ due to the water expansion and a positive coefficient of $+9.6 \times 10^{-5}/°C$ due to the nuclear parameter effect.

Heat Transfer Calculation

A calculation was carried out to determine the maximum power level at which the core could be operated without the occurrence of local boiling at the hottest point in the fuel elements. This calculation was made by a method of successive approximations of the average water density in the central fuel element as follows:

(1) $$dQ_z = q_z A dz \text{ (Btu/hr)} ,$$

(2) $$Q_z = xC_p(T_z - T_0) \text{ (Btu/hr)} ,$$

(3) $$x = A_w v_z \rho_z \text{ (lb/hr)} ,$$

(4) $$v_z = 2\left(\frac{\rho_0 - \overline{\rho}_z}{\overline{\rho}_z}\right) gz\, 3600 \text{ (in./hr)} ,$$

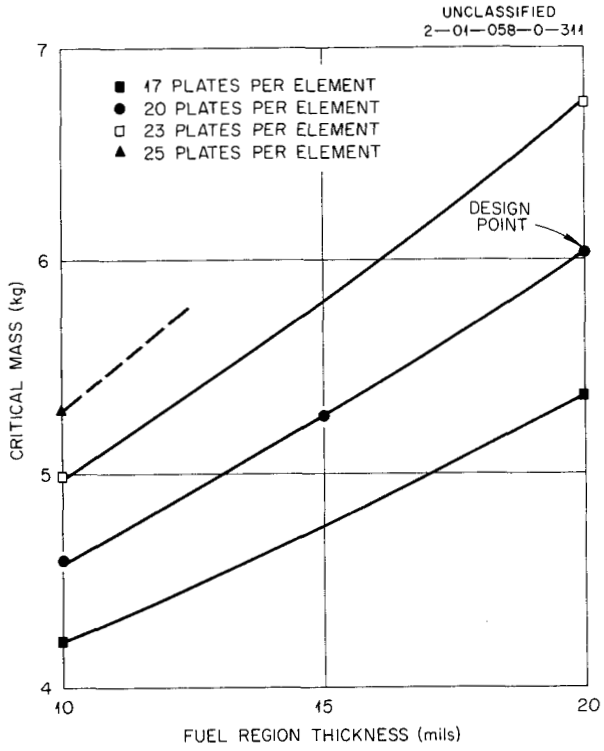

Fig. 2.1.6. Critical Mass as a Function of Fuel Region Thickness for Various Numbers of Plates per Element for the Proposed BSR-II.

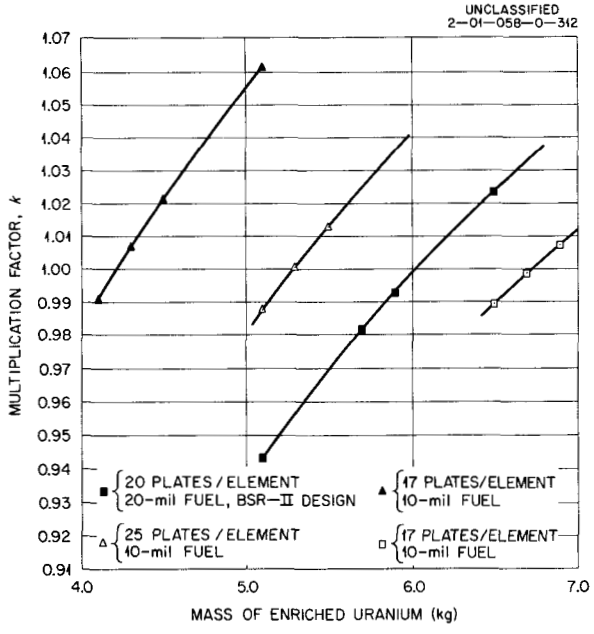

Fig. 2.1.7. Multiplication Factor k as a Function of Mass of Enriched Uranium in the Proposed BSR-II.

where

Q_z = total heat transferred to water in length z of fuel elements, Btu/hr,

q_z = heat generation rate at any point z in central fuel element, Btu·hr^{-1}·in.$^{-3}$,

A = gross cross section of fuel element, in.^{2},

z = length of fuel element, in.,

x = mass water flow, lb/hr,

C_p = heat capacity of water, Btu·lb^{-1}·(°F)$^{-1}$,

T_z = mean water temperature at point z, °F,

T_0 = water temperature in pool, °F,

A_w = cross section available for water flow, in.^{2},

v_z = average velocity of water flow over area A at point z, in./hr,

ρ_z = water density at point z, corresponding to temperature T_z, lb/in.^{3},

$\bar{\rho}_z$ = average water density in length z, lb/in.^{3},

g = acceleration of gravity, in./sec^2.

The calculated flux shape in the core was then approximated with a cosine distribution of which only a central part was used. The portion used was chosen to have the same peak-to-average flux ratio as that of the calculated flux shape, as shown in Fig. 2.1.8. This ratio was 1.89:

$$(5) \qquad q_z = \frac{1.89P}{3300} \sin\left(\frac{\pi z}{15}\right) \text{(Btu·hr}^{-1}\text{·in.}^{-3}) ,$$

where P is the reactor thermal power level, Btu/hr.

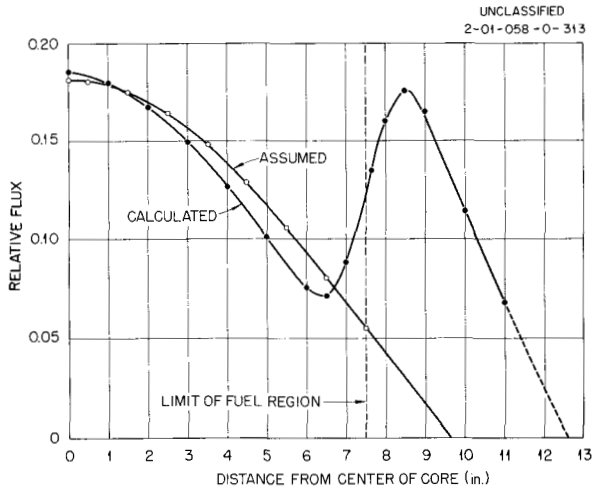

Fig. 2.1.8. Comparison of Calculated Flux in the Proposed BSR-II with Flux Shape Assumed for Heat Transfer Calculations.

The method used was to find the value Q_z by use of Eqs. 1 and 5; x was then plotted as a function of $(T_z - T_0)$. A value for $(T_z - T_0)$ was then assumed, and a value of $\overline{\rho}_z$ was obtained from a curve of ρ vs T. Using this value of $\overline{\rho}_z$, a value of v_z was found from Eq. 4, after which a value of x was found from Eq. 3. This x, substituted back into Eq. 2, should yield the originally assumed $(T_z - T_0)$. If it did not, a new value of $(T_z - T_0)$ was assumed, and resultant temperature differences were checked.

The temperature of the fuel-plate surface was then found from

$$T_w = \frac{Q_z}{ha} + \overline{T}_z \ , \tag{6}$$

where

T_w = fuel-plate wall temperature at point z, °F,
h = average heat transfer coefficient over length z, Btu·hr^{-1}·(°F)$^{-1}$·ft^{-2},
a = surface area available for heat transfer in length z, ft^2,
$\overline{T}_z$ = average fluid temperature over length z, °F.

With 20 fuel plates per element, the plate surface temperature, T_w, in the central fuel element was found to reach 239°F, the boiling point for water under a head of 20 ft at a reactor power of about 1000 kw (Fig. 2.1.9). The effective transfer coefficient h was 140 Btu·hr^{-1}·(°F)$^{-1}$·ft^{-2}. At this same power level, the average water temperature rise in passing through the fuel element was 62°F (Fig. 2.1.10). Thus the stainless-steel-clad reactor would be limited in power level to below 1 Mw. Based on past experience with the aluminum-clad core, it is not anticipated that such a power-level limitation would present any difficulties for the performance of shielding experiments.

An identical calculation for loading No. 33 of the aluminum-clad BSR-I was compared with measured temperatures of the water. Good agreement was obtained, well within experimental accuracy. The measured wall temperatures, however, indicate that a heat transfer coefficient of 140 Btu·hr^{-1}·(°F)$^{-1}$·ft^{-2} is conservative.

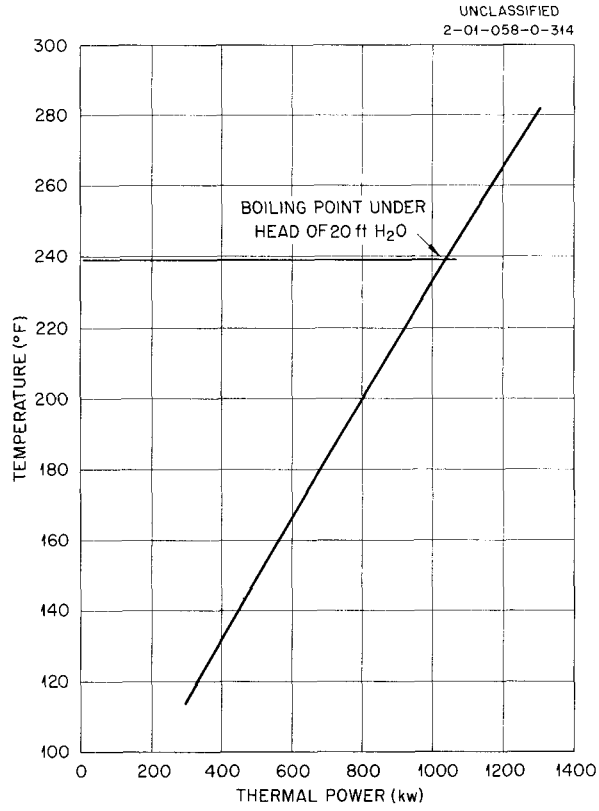

Fig. 2.1.9. Maximum Fuel Plate Surface Temperature as a Function of Reactor Power of the Proposed BSR-II.

Reactor Control Considerations

The thermal-neutron lifetime in the proposed core is given approximately by

$$l_{th} = \frac{1}{v\Sigma_a(1 + L^2B^2)} \ ,$$

where

l_{th} = prompt-neutron thermal lifetime,
v = mean neutron velocity of thermal neutrons = 2.2×10^5 cm/sec,
Σ_a = thermal-neutron absorption cross section in the core = 0.223 cm^{-1},
L = thermal diffusion length = 0.986 cm,
B^2 = buckling of the equivalent bare core = 0.0147 cm^{-2}.

The result for l_{th} is 20.1 μsec. In order to find the effective prompt-neutron generation time, the

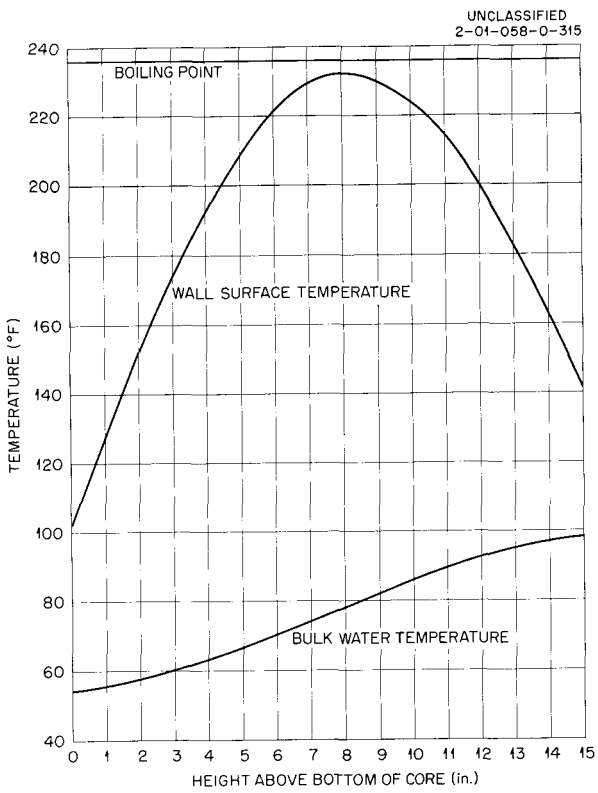

Fig. 2.1.10. Calculated Wall Surface and Bulk Water Temperatures in Central Water Channel of Proposed BSR-II at 1 Mw.

slowing-down time[6] must also be taken into account, and is assumed to be 10 μsec. In this reactor 19% of the fissions are initiated by neutrons above 0.1 ev. Taking this as the epithermal fission fraction, it is found that the prompt-neutron generation time is

$$0.19(10\ \mu\text{sec}) + 0.81(10\ \mu\text{sec} + 20.1\ \mu\text{sec}) = 26\ \mu\text{sec} .$$

Safe control of a reactor with such a short generation time requires a faster safety system than is necessary in reactors with longer neutron generation times.

The safety of a reactor in the case of a fast, positive period depends on the speed with which negative reactivity can be added to the reactor; that is to say, it is desired to make

$$\int_0^{\tau} - \frac{dk}{dt}\, dt$$

as large in magnitude as possible for short times, τ. Several ways to achieve this have been incorporated in the present design:

1. The control plates are spring-driven rather than gravity-dropped, over the first few inches of their travel.
2. The control elements are inserted into the core to a depth of 1.0 in. in the fully withdrawn position. This makes the initial plate motion more effective, since the initial poison addition is made at a more effective location.
3. The control elements are made to have as large a total worth as possible, in order to gain both rapid insertion of negative reactivity during a scram and large reactivity override.

These design parameters and their effect will be discussed below.

Control-Element Worth. – The control of this reactor, as presently proposed, is to be achieved by means of eight plates, each containing 4.5 g of 90% B^{10}. This makes the plates equivalent to ones containing 22.5 g of natural boron. In order to determine the effectiveness of such plates, a series of experiments was performed with BSR-I loading 64, in which plates of aluminum containing natural boron were inserted in location E_1 of position 24, each boron-loaded plate replacing a single fuel plate. (These tests are described in Sec 1.1.) The results are shown in Fig. 2.1.11 along with additional data taken for location W_1 in position 14.

The BSR-I experiments were used to infer the new control-plate design on the assumption that a control plate extending to the full height of the core is equally effective for the same amount of poison per unit plate area in either the 15- or 24-in.-high reactor. On this basis, a plate containing 4.5 g of B^{10} has the same effect in the proposed new core as a plate containing 36 g of natural boron in the BSR-I.

Figure 2.1.12 shows that such a plate may be considered to be, in effect, "black" to thermal neutrons, if the poison in the plate can be considered to be homogeneously distributed. The experiment showed that in the BSR-I, the worth of such a plate is 3.2% $\Delta k/k$ at location E_1 of position 24, which would be 3.33% at the center of the

[6] S. Glasstone and M. C. Edlund, *The Elements of Nuclear Reactor Theory*, Table 6.147, p 184, Van Nostrand, New York, 1952.

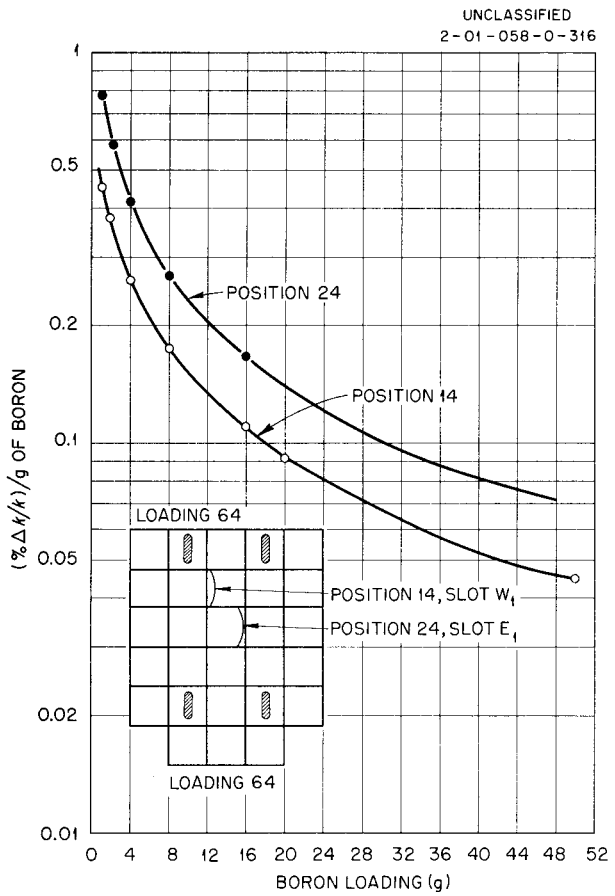

Fig. 2.1.11. Per Cent Change in Reactivity per Gram of Boron in a Single Plate in Positions 24 (Slot E_1) and 14 (Slot W_1) of BSR-I Loading 64.

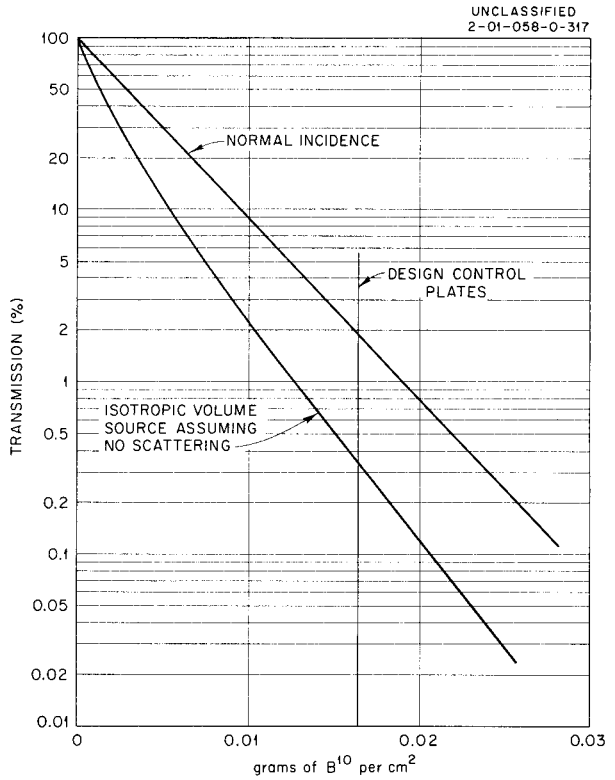

Fig. 2.1.12. Calculated Transmission of Thermal Neutrons Through a B^{10} Slab.

core (Fig. 2.1.13). If the effect of an average control rod in the Materials Testing Reactor (MTR), which has a core composition similar to that of the BSR-I, is compared with the effect of a rod of similar shape in the APPR, which has a core composition similar to that of the proposed BSR-II, it is found that a control plate is worth about 50% as much in the stainless steel core as in the aluminum core. Thus a worth of the order of 1.7% per plate at the center of the proposed core loading results.

The question of the interference effects between plates was experimentally investigated in the BSR-I with plates containing 2.0 g of boron. Figure 2.1.14 shows the effect of two such plates as a function of their separation distance. This experiment was conducted by comparing the reactivity with the two plates inserted at the specified separation with the reactivity when fuel plates were put in the place of these two plates.

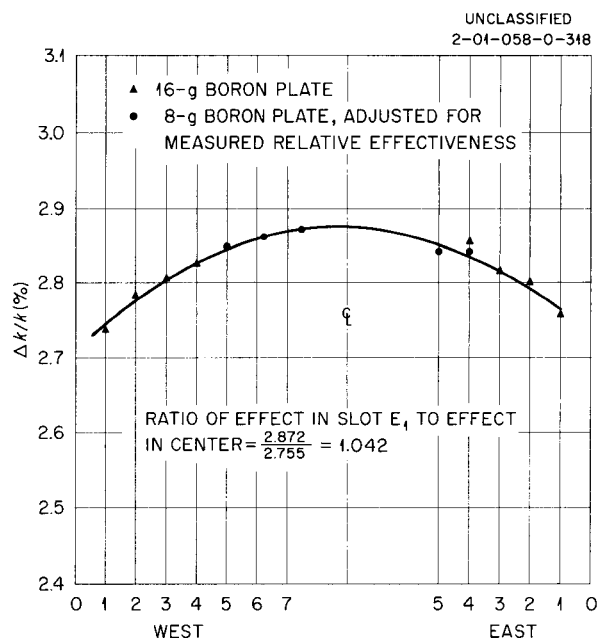

Fig. 2.1.13. Measured Effectiveness of Boron Plate in Position 24 of BSR Loading 64.

Since the effect of single boron-loaded plates on the reactivity was compared with the effect of a water space in the same location, and since the effect of two plates was compared with that of fuel in the same locations, the two sets of data are not directly comparable. However, it may be seen that the effect of separation is saturated for distances of 4.0 cm or more between the plates. The normalization of the curve of Fig. 2.1.14 in order to compare it with the single-plate data can be made from the following experimental data.

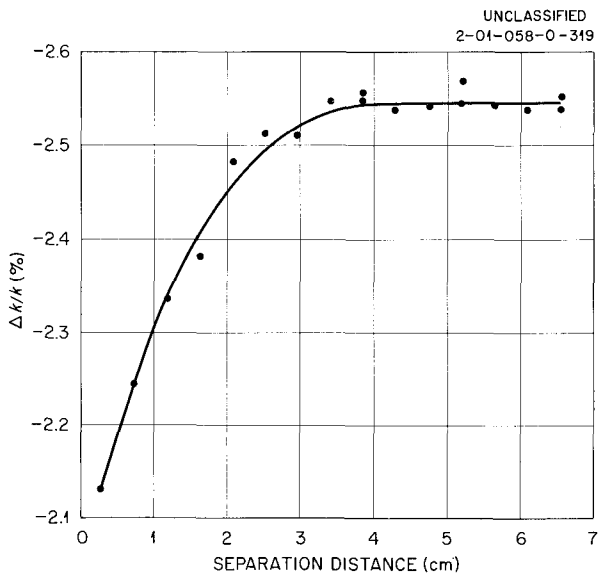

Fig. 2.1.14. Per Cent Change in Reactivity as a Function of Separation Distance Between Two 2-g Boron Plates in Position 24 of BSR-I Loading 64.

In the two most widely separated slots, 6.7 cm apart, data were taken with 2-g boron-loaded plates as follows:

Boron plates in both positions	Excess $k = 0.39\%$
Water in both positions	Excess $k = 2.75\%$
Boron in one position, water in the other	Excess $k = 1.56\%$

The difference in excess reactivity due to inserting one plate is thus 1.23%, whereas the difference due to inserting two plates is 2.42%. The effect of two plates then is about equal to twice the effect of a single plate at a separation of 6.7 cm, and reference to Fig. 2.1.14 shows that this holds true from about 4.0 cm on. In the proposed core, where the thermal-neutron diffusion lengths are much shorter than in the BSR-I, less interaction would be expected for the ~~small~~ same plate separation. It may be concluded, therefore, that at the design separation of 7.08 cm for the paired control plates in the proposed core the effect of interference is negligible.

Since not all the plates can be inserted at the center of the core, the total reactivity worth of the plates will be less than the 13.6% calculated from the center plate measurements. However, there is an added effect which may be gained by judicious placement of the control elements. If, for example, they are so arranged as to surround the central fuel element completely, which is a possible arrangement, then, in effect, this fuel element is removed from thermal interactions with the rest of the core, which will increase the effectiveness of the plates. Enhancement in the value of any given plate can also result because of the flux distortion occasioned by all the plates. A total worth of the control plates of 6.0 to 10.0% is thus reasonable.

Kinetic Behavior of Reactor and Control System. – Due to the decreased neutron lifetime in the reactor, an increase in the rate of control-plate insertion in a reactor scram over the rate available from the action of gravity alone was incorporated. Within the limitations of cost, space, and reactor loading procedure, it did not prove feasible to accelerate the control plates throughout the entire length of the plate travel. Instead, a simple coil-spring system provides a maximum of acceleration at the beginning of plate travel in a reactor scram. The spring is compressed, through a special accelerator tube, against the face of the magnet armature by the drive motor and is held compressed by the attractive force of the magnet on the armature. When magnet current is cut off, at any position of the control plates, the spring force will drive the entire paired control-plate assembly downward.

Each control assembly of the BSR-II consists of two relatively thin plates that move in water channels on either side of a special fuel element. Both plates are attached to a common yoke above the fuel element, and the yoke is, in turn, attached to one lift tube. At the upper end of the lift tube is fixed a decelerator piston, and above it is the magnet armature (Fig. 2.1.15). A coil spring mounted above the magnet gives the entire assembly of two plates, lift tube, piston, and armature an initial downward acceleration (Fig. 2.1.16).

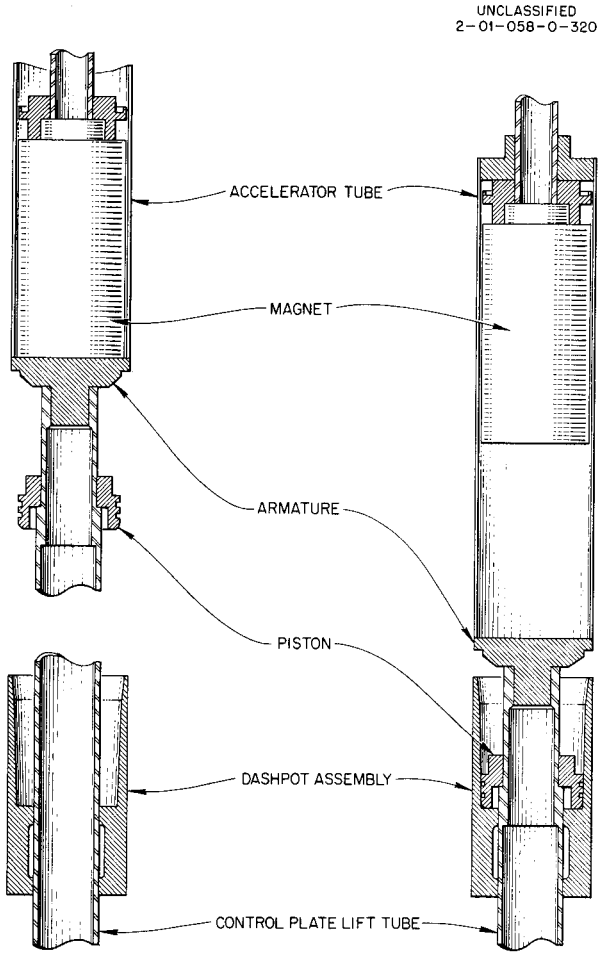

Fig. 2.1.15. Proposed BSR-II Magnet and Decelerator Design.

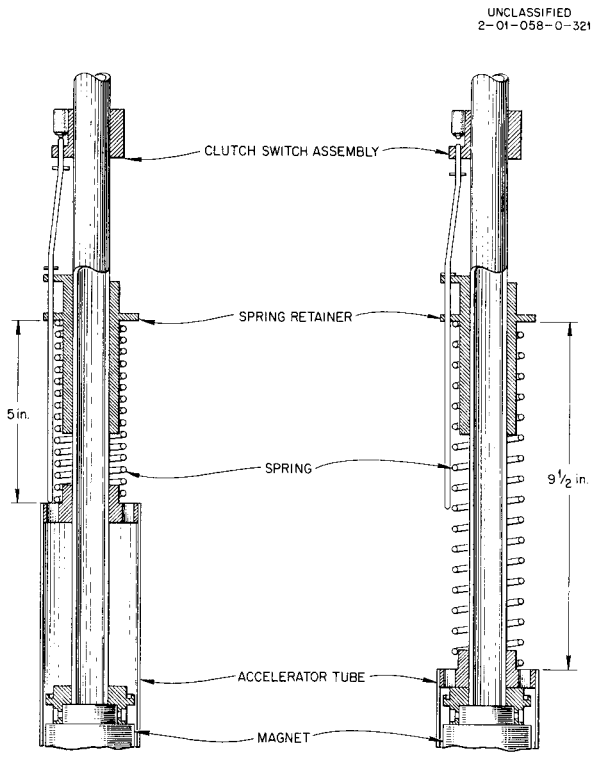

Fig. 2.1.16. Proposed BSR-II Control Plate Accelerator Spring Drive.

The control-plate lift tube is guided through a cylindrical hole in the decelerator body. Downward motion of the entire assembly is limited by the bottoming of the piston in the decelerator.

The equation used to predict the performance of the decelerators is

$$\ddot{S} = K_1 - S^2 K_2 \left[\frac{1}{(A_{co} + A_{vo})^2 C_v^2 C_D^2} \right],$$

where

$\ddot{S}$ = acceleration in in./sec^2 at time t, positive downward,

K_1 = $(W - F_{H_2O} - q)/M$,

W = weight of parts in air, lb,

F_{H_2O} = buoyant force of water, lb,

q = dynamic water drag $+ \frac{1}{2} \rho \dot{S}^2 A C_D n$,

ρ = density of water,

$\dot{S}$ = velocity,

A = 2.65 in.^{2},

C_D = drag coefficient,

n = a constant depending on geometry,

M = mass of moving parts,

K_2 = $A^3 \rho / 2W$,

A_{co} = area of constant annular orifice formed by clearance between the lift tube and decelerator bushing,

A_{vo} = area of varying annular orifice formed by clearance between the piston and the wall of the decelerator

$$= \frac{\pi}{4} \left[D_1 - \frac{S}{S_0} (D_1 - 2.376) \right]^2 - 4.632.$$

The terms C_v and C_D are the coefficients of velocity of efflux and of discharge for the orifices. The varying annular orifice was defined as shown

in Fig. 2.1.17. To design the decelerator, various combinations of D_1 and S_0 were tried in the equations for several assumed values of C_v and C_D. The equations were solved on an analog computer, and the results were compared for minimum final velocity and most nearly uniform decelerating force. The decelerator finally used in the tests has the dimensions shown in Fig. 2.1.17. Although a straight-line taper of D_S does not yield the theoretically optimum shape of decelerator wall, it is by far the easiest to fabricate and was used for this reason. The test results showed that the straight-line taper approximated the best theoretical curve quite well, since the plate assembly decelerated to a velocity of about 1 in./sec in each case before hitting the stop.

The entire control-plate configuration was tested in a water tank; position vs time after magnet current cutoff was obtained for initial accelerations of 1, 8.2, and 10.5g. Figure 2.1.18 shows the assembled test setup.

UNCLASSIFIED
2-01-058-0-322

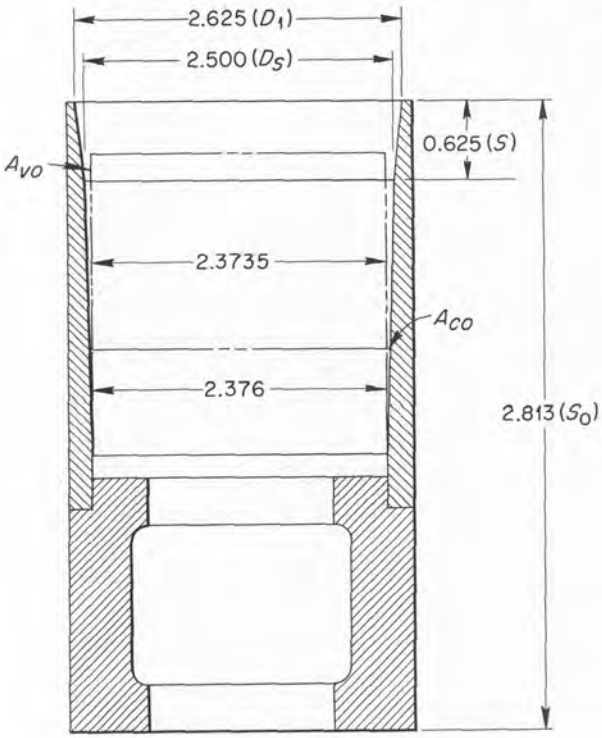

ALL DIMENSIONS ARE IN INCHES

Fig. 2.1.17. Proposed BSR-II Decelerator Design.

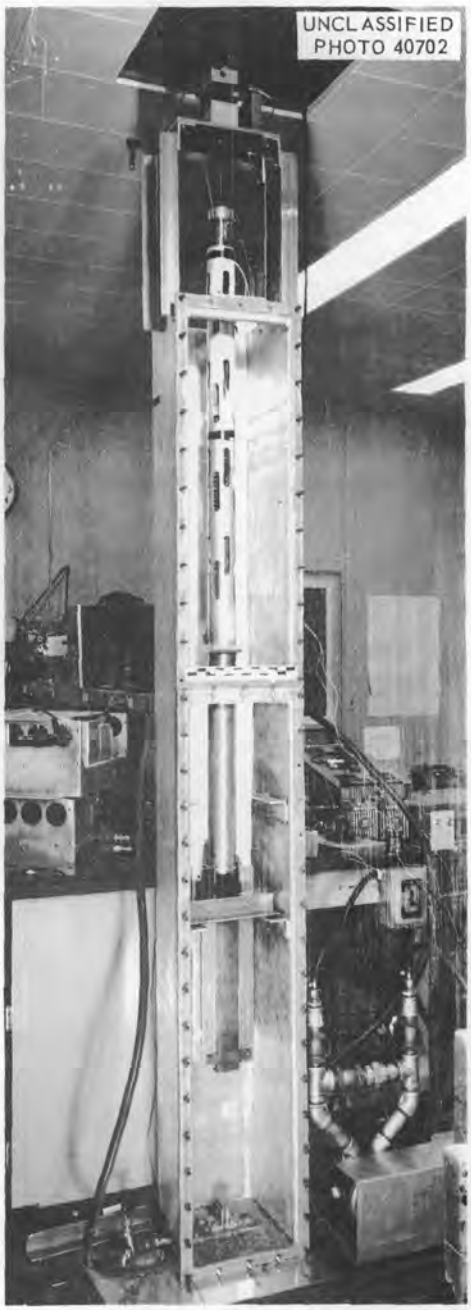

Fig. 2.1.18. View of Assembled BSR-II Control Drive System Test Rig.

During the tests a Plexiglas plate was bolted to the face of the test tank, which was filled with water at room temperature. All working parts were thus immersed in water.

In order to measure plate position vs time, a Fastax camera running at 2000 frames/sec was used to photograph simultaneously the graduated edge of one of the control plates and the face

of a disk rotating at 3600 rpm. In addition, two lamps were placed in the field of view of the camera. One lamp flashed when the magnet current was cut off, and the other flashed when the clutch switch opened, thus indicating that the control-plate assembly had begun to move. The time interval between the flashing of the magnet lamp and of the clutch-switch lamp represents the time required for the magnet to release plus any overtravel in the clutch switch.

A record of the motion was thus obtained. The film could be read with an accuracy of ±0.15 turn, and, since each full turn of the disk represented 0.0167 sec, the accuracy with which the motion could be determined was ±0.0022 sec. The position of the control plate could be read on most of the films with an accuracy of $\pm \frac{1}{16}$ in. or better. The plates were dropped under the following conditions:

1. initial spring compression to a force of 66 lb, decaying to zero in 3.3 in. (8.2*g*) (design case);
2. initial spring compression to a force of 86 lb, decaying to zero in 4.3 in. (10.2*g*);
3. fall under force of gravity only;
4. fall under force of gravity only, with one control plate removed from the assembly;
5. fall under force of gravity only, with both control plates removed from the assembly; that is, only the lift tube, yoke, piston, and magnet armature were dropped.

In addition, the tests were further divided into two parts, with different details for the upper guide tube and the plate lift tube. In the first tests the upper guide tube had no openings in the lower 6 in. of its length, and the lift tube had no openings at its upper end, so that the water inside the lift tube was trapped. Since it was felt that the lack of openings for water passage might affect the motion of the plate assembly, and particularly the performance of the decelerator, the additional holes were cut and the tests repeated. The results showed that this induced only an insignificant change in the control-plate motion.

The essential results of the tests are combined in one graph in Fig. 2.1.19. This graph shows the plate position as a function of time after scram. Figure 2.1.20 is a plot of velocity during the first 80 msec of travel. This was made by measuring the slopes of the position vs time

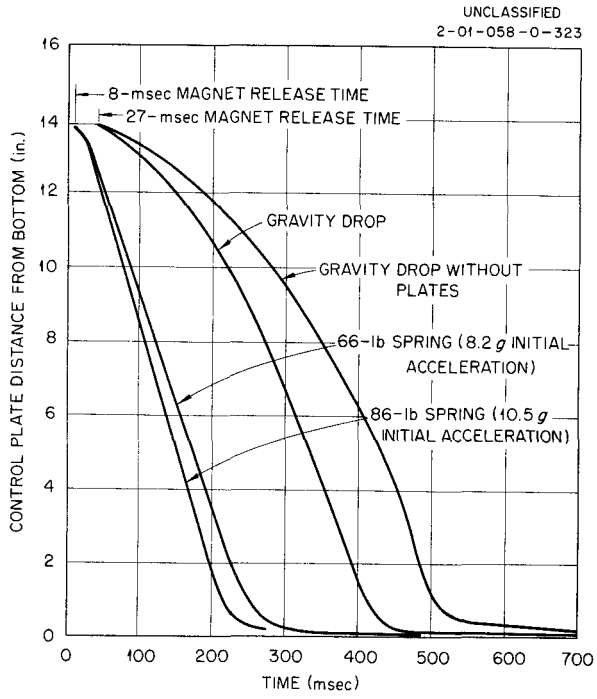

Fig. 2.1.19. Control Plate Position as a Function of Time After Scram Signal in Rod-Drop Tests.

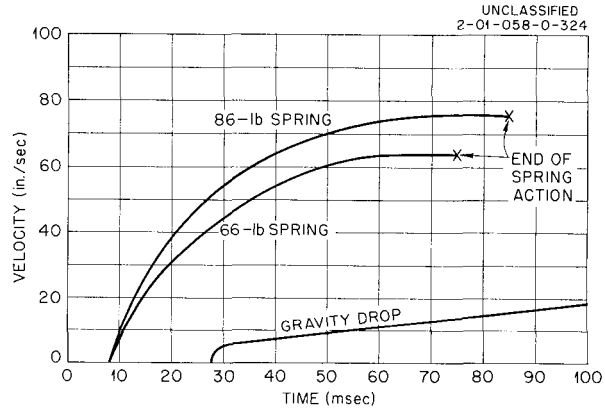

Fig. 2.1.20. Control Plate Velocity as a Function of Time After Scram Signal in Rod-Drop Tests.

curves drawn to a greater scale than was used in Fig. 2.1.19.

The results of the drop tests, in terms of control-plate location as a function of time, were applied to a measured position vs reactivity curve obtained[7] for the BSR-I. It was assumed that the shape of the curve would be the same,

[7]R. G. Cochran *et al.*, *Reactivity Measurements with the Bulk Shielding Reactor*, ORNL-1682 (Nov. 9, 1954).

scaled to the 15-in. total core height of the BSR-II instead of the 24-in. height of the BSR-I.

Figure 2.1.21 compares the reactivity removal rates of the gravity-dropped and spring-driven control systems. The worst case, from the point of view of safety, arises with the initial position of the control plate in its most withdrawn position (inserted 1 in.). The total drop in this case is 14 in. For comparison, more favorable cases, in which the initial insertion is 3 and 5 in., are also shown.

The information as to poison insertion rate and neutron generation time has been evaluated by means of the analog computer. F. P. Greene has carried out a series of calculations by using the experimental rod-drop data presented above, in order to determine the shortest reactor period that would be reversed within a power excursion limit of three orders of magnitude. The study technique was based upon a simulation system

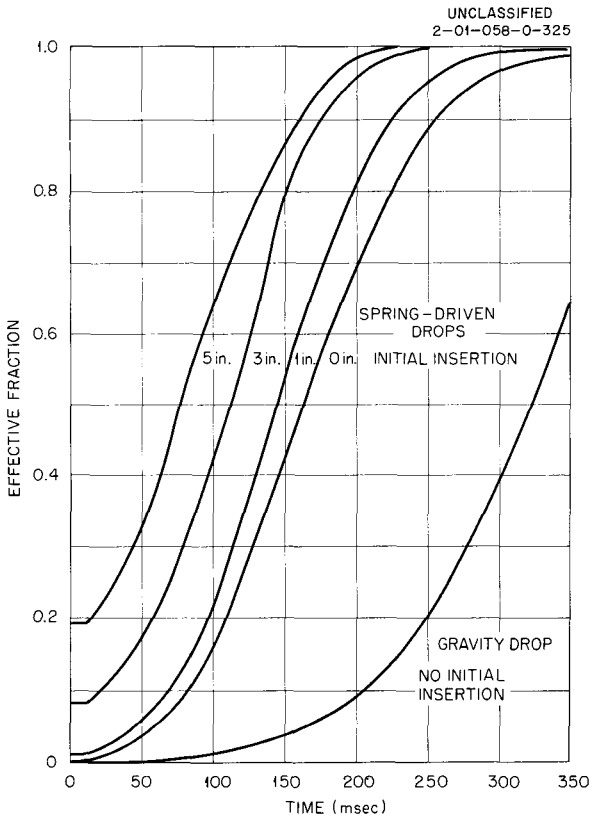

Fig. 2.1.21. Effective Fraction of Total Control Plate Worth as a Function of Time After Scram Signal in Rod-Drop Tests.

described previously.[8] In this technique the reactor is initially maintained critical at a low power level; a calibrated positive reactivity step function is then inserted, and at an arbitrary power level a reactivity decrease is initiated of the shape described above. By a sequence of runs, that step function is found which causes an excursion that can just be reversed by the corrective action within three decades of power increase from the moment of initiation of the corrective action.

The excursion is then repeated with no corrective action in order to measure the stable period induced by the step function.

Figure 2.1.22 shows the effect of preinsertion of the control plates for two different springs and prompt-neutron generation time. It will be observed that the gain due to 1 in. of initial insertion is from 9.2 msec down to 7.3 msec.

Figure 2.1.23 presents the shortest period, as well as the excess reactivity, that can be reversed within a three-decade power rise for various total plate worths. It will be seen from the figure that this corresponds in all cases to an excess reactivity of about 1.0 to 1.2%. This means, in turn, that the amount of reactivity that can be controlled does not depend much on the plate worth, since the total effect of a plate-worth change from 8 to 4% only decreases the reactivity that can be reversed from 1.19% to 1.06% in the design situation. The inhour curve for this core is presented in Fig. 2.1.24. The low sensitivity to the plate worth of the excess reactivity that can be handled is due to the sensitivity of a short generation time system to the excess that can be handled above prompt criticality, which is only about 0.30%; this amount of reactivity is removed quickly, even with small total plate worth, once the plate starts to move. The delay time in the release of the magnet, which is found to be about 7 msec, is significant in the control of excursions.

Proposed Procedure for Safe Operation

The control and kinetic situation discussed above has implications for the safety of the reactor system and its operation.

It is observed that it is not possible to increase, much above 1%, the amount of excess reactivity

[8] F. P. Greene "Analog Simulation of Corrective Action for A Nuclear Excursion," in *Reactor Safety System Response*, ORNL-2318 (to be published).

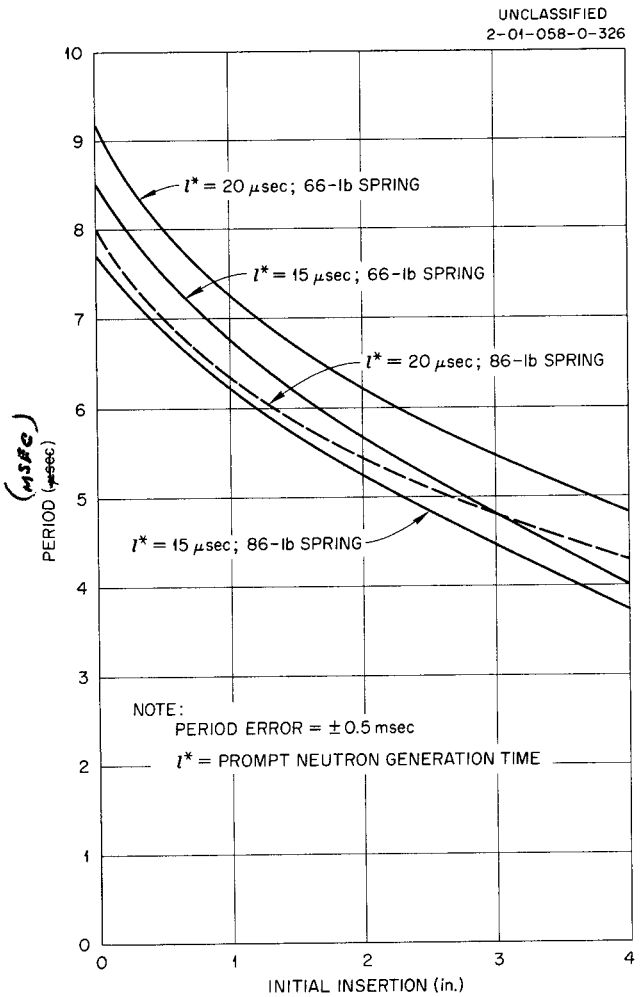

Fig. 2.1.22. Period That Can Be Reversed Within a Three-Decade Power Excursion as a Function of Initial Control Plate Insertion.

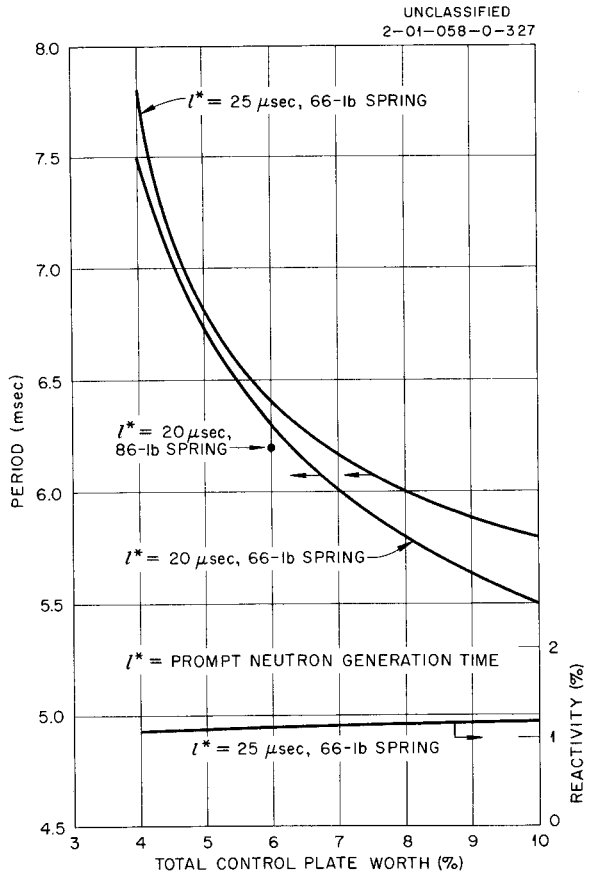

Fig. 2.1.23. Period and Per Cent Reactivity That Can Be Reversed Within a Three-Decade Power Excursion as a Function of Total Control Plate Worth.

which can be handled by increasing the total control-plate worth. On the other hand, this implies that a situation which is safe when all plates function is not greatly more dangerous if one or even two of the control drives should fail to release, since the amount of reactivity which the full ~~8%~~ eight plates worth can control is not much more than that which can be controlled by the insertion of a ~~4%~~ four plates at the same speed.

The calculations for the power increase due to step reactivity insertions are conservative, in that they did not include any boiling or other temperature effects, which might be expected to function so as to diminish the severity of the

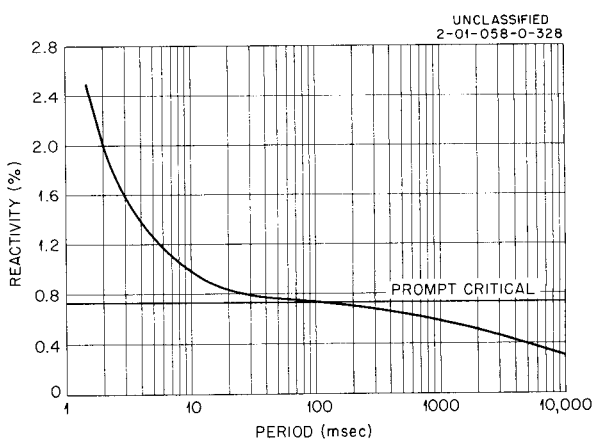

Fig. 2.1.24. Period as a Function of Reactivity for a 26.3-μsec Prompt-Neutron Generation Time.

excursion. The Borax experiments do indicate that, for an aluminum-clad reactor under the conditions of the tests, the ability to control reactivity was better than that indicated in the calculations carried out by the means used here. However, a scheme of operation, safe within the limitations of calculations as carried out, is proposed as follows:

1. The potential excess reactivity of the core will be kept at less than prompt critical.
2. The loading of the reactor will at all times be carried out in such a manner as to exclude the formation of a void in the core into which fuel might be dropped accidentally.

The latter restriction carries with it a safeguard against accidental step increases of reactivity above prompt criticality. If the loading of the reactor has no void space, it will not be possible to place fuel accidentally near the center of the core. The worst that could happen would be the dropping of an element on top of, or next to, the core. In an experiment with the BSR-I it was observed that the reactivity effect of a single fuel element, when placed on the center line immediately adjacent to a loading of compact symmetry, was 0.62%. It is therefore not probable that a mishap, in the absence of core voids, would occasion a period too short to be readily controlled.

It is intended that the first core of the proposed design be tested at SPERT (Special Power Excursion Reactor Tests) in order to determine the actual safety limitations, which are expected to be well beyond the initially proposed operation limits. After these tests, the excess reactivity limit will be re-examined, and proposals to alter operating procedure will be advanced.

Part 3

DESIGN FOR A SPHERICAL TOWER SHIELDING REACTOR (TSR-II)

3.1. DESIGN FOR A SPHERICAL TOWER SHIELDING REACTOR (TSR-II)

C. E. Clifford L. B. Holland

Much of the work at the Tower Shielding Facility (TSF) has been devoted to a study of the interaction of neutrons and gamma rays with air. It has become clear in explorations with the present reactor at the TSF (the TSR) that the most rewarding research in this field will be done with either an isotropic or a collimated source. With the collimated source the direction of the beam as well as the energy spectrum should be variable (the spectrum would be changed by interposed absorbers), and the detector to be used in either case should be equipped with a collimator and be capable of measuring the spectra of scattered radiation. The present parallelepiped-shaped reactor does not constitute an isotropic source of radiation nor is it well suited to a collimator which is to point in various directions. In fact, the limitation of a 400-kw maximum operating power level for the present reactor precludes its use for doubly collimated experiments (i.e., experiments in which a collimator is used both at the reactor and at the detector). A further difficulty has been that the distribution of power within the core changes with the control-rod position, thus changing the effective source strength of a collimator at the reactor. A new reactor, which will be called the Tower Shielding Reactor II (TSR-II), is being designed to overcome these difficulties. In the discussion below, the presently conceived design of the TSR-II and the studies which led to this design are given.

Description of the Reactor

In many respects the TSR-II will be like the present reactor; that is, it will be heterogeneous, [illegible] enriched, and light-water-cooled and -moderated. Major differences will be a higher operating power (5 Mw), a nearly spherically symmetric annular fuel region, and an internal water reflector in which curved boron-filled plates will move radially to control the operation of the reactor without appreciably perturbing the symmetry of the leakage radiation. As shown in Fig. 3.1.1, the reactor core will be mounted in the bottom of a long cylindrical tank which has a hemispherical lower end.[1] A central pipe, which will contain the control chambers and the control mechanism positioning device, will divide the core into two regions. The cooling water will enter at the top of the central pipe and flow downward through the central core region and the internal reflector, and will turn at the bottom and go up through the outside core region and the annular space between the pipe and the tank.

In the internal water reflector region, umbrella-shaped boron-loaded plates will be located to serve as a control device for the reactor (see Fig. 3.1.2). When moved radially inward, away from the fuel, the plates will cause the reactivity to increase, and vice versa. Movement of the plates will be achieved by a combination of mechanical and hydraulic devices.

A lead-boral-water region adjacent to the core periphery will reduce the reactivity coupling between the reactor and the close-fitting shields. It will also provide a minimum gamma-ray shield, thereby reducing the problems associated with changing the shield configurations. Shields will be mounted directly to the cylindrical support tube by means of flanges so that the reactor and its shields will rotate as a unit.

Preliminary Studies to Establish Reactor Dimensions

In order to establish the dimensions of a core configuration that would fit the requirements of the reactor, the following calculational procedures were followed: A nuclear-parameter study was first carried out to determine the critical mass and control available for various core sizes, internal water reflector thicknesses, and aluminum-to-water volume ratios. From this study a configuration was selected which appeared to be the optimum configuration from the viewpoint of critical mass and small reactor diameter. This configuration was then examined to ensure that the surface density of the U^{235} in the fuel plates would be

[1] The mechanical design of the TSR-II is being done by the Engineering Department.

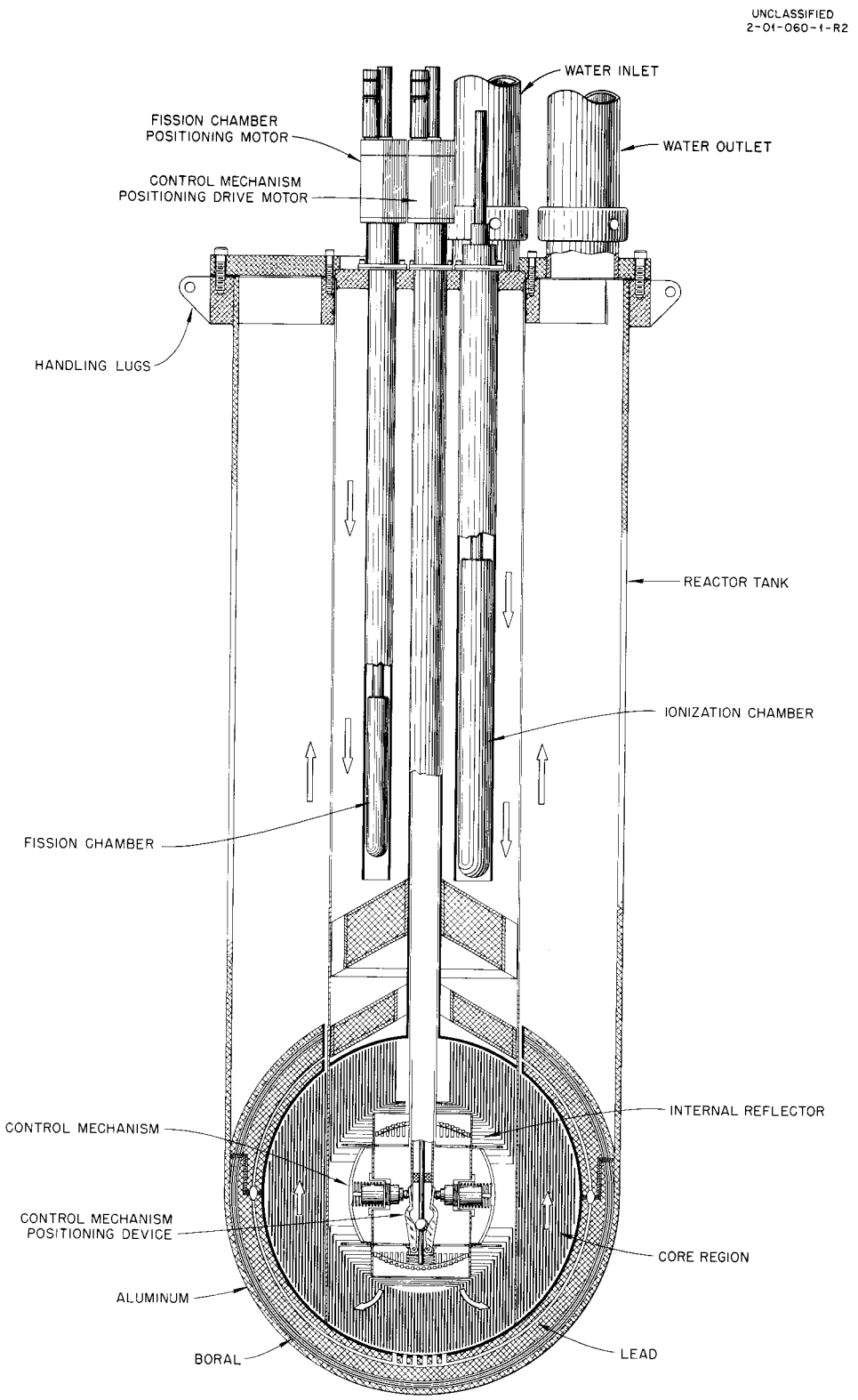

Fig. 3.1.1. Proposed TSR-II (Vertical Section).

UNCLASSIFIED
2-01-060-2

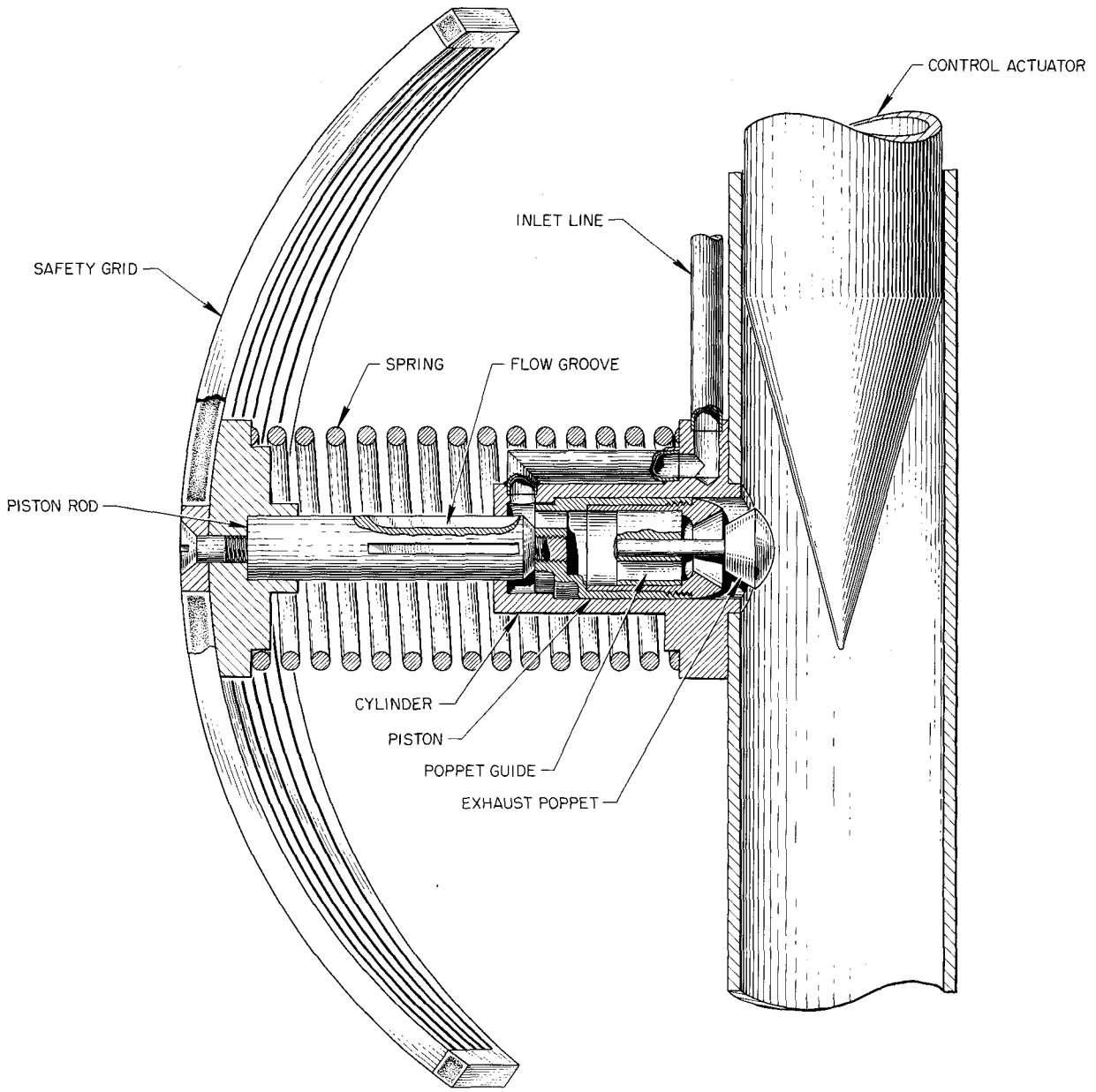

Fig. 3.1.2. Proposed TSR-II Control Mechanism.

below 0.0285 g/cm^2, a density which was established during operating experience[2] with the MTR. Finally, the configuration was examined to determine whether the water flow available to remove the heat from the core was sufficient to prevent local boiling.

[2]R. J. Beaver, Metallurgy Division, private communication.

Nuclear-Parameter Study. – Calculations[3] by use of the three-group, three-region reactor code (the 3G3R code) as a two-group, three-region code were performed on the Oracle to determine the critical mass and control available in reactor

[3]These calculations were performed by M. E. LaVerne; previous calculations by E. G. Silver were helpful in setting up the present problems, see *Appl. Nuclear Phys. Ann. Rep. Sept. 10, 1956*, ORNL-2081, p 47.

configurations having internal water reflector diameters of 32, 40, and 50 cm, and core thicknesses of 16, 20, and 25 cm. The aluminum-to-water volume ratios in the cores ranged from 0.250 to 2.000. All possible reflector-core combinations were investigated for each aluminum-to-water ratio. The external reflector was fixed at 20 cm of water, which was used instead of the lead-water reflector proposed for the actual reactor. A sketch of the geometry used in the calculation is shown in Fig. 3.1.3, and some of the constants are presented in Table 3.1.1.

Calculations were first made to determine the effective multiplication factor for several concentrations of U^{235} in the fuel plates. Typical results for one geometry and all aluminum-to-water volume ratios are shown in Fig. 3.1.4. Earlier calculations for this reactor have shown that 4% excess reactivity would be necessary to compensate for temperature rise, xenon poisoning, and burnup and to provide 1% for control. (More recent calculations indicate that the excess reactivity could be reduced to 3%.) The concentration that gave an excess reactivity of 4% in a particular configuration was used to compute the mass of U^{235} that would be required for that configuration.

In Figs. 3.1.5 through 3.1.7 the critical mass is shown as a function of internal reflector radius for various aluminum-to-water volume ratios and all core geometries considered. As expected, the smallest internal reflector and lowest aluminum-to-water volume ratio will give the minimum critical mass.

The amount of excess reactivity that it is possible to control for the various geometries was next determined. This calculation was performed in a straightforward manner (as provided in the 3G3R Oracle code) by the insertion of a boron-loaded shell between the internal reflector and the core region. The results shown in Fig. 3.1.8 are for a very light loading of boron in the shell (0.0022 g/cm^2). Although it is possible to obtain a larger amount of control by using higher aluminum-to-water volume ratios and larger internal reflector regions, the greatest increase in control is realized by decreasing the thickness of the core region. This is fortunate, since the thinner core region also reduces the heat transfer problem.

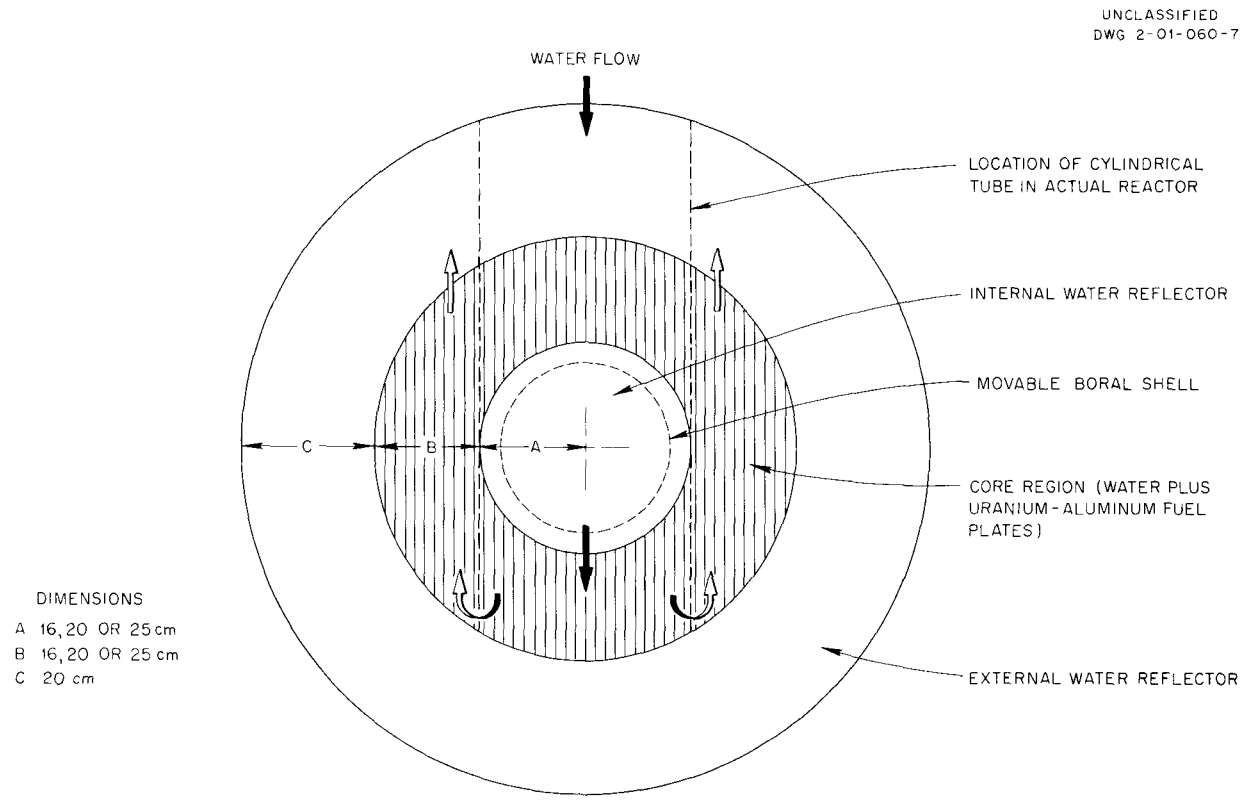

Fig. 3.1.3. Vertical Section of Reactor Core Model Used in Nuclear Parameter Study for the Proposed TSR-II.

Table 3.1.1. Nuclear Parameters Used with the 3G3R Oracle Code for Calculations of the Critical Mass of the TSR-II with an Aluminum-to-Water Volume Ratio of 0.707

Region	Absorption Cross Section* (cm^{-1})		Diffusion Coefficient** (cm)		Transfer Cross Section** (cm^{-1})		Temperature (°C)
	Σ_{a_f}	Σ_{a_s}	D_f	D_s	Σ_{x_f}	Σ_{x_s}	
Internal reflector	0	0.01837	1.190	0.160	0.0361	0	50
Core	0	$0.01535 + 0.47127\nu\Sigma_{f_s}$	1.315	0.2655	0.0210	0	60
External reflector	0	0.01949	1.190	0.160	0.0361	0	20

*Values of Σ_{a_s} were obtained from BNL-325, *Neutron Cross Sections*, by D. J. Hughes and J. A. Harvey (July 1, 1955), with correction applied for (1) non-$1/v$ behavior, (2) Maxwellian distribution of neutron speeds, and (3) temperature effect on density.

**Values of D_f, D_s, Σ_{x_f}, and Σ_{x_s} were taken from IDO-16133, *Reactivity Effect of Reducing the Al/H_2O Ratio in the MTR Core*, by J. W. Webster (Oct. 26, 1953).

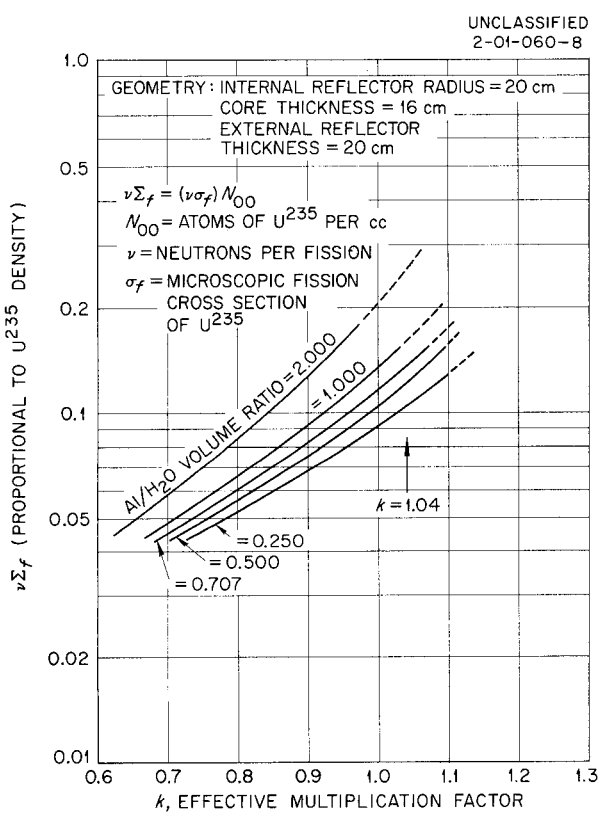

Fig. 3.1.4. Effective Multiplication Factor in the TSR-II as a Function of the U^{235} Concentration for Various Aluminum-to-Water Volume Ratios. Reactor geometry: 40-cm-thick internal reflector, 16-cm-thick core, 20-cm-thick external water reflector.

Subsequent calculations involving a more sophisticated use of the code were made in which the transmission of thermal neutrons through the boron-loaded shell was varied from 0 to 100%. [These calculations were made after the reflected diameter was set at 17.5 in., the core thickness at 5.5 in., and the aluminum-to-water volume ratio at 0.57 (see below).] With zero transmission of thermal neutrons the reactivity that could be controlled was found to be 11%. For these calculations the transmission of fast neutrons was assumed to be 100%, which should give a conservative result. The change in the thermal-neutron flux produced by the insertion of the zero transmission shell is shown in Fig. 3.1.9.

A calculation performed to determine the amount of separation required between the fuel and the control plates, in order to reduce the effect of the control plates sufficiently to permit operation of the reactor, involved a more subtle use of the 3G3R code (see Sec. 8.8). In this case it was necessary to artificially maintain the neutron flux and current at the outer water reflector and core boundary so that the internal reflector could be divided into two regions with a boron shell between them, the core making the third region. It was then possible to vary the thickness of the water regions in the internal reflector and effectively simulate movement of the control plates. The calculation was made for only two aluminum-to-water volume ratios, 1.0 and 0.707, and one

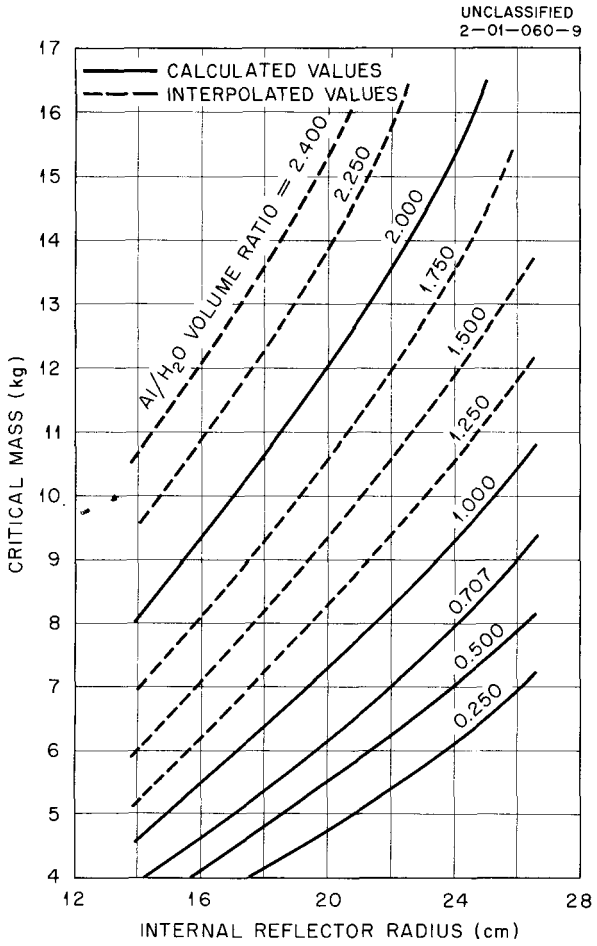

Fig. 3.1.5. Critical Mass in the Proposed TSR-II as a Function of the Internal Water Reflector Radius for Various Aluminum-to-Water Volume Ratios. Reactor geometry: 16-cm-thick core, 20-cm-thick external water reflector.

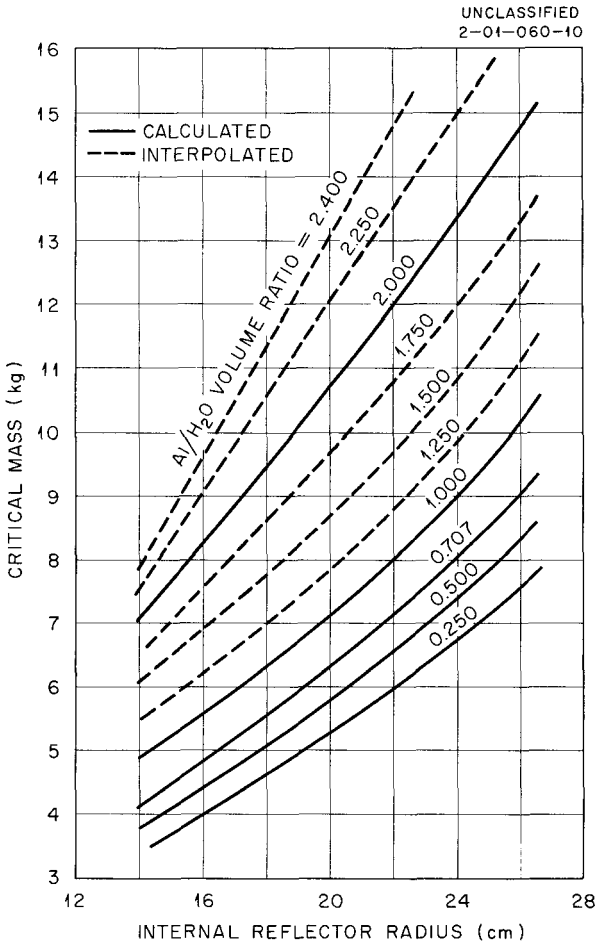

Fig. 3.1.6. Critical Mass in the Proposed TSR-II as a Function of the Internal Water Reflector Radius for Various Aluminum-to-Water Volume Ratios. Reactor geometry: 20-cm-thick core, 20-cm-thick external water reflector.

geometry. The results for the 0.707 ratio are plotted in Fig. 3.1.10 and show that no more than 2.5 in. (~6.5 cm) of travel will be required to reduce the control-plate effectiveness to 0.1 of its full value. The results of an experiment at the Bulk Shielding Reactor (BSR), which has an aluminum-to-water ratio of 0.7, normalized to the calculated value for the TSR-II, are also shown. A description of the test setup and other results are described later in this section.

Although the information was not required to establish the dimensions of the TSR-II, the effect of the control plates on the fast- and thermal-neutron flux throughout the reactor was also calculated as shown in Fig. 3.1.11. Cases *b* and *c* show the effect on the flux of having the boral shell adjacent to the core or 5 cm from the core, respectively. Case *a* represents the same geometry shown in case *b* and is included only to show the validity of the method used, that is, with the external water reflector region left off and with the neutron flux artificially maintained at the outer core boundary. The effect of the boral shell position on the fast- and thermal-neutron leakage from the TSR-II for two aluminum-to-water volume ratios, 0.707 and 1.000, is shown in Table 3.1.2. In this calculation the internal water reflector was 40 cm in diameter, and the core region and

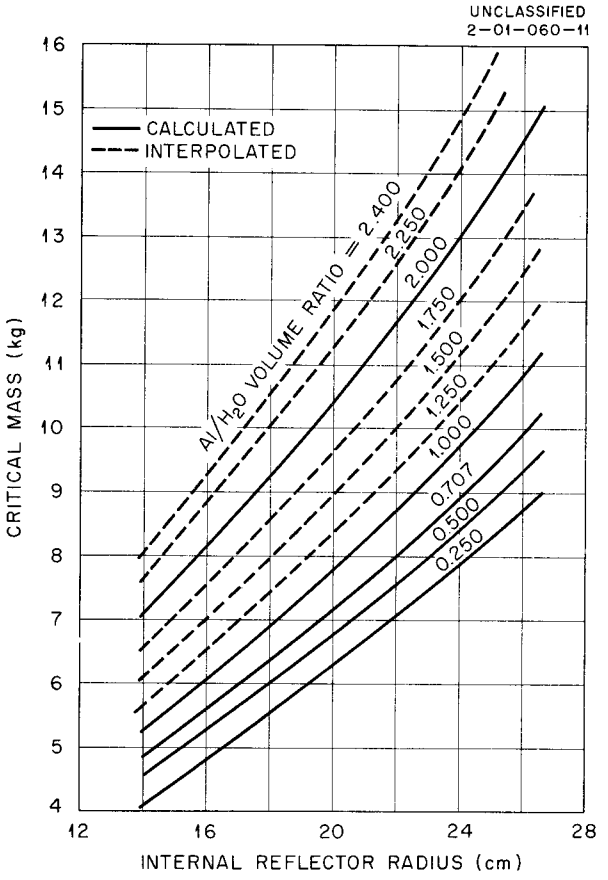

Fig. 3.1.7. Critical Mass in the Proposed TSR-II as a Function of the Internal Water Reflector Radius for Various Aluminum-to-Water Volume Ratios. Reactor geometry: 25-cm-thick core, 20-cm-thick external water reflector.

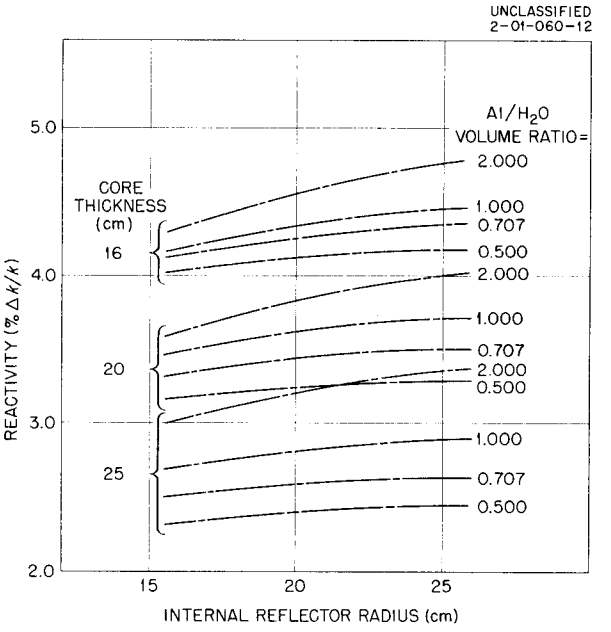

Fig. 3.1.8. Change in Reactivity Produced in the Proposed TSR-II by the Presence of a Boral Shell Between the Internal Water Reflector and the Core as a Function of the Internal Reflector Radius for Various Core Thicknesses and Aluminum-to-Water Volume Ratios. External water reflector thickness: 20 cm.

the external water reflector were each 20 cm thick. Changing the aluminum-to-water volume ratio produces less than 1.5% change in the fast-neutron leakage. Over the probable operating range of the control plates (3 to 5 cm), the variation in fast-neutron leakage will be less than 1.5%.

The space required to house the proposed control mechanism and also allow it to be withdrawn 2.5 in. from the core will necessitate that the internal water reflector be no smaller than 17.5 in. in diameter. With this parameter fixed it was then necessary to carry out a study to determine the corresponding core parameters which would give a minimum fuel loading. This was done by plotting the critical mass as a function of core thickness for various aluminum-to-water volume ratios (see Fig. 3.1.12). As would be expected, the mass decreased with a decrease in the aluminum-to-water volume ratio; however, it does not seem practicable to go below the ratio of 0.7 used in the BSR. (In the BSR the fuel plates and water coolant have an aluminum-to-water ratio of 0.5; the side plates required to hold the fuel plates raise the over-all aluminum-to-water volume ratio to approximately 0.7.) Also, if this ratio is used, the standard arrangement of 60-mil-thick fuel plates separated by 120 mils of water can be used. Since the amount of control available increases with a decrease in core thickness, an approximately 14-cm core thickness (5.5 in.) appears to be the optimum one. This thin core, requiring less than 6.5 kg of U^{235} for criticality, will also be an advantage with respect to the heat removal problem (see below).

The configuration having a 17.5-in.-dia internal water reflector and 5.5-in.-thick core region was then examined to ensure that the U^{235} fuel plate loading would not exceed the 0.285 g/cm^2 surface

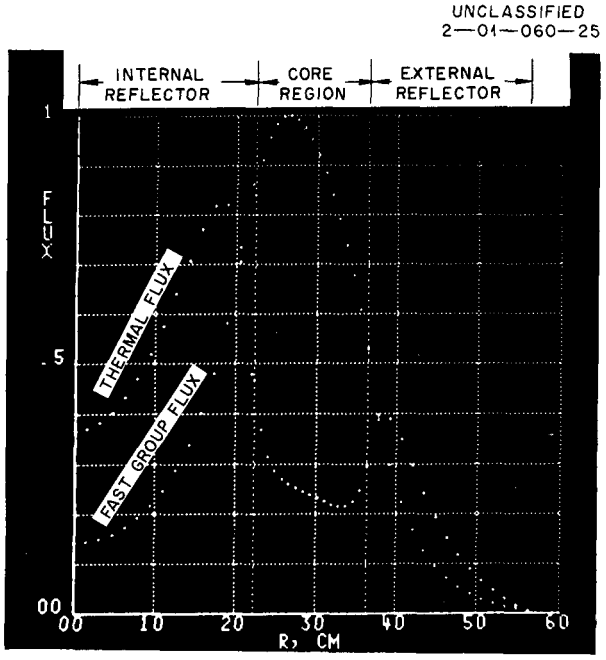

(*a*) No Boral Shell.

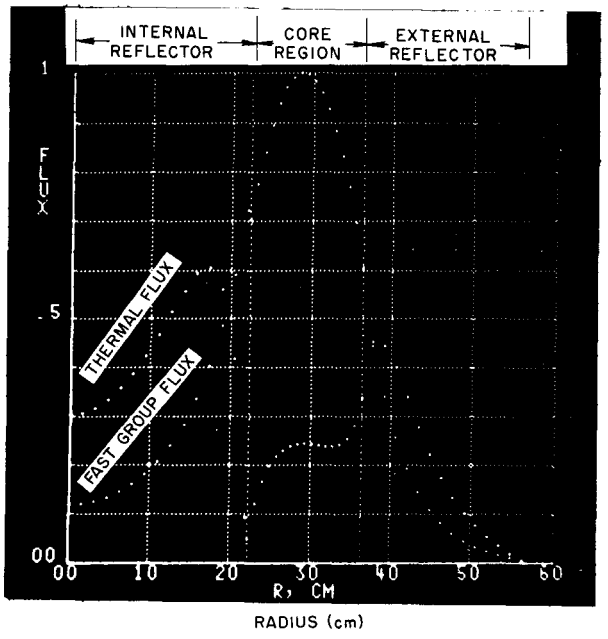

(*b*) Thermally Black Shell at Interface of Core and Internal Reflector.

Fig. 3.1.9. Fast- and Thermal-Neutron Flux in the Proposed TSR-II as a Function of Distance from the Center of the Internal Reflector.

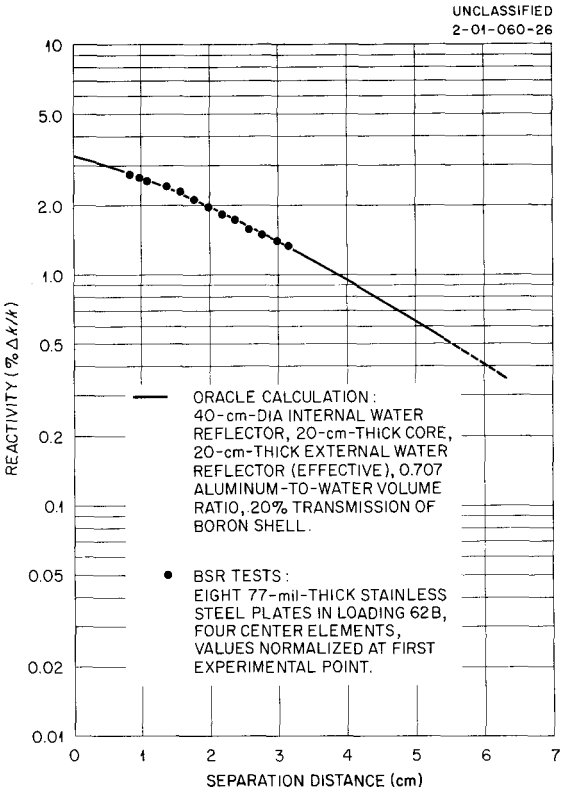

Fig. 3.1.10. Change in Reactivity Produced in the Proposed TSR-II by the Presence of a Boral Shell in the Internal Water Reflector as a Function of the Distance Between the Shell and the Core, Compared with BSR Test.

density previously designated. It was found that the maximum loading possible for this surface density was 9.5 kg. This allows for an error as high as 45% in the critical mass obtained from the two-group Oracle calculations.

Subsequently a set of calculations was run on the Oracle for the simplified geometry with a 17.5-in.-dia internal water reflector, a 5.5-in.-thick core region, a 7.875-in.-thick external water reflector, and an aluminum-to-water volume ratio of 0.57. The same calculations were run on the UNIVAC by using the Murine code, and the values of concentration vs reactivity from the two calculations were compared. It was found that a change of 0.3% in the thermal macroscopic absorption cross section, Σ_a, for the Oracle calculations was all that was required to obtain complete agreement.

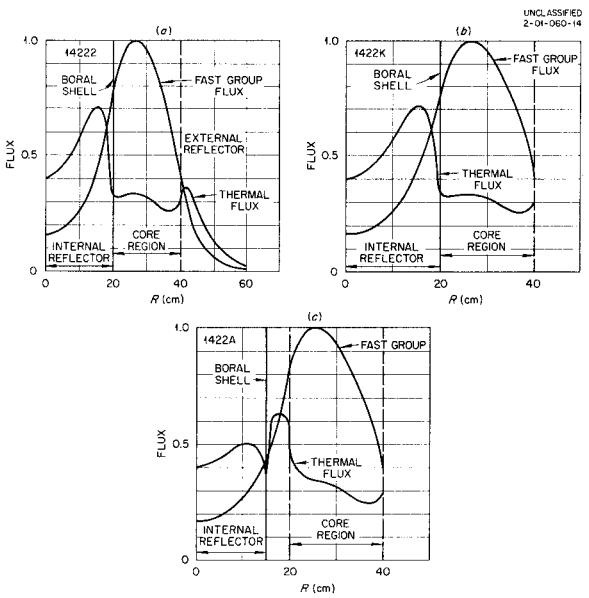

Fig. 3.1.11. Neutron Flux as a Function of the Radial Position in the Proposed TSR-II for Various Positions of a Boral Shell in the Internal Water Reflector. Reactor geometry: 0.707 aluminum-to-water volume ratio, 40-cm-dia internal water reflector, 20-cm-thick core, 20-cm-thick external water reflector (effective).

Results of Oracle calculations with the revised value of Σ_a are compared with the UNIVAC calculations in Fig. 3.1.13. The agreement is such that control problems and the effects of various shells in the design will be investigated with the Oracle 3G3R code, and only the final results will be checked with a multigroup code.

Heat Removal Study. – The heat flux from the fuel plates will be approximately 5×10^4 $Btu \cdot ft^{-2} \cdot hr^{-1}$. To remove this a two-pass cooling system has been proposed.[4] It has previously been determined[5] that a 1000-gpm flow rate with a 40°F temperature rise of the water over the inlet water temperature would provide sufficient cooling to prevent boiling or excessive fuel plate temperatures in a reactor core with higher aluminum-to-water volume ratios. It was also stated that a larger internal reflector and a thinner core region would make conditions even better. The 17.5-in.-dia internal reflector and 5.5-in.-thick core meet

[4]The cooling system for the TSR-II is being developed by the Heat Transfer and Physical Properties Section of the ARE Division.

[5]P. Stover, USAF, private communication.

Table 3.1.2. Predicted Fast- and Thermal-Neutron Leakage from the TSR-II for 0.707 and 1.000 Aluminum-to-Water Volume Ratios and Various Core–Boral Shell Separation Distances

Core–Boral Shell Separation Distance (cm)	Fast-Neutron Leakage		Thermal-Neutron Leakage	
	$Al:H_2O$ Ratio = 0.707	$Al:H_2O$ Ratio = 1.000	$Al:H_2O$ Ratio = 0.707	$Al:H_2O$ Ratio = 1.000
0	0.1070	0.1083	0.01294	0.01322
0.5	0.1064	0.1080	0.01291	0.01325
1.0	0.1057	0.1074	0.01284	0.01318
1.5	0.1051	0.1067	0.01276	0.01306
2.0	0.1044	0.1060	0.01269	0.01300
2.5	0.1038	0.1053	0.01258	0.01291
3.0	0.1033	0.1048	0.01252	0.01285
3.5	0.1028	0.1043	0.01247	0.01276
4.0	0.1024	0.1038	0.01243	0.01271
4.5	0.1020	0.1035	0.01235	0.01267
5.0	0.1018	0.1032	0.01235	0.01264
No shell	0.1083	0.1120	0.0142	0.0169

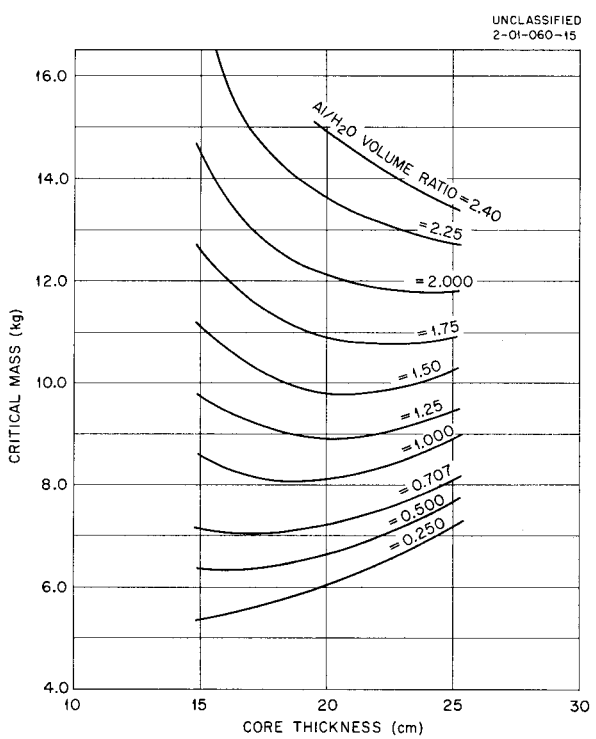

Fig. 3.1.12. Critical Mass in the Proposed TSR-II as a Function of the Core Thickness for a 44.5-cm-dia (17.5-in.-dia) Internal Water Reflector and Various Aluminum-to-Water Volume Ratios. External water reflector thickness: 20 cm.

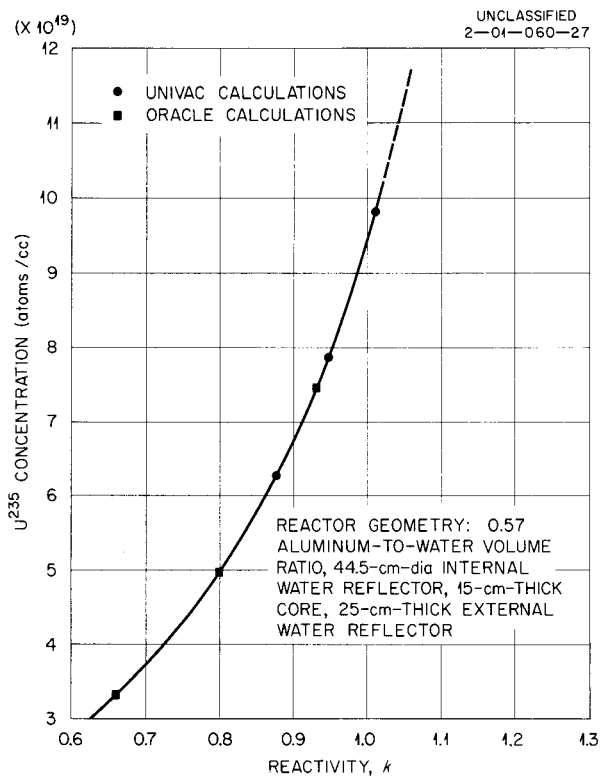

Fig. 3.1.13. Concentration of U^{235} in the Proposed TSR-II as a Function of Reactivity. Reactor geometry: 0.57 aluminum-to-water volume ratio, 44.5-cm-dia internal water reflector, 15-cm-thick core, 25-cm-thick external water reflector.

these conditions, but the larger water volume in the core dictated by the lower aluminum-to-water ratio is somewhat detrimental. It is felt that if a turbulent water flow could be maintained in each channel, adequate cooling could still be achieved with the 1000-gpm flow rate. By using a log mean flow area and assuming equal flow per channel, the Reynolds number was calculated and found to vary from 11,000 in the inner channels to 8500 in the outer channel. It appears, therefore, that sufficient latitude will exist over which to adjust flow rates experimentally in order to obtain a uniform outlet temperature and still maintain turbulent flow.

Since the fuel-element development has proceeded satisfactorily, it is planned to set up a full-scale, quarter-section dummy core with which to perform experimental flow studies for the proposed cooling system. In these studies the water flow rate in the various channels between the fuel plates will be measured. With this information and the calculated power distribution in the core, it will be possible to calculate the exit temperature that could be expected from each channel in the actual reactor. Adjustments in the flow will be made until a fairly uniform exit temperature from all channels is achieved. Experiments to determine the cooling flow required in the lead region will be conducted with the same device.

Removing the heat generated in the lead-boral-water region presents other problems. First, the lead must be canned to prevent excessive corrosion of the aluminum fuel plates. Second, the heat generation rates in the lead must be determined.

If the lead is canned, a good bond must exist between the lead and the aluminum to ensure proper heat transfer from the lead to the water.[6]

[6] At Los Alamos attempts to cool lead canned in aluminum without bonding were unsuccessful for a similar situation on the Omega West Reactor; private communication from W. F. Schaffer, Jr.

Two methods, both satisfactory, have been investigated by the ORNL Mechanical Department. One method utilizes an ultrasonic technique to clean the aluminum in the presence of molten lead. The other method employs electrolytic plating with zinc, then copper, and finally lead. Neither of these bonds has been tested in the neutron and gamma-ray fluxes to which they will be subjected in the TSR-II.

Calculation of Gamma-Ray Heating in the Lead

Calculations[7] have been carried out to determine the gamma-ray heating of the lead region around the TSR-II core. For these calculations the core was assumed to contain 9 kg of U^{235} and to have an aluminum-to-water core volume ratio of 0.57. The shield was of the size and composition shown in Fig. 3.1.14.

In the first step of the calculation the gamma-ray heating at the core-shield interface was determined. This was accomplished by first dividing the core into seven spherical-shell source regions and then by dividing the gamma-ray source spectrum from each shell into six energy groups, 0.5, 1, 2, 4, 6, and 8 Mev. The spherical-shell sources were converted to equivalent infinite plane sources, and the gamma-ray heating from each energy group within each plane source was calculated by computing the uncollided flux and using NDA buildup factors. The total gamma-ray heating was then the sum of the heating contributions from each energy group and each source plane. The heating in the first aluminum layer of the shield was then estimated by multiplying the calculated core heating from each energy group by the ratio of the aluminum and the core energy absorption coefficients for that energy. The heating in the initial layer of lead was estimated in a like manner by using the heating calculated in the aluminum and the ratio of the absorption coefficients. The assumption that the flux does not vary in going from the core through the aluminum and into the lead is quite valid for the aluminum but is rather poor for the lead.

The second step of the calculation utilized the Oracle Monte Carlo code for heat generation resulting from gamma radiation that penetrated shields with stratified slab geometries (see Secs 9.8, 9.9, and 9.10). This step yielded gamma-ray heating, as a function of initial energy and angle of incidence, in a number of arbitrary regions within the shield. To apply this information it was necessary to find the energy and angular distribution of the flux incident upon the shield.

The energy flux incident upon the shield was estimated by dividing the calculated heating at the core-aluminum interface into collided and uncollided portions in each initial energy group. The uncollided heating divided by the energy absorption coefficient for that energy group gave directly the uncollided flux for each energy group. The collided energy flux for each energy group was determined by assuming that it had a differential energy spectrum of the type given by Goldstein and Wilkins[8] for a point isotropic source after passage through one mean free path of water. This was possible, since the relative spectrum for each E_0 is nearly independent of distance from the source for a number of mean free paths. The collided flux spectrum was divided into the same energy groups as was the uncollided flux, and the sum of the collided and uncollided flux gave the total flux for each energy group penetrating the shield.

The angular distribution was determined by assuming that the uncollided flux was essentially isotropic at the infinite plane sources, and the angular dependence at the shield was determined by weighting the contribution per solid angle with the exponential attenuation with distance. To get a limiting case it was assumed that the collided flux had the same angular dependence as did the uncollided flux.

The total heating evaluated in each region in the shield by the Monte Carlo technique is tabulated in Table 3.1.3 and is shown in the form of a histogram in Fig. 3.1.15. The heating in the aluminum-water-aluminum region and in the final lead and aluminum region was not significant, compared with the heating in the other regions. The estimated heating near the core-shield interface is also shown in Fig. 3.1.15.

---

[7] These calculations were carried out by D. K. Trubey, Applied Nuclear Physics Division, and W. W. Dunn, USAF, on loan to ORNL.

[8] H. Goldstein and J. E. Wilkins, Jr., *Calculations of the Penetrations of Gamma Rays. Final Report*, NYO-3075 (June 30, 1954).

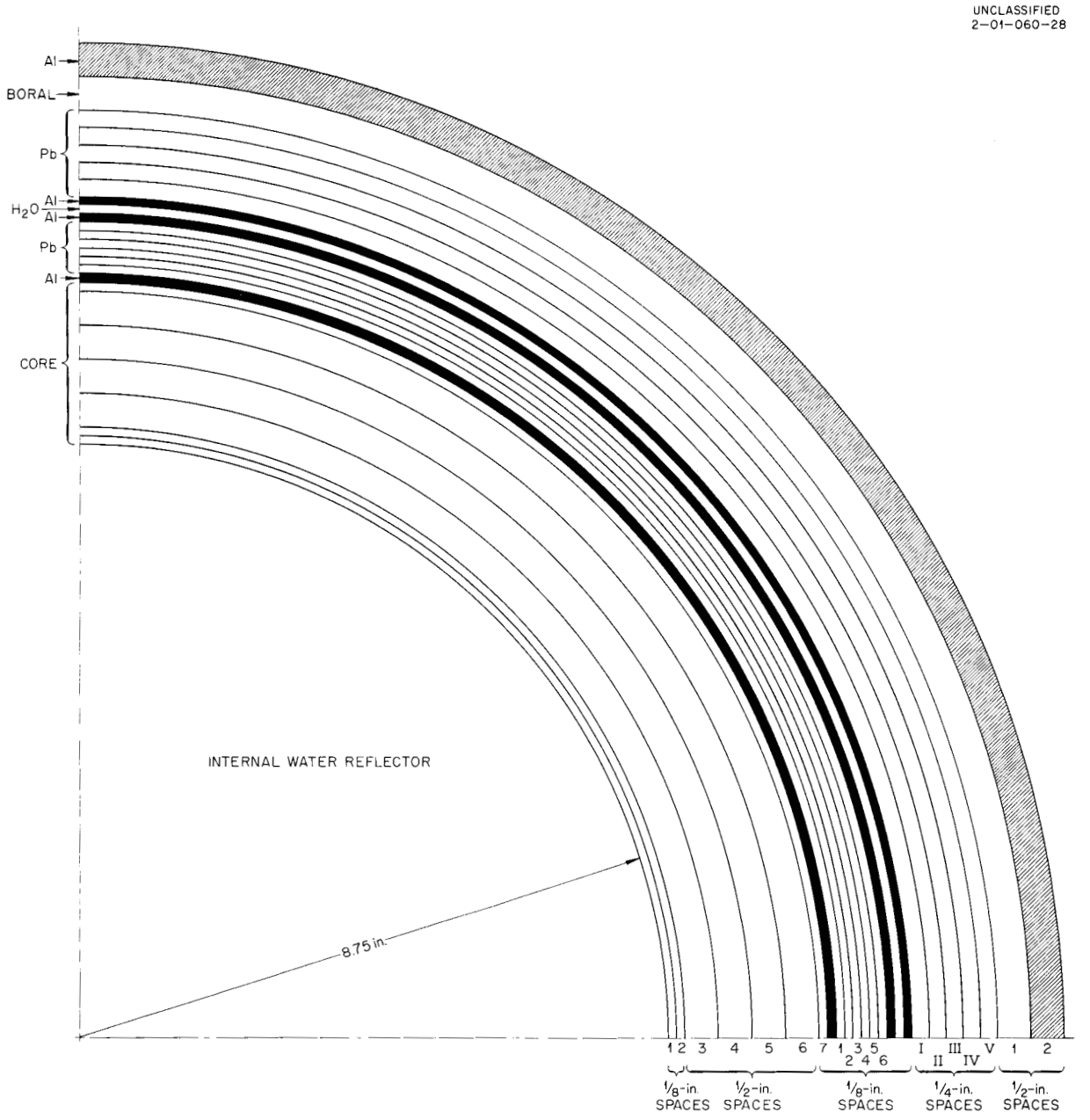

Fig. 3.1.14. Shield Configuration Used to Calculate Gamma-Ray Heating in the TSR-II.

Fuel-Element Development[9]

The fuel plates for the TSR-II will be fabricated by means of the MTR techniques and assembled into elements; however, it will be necessary to alter the shape of the elements to attain a spherical-shell core with an internal water reflector. In order to accomplish this, each plate in each element will have its own distinct size and radius of curvature. At the ends of the reactor, that is, above and below the internal reflector when the fuel elements are in a vertical geometry, there will be four pie-shaped elements consisting of plates that will increase in length with distance from the reactor axis (see Fig. 3.1.16). The

[9]The fuel element development work is being performed by the Metallurgy Division.

Table 3.1.3. Gamma-Ray Heating in the TSR-II Lead Regions (Monte Carlo Technique)

Shield Region	Heating ($w \cdot cc^{-1} \cdot Mev^{-1}$)
Al	0.197
Pb_1	1.40
Pb_2	0.594
Pb_3	0.401
Pb_4	0.280
Pb_5	0.210
Pb_6	0.174
Pb_I	0.107
Pb_{II}	0.064
Pb_{III}	0.043

arrangement of these elements around the reactor axis will be such that plates of the same size in the four elements will form nearly cylindrical shells. The other fuel elements, that is, the outer elements, will consist of plates that will decrease in length with distance from the reactor axis. The plates in these elements also will form nearly cylindrical shells whose mid-points, in this case, will be at the center of the reactor.

The fuel-element development work was divided into two phases. The first phase was concerned with establishing the correct fuel core sizes before rolling and the rolling sequence that would produce the correct final dimensions for each fuel plate. The second phase involved the mechanics of forming the correct radius of curvature in each plate and then assembling the plates into elements. The use of an aluminum alloy (type 6951), which is much harder than the conventional pure aluminum

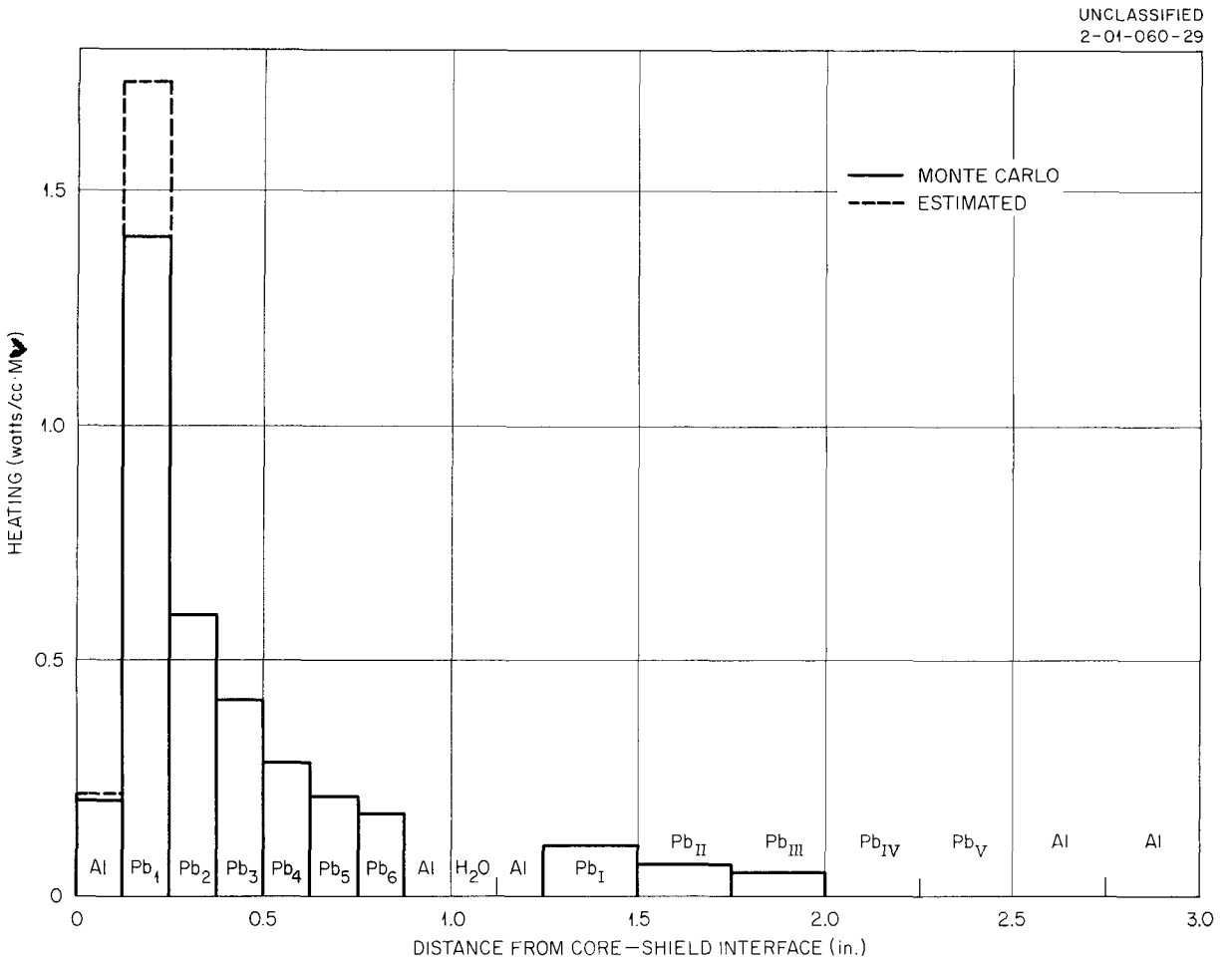

Fig. 3.1.15. Gamma-Ray Heat Generation Rates in the Proposed TSR-II Lead Shield Region as a Function of Distance from the Core-Shield Interface.

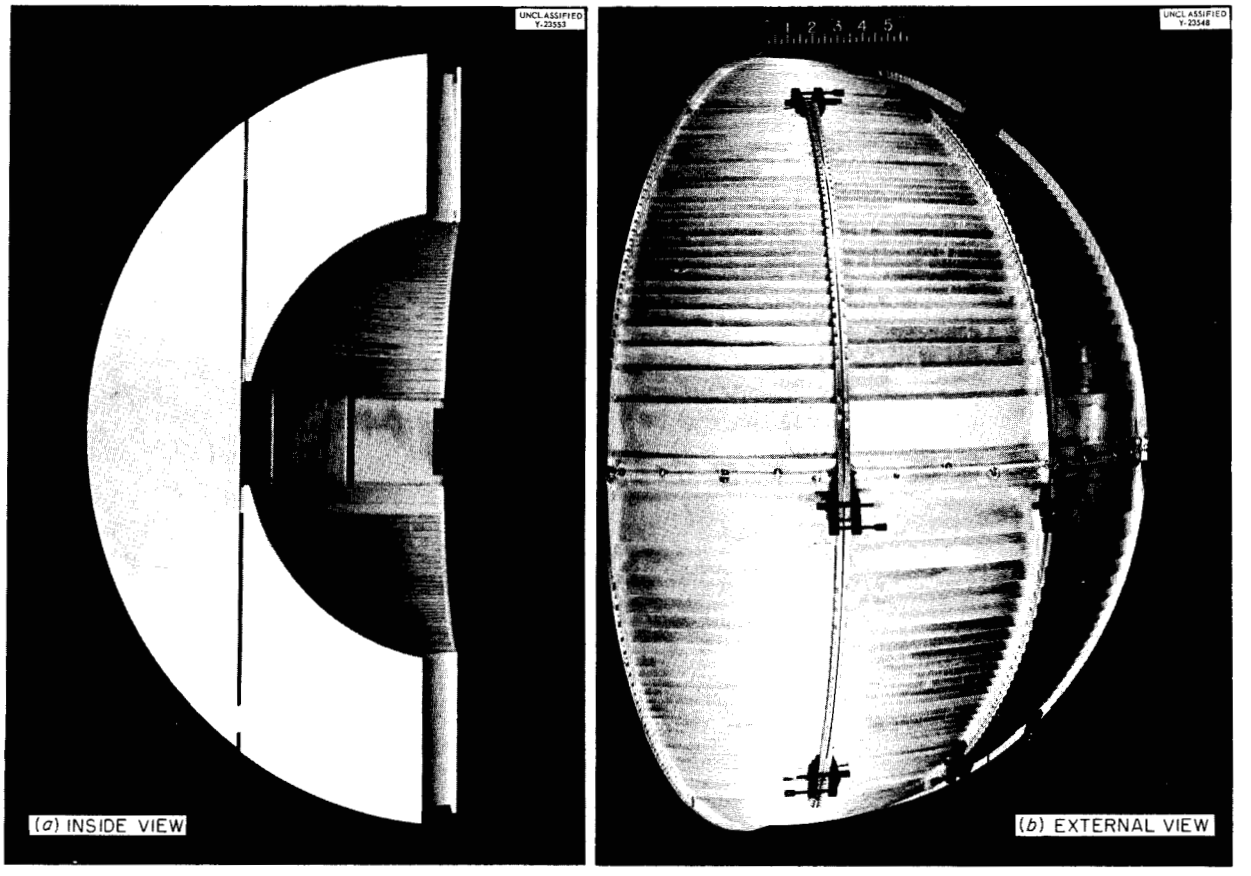

Fig. 3.1.16. Dummy Fuel Elements for the Proposed TSR-II, Assembled in a Quarter Sphere.

(type 1100), makes it feasible to use a three-roll hand roll to curve the fuel plates. The most satisfactory method of assembly tried is a combination of peening and tack-welding the plates into the side plates, as shown in Fig. 3.1.17 for one of the central elements. The elements shown in Fig. 3.1.16 are not completely satisfactory due to some variation in curvature of the longer fuel plates. A change in the design of the hand rolls has reduced this to a tolerable difference.

Control-System Studies

As mentioned previously, the TSR-II will be controlled by umbrella-shaped boron-loaded plates located in the internal water reflector. The development of this mechanism has been divided into two studies. The first study is concerned only with determining the amount of excess reactivity that can be controlled in the TSR-II. This study includes both the Oracle calculations discussed above and experimental mockup tests with the BSR. The second study is concerned with the development of a mechanism for obtaining control under normal operation and for quickly shutting down the reactor in any potentially unsafe condition.

BSR Mockup Studies.[10] – In order to obtain some experimental information with which the results of the Oracle calculations could be compared, poison plates simulating the proposed TSR-II control device were operated in a 6-in.-square water-filled hole in the center of the BSR. The fuel loading used for this experiment was as shown in Fig. 3.1.18. The control device consisted of four or eight stainless steel or boron-loaded aluminum plates mounted parallel to the sides of the aluminum can in which they were operated. A sketch of a top view of the assembly is shown in Fig. 3.1.19. On the top of the can were placed two diagonal guide rods along which angles supporting the

[10]This experiment was performed by K. M. Henry, E. B. Johnson, and J. D. Kington.

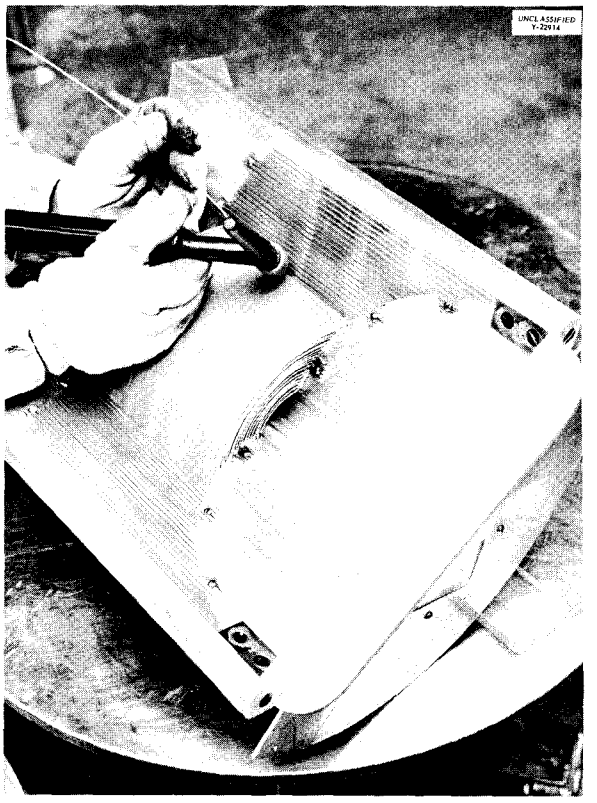

Fig. 3.1.17. Partially Assembled Central Dummy Element for the Proposed TSR-II, Showing Tack-welding Technique.

control plates were moved toward the center of the can. The size of the opening limited the normal travel of the control plates to about 1 in.

When all the eight plates shown in Fig. 3.1.19 were used, a complete shell was formed within the water region. When only four plates were used, alternate plates were removed, leaving some internal fuel areas without adjacent control plates.

The boron-loaded plates did not give any worthwhile data because the excess loading of the reactor was not sufficient to permit operation of the reactor with the plates in any position. Both solid and slotted stainless steel plates were used in two configurations. The results of these experiments are shown in Fig. 3.1.20.

Development of the Control Device.[11] – A prototype of the proposed TSR-II control mechanism shown in Fig. 3.1.2 was designed and fabricated for tests to obtain a comparison between the actual and the calculated values of the pressure required to operate the mechanism and to determine the time required for the full travel of the control plate under scram conditions. The prototype, which had a stroke of 1 in., as opposed

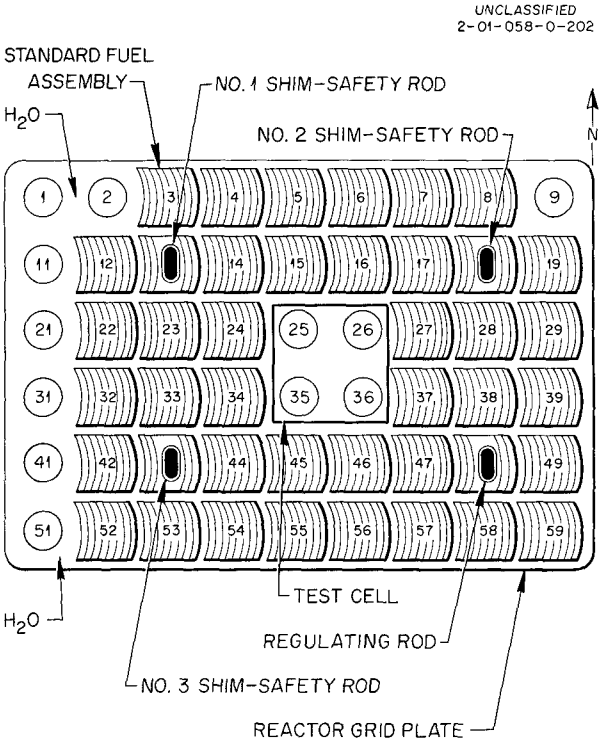

Fig. 3.1.18. BSR Loading 62B.

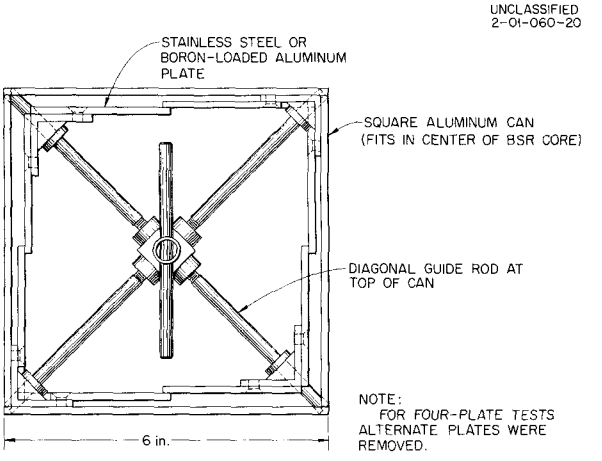

Fig. 3.1.19. Top View of Experimental Apparatus for BSF Experiments to Test Mockup of Proposed TSR-II Control-Plate Device.

[11]The controls system for the TSR-II is being developed by the Reactor Controls Group.

to the 2.5-in. stroke region, was operated by a combination of hydraulic and mechanical forces. The water pressure required to operate the mechanism was obtained by boosting the main pressure, changes in the pressure being indicated by a fast-acting pressure cell. The pressure required to operate the piston in the cylinder was indicated by a Bourdon gage. Calculations had indicated that a 66-psi line pressure should be sufficient to hold the poppet against the positioning device for normal operation; reducing the pressure below 50 psi should allow the spring force to overcome the pressure in the cylinder, and the mechanism would move away from the positioning device (in the reactor the control plates would then move toward the fuel). The actual pressures observed were 72 psi to operate the mechanism satisfactorily and less than 53 psi to permit the spring to overcome the hydraulic force.

The control-plate travel as a function of time under scram conditions was obtained by observing with an oscilloscope, which has a persistent screen, the time required for the piston and control plate to traverse a known part of its travel. The time was defined by having the control plate break an electrical contact when motion started and then make electrical contact when the desired distance had been covered. The change in contact appeared as pips on the sweep signal moving across the oscilloscope screen. The values of distance traveled as a function of time thus obtained are shown in Fig. 3.1.21, together with the same values obtained by an iterative solution of a force balance equation that was written to design the prototype. A full-scale model is being designed on the same principles.

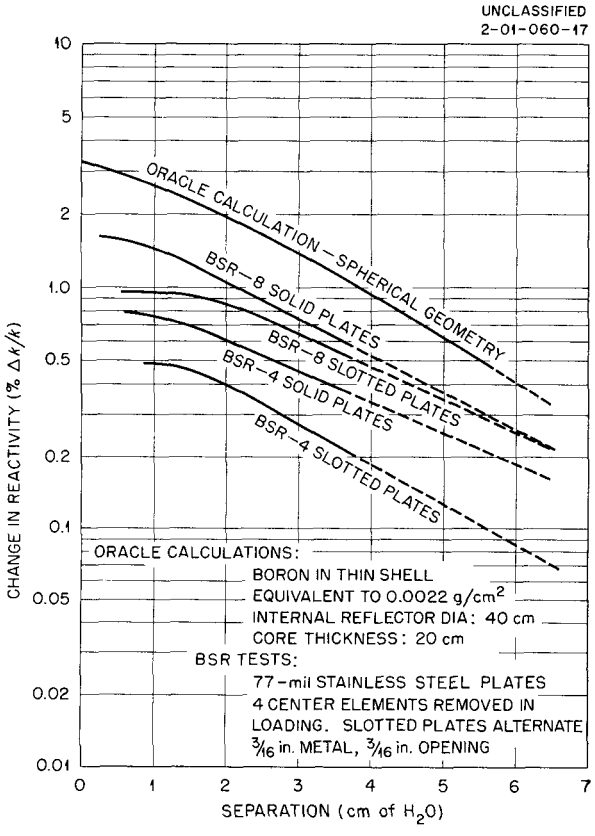

Fig. 3.1.20. Reactivity of Control Plates in an Internal Water Reflector as a Function of the Distance Between the Plates and the Inner Edge of the Core (BSR Experiment).

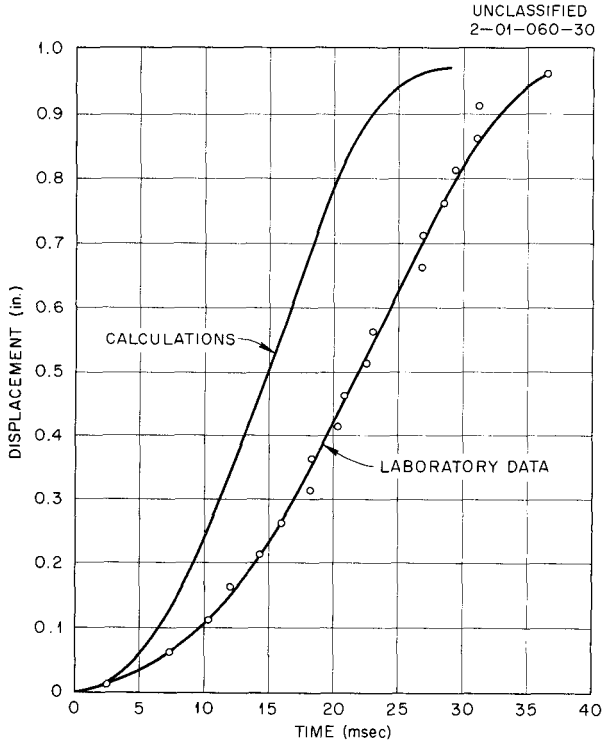

Fig. 3.1.21. Piston Displacement in Control Mechanism Test for Proposed TSR-II as a Function of Time.

Part 4

CRITICAL EXPERIMENTS

4.1. CRITICAL PARAMETERS OF AQUEOUS SOLUTIONS OF U^{235}

J. K. Fox L. W. Gilley

The series of experiments to determine the critical parameters of aqueous solutions of UO_2F_2 highly enriched in U^{235} has continued.[1] In one set of the experiments reported below, the critical parameters of unreflected and water-reflected solutions in single vessels of varying size were determined. Both cylindrical and slab-type vessels were used. In another group of experiments, similar vessels were used under special reflector conditions. In a third set the critical parameters of arrays of interacting vessels were determined. For all the experiments the U^{235} enrichment of the solutions was 93.2%.

ENRICHED U^{235} SOLUTIONS IN VESSELS OF SIMPLE GEOMETRY

A study of the conditions under which various enriched U^{235} solutions contained in aluminum and stainless steel cylinders become critical was initiated several years ago.[2] Results of experiments which extended this study to aluminum cylinders with diameters up to 30 in. were reported previously.[1] This work has now been supplemented with additional experiments performed with solutions contained in unreflected, partially water-reflected, and totally water-reflected, and totally water-reflected aluminum cylinders having diameters that ranged from 5.5 to 30 in. The solution concentrations varied from 0.532 to 0.0779 g of U^{235} per milliliter. The total water reflector was effectively infinite, while the partial water reflector was effectively infinite on the bottom and on the lateral surface to a height equal to the critical solution height. Experiments were also performed with solutions in an 8.5-in.-dia stainless steel cylinder and in an aluminum vessel that was rectangular (20 in.^{2}) in cross section. The containers used in this group of experiments had $\frac{1}{16}$-in.-thick walls, and the aluminum vessels were coated on the inside with Heresite.

All the results of the experiments in this series are presented in Table 4.1.1. It is to be noted that a few of the unreflected experiments were performed in a 9.5-ft-dia steel tank which acted as a neutron reflector.

A plot of the critical heights of the solutions in unreflected aluminum cylinders as a function of the $H:U^{235}$ atomic ratios of the solutions is shown in Fig. 4.1.1. In order to show more accurately the variation of critical height with concentration for values of concentrations near the minimum volume, the data for the 8.76- and 10-in.-dia unreflected cylinders have been replotted in Fig. 4.1.2 on an expanded scale. From these data it is seen that the concentration for a minimum critical volume of an unreflected enriched aqueous solution of UO_2F_2 in a cylindrical aluminum container is about 0.374 g of U^{235} per milliliter, corresponding to an $H:U^{235}$ atomic ratio of 66.

The data for solutions contained in totally water-reflected aluminum cylinders indicate that the minimum critical diameter for these conditions is between 5.5 and 6 in., since the solution concentrations used are near the concentration for minimum volume (for water-reflected cylinders). Also it was found that an unreflected 8.5-in.-dia stainless steel cylinder was not critical at a concentration near that for minimum volume. Then certainly an unreflected 8.5-in.-dia aluminum cylinder would not be critical; however, an unreflected 8.76-in.-dia aluminum cylinder was found to be critical. Since an unreflected 8.76-in.-dia stainless steel cylinder would also be critical, the minimum critical diameter for both unreflected stainless steel cylinders and unreflected aluminum cylinders is between 8.5 and 8.76 in.

The measured critical parameters of these experiments are obviously affected by the materials of the containing vessels, especially by the $\frac{1}{2}$-in.-thick bottom plate of the aluminum vessels. The effect of this bottom plate in unreflected systems was determined in an experiment reported below, and an appropriate correction (0.4 cm) was applied to all critical heights of unreflected aluminum cylinders reported here. The critical heights of totally water-reflected vessels were

---

[1] J. K. Fox and L. W. Gilley, *Appl. Nuclear Phys. Ann. Rep. Sept. 10, 1956*, ORNL-2081, p 61.

[2] C. K. Beck *et al.*, K-343 (April 19, 1949) (classified).

Table 4.1.1. Critical Parameters of Enriched U^{235} Solutions in Simple Geometry: With and Without Water Reflectors

Solution Container and Diameter (in.)	Solution Concentration		Critical Values		
	U^{235} (g/cc)	$H:U^{235}$ Atomic Ratio	Height (cm)	Volume (liters)	Mass (kg of U^{235})
Totally Water-reflected					
Aluminum cylinder					
5.5	0.532	44.7	*		
6	0.537	43.2	70.1	12.8	6.87
8	0.537	43.2	18.6	6.05	3.25
10	0.537	43.2	12.5	6.34	3.40
10	0.470	51.5	11.4	5.78	2.72
Partially Water-reflected					
Aluminum cylinder					
8	0.470	51.5	23.8	7.74	3.64
10	0.537	43.2	17.3	8.77	4.71
No Reflector					
Stainless steel cylinder					
8.5	0.385	63.7	*		
Aluminum cylinder					
8.76	0.532	44.7	175.0**	68.1	36.2
	0.480	50.1	202.2	78.7	37.8
	0.470	51.5	149.1	58.0	27.2
	0.437	55.4	171.6	66.8	29.2
	0.402	60.8	162.5	63.2	25.4
	0.373	66.1	159.8	62.2	23.2
	0.350	71.5	163.2	63.5	22.2
9.5	0.532	44.7	44.4**	20.3	10.8
	0.470	51.5	43.4**	19.9	9.35
10	0.537	43.2	34.9**	17.7	9.50
	0.532	44.7	34.7**	17.6	9.36
	0.480	50.1	34.8	17.5	8.40
	0.470	51.5	33.5**	17.0	7.99
	0.437	55.4	34.3	17.4	7.60
	0.402	60.8	34.1	17.3	6.96
	0.373	66.1	34.1	17.3	6.45
	0.350	71.5	34.1	17.3	6.06

*This cylinder was not critical at a height of at least 203 cm and probably could not have been made critical at any height.

**These experiments were performed inside a 9.5-ft-dia steel tank which acted as a neutron reflector; consequently, the values reported here are too low.

Table 4.1.1 (continued)

Solution Container and Diameter (in.)	Solution Concentration		Critical Values		
	U^{235} (g/cc)	$H:U^{235}$ Atomic Ratio	Height (cm)	Volume (liters)	Mass (kg of U^{235})
		No Reflector			
Aluminum cylinder					
10	0.300	83.1	34.4	17.4	5.22
	0.291	85.7	34.9	17.7	5.15
	0.0785	328	147.8	74.9	5.83
	0.0779	331	170.1	86.2	6.72
12	0.480	50.1	22.6	16.5	7.92
	0.470	51.5	22.6**	16.5	7.76
	0.437	55.4	22.7	16.6	7.25
	0.402	60.8	22.7	16.6	6.67
	0.0779	331	32.8	23.9	1.86
15	0.480	50.1	17.9	20.4	9.79
	0.0779	331	22.9	26.1	2.03
20	0.480	50.1	15.4	31.0	14.9
	0.402	60.8	15.3	31.0	12.5
	0.0791	325	18.7	37.9	2.97
20 × 20 square cross section	0.0779	331	17.9	46.2	3.60
30	0.480	50.1	13.8	62.9	30.2
	0.470	51.5	13.3**	60.0	28.2
	0.0779	331	16.3	74.3	5.79

*This cylinder was not critical at a height of at least 203 cm and probably could not have been made critical at any height.

**These experiments were performed inside a 9.5-ft-dia steel tank which acted as a neutron reflector; consequently, the values reported here are too low.

corrected by –0.7 cm, a correction which was determined in earlier experiments.

CRITICAL PARAMETERS OF ENRICHED U^{235} SOLUTIONS IN VESSELS OF SIMPLE GEOMETRY WITH SPECIAL REFLECTOR CONDITIONS

A number of experiments have been performed with enriched aqueous solutions of UO_2F_2 contained in aluminum vessels of simple geometry under a variety of reflector conditions. In particular, an evaluation was made of the effect of the 0.5-in.-thick bottom plates on the critical heights of solutions in unreflected aluminum cylinders having $\frac{1}{16}$-in.-thick walls. The procedure used was to determine the critical height as a function of bottom plate thickness (0.5 to 1.75 in.), to plot the results, and to extrapolate linearly to a bottom plate thickness of zero. The difference between the extrapolated critical height and the critical height corresponding to a 0.5-in. thickness is a measure of the effect of the bottom plate on unreflected aluminum cylinders used in these experiments. This procedure was used with 10-, 15-, 20-, and 30-in.-dia cylinders containing solutions of various concentrations. All the critical parameters for these experiments are given in Fig. 4.1.3. It is felt that there is not sufficient data to justify usual curve-fitting techniques, and, therefore, only linear curves representing the limits of the data have been drawn by inspection along with an "averaged" curve representing the data as a whole. This

averaged curve indicates that a correction of 0.4 cm should be applied to the measured critical heights. This is obviously an approximation and is subject to a relatively large percentage of error.

The effect of the ⅛-in.-thick walls of an aluminum containing vessel on the critical height of a 6-in.-thick slab of solution was also determined. In these experiments the thickness of the aluminum on the two faces was varied. The data are presented in Fig. 4.1.4.

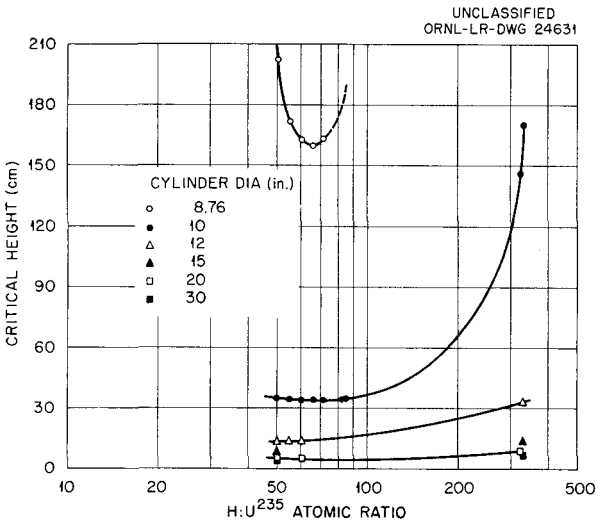

Fig. 4.1.1. Critical Height of Unreflected Enriched U^{235} Solutions Contained in Aluminum Cylinders as a Function of the $H:U^{235}$ Atomic Ratio of the Solutions.

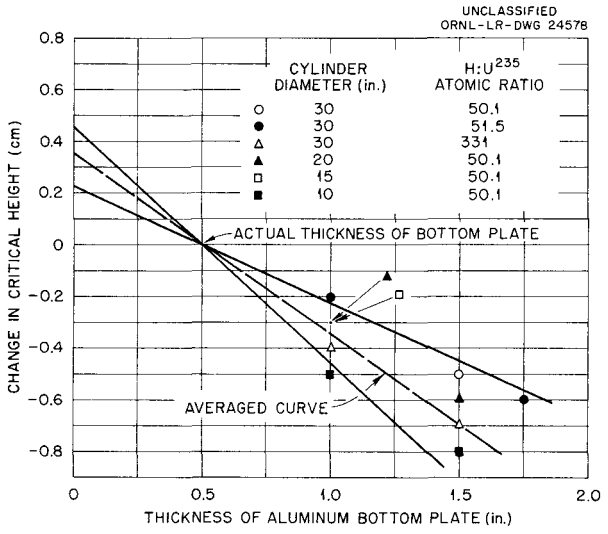

Fig. 4.1.3. Change in Critical Height of Unreflected Enriched U^{235} Solutions Contained in Aluminum Cylinders as a Function of the Thickness of the Bottom Plate of the Cylinders.

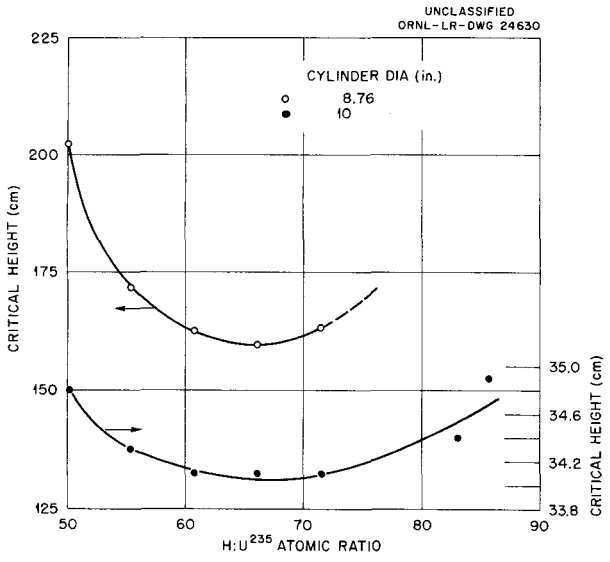

Fig. 4.1.2. Critical Height of Unreflected Enriched U^{235} Solutions Contained in Aluminum Cylinders as a Function of the $H:U^{235}$ Atomic Ratio of the Solutions. Ratios from 50 to 86.

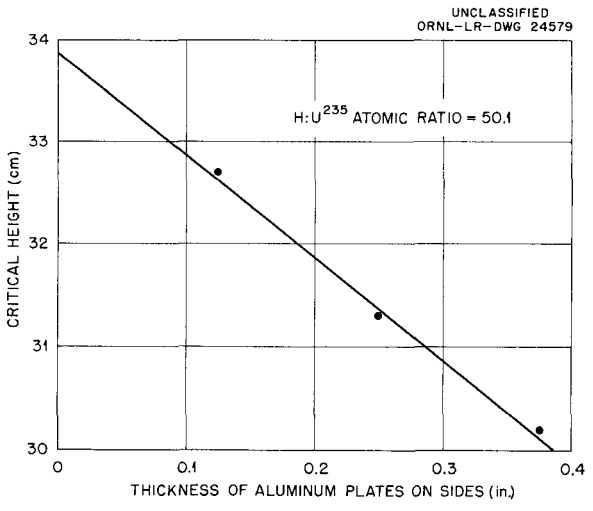

Fig. 4.1.4. Critical Height of a 6-in.-Thick Slab of Enriched U^{235} Solution Contained in an Aluminum Vessel as a Function of the Thickness of Aluminum on the Two Faces of the Slab.

A group of experiments also was performed to determine the relative neutron-reflecting properties of Plexiglas and water. A 30-in.-dia aluminum cylinder ($\frac{1}{16}$-in.-thick walls) was placed in a 9.5-ft-dia steel tank in which water could be raised to any desired height. The level of the water was adjusted to the same height as the bottom of the solution, and critical heights were measured for various thicknesses of Plexiglas replacing the water immediately beneath the cylinder. The data, presented in Table 4.1.2, indicate that, to within the accuracy of these experiments, Plexiglas and water have the same neutron-reflecting properties; however, it was discovered in later experiments (see "Critical Parameters of Arrays of Interacting Enriched U^{235} Solutions," below), in which more sensitive measurements were taken, that Plexiglas is more effective than water.

A few rather specialized experiments were performed to determine the critical height of solutions in partially water-reflected aluminum cylinders ($\frac{1}{16}$-in.-thick walls). The critical height of an otherwise totally water-reflected 10-in.-dia cylinder was measured as a function of the thickness of a void immediately above the solution. These data are presented in Fig. 4.1.5. Experimental results were also obtained from which a comparison of the critical heights of an unreflected and a one-half water-reflected 10-in.-dia cylinder could be made. In addition, data were obtained for comparing an 8-in.-dia cylinder water-reflected on one-half the lateral surface (one-half shell reflector). One experiment was performed in which the critical height was measured for an 8-in.-dia cylinder surrounded by a 6-in.-thick annular void on the lateral surface and an effectively infinite water reflector on the lateral surface outside the void. All these data are shown in Table 4.1.3.

The critical parameters of a 6-in.-thick slab of solution contained in an aluminum vessel ($\frac{1}{8}$-in.-thick walls) were determined for several

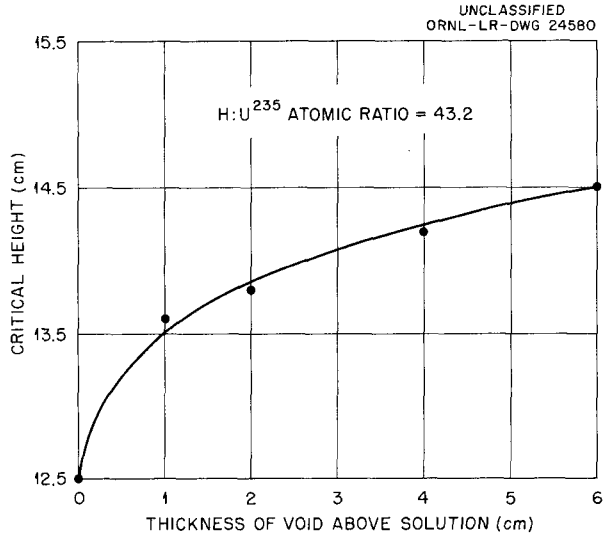

Fig. 4.1.5. Critical Height of Water-reflected Enriched U^{235} Solutions Contained in 10-in.-dia Aluminum Cylinders as a Function of the Thickness of a Void Immediately Above the Solution.

Table 4.1.2. Critical Parameters of Enriched U^{235} Solutions Contained in 30-in.-dia Aluminum Cylinders Reflected on the Bottom by Plexiglas and/or Water

Solution concentration: 0.470 g of U^{235} per cc
$H:U^{235}$ atomic ratio = 51.5

Bottom Reflector	Critical Values		
	Height (cm)	Volume (liters)	Mass (kg of U^{235})
None	13.3	60.0	28.2
Infinite water	9.8	44.6	21.0
0.5-in.-thick Plexiglas + infinite water	9.8	44.6	21.0
1.5-in.-thick Plexiglas + infinite water	9.8	44.6	21.0

reflector conditions. In one group of experiments the critical height was measured for the following reflector conditions: (1) unreflected, (2) 3-in.-thick water reflector on one face of the slab, (3) 6-in.-thick water reflector on one face of the slab, and (4) 6-in.-thick water reflector on one face of the slab plus a 6-in.-thick Plexiglas reflector on one end and the bottom of the slab. These data are presented in Table 4.1.4.

In another group of experiments, the results of which are given in Table 4.1.5, the critical height of the slab was determined as a function of the separation distance between one edge of the slab and a 48 × 48 × 6 in. slab of water placed perpendicular to and symmetrical with the edge of the solution slab. In a third group of experiments a study was made of the critical parameters of the slab as a function of the separation distance between the slab and a 5-ft-thick concrete wall parallel to the slab. In some of these experiments a sheet of boral (60 × 48 × ¼ in.) was placed adjacent to the concrete wall on the side facing the slab. In other experiments the boral sheet was placed adjacent to the slab on the

Table 4.1.3. Critical Parameters of Partially Water-reflected Enriched U^{235} Solutions Contained in Aluminum Cylinders

Water Reflector	Solution Concentration		Critical Values		
	U^{235} (g/cc)	$H:U^{235}$ Atomic Ratio	Height (cm)	Volume (liters)	Mass (kg of U^{235})
10-in.-dia Cylinders					
None	0.0785	328	147.8	74.9	5.88
4 in. thick on bottom and on one-half (180 deg) of lateral surface	0.0785	328	38.0	19.3	1.52
8-in.-dia Cylinders					
6 in. thick on one-half (180 deg) of lateral surface only	0.470	51.5	46.1	15.0	7.05
6 in. thick over entire lateral surface	0.470	51.5	25.3	8.2	3.85
Effectively infinite water reflector outside 6-in.-thick void over entire lateral surface	0.470	51.5	66.4	21.6	10.2

Table 4.1.4. Critical Parameters of a 6-in.-thick Slab of Enriched U^{235} Solution Under Various Reflector Conditions

Solution concentration: 0.779 g of U^{235} per cc
$H:U^{235}$ atomic ratio = 331

Reflector	Critical Values		
	Height (cm)	Volume (liters)	Mass (kg of U^{235})
None	121.5	221.1	17.2
3 in. of water on one face	34.5	62.8	4.89
6 in. of water on one face	33.7	61.3	4.78
6 in. of water on one face; 6 in. of Plexiglas on one end and bottom	30.5	55.5	4.32

Table 4.1.5. Critical Parameters of a 6-in.-thick Slab of Enriched U^{235} Solution Perpendicular to and at Various Distances from a 6-in.-thick Slab Water Reflector

Solution concentration: 0.0791 g of U^{235} per cc
$H:U^{235}$ atomic ratio = 325

Separation Distance (in.)	Critical Values		
	Height (cm)	Volume (liters)	Mass (kg of U^{235})
1.1	100.8	183.5	14.5
5.1	105.6	192.2	15.2
15.6	109.6	199.5	15.8
42.6	111.3	202.6	16.0
∞	111.3	202.6	16.0

side facing the concrete wall. The critical height of the solution slab as a function of the separation distance from the concrete wall is plotted in Fig. 4.1.6. Placing the boral sheet adjacent to the concrete wall reduced the critical height somewhat, the difference becoming less as the separation increased. This was due, at least partly, to the smaller fractional solid angle subtended by the boral at larger separations.

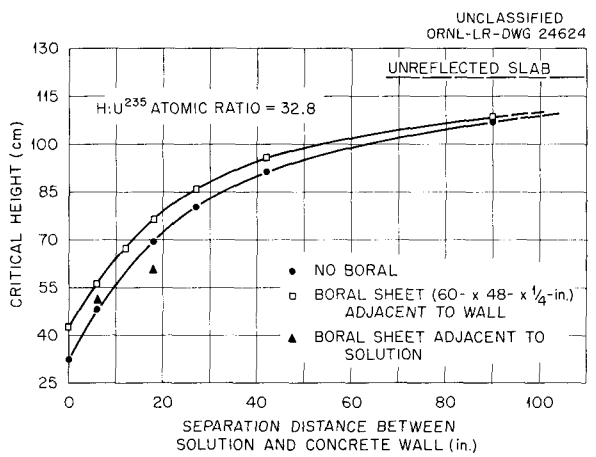

Fig. 4.1.6. Critical Height of a 6-in.-Thick Slab of Enriched U^{235} Solution Contained in an Aluminum Vessel as a Function of the Distance from a 5-ft-Thick Concrete Wall: With and Without Boral Adjacent to the Wall or Solution.

CRITICAL PARAMETERS OF ARRAYS OF INTERACTING ENRICHED U^{235} SOLUTIONS

Interacting Parallel Slabs

The critical parameters of systems of parallel 3- and 6-in.-thick slabs of solutions contained in type 2S aluminum vessels 4 ft wide and 5 ft high were determined. The thickness of the lateral walls of the containers was 0.125 in., and wall distortion was minimized by ¼-in.-dia tie rods welded in place on 12-in. centers. In all plots of the data obtained in this series, the separation distances include the wall thicknesses of the containing vessels.

In one group of experiments three parallel 3-in.-thick slabs were separated equally, and the common critical height was measured for various distances between the slabs. The slab solution had an $H:U^{235}$ atomic ratio of 337. Both unreflected and water-reflected systems were used; however, it should be pointed out that the unreflected experiments were performed in a 9.5-ft-dia steel tank which, as is noted below, acted as a neutron reflector. The water-reflected slabs were reflected to the height of the fuel; that is, there was no top reflector. The critical heights measured in these experiments are plotted as a function of the separation distance between the slabs in Fig. 4.1.7. Corresponding data for two water-reflected slabs are also shown for comparison.

In another group of experiments the effect of replacing some of the water reflector in the two-slab system with Plexiglas was determined. In all cases the Plexiglas was placed adjacent to the inner or outer lateral faces of the slabs. Use of Plexiglas resulted in a lowering of the critical height, which indicates that Plexiglas is superior to water as a moderator or reflector. The results of these experiments are given in Table 4.1.6.

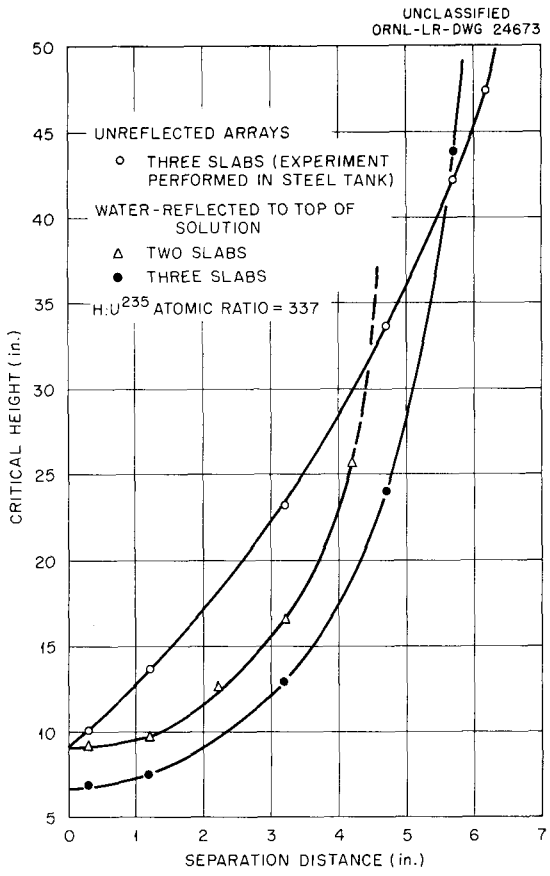

Fig. 4.1.7. Critical Height of Equally Spaced 3-in.-Thick Slabs of Enriched U^{235} Solution as a Function of the Distance Between the Slabs (Aluminum Vessels).

Since it was known that the 9.5-ft-dia steel tank in which the totally water-reflected experiments were performed would act as a neutron reflector and thus affect the results of unreflected experiments to some extent, it was decided to determine the magnitude of the effect. Thus a series of experiments was performed with two- and three-slab arrays, both in the reflector tank and outside the tank. The results, which are presented in Table 4.1.7, verified that the tank had an appreciable effect on the measured critical heights, and unreflected arrays were subsequently performed outside the tank.

A series of experiments was performed in which two parallel 3-in.-thick slabs were placed in water at an $H:U^{235}$ atomic ratio of 50.1. The data are presented in Fig. 4.1.8. The graph shows clearly that the interacting slabs are essentially isolated when separated by 12 in. of water, even though the solid angle between the reactors is large. This result agrees with earlier data obtained by using cylinders.[3] The critical height for two unreflected slabs is plotted in Fig. 4.1.9.

A group of unreflected experiments was performed with a nominally 6-in.-thick slab of solution ($H:U^{235}$ atomic ratio = 337) in various combinations with 3-in.-thick slabs. In one series, two 3-in.-thick slabs were placed adjacent to each other to mock up a 6-in.-thick slab, and the common critical height of the two 6-in.-thick slabs was studied as a function of their separation distance. The same experiment was performed by using a 6-in.-thick slab and one 3-in.-thick slab. In another experiment a 3-in.-thick slab was placed on each side of the 6-in.-thick slab at equal distances. The results of all these experiments are plotted in Fig. 4.1.10.

In order to investigate the dimensional uniformity of the nominally 3-in.-thick slabs, one series of experiments was performed in which some of the slabs were interchanged. Plots of the resulting critical heights in Fig. 4.1.10 show that the difference in thickness was sufficiently large to affect the data.

Two interacting 6-in.-thick slabs with a 6-in.-thick water reflector on the two outer faces only were studied at $H:U^{235}$ atomic ratios of 254 and 325. The data are plotted in Fig. 4.1.11. The variation of the common critical height with separation is roughly equivalent to that obtained for an unreflected system (see, e.g., the lower curve in Fig. 4.1.12), the effect of the outside reflector being mainly an increase in individual slab reactivity.

Interacting Nonparallel Slabs

The interaction of unreflected slabs was further studied in a series of experiments in which two slabs were used to form T- and L-shaped assemblies. The common critical height as a function of the separation distance between the two arms of each assembly is shown in Fig. 4.1.13. The data for two parallel 6-in.-thick slabs at an $H:U^{235}$ ratio of 337 are also plotted for purposes of comparison.

---

[3] J. K. Fox and L. W. Gilley, *Critical Mass Studies, Part IX*, ORNL-2367 (to be published).

Table 4.1.6. Critical Parameters of Two 3-in.-thick Slabs Reflected by Plexiglas and/or Water

Solution concentration: 0.0763 g of U^{235} per cc
$H:U^{235}$ atomic ratio = 337

Reflector*	Separation Distance** (in.)	Critical Values		
		Height (in.)	Volume (liters)	Mass (kg of U^{235})
Water	2.2	12.63	59.1	4.51
	4.2	25.63	120	9.14
Water plus a 1-in.-thick Plexiglas plate (area = 12 × 48 in.) against inner surface of each slab	2.2	11.94	55.8	4.26
Water plus a 1-in.-thick Plexiglas plate (area = 22 × 48 in.) against inner surface of each slab	4.2	22.11	103	7.89
Water plus a 1-in.-thick Plexiglas plate (area = 22 × 48 in.) against outer surface of each slab	4.2	22.47	105	8.02

*Water reflector was always to the height of the fuel, with no top reflector.
**Includes wall thicknesses of containers.

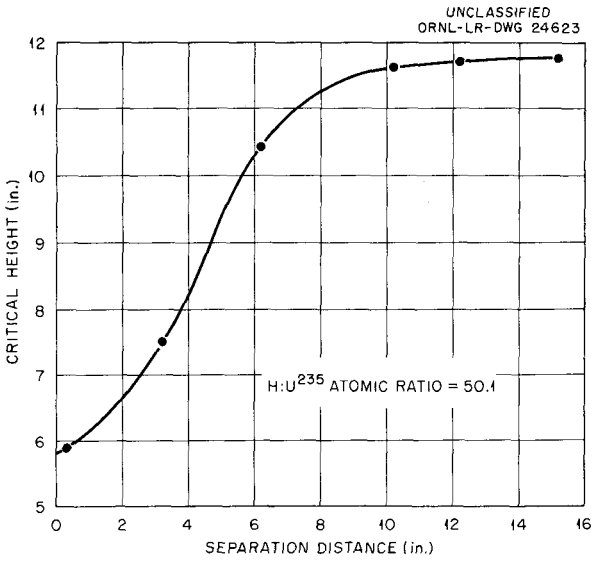

Fig. 4.1.8. Critical Height of Two Water-reflected (Except at Top), Parallel Slabs of Enriched U^{235} Solution as a Function of the Distance Between the Slabs (Aluminum Vessels).

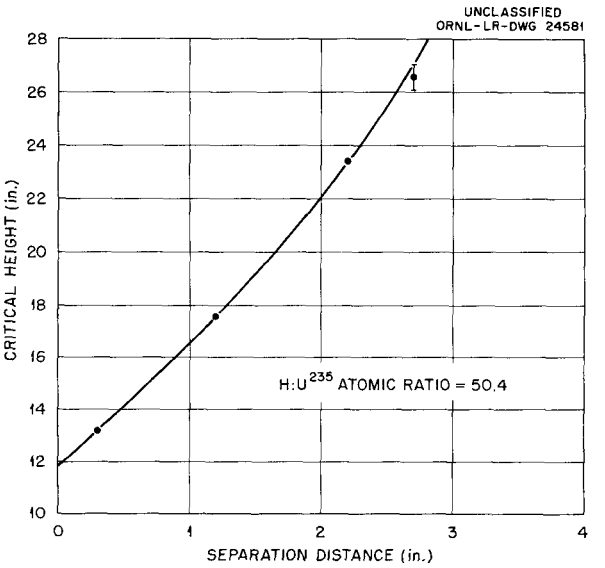

Fig. 4.1.9. Critical Height of Two Unreflected, Parallel 3-in.-Thick Slabs of Enriched U^{235} Solution as a Function of the Distance Between the Slabs (Aluminum Vessels).

Table 4.1.7. Comparison of Critical Parameters of Unreflected Slab Arrays of Enriched U^{235} Solutions to Show Effect of 9.5-ft-dia Steel Tank

Description of Array	Separation Distance (in.)	Solution Concentration		Critical Values		
		U^{235} (g/cc)	$H:U^{235}$ Atomic Ratio	Height (in.)	Volume (liters)	Mass (kg of U^{235})
Experiments Performed Inside Tank						
One 6-in.-thick[a] slab and one 3-in.-thick slab	6.2	0.0792	337	17.74	125	9.50
	12.2			22.91	161	12.3
	18.2			26.89	189	14.4
	30.2			32.72	229	17.5
	∞			39.80	279	21.2
Two 3-in.-thick slabs	0.3	0.480	50.1	12.54	58.7	28.2
	1.2			16.8	~79	~38
	3.2			*b*		
Experiments Performed Outside Tank						
One 6-in.-thick slab and one 3-in.-thick slab	2.2	0.0792	337	12.75	88.8	6.77
	6.2			17.55	122	9.32
	15.2			25.91	180	13.8
	30.2			36.41	254	19.4
	48.2			44.82	312	23.8
	∞			51.87	362	27.6
Two 3-in.-thick slabs	0.3	0.481	50.4	13.13	61.5	29.6
	1.2			17.53	81.9	39.4
	2.2			23.4	109	52.4
	2.7			26–27[c]	~124	~60

[a]One 6-in.-thick slab mocked up with two adjacent 3-in.-thick slabs.
[b]Subcritical; probably subcritical even at an infinite height.
[c]Extrapolated from an actual solution height of 24.7 in.

Interacting Cylinders

The data on interacting cylinders has been extended beyond those previously reported,[3] the interaction between two 10-in.-dia aluminum cylinders having been studied in some detail. A series of experiments was performed with unreflected cylinders containing solutions that varied in $H:U^{235}$ atomic ratios from 49.2 to 328. A series was also performed in which two interacting cylinders contained solutions that differed in concentrations. All these data are presented in Fig. 4.1.14, along with data reported earlier[4] for two unreflected cylinders containing a solution with an $H:U^{235}$ atomic ratio of 329. The data for solutions with $H:U^{235}$ atomic ratios of 325 and 328 are shown on the same curve, since the effect of the difference in concentration is probably within the experimental error. The difference between the new curve and that from K-406 is felt to be mainly due to the reflector tank present in the earlier experiments.

The data for two interacting cylinders, one of which contains a solution with an $H:U^{235}$ atomic ratio of 50 and the other a solution with a ratio of 328, show that the common critical height is very close to the critical height of two cylinders, each of which contains a solution with an $H:U^{235}$

[4]D. Callihan *et al.*, K-406 (Nov. 28, 1949) (classified).

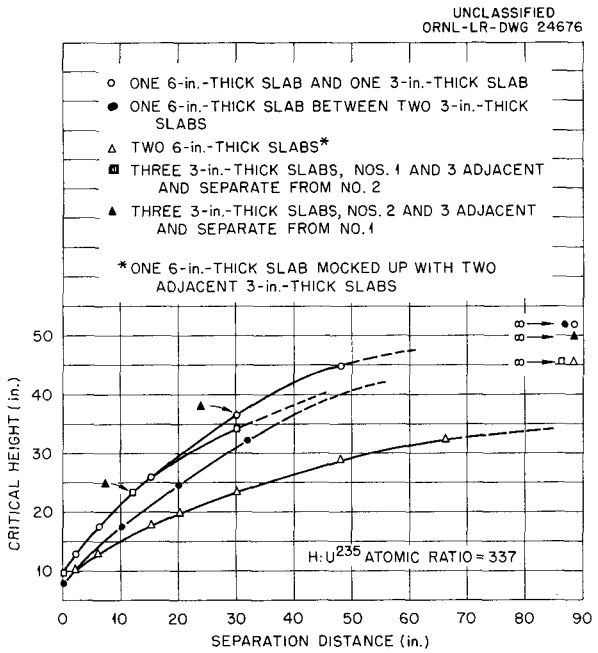

Fig. 4.1.10. Critical Height of Unreflected Arrays of Interacting Parallel 3-in.-Thick Slabs of Enriched U^{235} Solution as a Function of the Distance Between the Slabs (Aluminum Vessels).

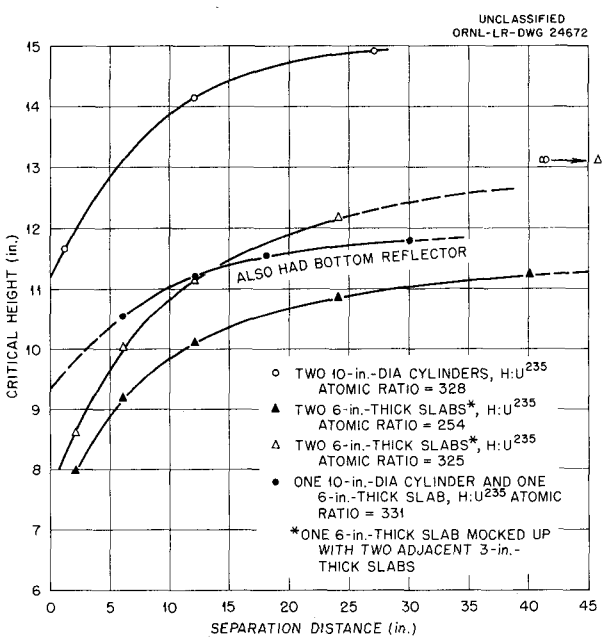

Fig. 4.1.11. Critical Height of Partially Water-reflected Arrays of Interacting Vessels of Enriched U^{235} Solutions as a Function of the Separation Distance Between the Vessels: Water Reflector on Sides Opposite the Interacting Surfaces.

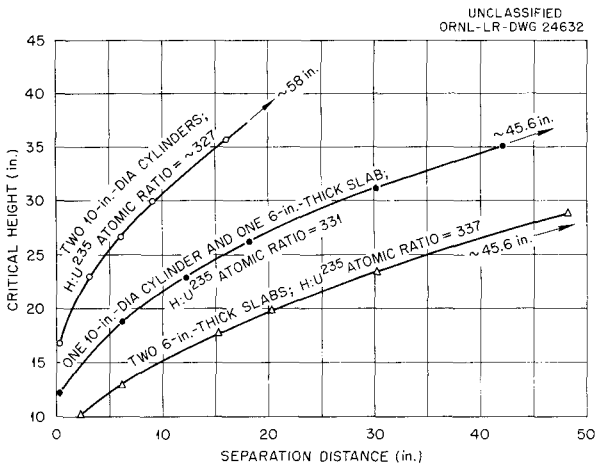

Fig. 4.1.12. Critical Height of Unreflected Arrays of Interacting Vessels of Enriched U^{235} Solutions as a Function of the Separation Distance Between the Vessels.

atomic ratio of 50. In one set of experiments, the two atomic ratios were 49 and 83. Data obtained in experiments with unreflected single 10-in.-dia cylinders (Table 4.1.1) indicate that the critical height of a solution having an $H:U^{235}$ atomic ratio of 49 is very nearly the same as in one having a ratio of 83, since the atomic ratio yielding a minimum critical volume is about 65.

Three experiments were also performed in which the cylinders had half shells of reflector water $3\frac{1}{2}$ in. thick on the sides opposite the interacting surfaces. The results are shown in Fig. 4.1.11.

The study of arrays of seven interacting aluminum cylinders[3] also has been extended to include data for 5-in.-dia cylinders at an $H:U^{235}$ atomic ratio of 50. As shown in Fig. 4.1.15, unreflected hexagonal arrays become infinitely high cylinders at about a 2-in. separation. Water-reflected arrays require about a 4.6-in. separation. A line of seven water-reflected cylinders has an infinite height at about a 3.5-in. separation. Removal of one of the seven cylinders in line has little effect at a separation of 2 in. Hence an infinite plane of cylinders at a 3.5-in. separation probably would not be critical.

Interacting Slabs and Cylinders

The critical parameters for an interacting 6-in.-thick slab and a 10-in.-dia cylinder have been studied for two reflector conditions. The common critical heights of two unreflected 10-in.-dia

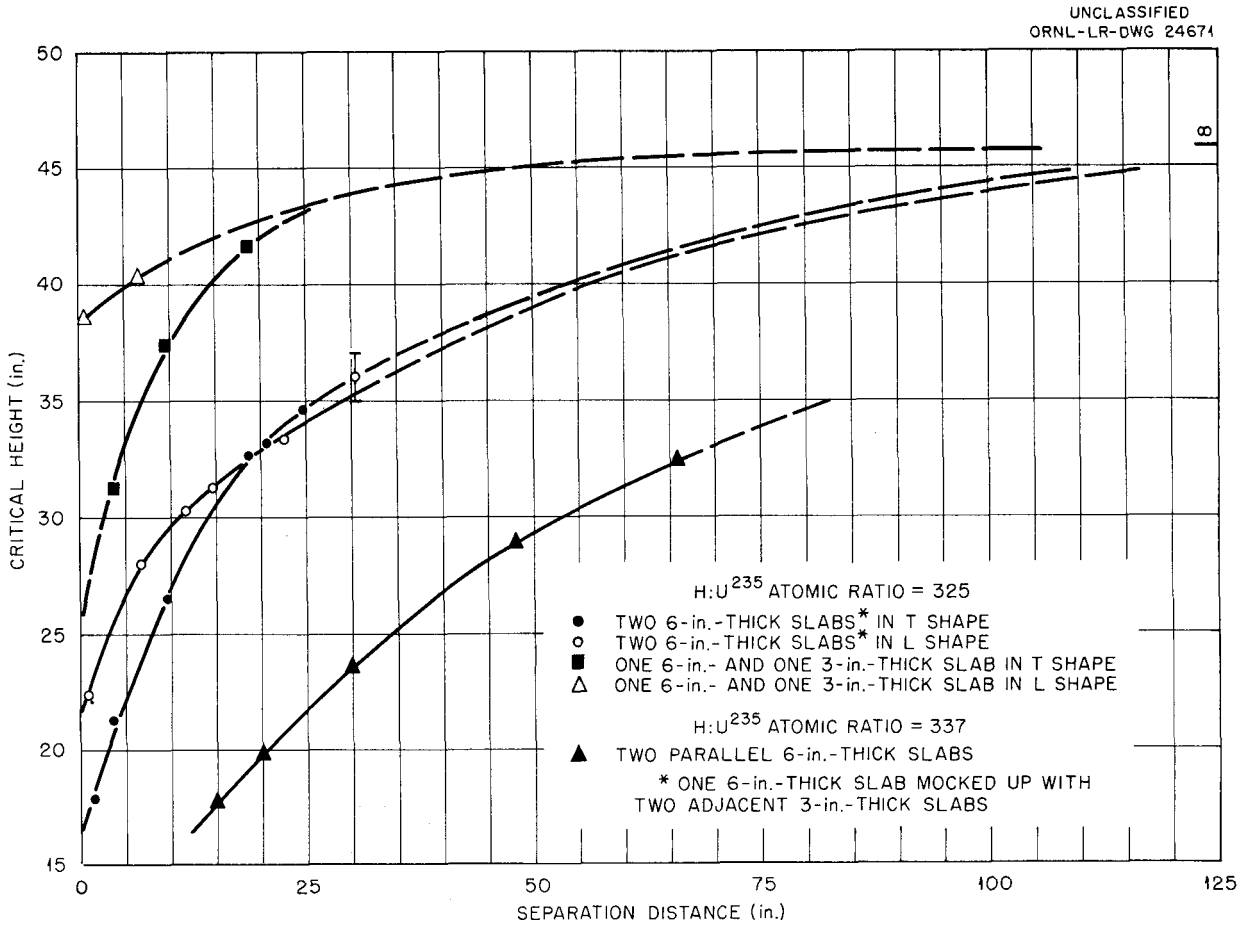

Fig. 4.1.13. Critical Height of Unreflected Arrays of Interacting Nonparallel 3-in.-Thick Slabs of Enriched U^{235} Solution as a Function of the Distance Between the Slabs (Aluminum Vessels).

cylinders, of two unreflected 6-in.-thick slabs, and of one unreflected 10-in.-dia cylinder combined with one unreflected 6-in.-thick slab, all containing solutions with approximately the same $H:U^{235}$ atomic ratio, are shown in Fig. 4.1.12. The curve for the cylinder-slab combination lies between the curves for the two other systems but is somewhat closer to that for the two slabs, since they are the more reactive vessels. Some data were obtained for the slab-cylinder combination reflected on the back sides and the bottom (see Fig. 4.1.11). For large separation distances the bottom reflector was sufficient to lower the critical height of the slab-cylinder combination below that for two slabs reflected on the back sides only (also shown in Fig. 4.1.11).

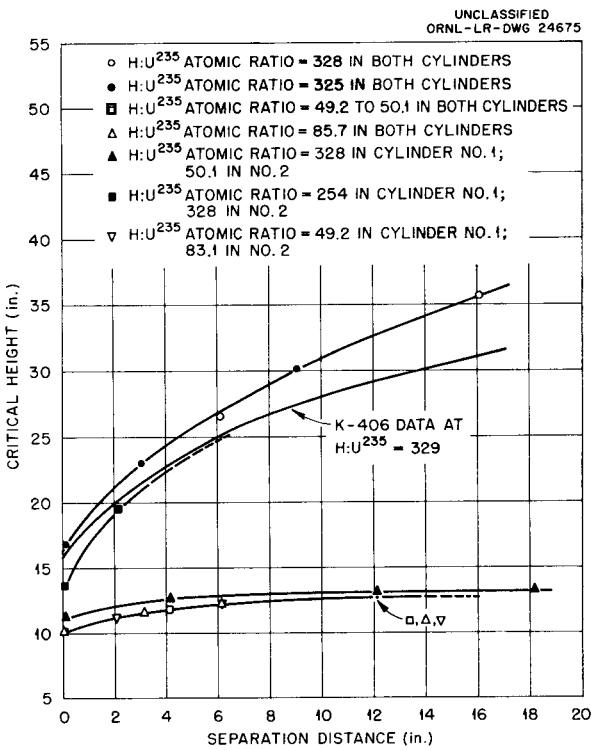

Fig. 4.1.14. Critical Height of Two Unreflected Interacting 10-in.-dia Cylinders Containing Enriched U^{235} Solution as a Function of the Distance Between the Cylinders.

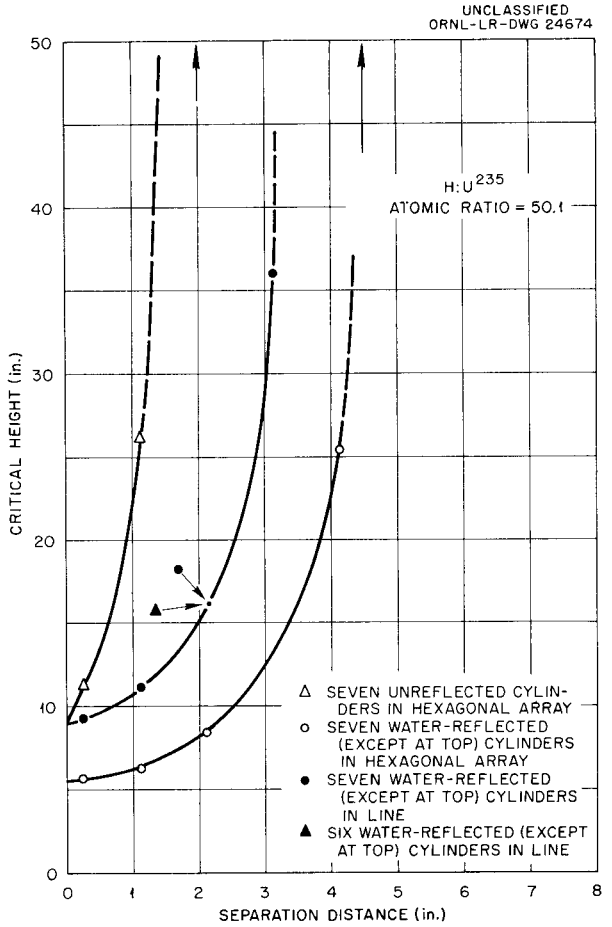

Fig. 4.1.15. Critical Height of Arrays of 5-in.-dia Cylinders Containing Enriched U^{235} Solution.

4.2. DETERMINATION OF UNREFLECTED REACTOR PARAMETERS

R. Gwin

An experimental program designed to provide suitable data on unreflected reactors for theoretical analysis is in progress.[1] Critical volumes and stable reactor periods in cylindrical and parallelepipedal geometries have been measured for aqueous solutions of uranyl fluoride, the U^{235} enrichment being 93.2%. The solution density was 1.0947 g/cm^3, corresponding to a U^{235} density of 0.0764 g/cm^3 and an H:U^{235} atomic ratio of 331.

Most theoretical calculations of unreflected reactors introduce the concept of geometric buckling which, for criticality, must be equated to a material buckling calculated from microscopic cross sections and/or experimentally determined slowing-down kernels. In analyses of unreflected reactors by the diffusion theory the boundary condition at the surface of the reactor may be approximated by at least two methods. In one, referred to as the "extrapolated end-point" method, the flux is assumed to go to zero at some fixed distance beyond all reactor surfaces (plane or convex).[2] In the other, referred to as the "current" method, the net return of neutrons into the reactor at its surface is set equal to zero. Although the latter condition is certainly correct on the basis of diffusion theory, there is, at the present time, some question as to which method is more properly applicable. In the analyses of the experimental data given below both methods have been used. Values of B^2 obtained by the two methods differ by about 15%.

The experimental data were first corrected for the neutron-reflector effect of the aluminum walls of the reactor vessels. This was determined by measuring the effect on the critical heights of the thickness of the aluminum plate on the bottom of various reactors (see Sec 4.1). The resulting changes in height were found to be linear as the aluminum thickness was varied between 0.5 and 1.5 in. A correction for the $\frac{1}{16}$-in.-thick lateral walls was made by assuming that the reflector savings were also linear for smaller thickness. The indicated correction to the heights for the 0.5-in.-thick bottom was +0.4 ± 0.1 cm and that to the diameters was +0.1 cm. Corrections were made to the observed stable reactor periods in the same way. The precision of the critical solution height measurements is about ±0.1 cm. Each of these two uncertainties in the critical dimensions gives a maximum error in B^2 of approximately 1%. Errors due to nonuniform cross sections of the reactors are unknown but are considered to be small. During the course of the experiments the U^{235} concentration of the solution was increased slightly by evaporation of water; consequently, control experiments showed an additional maximum variation in B^2 of about 0.5%. The solution temperature was maintained at 77 ± 1°F from day to day, and during an experiment the variation was less than 0.5°F. The effect of neutrons reflected by room walls and equipment was minimized by the location of the reactor vessel and is believed to be small. The period measurements were reproducible to within 5% in reactivity measured in cents.

The analysis of the experiments is based on the following relations (the notation used throughout this section is that of Glasstone and Edlund,[3] and the subscript 0 refers to the value of the term at critical):

$$k_{\text{eff}} = (1 - \beta)\, kK_p(B) + \beta k K_d(B) \,, \tag{1}$$

where K_p and K_d are the nonleakage probabilities for prompt and delayed neutrons, respectively; and

$$B^2 = B^2_{(xy)} + B^2_h \,, \tag{2}$$

$$\frac{\sum \beta_i/(1 + \lambda_i T)}{\Delta h} = 2CB_{h_0} \left[\frac{\partial B_h}{\partial h}\right]_{h=h_0} \,, \tag{3}$$

$$C = \frac{(1-\beta)\left[\dfrac{\partial K_p(B)}{\partial B_h}\right]_{h=h_0} + \left[\dfrac{\beta \partial K_d(B)}{\partial B_h}\right]_{h=h_0}}{2B_{h_0} K_d(B)} \,. \tag{4}$$

[1] R. Gwin, *Appl. Nuclear Phys. Ann. Rep. Sept. 10, 1956*, ORNL-2081, p 84.

[2] A discussion of this topic is given by B. Davison, *Neutron Transport Theory*, sec 8.3, p 97, Clarendon Press, Oxford, 1957.

[3] S. Glasstone and M. C. Edlund, *The Elements of Nuclear Reactor Theory*, Van Nostrand, New York, 1952.

The two methods of considering the boundary condition of interest here are expressed by

$$\phi(r + d) = 0 \tag{5}$$

and

$$[\phi + (\nabla\phi)_n d]_{\text{boundary}} = 0 \ . \tag{6}$$

With the use of Eqs. 5 and 6 the relations for B_h are, respectively,

$$B_h = \frac{\pi}{h + 2d} \ , \tag{7}$$

$$B_h = \frac{\pi}{h + (2\tan^{-1} B_h d/B_h)} \ . \tag{8}$$

The value of d in Eqs. 7 and 8 was adjusted to minimize the standard deviation of B^2 from its mean. The best values were 2.6 cm in Eq. 5, by the extrapolated end-point method, and 3.7 cm in Eq. 6 by the current method. These values of d and the corresponding values for B_h, $\partial B_h/\partial h$, and

$$\frac{\sum \beta_i/(1 + \lambda_i T)}{\Delta h}$$

were used in Eq. 3 to determine C, a constant for all reactor vessels. The expressions used for $K_p(B)$ and $K_d(B)$ were

$$K_p(B) = \frac{e^{-l^2B^2}}{(1 + l_1^2B^2)(1 + l_2^2B^2)^2(1 + L^2B^2)}$$

and

$$K_d(B) = \frac{1}{(1 + \tau_d B^2)(1 + L^2B^2)} \ ,$$

in which L is the thermal diffusion length and τ_d is the age of delayed neutrons.

The constants l^2, l_1^2, and l_2^2 of the first expression were derived by Trubey *et al.* (see Sec 8.10) to be 1, 26.27, and 2.26 cm^2, respectively, for a fission neutron source in pure water. In this analysis, however, l_1 and τ_d were chosen to fit the experimental data.

The critical dimensions, the term

$$\frac{\sum \beta_i/(1 + \lambda_i T)}{\Delta h} \ ,$$

and the values of B^2 and C derived by the two methods are shown in Table 4.2.1. The properties

Table 4.2.1. Critical Kinetic Data for Unreflected Cylinders and Parallelepipeds and the Derived Values for B^2 and C

UO_2F_2 solution density, 1.0947 g/cm^3; U^{235} density, 0.0764 g/cm^3; H:U^{235} atomic ratio, 331; U^{235} enrichment, 93.2%

Reactor Cross Section	Critical Height (cm)	$\sum \frac{\beta_i}{1 + \lambda_i T} \times 10^4 / \Delta h$ (cm^{-1})	B^2 (cm^{-2}) Extrapolated End-Point Method, $d = 2.6$ cm	B^2 (cm^{-2}) Current Method, $d = 3.7$ cm	C (cm^2) Extrapolated End-Point Method, $d = 2.6$ cm	C (cm^2) Current Method, $d = 3.7$ cm
Cylinders						
25.5-cm-dia*	170.1	0.77	0.02489	0.02135	21.1	21.2
30.6-cm-dia	32.8	60	0.02492	0.02194	16.7	19.3
38.2-cm-dia	22.9	151	0.02478	0.02197	17.0	20.1
51.0-cm-dia	18.7	220	0.02460	0.02176	15.2	18.2
76.3-cm-dia	16.3	303	0.02483	0.02168	15.3	18.3
Parallelepipeds*						
15.3 × 121.5 cm	116.6	2.2	0.02476	0.02167	20.1	21.2
50.9 × 50.9 cm	17.9	247	0.02477	0.02186	15.4	18.5
Average values			0.02479	0.02174	17.3	19.5

*The dimensions of these vessels were slightly irregular.

of delayed neutrons reported by Keepin *et al.*[4] were used in the calculations.

The results of calculations in which the boundary conditions are applied by either method agree with the critical data within experimental error. The fit of the analysis by the current method to the kinetic data is at the limit of experimental error, while for the extrapolated end-point method the fit is well outside the experimental error. It should be pointed out, however, that if the data obtained in the vessels which have slight dimensional irregularities are omitted from the analysis, the results by both methods fit the data within experimental error. However, this is not considered a valid omission since the values of the geometric bucklings are consistent with the average. Thus some uncertainty in the choice of analytical methods still exists.

The resulting values for the constant l_1^2, the ages (to thermal) of delayed and prompt neutrons, and the effective fraction of delayed neutrons are given in Table 4.2.2. For these calculations k_∞' was taken to be 1.79 and L^2 to be 1.2 cm^2.

The kernel used by Trubey (see Sec 8.10) gives an age to thermal of 31.8 cm^2 for a fission source in pure water.

Table 4.2.2. Ages and Effective Delayed Neutron Fractions

	Extrapolated End-Point Method, $d = 2.6$ cm	Current Method, $d = 3.7$ cm
l_1^2, cm^2	20.7	25.3
Age of delayed neutrons, cm^2	4.5 ± 1	11.4 ± 2
Age of prompt neutrons, cm^2	26.2 ± 0.5	30.8 ± 0.5
Effective delayed neutron fraction, %	1.0	0.9

[4] G. R. Keepin, T. F. Wimett, and R. K. Zeigler, *Delayed Neutrons from Fissionable Isotopes of Uranium, Plutonium, and Thorium*, LA-2118 (July 23, 1957).

4.3. CRITICAL PARAMETERS OF A PROTON-MODERATED AND PROTON-REFLECTED SLAB OF U^{235}

J. K. Fox L. W. Gilley
J. H. Marable

The thickness of a critical slab-shaped volume of fissionable material is of practical interest in setting limiting vessel dimensions and is of importance in elementary reactor analyses if the area-to-thickness ratio is sufficiently large to make the system essentially unidimensional. To measure the thickness of a critical slab of a solution when all the other parameters are optimized is of even more practical interest. Evaluations of this so-called "minimum thickness of an infinite slab" have been made previously by extrapolation of the critical dimensions of water-reflected cylinders of finite area.[1] Other estimates of the thickness of water-reflected slabs have been obtained from the extrapolation of measurements on partially reflected vessels.[2]

An attempt has now been made to measure directly the critical thickness of a hydrogen-reflected slab of aqueous solution of UO_2F_2 (enriched to 93.2% in U^{235}) at chemical concentrations selected to give the minimum critical volume. For this purpose a reactor vessel was constructed from ¾-in.-thick Lucite sheets reinforced by stiffening members, also of Lucite, attached to the outside. The nominal inside dimensions were 58 × 71 × 2.25 in. The slab was mounted with the 71-in. dimension vertical in such a manner that it could be filled with UO_2F_2 solution and surrounded, except for the top surface, by an effectively infinite water reflector. The size of the slab was altered by inserting plastic sheets of various thicknesses adjacent to one inside surface. Blocks of plastic about 1 in. square and of appropriate length were placed within the slab on 12-in. centers in two directions in an attempt to maintain constant thickness as the hydrostatic pressures varied with the inner and outer liquid heights.

In the experiment, critical heights of solutions of two concentrations were measured over a narrow range of slab thicknesses with, of course, the other horizontal dimension fixed at 58 in. The temperature of the solution was between 72 and 75°F. The extent of the measurement was limited by the volume of solution available. It is apparent from the data recorded in Table 4.3.1 that the critical dimensions were sensitive to the water height because of its effect as a neutron reflector above the solution and, more importantly, because of deformations of the plastic by variations in hydrostatic forces. In some instances the slab thickness was measured with gage blocks with the liquids only slightly below the critical levels and with a neutron absorber inserted in the solution. This dimension varied by as much as ±0.01 in. over the area of the slab. Data in which there is greatest confidence have been extrapolated to an infinite height as shown in Fig. 4.3.1. The extrapolated value is 1.81 in.

It is obvious that a 50-in. height is not "infinite," and the extrapolation of the graph evaluates this effect in only one dimension. Were the finite width (58 in.) of the slab extended indefinitely, it is estimated, from Fig. 4.3.1, that the thickness would be reduced by 0.15 ± 0.05 in.

An evaluation of the effect on the critical thickness of the infinite slab of replacing the Lucite with water was made by equating the geometric buckling of the water-reflected slab to the geometric buckling of the water- and Lucite-reflected slab and solving for the thickness. The extrapolation distance into the water-Lucite medium had been determined previously by equating the bucklings of two similarly water-reflected and water- and Lucite-reflected critical slabs. These results indicate that replacing the Lucite with water would increase the critical thickness of the infinite slab by 0.1 in. These considerations yield for the minimum critical thickness of an infinite slab of solution with a water reflector the value of 1.76 in.

It is estimated that an uncertainty of ±0.07 in. should be attached to these results because of uncertainties in measurements of the experimental slab thicknesses, the extrapolations of the data, and the deviation of the experimental solution concentration from the optimum concentration.

---

[1] C. L. Schuske and J. W. Morfitt, Y-533 (Dec. 6, 1949) (classified); Y-829 (Dec. 5, 1951) (classified).

[2] A. D. Callihan *et al.*, *Phys. Semiann. Prog. Rep. March 10, 1954*, ORNL-1715, p 12 (classified).

Table 4.3.1. Critical Dimensions of a Proton-reflected and -moderated Slab

Slab Thickness (in.)	Critical Solution		Reflector Water Height* (in.)	Critical Values		
	Height (in.)	Height^{-1} (in.$^{-1}$)		Volume (in.^{3})	Volume (liters)	Mass (kg of U^{235})
			$H:U^{235}$ = 44.7; 0.532 g of U^{235} per cm^3			
2.12 ± 0.01	28.18	0.0355	45.7	3465	56.8	30.2
2.06 ± 0.01	35.02	0.0286	53.5	4185	68.5	36.4
2.06 ± 0.01	34.91	0.0286	51.0	4170	68.3	36.3
2.00 ± 0.01	42.09	0.0238	54.5	4885	80.0	42.6
2.00 ± 0.01	43.08	0.0232	56.7	5000	81.9	43.6
1.995 ± 0.005	45.38	0.0220	59.0	5250	86.0	45.7
1.995 ± 0.005	47.20	0.0212	64.0	5460	89.5	47.6
			$H:U^{235}$ = 51.5; 0.469 g of U^{235} per cm^3			
2.06 ± 0.01	36.73	0.0272	53.5	4390	71.9	33.7
2.06 ± 0.01	37.62	0.0266	64.0	4495	73.7	34.6
1.995 ± 0.005	51.99	0.0192	65.5	6015	98.6	46.2
1.995 ± 0.005	51.28	0.0195	64.0	5935	97.2	45.6

*Measured from bottom of liquid slab.

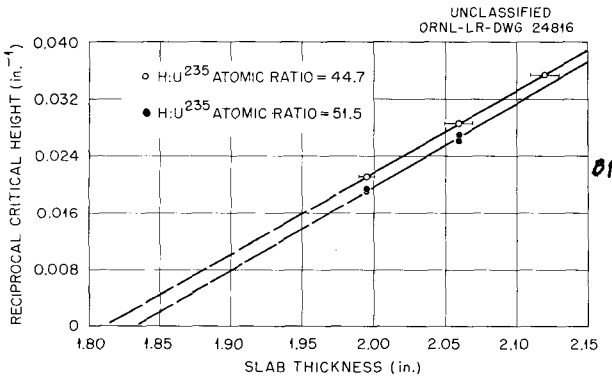

Fig. 4.3.1. Reciprocal Critical Height of a Slab of Enriched U^{235} Solution as a Function of the Thickness of the Slab.

In an attempt to analyze the experimental data, several water-reflected finite and infinite slab reactors were calculated on the Oracle, using the three-group, three-region (3G3R) reactor code. The core was assumed to be an aqueous solution of UO_2F_2 (uranium 93.2% enriched) with a U^{235} concentration of 0.532 g/cc, corresponding to the experimental conditions which yielded the value of 1.76 in. for the infinite slab. The Lucite containers used in the critical experiments were assumed to be water.

Group constants were obtained from the Eyewash multigroup cross-section compilation using the Group Constant Preparation Routine (GCPR) (see ORNL-CF-55-1-76) ~~see 8.5~~. The multiplication factors calculated by this method for three finite slabs which were critical experimentally were each 1.125. The thickness of the infinite slab which gave a calculated multiplication factor of 1 was 1.38 in. The thickness of the infinite slab which gave a calculated multiplication factor of 1.125 was 1.88 in.

The large values obtained for the multiplication factors may be due to the method of calculating the group transfer cross sections Σ_x. These are calculated in the GCPR from ages which are obtained by an empirical method. Another method of calculating the transfer cross section from the slowing down in unreflected spheres yielded smaller values for the transfer cross sections with a corresponding value of 0.92 for the calculated multiplication factor of the finite reflected slabs. This shows that the calculated multiplication factor is very sensitive to the model used to determine transfer cross sections.

Part 5

RESONANCE REACTOR PROGRAM

5.1. RESONANCE REACTOR PROGRAM

L. Dresner
S. H. Hanauer
D. W. Magnuson
C. D. Zerby

Historically, interest in reactors with a resonance-energy spectrum (1 to 100 kev) first came about in the hope that it would be possible to achieve a high breeding ratio in the resonance energy range. It was soon discovered[1,2] that the capture-to-fission ratio in the fuels U^{235} and Pu^{239} was high, and hope for an efficient resonance-energy breeder waned. Nevertheless, by the time this discovery was made, three resonance-energy critical assemblies had been built and studied.[3] These studies proved to be interesting in themselves, as will be indicated in detail below, and will be continued in a resonance reactor program at ORNL.

Among the first things of importance in a resonance reactor program are an experimental survey of the critical conditions and a comparison of the results with those obtained by various methods of calculation. The method of calculation used for the three critical assemblies discussed by Hurwitz and Ehrlich[3] was multigroup age-diffusion theory.[4] However, important effects exist which necessitate various refinements in ordinary age-diffusion theory: (1) The presence of hydrogen invalidates the use of age theory.[5,6] (2) Anisotropy in scattering in the center-of-mass system is possible because of the appearance of p waves in the 100-kev range; this may be accounted for at various levels, for example, transport corrections to $\bar{\mu}$ and ξ in age-diffusion theory, use of a consistent P_1 approximation to the Boltzmann equation,[6] etc. (3) Certain materials, for example, F^{19}, U^{238}, and U^{235}, cause strong inelastic scattering in the resonance energy range. It is of considerable importance to try to develop workable methods of calculation which include these effects and which will give reliable results for critical masses and for neutron flux spectra and their adjoints. The latter quantities are particularly important, since the interpretation of perturbation measurements, for example, pile oscillator danger coefficient measurements, depends on their being known. At the present, instrumentation is not available for measuring flux spectra in the resonance range, so that reliance for these quantities must be on calculation.

Among the measurements which a resonance-energy reactor is uniquely well suited to make is the measurement of radiative cross sections in which neutron capture does not lead to subsequent radioactivity.[3,7] Such measurements can be made on separated isotopes as well as on special groups of isotopes, such as the fission products.[8] Of course, such cross sections will be averaged over a wide range of energies and will not directly supply any information on the detailed shape of the cross sections; however, theories of the radiative cross section must reproduce these reactor-spectrum averages.

In a resonance reactor it is also possible to measure the capture-to-fission ratio, α, in fissionable materials by perturbation techniques.[3] Such measurements are particularly important because they are independent of the usual chemical-mass spectrometric determinations, which are in some disagreement with theory. In particular, theory[1,2] requires a somewhat larger fission width than is observed.[9] Moreover, the resonance reactor is an excellent device with which to investigate the dependence of α on sample thickness.

---

[1] H. A. Bethe, *Progress in Nuclear Energy* (ed. by R. A. Charpie *et al.*), Series I, vol I, chap. 3, p 91, McGraw-Hill, New York, 1956.

[2] S. Oleksa, *Proceedings of the Brookhaven Conference on Resonance Absorption of Neutrons in Nuclear Reactors, September 24 to 25, 1956*, BNL-433, p 59 (July 1957).

[3] H. Hurwitz, Jr., and R. Ehrlich, *Progress in Nuclear Energy* (ed. by R. A. Charpie *et al.*), Series I, vol I, chap. 11, p 343, McGraw-Hill, New York, 1956.

[4] R. Ehrlich and H. Hurwitz, Jr., *Nucleonics* 12(2), 23 (1954).

[5] G. Goertzel, *Criticality of Hydrogen Moderated Reactors*, TAB-53 (July 25, 1950).

[6] P. F. Zweifel and H. Hurwitz, Jr., *J. Appl. Phy.* 25, 1241 (1954).

[7] J. Codd, L. R. Shepherd, and J. H. Tait, *Progress in Nuclear Energy* (ed. by R. A. Charpie *et al.*), Series I, vol I, chap. 9, p 251, McGraw-Hill, New York, 1956.

[8] P. Greebler, H. Hurwitz, Jr., and M. L. Storm, *Nuclear Sci. and Eng.* 2, 334 (1957).

[9] R. B. Schwartz, *Conference on Neutron Physics by Time-of-Flight, Held at Gatlinburg, Tennessee, November 1 and 2, 1956*, ORNL-2309, p 192 (June 17, 1957).

In order to carry out a program similar to the one outlined above, steps are being taken to establish the parameters of a critical assembly which will be built at the ORNL Critical Experiments Facility. Some of the calculations of the critical mass and a discussion of the current design of the experiment are given below.

Calculations of Critical Mass

In order to perform initial calculations of the critical size of the resonance reactor, it was necessary to write a special multigroup reactor code for the Oracle. This code was patterned after the Eyewash code[10] except for obvious simplifications resulting from the fact that the resonance reactor will be unreflected. The energy spectrum was separated into 30 groups with energy limits the same as in the Eyewash code.[11] Results of the calculation for an unreflected bare spherical assembly are given in Fig. 5.1.1.

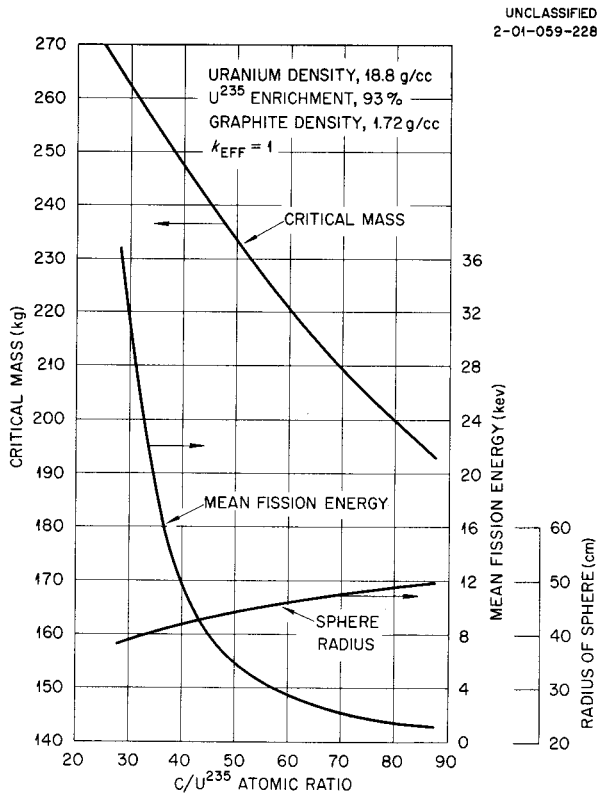

Fig. 5.1.1. Critical Mass, Radius, and Mean Fission Energy of an Unreflected Uranium-Graphite Sphere.

Experimental Design

Critical experiments for the resonance reactor program are being planned. The cores of the initial assemblies will be rectangular parallelepipeds of uranium (enriched to 93% in U^{235}) and graphite made as homogeneous as is practically possible. Since the necessary supporting structure of a nominally unreflected reactor will provide at least a partial reflector, the top and bottom of the cores used in these experiments will be reflected by lead 6 in. thick. The design of the experiment has been guided by the results of the reactor calculations presented in Fig. 5.1.1. Table 5.1.1 gives the characteristics of three unreflected reactors, each 30 by 30 in. in area and built up of alternating laminae of uranium metal foil and graphite. The first assembly will have a $C:U^{235}$ atomic ratio of 42.6, in which the mean energy of the neutrons producing fission is calculated to be 9.4 kev.

The assembly will be built in two adjacent parts, one of which is to be placed on a movable table that can be driven by remote control. Safety rods, consisting of fuel and moderator, will operate in the horizontal plane. Three additional horizontal holes and one vertical access hole at the interface, all lined with brass wave guide, will be used for control rods and for experimental measurements.

The reactivity of the assembly will be controlled by four safety rods, two control rods, and a sensitive regulating rod for experimental measurements, as well as by the separation of the sections as described above. Both safety and control rods will be made from uranium foils and thin graphite sheets, in a pattern matching the core, and their removal will decrease the reactivity of the assembly. The safety rods will be inserted by pressurizing a pneumatic cylinder and will be held in the core against a compressed spring by a d-c electromagnet when the pressure is removed. Only one rod may be inserted at a time. Signals from an array of conventional instrumentation will de-energize the magnets at a predetermined radiation level or rate of level change, allowing the springs to eject the rods from the lattice. It is estimated that each of the four safety rods will control $0.01\Delta k/k$. The control rods will be driven

[10] J. H. Alexander and N. D. Given, *A Machine Multigroup Calculation, The Eyewash Program for UNIVAC*, ORNL-1925 (Sept. 6, 1955).

[11] *Ibid.*, Table A, p 31.

Table 5.1.1. Characteristics of Unreflected Uranium-Graphite Critical Assemblies (Parallelepipeds)

Mean Energy of Fission (kev)	$C:U^{235}$ Atomic Ratio	Lamina Thickness (in.)		Number of Uranium (or Graphite) Laminae	Critical Dimensions (in.)	Critical Mass (kg of U^{235})
		Uranium	Graphite			
1.8	75.0	0.009	0.348	117	$30 \times 30 \times 41.6$	268
9.4	42.6	0.009	0.198	130	$30 \times 30 \times 27.3$	305
24.6	32.4	0.009	0.150	144	$30 \times 30 \times 22.8$	330

by a-c induction motors through a reduction worm gear and a screw and nut at a speed of 17 in./min over a 30-in. travel. Each will have a value of approximately $3 \times 10^{-3} \Delta k/k$.

In addition to the usual instruments of a critical experiment, there will be installed a regulating rod and a sample-changing mechanism so that reactivity-coefficient measurements may be made with the greatest possible sensitivity. The regulating rod, to be designed empirically in the assembly to be worth about $10^{-4} \Delta k/k$, will be operated by a servo system which will keep the neutron flux as nearly constant as possible. As the sample is quickly inserted into the core, the regulating rod will move to a new position to compensate for the reactivity change made by the introduction of the sample. After a pause, the sample will be quickly withdrawn, and the regulating rod again compensates for the change – this time in the reverse direction. A standard sample may also be oscillated in this way. The data to be observed are the equilibrium positions of the regulating rod corresponding to the extremes of the sample displacement. DeBoisblanc and co-workers[12] estimate that a sensitivity of greater than $10^{-6} \Delta k/k$ may be achieved by this method.

[12] D. R. DeBoisblanc, E. E. Burdick, and G. L. Smith, *The RMF Pile Oscillator*, Paper No. 5-6, Third Annual American Nuclear Society Meeting, Pittsburgh, June 10–12, 1957; also private communication.

Part 6

FISSION PHYSICS

6.1. SPECTRA OF SHORT-LIVED FISSION-PRODUCT GAMMA RAYS

W. Zobel
R. W. Peelle
T. A. Love
G. M. Estabrook

The final analysis of the data taken in the fission-product gamma-ray experiment reported previously[1] is continuing. In particular, the method used to determine the number of fissions in the samples was changed subsequent to the preliminary analysis, and attempts are under way to remove the so-called "nonuniqueness" effect of the scintillation spectrometer. These changes are described below.

Source Strength Determination

In the preliminary analysis[1] the number of fissions in a sample was determined from the sample weight and the effective thermal-neutron flux. The latter was obtained by exposing bare and cadmium-covered gold foils to the same conditions under which the uranium samples had been exposed. However, the gold foils and the uranium samples differed in size, so that it would have been necessary to apply flux depression corrections, which are difficult calculations at best. Hence it was decided to determine the number of fissions in a sample experimentally.

The samples used during the experiment were of four sizes: approximately 2 mg ($\frac{1}{16}$-in.-dia by 0.002-in.-thick), approximately 7 mg ($\frac{1}{8}$-in.-dia by 0.002-in.-thick), approximately 15 mg ($\frac{1}{8}$-in.-dia by 0.004-in.-thick), and approximately 32 mg ($\frac{3}{16}$-in.-dia by 0.004-in.-thick). Five samples from each of these four groups, as well as five samples of approximately 3.5 mg ($\frac{1}{8}$-in.-dia by 0.001-in.-thick), were exposed for the same period of time in the same experimental arrangement as was used in the original experiment. The integral number of counts, taken for the same counting time interval, above a given pulse-height level was determined for each sample, and the average was taken for each group. Thus the relative number of fissions in all the samples was determined.

It now remained only to determine the absolute number of fissions in samples of any one group for the different bombarding times used. Gold foils $\frac{1}{8}$ in. in diameter were used for this purpose. In order to eliminate the need for flux depression corrections, their thickness was so chosen as to be approximately equal to that of the $\frac{1}{8}$-in.-dia uranium foils, when both thicknesses were measured in mean free paths. This led to the use of 0.005- and 0.010-in.-thick gold foils for comparison with 0.001- and 0.002-in.-thick uranium foils. The total activations of the gold foils were determined in the calibrated high-pressure ion chamber of the ORNL Radioisotopes Control Laboratory. The number of fissions in the uranium samples was then determined by comparison with the gold-foil activation due to the cadmium difference flux. No attempt has yet been made to take into account epithermal fissions in the samples.

Nonuniqueness Correction

The nonuniqueness effect of the scintillation spectrometer is a short name for the following phenomenon: When monoenergetic gamma rays are allowed to fall on a scintillation spectrometer, it is found that pulses are recorded on the associated multichannel analyzer in channels other than (mostly below) the channel which would correspond to the pulse generated by the absorption of the full energy of the gamma ray. Thus a response curve is obtained which extends over many channels. The shape of this response curve depends on the type of spectrometer, and the multiple-crystal type was chosen for the experiment because it minimizes this effect. The peak-to-total ratio, which is a measure of the uniqueness, is never less than 0.5 over the energy range used in this experiment. It is, however, desirable to try to remove the effects of the nonuniqueness from the data.

Assume that there exists a true fission-product pulse-height spectrum Γ, which can be represented by a 60-component vector. Call the measured pulse-height distribution (also a 60-component vector) N. Then there should exist a matrix, call it U, which will transform Γ into N; that is, $\Gamma U = N$. This matrix U will have for its rows the vectors which describe the response functions of the instrument to monoenergetic gamma rays of energies corresponding to those associated with

[1] W. Zobel and T. A. Love, *Appl. Nuclear Phys. Ann. Rep. Sept. 10, 1956*, ORNL-2081, p 95.

the components of the vector Γ. To obtain Γ from the known N it is then merely necessary to invert U and to multiply N on the right by this inverse, or $\Gamma = NU^{-1}$. Of course the inversion of a large matrix, in this case 60×60, must be carried out on a high-speed computer. Fortunately, a matrix inversion routine[2] which could be used, as well as a matrix multiplication code,[3] had been written for the Oracle.

To utilize this method the response functions were approximated by analytic functions, by use of data obtained with radioactive sources which emitted one or, at the most, two gamma rays of known energy. A matrix was then calculated by hand and inverted on the Oracle. When the inverse was multiplied into the experimental pulse-height distributions, however, the results were apparently meaningless because they oscillated wildly.

It was pointed out by L. Dresner that if the Gaussian function chosen to approximate the peak of the response function is too broad, the result will be just such oscillations as have been observed. As a result a code has been written with which the Oracle calculates the matrix elements for an arbitrary width of the Gaussian peak. No successful choice of a matrix has yet been made. However, calculations are continuing, and it is hoped that positive results will be obtained soon.

[2]By M. R. Arnette, Mathematics Panel.

[3]By G. W. Medlin, Mathematics Panel.

6.2. ENERGY SPECTRUM OF PROMPT GAMMA RAYS ACCOMPANYING THE FISSION OF U^{235}

F. C. Maienschein R. W. Peelle
T. A. Love

The design of shields for nuclear reactors can be carried out intelligently only if the nature of the radiations being shielded against is understood. That aspect of the nature of the radiations which is most essential for the performance of penetration calculations is the energy spectrum.

It is clear that the radiations produced in the fission process will constitute a significant contribution to the sources in the core of a nuclear reactor. For neutrons, this fission source dominates. For gamma rays, the contribution due to those gamma rays accompanying fission is usually of the same order of magnitude as the gamma-ray source resulting from neutron interactions other than fission. Thus a knowledge of the energy spectrum of fission-associated gamma radiation is essential for correct shield design.

A knowledge of the energy spectrum of the gamma rays accompanying fission should ultimately also increase the understanding of the fission process. However, with the present theories of fission, it is not possible to make predictions of the energy distribution of the fission-associated gamma radiation.

Some ORNL measurements of gamma-ray spectra accompanying the fission of U^{235} have been reported previously.[1,2] The first of these measurements[1] suffered from the use of a small ($1\frac{1}{2} \times 1$ in.) NaI(Tl) crystal, with the concomitant small peak-to-total ratios which introduce uncertainties in the conversion from pulse-height spectra to energy spectra. The second measurement[2] included energies from only 0.5 to 2.25 Mev.

In addition, both these energy spectra measurements included a background due to the prompt neutrons from fissions. The magnitude of this background was not appreciated at the time the measurements were taken, so that no accurate determination of its size was made. An estimate of the magnitude of the neutron-induced background is given later in this section, and attempts to reduce the background are described.

A measurement of the gamma rays accompanying the spontaneous fission of Cf^{252} has been reported.[3] This spectrum, which is easier to measure than that due to neutron-induced fission because of the relatively lower backgrounds, may have some relationship to the spectrum accompanying U^{235} fission.

The emission of gamma radiation from the radioactive fission fragments also has long been appreciated as being of unique importance for reactor shielding. However, only recently has it been demonstrated[4] (see, also, Sec. 6.1) that about 75% of the known energy corresponding to fission-product gamma radiation is emitted in the time range from 1 to 1600 sec after fission.

The existence of gamma radiation delayed for shorter times after fission has not been demonstrated, although several searches have been made.[1,3,5] The division of fission-associated gamma radiation into prompt and delayed components has been based on the resolving time employed in a given experiment. Radiation occurring within the resolving time of the apparatus has been called "prompt." However, none of the experimental resolving times approach the estimated time,[6] $\sim 10^{-14}$ sec, required for the emission of the "prompt" radiation.

Beta-ray emitters would not be expected to have half lives less than 10^{-3} sec, because the excitation energy required by beta-ray decay theory would be unreasonably large. Isomeric transitions, on the other hand, would not appear to be unlikely.

The existence of small quantities of gamma radiation delayed by only a short time (compared with a second) after fission would be of especial practical importance in the effects of nuclear weapons. This follows because the prompt gamma radiation is well-shielded by the dense bomb

[1] J. E. Francis and R. L. Gamble, *Phys. Semiann. Prog. Rep. March 20, 1955*, ORNL-1879, p 20.

[2] F. C. Maienschein *et al.*, *Phys. Semiann. Prog. Rep. March 20, 1955*, ORNL-1879, p 51.

[3] A. B. Smith, P. R. Fields, and A. M. Friedman, *Phys. Rev.* 104, 699 (1956).

[4] R. W. Peelle, W. Zobel, and T. A. Love, *Appl. Nuclear Phys. Ann. Rep. Sept. 10, 1956*, ORNL-2081, p 91.

[5] J. E. Brolley, Jr., *et al.*, *Phys. Rev.* 83, 990 (1951).

[6] A. M. Weinberg and E. P. Wigner, *Preliminary Draft, Theory of Neutron Chain Reactions*, ORNL CF-56-11-43, vol I, p 5.10 (Nov. 27, 1956).

materials. The shielding is reduced upon the rapid destruction of the bomb and mixing of its components, and thus any delayed gamma radiation is enhanced in importance by almost two orders of magnitude.[7]

Because of the uncertainties associated with the earlier measurements of the U^{235} prompt gamma-ray energy spectrum, and the limited energy range studied in one of them, the experiment described below was performed with improved apparatus.

[7] S. Glasstone (ed.), *The Effects of Nuclear Weapons*, p 343, USAEC, Washington, 1957.

Experimental Arrangement

The apparatus used in this measurement was similar to that employed at the Bulk Shielding Facility (BSF) previously.[2] Fissions were produced in a standard U^{235} spiral fission chamber by thermal neutrons from the BSF thermal column, and an announcement that a fission had occurred was made by a pulse from the chamber. The energies of the gamma rays emitted during the fission were analyzed with a multiple-crystal scintillation spectrometer positioned close to the fission chamber, as shown in Fig. 6.2.1. This

UNCLASSIFIED
ORNL-LR-DWG 5893R1

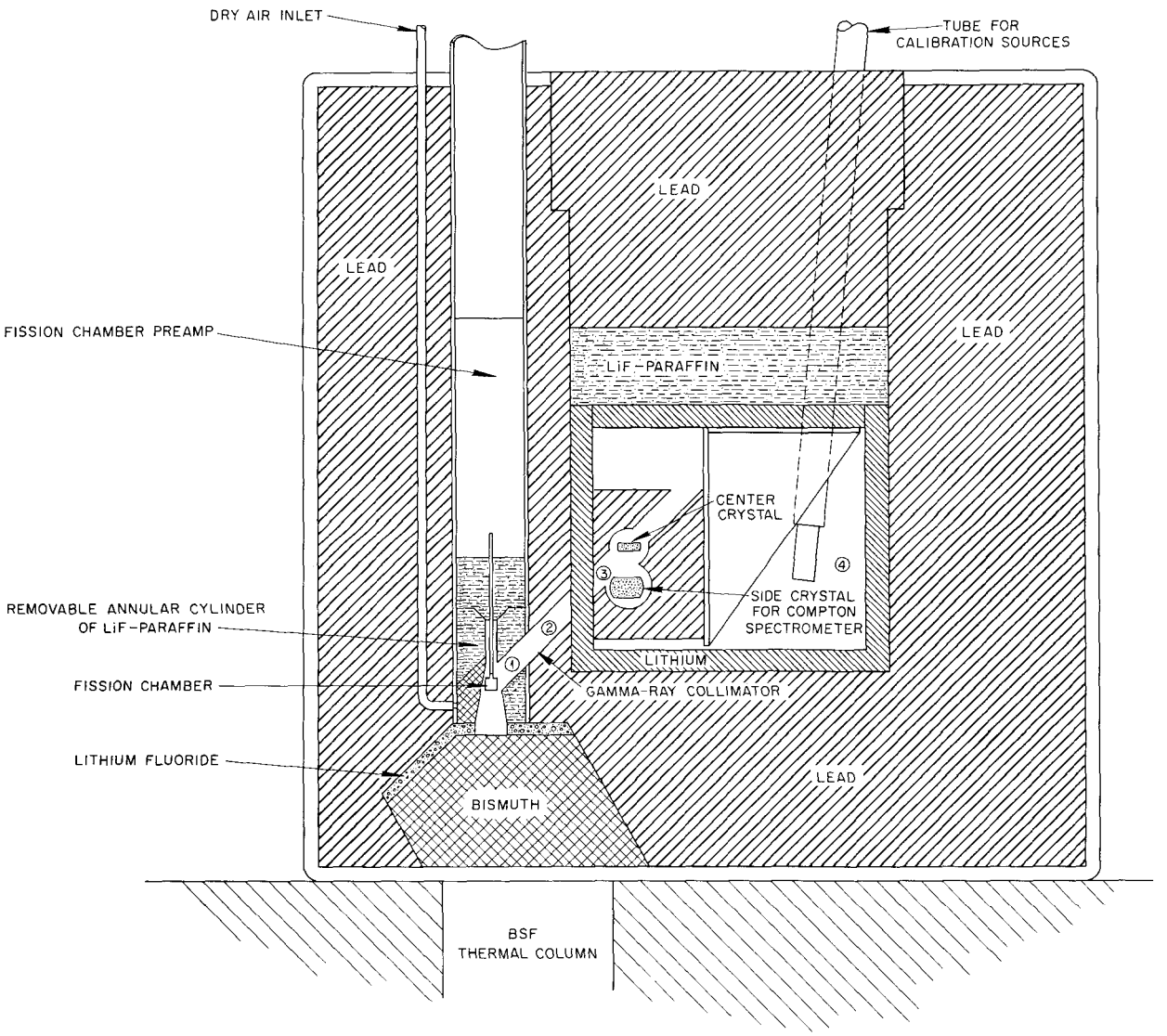

Fig. 6.2.1. Shield Housing for the Gamma-Ray Spectrometer Used to Measure the U^{235} Prompt Gamma-Ray Energy Spectrum. The effect on the background of changing the shielding in the numbered portions of the housing has been determined.

spectrometer was chosen because of its relatively large peak-to-total ratio, which tends to maximize the diagonal elements of the response matrix which relates observed pulse-height distributions to energy spectra. Analysis of spectral results in order to remove the effects of low-energy pulse tails requires the application of the inverse of the response matrix to the observed pulse-height spectra. In order for such an analysis to proceed in a straightforward manner, the fraction of the response matrix embodied in the near-diagonal elements must approach unity.

The shield housing for the gamma-ray spectrometer is also shown in Fig. 6.2.1. The effectiveness of various components of the shield has been measured, with results described below. Since the spectrometer was located within the BSF pool atop the BSF thermal column, an insulated enclosure was placed around the spectrometer shield in order to protect the instrument against changes in pool water temperature. The water within this enclosure was cooled by a small water chiller.

Although the same general types of electronic equipment used in this experiment were employed in the earlier measurements,[8] almost all the individual components were replaced. A block diagram of the equipment is shown in Fig. 6.2.2.

The crystal-photomultiplier combination was chosen as a result of some of the tests described below. The preamplifier was changed to a stacked cathode follower for the photomultiplier channels. All amplifiers were changed to the DD-2 type,[9] a double-delay-line differentiated-pulse amplifier. This unit permits determination of the time of a pulse to an extent impossible with a single-delay-line differentiated amplifier of comparable rise time. The lack of base-line shift associated with double differentiation is also essential in the fission-chamber channel wherein high counting rates prevail.

The analysis unit for determining the time of initiation of a pulse is described in this report (see Sec 10.3). The differential pulse-height analyzers were of the standard ORNL-Q-1192 type. Variable delay was provided by Helidels. Coincidence circuitry was essentially unchanged from that described previously.[8] Pulse-height analysis was carried out by means of the 256-channel magnetic-core memory pulse-height analyzer designed at the Argonne National Laboratory.[10] The linearity of this unit was almost adequate for the necessary pulse-height analysis.

Additional electronics, not shown in Fig. 6.2.2, included a monitor for the high-voltage power supply and count-rate monitors for six pulse outputs. An automatic timing circuit for control of the analyzer was developed (described in Sec 10.7).

Background Analysis

A major emphasis in data accumulation during the past year has been directed toward determining the most effective means of reducing the background in the observed spectrum. It has already been pointed out that neutron-induced gamma-ray backgrounds cast doubt on the data obtained earlier. In the paragraphs below, the source of the neutron-induced background is discussed, and the tests to determine a more favorable shield configuration to eliminate all backgrounds are described.

Demonstration of Neutron-induced Background. – The response of a sodium iodide crystal to the fast neutrons from fission is difficult to calculate because of the lack of data on inelastic scattering for sodium and iodine. However, data for iodine are available for neutron energies[11] up to 1.2 Mev. The probabilities of gamma rays being produced by 1.2-Mev neutrons, which enter a 1-in.-dia by 1-in.-long NaI crystal radially and scatter inelastically in the iodine, are given in Table 6.2.1. The gamma-ray collision probabilities are taken from those calculated for an infinite cylinder by Case, de Hoffman, and Placzek[12] and hence represent an overestimate.

The probability of interaction for a 1.2-Mev gamma ray in the same size crystal is 0.32. Thus if the fission radiations consisted of equal numbers of 1.2-Mev neutrons and 1.2-Mev gamma rays, and if all gamma rays above 0.062 Mev were detected, the neutron background in a 1-in.-dia single-crystal measurement would be of the order of 8% of the gamma-ray foreground.

[8] T. A. Love, R. W. Peelle, and F. C. Maienschein, *Electronic Instrumentation for a Multiple-Crystal Gamma-Ray Scintillation Spectrometer*, ORNL-1929 (Oct. 25, 1955).

[9] E. Fairstein, *Rev. Sci. Instr.* 27, 475 (1956).

[10] R. W. Schumann and J. P. McMahon, *Rev. Sci. Instr.* 27, 675 (1956).

[11] D. J. Hughes and R. B. Schwartz, *Neutron Cross Sections*, BNL-325, Supplement No. 1 (Jan. 1, 1957).

[12] K. M. Case, F. de Hoffman, and G. Placzek, *Introduction to the Theory of Neutron Diffusion*, Los Alamos Scientific Laboratory, Los Alamos, 1953.

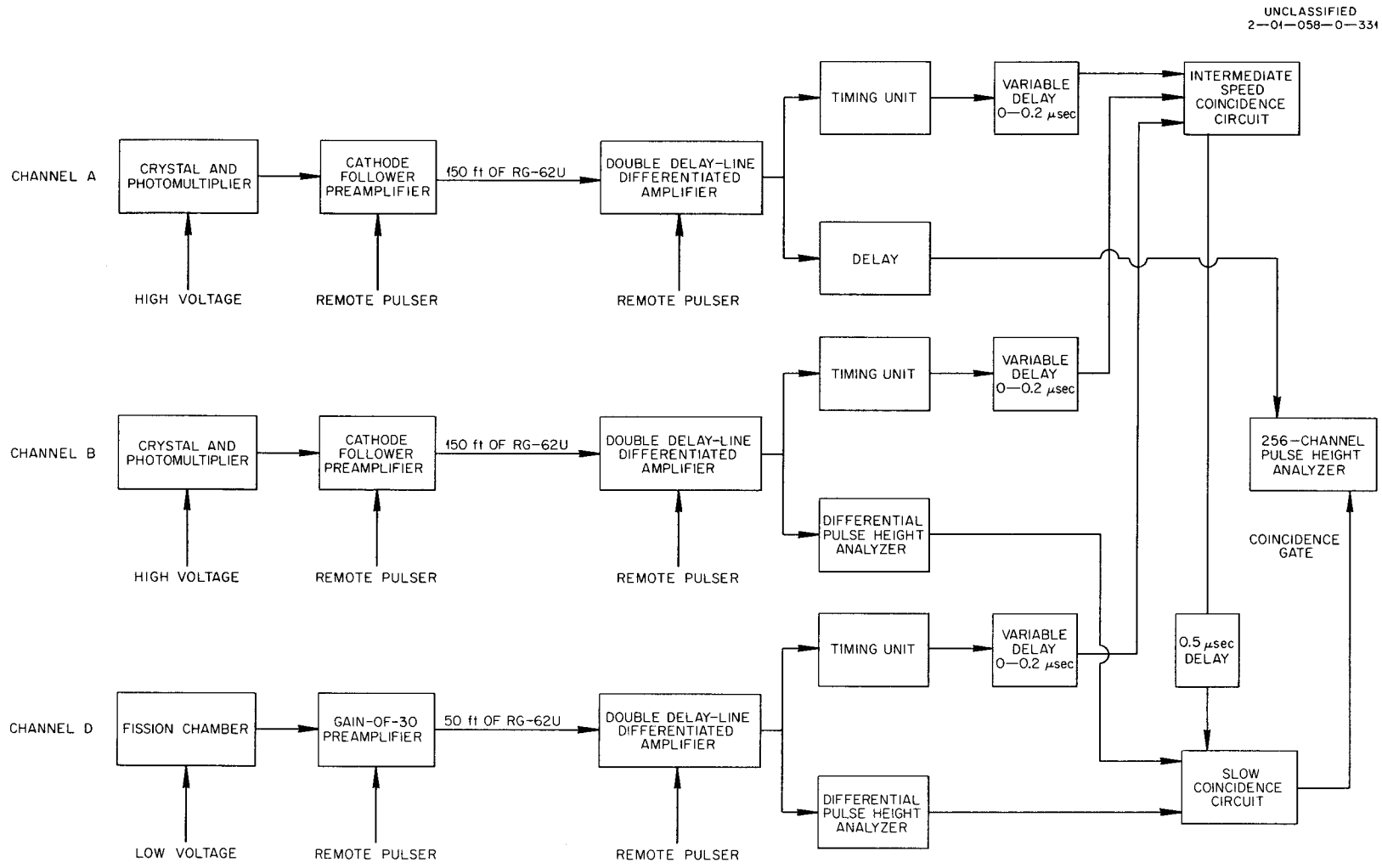

Fig. 6.2.2. Block Diagram of Electronic Components Used in Experiment to Measure the U^{235} Prompt Gamma-Ray Energy Spectrum. This circuit arrangement is the one employed for the Compton spectrometer; an additional crystal channel is employed for the pair spectrometer.

Table 6.2.1. Probability of Interaction and Gamma-Ray Production by 1.2-Mev Fast Neutrons Entering a 1 by 1 in. NaI(Tl) Crystal

Gamma-Ray Energy (Mev)	Probability of Production	Probability of Collision	Over-all Probability of Interaction
0.632	0.019	0.28	0.005
0.435	0.013	0.38	0.005
0.208	0.009	0.69	0.006
0.062	0.009	1.0	0.009
		Total	0.025

The above calculation neglects the possibility of neutrons scattering into the crystal, an effect which would increase the background. For fission neutrons, additional, higher energy levels will surely be excited, thus increasing the possible number of neutron-induced gamma-ray transitions.

In all considerations of backgrounds induced by inelastic scattering of neutrons, it must be remembered that the energies of the gamma rays produced will tend to be low. Thus none of the known gamma rays from inelastic scattering would interfere with the fission-associated gamma-ray spectrum above 0.632 Mev.

In order to measure the extent of the neutron-induced background, the experiments described below were carried out with the crystal and shielding arrangement previously used.[13] The center crystal was a 1-in.-long by 1-in.-dia cylinder of NaI(Tl), and the shield housing for the spectrometer was similar to that shown in Fig. 6.2.1. Plugs of lead and polyethylene, each 10.5 cm long, were inserted into the regions labeled (1) and (2). The gamma-ray pulse-height spectra observed in the center crystal in coincidence with the fission chamber (resolving time $\cong 10^{-7}$ sec) are plotted in Fig. 6.2.3.

The data of Fig. 6.2.3 show that filtration of the fission-associated radiation through lead gives rise to marked peaks in the observed energy spectra. Since these peaks correspond, within the limitations imposed by poor energy calibration, to the energies of gamma rays observed due to the inelastic scattering of neutrons,[10] the conclusion appears inescapable that the neutrons from fission are being detected in spite of the various shields of lithium, lithium fluoride, paraffin, etc. The data obtained with the polyethylene do not show these peaks, as would be expected, because of the selective attenuation of neutrons by this hydrogenous material.

If the pessimistic assumption is made that the lead plug in the above experiment stops all the gamma rays and none of the neutrons, the neutron-induced background would appear to contribute 19% of the prompt fission gamma-ray spectrum from 0.05 to 0.6 Mev.

Experiments to Determine the Shielding Configuration. – Although the reduction of backgrounds has been an essential part of this experiment from the very beginning, portions of the shielding in the spectrometer housing have not yet been optimized. The experiments described below were attempted in order to achieve a more favorable configuration.

Variation of Materials of Cylinder Around Fission Chamber. – The irregular volume of lithium fluoride and paraffin, roughly an annular cylinder, which surrounds the fission chamber, was designed primarily to remove by capture in lithium the thermal neutrons not captured in the fission chamber. However, the paraffin was placed there in an attempt to reduce the escape of fast neutrons into the lead region. Various other materials have been tested in this region, including bismuth, for which data were previously reported.[13]

More recent data demonstrate that the coincidence counting rate is not dependent on the presence of a lithium fluoride cylinder if the backgrounds are properly subtracted. The spectrum observed in the center crystal in coincidence with the fission chamber is shown in Fig. 6.2.4. Of the two coincidence curves, one shows the data taken with an

[13] F. C. Maienschein *et al.*, *Phys. Semiann. Prog. Rep. March 20, 1955*, ORNL-1879, p 51.

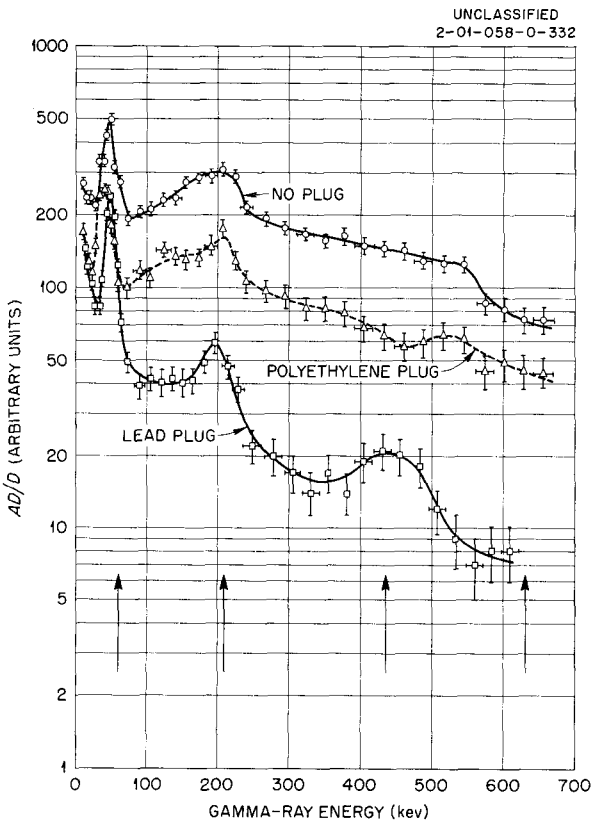

Fig. 6.2.3. Demonstration of Neutron-induced Gamma-Ray Background. Three curves are shown of the AD (center crystal A and fission chamber D) coincidence rate per channel of the multichannel analyzer per count in the fission chamber. All measurements were made with the "old" geometry used in an earlier experiment (see ref 2). The top center and bottom curves respectively show data taken with no plug, with a 10.5-cm-long polyethylene plug, and with a 10.5-cm-long lead plug. The plugs were located in positions 1 and 2 shown in Fig. 6.2.1. Data from adjacent channels of the pulse-height analyzer were combined to improve the apparent counting statistics. The number of channels combined varied from 1 at 0.05 Mev to 8 at high energies. The lengths of the horizontal bars indicate the energy range over which channels were combined. The vertical bars show the usual standard deviation errors based on counting statistics. The arrows represent the energies of gamma rays observed due to the inelastic scattering of fast neutrons in iodine. The energy calibration in this figure is only approximate, owing to instabilities in the pulse-height analyzer zero at the time the data were accumulated. This difficulty has since been minimized but not entirely eliminated.

LiF-paraffin cylinder, and the other shows data for no cylinder at all. The counting rates above ten channels (~0.05 Mev) agree to within 5%. The background rates due to random coincidences are shown at the bottom of the figure. The variation in these rates reflects the fact that the background in the single counts of the center crystal (crystal A) is reduced by the cylinder by about 60%.

The aperture in the bottom end of the cylinder (Fig. 6.2.1) has been enlarged since the earlier experiments. This change increased the fission rate in the fission chamber for a given reactor power by a factor of 5. In addition, a bismuth

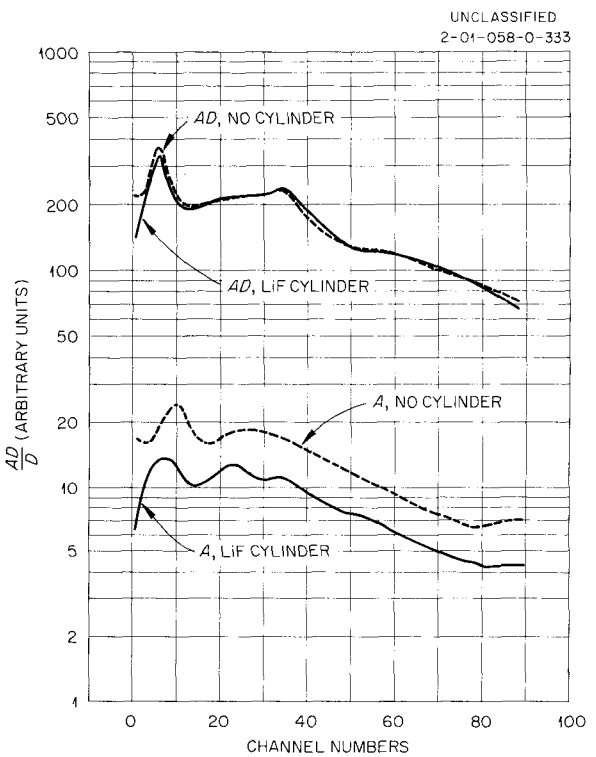

Fig. 6.2.4. Variations in the Coincidence Counting Rate as a Function of Different Cylinder Materials Surrounding the Fission Chamber. AD/D is the number of AD coincidences per channel per fission event expressed on an arbitrary scale. The curves labeled A are the chance rates per D count calculated on the basis of the measured single rates, A and D, and the known resolution time of the coincidence circuit. As an energy calibration, it may be noted that channel No. 90 corresponds to approximately 0.5 Mev. The errors on the AD curves are about ±3% in the ordinate.

insert has been mounted in the portion of the cylinder opposite the collimator leading to crystal A. Bismuth was chosen because of its supposed low neutron inelastic scattering cross section and also because the high density would tend to shield gamma rays produced within the bismuth.

Addition of Lead Around Crystals. – The addition of a lead region around the crystals within the lithium box shown in Fig. 6.2.1 reduced the background response (measured with fission chamber removed but with reactor operating) more than it reduced the response to either the fission-associated radiation from the fission chamber or the monoenergetic sources. The reduction in the foreground arises because the lead obscures a portion of the crystal. These reduction factors are listed in Table 6.2.2.

Table 6.2.2. Effect on Crystal Response of Adding Lead Around Crystals

Source	Reduction Factor
Foreground-monoenergetic sources	
0.66-Mev gamma ray	0.81
0.90-Mev gamma ray	0.90
1.85-Mev gamma ray	0.79
Foreground—fission-associated gamma rays	0.84
Background (proportional to counting rate in crystal A)	0.45

Addition of Hydrogenous Shielding. – A possible source of background that has been mentioned previously is that due to the scattering of fast neutrons in the lead to the crystal and subsequent production of gamma rays by inelastic scattering. In order to attempt to determine the magnitude of this effect, additional hydrogenous material was introduced within the spectrometer shield to capture neutrons. Region 4 in Fig. 6.2.1 was filled with LiF-paraffin, and measurements of the coincident rate, BD, were made with and without this additional shielding; BD was measured rather than AD because the B crystal is larger than A and thus should respond more sensitively to neutrons. The results obtained indicated that the additional hydrogenous shield did not affect the observed coincidence counting rates within the limits of error (about 3%).

Choice of Crystal Configuration. – Once the presence of the appreciable neutron background had been established, it was immediately apparent that smaller crystals might improve the gamma-ray-to-neutron sensitivity ratio. This reduction in background would follow because the crystals were thicker than necessary for efficient detection of the Compton-scattered gamma rays. It is assumed that the neutron sensitivity of the crystals is proportional to the crystal volume. Further, neutron-induced counts arise from double interactions, and thus the probability of their detection decreases more rapidly with crystal size than does that for gamma rays. Consequently, smaller crystals were employed, shaped as shown in Fig. 6.2.1.

The results obtained with the small crystals are compared with those of the old 1 by 1 in. crystals in Fig. 6.2.5. The two curves of peak-to-total area ratios demonstrate that this essential parameter is not appreciably affected by the change to the small crystals. The lower curves present the ratios of peak efficiencies for the small crystals to those for the large crystals. The fact that the ratios for the fission source lie consistently below the monoenergetic source data demonstrates that the background has been reduced more than the foreground by the change from large to small crystals.

In order to reduce the distance between crystals A and B, the photomultiplier for crystal A was changed to a smaller one, a nominal 1.5-in.-dia DuMont No. 6291.

Collimator-Plug Studies of the Final Compton Configuration. – As one approach to the determination of the magnitude of the neutron-induced background, studies were made of the attenuation of radiations by plugs of lead or polyethylene inserted in the spectrometer collimator into position 2 or 1 in Fig. 6.2.1. These measurements differ from those shown in Fig. 6.2.3 in that they were made with the altered shield and crystal configurations chosen for the "final" Compton configuration. Measurements were made with and without the plugs for both the fission-associated gamma radiation and for monoenergetic sources. The results obtained are shown in Fig. 6.2.6, where the ratios of the counting rate with each plug to the counting rate without a plug are plotted. All

data were taken with the Compton spectrometer. The results indicate that the attenuation of the fission radiation in the polyethylene plug is consistent with the source attenuations within the combined limits of error. The approximate limits of deviation of the fission radiation attenuation are indicated by the solid lines in Fig. 6.2.6.

For the lead-plug data, the transmission of the fission radiation is consistent with the measured radioactive source transmission for energies >1 Mev. For energies <1 Mev, the transmission is greater than that for sources. An explanation of this behavior is believed to follow from the fact that even the Compton spectrometer does not have a unique response, that is, a peak-to-total ratio of 1. Thus for a spectrum distributed continuously in energy, a significant error is introduced in the low-energy region of the corresponding pulse-height spectrum. A correction can be made for this effect (see Sec 6.1), but it was not considered worthwhile in this case at this time.

As a result of the above attenuation measurements with the small crystals, it is possible to estimate the magnitude of the neutron-induced background in the spectrum of fission-associated gamma radiation. From the polyethylene-plug data, the background would appear to constitute about 4% of the gamma-ray counts. From the lead data the corresponding number is 10%. The error in each case is about equal to the number itself.

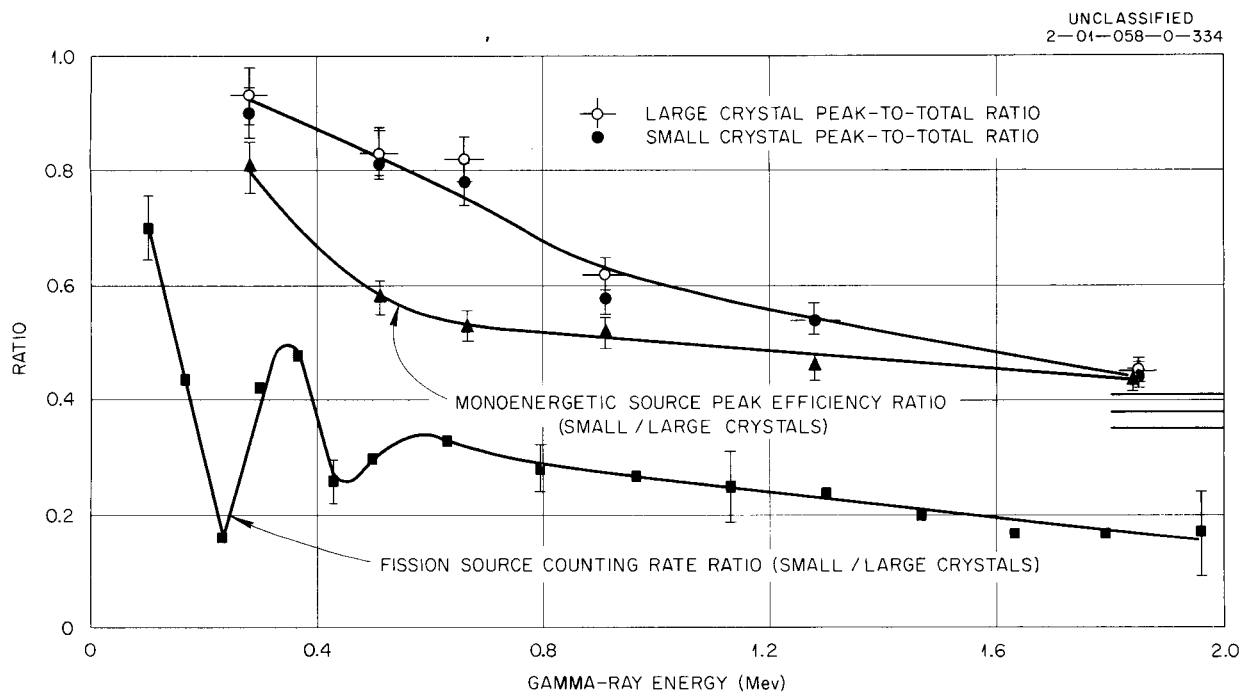

Fig. 6.2.5. Comparison of Gamma-Ray Measurements Made with New $\frac{3}{8} \times \frac{3}{4}$ in. Sodium Iodide Crystals and Those Obtained with Old 1 × 1 in. Crystals. Two types of data are shown. The P/T curves show values of the ratios of the peak area to the total area for the pulse-height spectra observed when the Compton spectrometer was exposed to monoenergetic gamma-ray sources of the energies shown. The second curve from the top shows the ratios of peak efficiency observed when the Compton spectrometer was exposed to the same sources. The ratio is defined as the peak efficiency for small crystals divided by the peak efficiency for large crystals. The bottom curve shows the corresponding ratio of coincidence counting rates, AD, due to the fission source. The two marked valleys in this curve correspond to two of the known gamma rays resulting from inelastic scattering of fast neutrons. The straight line represents the ratio for the response of the Compton spectrometer. It is not shown as a function of energy, since sufficient statistical data were not accumulated during the Compton run to permit an energy differentiation. The two outside lines represent the probable error based on statistics for the Compton run. The errors shown on the other data points are approximate.

Thus these data are not inconsistent with the absence of neutron-induced background.

Time Relation Analysis

Measurements of the time relationships between pulses in the fission chamber and those in crystal A were made for the reasons given earlier, as well as to determine the magnitude of the fission-neutron induced background by neutron time-of-flight methods. Additional measurements were made for monoenergetic gamma-ray sources in order to determine the time-resolving capabilities of the equipment employed.

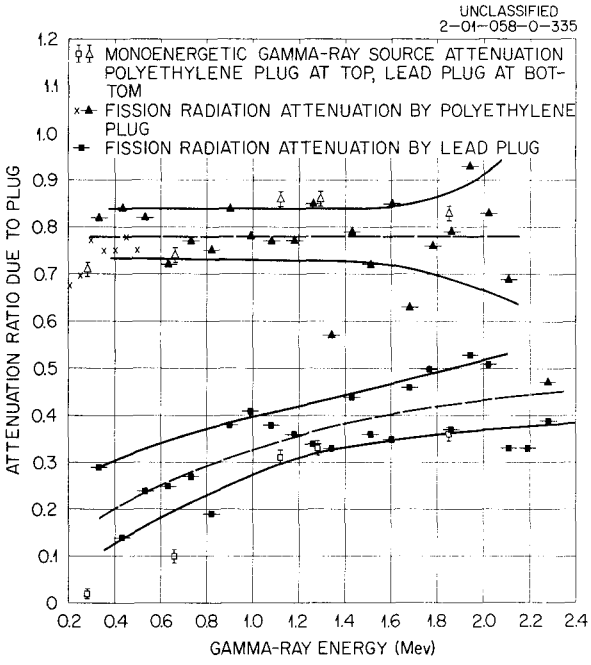

Fig. 6.2.6. Attenuation of Fission-associated and Monoenergetic Source Gamma Rays by Plugs of Lead and Polyethylene. For the lead attenuation measurement (bottom curve) a 1.95-cm-long lead plug was located in position 2 in Fig. 6.2.1. For the polyethylene attenuation measurement (top curve) a 4.2-cm-long polyethylene plug was located in position 1. The data plotted are the ratios of counting rates observed by the Compton spectrometer with and without a plug. The monoenergetic source attenuations are shown as points at five energies. The fission-associated attenuations are shown as horizontal bars which define the energy limits associated with each point. Low-energy fission-associated radiation attenuations are shown by the crosses. The solid lines include two-thirds of the attenuation ratios observed with the fission data.

Improvements in Circuitry. – A fundamental limitation in the analysis of the time of occurrence of an event in a detector would appear to arise from the rise time of the detector and the associated electronic amplification. For the fission channel, the longest rise time is that associated with the DD-2 pulse amplifier. For the scintillation channels, on the other hand, the rise time due to the sodium iodide scintillation is comparable with that of the amplifier. By the introduction of a new type of pulse-announcement circuit described elsewhere in this report (see Sec 10.3), it has been demonstrated that time resolutions of the order of a few per cent of the amplifier rise time may be achieved.

The limitation in detector rise times is more fundamental and presumably could only be modified by changing detectors. The gas scintillation fission chamber might yield a faster rise time than would the spiral fission chamber being used, but this change has not been made, since the fission chamber rise time is already small compared with that of the amplifier.

With the very considerable improvement in time resolution described above, it became profitable to introduce a multichannel time analyzer. Such an instrument was readily obtained by adaptation of the 256-channel magnetic-core-memory pulse-height analyzer. The use of a variable external sweep for timing permits the observation of a wide range of times (from 3×10^{-9} to 10^{-5} sec/channel). The time analyzer is described in detail elsewhere in this report (see Sec 10.5).

Measured Time Dependence. – In order to cover a wide range of times after fission, two sweeps of different speeds were used in the time analyzer. Data taken with the slower sweep are shown in Fig. 6.2.7. The time range covered for the fission-associated radiation in this measurement was $(2.65 \pm 0.03) \times 10^{-8}$ sec/channel, or a total time of about 5 μsec. Data were accumulated for a similar sweep speed for a gamma-ray source of Cs^{137} in order to check the performance of the time analysis equipment. For this experiment, channels A and B were employed, with channel B detecting scattered radiation as it normally does during a Compton spectrometer run. It should be noted that the calculated chance coincidence rate is consistent with the coincidence rate observed for channel numbers away from the coincident peak. This background coincidence rate is less than the peak rate by a factor of about 4000.

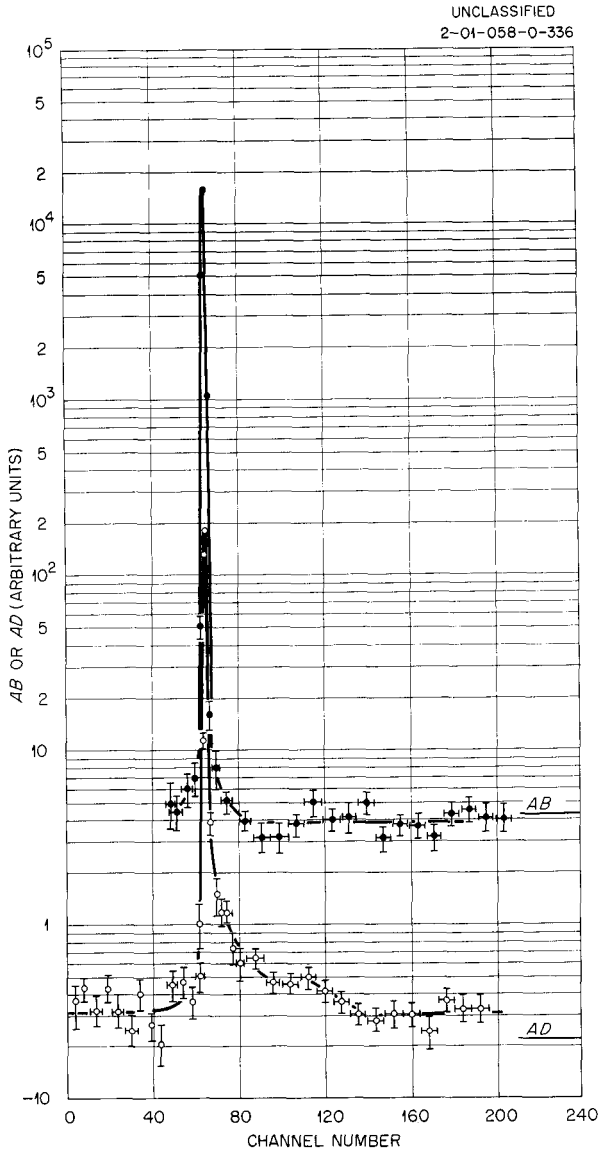

Fig. 6.2.7. Intermediate-Speed Time Analyses. The top curve represents the AB coincidence counting rate observed in the time analyzer plotted as a function of channel number. The source was Cs^{137} positioned at the fission chamber location. Thus the coincidences correspond to those normally observed in the Compton spectrometer. The energy range covered in channel A extended from 0.30 to 2.25 Mev; that in channel B from 0.1 to 0.4 Mev. For this run the sweep was triggered by channel B and cut off by channel A. The time calibration for the measurement was about 5.3×10^{-8} sec/channel. The calculated chance coincidence rate is shown as a solid line on the right-hand side of the graph. Adjacent channels were combined to improve the statistics; horizontal bars on the points indicate the time spread, while the vertical bars represent the probable statistical error. The lower curve represents data obtained with the fission chamber. The AD coincidence rate is plotted as a function of channel number. The energy range covered by channel A extended from 0.25 to 2.50 Mev. The time for each channel was $(2.65 \pm 0.03) \times 10^{-8}$ sec. The calculated chance coincidence rate is shown on the right-hand side of the graph. The time scale is not absolute in any sense, since it depends upon the delays introduced into each channel. Therefore the peaks have been normalized to fall in the same channel.

For the measurement of fission-associated radiation as a function of time, the calculated chance background is ~50% lower than that observed. The observed background is equal to the counting rate to the left of the peak, assuming that no fission-associated radiation is emitted *before* fission. The discrepancy between calculation and experiment is presumed to be due to the presence of electrical noise of sufficient magnitude to activate both coincidence channels. This assumption is made, since the *discrepancy* appears to be of roughly constant magnitude, independent of the fission rate. Thus when the fission rate was increased by a factor of 10, the observed and calculated chance coincidence rates agreed within the error of 4%.

For the measurement shown in Fig. 6.2.7, channel D was arranged to initiate the sweep in the time analyzer, and channel A was arranged to cut off the sweep. By reversing the two functions it was possible to obtain curves which were essentially the mirror image of those shown in Fig. 6.2.7. In Fig. 6.2.8 the observed coincidence rate for times after fission does not fall to the level of the rate for times before fission for 68 channels, or 1.65 μsec. The excess counts for times after fission, although apparently real, represent only a small fraction of the total fission-associated counts. From Fig. 6.2.7 this fraction is calculated to be of the order of 6%. The contribution of the previously known (>1 sec) fission-product gamma rays to the observed counting rate would be less than 10^{-4}. Even a 6% contribution of

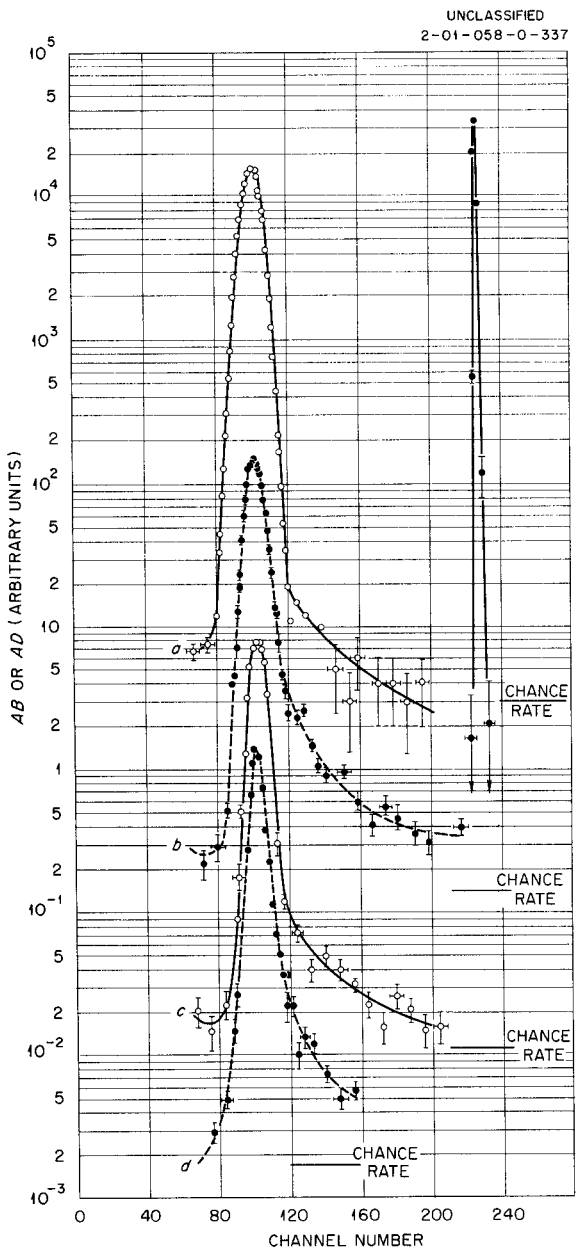

Fig. 6.2.8. Fast-Speed Time Analysis. The time calibration for all curves in this figure is $(3.13 \pm 0.1) \times 10^{-9}$ sec/channel. Curve *a* represents the AB coincidence counting rate observed as a function of the channel number. The source was Cs^{137} positioned at the fission-chamber location. The energy range covered in channel A extended from 0.20 to 2.25 Mev; that in channel B from 0.10 to 0.40 Mev. The sweep was triggered by channel B and cut off by channel A. Curve *b* represents the coincidence rate, AD, observed with the fission source. The energy range covered in channel A extended from 0.175 to 2.25 Mev. For curve *c* the range in channel A was changed to 0.55 to 2.25 Mev. Finally, for curve *d*, a 4-cm-long polyethylene plug was inserted into position 1 shown in Fig. 6.2.1. The calculated chance coincidence rates for all curves are shown on the right side of the figure. As in Fig. 6.2.7, the time calibration at the given channel is arbitrary so that all curves are normalized to make the peaks coincide. Data for adjacent channels are combined in regions of all curves. The narrow peak on the right-hand side of the figure represents the response of the time analyzer to 60-cps pulses introduced into channels A and B simultaneously by the coincident pulser (see Fig. 6.2.2). The full width at half maximum is approximately two channels, or 6×10^{-9} sec. The pulse heights for this measurement corresponded to about 0.3 Mev in both channels.

---

delayed gamma radiation in this time region would be of appreciable importance in the effects of nuclear weapons for the reasons outlined above.

In order to examine the region of shorter times after fission, a faster sweep was employed. The data shown in Fig. 6.2.8 were accumulated with a time corresponding to $(3.13 \pm 0.1) \times 10^{-9}$ sec/channel, or a total time for 100 channels of about 0.3 μsec. The performance of the time analyzer is illustrated by the peak showing its response to the coincidences produced by the multichannel 60-cps pulser. For pulses lying approximately halfway between the pulse-height discriminator settings, the apparent time resolution in terms of full width at half maximum is 6×10^{-9} sec. Since the pulser run was short, gain and zero drifts were not included in this time resolution. The data obtained with a monoenergetic gamma-ray source (curve *a* in Fig. 6.2.8) illustrate the widening of the time resolution due to the indeterminacy of the time of pulse formation in the detector and analysis in the pulse-announcement circuit. The resolution for the source run is about 4.5×10^{-8} sec. The background counting rate is reduced, compared with the peak, by a factor somewhat greater than 1000. The calculated chance coincidence rate is shown on the right-hand side of the graph as a horizontal line.

The data accumulated with the fission source (curves *b*, *c*, and *d* in Fig. 6.2.8) present markedly asymmetric peaks, with tails on the right or "time-after-fission" side of the main peak. It may be noted that 100 channels in Fig. 6.2.8 correspond to 12.5 channels in Fig. 6.2.7. Upon comparison, the "excess" counting rate above background in both figures appears to be of the same order for similar times after fission.

One purpose of examining the shortest possible time region after fission was to determine whether prompt neutrons could be detected by time-of-flight methods. Neutrons having an energy of 0.10 Mev would have a flight time through the spectrometer collimator of 6×10^{-8} sec. This time corresponds to about 20 channels in Fig. 6.2.8. Neutrons with energies >1 Mev would have flight times $<2 \times 10^{-8}$ sec. In order to determine how much of the "tail" was due to neutrons, the energy bias on channel A was increased to 0.55 Mev, thus excluding most of the known inelastic scattering gamma rays. The results, shown as curve *c* in Fig. 6.2.8, do show a lowering of the tail region relative to the main peak of the order of 30%. This reduction could, of course, be simply due to the fact that gamma radiation of low energy (<0.55 Mev) was emitted in this time region. Therefore a polyethylene plug was inserted in the collimator (in position 1 of Fig. 6.2.1) and the measurement repeated. The energy range of channel A was again 0.175 to 2.25 Mev. The results shown in curve D of Fig. 6.2.8 indicate that the tail is reduced relative to the peak by about 20%.

If these delayed counts are interpreted as corresponding to neutrons, an estimate of the neutron background in the gamma radiation may be obtained. If the neutron-induced counts are assumed to have a distribution in time corresponding to that which would be calculated by using the known neutron fission spectrum,[14] the neutron-induced background would correspond to a maximum of 4% of the total fission radiation. This value for the background is consistent with the values discussed earlier. No mechanism is postulated by which *prompt* neutrons could account for the excess counts in the time region from 0.75 to 1.5 μsec after fission. The possibility that the delayed counts are due to delayed gamma rays has not been eliminated.

Future Studies

In future studies crystal A will be moved away from the fission source in an attempt to improve the resolution for time-of-flight measurements. A factor of approximately 2 in time resolution may be obtained in this manner.

Attempts may be made to employ longer sweeps of the order of milliseconds in a search for longer-lived fission-associated gamma radiation.

After the extent of the neutron-induced background has been established, measurements of the pulse-height spectra of the fission-associated gamma radiation should be relatively straightforward but time-consuming.

[14] L. Cranberg *et al.*, *Phys. Rev.* 103, 662 (1956).

6.3. U^{233} PROMPT-NEUTRON FISSION SPECTRUM

K. M. Henry

Since a previous measurement of the U^{233} neutron fission spectrum[1] was subject to large experimental errors, the measurement has been repeated. In addition, a measurement of the neutron fission spectrum of U^{235} was made. The results of both tests are given below.

The physical arrangement of the apparatus used in the previous U^{233} experiment[1] was modified only slightly for the new measurements. As before, the Bulk Shielding Reactor (BSR) was utilized to produce neutrons which were thermalized by a large (5 × 4 × 2 ft) slab of graphite canned in aluminum. The thermalized neutrons were absorbed by the fission sample plate with the resultant production of prompt fission neutrons. The fission neutrons were detected by the proton-recoil neutron spectrometer from which energy spectra were obtained.

Background considerations dictated the use of 5 in. of lead between the reactor and the graphite to filter out the reactor gamma rays. For the same reason it was also necessary to position the spectrometer collimator at an angle of 29 deg to the thermal column. This required that a small air wedge be inserted between the graphite and the collimator.

The experimental arrangement was dictated by the size and shape of the U^{233} source, which had been fabricated for another experiment. The source container was polystyrene, the external dimensions of which were originally 8 by 8 by 1 in. It was machined so that a 6-in.-dia by 0.170-in.-thick volume was located in the center. The faces parallel to the source had been undercut so that the remaining wall was 0.125 in. thick. The central space was then filled with 250 g of U^{233} in the form of U_3O_8 powder and the filling hole sealed. The container was enclosed in a water-tight aluminum box (0.062-in.-thick walls), which was then attached to the large end of a 1-ft-long, 6-in.- to 1½-in.-dia conical neutron collimator.

The U^{235} source container was identical to that for the U^{233}. The sample used was 254 g of highly enriched U^{235} in the form of uranium metal rolled and trimmed to fit the allotted space. The two sources and their containers were used interchangeably in the water-proof container.

The operation of the neutron spectrometer has been reported previously.[2] Using large samples and placing the spectrometer collimator at an angle to the thermal column reduced the effects of fast-neutron streaming from the reactor to less than 3% of the source plate spectra.

The resultant spectra are plotted in Fig. 6.3.1. The use of samples of nearly equal masses (and having comparable cross sections) in identical fluxes and geometries yielded curves which were separated by an order of magnitude on the intensity axis to prevent overlap of information in the figure. Arbitrary intensity units were used, since the fission rate was not determined.

In the 1.4- to 10-Mev energy interval the observed U^{233}/U^{235} neutron yield per unit mass is 1.30. Yield ratios for various energy groups are tabulated in Table 6.3.1. Above 6.2 Mev the statistical errors make comparison meaningless.

---

[1] K. M. Henry and M. P. Haydon, *The Fission Neutron Spectrum of U^{233}*, ORNL CF-55-4-22 (April 22, 1955); *Appl. Nuclear Phys. Ann. Rep. Sept. 10, 1956*, ORNL-2081, p 108.

[2] R. G. Cochran and K. M. Henry, *Rev. Sci. Instr.* **26**, 757 (1955).

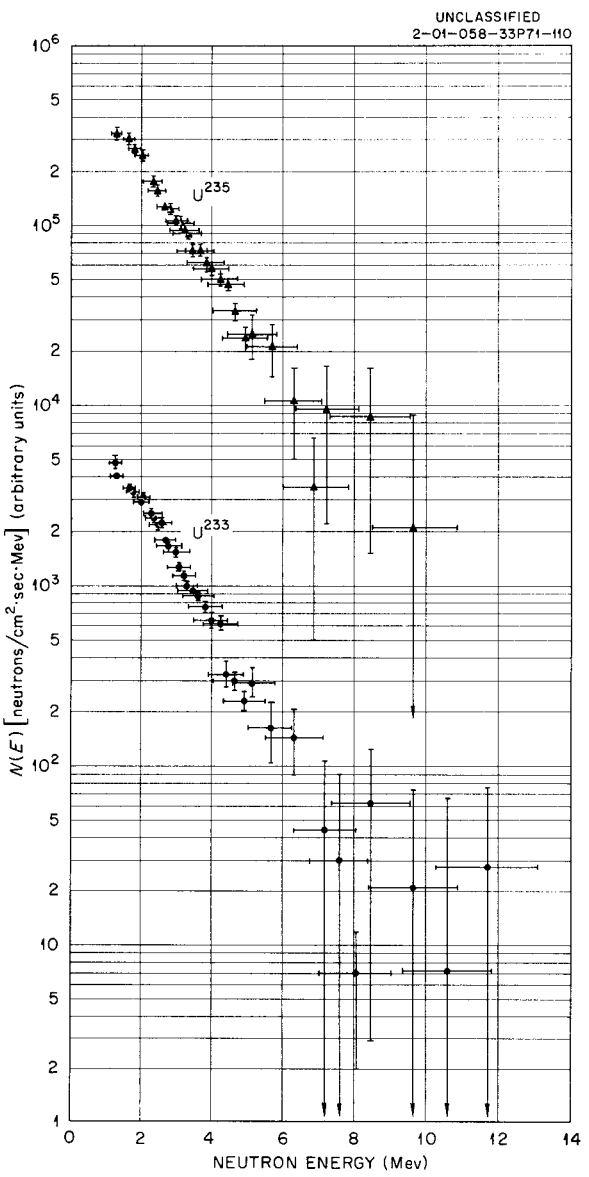

Fig. 6.3.1. Response of the BSF Proton Recoil Spectrometer to U^{233} and U^{235} Fission Neutrons. The intensity scale is arbitrary, and the two curves have been displaced so that both may be seen. The errors in intensity are based on the counting statistics. The energy errors are derived from the spectrometer constants, as discussed in the text.

Table 6.3.1. Relative Prompt-Neutron Yield of U^{233} and U^{235} Samples per Energy Interval

Neutron Energy (Mev)	Relative Yield per Unit Mass		U^{233}/U^{235} Ratio
	U^{235}	U^{233}	
1.4–2.2	2710 ± 100	3540 ± 90	1.32 ± 0.06
2.2–3.0	1420 ± 100	2100 ± 100	1.53 ± 0.15
3.0–3.8	846 ± 80	1080 ± 80	1.28 ± 0.18
3.8–4.6	500 ± 60	610 ± 60	1.22 ± 0.24
4.6–5.4	276 ± 60	336 ± 60	1.21 ± 0.44
5.4–6.2	220 ± 80	216 ± 80	1.0 ± 0.9

The numerical statistics, while smaller than those in the previous work, are large. This is accounted for by the fact that a proton-recoil spectrometer has a large background when it is in a flux of high-energy neutrons. The error was calculated by the use of the equation

$$\Delta N(E) = \frac{\sqrt{(\text{foreground})^2 + (\text{background})^2}}{\text{foreground} - \text{background}} N(E) \ .$$

The energy errors at each energy were determined in the same manner for this measurement as were those for the previous work.[1] These errors arise from proton straggling, uncertainty of proton range as a result of finite radiator and detector thickness, and finite proton collimation. The instrument design was such that the error in E was $\pm 0.1E$.

The statistical error could be improved by (1) increasing the number of counts by increasing the counting time, since the rate is already optimum, (2) reducing the number of background pulses by redesigning the equipment, or (3) decreasing the energy resolution. Since other types of spectrometers appear to offer more promise for future development (see Sec 10.2), none of these approaches are being followed at present.

6.4. COMPARISON OF THE AVERAGE NUMBER OF PROMPT NEUTRONS EMITTED IN THE FISSION OF U^{233}, U^{235}, Pu^{239}, AND Pu^{241}

G. deSaussure E. G. Silver

The average number of neutrons released per thermal fission of any isotope is an important parameter of reactor theory; furthermore, an accurate knowledge of how the average number of neutrons emitted when fission occurs varies with the isotopes may help to reveal the nature of the fission process itself. The neutrons emitted as a result of the fission process can be divided into "prompt neutrons" and "delayed neutrons." The prompt neutrons constitute over 99% of the total number of fission neutrons and are emitted within a very short time (about 10^{-14} sec) after the fission process, whereas the delayed neutrons are emitted, with gradually decreasing intensity, over a period of minutes. Preliminary measurements of the relative prompt-neutron yield per fission of Pu^{241} and U^{235} have been made previously at this laboratory.[1] Later measurements have been made of the relative neutron yields of U^{233}, U^{235}, Pu^{239}, and Pu^{241}. Because of the nature of the experimental technique employed, the yields reported do not include delayed neutrons.

[1]G. deSaussure and E. G. Silver, *Appl. Nuclear Phys. Ann. Rep. Sept. 10, 1956*, ORNL-2081, p 105.

A block diagram of the experimental apparatus is given in Fig. 6.4.1. A description of the experimental technique was presented in the earlier report[1] and will not be repeated here. Essentially, it consists of placing a sample of the fissionable isotope on nickel foils which form the electrodes of a fission chamber and then counting simultaneously the number of fissions occurring in the sample and the number of coincidences between fission neutrons and fission events. As long as the probability ϵ with which a prompt neutron can be detected in coincidence with a fission event is small, the coincidence rate r is given by the relation

$$r = r_f(\nu\epsilon + 2r_b t) , \qquad \epsilon \ll 1 , \tag{1}$$

where

ν = number of neutrons per fission in the isotope,

r_f = counting rate at the fission detector,

r_b = counting rate at the neutron detector,

t = resolving time of the coincidence circuit.

UNCLASSIFIED
2-01-058-0-350

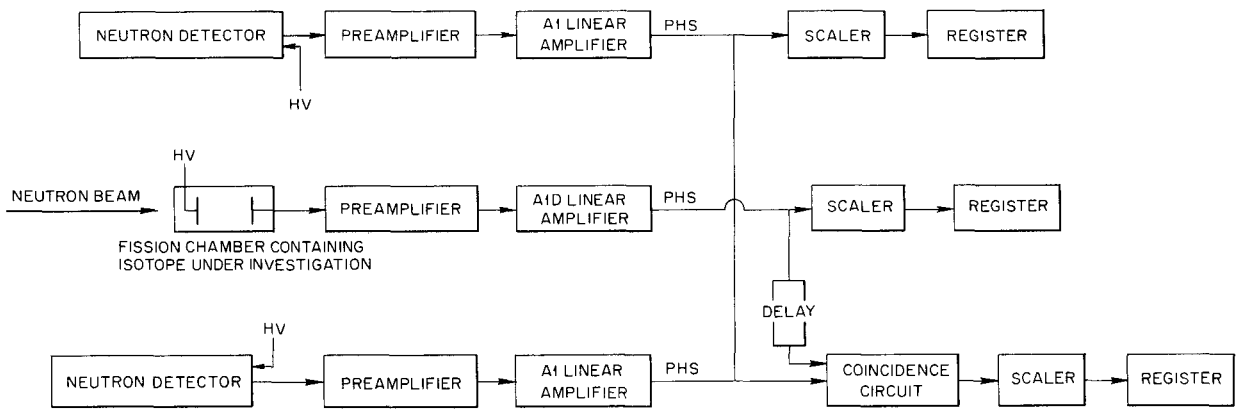

Fig. 6.4.1. Experimental Arrangement for the Measurement of ν^{23}, ν^{25}, ν^{49}, and ν^{41}.

If ϵ is the same for two isotopes A and B, the following relation holds:

$$\frac{\nu(A)}{\nu(B)} = \frac{n(A)}{n(B)}, \qquad n = \frac{r}{r_f} - 2r_b t, \tag{2}$$

where n is the ratio of coincidence rate to fission rate, corrected for accidental coincidences. It is evident from Eq. 2 that to obtain a high precision in the determination of the ratio of two values of ν, it is important to keep the correction factor $r_b t$ as small as possible, relative to r/r_f. It is not easy to reduce r_b because of a background of fast neutrons against which it is difficult to shield; thus it is advantageous to keep t as short as possible, consistent with the requirement that ϵ be kept reasonably large.

In all previous measurements employing this coincidence method,[2-4] the fast neutrons resulting from fission were first thermalized by a moderator surrounding the fissioning sample and then counted by a thermal-neutron detector. This places a lower limit on t of about 0.5 msec, since that is the time required to thermalize a fast neutron. In this experiment the fast neutrons resulting from fission were detected directly by a fast-neutron detector which recorded recoil protons associated with fast-neutron scattering. This permitted a reduction of t to about 1 μsec; consequently, a considerable reduction of the background effect $r_b t$ of Eq. 2 was accomplished.

The isotopic compositions of the four sets of sample foils are given in Table 6.4.1, and corresponding measurements of the ratio n/n^{25} are given in Table 6.4.2. No foils highly enriched in Pu^{241} were available, so the ratio n^{41}/n^{25} could not be measured directly; however, the measurements of n for foils containing approximately 50% Pu^{241}, together with measurements of n^{49}, were used to obtain a value of ν^{41}. Several determinations of the quantity n were made for each set of foils, the statistical error on each determination being

[2] F. R. Barclay and W. J. Whitehouse, *Proc. Phys. Soc. (London)* **A66**, 447 (1953).

[3] V. I. Kalashnikova *et al.*, *Conf. Acad. Sciences U.S.S.R. Peaceful Uses of Atomic Energy. Moscow, 1955. Session Div. Phys. Mathe. Sci.* p 123 (1956).

[4] J. E. Sanders, *J. Nuclear Energy* **2**, 247 (1956).

Table 6.4.1. Isotopic Composition of Foils of U^{233}, U^{235}, Pu^{239}, and Pu

Isotope	Composition (%)
	U^{235} Foils*
U^{234}	0.048 ± 0.006
U^{235}	99.806 ± 0.015
U^{236}	0.062 ± 0.006
U^{238}	0.084 ± 0.006
	U^{233} Foils*
U^{233}	98.86 ± 0.09
U^{234}	0.74 ± 0.09
U^{238}	0.40 ± 0.09
	Pu^{239} Foils**
Pu^{239}	99.81 ± 0.03
Pu^{240}	0.15 ± 0.05
Pu^{241}	0.04 ± 0.03
Pu^{242}	<0.003
	Pu Foils**
Pu^{239}	24.76 ± 0.37
Pu^{240}	25.27 ± 0.21
Pu^{241}	49.20 ± 0.22
Pu^{242}	0.77 ± 0.03

*Supplied by R. Green, Isotopes Standards Section, Uranium Measurements Group, Oak Ridge Gaseous Diffusion Plant.

**Prepared by F. Moore, Analytical Chemistry Division, with isotopes separated by the Electronuclear Research Division.

Table 6.4.2. Ratios of n/n^{25} for Various Samples

Foil	n/n^{25}
U^{233}	1.024 ± 0.005
U^{235}	1.000
Pu^{239}	1.227 ± 0.005
Pu	1.275 ± 0.005

smaller than 0.1%. However, discrepancies of the order of 0.3% existed between successive determinations of the same n. This was attributed to small changes in the gain of the fast-neutron detector sensitivity. To avoid making a systematic error in these ratios the determinations of n for the various isotopes were alternated.

As described above, values of the ratios ν/ν^{25} for various isotopes were obtained from the measured values of the ratios n/n^{25}. These values of ν/ν^{25} are summarized in Table 6.4.3, and they are based on the assumption that the efficiency of the neutron detectors is the same for the prompt fission neutrons from all four isotopes. This requirement will be met if either of the two following conditions is satisfied: (1) if the efficiency of the neutron detector is independent of energy over the range of the fission spectrum, or (2) if the prompt-neutron fission spectra of all isotopes investigated are similar. The variation of the efficiency of this type of neutron detector with energy has not been published, but it certainly is not constant over the entire fission spectrum. Thus the values of ν reported here rest on the assumption that the prompt fission neutron spectra of U^{233}, U^{235}, Pu^{239}, and Pu^{241} have no significant differences. The spectra of U^{233}, U^{235}, and Pu^{239} have been measured by various authors[5] and were found to agree reasonably well in shape. An error of 0.5% has been estimated for possible differences in the fission spectra and is included in the reported values of ratios ν/ν^{25}.

Since a value of n^{41}/n^{25} could not be measured directly, a value of ν^{41}/ν^{25} was deduced from the ratios $n(\mathrm{Pu})/n^{25}$ and n^{49}/n^{25}. If Σ^{49} and Σ^{41} represent the macroscopic fission cross sections of Pu^{239} and Pu^{241} in the plutonium foils, averaged over the flux of thermal neutrons causing the fission, the following relation holds:

$$(3)\quad \frac{n(\mathrm{Pu})}{n^{25}} = \frac{\Sigma^{49}\ \nu^{49}/\nu^{25} + \Sigma^{41}\ \nu^{41}/\nu^{25}}{\Sigma^{49} + \Sigma^{41}}\ .$$

From this relation,

$$(4)\quad \frac{\nu^{41}}{\nu^{25}} = \frac{n(\mathrm{Pu})}{n^{25}} + \left[\frac{n(\mathrm{Pu})}{n^{25}} - \frac{\nu^{49}}{\nu^{25}}\right]\frac{\Sigma^{49}}{\Sigma^{41}}\ .$$

The value of the ratio Σ^{49}/Σ^{41} was obtained as follows. The ratio of the number of atoms of Pu^{239} to the number of atoms of Pu^{241} in the plutonium foils (obtained from Table 6.4.1) was corrected for the decay of Pu^{241}, with a resulting value of 0.52 ± 0.01. The ratio of the microscopic cross section was then weighted by the neutron flux seen by the fission foils. This flux is not accurately known, but the fission cross sections of both isotopes have approximately the same energy dependence[6] in the thermal region, and most of the fission occurred in the thermal region. (This was shown[7] by covering the beam with a cadmium foil and observing that the fission rate was reduced by a factor larger than 20.) Thus instead of using the ratio of the fission cross sections averaged over the beam energy, the ratio of the cross sections for a 2200-m/s flux was used. This ratio[6] is 0.8 ± 0.1. The large limit of error was

[5] N. Nereson, *Phys. Rev.* **88**, 823 (1952); K. M. Henry and M. P. Haydon, *The Fission Neutron Spectrum of U^{233}*, ORNL CF-55-4-22 (April 22, 1955); *Appl. Nuclear Phys. Ann. Rep. Sept. 10, 1956*, ORNL-2081, p 108.

[6] D. J. Hughes and R. B. Schwartz, *Neutron Cross Sections*, BNL-325, Supplement No. 1 (Jan. 1, 1957).

[7] W. W. Pratt, F. J. Muckenthaler, and E. G. Silver, *Appl. Nuclear Phys. Ann. Rep. Sept. 10, 1956*, ORNL-2081, p 104.

Table 6.4.3. Values of ν^{23}/ν^{25}, ν^{49}/ν^{25}, and ν^{41}/ν^{25} Reported by Various Investigators

Investigator	ν^{23}/ν^{25}	ν^{49}/ν^{25}	ν^{41}/ν^{25}	Ref
This work, 1956–57	1.024 ± 0.01	1.23 ± 0.01	1.295 ± 0.02	
KAPL, 1955	1.017 ± 0.02	1.251 ± 0.03	1.305 ± 0.04	8
Harwell, 1955	1.005 ± 0.016	1.168 ± 0.022	1.232 ± 0.052	4
USSR, 1955	1.03 ± 0.01	1.19 ± 0.01	1.24 ± 0.01	3

assumed to take into account the uncertainty in the averaging. This gives

$$\frac{\Sigma^{49}}{\Sigma^{41}} = 0.416 \pm 0.06 \tag{5}$$

and

$$\frac{\nu^{41}}{\nu^{25}} = 1.275 + (1.275 - 1.227)\,0.416 = 1.295 \pm 0.02 \ . \tag{6}$$

All the results of this experiment are compared with those obtained by other researchers in Table 6.4.3. Although the values of ν/ν^{25} obtained in this experiment agree very well with values obtained by a group at KAPL by a completely different method,[8] they disagree significantly, in the case of the plutonium isotopes, with values obtained by Sanders[4] at Harwell and by the Russian workers.[3]

---

[8] D. E. McMillan *et al.*, *A Measurement of Eta and Other Fission Parameters for* U^{233}, Pu^{239}, *and* Pu^{241}, *Relative to* U^{235}, *at Sub-Cadmium Neutron Energies*, KAPL-1464 (Dec. 15, 1955).

Part 7

REACTOR PHYSICS

7.1. TIME-DEPENDENT NEUTRON-DIFFUSION MEASUREMENTS

G. deSaussure E. G. Silver

An experiment is being designed to measure the diffusion properties of crystalline moderators at various temperatures by the pulsed-neutron-source method. Some preliminary experiments have already been performed with beryllium and graphite.

Theory of the Pulsed-Neutron-Source Method

In the last few years the pulsed-neutron-source method has been used extensively to measure neutron-diffusion parameters in various moderators.[1-9] With this method a sample of moderator is irradiated by a short burst of fast neutrons (from a few microseconds to a few milliseconds), and the decay of the neutron density at the surface of the sample is observed. The fast neutrons inside the sample rapidly slow down to thermal velocities (slowing down time in beryllium $\cong$ 100 μsec). When the neutrons approach thermal equilibrium with the moderator, the neutrons continue to leak "slowly" out of the system or are absorbed. The thermal-neutron density, n, then satisfies the following differential equation:

$$D\Delta n - v\Sigma_a n = \frac{\partial n}{\partial t} , \qquad D = \frac{\lambda_{tr}}{3} v , \tag{1}$$

where

D = diffusion coefficient,
λ_{tr} = transport mean free path,
v = velocity of the neutrons,
Σ_a = macroscopic absorption cross section,
$\partial n/\partial t$ = time derivative of the neutron density, n.

The solution of Eq. 1 which satisfies the proper boundary condition (the condition that the flux vanishes at the extrapolated boundary, $\vec{R}$, of the moderator) is

$$n(t,\vec{r}) = \sum_{l,m,n} A_{lmn} S_{lmn}(\vec{r})\, e^{-(v\Sigma_a + DB^2_{lmn})t} , \tag{2}$$

where the values of A_{lmn} are constants that depend on the source position, and S_{lmn} and B^2_{lmn} are, respectively, the eigenfunctions and eigenvalues (also called bucklings) of the equation

$$\Delta S_{lmn}(\vec{r}) = B^2_{lmn} S_{lmn}(\vec{r}) , \tag{3}$$

which corresponds to the given boundary condition

$$S_{lmn}(\vec{R}) = 0 . \tag{3a}$$

Equation 2 shows that the neutron density $n(t,\vec{r})$ can be represented as a sum of exponential terms (modes). The term with the lowest decay constant (fundamental mode) will eventually become the dominant term. Thus, after a short time, Eq. 2 reduces to

$$n(t,\vec{r}) \cong AS(r)\, e^{-\lambda t} , \qquad \lambda = v\Sigma_a + DB^2 , \tag{4}$$

where the indices $l = m = n = 1$ have been dropped for simplification.

Hence a measurement of the decay constant λ of the neutron population as a function of the size or buckling B^2 of the moderating assembly will permit the determination of the absorption cross section Σ_a and of the diffusion coefficient D.

Equation 1 describes the diffusion of monoenergetic neutrons. In reality the neutrons are not monoenergetic, but the neutron density still

---

[1] G. F. von Dardel, *Kgl. Tek. Högskol. Handl.* **No. 75** (1954).

[2] G. von Dardel and N. G. Sjöstrand, *Phys. Rev.* **96**, 1245 (1954).

[3] A. V. Antonov *et al.*, *Proc. Intern. Conf. Peaceful Uses Atomic Energy, Geneva, 1955* **5**, 3 (1956).

[4] R. Ramanna *et al.*, *Proc. Intern. Conf. Peaceful Uses Atomic Energy, Geneva, 1955* **5**, 24 (1956).

[5] K. H. Beckurts, *Nichtstationare Neutronenfelder*, Thesis, Gottingen (1956).

[6] K. H. Beckurts, *Nuclear Sci. and Eng.* **2**, 516 (1957).

[7] A. Bracci and C. Coceva, *Nuovo cimento* **Serie X, IV**, 59 (1956).

[8] E. C. Campbell and P. H. Stelson, *Phys. Semiann. Prog. Rep. March 10, 1956*, ORNL-2076, p 32.

[9] R. L. Macklin, *Graphite Sphere Neutron Detector* (to be published).

satisfies Eq. 1 in most cases if the parameters are properly averaged over the flux. Neutrons diffusing in an infinite medium of negligible absorption have a Maxwell-Boltzmann distribution in thermal equilibrium with the moderator. In this case the properly averaged transport mean free path is[10,11]

$$(5)\quad \lambda_{tr} = \frac{A}{L\rho} \frac{\int [\, E\, e^{-E/kT}/\sigma_{tr}(E,T)\,]\; dE}{\int E\, e^{-E/kT}\; dE} ,$$

where

L = Avogadro's number,
A = atomic weight of the moderator,
ρ = density of the moderator,
$\sigma_{tr}(E,T)$ = microscopic transport cross section for neutrons of energy E in the moderator at absolute temperature T,
k = Boltzmann's constant.

On the other hand, neutrons diffusing through a moderator of finite size (or large absorption cross section) may never have a Maxwell-Boltzmann distribution in thermal equilibrium with the moderator.[1-9] The neutrons that have a large diffusion coefficient (large velocity or large transport mean free path) leak first out of the system. In crystalline moderators the transport mean free paths have a rather sharp variation and become very much larger for those "cold" neutrons that have a wavelength larger than the Bragg cutoff (see below). For neutrons diffusing in such a medium, a two-group approximation will lead to a better understanding of the diffusion process than will the monoenergetic approximation of Eq. 1. Two energy groups, n_1 and n_2, with diffusion coefficients D_1 and D_2, respectively, will be considered. They satisfy the following pair of differential equations:

$$(6)\quad \left(-D_1B^2 - v\Sigma_a - \beta_{12} - \frac{\partial}{\partial t} \right) n_1 + \beta_{21} n_2 = 0 ,$$

$$(7)\quad \left(-D_2B^2 - v\Sigma_a - \beta_{21} - \frac{\partial}{\partial t} \right) n_2 + \beta_{12} n_1 = 0 ,$$

where the absorption cross section Σ_a, the buckling B^2, and the velocity v are considered to be the same for the two groups for simplification; β_{12} and β_{21} are the probabilities per unit time for neutrons of group n_1 to be scattered into group n_2 and for neutrons of group n_2 to be scattered into group n_1. If it is assumed that $\beta_{12} = \beta_{21}$, the solution of Eqs. 6 and 7 is given by

$$(8)\quad n = n_1 + n_2 = e^{-(\lambda+\beta)t} \left(P\, e^{\mu t} + Q\, e^{-\mu t} \right) ,$$

where P and Q are constants and

$$(9)\quad \lambda = v\Sigma_a + \frac{D_1 + D_2}{2} B^2 , \qquad \mu^2 = \beta^2 + \left(\frac{D_1 - D_2}{2} \right)^2 B^4 .$$

Equation 8 is the sum of two terms decaying with different periods, and after a certain time only the term with the smaller period $(\lambda + \beta - \mu)$ will remain. Furthermore, for moderating geometries of large size (small buckling), μ^2 can be developed in series, leading to

$$(10)\quad n \cong P\, e^{-\lambda' t} ,$$

where

$$\lambda' \cong v\Sigma_a + \bar{D}B^2 - \frac{(D_1 - D_2)^2}{8\beta} B^4 ,$$

$$\bar{D} = \frac{(D_1 + D_2)}{2} .$$

The two-group assumption used to obtain Eq. 10 is only a very rough approximation of the true situation, but it indicates, through Eq. 10, that for large sizes of the diffusing media the plot of the decay constants λ of the neutron population vs the buckling B^2 should be a parabola:

$$(11)\quad \lambda = v\Sigma_a + \bar{D}B^2 - CB^4 ,$$

where C is a positive parameter that increases with increasing spread of the diffusion coefficient $D(E)$ over the neutron spectrum. Parameter C of Eq. 11 was observed experimentally by many researchers. A theoretical interpretation was given first by von Dardel[1,2] but was on a somewhat different basis than the one discussed above. The "two-group theory" given above was first developed by Antonov *et al.*[3]

[10] A. M. Weinberg and L. C. Noderer, *Theory of Neutron Chain Reactions, Volume I, Diffusion and Slowing Down of Neutrons*, ORNL CF-51-5-98, p I-39 (May 15, 1951).

[11] A. M. Weinberg and E. P. Wigner, *Preliminary Draft, Theory of Neutron Chain Reaction*, ORNL CF-56-11-43, vol I, p 8.42 (Nov. 17, 1956).

Estimation of the Temperature Dependence of the Transport Mean Free Path

For very large moderating assemblies, where the neutron flux is in a Maxwell-Boltzmann distribution in thermal equilibrium with the moderator, the transport cross section $\sigma_{tr}(E,T)$ is a function of both the energy of the neutrons and the temperature of the moderator. For crystalline media, the transport cross section exhibits well-known coherence effects. These effects have not been investigated very much, which makes it difficult to predict the temperature dependence of the transport mean free path in crystalline materials. (The total cross section of various crystalline materials has been measured as a function of the temperature of the material and of the energy of the neutron; see refs 12, 13, and 14. Various attempts have also been made to calculate the scattering and transport cross sections of crystalline moderators; see refs 15, 16, and 17.)

In order to obtain a very rough estimate of the change in transport mean free path in, say, beryllium with temperature and in order to consider the factors that cause this change, a simplified model of the behavior of the total microscopic transport cross section of beryllium will be used; the scattering cross section of beryllium will be assumed to be constant and equal to $\sigma = 6$ barns for all energies above $E_c = 0.005$ ev. Below this energy it will be assumed to be constant again and equal to $\sigma_1 = 0.6$ barn for a moderator temperature of 300°K and $\sigma_2 = 0.06$ barn for a moderator temperature of 100°K. The experimentally determined behavior of the total cross section of beryllium is given in BNL-325 (ref 18) and is reproduced in Fig. 7.1.1 along with the simplified model indicated above. The experimental cross section follows a much more complicated behavior than the one described in the model. The sharp jump associated with the Bragg cutoff does not occur at 0.005 ev but extends from 0.004 to 0.007 ev. Furthermore, the cross sections above and below the Bragg cutoff are not constant but vary somewhat with energy. Yet the model proposed above permits an easy analytical evaluation of the change in transport mean free path with temperature, and since it approximates the real behavior of the cross section, it should give a good estimate of the order of magnitude of the effect.

The absorption cross section in beryllium is so small that the scattering cross section is almost equal to the total cross section given in Fig. 7.1.1, even for neutrons with wavelengths larger than the Bragg cutoff.

In this simplified model it will be assumed that the transport cross section is proportional to the scattering cross section. Then the ratio of the transport mean free path of "thermal neutrons" in beryllium at temperature $T_1 = 300°K$ and at temperature $T_2 = 100°K$ can be roughly estimated as

$$(12)\quad \frac{\lambda_{tr}(300°K)}{\lambda_{tr}(100°K)} \cong \frac{\rho(100°K)}{\rho(300°K)} \frac{\frac{1}{\sigma_1}\int_0^{x_1} x\, e^{-x}\, dx + \frac{1}{\sigma}\int_{x_1}^{\infty} x\, e^{-x}\, dx}{\frac{1}{\sigma_2}\int_0^{x_2} x\, e^{-x}\, dx + \frac{1}{\sigma}\int_{x_2}^{\infty} x\, e^{-x}\, dx}$$

$$= \frac{(1 + x_1)\, e^{-x_1}\left(\frac{1}{\sigma_1} + \frac{1}{\sigma}\right) - \frac{1}{\sigma_1}}{(1 + x_2)\, e^{-x_2}\left(\frac{1}{\sigma_2} + \frac{1}{\sigma}\right) - \frac{1}{\sigma_2}} \cong \frac{1}{10},$$

[12] O. Halpern, M. Hamermesh, and M. H. Johnson, *Phys. Rev.* **59**, 981 (1941).

[13] E. Fermi, W. J. Sturm, and R. G. Sachs, *Phys. Rev.* **71**, 589 (1947).

[14] D. J. Hughes, *Pile Neutron Research*, p 249, Addison-Wesley, Cambridge, 1953.

[15] R. Weinstock, *Phys. Rev.* **65**, 1 (1944).

[16] R. C. Bahndari, private communication.

[17] J. F. Hogerton and R. C. Grass (eds.), *The Reactor Handbook, Volume 3 — Section I, General Properties of Materials*, AECD-3647 (March 1955).

[18] D. J. Hughes and J. A. Harvey, *Neutron Cross Sections*, BNL-325 (July 1, 1955).

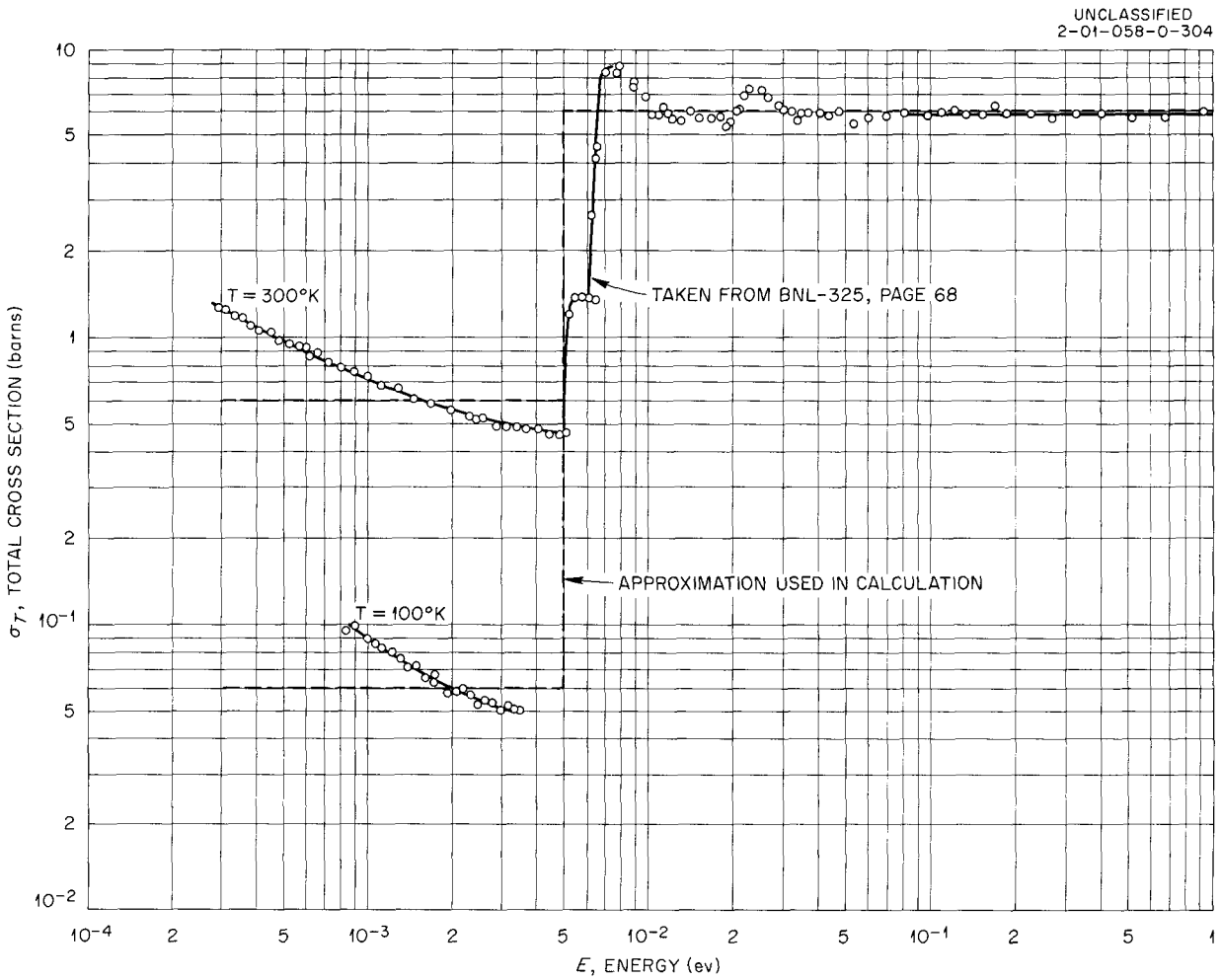

Fig. 7.1.1. Total Cross Section of Beryllium for Thermal Neutrons: Comparison of BNL-325 Values with an Approximate Scattering Cross Section Used for Calculation of the Temperature Variation of the Transport Mean Free Path.

where the density effect $\rho(100°K)/\rho(300°K)$ has been neglected, where $x_1 = E_c/kT_1 = 0.2$ and $x_2 = E_c/kT_2 = 0.6$, and where the other symbols are defined above.

It results from this simplified calculation that the change in transport mean free path in beryllium, when the metal is cooled from room temperature to liquid-nitrogen temperature (about 100°K), should be of the order of a factor of 10.

Experimental Arrangement

A series of experiments is being planned to measure the diffusion parameters of beryllium, graphite, and perhaps beryllium oxide and lampblack, at room temperature, at liquid-nitrogen temperature (100°K), at 260°K, and at 500°K. A block diagram of the experimental arrangement is shown in Fig. 7.1.2. The equipment consists of a neutron-pulsing system, a detector, a time analyzer, and various moderating geometries. All the components, which are described below, are now available with the exception of the SAMES (Société Anonyme de Machines Electrostatiques) electrostatic generator, which will not be available before February 1958.

Pulsed Neutron Source. Fast-neutron bursts will be produced by a particle accelerator, and the $d(d,He^3)n$ reaction will be used. If very high intensities are required, the $d(t,He^4)n$ reaction will be used. This accelerator is being assembled

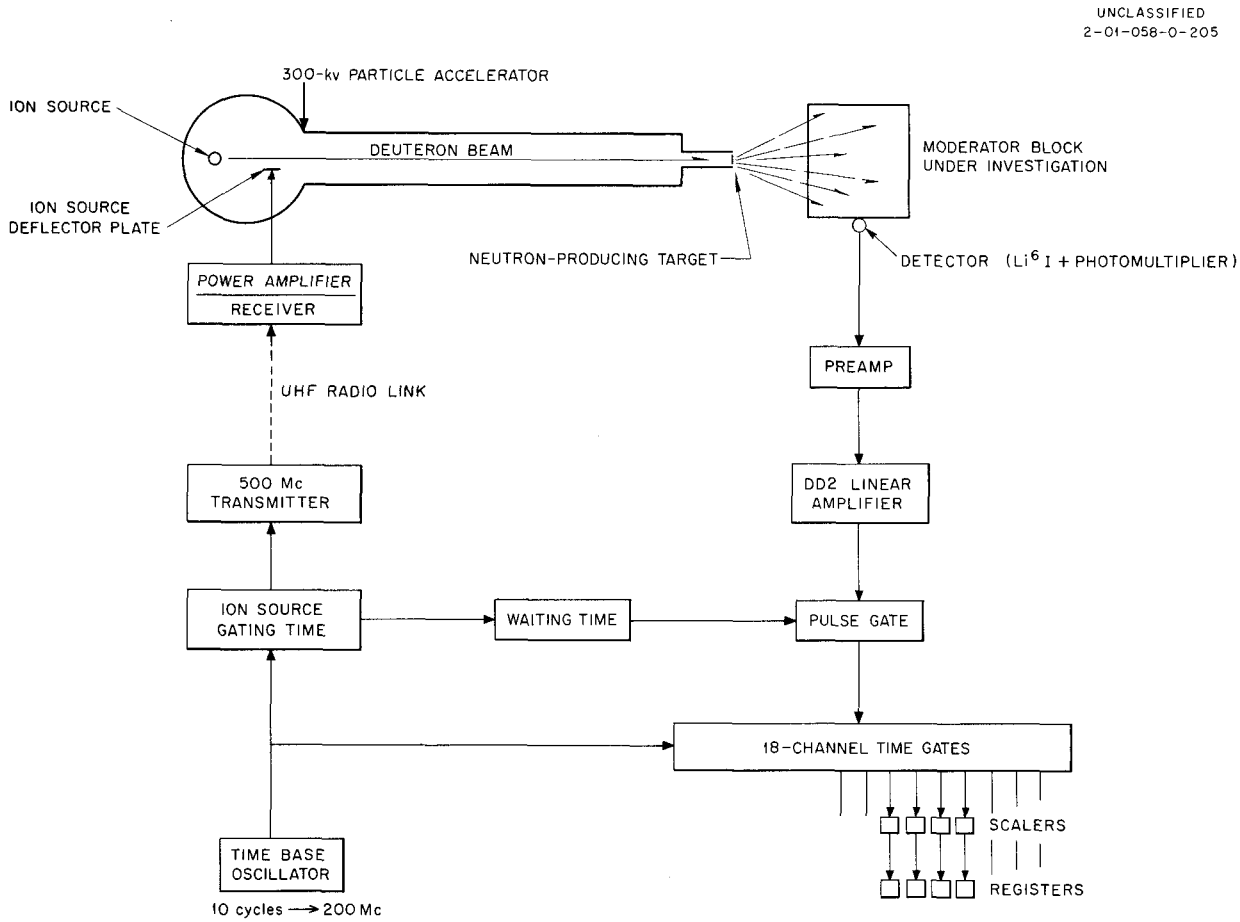

Fig. 7.1.2. Block Diagram of the Experimental Arrangement for Measurements of the Diffusion Parameters of Neutrons in Various Moderating Materials.

and will be located on the first floor of Building 3010. It will be operated at 300 kv with an SAMES high-voltage electrostatic generator delivering an output current of 1.2 ma. A UHF radio link will connect a transmitter at ground potential to a receiver in the high-voltage end of the accelerator. Through this link the length and repetition rate of the deuterium pulses will be controlled with a set of deflection plates just below the deuterium ion source.[19]

Detector. The detector will consist of an $Li^6I(Eu)$ scintillation crystal, about 1 cm in diameter and 0.3 cm in thickness, optically connected through a Lucite light piper to an RCA 6655 2-in.-dia photomultiplier. The signals from the photomultiplier will be amplified through a preamplifier and a DD2 amplifier.[20] The signal from the differential pulse-height analyzer of the amplifier will be fed to the time analyzer (built by F. Glass, Instrumentation and Controls Division). The Li^6I crystal is black to thermal neutrons. [It responds to neutrons by means of the reaction $Li^6(n,\alpha)H^3$.] The disintegration products lose their energy in the crystal and cause a large and well-defined scintillation pulse, which can easily be discriminated from pulses caused by gamma rays or other sources of scintillation. A photon of about 3.5 Mev, spending all its energy in the crystal, would produce a scintillation of the same amplitude as the scintillation caused by the

[19] This method has been described by R. F. King and V. E. Parker, *Phys. Semiann. Prog. Rep. Sept. 10, 1955*, ORNL-1975, p 65.

[20] E. Fairstein, *Rev. Sci. Instr.* **27**, 475 (1956).

$Li^6(n,\alpha)H^3$ reaction.[21] However, the probability of a photon expending 3.5 Mev energy in such a small crystal is unlikely.

Time Analyzer. The pulses from the neutron detector are fed into an 18-channel time analyzer. The width of the time channels can be varied from a few microseconds to a few hundred milliseconds. The length of the waiting time between the end of the neutron pulse and the beginning of the counting can be varied, as well. The time analyzer records coincidences between the input signals and a time signal running down the 18 positions of two M010 Burroughs beam switching tubes.

Moderating Assemblies. The moderating assemblies will be almost cubical prisms of various sizes and materials. The bucklings of a cube with side dimension a are given by

$$B^2_{lmn} = \frac{\pi^2}{\tilde{a}^2}(l^2 + m^2 + n^2) , \tag{13}$$

where $\tilde{a} = a + 1.42\ \lambda_{tr}$ is the "extrapolated size" of the side of the cube. If the neutron source is on a center line of the cube and if the detector is on the center of another face of the cube, only "odd modes" will be detected (since "even modes" will have a mode at the detector or at the source). The lowest odd mode after the fundamental, B^2_{113}, decays about $1\frac{1}{3}$ times faster than the fundamental mode (in most sizes of moderator considered, the leakage DB^2 is much larger than the absorption $v\Sigma_a$). Under those conditions it should be easy to separate the fundamental mode from its higher harmonics, so as to use Eq. 4.

Equipment has been prepared for cooling three beryllium prisms to liquid-nitrogen temperatures. The sizes of the prisms are about 8 × 9 × 9 in., $11\frac{1}{2} \times 11\frac{1}{2} \times 12$ in., and $14\frac{1}{2} \times 14\frac{1}{2} \times 16$ in. Each prism will be enclosed in a brass can (lined inside with 30-mil-thick cadmium sheets to obtain a well-defined buckling). The brass cans will be placed inside a liquid-nitrogen bath in front of the accelerator tube. These assemblies have already been tested, and it was found that a fairly homogeneous temperature distribution inside the beryllium assembly could be obtained in a few hours.

[21] R. B. Owen, AERE EL-L-10 (March 16, 1954) (Classified).

Preliminary Results

Although the apparatus just described has been designed to be placed on a 300-kv accelerator that will be set up in Building 3010, some preliminary experiments, mainly to check on the performance of the equipment, have been made with a 200-kv accelerator that has been available on part-time basis in Building 5500 (the Van de Graaff building). The decay periods of various assemblies of beryllium and graphite have been measured at room temperature. Figure 7.1.3 shows the decay of the neutron density in a 20 × 20 × 24 in. block of beryllium. Figure 7.1.4 shows the decay of the neutron density in a 28-in. cube of AGHT graphite. Figure 7.1.5 shows a curve of the decay period vs the buckling for beryllium prisms of various sizes. The corresponding plot for AGHT graphite is shown on Fig. 7.1.6.

As indicated by Eq. 4 or 11, the intercept of the curves of Figs. 7.1.5 and 7.1.6 on the axis $B^2 = 0$ is equal to the inverse of the lifetime τ_a of

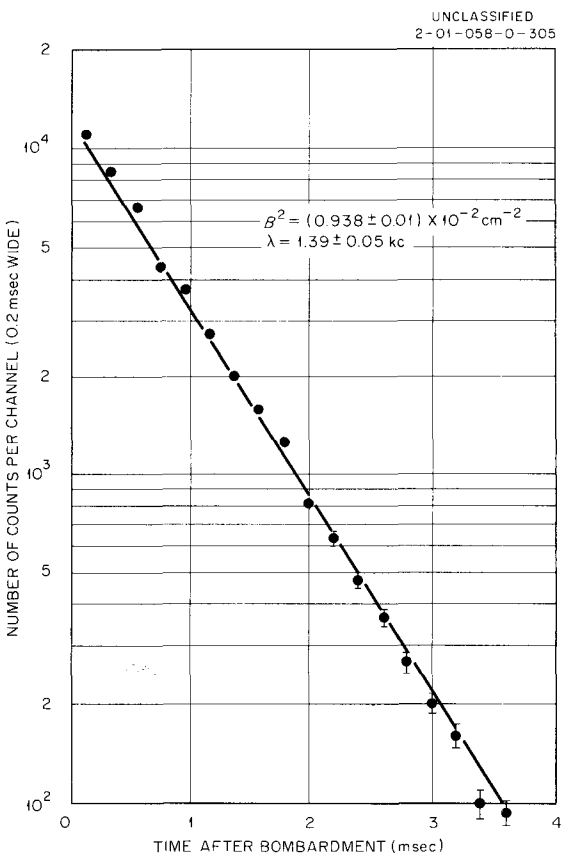

Fig. 7.1.3. Decay of the Neutron Density in a 20 × 20 × 24 in. Prism of Beryllium.

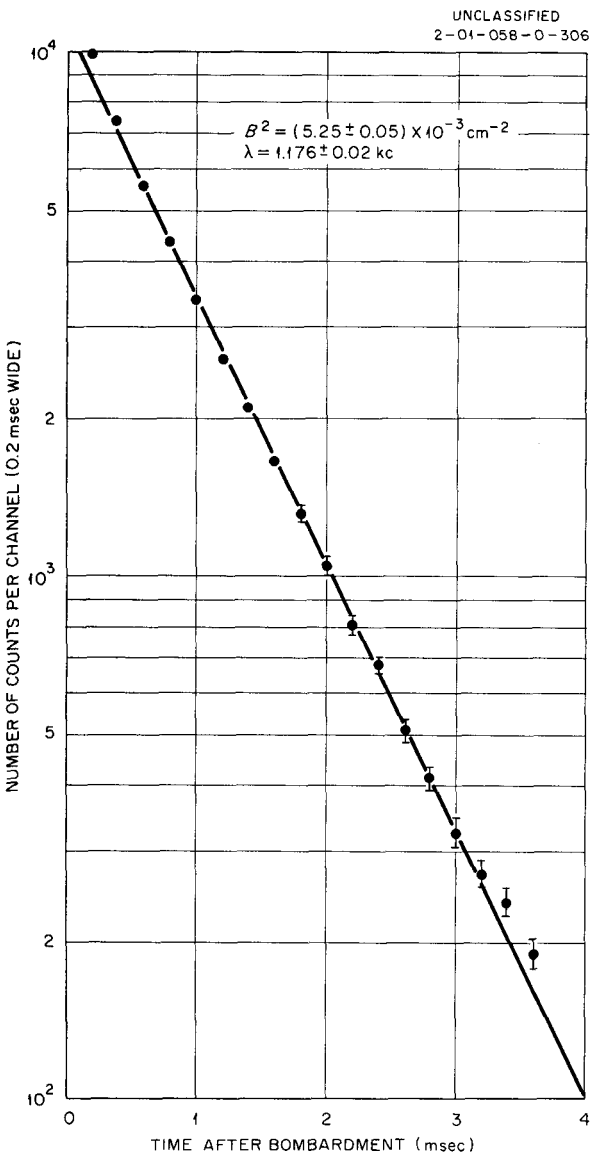

Fig. 7.1.4. Decay of the Neutron Density in a 28-in. Cube of AGHT Graphite.

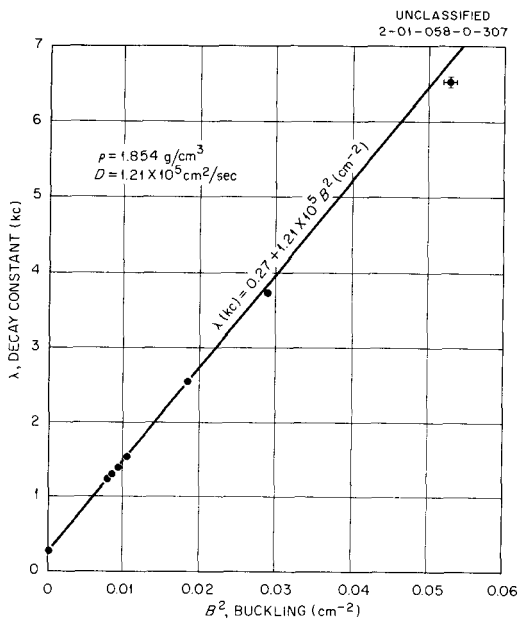

Fig. 7.1.5. Neutron Density Decay Constant as a Function of Buckling for Beryllium.

thermal neutrons in a prism of infinite dimensions. An experimental determination of this lifetime will allow the determination of the absorption cross section, or, conversely, a knowledge of the absorption cross section will permit the calculation of the intercept of the curve λ vs B^2 described by Eqs. 4 and 11.

The sizes of the prisms of graphite investigated were too small to allow a precise extrapolation of the curve λ vs B^2 to the axis $B^2 = 0$. Rather, the intercept in Fig. 7.1.6 was calculated from the known absorption cross section of AGHT graphite, Σ_a (2200 m/sec) = (0.40 ± 0.05) × 10^{-2} cm^{-1}. (This value of Σ_a was determined from the value σ_a (2200 m/sec) = 4.8 mb reported[17] for AGOT graphite. The appropriate corrections were made for the difference in density between AGHT and AGOT graphite.) Table 7.1.1 lists the mean lifetime τ_a and the diffusion coefficient D of thermal neutrons in room-temperature beryllium and AGHT graphite, as determined from Figs. 7.1.5 and 7.1.6; it also lists the microscopic absorption cross section σ_a (2200 m/sec) and the transport mean free path λ_{tr}, derived from the mean lifetime and the diffusion coefficient. Table 7.1.2 lists some published values of the diffusion parameters in beryllium and graphite.

Conclusion

The preliminary experiments just described permitted a better knowledge to be acquired of the performance of the various parts of the equipment and provided some experience with the pulsed-neutron technique. Although results have been obtained that agree with published values, various aspects of the technique will still have to be improved on. For example, the decay constants of the various moderating assemblies were determined

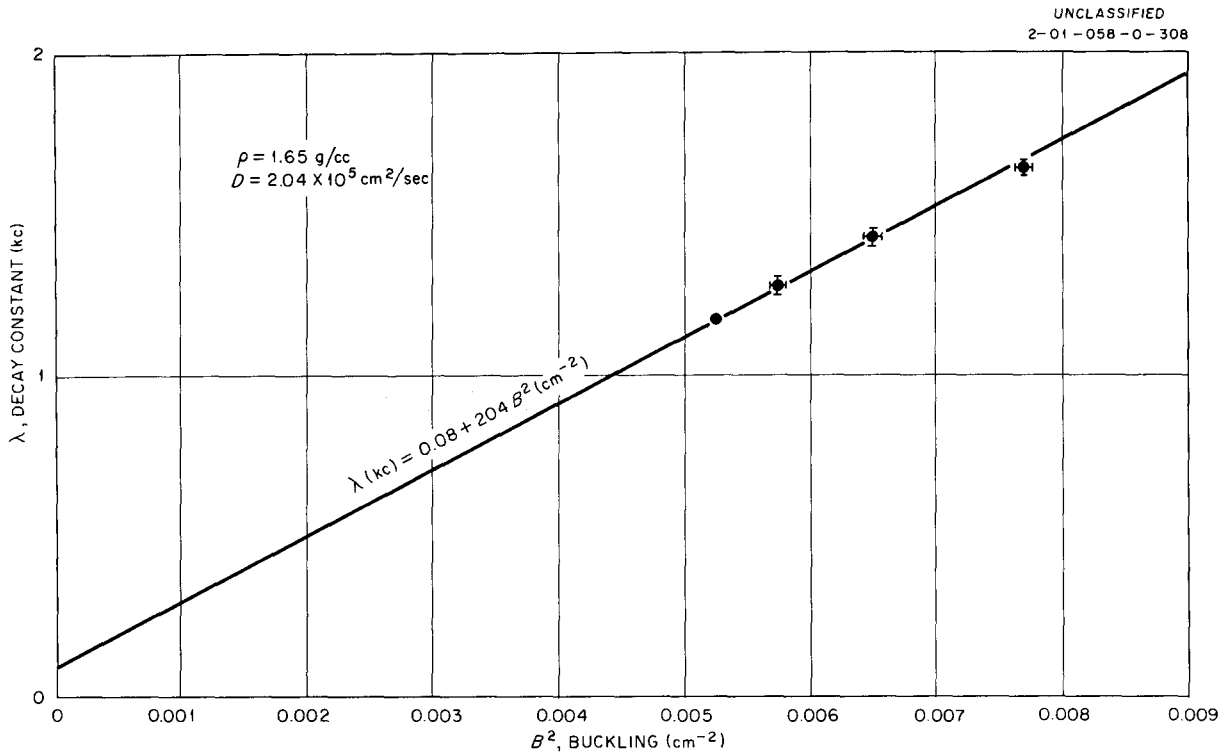

Fig. 7.1.6. Neutron Density Decay Constant as a Function of Buckling for AGHT Graphite.

Table 7.1.1. Measured Diffusion Parameters of Thermal Neutrons in Beryllium and AGHT Graphite at Room Temperature

Parameter	Beryllium	AGHT Graphite
ρ, density (g/cm^3)	1.85 ± 0.01	1.65 ± 0.01
τ_a, mean lifetime (msec)	3.7 ± 1	(11.5 ± 1.5)
D, diffusion coefficient (cm^2/sec)	1.21 ± 0.05 × 10^5	2.04 ± 0.06 × 10^5
σ_a (2200 m/sec), absorption cross section (mb)	10 ± 3	(4.8 ± 0.5)*
λ_{tr}, transport mean free path (cm)	1.45 ± 0.06	2.45 ± 0.08

*Calculated.

analytically by the well-known method of Peierls,[22] a method that can be applied only to a simple exponential decay. A close examination of Fig. 7.1.4 shows that for the graphite prisms, for instance, the decay is not a simple exponential; actually the decay constant seems to decrease with increasing time. In such a case, a portion of the decay curve was selected that seemed to be purely exponential, and the decay constant of this portion was determined. The change of period with time observed in Fig. 7.1.4 could be explained in various ways: contamination by higher modes (Eq. 2), the presence of a small background, or slow thermalization of the neutron population. (According to a theoretical calculation by Kothari and Singwi,[23] neutrons slowing down from 2 Mev in an infinite beryllium moderator at 300°K are slowed to 1.4 ev in about 13 μsec and from 1.4

[22] R. Peierls, *Proc. Roy. Soc. (London)* **A149**, 467 (1935).

[23] L. S. Kothari and K. S. Singwi, *Slowing Down of Neutrons in Beryllium from 1.44 ev to Thermal Energy* (to be published).

Table 7.1.2. Various Published Values of the Diffusion Parameters of Thermal Neutrons in Beryllium and Graphite at Room Temperature[a]

	Reference	Beryllium	Graphite
σ_a, absorption cross section (mb)	*b*	10 ± 1	3.2 ± 0.2
	c	9.0 ± 0.5	4.8
D, diffusion coefficient (cm^2/sec)	*d*	$1.17 \pm 0.05 \times 10^5$	$2.00 \pm 0.03 \times 10^5$
	e		$2.08 \pm 0.02 \times 10^5$
	f	1.25×10^5	
	g	1.21×10^5	
τ_a, mean lifetime (msec)	*b*	3.7 ± 0.4	
	f	6.6	
	h	4.3	
	i	3.2	

[a]All values dependent on density were corrected to a beryllium density of 1.85 g/cc and a graphite density of 1.65 g/cc.

[b]Calculated from value of σ_a in *Neutron Cross Sections*, by D. J. Hughes and J. A. Harvey, BNL-325 (July 1, 1955).

[c]J. F. Hogerton and R. C. Grass (eds.), *The Reactor Handbook, Volume 3 – Section I, General Properties of Materials*, AECD-3647 (March 1955).

[d]A. V. Antonov *et al.*, *Proc. Intern. Conf. Peaceful Uses Atomic Energy, Geneva, 1955* **5**, 3 (1956).

[e]K. H. Beckurts, *Nichtsationare Neutronenfelder*, Thesis, Gottingen (1956); see also *Nuclear Sci. and Eng.* **2**, 516 (1957).

[f]E. C. Campbell and P. H. Stelson, *Phys. Semiann. Prog. Rep. March 10, 1956*, ORNL-2076, p 32.

[g]R. C. Bahndari, private communication.

[h]S. Glasstone, *Principles of Nuclear Reactor Engineering*, p 167, Van Nostrand, New York, 1955.

[i]Calculated from value of Σ_a in *Preliminary Draft, Theory of Neutron Chain Reactions*, by A. M. Weinberg and E. P. Wigner, ORNL CF-56-11-43, vol I, p 8.42 (Nov. 27, 1956).

ev to 300°K in 100 μsec. In graphite the slowing down time is obviously even longer.) A precise investigation of the decay of the neutron population in various small moderating assemblies and over long periods after the end of the fast-neutron bombardment will permit the determination of the pertinent decay period with more precision. But since such an investigation will require higher counting rates at the neutron detector than were available in the preliminary experiments, various methods of increasing the counting rate are being considered. As one means, larger Li^6I crystals have been ordered. The size of these crystals is limited by the necessity of discriminating against background due to gamma radiation. However, a simple test has shown that, at least for the 1-cm-dia, 0.3-cm-thick crystals, this background is completely negligible. (No counts can be observed when the crystals are covered with cadmium foils.)

The results reported here have been obtained with a deuteron beam smaller than 200 μa. It is hoped that with the new accelerator assembled in Building 3010 somewhat larger beam currents will be available. If the counting rates cannot be sufficiently increased by the methods described above, the $d(t,He^4)n$ reaction will be used, since it has a yield about 10 times larger than the $d(d,He^3)n$.

Part 8

REACTOR THEORY

8.1. SOME ANALYTICAL SOLUTIONS OF THE SLOWING-DOWN PROBLEM IN HYDROGEN

L. Dresner A. Simon

Because the continuous slowing-down model is inapplicable to moderation by hydrogen, Selengut and Goertzel[1] introduced an approximate method which correctly accounts for the neutron energy distribution after scattering. Their method, however, computes neutron leakage by the usual age-diffusion theory. This approximation has the well-known consequence that the age in water is overestimated.[2] The most elementary approximation to the Boltzmann equation in which the age is given correctly is the P_1 approximation.[3] For large reactors, in which only the second moment of the slowing-down distribution is significant, the P_1 approximation ought to represent an improvement over the Selengut-Goertzel method. In small reactors, in which several moments of the slowing-down distribution are important, this may not necessarily be true. In particular, the slowing-down density in the P_1 approximation becomes negative for large bucklings for certain assumed variations of the cross sections with energy.[4] This pathologic behavior is a result of the attempt to represent the highly anisotropic angular distribution of the flux in a small reactor with only the first two Legendre polynomials.[4] There is another[2] approximation to the Boltzmann equation, called the B_1, in which terms of order P_1 and P_0 in the angular distribution of scattered neutrons in the laboratory system are retained. Terms of all orders, P_l, in the angular expansion of the neutron flux are retained, however, so that even quite anisotropic fluxes can be represented. This improves the accuracy of the approximation and results in a positive slowing-down density for all values of the buckling.

Several problems in which analytic solutions for the Fourier transform of the slowing-down density exist in both the P_1 and Selengut-Goertzel approximations have been considered previously,[4] and from a study of these solutions some insight into the behavior of the two approximations was obtained. It is the purpose of this paper to report a study of two problems in which analytic solutions in the P_1, B_1, and Selengut-Goertzel approximations exist. The first is the case of all cross sections constant in energy. Plotted in Fig. 8.1.1 is $q(ku)$ vs $(k/\Sigma_{SH})^2$, where k is the buckling and Σ_{SH} is the scattering cross section of hydrogen, and $q(ku)$ is the slowing-down density at lethargy u for a particular choice of constant cross sections. The curves must all intersect at one point whose ordinate is the resonance escape probability when $k^2 = 0$; their slopes at the origin are numerically equal to $-\Sigma_{SH}^2\tau$, where τ is the age to u. It appears that the Selengut-Goertzel age is smaller than the true age, and computation verifies that it is smaller by about 2%. On the other hand, if $\Sigma_a = \Sigma_{SM} = 0$, then the true age is always smaller than the Selengut-Goertzel age, the latter becoming asymptotically correct[5] for large u. Here Σ_a is the absorption cross section, and Σ_{SM} is the scattering cross section of an infinitely heavy scattering material.

[1] G. Goertzel, *Criticality of Hydrogen Moderated Reactors*, TAB-53 (July 25, 1950); D. Selengut, private communication to G. Goertzel.

[2] H. Hurwitz, Jr., and P. F. Zweifel, *J. Appl. Phy.* 26, 923 (1955).

[3] R. E. Marshak, *Revs. Modern Phys.* 19, 201 (1947).

[4] A. Simon, *Neutron Slowing Down by Hydrogen in the Consistent P_1 Approximation*, ORNL-2098 (July 5, 1956).

[5] L. C. Biedenharn and T. A. Welton, *Some Remarks on the Slowing Down of Neutrons in Hydrogen*, ORNL-2107 (Aug. 10, 1956).

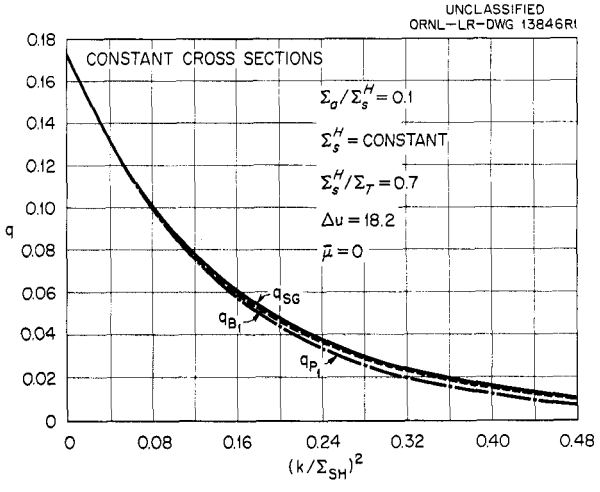

Fig. 8.1.1. Variation of Slowing-Down Density with Buckling.

In the limit of large buckling, and for the case $\Sigma_a = \Sigma_{SM} = 0$, the three curves have the following asymptotic behavior:

$$(1a) \quad q(ku) \sim \frac{\Sigma_{SH}^2}{k^2} e^{-u} \qquad \text{(Selengut-Goertzel)}$$

$$(1b) \qquad \sim -\frac{3\Sigma_{SH}^2}{k^2} e^{-u} \qquad (P_1)$$

$$(1c) \qquad \sim \frac{\pi}{2}\frac{\Sigma_{SH}}{k} e^{-u} \qquad (B_1) \ .$$

It is possible to show that the asymptotic behavior of the B_1 approximation is actually the correct asymptotic behavior of the true solution of the Boltzmann equation. This can be done, for example, directly from Eq. 1. A more physical method is as follows: $q(ku)$ can be interpreted[6] as the fast neutron nonleakage probability to lethargy u from a slab of thickness π/k of an isotropic, monoenergetic neutron source whose spatial dependence is given by cos (kx), where x is measured from the center line of the slab. If the buckling k is sufficiently large, the reactor will be so thin that only those neutrons that are thrown below lethargy u in their first collision will not leak out. The leakage is given by the current normal to the faces of the slab, and for a thin reactor is essentially due to the uncollided flux. Specifically, the nonleakage probability per unit surface from an isotropic unit plane source placed at x in the slab is $\pi\Sigma_{SH}/2k$ to the lowest order in $1/k$. Since this result is independent of x, to the lowest order in $1/k$, the over-all nonleakage probability for the cosine distribution is equal to $\pi\Sigma_{SH}/2k$. Of the neutrons which collide, the fraction thrown below u on the first (and in this approximation, the only) collision is $K_0(u) = e^{-u}$. Multiplying this quantity by the nonleakage probability gives Eq. 1c.

The physical reason for the correctness of the asymptotic behavior of the B_1 approximation lies in the fact, obvious from the previous paragraph, that all solutions of the slowing-down problem with an isotropic, monoenergetic source and the same angle-integrated scattering kernel, K_0, have the same asymptotic solution. The B_1 approximation to hydrogen moderation is the *exact* solution of the slowing-down problem with scattering kernel $K(U,\mu_0) = (4\pi)^{-1}(e^{-U} + 3e^{-3U/2}\mu_0)$, which has the same K_0 value as the complete slowing-down problem in hydrogen. The P_1 approximation, on the other hand, is not the *exact* solution to any slowing-down problem because it lacks terms in P_2 and higher in the flux. A similar conclusion applies to the Selengut-Goertzel approximation.

The fact that the B_1 approximation must be a good solution of the slowing-down problem, in the limit of both small and large buckling, implies that it should be quite a good approximation for all buckling. Hurwitz and Zweifel[2] have calculated some integrated fluxes,

$$\int_0^\infty N_0(ku)du \ ,$$

in the case of constant cross sections ($\Sigma_a = \Sigma_{SM} = 0$) for $k = \Sigma_{SH}$ and $k = 5\Sigma_{SH}$. In the first case the B_1 is only 10% smaller than the exact result; the P_1 is smaller by nearly a factor of 2. In the second case the P_1 is smaller than the exact result by nearly a factor of 10; the B_1 is only 10% smaller. From the closer agreement of the Selengut-Goertzel and the B_1 approximations, as compared with the P_1 and the B_1 approximations, it may be conjectured that for small reactors ($\sim$5 to 10 mean free paths in diameter) the Selengut-Goertzel method is better than the P_1 approximation.

Another problem in which the P_1, B_1, and Selengut-Goertzel approximations may all be solved analytically is $\Sigma_a = \Sigma_{SM} = 0$, $\Sigma_{SH} \propto v^3$, where the last term is the cube of the neutron velocity. If the source energy is made high enough, then $q(ku)$ becomes independent of the source energy. The physical reason is that the cross section is sufficiently large at the source energy so that the neutrons slow down for a while without migrating at all. Plotted in Fig. 8.1.2 is the $q(ku)$ in the P_1, B_1, and Selengut-Goertzel approximations in the case where q is independent of the source energy. In this case it is seen that both the P_1 and Selengut-Goertzel approximations underestimate the B_1 value of $q(ku)$, the underestimate being larger for the Selengut-Goertzel approximation. The age in the Selengut-Goertzel approximation is greater than the exact age; calculation shows it to be $\frac{1}{3}\Sigma_{SH}^2(u)$, which is twice the exact age.

[6] S. Glasstone and M. C. Edlund, *Elements of Nuclear Reactor Theory*, p 349 ff, Van Nostrand, New York, 1952.

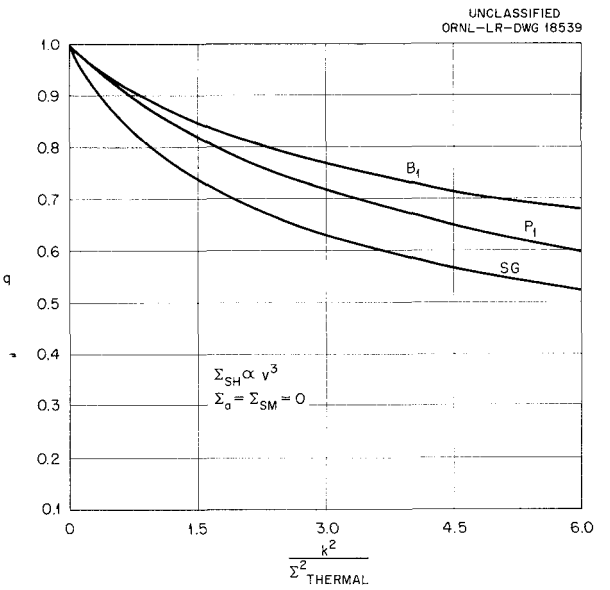

Fig. 8.1.2. Variation of Slowing-Down Density with Buckling.

8.2. EFFECT OF FLUCTUATIONS IN WIDTHS ON NEUTRON REACTION CROSS SECTIONS

L. Dresner

The cross section for reaction from channel α to channel α' averaged over many levels of the compound nucleus can be written as[1]

$$\sigma(\alpha,\alpha') = \frac{\pi \lambda\!\!\!^{-2}_{\alpha}}{2(2I+1)} \sum_{J,\pi,l,l',S,S'} \frac{2J+1}{D_{J\pi}} \left\langle \frac{\Gamma^{J\pi}_{\alpha l S} \Gamma^{J\pi}_{\alpha' l' S'}}{\Gamma^{J\pi}} \right\rangle , \tag{1}$$

where $\lambda\!\!\!^{-}_{\alpha}$ is the reduced neutron width in channel α, I is the target spin, J and π are the spin and parity of the compound state, respectively, and l and S are the orbital angular momentum and channel spin, respectively, in channel α. The total width, $\Gamma^{J\pi}$, of the compound state is the sum of the partial widths, $\Gamma^{J\pi}_{\alpha l S}$, over all values of α, l, and S. The braces in Eq. 1 represent an average taken over the distributions of the various partial widths. In the past, largely because little was known about these distributions, averages of the sort $\langle \Gamma_S \Gamma_t / \Gamma \rangle$ were replaced by $\langle \Gamma_S \rangle \langle \Gamma_t \rangle / \langle \Gamma \rangle$. Recently, however, it has been shown that the neutron widths of nuclear resonance levels are distributed in a chi-squared distribution of one degree of freedom and that the radiative widths are essentially constants.[2] Hence it is now possible to evaluate the averages appearing in Eq. 1, and it is the purpose of this paper to do so.

Before proceeding, however, another form of Eq. 1, which is of importance, should be noted. It is often assumed[3] in schematic theories of nuclear reactions that the average partial widths, $\langle \Gamma^{J\pi}_{\alpha l S} \rangle$, are independent of the channel spins, S. If this is so, and if it is further assumed that the partial widths for different channel spins are statistically independent, the sums over S and S' in Eq. 1 can be carried out:

$$\sigma(\alpha,\alpha') = \frac{\pi \lambda\!\!\!^{-2}_{\alpha}}{2(2I+1)} \sum_{J,\pi,l,l'} \frac{2J+1}{D_{J\pi}} \left\langle \frac{\epsilon(J\pi\alpha l)\, \Gamma^{J\pi}_{\alpha l} \cdot \epsilon(J\pi\alpha' l')\, \Gamma^{J\pi}_{\alpha' l'}}{\Gamma^{J\pi}} \right\rangle , \tag{2a}$$

where

$$\Gamma^{J\pi} = \sum_{\alpha l} \epsilon(J\pi\alpha l)\, \Gamma^{J\pi}_{\alpha l} + \Gamma^{J\pi}_{\gamma} . \tag{2b}$$

The symbol $\epsilon(J\pi\alpha l)$, of Hauser and Feshbach,[3] represents the number of channel spins with which the states J,π can be formed with orbital angular momentum l in channel α. For neutrons it can only be 0, 1, or 2. For the purposes of computing the indicated average, the symbol $\epsilon(J\pi\alpha l)\, \Gamma^{J\pi}_{\alpha l}$ is to be interpreted as the sum of $\epsilon(J\pi\alpha l)$ independent, identically distributed, random variables, each with mean $\langle \Gamma^{J\pi}_{\alpha l} \rangle$. If the widths, $\Gamma^{J\pi}_{\alpha l S}$, are distributed in chi-squared distributions of one degree of freedom,

[1] J. M. Blatt and L. C. Biedenharn, *Revs. Modern Phys.* 24, 258 (1952).

[2] C. E. Porter and R. G. Thomas, *Phys. Rev.* 104, 483 (1956).

[3] W. Hauser and H. Feshbach, *Phys. Rev.* 87, 366 (1952).

then, by the addition theorem for the chi-squared family,[4] $\epsilon(J\pi\alpha l)\ \Gamma_{\alpha l}^{J\pi}$ represents a random variable with $\epsilon(J\pi\alpha l)$ degree of freedom and with mean $\epsilon(J\pi\alpha l)\ \left\langle \Gamma_{\alpha l}^{J\pi} \right\rangle$.

The averages in Eqs. 1 or 2 are conveniently expressed in terms of a quantity, R_{St}, defined as

$$R_{St} = \left\langle \frac{\Gamma_s \Gamma_t}{\Gamma} \right\rangle \frac{\langle \Gamma \rangle}{\langle \Gamma_s \rangle \langle \Gamma_t \rangle} \ . \tag{3}$$

Here R_{St} is a correction factor to be applied to the old theory in which the neutron widths were taken to be constant; this factor obeys several inequalities in a manner which is quite independent of how the widths are distributed. It is possible to show generally that $R_{kk} \geqq 1$; hence the effect of fluctuations is always to increase compound elastic scattering. It is also true that

$$\sum_m \langle \Gamma_m \rangle (R_{km} - 1) = 0 \ ,$$

so that at least some of the nondiagonal R's must be less than unity. However, they all do not necessarily have to be, and some may exceed unity. If $\Gamma = \Gamma_s + \Gamma_t$ only, that is, if there are no competing processes, then $R_{St} \leqq 1$.

In general, the evaluation of R_{St} involves performing a multiple integration, with one integration for each nonconstant partial width present. However, if the partial widths are distributed in members of the chi-squared family, it is always possible to reduce this multiple integral to a single, infinite integral, namely,

$$R_{St} = \langle \Gamma \rangle \int_0^\infty \left(1 + \lambda \frac{\langle \Gamma_s \rangle}{\rho_s}\right)^{-(\rho_s+1)} \left(1 + \lambda \frac{\langle \Gamma_t \rangle}{\rho_t}\right)^{-(\rho_t+1)} \prod_r \left(1 + \lambda \frac{\langle \Gamma_r \rangle}{\rho_r}\right)^{-\rho_r} d\lambda \ . \tag{4}$$

The product in the integral is over all competing widths, Γ_r, and ρ_k is a positive integer or half-integer equal to half the number of degrees of freedom, ν_k, of Γ_k. If Γ_k is constant, it has infinitely many degrees of freedom. When ν_k approaches infinity the corresponding bracket in Eq. 4 approaches $\exp -\lambda \langle \Gamma_k \rangle$.

The cases in which the integral in Eq. 4 has been explicitly evaluated are listed in Table 8.2.1. In view of the discussion following Eq. 2, ν has been restricted to 1, 2, and ∞. The resulting formulas are lengthy and will not be included here, but can be found in another report.[5] However, the results for the cases in which Γ_r is absent are plotted in Figs. 8.2.1 and 8.2.2.

The analytic formulas derived from Eq. 4 suffer two defects: (1) Since in the numerous cases in which there are four or more partial widths the integral for R_{St} is very difficult to evaluate, such cases have not been done. Hence the effect of all competing channels must be approximated with one partial width for which ν can only equal 1, 2, or ∞. (2) The numerical evaluation of R_{St} in these cases is quite

[4] H. Cramér, *Mathematical Methods of Statistics*, Princeton University Press, Princeton, 1946.

[5] L. Dresner, *The Effect of Fluctuations in the Widths on Neutron Reaction Cross Sections*, ORNL CF-57-6-2 (June 1, 1957).

Table 8.2.1. Cases in Which the Integral Expressing R_{St} Has Been Explicitly Evaluated*

Γ_s	Γ_t	Γ_r
1	1	Absent, 1, 2, ∞
	2	Absent, 1, 2, ∞
	∞	Absent, 1, 2
2	2	Absent, 1, 2, ∞
	∞	Absent, 1, 2

*The entries represent the number of degrees of freedom in the distribution of the corresponding width.

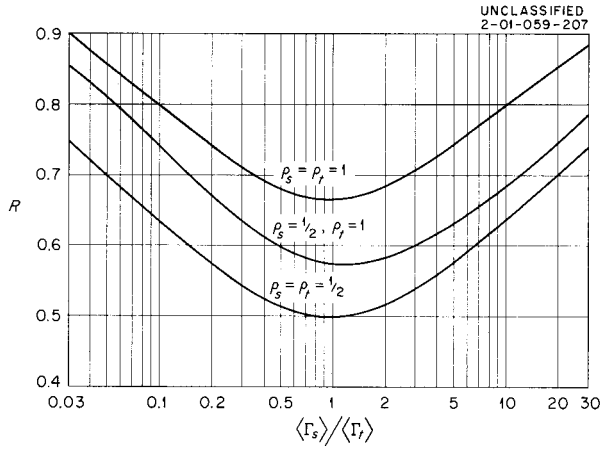

Fig. 8.2.1. R **as a Function of** $\langle\Gamma_s/\Gamma_t\rangle$.

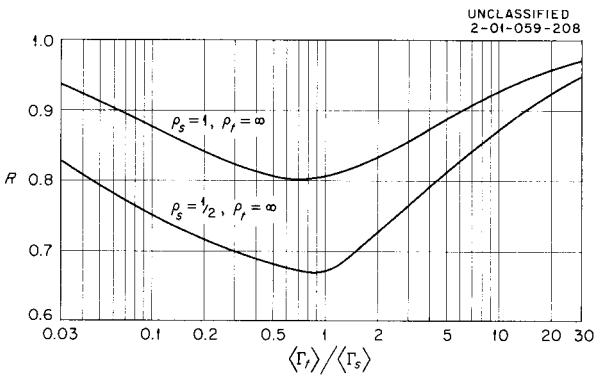

Fig. 8.2.2. R **as a Function of** $\langle\Gamma_t/\Gamma_s\rangle$.

tedious and time-consuming. For these reasons computation of R_{St} has been coded for the Oracle. A Monte Carlo code is used in which a large number of values of R_{St} are formed by choosing each partial width from its appropriate distribution and substituting these choices in Eq. 3. The values of R_{St} so obtained are then averaged. If the number of values is large, this average will be a good estimate of the true value of R_{St}.

The code contains subroutines for choosing from chi-squared distributions with $\nu = 1$ or 2. This restriction is not essential, however, for if it is desired to compute averages in which one of the partial widths, Γ_s, has, say, $\nu = 3$, the addition theorem can be employed to write Γ_s either as the sum of three independent widths, with $\nu = 1$ and mean $\frac{1}{3}\langle\Gamma_s\rangle$, or as the sum of two independent widths, one with $\nu = 2$ and one with $\nu = 1$, and both with mean $\frac{1}{2}\langle\Gamma_s\rangle$. As a matter of fact, the two subroutines used to choose from the $\nu = 1$ and 2 distributions are related by the addition theorem. The $\nu = 2$ distribution is an exponential, and the manner of choosing from it is a well-known one, attributed to Von Neumann and described by Kahn.[6] When $\nu = 1$, a choice is made from $e^{-z}\,dz$, using the technique mentioned above. Then a pair of random numbers, u, v, which satisfy the inequality $u^2 + v^2 \leqq 1$, is picked from a uniform distribution on the interval $0 \leqq u, v \leqq 1$. Finally, $x = 2z\,u^2/(u^2 + v^2)$ and $y = 2z\,v^2/(u^2 + v^2)$ are constructed. It can then be shown that both x and y are independent random variables with a mean of unity and with $\nu = 1$. The first time the routine is entered, both x and y are computed and x is used as output; the second time the routine is entered, y is used as output and the routine is returned to its original state.

[6]H. Kahn, *Applications of Monte Carlo*, RM-1237-AEC (April 19, 1954).

The running time for the code is $\frac{1}{4}\{(N+2)/2\}\,2^{(K-10)}$ min, where 2^K is the number of histories desired and N is the number of widths. The input tape has the form

$$\text{Key word}\,|\,N^*\,|\,K^*\,|\,\langle\Gamma_1\rangle\,|\,\langle\Gamma_2\rangle\,|\,\ldots\,|\,\langle\Gamma_N\rangle\,|\,CR\ .$$

The starred quantities are required in hexadecimal form; the average widths, $\langle\Gamma_i\rangle$, are required in decimal form but must be <1. From the form of Eq. 3 it is clear that scaling all the widths $\langle\Gamma_i\rangle$ by the same amount will not affect the value of R_{St}. The key word is formed as follows: If $\nu_i = 1$, then $\alpha_{2i} = 0$ and $\alpha_{2i+1} = 0$; if $\nu_i = 2$, $\alpha_{2i} = 0$ and $\alpha_{2i+1} = 1$; if $\nu_i = \infty$, $\alpha_{2i} = 1$ and α_{2i+1} is irrelevant. The key word is then $\alpha_0\alpha_1 \ldots \alpha_{38}\alpha_{39}$ in binary form. No more than $2N$ binary bits of the key word are utilized; the rest are irrelevant.

The code punches out the input tape, followed by $R \times 2^{-5}$ in decimal form. It also tallies the number of R's, by intervals of 2^{-6}, for $0 \leqq R \leqq 24$. In general, this information is superfluous and will not be punched out. However, if it is desired, a correction tape at the end of the main tape will alter the code appropriately and punch out, in decimal form, the number of histories in each interval. The interval can be changed by altering the appropriate order.[7]

---

[7]The author gratefully acknowledges the extensive help of R. R. Coveyou in the coding of this problem, and thanks him particularly for the invention and coding of the subroutine for choosing from the chi-squared distribution of one degree of freedom. The author also wishes to thank J. G. Sullivan for operating the Oracle program compiler and aiding with the "debugging" of the compiled code.

8.3. AN ANALYSIS OF LOW-ENERGY NEUTRON REACTIONS IN U^{238}

L. Dresner

A considerable amount of experimental data[1-9] has been reported for neutron reactions in U^{238}. It is of some interest to try to explain these data on the basis of the statistical theory of nuclear reactions.[10,11] The rationale adopted in this section is to deduce the strength functions for the various partial waves from experimental cross sections. As shall be seen, theoretical considerations, together with the low-energy resonance data, serve to determine everything but the p-wave strength function. As it happens, there are enough reaction data to overdetermine the p-wave strength function, so that agreement of independent determinations will give the theory an absolute significance.

In order to carry out the analysis of the data, it is necessary to know the spins and parities of any states that are excited in the reaction. A 2+ state has been observed[12,13] at 44 kev, and states have been observed[3,6] at 146 and 306 kev. From the energy ratios it has been concluded that the latter states are the 4+ and 6+ members of the ground-state rotational band. States have also been observed at 700 kev and above,[6,8] but no information on spins and parities is available. For this reason, only the reactions between 0 and 0.5 Mev, where only the ground-state rotational band is excited, will be considered.

Theory

The cross sections were calculated with Eq. 2 of the preceding section (Sec 8.2). The effect of fluctuations in the neutron widths has been taken into account, and the spin and energy dependences of the various quantities in Eq. 2 have been chosen as follows:

1. Γ_γ is taken to be constant in energy and independent of $J\pi$,
2. $D_{J\pi}$ is taken to be proportional to $(2J+1)^{-1}$ with the energy dependence given by Lang and Le Couteur,[14]
3. $\left\langle \Gamma_l^{J\pi} \right\rangle = 2s_l \left\langle \gamma_{J\pi l}^2 \right\rangle$, where s_l is the penetration factor defined by Blatt and Weisskopf,[15] and $\left\langle \gamma_{J\pi l}^2 \right\rangle$ is the average reduced width,
4. $\left\langle \gamma_{J\pi l}^2 \right\rangle / D_{J\pi} = S_l$, the strength function, is taken to be independent of $J\pi$; it is also assumed that $S_0 = S_2$ and $S_3 = 3S_1$.

Some discussion of the reasons for these choices can be found in a summary article by Lane.[16] Because there are no s or d levels near zero neutron energy, it can be shown that it is reasonable to expect $S_0 = S_2$; this point is discussed in much more detail in the original report on which this summary is based.[17] The plausibility of the choice $S_3 = 3S_1$ is also discussed there; this choice, however, is not a critical one, since f waves are relatively unimportant below ½ Mev. Values of the parameters consistent with the resonance data are $\Gamma_\gamma = 24$ mv, $D_{1/2} = 18$ ev, and $S_0 = 0.0358$.

---

[1] D. J. Hughes and J. A. Harvey, *Neutron Cross Sections*, BNL-325 (July 1, 1955).

[2] D. J. Hughes and R. B. Schwartz, *Neutron Cross Sections*, BNL-325, Supplement 1 (Jan. 1, 1957).

[3] R. C. Allen, *Phys. Rev.* **105**, 1796 (1957).

[4] R. L. Zimmerman, *Conference on Neutron Physics by Time-of-Flight, Held at Gatlinburg, Tennessee, November 1 and 2, 1956*, ORNL-2309, p 10 (June 17, 1957).

[5] L. M. Bollinger *et al.*, *Phys. Rev.* **105**, 661 (1957).

[6] L. Cranberg and J. Levin, private communication.

[7] H. W. Newson, *Conference on Neutron Physics by Time-of-Flight, Held at Gatlinburg, Tennessee, November 1 and 2, 1956*, ORNL-2309, p 138 (June 17, 1957).

[8] R. Batchelor, *Proc. Phys. Soc. (London)* **A69**, 214 (1956).

[9] B. Rose, *A Determination of the Cross-Section for the Reaction U^{238} (n,γ) U^{239} as a Function of Neutron Energy in the Range 30–900 kev*, AERE-NP/R-1743 (June 22, 1955).

[10] W. Hauser and H. Feshbach, *Phys. Rev.* **87**, 366 (1952).

[11] B. Margolis, *Phys. Rev.* **88**, 327 (1952).

[12] N. P. Heydenburg and G. M. Temmer, *Phys. Rev.* **93**, 906 (1954).

[13] A. S. Devatia *et al.*, *Phys. Rev.* **100**, 1266 (1955).

[14] J. M. B. Lang and K. J. Le Couteur, *Proc. Phys. Soc. (London)* **A67**, 586 (1954).

[15] J. M. Blatt and V. F. Weisskopf, *Theoretical Nuclear Physics*, Wiley, New York, 1952.

[16] A. M. Lane, *Conference on Neutron Physics by Time-of-Flight, Held at Gatlinburg, Tennessee, November 1 and 2, 1956*, ORNL-2309, p 113 (June 17, 1957).

[17] L. Dresner, *An Analysis of Low-Energy Neutron Reactions in U^{238}* (to be published).

Comparison with Experiment

Data for $E = 150$ kev. – The lowest energy at which data are available on inelastic scattering is 150 kev. Table 8.3.1 summarizes the available experimental data at this energy. The only state inelastically excited at this energy is the one at 44 kev.

In comparing these data with theory, it is not necessary, fortunately, to compute results at more than one value of the ratio of p- to s-wave strength functions, the ratio being denoted as R. This is a consequence of a very convenient property of the states of a rotational band, namely, that they all have the same parity. Therefore all the widths which appear in a given term of Eqs. 1 or 2 in Sec 8.2 have the same parity. Because of the fixed ratios that are assumed between the s and d strength functions and the p and f strength functions, the terms in the expression for the radiative cross section will be homogeneous functions of order zero, while the terms for the inelastic cross section will be homogeneous functions of order one, in the s- and p-wave strength functions. Hence the radiative cross section should not vary with R, while the inelastic cross section should vary linearly with R. The only exception to this predicted behavior will occur when R is quite near zero, so that the radiative width exceeds the neutron widths. By this time the odd-wave contribution will be so small in the inelastic cross section that a significant departure from linearity will not be noticed. In the radiative cross section, however, a sharp drop will occur for very small R.

In order to check these points, the cross sections for $R = 0$, 1, and 3 have actually been calculated. The results of these calculations are presented in Table 8.3.2. As predicted, the cross section for radiative capture exhibits very little dependence on R, while the inelastic cross section is given by the relationship $\sigma(n,n') = (190 + 490R)$ mb, derived from the values for $R = 0$ and 1. This gives 1660 mb at $R = 3$, which compares well with the directly calculated value. The nonelastic cross section varies nearly linearly according to the law $\sigma_{\text{nonelastic}} = (310 + 550R)$ mb, except near $R = 0$, where the error is only about 12%.

Table 8.3.1. Experimental Values of Cross Sections for $E = 150$ kev

Cross Section	Measurement (mb)	Reference
$\sigma(n,\gamma)$	160 ± 8	*a*
	200 (interp)	*b*
	240 (interp)	*c*
$\sigma_{\text{nonelastic}}$	800 ± 200	*d*
	630 ± 200	*e*

[a]B. Rose, *A Determination of the Cross-Section for the Reaction U^{238} (n,γ) U^{239} as a Function of Neutron Energy in the Range 30–900 kev*, AERE-NP/R-1743 (June 22, 1955).

[b]D. J. Hughes and J. A. Harvey, *Neutron Cross Sections*, BNL-325 (July 1, 1955).

[c]H. W. Newson, *Conference on Neutron Physics by Time-of-Flight, Held at Gatlinburg, Tennessee, November 1 and 2, 1956*, ORNL-2309, p 138 (June 17, 1957).

[d]M. Walt, *Proc. Inter. Conf. Peaceful Uses Atomic Energy, Geneva, 1955* 2, 18 (1956).

[e]R. C. Allen, *Phys. Rev.* 105, 1796 (1957).

Table 8.3.2. Calculated Values of Cross Sections for $E = 150$ kev – Including Fluctuations

Cross Section	Calculated Value (mb)		
	$R = 0$	$R = 1$	$R = 3$
$\sigma(n,\gamma)$	86	180	205
$\sigma(n,n')$	190	680	1760
$\sigma_{\text{nonelastic}}$	276	860	1965

By comparing the theoretical and the experimental nonelastic cross sections, it can be seen that R is found to be near unity. Indeed, if equal weight is given to the two reported values of the nonelastic cross section, R is found to be 0.75 ± 0.25. The insensitivity of the radiative capture cross section to R makes it useless for the determination of R. However, if $R \cong 1$ is taken, the agreement of the radiative cross section serves as a check on the validity of the assumptions used in the calculations. For example, if $D_{J\pi}$ is chosen to be independent of J rather than proportional to $(2J + 1)^{-1}$, the inelastic cross section remains unchanged, but the radiative cross section falls by about 45% to 125 mb, which is too low. Again,

if the decrease of about 30% in the level spacing predicted by Lang and Le Couteur[14] in going from zero bombarding energy to 150 kev is not permitted, the inelastic cross section remains unchanged, but the radiative cross section falls by 30% to 140 mb, which is also too low. The necessity for using the level-density law by Lang and Le Couteur to calculate the radiation cross section correctly has been carefully pointed out by Lane and Lynn.[18]

It is of some interest to exhibit explicitly the importance of the neutron width fluctuations in these calculations. Table 8.3.3 is a replica of Table 8.3.2, except that the entries have been computed under the assumption that the reduced neutron widths have a δ-function distribution. The effect on the inelastic scattering is quite evident, but there seems to be little effect on the radiative cross section. This is apparent and not real, however, for the individual terms in the expression for the cross section are quite strongly affected; some are increased and others are decreased.

Table 8.3.3. Calculated Values of Cross Sections for E = 150 kev – Ignoring Fluctuations

Cross Section	Calculated Value (mb)		
	$R = 0$	$R = 1$	$R = 3$
$\sigma(n,\gamma)$	66	175	185
$\sigma(n,n')$	265	1125	2970
$\sigma_{\text{nonelastic}}$	331	1300	3155

Data for E = 550 kev. – As was seen in the preceding paragraphs, the radiative capture cross section is not of much value for determining R at high energies. Hence, although enough data exist to draw a continuous curve of $\sigma(n,\gamma)$, no attempt will be made to fit this curve in detail. Instead, an attempt will be made to fit the inelastic scattering data and to compute $\sigma(n,\gamma)$ only at the same point as a check. Insofar as the reported data on the nonelastic cross section are concerned, enough information is available to draw a continuous curve from 150 kev to about 2 Mev. Unfortunately, most of these data suffer from a systematic defect, namely, only partial resolution of elastic neutrons and neutrons scattered from the state at 44 kev. Perhaps the easiest way to see this is to compare the time-of-flight measurements at 550 kev with measurements by other techniques at the same energy. The time-of-flight measurements,[19] which resolve the 44-kev level, as can be seen by a study of the reported time spectra, give a total nonelastic cross section of about 1800 mb. On the other hand, the work of Allen[20] and the work of Batchelor,[21] both of which were done by sphere transmission and proportional counting, fail to resolve the 44-kev level, as can be seen by a study of the reported pulse-height spectra. The subtraction of "sphere-on" from "sphere-off" spectra is therefore very uncertain for these experiments. Both these experiments give a nonelastic cross section of about 800 mb, which is significantly lower than the time-of-flight value. The data reported by Allen[20] at 250 kev appear also to be in error, as is indicated by the low value of the excitation cross section for the 44-kev level at this energy, compared with its value at 150 kev. Such a sharp drop in such a small energy interval is quite contrary to theory. Hence, in sum, it appears that the only reliable experiments are those from the time-of-flight work at 550 kev and the reported work at 150 kev. Even in the latter case there may possibly be some systematic error due to resolution difficulties. Such errors are not believed to be large, mainly because the value of R determined by the time-of-flight work agrees, as shall be seen below, with that determined from the work at 150 kev.

The available experimental data at 550 kev are summarized in Table 8.3.4. In this table, $B(2+)$ represents the coefficient of the $\cos^2\theta$ term in the angular distribution, $1 + B\cos^2\theta$, of the neutrons scattered from the 44-kev (2+) state. It has been determined experimentally that the coefficients of higher powers of $\cos\theta$ are zero. Only one value of $\sigma(n,\gamma)$ is given, and it represents an average of the various values reported, all of which are in excellent agreement.

[18] A. M. Lane and J. E. Lynn, *Proceedings of the Tripartite Conference on Cross-Sections of Fissile Nuclei*, AERE-NP/R-2076 (1956).

[19] L. Cranberg and J. Levin, private communication.

[20] R. C. Allen, *Phys. Rev.* 105, 1796 (1957).

[21] R. Batchelor, *Proc. Phys. Soc. (London)* **A69**, 214 (1956).

Table 8.3.4. Experimental Values of Cross Sections for $E = 550$ kev

Cross Section	Measurement (mb)	Reference
$\sigma(2+)$	1430 ± 200	*
$\sigma(4+)$	290 ± 60	*
$B(2+)$	-0.45 ± 0.10	*
$\sigma(n,\gamma)$	135 ± 15	**

*L. Cranberg and J. Levin, private communication.

**B. Rose, *A Determination of the Cross-Section for the Reaction U^{238} (n,γ) U^{239} as a Function of Neutron Energy in the Range 30–900 kev*, AERE-NP/R-1743 (June 22, 1955).

Calculations have been carried out with $R = 0$ and 1, and, in view of the linear law for $\sigma(2+)$ and $\sigma(4+)$,

$$(1a) \qquad \sigma(2+) = (570 + 760R) \text{ mb} ,$$

$$(1b) \qquad \sigma(4+) = (88 + 180R) \text{ mb} ,$$

$$(1c) \qquad \sigma(n,\gamma) = 140 \text{ mb } (R = 1) ;$$

$B(2+)$ can be written as the quotient of two linear expressions in R, namely,[22]

$$(1d) \qquad B(2+) = -\frac{120 + 230R}{1100 + 1440R} .$$

Equations 1*a* and 1*b* yield, respectively, $R = 1.13 \pm 0.26$ and $R = 1.12 \pm 0.33$. These two independent determinations of R are in excellent agreement and give the theory a measure of internal consistency. The (n,γ) cross section for $R \cong 1$ agrees well with experiment. However, when the value $R = 1.13$ is used in Eq. 1*d*, $B(2+)$ is found to be -0.14, which is too low by a factor of 3. For this last discrepancy no explanation can be offered. It has been suggested that if a component of the excitation were direct excitation of the 44-kev level by surface interaction with a nonspherical nucleus, the anisotropy of the calculated angular distribution would be increased. Calculations by Chase and Wilets[23] of the direct excitation cross section have been reported, and they find this effect insignificant below 0.5 Mev.

Radiative Capture Below Inelastic Threshold. – In the discussion above, the ratio R has been determined to be near unity from an analysis of the available inelastic scattering data. In the relevant energy range $\sigma(n,\gamma)$ was found to be an insensitive function of R. Below the inelastic threshold (44 kev), however, this is no longer true and the radiative capture cross section can be used to determine R.

The experimental points of Newson[24] below 45 kev, together with the 95% confidence limits of error, are plotted in Fig. 8.3.1 along with three calculated curves (solid lines) corresponding to $R = 0$, 1, and 3, and an interpolated curve (dotted line) corresponding to $R = 1.35$. The last four experimental points agree very well with the dotted

[22]The calculation of angular distributions on the statistical model is described by J. M. Blatt and L. C. Biedenharn, *Revs. Modern Phys.* **24**, 258 (1952). It involves evaluating expressions similar to the right hand side of Eq. 1 in Sec 8.2 with the exception that the factor $2J + 1$ is replaced by a product of Z coefficients. The effect of fluctuations is still through the evaluation of averages, $\langle \Gamma_s \Gamma_t / \Gamma \rangle$.

[23]D. M. Chase and L. Wilets, results to be included in paper by L. Cranberg.

[24]H. W. Newson, *Conference on Neutron Physics by Time-of-Flight, Held at Gatlinburg, Tennessee, November 1 and 2, 1956*, ORNL-2309, p 138 (June 17, 1957).

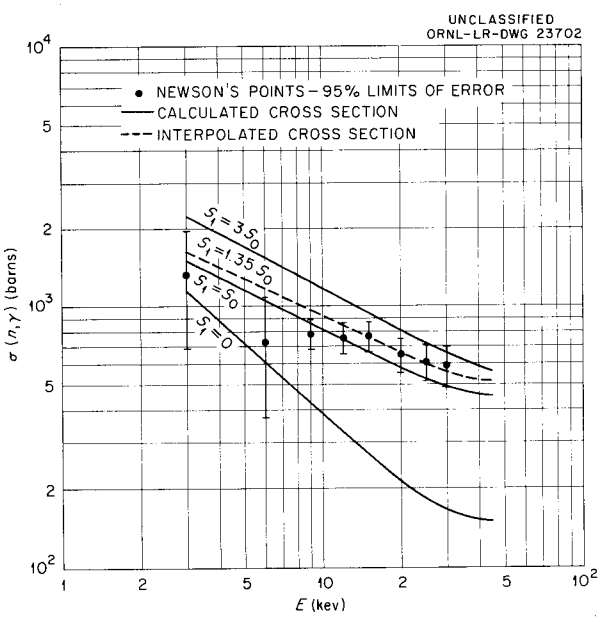

Fig. 8.3.1. Radiative Capture Cross Section as a Function of Energy.

curve, but the first four points do not agree at all with any curve of constant R.

If it it is believed that the first four data points are free of systematic error, then with the statistical errors estimated, it must be believed that there is an inflection point in the radiative cross section near 10 kev. Newson has suggested that this inflection is due to the appearance of a rapidly rising p-wave contribution. A comparison with the calculated curves of Fig. 8.3.1 seems to rule this out emphatically. Hence one is inclined to believe that systematic errors are present in the first four data points. On the other hand, the last four data points are probably correct; first, because the one at 25 kev is confirmed by an Sb-Be activation experiment of Macklin *et al.*,[25] and, second, because all four points lie quite accurately on a curve of constant R.

[25] R. L. Macklin, W. S. Lyon, and N. H. Lazar, unpublished information, 1956.

Conclusions

The available, credible experimental data on inelastic scattering and radiative capture in U^{238} indicate a p-wave strength function somewhat larger than the s-wave strength function. The inelastic scattering data at 550 kev give a value of R of 1.13 ± 0.20, if the two determinations (2+ and 4+ states) are taken as independent. The Sb-Be radiative capture data of Macklin *et al.* give $R = 1.60 \pm 0.50$. When combined, these determinations give a best value of $R = 1.24 \pm 0.19$. The predicted angular distribution at 550 kev is more isotropic than is experimentally observed, and the cause of this discrepancy is not known.

8.4. EFFECT OF FLUCTUATIONS IN THE REACTION WIDTHS ON RESONANCE INTEGRALS

E. Kuhn[1] L. Dresner

An estimate was previously given[2] for the resonance integral of nonfissile nuclei in terms of certain average resonance parameters, namely, $\bar{\Gamma}_n^0$, the average reduced neutron width, $\bar{\Gamma}_\gamma$, the average radiative width, and D^*, the average spacing between resonances of the same spin and parity. The estimate is

$$(1) \qquad \int_{E_1}^{\infty} \sigma_a \frac{dE}{E} = \frac{1.3 \times 10^6 \text{ barns-ev}}{E_1} \left(\frac{2\pi\bar{\Gamma}_\gamma}{D^*}\right) \frac{\beta - \log(1+\beta)}{\beta^2} ,$$

where $\beta = \bar{\Gamma}_\gamma/\bar{\Gamma}_n^0 E_1^{1/2}$. This formula is based on the assumption that the reduced neutron width is a constant for all resonances. Recently, Porter and Thomas[3] have shown that this is not a good assumption and that the reduced neutron widths are distributed in a chi-squared distribution of one degree of freedom. It is possible to show that this latter assumption leads to the following equation for the resonance integral:

$$(2) \qquad \int_{E_1}^{\infty} \sigma_a \frac{dE}{E} = \frac{1.3 \times 10^6 \text{ barns-ev}}{E_1} \left(\frac{2\pi\bar{\Gamma}_\gamma}{D^*}\right) \int_0^{\infty} \frac{(\beta/x) - \log(1+\beta/x)}{(\beta/x)^2} (2\pi x)^{-1/2} e^{-x/2}\, dx .$$

The second factor in the second integral in Eq. 2 is the normalized chi-squared distribution of one degree of freedom.

When $\beta \gg 1$ it is possible to derive an asymptotic series for the integral, I, in Eq. 2 by rearranging the terms and using the MacLaurin expansion for $\ln(1 + x/\beta)$. The resulting series is

$$(3) \qquad I = \frac{1}{\beta} + \frac{8 - 3(\ln\beta + C + \ln 2)}{\beta^2} + \sum_{k=1}^{\infty} (-)^k \frac{(2k+3)!!}{k\beta^{k+2}} ,$$

where C is the Euler-Mascheroni constant, equal to 0.577216. It is possible to show that the absolute error in this expression is less than the first term of the series neglected. The estimate of I can also be improved by at least a factor of 2, and possibly much more, by adding half the first term ordinarily neglected. In this way it can be shown that for $\beta = 10$ the error in I is less than 2%, and decreases as β increases.

When $\beta \ll 1$ it is possible to derive a power series in $\sqrt{\beta}$ for I by the technique of repeated integration by parts. The result of this procedure is the series

$$(4) \qquad I = \frac{1}{2} - \frac{\sqrt{2\pi}}{5}\beta^{1/2} + \frac{1}{3}\beta - \frac{\sqrt{2\pi}}{14}\beta^{3/2} + \dots .$$

---

[1]Oak Ridge School of Reactor Technology.

[2]L. Dresner, *J. Nuclear Energy* **2**, 118 (1955); a summary of this work is given by L. Dresner, *Appl. Nuclear Phys. Ann. Rep. Sept. 10, 1956*, ORNL-2081, p 116.

[3]C. E. Porter and R. G. Thomas, *Phys. Rev.* **104**, 483 (1956).

It is possible to show for this series also that the error is less than the term neglected. Thus when $\beta = 0.1$, the maximum error in I is about 1.5% and decreases with decreasing β.

When $\beta \cong 1$, recourse to numerical integration is necessary. By combining these techniques, the curve plotted in Fig. 8.4.1 is obtained for the ratio of Eq. 2 to Eq. 1.

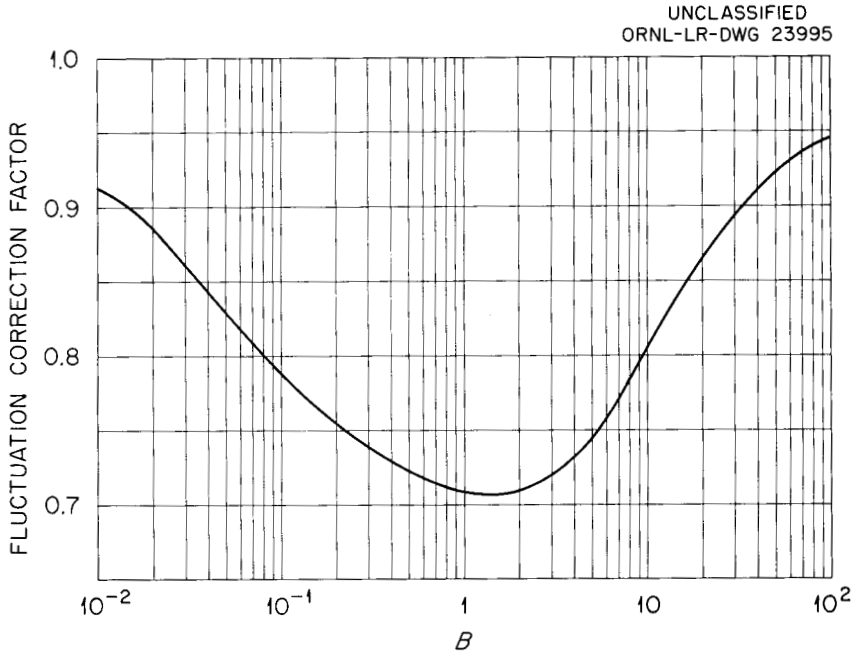

Fig. 8.4.1. Reduction in the Resonance Integral Due to Fluctuations in the Neutron Width.

8.5. "CORN PONE" – A MULTIGROUP, MULTIREGION REACTOR CODE

R. R. Coveyou W. E. Kinney J. G. Sullivan, Jr.

The theory of "Corn Pone," a multigroup code for the Oracle developed to calculate the parameters of a multiregion reactor, has been previously described.[1,2] Descriptions of the four subcodes which comprise Corn Pone are given below.

Group Constant Preparation Routine (GCPR)

The GCPR uses paper-tape input specifications and data from the master cross-section tape[3] in order to construct a desired group structure. The following information is required by the GCPR:

1. The number of isotopes in the group structure and a list of the isotopes are required. The isotopes are identified by a five-digit code number which selects the isotope from the master cross-section tape. A two-digit Corn Pone code number is assigned to each isotope by the user, and the number must be specified. This code number will later be used in referring to the isotope for reactor calculations. The Corn Pone code numbers are the hexintegers from 00 through 32. The number of isotopes and alloys is limited to 51 per group structure.

2. The number of alloys or mixtures in the group structure is required. Each alloy is described by a word which gives the number of isotopes in the alloy and the Corn Pone code number assigned to the alloy. Following the description word, the concentrations and the Corn Pone code number of each of the isotopes in the alloy must be given. The sum of the number of isotopes in all the alloys must not exceed 64.

3. The number of fast groups is needed. Following this are listed the lethargy widths of the fast groups. The number of fast groups is limited by the length of the Oracle magnetic tape, and could be as large as 1000. The first fast group starts at the lethargy where fission neutrons first appear. The zero of lethargy is 10^8 ev.

4. The number of epithermal groups is required. The lower lethargy limit and the lethargy width of each epithermal group must be listed. An epithermal group is here defined as that group immediately above the thermal group, and the presence of a number of such groups will allow flexibility in the joining of the fast groups to the thermal group. There may be no more than 64 epithermal groups in a group structure.

5. The number of thermal groups and the temperature of each must be given. There may be no more than 128 thermal groups.

Five fuels, with Corn Pone code numbers lying between and including 00 and 04, are allowed in a group structure. Isotopes and alloys, as well as epithermal and thermal groups, may be added rather simply to an existing group structure.

Scattering, absorption, and fission cross sections are averaged over the fast and epithermal groups in the prescribed manner.[2] The thermal cross sections are averaged over a Maxwell-Boltzmann distribution characterized by the designated T.

Slowing-down parameters, combinations of these parameters and the averaged cross sections, and the cross sections for each group are written on drive 0, and then are edited on the curve plotter. A typical page from the edit for a nonfuel isotope is shown in Fig. 8.5.1.

UNCLASSIFIED
2-01-059-230

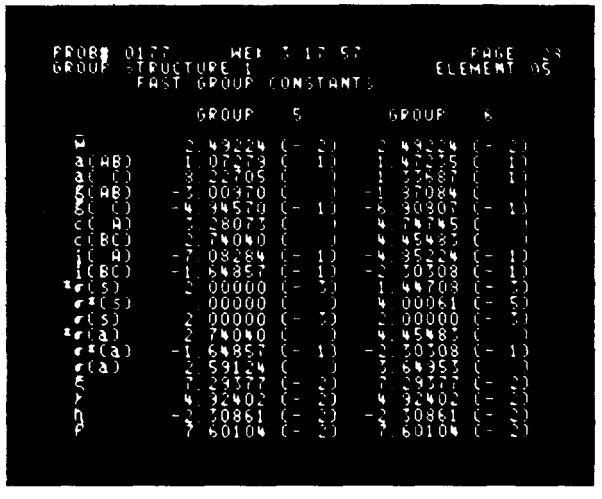

Fig. 8.5.1. Typical Page from the Edit of a Nonfuel Isotope, GCPR, RCPR, IR, and ER.

[1] B. J. Garrick, *Multigroup-Multiregion Theory for the Consistent* P_1 *Approximation to the Boltzmann Equation*, ORNL CF-55-8-189 (Aug. 1955).

[2] W. E. Kinney *et al.*, *Appl. Nuclear Phys. Ann. Rep. Sept. 10, 1956*, ORNL-2081, p 133.

[3] R. R. Bate, J. H. Marable, and J. W. Niestle, *Appl. Nuclear Phys. Ann. Rep. Sept. 10, 1956*, ORNL-2081, p 140.

The GCPR is debugged, and has been used to construct a group structure for testing the other Corn Pone codes.

Reactor Constant Preparation Routine (RCPR)

The RCPR uses paper-tape input describing a reactor, together with group constants prepared by GCPR, to compute the reactor constants required by the integration routine (see below). The quantities needed in order to specify a reactor are discussed below.

The geometry factor, which indicates slab, cylindrical, or spherical geometry, is required. For finite reactors the half dimensions are specified for the geometries to which they apply. The total number of groups to be computed is indicated, and a choice is made between zero flux and zero return current as an external boundary condition. A choice is available as to the slowing-down models desired. It is also possible to converge on the source, the thermal flux, or the multiplication constant and to specify the desired degree of convergence.

The thickness, the epithermal group number, and the thermal group number must be designated in order to describe a region. The materials for the region must then be listed along with their nuclear densities or, in the case of alloys, their volume fractions. Each region may contain all the materials in the group structure as class A materials. Only four materials, however, may be treated as class B or C. There may be no more than 128 regions in a reactor.

The RCPR computes the number of lattice intervals for each region required to keep certain constants small enough for satisfactory solution of the difference equations. The number is displayed, if desired, and may be increased. If the number of lattice intervals is decreased, the P_1 difference equations may fail.

The RCPR is debugged, and has been used in the debugging of the integration routine. An addition is to be made which will facilitate the input.

Integration Routine (IR)

The IR uses the output of the RCPR to integrate the P_1 equations. It was found necessary to change the method of computing the first derivative of the flux in the calculation of the current. A numerical differentiation was used, but this did not ensure the continuity of current at region interfaces to a sufficiently high degree of accuracy. With the present method of using the original differential equation in the computation of the first derivative of the flux, the currents are continuous within acceptable limits.

The IR is nearly debugged. A test calculation has compared quite favorably with results of an Eyewash calculation in the multiplication constant computed. The test calculation, which had 31 groups, 3 regions, and 216 space points, required 13 min for an iteration and about 10 min for preparing the reactor constant. When fewer than 120 space points were used, the iteration time was reduced to about 6 min.

Edit Routine (ER)

The ER will print results of the calculation on the curve plotter. The initial conditions and the multiplication constant will be printed for each case. The user may have additional results presented in the form of tables, or as graphs or histograms.

The events per neutron, which may be obtained for each region and each group, include absorptions, fissions, leakages parallel to r (r = radius vector), leakages perpendicular to r, and source contributions. The fissions and absorptions in specified materials may be edited for each group. The results of a neutron balance, the source integral and sources, and the spatial integrals of the fluxes may also be obtained.

Absorption, fission, neutron-producing, scattering, and perpendicular-leakage cross sections will be available for each group and region.

The reactor quantities which may be edited include average fluxes, end-point fluxes, Q slowing-down densities, source contributions, average currents, end-point currents, and P slowing-down densities. Coding has not yet been started on the edit routine.

8.6. "MANFRED" – A "FEW"-GROUP, MULTIREGION REACTOR CODE

J. F. Wett[1] R. R. Coveyou

A program designated as "Manfred" has been initiated in order to develop a "few"-group, multiregion reactor code for the Oracle. Manfred will allow the diffusion coefficient and the removal cross section to be spatially dependent. The code, by using the concept of albedos, collapses each region into a set of boundary conditions until the reactor is reduced to a core with a somewhat peculiar set of boundary conditions. Thus, in essence, the code reduces the problem to only one region, and, consequently, all the space points may be used in the core. After the calculation of the flux in the core has been made, the fluxes in the other regions can be calculated by again making use of all the space points available. A brief description of the theory, expected properties, and status of the code follows.

Theory of Manfred

The diffusion equation is

$$(1) \qquad D_{ij}(r) \frac{\partial^2}{\partial r^2} \phi_{ij}(r) + \left[\frac{\gamma}{r} D_{ij}(r) + \frac{\partial}{\partial r} D_{ij}(r)\right] \frac{\partial}{\partial r} \phi_{ij}(r) - \Sigma_{ij}(r) \phi_{ij}(r) + \nu_{ij}(r) = 0 ,$$

where

$D_{ij}(r)$ = diffusion coefficient for group i in region j at point r,

$\phi_{ij}(r)$ = flux for group i in region j at point r,

$\Sigma_{ij}(r)$ = removal cross section for group i in region j at point r (contains absorption, slowing down, and buckling),

$\nu_{ij}(r)$ = source into group i in region j at point r (i.e., the sum of fission neutrons, neutrons slowing down from higher energy groups, and extraneous neutrons),

γ = 0 for slabs, 1 for cylinders, and 2 for spheres.

This can be written as

$$(2) \qquad \frac{\partial^2}{\partial r^2} \phi_{ij}(r) + A_{ij}(r) \frac{\partial}{\partial r} \phi_{ij}(r) + B_{ij}(r) \phi_{ij}(r) + C_{ij}(r) = 0 ,$$

where

$$A_{ij}(r) = \frac{\gamma}{r} + \frac{1}{D_{ij}(r)} \frac{\partial}{\partial r} D_{ij}(r) ,$$

$$B_{ij}(r) = - \frac{\Sigma_{ij}(r)}{D_{ij}(r)} ,$$

$$C_{ij}(r) = \frac{\nu_{ij}(r)}{D_{ij}(r)} .$$

---

[1]Reactor Operations Division.

When difference approximations are made, good to order h^4, where h is the lattice spacing, the difference equation at a space point is found to be

(3) $$P_{ij}(r,h)\,\Omega_{ij}(r+h) - Q_{ij}(r,h)\,\Omega_{ij}(r) + R_{ij}(r,h)\,\Omega_{ij}(r-h) + S_{ij}(r,h) = 0 \ ,$$

where

$$P_{ij}(r,h) = \frac{1}{2} + \frac{A_{ij}(r)}{4}\,h + \frac{A_{ij}^2(r) + 2\,\frac{\partial}{\partial r}A_{ij}(r) + B_{ij}(r)}{24}\,h^2 +$$

$$+ \frac{\frac{\partial^2}{\partial r^2}A_{ij}(r) + A_{ij}(r)\,\frac{\partial}{\partial r}A_{ij}(r) + A_{ij}(r)\,B_{ij}(r) + 2\,\frac{\partial}{\partial r}B_{ij}(r)}{48}\,h^3 \ ,$$

$$Q_{ij}(r,h) = 1 + \frac{A_{ij}^2(r) + 2\,\frac{\partial}{\partial r}A_{ij}(r) - 5B_{ij}(r)}{12}\,h^2 \ ,$$

$$R_{ij}(r,h) = \frac{1}{2} - \frac{A_{ij}(r)}{4}\,h + \frac{A_{ij}^2(r) + 2\,\frac{\partial}{\partial r}A_{ij}(r) + B_{ij}(r)}{24}\,h^2 -$$

$$- \frac{\frac{\partial^2}{\partial r^2}A_{ij}(r) + A_{ij}(r)\,\frac{\partial}{\partial r}A_{ij}(r) + A_{ij}(r)\,B_{ij}(r) + 2\,\frac{\partial}{\partial r}B_{ij}(r)}{48}\,h^3 \ ,$$

$\Omega(r)$ = flux at space point r ,

$$S_{ij}(r,h) = \frac{C_{ij}(r)}{2}\,h^2 \ .$$

Assuming that

(4) $$\Omega(r) = \Gamma(r)\,\Omega(r+h) - \Delta(r) \ ,$$

it follows that

(5) $$\Gamma(r) = \frac{P(r)}{Q(r) - R(r)\,\Gamma(r-h)} \ ,$$

(6) $$\Delta(r) = \frac{\Gamma(r)}{P(r)}\,[R(r)\,\Delta(r-h) + S(r)] \ .$$

The boundaries of a region must be investigated. Let r_0 be the inner boundary of a region and r_N be its outer boundary. Now it is postulated that

$$\overleftarrow{J}_{ij}(r_N) = \beta_{i+1,j\to j}\overrightarrow{J}_{ij}(r_N) + \beta_{i+1,j-1\to j}\overrightarrow{J}_{i,j-1}(r_N) + \cdots + \beta_{i+1,1\to j}\overrightarrow{J}_{i1}(r_N) , \tag{7}$$

$$\overleftarrow{J}_{ij}(r_N) = \beta_{i+1,j\to j}\overrightarrow{J}_{ij}(r_N) + \sum_{k=1}^{j-1} \beta_{i+1,k\to j}\overrightarrow{J}_{ik} , \tag{8}$$

where

$\overleftarrow{J}_{ij}(r_N)$ = current from region $i+1$ to region i, group j,

$\overrightarrow{J}_{ik}(r_N)$ = current from region i, group k, to region $i+1$,

$\beta_{i+1,k\to j}$ = reflection coefficient of region $i+1$ for neutrons that slow down from group k to j.

Also

$$\begin{aligned} \overleftarrow{J}_{ij}(r_N) &= \phi(r_N) + 2D(r_N)\frac{\partial}{\partial r}\phi(r_N) , \\ \overrightarrow{J}_{ij}(r_N) &= \phi(r_N) - 2D(r_N)\frac{\partial}{\partial r}\phi(r_N) . \end{aligned} \tag{9}$$

Then

$$\frac{\partial}{\partial r}\phi_{ij}(r_N) + \frac{1}{2D_{ij}(r_N)}\left(\frac{1-\beta_{i+1,j\to j}}{1+\beta_{i+1,j\to j}}\right)\phi_{ij}(r_N) - \frac{\sum_{k=1}^{j-1}\beta_{i+1,k\to j}J_{ik}(r_N)}{2D_{ij}(r_N)(1+\beta_{i+1,j\to j})} = 0 . \tag{10}$$

Further,

$$\begin{aligned} \overrightarrow{J}_{ij}(r_0) &= \phi_{ij}(r_0) - 2D_{ij}(r_0)\frac{\partial}{\partial r}\phi_{ij}(r_0) , \\ \frac{\partial}{\partial r}\phi_{ij}(r_0) - \frac{1}{2D_{ij}(r_0)}\phi_{ij}(r_0) &+ \frac{\overrightarrow{J}_{ij}(r_0)}{2D_{ij}(r_0)} = 0 . \end{aligned} \tag{11}$$

Now $\partial\phi_{ij}(r_N)/\partial r$ and $\partial\phi_{ij}(r_0)/\partial r$ must satisfy the original diffusion equation (Eq. 2), and Eqs. 10 and 11, respectively. Difference approximations were found, and coefficients similar to $P_{ij}(r)$, $Q_{ij}(r)$, $R_{ij}(r)$, and $S_{ij}(r)$ were found. The above-mentioned coefficients are used to compute $\Gamma(r_{-1})$, $\Delta(r_{-1})$, and $\Omega(r_{N+1})$. It should be noted that Eqs. 7, 8, 9, 10, and 11 are for regions outside the core; that is, the core lies between the region under study and the origin. It can be seen that for regions inside the core, r_0 and r_N change roles in Eqs. 7 through 11.

During a solution the extreme outside region is handled first, unless by some oddity it is the core. It is known that all the reflection coefficients for the next region out are zero. If a current of 1 neutron·cm^{-2}·sec^{-1} is introduced across r_0 into the region, and the currents across the boundary r_0 out of the region are calculated, the β's for that region are obtained. (Similar currents must be introduced into each group.) When all the β's for that region are computed, the next region in toward the core is treated in a corresponding manner. (However, now the β_{i+1}'s are not zero but are those just computed.) This is continued until the core is reached. If there are reflector regions on the other side of the core, they are handled in a similar fashion; remember that r_0 and r_N now change roles and that $\overleftarrow{J}(0) = \overrightarrow{J}(0)$.

The problem is now reduced to the core, with somewhat unusual boundary conditions. A flat source is imposed on the core, Eq. 3 is solved for each group, and a source for the next iteration is computed. (Equation 10 holds for both r_0 and r_N if the core is not at the origin.) The initial and the computed sources are compared in order to determine k. The new source is divided by k in order to enforce steady state, and another iteration is started. The process is continued until the thermal flux converges.

Properties of Manfred

Manfred will be a one-dimensional calculation in which the critical properties of parallelepipeds, spheres, and cylinders will be computed. The physical limitations as to the number of regions and groups have not yet been determined. The code will have a maximum of 60 space points.

Calculation will halt after the thermal flux converges, if k is all that is desired. If the fluxes in the reflectors are desired, they will be computed after convergence of the core flux. It is expected that the programmer will have a choice of several edit routines.

The code is expected to have several advantages; for example, iterations do not have to be carried out over regions containing no fissionable material, all available space points are used in the core, etc. If the combination of all the regions on either side of the core is self-critical, the code will fail.

Status of the Code

The analysis of the code has been completed and coding has begun.

8.7. A PROGRAM COMPILER FOR THE ORACLE

M. E. LaVerne

In the period since the last report[1] on the Compiler, changes have consisted principally in adapting it to the new input-output equipment installed on the Oracle. Operation of the Compiler has been somewhat simplified, and a number of the programed stops are now monitored[2] on the console typewriter for the edification of the programmer.

A report on the present Compiler is being made in two sections,[3] the first being a description of the coding system, and the second being a manual for the operation of the Compiler.

Current work on the Compiler centers on a rewriting in order that the Compiler itself may be compiled, a procedure carrying with it a number of advantages. The most obvious advantage is the elimination of the necessity for code "patches" (with which the present Compiler is heavily laden) that normally attend the inevitable changes. No less important is the ability to add new features or modify old ones with the assurance that the remainder of the code has not been disarranged thereby.

Of the four segments of the Compiler, only one, Compiler I, requires any substantial revamping of its logic. The majority of these changes have already been worked out and debugged (with the assistance of J. Harrison, ORNL Mathematics Panel). The remaining three segments require principally a rewriting in convenient length hunks.

---

[1] R. R. Bate and M. E. LaVerne, *Appl. Nuclear Phys. Ann. Rep. Sept. 10, 1956*, ORNL-2081, p 141.

[2] This work was performed by J. G. Sullivan.

[3] R. R. Bate and M. E. LaVerne, *The Oracle Compiler. Part I: The Coding System*, ORNL CF-57-8-89; M. E. LaVerne, *Part II: Operating Manual*, ORNL CF-57-8-90 (to be issued).

8.8. EFFECTIVE BOUNDARY CONDITIONS IN THE THREE-GROUP, THREE-REGION REACTOR CODE

M. E. LaVerne

The material reported below is the result, thus far, of curiosity as to the effects of tampering with the boundary conditions of the Oracle three-group, three-region (3G3R) reactor code. Several interesting and useful results have appeared, among them being the simulation of reactor regions and the relation of the physically rather obscure 3G3R β's to quantities such as shell transmission and reflection coefficients. In addition, a simple means for evaluating the shell coefficients and an adaptation of the 3G3R code for lattice calculations have been devised.

Simulated Regions in the 3G3R Reactor Code

In the course of some recent reactor calculations (see Part 3) with the 3G3R code, a need arose for more than the available three regions. A means was therefore sought for mocking up the effect of the outer reactor regions, thus making available the three regions for study of the inner portions of the reactor. An adaptation of the 3G3R code has been devised to accomplish such a mockup and is presented below.

The condition on the fictitious outer-boundary flux is expressed by Eq. 44 from the manual for this code.[1] If this equation is solved for β_5, then

(1)
$$\beta_5 = -\frac{\Omega_N}{2D_1^*(L_N\Omega_{N-1} + M_N\Omega_{N+1} + N_N\Omega_{N+1} + X_N)},$$

where the Δ's and Γ's have been eliminated by use of Eq. 37 from the manual.[2]

The procedure for mocking up effective regions then is as follows:

1. Calculate a reactor in the normal fashion, using all three regions.

2. Select the radius at which the reactor is to be split and compute β_5 for each group from Eq. 1. The region constants to be used are those for the inner region immediately adjacent to the dividing radius. The required fluxes are those at the dividing radius and at radii one space point either way. If the dividing radius is at an original boundary, one of the required fluxes is the "fictitious" flux[3] beyond the boundary.

3. Compute a new reactor in which the dividing radius is the new outer boundary, the β_5's in the initial conditions are those determined in step 2, and the regions inside the dividing radius substantially match the corresponding regions from step 1. It is desirable that at least the region adjacent to the dividing radius be identical with the corresponding portion in the original calculation.

The results from a sample calculation testing the above procedure are shown in Fig. 8.8.1. The solid lines are the fluxes from a standard calculation of a reflected reactor. The superimposed circles and squares represent the fluxes for an "effectively reflected" reactor in which the outer boundary conditions match those at the

[1] R. R. Bate, L. T. Einstein, and W. E. Kinney, *Description and Operating Manual for the Three Group, Three Region Reactor Code for Oracle*, ORNL CF-55-1-76 (Jan. 13, 1955).

[2] *Ibid.*, p 9.

[3] *Ibid.*, Fig. 1, p 7.

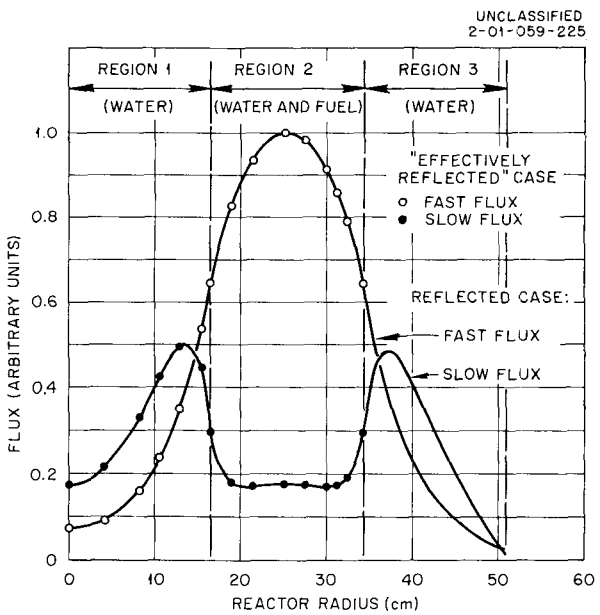

Fig. 8.8.1. Comparison of Fluxes for Reflected and "Effectively Reflected" Reactors. Oracle 3G3R reactor code; slab geometry; two groups.

outer fuel-reflector interface of the original reactor. The agreement is clearly excellent.

The modification required in the 3G3R code is simply that of rescaling one number. "Normal" scaling on β_5 is 2^{-1}, allowing values of β_5 up to ± 2. Since values of β_5 computed from Eq. 1 may run of the order of ± 10 or more, a scaling of, say, 2^{-5} seems desirable. This rescaling may be accomplished by simply changing the contents of memory location 22F (in the 3G3R program) from its normal value of 2^{-12} to a value of 2^{-16}.

The use of this means of, in effect, "peeling off" the outer reactor layers involves the tacit assumption that the effects of any perturbations in the inner regions of the original reactor will not be felt (or, if felt, only weakly) at the dividing radius. It is for this reason that the limitations mentioned above (under step 3) have been made. Perturbations will, in fact, change the boundary conditions at the radius for which matching is attempted, but if a sufficient buffer region is provided and radical changes are not made in the inner regions, the mismatching should not be serious.

It is recognized that the procedure outlined could have been made exact (see ref 4 and Sec 8.6, this report). However, the desire here was to adapt an existing and operational code with a minimum of reworking. The facility with which this procedure works is interesting because it shows that the full-fledged matrix albedo is not always essential.

Shell Transmission and Reflection Coefficients in Terms of 3G3R β's

In the boundary-crossing conditions for the 3G3R reactor code, certain combinations of the shell coefficients appear. The physical significance of these combinations, the β's, is somewhat obscure. The relations between these β's and the transmission and reflection coefficients for the shells follow.

Equations 5 and 6 of the 3G3R code manual[1] lead to

$$(2) \qquad I^{\gamma}(\beta_4\phi_1 + 2D_1\beta_2\phi_1') = J^{\gamma}(2D_2\beta_1\phi_2') \ ,$$

$$(3) \qquad I^{\gamma}(\beta_2\phi_1 - 2D_1\beta_3\phi_1') = J^{\gamma}(\beta_1\phi_2) \ .$$

[4]H. L. Garabedian, D. Mumford, and R. R. Schiff, *Boundary Conditions in Multi-Region Reactor Theory*, WAPD-TN-516 (June 1955).

The partial exit currents from the shell may be written in terms of left and right transmission coefficients, T_L and T_R, left and right reflection coefficients, R_L and R_R, and the incident partial currents as

$$(4) \qquad I^{\gamma}(\phi_1 + 2D_1\phi_1') = J^{\gamma}T_L(\phi_2 + 2D_2\phi_2') + I^{\gamma}R_L(\phi_1 - 2D_1\phi_1') \ ,$$

$$(5) \qquad J^{\gamma}(\phi_2 - 2D_2\phi_2') = I^{\gamma}T_R(\phi_1 - 2D_1\phi_1') + J^{\gamma}R_R(\phi_2 + 2D_2\phi_2') \ ,$$

where I and J are inside and outside shell radii, respectively, and γ is the geometry factor (0 for a slab, 1 for a cylinder, and 2 for a sphere). Subscripts 1 and 2 refer to the regions inside and outside the shell, respectively.

If a linear combination of Eqs. 2 and 3 is now formed, and coefficients in the resulting equation are compared with the corresponding coefficients in Eq. 4, expressions are obtained for T_L and R_L in terms of the four β's. A comparison with Eq. 5 yields expressions for T_R and R_R that are identical with those for T_L and R_L, respectively. Hence, dropping the L and R subscripts gives

$$(6) \qquad T = \frac{2\beta_1}{2\beta_2 + \beta_3 + \beta_4} \ ,$$

$$(7) \qquad R = \frac{\beta_3 - \beta_4}{2\beta_2 + \beta_3 + \beta_4} \ .$$

Evaluation of 3G3R Shell Coefficients for Heavily Absorbing Shells

In the 3G3R reactor code, provision is made for calculation of the effects of thin shells, taking into account both the angular distribution of the incident neutrons and the scattering law within the shell. Unfortunately, use of the polynomial approximations, given for the shell coefficient, limits the calculation to shells for which $\Sigma_t t$ is of the order of 0.1, where t is the shell thickness, and an attempt to use the exact expressions for the coefficients entails the evaluation of rather intractable convolutions of exponential integrals. The calculation of heavily absorbing shells thus becomes difficult unless the shells are made immoderately thin. The following is an attempt to alleviate this difficulty. The sole assumption made is that the shell albedo is negligible.

Transmission and reflection coefficients for the shell, T and R, may be written in terms of the shell β's as

$$T = \frac{2\beta_1}{2\beta_2 + \beta_3 + \beta_4} , \tag{8}$$

$$R = \frac{\beta_3 - \beta_4}{2\beta_2 + \beta_3 + \beta_4} . \tag{9}$$

If the shell is such that scattering is negligible compared with absorption, an easily evaluated set of β's is obtained. Setting $R = 0$ in Eq. 9 gives

$$\beta_3 = \beta_4 , \tag{10}$$

and hence

$$T = \frac{\beta_1}{\beta_2 + \beta_4} . \tag{11}$$

From the defining equations[5] for the β's, the coupling relation

$$\beta_1^2 = \beta_2^2 - \beta_3\beta_4 \tag{12}$$

may be obtained. Then from Eqs. 11 and 12,

$$\begin{aligned} \frac{\beta_1}{\beta_4} &= \frac{2T}{1 - T^2} , \\ \frac{\beta_2}{\beta_4} &= \frac{1 + T^2}{1 - T^2} , \\ \frac{\beta_3}{\beta_4} &= 1 , \\ \frac{\beta_4}{\beta_4} &= 1 . \end{aligned} \tag{13}$$

A convenient choice for β_4 (arbitrary thus far) is

$$\beta_4 = 1 - T , \tag{14}$$

giving, finally,

$$\begin{aligned} \beta_1 &= \frac{2T}{1 + T} , \\ \beta_2 &= \frac{1 + T^2}{1 + T} , \\ \beta_3 &= 1 - T , \\ \beta_4 &= 1 - T . \end{aligned} \tag{15}$$

A check on Eqs. 15 is provided by noting that they reduce to the following (correct) values for the two extremes of zero and complete transmission (where the reflection is, indeed, zero):

	Black Shell	Transparent Shell
T	0	1
β_1	0	1
β_2	1	1
β_3	1	0
β_4	1	0

The thermal fluxes from sample two-group calculations for both a thermally black and a transparent shell are shown in Fig. 8.8.2. The shell was considered to be transparent for the fast group in both cases.

Lattice Calculations with the 3G3R Reactor Code

Because of the symmetry with respect to the outer boundary of each cell in a lattice, a natural

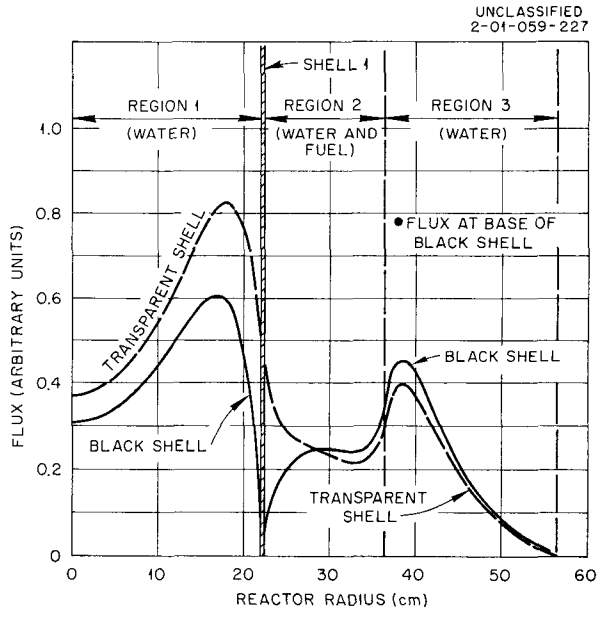

Fig. 8.8.2. Comparison of Thermal Fluxes for a Transparent and a Black Shell. Oracle 3G3R reactor code; spherical geometry; two groups.

[5] R. R. Bate, L. T. Einstein, and W. E. Kinney, *Description and Operating Manual for the Three Group, Three Region Reactor Code for Oracle*, ORNL CF-55-1-76, Eq. 23, p 6 (Jan. 13, 1955).

boundary condition is the zero slope of the flux at that point. This condition, unfortunately, leads to an infinite β_5, an impracticably large value. A prescription has been found, however, involving a minor change in the 3G3R code, that *effectively* imposes an infinite β_5.

Equation 44 of the 3G3R manual[6] is

$$\Omega_{N+1} = -\frac{2\beta_5 D_1^* X_N + \Delta_N \left[1 + 2\beta_5 D_1^* \left(\frac{L_1 \Delta_{N-1}}{\Delta_N} + N_1 + L_1 \Gamma_{N-1}\right)\right]}{2\beta_5 D_1^* M_1 + \Gamma_N [1 + 2\beta_5 D_1^* (N_1 + L_1 \Gamma_{N-1})]} . \tag{16}$$

It can be seen that

$$\lim_{\beta_5 \to \infty} \Omega_{N+1} = -\frac{2D_1^* X_N + \Delta_N \left[0 + 2D_1^* \left(\frac{L_1 \Delta_{N-1}}{\Delta_N} + N_1 + L_1 \Gamma_{N-1}\right)\right]}{2D_1^* M_1 + \Gamma_N [0 + 2D_1^* (N_1 + L_1 \Gamma_{N-1})]} . \tag{17}$$

Comparison of Eqs. 16 and 17 shows that the *effect* of an infinite β_5 may be obtained simply by inserting 0 where Eq. 16 calls for a 1. It would also appear, at first sight, that the *input* β_5 should equal 1. However, in Eq. 16 the terms that involve the input β_5 appear as common factors in the numerator and denominator. Hence the effect of the input β_5 cancels out, and the actual value used proves to be irrelevant.

The net result is that if, in the 3G3R program, the contents of cell 22F (the memory location of the "1" used in Eq. 16) is set equal to 0, the condition of zero slope for the flux at the outer reactor boundary is automatically satisfied.

[6] R. R. Bate, L. T. Einstein, and W. E. Kinney, *Description and Operating Manual for the Three Group, Three Region Reactor Code for Oracle*, ORNL CF-55-1-76 (Jan. 13, 1955).

8.9. ORACLE SUBROUTINES

J. G. Sullivan J. H. Marable
R. R. Coveyou M. E. LaVerne
W. E. Kinney

In the process of preparing Oracle programs for the solution of various problems, it is frequently desirable to write subroutines specially adapted to the needs of these problems. Since many such subroutines are also of general use, they are published separately. A list of such published subroutines prepared by the Reactor Theory Group of the Applied Nuclear Physics Division is as follows:

Subroutine No.	Operation
00E14	A list of binary fixed-point numbers is multiplied by $2^{-b}10^{d}$ and stored
00E1E	A list of binary fixed-point numbers is multiplied by $2^{b}10^{-d}$ and stored
00E38	A specified number of blocks of information are copied from one magnetic-tape drive onto another
00E39	A tape drive is searched for a specified sentinel
00E3A	Words of specified length are printed in columns on the curve plotter
00E3B	A specified number of characters are printed in columns on the curve plotter
00E3C	A list of words is printed in rows on the curve plotter
00E41	A list of 8-32 floating-point numbers is converted to decimal floating points and printed on the curve plotter
00E3D	A specified number of characters are printed on the curve plotter in rows of a specified length
00E3F	The appropriate sign is appended to decimal numbers printed on the curve plotter, and the position of the decimal point can be indicated
00E40	A list of binary fractions is converted to decimal with scaling $2^{b}10^{-d}$ and printed on the curve plotter
00E3E	An executive routine using 00E3A, 00E3B, 00E3C, and 00E3D
00ABE	A list of symbols available in output on the curve plotter
00E46	A curve plotter frame is titled with the page number being automatically kept track of
00E5C	The left half of a hexadecimal word is converted to an alphameric word
00E5D	A list of words ended by a zero sentinel is put out on paper tape, narrow magnetic tape, or the console typewriter
00E5E	A list of words is either loaded through paper tape or the console keyboard, or put out through paper tape, narrow magnetic tape, or the console typewriter
00F5C	The number of words preceding the sentinel is reported
00E06	The right and left halves of the words in a list are interchanged, and the number of words in the list is reported
00E02	A list of words is partially erased, and the number of words in the list is reported
00F8E	A specified number of consecutive cells are erased
00F8D	The sum of a specified number of consecutive cells is reported
00F72	A list of integers is stored in the memory

Subroutine No.	Operation
00F96	A list of words is copied from one section of the memory to another
00FFF	A specified portion of a cell is compared with the corresponding portion of a list of words and, depending on the results of the check, various information is reported
00FD1	The logical product of two words is determined
00FAF	A specified number of consecutive words are punched on paper tape
00FCB	The right half of Q replaces the left half
00F74	The differences of the corresponding members of two lists are stored
00F76	The contents of Q are squared
00F7F	The routine reports whether or not two lists match word for word
00F73	A list of random numbers uniform on the interval -1 to $+1$ is stored in the memory
00F7D	An originally Q to Q type subroutine is converted to operate as a memory-to-memory type subroutine
00F77	The squares of a list of numbers are stored in the memory
00FD3	A list of words is changed from the type "X*" to "*X*"
00F75	A list of words is checked for any nonzero word
00F95	A list of words is copied from one portion of the memory to another

Although not a subroutine, a code has been written that is known as the "Servi-seer," which enables subroutines to be used as "bootstrap" codes for the debugging of large programs.

8.10. AN ESTIMATE OF THE NONLEAKAGE PROBABILITY FOR BARE AQUEOUS HOMOGENEOUS U^{235} REACTORS

D. K. Trubey H. S. Moran A. M. Weinberg

According to the usual theory of bare homogeneous neutron chain reactors,[1] the nonleakage probability in a finite reactor may be computed from the neutron slowing-down distribution in an infinite system, the relation between them being that the nonleakage probability is the Fourier transform of the fission-neutron, point-source, slowing-down distribution. Thus if $K(B)$ is the nonleakage probability for a bare reactor with geometric buckling B^2, and $G(r)$ is the point-source slowing-down kernel, then

$$(1) \qquad K(B) = \frac{\int_0^\infty G(r) \frac{\sin Br}{Br} 4\pi r^2 \, dr}{\int_0^\infty G(r) \, 4\pi r^2 \, dr} ,$$

where r is the distance from the source.

In the case of moderators which are heavier than deuterium, and to a lesser extent for deuterium itself, continuous slowing-down theory is applicable, and both $G(r)$ and $K(B)$ are superpositions of Gaussians. In the case of moderation by hydrogen, however, the continuous theory is not at all applicable; the experimentally observed kernel $G(r)$ deviates very strongly from a Gaussian shape. Such formalisms as the Goertzel-Selengut (G-S) method[2] give fairly good values for the slowing-down kernel at small distances – in fact, rather better values than can be derived from the exact transport equation with presently known cross sections. However, since the G-S method is not rigorous, it can be said that a reliable and consistent calculation of $G(r)$ and $K(B)$ for H_2O which agrees with experiment is lacking at present.

On the other hand, there is an abundance of measured data of $G(r)$ for neutrons in H_2O originating from a point source of fissioning U^{235} (see refs 3 and 4 and Sec 9.2, this report). It was therefore deemed worth-while to compute $K(B)$ directly from the observed $G(r)$ for various values of B. The resulting Fourier transform should be useful for helping in the computation of nonleakage probabilities (and therefore critical masses) in bare H_2O reactors (or H_2O-reflected H_2O reactors).[5] Furthermore, since in most of the theoretical calculations $K(B)$, not $G(r)$, is computed initially, tabulated values of $K(B)$ computed from the experimental values of $G(r)$ according to Eq. 1 should be useful for comparing theoretical computations of the slowing-down distribution with experiment. The present paper is a summary of such a computation of $K(B)$ for slowing down of U^{235} fission neutrons in H_2O.

Determination of $G(r)$

Values of $G(r)$ were obtained from two independent sets of experimental data. The first is the well-known slowing-down distribution to indium resonance of Hill and Roberts,[3] which gives results for distances from the source up to about 92 cm. This distribution to indium resonance will be denoted as the H-R distribution. The second is the measurement of the distribution of *thermal* neutrons from a fission source in the water tank of the Lid Tank Shielding Facility (LTSF) (see Sec 9.2, this report). Because the detector was sensitive to thermal neutrons and the intensity of the source was sufficiently large, the distribution in the LTSF experiments could be measured for distances much farther than the 92 cm of the H-R experiment; however, the depression of flux near the source was considerably larger than in the H-R experiment, and this makes unusable those results from the LTSF that were observed at locations closer than 15 cm to the source. The difficulty near the source was largely eliminated in the H-R experiment by using a small source, for one series of measurements, located 10 cm from

[1] S. Glasstone and M. C. Edlund, *The Elements of Nuclear Reactor Theory*, chap. 12, D. Van Nostrand, New York, 1952; see also A. M. Weinberg and E. P. Wigner, *Theory of Chain Reactions*, University of Chicago Press, Chicago (to be published).

[2] G. Goertzel, *Criticality of Hydrogen Moderated Reactors*, TAB-53 (July 25, 1950); D. Selengut, private communication to G. Goertzel.

[3] J. E. Hill, L. D. Roberts, and T. E. Fitch, *J. Appl. Phy.* 26, 1013–1017 (1955).

[4] L. M. Barkov and K. N. Mukhin, *J. Nuclear Energy*, 4, 91–93 (1957).

[5] N. C. Francis, H. Hurwitz, Jr., and P. F. Zweifel, *Nuclear Sci. and Eng.* 2, 253–287 (1957).

the bottom of the water tank. Even so, in order to obtain reliable data up to 2 cm from the source, it was necessary to extrapolate the data obtained at larger distances back to the source.

Since the LTSF data taken closer than 10 cm from the source were completely unusable, values of a thermal kernel for this region were based on the H-R indium-resonance kernel extrapolated to thermal energy. This extrapolation was actually performed for the entite distance covered by the H-R experiment, that is, out to 92 cm from the source, so that the overlapping regions of the two experiments could be compared.

The extrapolation of the H-R indium kernel to thermal energy was made by assuming that the indium-resonance slowing-down density and flux are proportional, that the slowing-down distribution from that energy to thermal energy is Gaussian (age theory), and that a diffusion kernel describes the diffusion of thermal neutrons from their point of origin. Thus if the H-R point kernel at a distance r is denoted as $G_{\text{In}}(r)$, and the thermal-neutron-flux kernel is denoted as $G_{\text{th}}(r)$,

$$G_{\text{th}}(r) \propto \iint_{\text{all space}} G_{\text{In}}(\vec{r}\,') \, e^{-(\vec{r}\,''-\vec{r}\,')^2/4\tau} \, \frac{e^{-|\vec{r}-\vec{r}\,''|/L}}{|\vec{r}-\vec{r}\,''|} \, d\vec{r}\,' \, d\vec{r}\,'' \, , \tag{2}$$

where τ is the age from indium resonance to thermal energy, and L is the diffusion length of thermal neutrons in water. This is equivalent to

$$G_{\text{th}}(r) \propto \int_0^\infty \int_0^\infty G_{\text{In}}(r') \frac{r'}{r''} \left[e^{-(r''-r')^2/4\tau} - e^{-(r''+r')^2/4\tau} \right] \times \frac{r''}{r} \left[e^{-|r-r''|/L} - e^{-|r+r''|/L} \right] dr' \, dr'' \, , \tag{3}$$

where $G_{\text{th}}(r)$ is now the point kernel for thermal neutrons [*not* for nascent thermal neutrons for which the kernel is denoted as $G_{\text{nas}}(r)$], and r is the scalar distance from the point source. Equation 3 follows from Eq. 2, since $G_{\text{In}}(r')$, the indium-resonance flux at a distance r' from a point source, acts as a spherical-shell source for the further slowing of the neutrons to thermal energies and their subsequent diffusion as thermal neutrons.[6]

[6] S. Glasstone, *Principles of Nuclear Reactor Engineering*, p 592–593, Van Nostrand, New York, 1955.

The expressions in the brackets are the spherical-shell kernels for age theory and diffusion theory, respectively. Thus the integration, which was carried out numerically by using the Oracle, a high-speed digital computer, was only double rather than sixfold. The resulting thermal-neutron kernel, based on the H-R indium-resonance data extrapolated to thermal energy, is shown in Fig. 8.10.1 for distances out to 90 cm from the source. The values very near the source (0 to 2 cm), which are based on data extrapolated back to the source, should be better than values obtained from the actual experimental data, since each point is based on two integrations over the entire curve.

Naturally, the constants τ and L are quite important to the calculation. The value of τ was taken to be 1.0 cm^2, which is the value determined experimentally by Barkov *et al.*[7] The value of L was taken to be 2.71 cm, which is the weighted average of the experimental results of various investigations summarized by Barkov *et al.*, and agrees within 1% with the experimental value obtained by Barkov *et al.*

As mentioned above, values of the thermal-neutron-flux kernel based on the LTSF[8] data were calculated for distances that extended out to 160 cm from the source, with the region from 15 to 90 cm overlapping with values based on the H-R data. The source used in this experiment was a 28-in.-dia plate of U^{235} activated by thermal neutrons streaming through a hole in the concrete shield of

[7] L. M. Barkov, V. K. Makarin, and K. N. Mukhin, *J. Nuclear Energy* 4, 94–102 (1957).

[8] The Lid Tank Shielding Facility has been described in various papers; see, for example, S. Glasstone, *Principles of Nuclear Reactor Engineering*, p 618, Van Nostrand, New York, 1955.

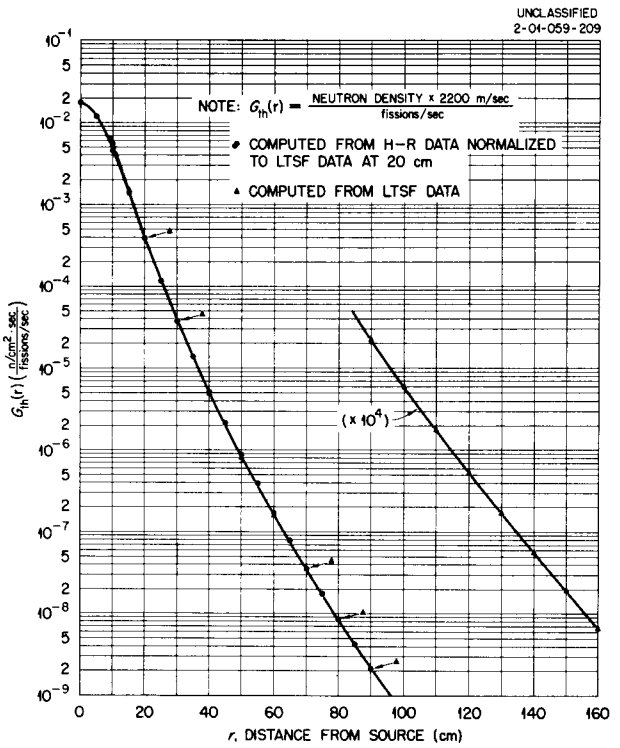

Fig. 8.10.1. Thermal-Neutron-Flux Kernel for an Infinite Water Medium as a Function of Distance from a Point U^{235} Fission Source.

the ORNL Graphite Reactor. The strength of this source is 1.62×10^{11} fissions/sec ± 5% as determined by estimating or measuring the following:[9] (1) the total number of thermal neutrons captured within the source plate, (2) the rate of neutron production within the source, and (3) the heat production in the source. It has been estimated on the basis of "effective removal cross sections" that, because of the intervening structural material between the uranium plate and the water in the tank, the effective source strength is 6% smaller, but this correction has not been applied in the normalization of the kernel calculated below, since this type of correction is not valid near the source.

The thermal-neutron flux measured in the experiment, designated as the "equivalent $1/v$" flux, is equivalent to the neutron density times 2200 m/sec and is plotted in Fig. 9.2.4 of Sec 9.2 in this report. Measurements out to distances of 60 cm from the source plate surface were made with bare and cadmium-covered gold foils, the other measurements taken with fission chambers and BF_3 counters were normalized to the foil measurements. The LTSF data close to the source plate are badly perturbed by the boundary, as was discussed above, and for this reason the data closer than 15 cm were not used in the subsequent analysis.

The transformation used to convert the LTSF data from a plane disk source to the point-source kernel was one developed by Blizard,[10] and may be derived as follows:

$$D(z,a) = S \int_0^a G(r)\, 2\pi\rho\, d\rho \ ,$$

where $D(z,a)$ is the flux at a distance z from a plane source of radius a (see Fig. 8.10.2). The source strength per unit area is S, and the differential source area is $2\pi\rho\, d\rho$. But

$$r^2 = z^2 + \rho^2 \ ,$$

and

$$2r\, dr = 2\rho\, d\rho \ .$$

Therefore

$$D(z,a) = 2\pi S \int_z^{\sqrt{z^2+a^2}} G(r)\, r\, dr \ .$$

[9] D. R. Otis, *Appl. Nuclear Phys. Ann. Rep. Sept. 10, 1956*, ORNL-2081, p 163.

[10] S. Glasstone, *Principles of Nuclear Reactor Engineering*, p 623, Van Nostrand, New York, 1955.

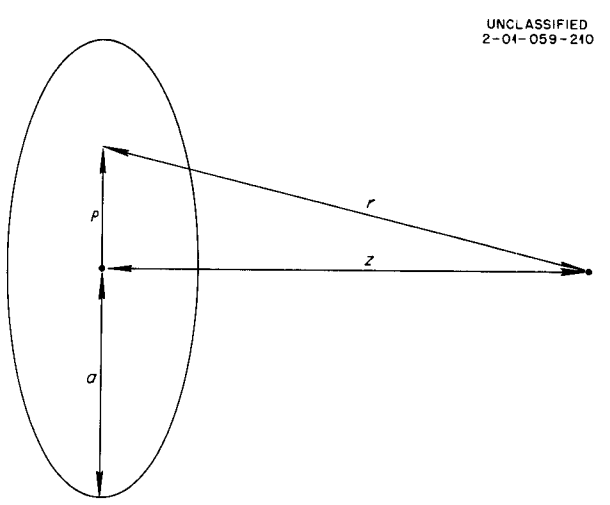

Fig. 8.10.2. Geometry Used in Calculation to Convert LTSF Plane-Disk-Source Data to a Point-Source Kernel.

Differentiating with respect to z,

$$(4) \quad \frac{1}{2\pi Sz} \frac{d}{dz} D(z,a) = G\sqrt{z^2 + a^2} - G(z) .$$

If a function $B(z)$ is defined by

$$B(z) \equiv -\frac{1}{2\pi Sz} \frac{d}{dz} D(z,a) ,$$

then it is found from the recursion formula of Eq. 4 that

$$(5) \quad G(z) = B(z) + B\sqrt{z^2+a^2} + B\sqrt{z^2+2a^2} + \ldots$$

$$= \sum_{\nu=0}^{\infty} B\sqrt{z^2+\nu a^2} ,$$

where $G(z)$ is the *point* kernel at the distance z (or r) from a point source.

Thus, from Eq. 5 applied to the LTSF data, a thermal-neutron point kernel $G_{th}(r)$ is obtained for r greater than 10 cm. This is plotted in Fig. 8.10.1 along with the thermal kernel calculated from the H-R indium kernel, which was normalized to the LTSF kernel at 20 cm. The agreement between the H-R and LTSF kernels is quite good over the region from 15 to 90 cm from the source, the region over which the two kernels overlap. It is unfortunate that the LTSF kernel for the region nearer the source is unobtainable, since the availability of such data might have served as a basis for explaining the difference between the H-R observed age in H_2O and the various theoretical calculations of the age.[11]

Determination of $K(B)$

Equation 1 was used to calculate the Fourier transform, $K_{th}(B)$, of the distribution $G_{th}(r)$ given in Fig. 8.10.1. Similarly, Eq. 1 was used to calculate $K_{In}(B)$ from the distribution reported by Hill and Roberts.[12] The integrations were carried out numerically by using the trapezoidal rule on the Oracle. It was found that the results were slightly greater than those obtained with Simpson's rule, and therefore were more accurate, since the trapezoidal rule integration must be an underestimate.

[11] J. E. Wilkins, Jr., R. L. Hellens, and P. E. Zweifel, *Status of Experimental and Theoretical Information on Neutron Slowing Down Distribution in Hydrogenous Media*, P/597 PICG V. p 62–76 (Aug. 1955).

[12] J. E. Hill, L. D. Roberts, and T. E. Fitch, *J. Appl. Phy.* **26**, 1013–1017 (1955).

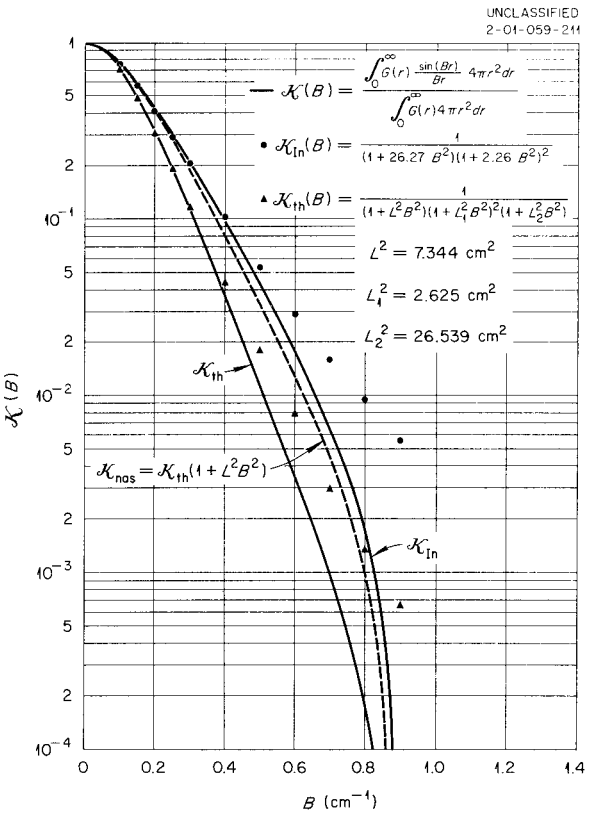

Fig. 8.10.3. Fourier Transforms of Indium-Resonance and Thermal-Neutron Slowing-Down Kernels in Water for $B < 0.9$. U^{235} fission source.

The results for both kernels are shown in Figs. 8.10.3, 8.10.4, and 8.10.5. For purposes of comparison, values of $K_{In}(B)$ obtained by Hurwitz *et al.*,[13] both by numerical integration and by the G-S method, are also plotted in Fig. 8.10.4. For large values of B the slope changes radically as shown in Fig. 8.10.3, and $K(B)$ even goes negative. This is believed to be due to the shape of the assumed kernel $G(r)$ near 0. In order to verify that the Oracle program was yielding the correct results, a Gaussian and an exponential kernel were computed analytically; the results were identical to those obtained in the Oracle numerical integration.

The transform $K_{nas}(B)$ of the nascent thermal kernel is also shown in Figs. 8.10.3 and 8.10.5.

[13] H. Hurwitz, P. Zweifel, and C. D. Petrie, private communication.

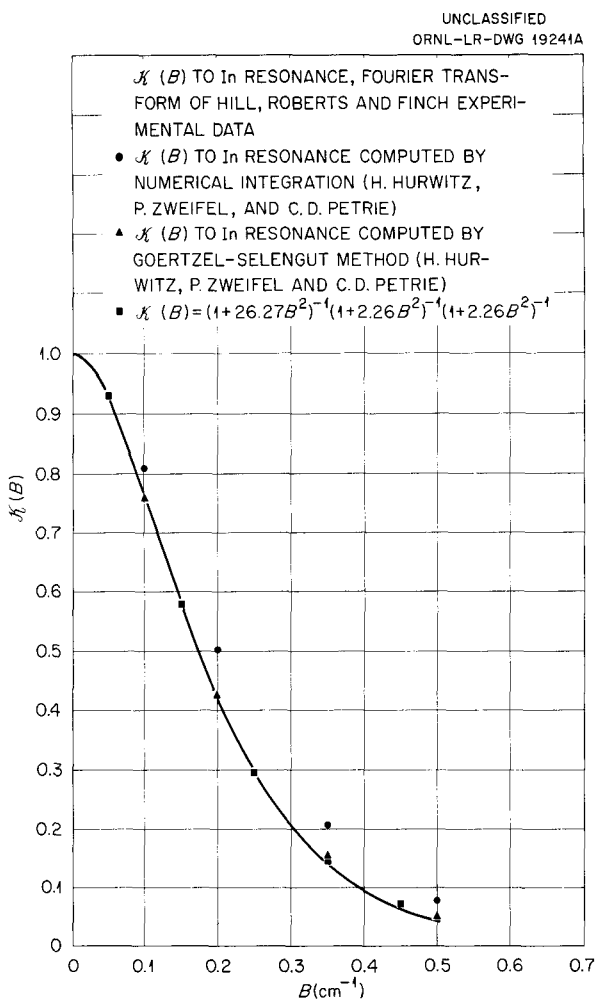

Fig. 8.10.4. Fourier Transforms of Indium-Resonance Slowing-Down Kernel in Water for $B < 0.5$. U^{235} fission source.

Since the thermal neutrons diffuse with a diffusion length L,

$$K_{nas}(B) = K_{th}(B)(1 + L^2B^2) \ . \tag{6}$$

On the other hand, since the age increment τ from indium resonance to thermal energy is 1 cm^2, the following is also very nearly true.

$$K_{nas}(B) = K_{In}(B)e^{-B^2} \ . \tag{7}$$

A comparison of the values of $K_{nas}(B)$ computed by these two methods is shown in Table 8.10.1.

In regard to the accuracy of $K_{th}(B)$, the numerator of Eq. 1 was integrated by hand from 0 to 15 cm, which covered the region where the kernel depends on the indium experiment, and the results are compared with the Oracle computations in Table 8.10.2. The table clearly shows that $K(B)$ is almost entirely dependent on the H-R indium experiment for values of B which are of most interest from a practical standpoint. However, it was found that $K(B)$ changed less than 0.5% for $B < 0.2$ cm^{-1}, even though the extrapolation of $G(r)$ to $r = 0$ was changed radically. For example, a Gaussian was fitted through the H-R data at $r = 3$ cm and $r = 4$ cm. This yielded a $G(0)$ value about 5% higher. A Gaussian was also fitted through LTSF points at $r = 10$ and $r = 20$ cm, which yielded a $G(0)$ value nearly 20% lower. For $B > 0.2$ cm^{-1}, the uncertainty in $K(B)$ becomes much larger.

Since for reactor calculations it is very useful to have a simple multigroup analytic approximation

Table 8.10.1. Ratio of the Fourier Transform $K_{nas}(B)$ Computed from $K_{In}(B)$ to that Computed from $K_{th}(B)$

B (cm^{-1})	$\dfrac{K_{In}(B)e^{-B^2}}{K_{th}(B)(1 + L^2B^2)}$
0.01	1.0000
0.05	1.0002
0.10	1.0020
0.15	1.0047
0.20	1.0067
0.30	1.0089
0.40	1.0190
0.50	1.0071
0.60	0.9450
0.70	0.9867

Table 8.10.2. Ratio of Numerator of Fourier Transform of $G_{th}(r)$ Computed by Hand to That Obtained on the Oracle

B (cm^{-1})	$\int_0^{15} \Big/ \int_0^{\infty}$
0.12	1.053
0.15	1.153
0.17	1.236

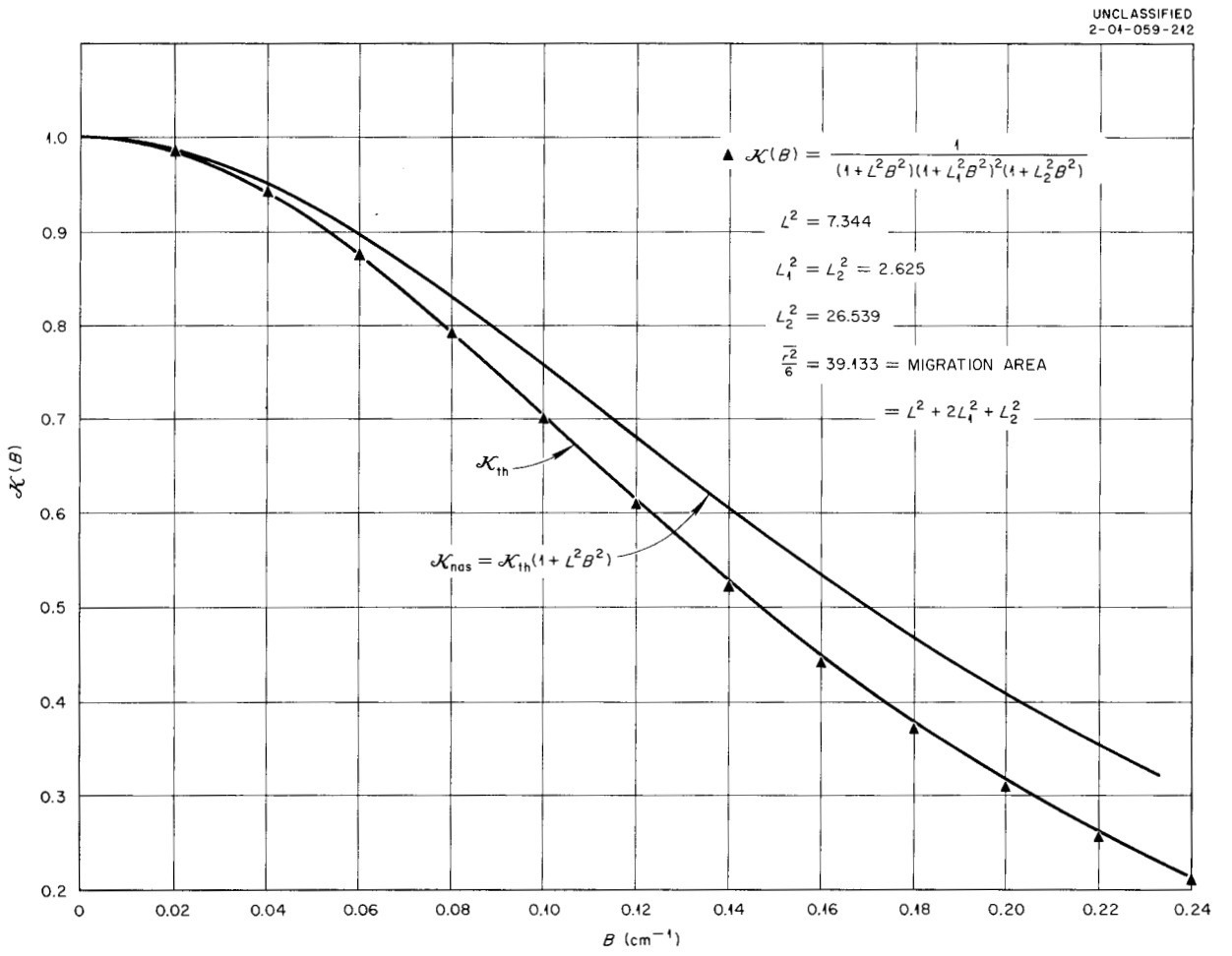

Fig. 8.10.5. Fourier Transform of Thermal-Neutron Slowing-Down Kernel in Water for $B < 0.25$. U^{235} fission source.

to the experimental Fourier transforms, attempts were made to develop such expressions for the data in Figs. 8.10.3, 8.10.4, and 8.10.5. The following expressions were obtained:

$$K_{1n}(B) = \frac{1}{(1 + 26.27B^2)(1 + 2.26B^2)^2},$$

$$K_{th}(B) = \frac{1}{(1 + L^2B^2)(1 + L_1^2B^2)^2(1 + L_2^2B^2)},$$

where

$$L^2 = 7.344 \text{ cm}^2,$$
$$L_1^2 = 2.625 \text{ cm}^2,$$
$$L_2^2 = 26.539 \text{ cm}^2.$$

These simple expressions agree very well with the computed values out to values of $B \cong 0.35$ cm^{-1}. The constants, whose sum equals the age or migration area, were chosen simply on the basis of making a good fit over a particular arbitrary region.

Moments of the Kernel

Quantities of interest are the moments, $\overline{r^n}$, of the distribution $G(r)$:

$$\overline{r^n} = \frac{\int_0^\infty G(r)\, r^n\, 4\pi r^2\, dr}{\int_0^\infty G(r)\, 4\pi r^2\, dr}. \tag{8}$$

The moments $\overline{r^n_{th}}$ determined from the kernel $G_{th}(r)$ are shown in Table 8.10.3 for n = 2, 4, 6, 8, and 10. The moments $\overline{r^n_{th}}$ determined from the Hill-Roberts kernel are also presented.

In order to compute the higher moments, both $G_{th}(r)$ and $G_{In}(r)$ had to be extrapolated by assuming $G(r) \propto e^{-r/\lambda}/r^2$, where λ_{th} = 11.017 cm for r > 160 cm and λ_{In} = 8.786 cm for r > 92 cm. The fractions of both $\overline{r^n_{th}}$ and $\overline{r^n_{In}}$ which depend on extrapolated data are also shown in Table 8.10.3. Since the extrapolated fraction of $\overline{r^n_{In}}$ is rather large (as much as 33%), it seems that a more accurate calculation of $\overline{r^n_{In}}$ could be made by using $G_{th}(r)$ rather than $G_{In}(r)$. The relationship between the various transforms may be written as follows:

$$K_{th}(B) = K_{In}(B)\, K_1(B)\, K_2(B) \ , \tag{9}$$

$$K_{th}(B) = K_{nas}(B)\, K_2(B) \ , \tag{10}$$

where $K_1(B)$, $K_2(B)$, and $K_{nas}(B)$ are the Fourier transforms of the Gaussian slowing-down distribution $e^{-r^2/4\tau}$, the diffusion kernel $e^{-r/L}/r$, and the nascent thermal slowing-down distribution. The moments of the Gaussian slowing-down distribution and the diffusion kernel are defined as $\overline{r^n_1}$ and $\overline{r^n_2}$, respectively.

If the transform is expressed in terms of the moments

$$K(B) = \sum_{i=0}^{\infty} \frac{(-1)^i}{(2i+1)!} B^{2i}\, \overline{r^{2i}} \ , \tag{11}$$

where $2i = n$, then by using Eqs. 9 and 10 and equating coefficients of powers of B, the moments of $G_{In}(r)$ and $G_{nas}(r)$ may be computed. This was carried out for n = 2, 4, 6, and 8, and the results appear in Table 8.10.3. Values for $\overline{r^n_1}$ and $\overline{r^n_2}$ are also given in Table 8.10.3.

It may be noted that the estimate for the migration area of U^{235} fission neutrons down to thermal energies in H_2O is the same, whether computed from the thermal or the indium second moment; that is,

$$\overline{r^2_{th}}/6 = 39.13 \text{ cm}^2$$

and

$$\overline{r^2_{In}}/6 + \tau + L^2 = (30.78 + 1.00 + 7.34) \text{ cm}^2 = 39.12 \text{ cm}^2 \ .$$

The contribution of the Hill-Roberts experiment (0 to 15 cm from the source) to the integral in computing $\overline{r^2_{th}}$ is only 30%.

Table 8.10.3. Summary of the Moments of Various Slowing-Down Distributions

n	$\overline{r^n_{th}}$, cm^n	$\overline{r^n_{th}}$, e.f.*	$\overline{r^n_{In}}$, From $G_{In}(r)$, cm^n	$\overline{r^n_{In}}$, e.f.*	$\overline{r^n_{In}}$, From $K_{th}(r)$, cm^n	$\overline{r^n_1}$, cm^n	$\overline{r^n_2}$, cm^n	$\overline{r^n_{nas}}$, cm^n
2	$(2.348 \pm 0.09) \times 10^2$**	3.08×10^{-6}	1.847×10^2	1.40×10^{-5}	1.847×10^2	6.0	4.406×10^1	1.907×10^2
4	$(1.592 \pm 0.13) \times 10^5$**	1.57×10^{-4}	1.222×10^5	7.95×10^{-4}	1.210×10^5	6.0×10^1	6.472×10^3	1.247×10^5
6	$(2.769 \pm 0.35) \times 10^8$**	2.75×10^{-3}	2.27×10^8	1.30×10^{-2}	2.23×10^8	8.4×10^2	1.996×10^6	2.278×10^8
8	$(1.084 \pm 0.18) \times 10^{12}$**	2.22×10^{-2}	8.6×10^{11}	8.57×10^{-2}	9.2×10^{11}	1.512×10^4	1.056×10^9	9.376×10^{11}
10	$(8.230 \pm 1.7) \times 10^{15}$**	9.59×10^{-2}		3.33×10^{-1}				

*Extrapolated fraction.

**Uncertainty due to estimated maximum possible error in measuring the slope of the kernel. Theory indicates a much larger error; see J. E. Wilkins, Jr., R. L. Hellens, and P. E. Zweifel, *Status of Experimental and Theoretical Information on Neutron Slowing Down Distribution in Hydrogenous Media*, P/597 PICG V. p 62–76 (Aug. 1955).

8.11. COMPILATIONS OF NEUTRON CROSS SECTIONS OF NITROGEN AND OXYGEN[1]

H. Lustig H. Goldstein M. H. Kalos
Nuclear Development Corporation of America

The purpose of this investigation is to present in convenient form the neutron cross sections of nitrogen and oxygen which are of use in reactor and shielding calculations. In part, the cross sections listed here are taken directly from experiment; in part, they are taken from a combination of scanty experiments and theoretical calculations of varying degrees of validity; and, in part, they are based on educated, artistic extrapolations. The lack of knowledge concerning some cross sections is so profound that no attempt was made to make estimates, for example, of the angular distribution of inelastically scattered neutrons. On the other hand, experimental data were at times more detailed than would be useful for reactor or shielding purposes, for example, some of the fine structure of resonances in the total cross section. The tabulated cross sections have been given at energy spacings thought to be more than adequate for the purposes at hand, but some of the finer detail has been averaged over. The range considered is from approximately thermal energy to 18 Mev. Work on nitrogen has been completed, and detailed tabulations of the pertinent cross sections have been prepared. A summary of the results, and the methods used in arriving at them, is presented below. The investigation on oxygen is still in progress, and only a brief discussion of its present status is given here.

NITROGEN

Nomenclature for the cross sections will follow the recent suggestions of the NCSAG;[2] since only neutrons will be considered as the incident particle, the subscript n will be omitted for the cross sections of specific reactions, for example, σ_γ instead of $\sigma_{n,\gamma}$. The total cross section σ_{nT} will be considered first, followed by the elastic scattering cross sections $\sigma_n(E)$ and $\sigma_n(E;\theta)$. In turn, the various cross sections making up the nonelastic cross section σ_{nX} will be discussed: the inelastic cross section $\sigma_{n'}$, the radiative capture cross section σ_γ, the remaining reactions making up the neutron disappearance cross section σ_{nD}, and finally the total nonelastic cross section σ_{nX}. Results will be given in the tables; the text will discuss mainly the procedures followed in arriving at the listed cross sections. Elemental nitrogen is made up almost entirely of N^{14}; only 0.37% is N^{15}, and no unusual reactions are known to take place in this isotope. All cross sections discussed below are therefore assumed to refer to N^{14}.

Total Cross Section $\sigma_{nT}(E)$

Table 8.11.1 lists the total cross section at 90 energy points spaced equally in log E from 200 kev to 18 Mev. Almost all the values have been taken from BNL-325 and supplements,[3] except for a short extrapolation from 14 to 18 Mev. In some cases the cross section has been averaged over the fine structure of the resonances in order to represent it properly at the energies chosen; these instances are indicated by a star in the table.

There is a gap in the measured cross section from 2 to 150 kev. As will be described below, the behavior on both sides of the gap indicates that the cross section is influenced by at least one, and possibly two, negative energy levels. One is quite broad and accounts for the general decrease in the cross section which terminates only around 500 to 600 kev; the other is much narrower and is perhaps evidenced by the decrease in the observed cross section at 2.5 kev. Table 8.11.2 presents an estimate of the behavior of σ_n from 0 to 200 kev, based on the assumed negative energy levels. No high certainty can be assigned to the listed values; it is even possible that a resonance similar to the one at 430 kev lurks in the unexplored gap. In any case, further measurements are definitely called for.

Elastic Scattering Cross Section σ_n

Total Elastic Scattering Cross Section, $\sigma_n(E)$. – No direct measurements of $\sigma_n(E)$ have been made for nitrogen, so that the cross section must be obtained by subtracting σ_X (to be discussed below)

[1]This work was performed under Subcontract 1069 with Nuclear Development Corporation of America.

[2]H. Goldstein, *A Proposed Nomenclature Scheme for Experimental Nuclear Cross Sections*, NDA-2-33 (May 28, 1956) revised Jan. 28, 1957.

[3]D. J. Hughes and J. A. Harvey, *Neutron Cross Sections*, BNL-325 (July 1, 1955); D. J. Hughes and R. B. Schwartz, *Neutron Cross Sections*, BNL-325, Supplement 1 (Jan. 1, 1957).

Table 8.11.1. Cross Sections and Elastic Angular Distribution Data for Neutron Scattering on Nitrogen

Energy	Cross Sections (barns)				Legendre Coefficients						
(Mev)	σ_{nT}	σ_{nD}	$\sigma_{n'}$	σ_n	f_1	f_2	f_3	f_4	f_5	f_6	f_7
18.0	1.80	0.261	0.455	1.084	0.763	0.545	0.390	0.325	0.205	0.1108	0.035
17.1	1.77	0.2675	0.4625	1.040	0.750	0.535	0.380	0.309	0.195	0.097	0.032
16.3	1.75	0.2735	0.470	1.0065	0.740	0.525	0.370	0.294	0.183	0.086	0.029
15.5	1.72	0.2785	0.4775	0.964	0.730	0.517	0.363	0.278	0.1725	0.077	0.0265
14.75	1.67	0.2825	0.4835	0.904	0.717	0.507	0.353	0.260	0.160	0.069	0.0240
14.0	1.60	0.2850	0.490	0.825	0.710	0.495	0.345	0.245	0.1475	0.0608	0.022
13.3	1.55	0.2880	0.4925	0.7695	0.690	0.482	0.335	0.227	0.1350	0.053	0.019
12.7	1.50	0.2895	0.4940	0.7165	0.680	0.475	0.325	0.215	0.125	0.049	0.0175
12.1	1.45	0.290	0.4940	0.660	0.667	0.460	0.315	0.195	0.113	0.042	0.0150
11.5	1.42	0.290	0.4900	0.640	0.650	0.450	0.310	0.180	0.105	0.037	0.0130
10.9	1.38	0.290	0.4840	0.606	0.640	0.440	0.298	0.168	0.0930	0.033	0.0115
10.4	1.35	0.2888	0.4750	0.5862	0.626	0.430	0.290	0.155	0.085	0.030	0.010
9.89	1.32	0.2875	0.4625	0.570	0.610	0.418	0.278	0.138	0.075	0.025	0.0085
9.41	1.29	0.2850	0.4450	0.560	0.595	0.405	0.268	0.125	0.0675	0.022	0.0070
8.95	1.28	0.2830	0.4230	0.574	0.580	0.395	0.260	0.113	0.0585	0.019	0.0060
8.51	1.30	0.2800	0.3980	0.622	0.565	0.380	0.248	0.102	0.0520	0.017	0.0050
8.10	1.48	0.2775	0.3735	0.829	0.550	0.370	0.238	0.090	0.0450	0.0145	0.0038
7.70	1.53	0.2745	0.3415	0.914	0.530	0.355	0.227	0.078	0.0380	0.0125	0.0030
7.33	1.43	0.2710	0.3150	0.844	0.525	0.340	0.215	0.068	0.0285	0.010	0.0023
6.97	1.37	0.2675	0.2880	0.8145	0.496	0.327	0.204	0.058	0.0220	0.0085	0.0016
6.63	1.35	0.2625	0.2570	0.8305	0.472	0.310	0.193	0.050	0.0155	0.0060	0.0012
6.30	1.40	0.2585	0.2275	0.914	0.450	0.295	0.178	0.042	0.010	0.0045	0.0008
6.00	1.48	0.2538	0.2000	1.0262	0.430	0.280	0.165	0.033	0.005	0.0028	0.0004
5.70	1.55	0.2485	0.1700	1.1315	0.405	0.265	0.150	0.025	0.0014	0.001	0
5.43	1.65	0.2430	0.1420	1.265	0.377	0.245	0.136	0.020	0	0.001	−0.0003
5.16	1.70	0.2375	0.1125	1.350	0.340	0.230	0.118	0.012	0.0025	0.0035	−0.0007
4.91	1.23	0.2325	0.0900	0.9075	0.300	0.210	0.103	0.005	0.0038	0.006	−0.0008
4.67	1.70	0.2270	0.0630	1.410	0.255	0.190	0.080	−0.006	0.0030	0.009	−0.0008
4.44	1.75	0.2220	0.0380	1.490	0.200	0.165	0.055	−0.018	0	0.009	−0.0009
4.23	1.65	0.2163	0.00910	1.4246	0.130	0.143	0.020	−0.030	−0.0025	0.0085	−0.0009
4.02	1.72	0.2085	0.00738	1.50412	+0.05	0.115	0.015	−0.025	−0.0050	0.005	−0.0008
3.82	1.67	0.2000	0.00575	1.46425	−0.060	0.085	0.028	−0.005	−0.0064	0.001	−0.0006
3.64	1.77	0.1880	0.00450	1.5775	−0.120	0.060	0.050	−0.003	−0.0070	−0.0025	−0.0004
3.46	1.72*	0.1625	0.00330	1.5542	−0.130	0.044	0.055	−0.006	−0.0039	−0.005	0
3.29	1.75*	0.1450	0.00245	1.60255	−0.090	0.050	−0.005	−0.007	0	+0.0035	+0.0002
3.13	1.65	0.1125	0.00163	1.53587	−0.050	0.070	−0.01	0.005	−0.0025	−0.0075	0.0007
2.97	1.70	0.1070	0.001	1.592	+0.01	0.090	+0.005	0.009	−0.0075	−0.009	0.0010
2.83	1.425	0.1130	0.0005	1.3115	0.10	0.105	0.023	0.010	−0.011	−0.008	0.0014
2.69	1.5	0.0880	0.00025	1.41175	0.18	0.100	0.040	+0.008	−0.012	−0.007	0.0017
2.56	1.5	0.0980	0.0001	1.4019	0.185	0.060	0.023	+0.006	−0.0080	−0.006	0.0018

Table 8.11.1 (continued)

Energy (Mev)	Cross Sections (barns)				Legendre Coefficients						
	σ_{nT}	σ_{nD}	$\sigma_{n'}$	σ_n	f_1	f_2	f_3	f_4	f_5	f_6	f_7
2.44	1.5	0.780	0	1.422	0.120	0.030	0.012	−0.005	−0.005	−0.0035	0.0018
2.32	1.55	0.1015	0	1.4485	0.12	0.055	0.0085	−0.005	−0.0030	−0.0025	0.0017
2.21	1.70	0.140		1.56	0.23	0.075	0.0075	+0.002	−0.0025	−0.002	0.0015
2.10	1.55	0.051		1.499	0.14	0.059	0.0028	0.0093	−0.002	−0.00165	0.0013
2.00	1.65	0.0414		1.6086	0.07	0.0465	0.0044	0.0065	−0.0014	−0.0013	0.0012
1.90	1.75	0.0466*		1.7034	0.04	0.040	0.0067	0.0008	−0.0013	−0.001	0.0011
1.81	2.70	0.1172*		2.5828	0.07	0.072	0.016	0.0065	−0.0012	−0.0008	0.0010
1.72	1.90	0.0815*		1.8185	0.01	0.037	−0.009	0.0042	−0.0011	−0.0006	0.0010
1.63	2.5*	0.0330		2.467	0.105	0.048	+0.00175	0.0015	−0.0010	0	0.0008
1.55	2.4*	0.0340		2.366	0.05	0.037	+0.0009	0.001	0		0.0007
1.48	1.95	0.0595		1.8905	0.125	0.026	+0.0025	0.0016			0.0005
1.41	2.5	0.220		2.280	0.275	0.056	+0.00025	0.0042			0.0004
1.34	3.10	0.0890		3.011	0.005	0.076	−0.009	0.04			0.0003
1.27	1.70	0.0232		1.6768	0.04	0.045	−0.0036	0.0026			0.0002
121	1.59*	0.0182		1.5718	0.390	0.003	−0.0014	0.0015			0.0001
1.15	1.63*	0.0092		1.6208	0.160	0.02	+0.002	0.010			0
1.096	2.70*	0.0069*		2.6931	−0.01	0.03	+0.0038	0.0075			
1.042	2.25	0.0064*		2.2436	−0.005	0.002	+0.0015	0.0006			
0.991	1.50	0.015*		1.485	+0.035	0.0022	0.0007	0.0005			
0.943	1.20	0.010		1.19	+0.055	0.00202	0.0004	0.00045			
0.897	1.40	0.0074		1.3926	+0.045	0.00185	0.0003	0.0004			
0.853	1.6	0.0094		1.5906	0.0375	0.00169	0.00025	0.0003			
0.812	1.8	0.0125		1.7875	0.036	0.001563	0.0002	0.0002			
0.772	1.9	0.0175		1.8825	0.035	0.001440	0.00015	0.00015			
0.734	2.05	0.0280		2.022	0.032	0.00135	0.0001	0.0001			
0.699	2.3	0.0400		2.26	0.024	0.00127	0	0			
0.666	2.5	0.1400		2.36	0.015	0.00127					
0.632	1.85	0.175		1.675	0.033	0.001625					
0.601	1.75	0.030		1.72	0.065	0.00245					
0.572	2.05	0.0076		2.0424	0.065	0.00241					
0.544	2.25	0.0070		2.243	0.0612	0.002325					
0.518	2.30	0.0275		2.2725	0.0563	0.00225					
0.492	2.50*	0.120*		2.38	0.0510	0.00231					
0.468	2.52	0.0030		2.517	0.045	0.00248					
0.445	3.20	0.0019		3.198	0.038	0.00295					
0.424	5.8*	0.00185		5.798	0.027	0.015					
0.403	3.00	0.0018		2.998	0.019	0.001225					
0.383	2.80	0.00175		2.798	0.0183	0.00034					
0.365	2.85	0.00170		2.848	0.0175	0.000225					
0.347	2.95	0.00168		2.948	0.0167	0.000175					

Table 8.11.1 (continued)

Energy (Mev)	Cross Sections (barns) σ_{nT}	σ_{nD}	$\sigma_{n'}$	σ_n	Legendre Coefficients f_1	f_2	f_3	f_4	f_5	f_6	f_7
0.330	3.20	0.00165		3.198	0.016	0.000150					
0.314	3.25	0.00162		3.248	0.0153	0.000138					
0.299	3.28	0.00160		3.278	0.0145	0.000125					
0.284	3.30	0.00158		3.298	0.0140	0.000108					
0.270	3.40	0.00156		3.398	0.0133	0.000100					
0.257	3.48	0.00155		3.478	0.0127	0.000088					
0.244	3.60	0.00155		3.598	0.0122	0.000075					
0.233	3.70	0.00154		3.698	0.0115	0.000070					
0.221	3.72	0.00153		3.718	0.0110	0.000068					
0.210	3.73	0.00152		3.728	0.0105	0.000055					
0.200	3.74	0.00150		3.739	0.0100	0.000050					

Table 8.11.2. Neutron Elastic Scattering Cross Section for Nitrogen Below 200 kev

Energy (kev)	$\sigma_n(E)$ (barns)
200	3.74
150	4.07
100	4.48
75	4.74
50	5.05
25	5.52
10	6.16
8	6.35
6	6.62
4	7.04
2	7.83
1.5	8.15
1.0	8.58
0.75	8.84
0.50	9.15
0.25	9.52
0.15	9.68
0.10	9.77
0.05	9.86
0.0	9.96

from the total cross section. The values of $\sigma_n(E)$ obtained in this manner are listed in Table 8.11.1 from 200 kev to 18 Mev. From 100 kev to 200 kev the total cross section, given in Table 8.11.2, can be taken as the elastic scattering cross section; below 100 ev the elastic cross section is constant at the 100-ev value.

Differential Elastic Scattering Cross Section, $\sigma_n(E;\theta)$. – Most transport calculations requiring detailed knowledge of the angular distribution use the cross section in the center-of-mass system. For a nucleus as heavy as nitrogen, the differences between the center-of-mass and the laboratory system are, in any case, usually insignificant. The discussion of the differential cross section will, therefore, refer only to the center-of-mass system.

Information about the differential distribution can be given in terms of the Legendre coefficients f_L' defined by

$$\sigma_n(E;\theta) = \lambda^2 \sum_{L=0}^{\infty} \frac{2L+1}{2} f_L'(E)\, P_L(\cos\theta) ,$$

$$f_L = \frac{f_L'}{f_0'} ,$$

where $\sigma_n(E;\theta)$ is the differential elastic scattering cross section (in the center-of-mass system), λ is the De Broglie wavelength (divided by 2π), and $P_L(\cos\theta)$ is the Legendre polynomial. Values of f_L are given in Table 8.11.1.

To obtain these f_L it was convenient to divide the energy region into the following three intervals, according to the laboratory energy of the incident neutron: (1) from 0 to 2.50 Mev, (2) from 2.50 to 4.15 Mev, and (3) from 4.15 to 18 Mev.

For $0 \leq E < 2.5$ Mev. – From 0.4 to 2.5 Mev there are at least 12 resonances, most of them well-resolved. Measurements of the differential scattering cross section have been reported by Fowler

and Johnson[4] at the following energies: 0.800, 0.970, 1.082, 1.110, 1.120, 1.130, 1.160, 1.280, 1.350, 1.377, 1.401, 1.540, 1.595, 1.682, 1.756, 1.779, 1.796, 2.07, 2.25, and 2.36 Mev. These angular distribution curves have been analyzed for the f_L. The necessary extrapolations in the forward and backward directions were suggested by the requirement that the integral of the differential scattering cross section should match closely the total elastic cross section (see above). No corrections have been made for the energy spread of the incident neutrons in the Fowler and Johnson experiment; the full width at half maximum varied from about 10 to about 40 kev, which is less than the energy spacings in the tabulation.

Because of the pronounced resonance structure, the experimental angular distributions are not closely enough spaced in energy to allow a determination of the f_L which is adequate for these calculations. Calculations have therefore been used, in effect, to interpolate in energy. Under the assumption that the scattering amplitude, at any given energy, may be written as the sum of a potential contribution and a contribution from a single resonance level in the compound nucleus, it is possible to adapt the formalism of Blatt and Biedenharn[5] for the calculation of the f_L in the neighborhood of the resonance. The actual calculation of the f_L in the neighborhood of a resonance requires knowledge of the potential phase shifts and of the parameters of the resonance. This information was obtained in the following way: Potential phase shifts were taken from the work of Fowler and Johnson,[4] in which only S and P waves were assumed, with spin-independent phase shifts. Resonance energies were taken directly from the total-cross-section measurements of Hinchey *et al.*[6] and of Meier *et al.*[7] The resonance widths, as analyzed by Hinchey *et al.*,[6] and apparently revised in BNL-325,[3] were also used. Considerable ambiguity is often present in fixing the total angular momentum of the resonance, J_0, the orbital angular momentum, l_0, and the channel spin mixture. Information on these parameters can be obtained in part from the total cross section, and more significantly from the angular distribution of elastic scattering and from the analysis of gamma radiation from the $C^{14}(p,\gamma)N^{15}$ reaction. On the basis of this information, reasonable values of J_0, l_0, and channel spin mixture have been assigned to the various resonances. These assignments were in excellent agreement with the results of a similar investigation conducted at Convair.[8]

Over this entire energy region, curves for the f_L have been drawn, which, in our judgment, best combine the experimental data and the theoretical predictions. Values taken from these curves are given in Table 8.11.1, averaged, where necessary, over our energy spacings. Below 400 kev, values have been obtained for f_1 and f_2 (the remaining ones being zero) by extrapolating as E^L toward zero. Although the tabulation stops at 200 kev, it is a simple matter to extend the f_1 linearly down to zero, while f_2 is zero below 200 kev.

For $2.50 \leqq E < 4.15$ *Mev.* – Relative angular distribution measurements have been reported by Huber and Striebel[9] and by Speiser[10] at the following energies: 2.63, 3.215, 3.30, 3.46, 3.52, 3.65, 3.78, 3.90, and 4.14 Mev; these have been analyzed for the f_L. Smooth curves have been drawn through these experimental points, and values taken from the resulting curves are listed in Table 8.11.1.

For $4.15 \leqq E < 18$ *Mev.* – In this region, use has been made of the experimental angular distribution measured by Smith[11] at 14 Mev and of the preliminary data of Bostrom *et al.*[12] at 4.85, 5.35, and 7.10 Mev. The forward peak of the 14-Mev angular distribution is in good agreement with the continuum model prediction, with a nuclear radius of 3.58×10^{-13} cm. In all cases the experimental results have been used to guide the drawing of smooth curves for the Legendre expansion coefficients. Results are presented in Table 8.11.1.

---

[4] J. L. Fowler and C. H. Johnson, *Phys. Rev.* **98**, 728 (1955).

[5] J. M. Blatt and L. C. Beidenharn, *Revs. Modern Phys.* **24**, 258 (1952).

[6] J. J. Hinchey, P. H. Stelson, and W. M. Preston, *Phys. Rev.* **86**, 483 (1952).

[7] R. Meier *et al.*, *Helv. Phys Acta* **26**, 451 (1953).

[8] Private communication.

[9] P. Huber and H. R. Striebel, *Helv. Phys. Acta* **27**, 157 (1954).

[10] D. Speiser, *Helv. Phys. Acta* **27**, 427 (1954).

[11] J. R. Smith, *Phys. Rev.* **95**, 730 (1954).

[12] N. A. Bostrum, I. L. Morgan, J. T. Prud'homme, A. S. Sattan, private communication, May 1957.

Inelastic Scattering Cross Section $\sigma_{n'}$

Measurements on the inelastic scattering of neutrons by nitrogen have been attempted by Day[13] at energies up to 4 Mev and by Smith[11] at 14 Mev. In observation of the de-excitation gamma ray arising from the 2.31-Mev level, Day found the surprisingly small cross section of 6 mb at 3.95 Mev, and this was the lowest energy at which the effect was seen. An estimate of the value expected in the decay of a compound nucleus is about an order of magnitude larger. The reason for the small measured value is obscure. Various suggested causes—selection rules on isobaric spin, unusually small matrix elements, selection rules suppressing gamma-ray emission—have been examined and found to be incapable of explaining the observed small cross section below 4 Mev. At higher energies a Hauser-Feshbach calculation[14] has been made for the excitation of the 3.95-, 4.91-, and 5.10-Mev levels of N^{14}, by using continuum model penetrabilities and including waves up to $l = 4$. This model, which requires that the assumptions of the statistical model of the nucleus be applicable to the compound nucleus, is not usually used for nuclei as light as N^{14}, but it may be at least qualitatively right, as an average, above 4 Mev. The results thus calculated for the three levels were used up to about 6 Mev.

By suppressing the $l = 0$ and $l = 1$ inelastic neutron waves, it was found possible to reduce the cross section to Day's value. This success should not be taken seriously, but the valuable corollary result was obtained that the cross sections for the other levels are not significantly altered by the change in the competition from the first excited state. The last results have been used as a guide in drawing a curve of $\sigma_{n'}$ from 2 to 6 Mev. From 4 to 6 Mev this curve shows a sharp rise. The curve was then drawn so as to continue to rise slightly above the value of 0.49 barn measured by Smith[11] at 14 Mev, and then to fall slowly. This behavior is suggested by the measurements of the nonelastic cross section of other light elements and by the continuum model predictions for the compound nucleus cross section. It is assumed, of course, that the competition of the charged-particle reactions remains at a constant ratio.

[13] R. B. Day, *Phys. Rev.* 102, 767 (1956).

[14] W. Hauser and H. Feshbach, *Phys. Rev.* 87, 366 (1952).

Radiative Capture Cross Section σ_γ, at Low Energies

At thermal energies recent measurements by Campion and Bartholomew[15] indicate that σ_γ is 80 ± 20 mb. The question arises, however, as to how σ_γ varies with energy above thermal. The answer depends on the proximity of levels in N^{15}.

The shape of the curve showing neutron-scattering cross section as a function of energy below about 300 kev indicates the presence of one or more negative energy resonances. Attempts have been made to analyze the scattering cross sections by means of the method described by Goldstein and Kalos,[16] which takes into account the interference of potential scattering with a negative energy resonance and a single positive energy resonance. Under these circumstances it is possible to plot a certain function of the scattering cross section as a straight line; however, the scattering data for N^{14} failed to give such a straight line. When the analysis was redone so as to include only the data above 100 kev, a satisfactory straight line was obtained whose parameters indicate a negative energy resonance between −220 and −450 kev. An extrapolation to thermal energies of the function of the scattering cross section resulting from this negative energy level indicates that it cannot account for more than about 7 barns of the thermal scattering cross section (which is about 10 barns). An analysis of the scattering data in the range 0 to 2 kev was carried out. The results are subject to considerable doubt, since the scattering data in this region (due to Melkonian[17]) are quite old and inaccurate, but the analysis indicates that the negative energy resonance occurs at a few kev below zero.

If a level at about −2.6 kev has roughly the same total radiative width as a level at about −370 kev, and if the rough estimates of the reduced neutron widths taken from the Goldstein-Kalos analysis (~4 to 10 ev and ~400 ev, respectively) are used, then the resonance closer to zero contributes practically all the thermal radiative capture. At +250 ev [where the (n,γ) cross section would fall

[15] P. J. Campion and G. A. Bartholomew, *Bull. Am. Phys. Soc.* 1, Series II, 28 (1956).

[16] H. Goldstein and M. H. Kalos, *Prediction of the Radiative Neutron Capture Cross Section of Iron Below 50 kev from Resonance Parameters*, NDA 2-62 (Jan. 21, 1957).

[17] E. Melkonian, *Phys. Rev.* 76, 1744 (1949).

below the thermal value by about a factor of 100; down to 0.8 mb] the deviation from a true $1/v$ behavior would be in the neighborhood of 20%. For almost all conceivable applications, σ_γ can be taken as decreasing indefinitely as $1/v$, but its true behavior can only be determined by fixing the existence and the location of the negative energy levels.

The scattering cross sections shown in Table 8.11.2 were computed by assuming that two negative energy levels contribute, one at –403 kev (in the laboratory system) with $\Gamma_n/2k = 136 \times 10^{-12}$ kev-cm, and the other at –2.62 kev with $\Gamma_n/2k = 0.60 \times 10^{-12}$ kev-cm.

Neutron Disappearance Cross Section σ_{nD} and Nonelastic Cross Section σ_{nX}

Besides inelastic scattering and radiative capture (which, as has been seen, is small), the nonelastic cross section is made up almost exclusively of the cross sections for the various charged-particle reactions (n,p), (n,d), (n,α), and (n,t). The $(n,2n)$ reaction has a threshold at about 11 Mev in the laboratory system; at 14.5 Mev the cross section for this process is less than 1% of the total nonelastic cross section.

The curves[3] of BNL-325 have been used to give σ_p and σ_α from 200 kev to 2.1 Mev. Below 200 kev the (n,p) reaction (which is exoergic) varies as $1/v$ to a value of 1.75 ± 0.05 barns at thermal. From 2.1 to 3.6 Mev the cross sections reported by Bollmann and Zünti[18] have been used. Above 3.6 Mev a curve has been drawn so that it passes through the value of 286 mb reported by Smith[11] for the cross section for two- and three-particle disintegration of N^{14}. This curve, which sums the contribution of all charged-particle reactions, is effectively the curve of the "neutron disappearance" cross section. The sum of σ_{nD} and $\sigma_{n'}$ gives the nonelastic cross section.[19]

OXYGEN

The neutron cross sections for oxygen form, in many ways, a simpler problem to tackle than do those for nitrogen. Below 4 or 5 Mev the only reaction of consequence is elastic scattering; the inelastic process has a threshold only at 6 Mev, and the zero nuclear spin greatly facilitates the analysis of the resonances. Total cross-section measurements, however, reveal that reasonably discrete resonance structure persists in oxygen at least up to 6 Mev and probably to 8 or 10 Mev. Above 3 Mev, inadequate energy resolution in the experiments and the complex shapes exhibited by many of the resonances (or groups of overlapping resonances) make determination of their parameters difficult. In addition, there are few dependable measurements of elastic scattering angular distributions above 3 Mev. These circumstances present formidable obstacles to any complete description of the neutron cross sections for oxygen in the region from 3 to 14 Mev, and a satisfactory picture has not yet been achieved. The following, therefore, presents merely a brief summary of the current status of knowledge about the oxygen cross sections in the same order as that employed for nitrogen.

Total Cross Section σ_{nT}

The available total-cross-section data are all contained in BNL-325 or its Supplement 1.[20] The entire region from thermal to 18 Mev is covered adequately for reactor and shielding needs. Indeed, the fine structure shown above 4 Mev is probably much more detailed than can be used in applied calculations, and some cross-section averaging must be done.

Elastic Scattering Cross Section σ_n

Total Elastic Scattering Cross Section, $\sigma_n(E)$. – Below the effective threshold for the $O^{16}(n,\alpha)$ reaction (~3.5 Mev), the total cross section is all due to elastic scattering. At higher energies, $\sigma_n(E)$ is best obtained by subtracting σ_{nX} from σ_{nT}, a procedure which is satisfactory up to the point where inelastic scattering becomes large (about 7 to 8 Mev).

Differential Elastic Scattering Cross Section, $\sigma_n(E,\theta)$. – Up to an energy of 2.6 Mev, the total-cross-section measurements plus the angular distribution experiments of Cohn and Fowler[21] permit

[18] W. Bollmann and W. Zünti, *Helv. Phys. Acta* **24**, 517 (1951).

[19] H. Lustig, H. Goldstein, and M. H. Kalos, *The Neutron Cross Sections of Nitrogen*, NDA-86-1 (to be published).

[20] D. J. Hughes and J. A. Harvey, *Neutron Cross Sections*, BNL-325 (July 1, 1955); D. J. Hughes and R. B. Schwartz, *Neutron Cross Sections*, BNL-325 Supplement 1 (Jan. 1, 1957).

[21] H. O. Cohn and J. L. Fowler, *Phys. Semiann. Prog. Rep. Sept. 10, 1956*, ORNL-2204, p 32; a more complete paper has been submitted to the *Revs. Modern Phys.* by the same authors for future publication.

a nearly definitive picture of $\sigma_n(E,\theta)$. Except for three very narrow resonances at 1.65, 1.85, and 1.92 Mev, the parameters of all the resonances in this region are adequately known. Cohn and Fowler have prepared curves of the phase shifts in this region and, on the basis of a reasonable single-particle potential well, have identified the 1.00-Mev resonance as a single-particle $d_{3/2}$ level. From the phase-shift curves, values have been calculated for the f_L coefficients in the Legendre polynomial expansion of $\sigma_n(E,\theta)$ up to about 2.7 Mev.

The situation above 2.7 Mev is much less satisfactory. The only angular distribution measurements covering any portion of this region in adequate detail are now quite old,[22] and involved a technique known to exaggerate the amount of small-angle forward scattering. Experiments at several spot energies from 3.6 to 7.1 Mev have been made at the Texas Nuclear Corporation.[23] These, however, are not adequately enough detailed in energy to indicate much more than that the older measurements are incorrect. Practically the only available recourse for obtaining resonance parameters (and from them, angular distributions) is, therefore, to analyze the total-cross-section data. The major part of the current effort is being devoted to this task.

From 3 to 4 Mev the total-cross-section curve is dominated by a broad, rounded peak, surmounted by a much narrower peak at 3.75 Mev. One obvious possibility is that the broad peak corresponds to a single-particle $P_{3/2}$ level, which might be expected in this region on the basis of some shell structure models. In order to investigate this situation, phase shifts have been calculated on the NDA Datatron for scattering from a potential well which is similar in shape to that used by Cohn and Fowler.[21] No reasonable combination of well parameters has yet been found, however, which will produce a single-particle resonance of the right energy and width. An empirical attempt at fitting the total-cross-section curve with combinations of one-level resonance curves has therefore been tried; the overlapping levels are assumed not to interfere. It has been found that the total-cross-section curve can be reproduced qualitatively by two levels, both about 450 kev wide, at 3.32 and 3.77 Mev and with angular momentum arrangements of $D_{3/2}$ and $D_{5/2}$, respectively. Computations are currently under way which seek to adjust the parameters so as to give a better quantitative fit.

Inelastic Scattering Cross Section $\sigma_{n'}$

Practically nothing is known about this cross section except the threshold (6.5 Mev in the laboratory system) and the 14-Mev value (0.5 barn). The excitation curve for production of 6.14-Mev gamma rays by inelastic scattering is currently being measured at Rice Institute and should throw some light on the cross section.

Cross Sections for Other Nonelastic Processes

In O^{16}, σ_γ is apparently not measurable even at thermal energies; it is given[20] in BNL-325 for O^{18} and falls off as $1/v$ until it is well below 1 μb. The only other nonelastic reactions of possible practical importance, therefore, appear to be the (n,p) and (n,α) reactions in O^{16} and O^{17}, respectively.

Although Q for the $O^{16}(n,\alpha)$ reaction is −2.2 Mev, the effective threshold is around 3.5 Mev. From this energy to 4.0 Mev, a curve of the cross section is given in Supplement 1 to BNL-325,[20] and this can be extended to 5.2 Mev from unpublished measurements made at the University of Wisconsin on this reaction and its inverse, $C^{13}(\alpha,n)O^{16}$. From the available data it is clear that the experimental resolution was not good enough to faithfully depict the resonance structure. However, practical application requires that the resonances be averaged in any case. Above 5.2 Mev the only known information is a cross section[24] of 310 ± 100 mb at 14 Mev. A smooth curve between 5 and 14 Mev has been estimated for σ_α so as to give this 14-Mev value and to fit in properly with the averaged curve below 5 Mev. For the $O^{16}(n,p)$ reaction, with an effective threshold at 10 Mev, it is fortunate (and almost unique) that a complete excitation curve is known, accurate in absolute magnitude to ±20%, which extends[25] above 18 Mev.

The (n,α) reaction in O^{17} is distinguished by having a positive Q (+1.85 Mev), so that it has a cross section at thermal energies of somewhere

[22] E. Baldinger, P. Huber, and W. G. Proctor, *Helv. Phys. Acta* 25, 142 (1952).

[23] Private communication.

[24] J. P. Conner, *Phys. Rev.* 89, 712 (1953).

[25] H. C. Martin, *Phys. Rev.* 93, 498 (1954).

between 0.2 and 0.5 barn. Beyond that nothing is known, nor does the reaction appear to have made itself manifest in bulk reactor or shielding experiments. For the $O^{17}(n,p)$ reaction, despite its high negative Q of −8.0 Mev, the situation is quite different. The product of this reaction, N^{17}, is a delayed neutron emitter. When water, even if it is of normal isotopic composition, is used as a coolant in a high-power reactor, the delayed neutrons from this reaction can be quite copious. Unfortunately no cross sections have been reported for this reaction beyond averages over the fission spectrum, with the range in the published values extending over two orders of magnitude. A detailed excitation curve, as in the $O^{16}(n,p)$ reaction, would be a very valuable measurement.

8.12. SOME RECENT CALCULATIONS OF THE AGE OF FISSION NEUTRONS IN WATER[1]

H. Goldstein J. Certaine
Nuclear Development Corporation of America

A number of rigorous calculations have been made[2,3] of the age of fission neutrons, from a point isotropic source, in water at the energy of the indium resonance, 1.44 ev. They have all given a result of about 26.0 ± 0.5 cm^2, which is considerably less than the value of approximately 30.0 ± 1.0 cm^2 which was obtained in two experiments.[4,5] In all the calculations, however, the oxygen cross-section data have been obtained from a compilation[6] which is now rather old and in need of revision. It can be shown that the only characteristic of the angular distribution for elastic scattering which is involved in the age is the average cosine in the laboratory system.[7] The oxygen data used in the previous calculations predicted that between resonances the scattering would be slightly backward ($\bar{\mu} < 0$) in the center-of-mass system. Recent experiments indicated that the scattering in these regions is slightly forward, which is in the direction to increase the age. It therefore seemed desirable to recalculate the age in water by using the best available cross-section data.

The measurements of Cohn and Fowler,[8] coupled with earlier work at the University of Wisconsin, provide a nearly definitive picture for the angular distribution, for scattering from oxygen, of neutrons with energies up to 2.6 Mev. Figure 8.12.1 compares the average cosine in the center-of-mass system, $\bar{\mu}$, computed on the basis of these measurements, with the values used in previous age calculations. Besides the slight forward scattering between resonances, as mentioned above, there are also considerable changes resulting from revised angular momentum assignments for the 1.00- and 1.30-Mev resonances. Above about 2.7 Mev there is little new information available, except for some indications that $\bar{\mu}$ in this region is smaller than the value previously accepted. An overestimate of the age should therefore be obtained if the new data below 2.7 Mev are merely faired into the old above 2.7 Mev. By using the oxygen angular distributions obtained by this prescription, the age in water was recalculated by the moments method.[2] The computations gave a value for the age of 26.51 cm^2, which is somewhat above the previously calculated result, but far short of the experimental value.

An attempt was then made to estimate the possible effect of cross-section changes above 2.7 Mev. The most drastic possible increase in the age would come if the oxygen scatterings were assumed to be entirely in the forward direction, that is, neglecting the oxygen completely except for the small absorption. Because of the manner in which the moments-method calculations are coded for machine operation, it is not feasible to make the computations with this assumption. Instead, the scattering was taken to have the same shape as at 18.0 Mev, where $\bar{\mu}$ is 0.81 in the center-of-mass system. A check calculation was first made by assuming the oxygen scattering to have this shape at all energies. The resulting age, about 36.4 cm^2, agrees reasonably well with the value of 41 cm^2 which is the result of unpublished calculations by Hellens,[9] in which oxygen was neglected. The oxygen scattering was then assumed to follow this behavior above 3.1 Mev and

[1]This work was performed under Subcontract 1069 with Nuclear Development Corporation of America.

[2]J. E. Wilkins, Jr., R. L. Hellens, and P. E. Zweifel, *Proc. Intern. Conf. Peaceful Uses Atomic Energy, Geneva, 1955* 5, 62 (1956).

[3]R. R. Coveyou, *Appl. Nuclear Phys. Ann. Rep. Sept. 10, 1956*, ORNL-2081, p 144.

[4]J. E. Hill, L. D. Roberts, and T. E. Fitch, *J. Appl. Phy.* 26, 1013 (1955).

[5]L. M. Barkov and K. N. Mukhin, *J. Nuclear Energy* 4, 91 (1957).

[6]H. Goldstein, *Fast Neutron Data for Oxygen*, NDA-Memo-15C-15 (Nov. 3, 1953).

[7]A. M. Weinberg and E. P. Wigner, *Theory of Neutron Chain Reactions*, Chapter 11, University of Chicago Press, Chicago (to be published).

[8]H. O. Cohn and J. L. Fowler, *Phys. Semiann. Prog. Rep. Sept. 10, 1956*, ORNL-2204, p 32; a more complete paper has been submitted to the *Revs. Modern Phys.* by the same authors for publication.

[9]Private communication.

was combined with the reliable low-energy data below 3 Mev. This set of cross-section data yielded an age of 28.0 cm^2, still 2.0 cm^2 short of the results of experimentation. The angular distribution for oxygen, assumed in the calculation, was certainly a gross exaggeration of possible changes in the actual distribution, and it is quite likely that the change is in the opposite direction. There seems to be little question therefore that the discrepancy between theory and experiment does not arise from errors in the oxygen cross sections.

It has also been suggested that errors in the fission spectrum might be the source of the discrepancy between the observed and the calculated age. The published measurements of the fission spectrum are most uncertain at the high-energy end, above 5 Mev, but it has already been shown above that this portion of the spectrum has little effect on the age. The consequences of modifying the low-energy end of the spectrum were therefore examined. A calculation of the age was performed in which it was assumed that the fission spectrum cut off completely below 330 kev, but was unaltered above that. The result was 27.3 cm^2, still well below the experimental value. Not until the cutoff was raised to 600 kev could the calculated age be increased to 29.9 cm^2. Almost one-fourth of the fission neutrons should be below this cutoff, and it seems highly improbable that the low-energy end of the fission spectrum could be so grossly uncertain as to account for the discrepancy. The only remaining modification in the fission spectrum which might explain the discrepancy is an alteration in the shape of the spectrum around 1 to 2 Mev. It seems very unlikely, however, that the experiments in this region can be so greatly in error as to increase the average fission neutron energy by the 300 to 400 kev that would probably be needed to raise the age to 30 cm^2.

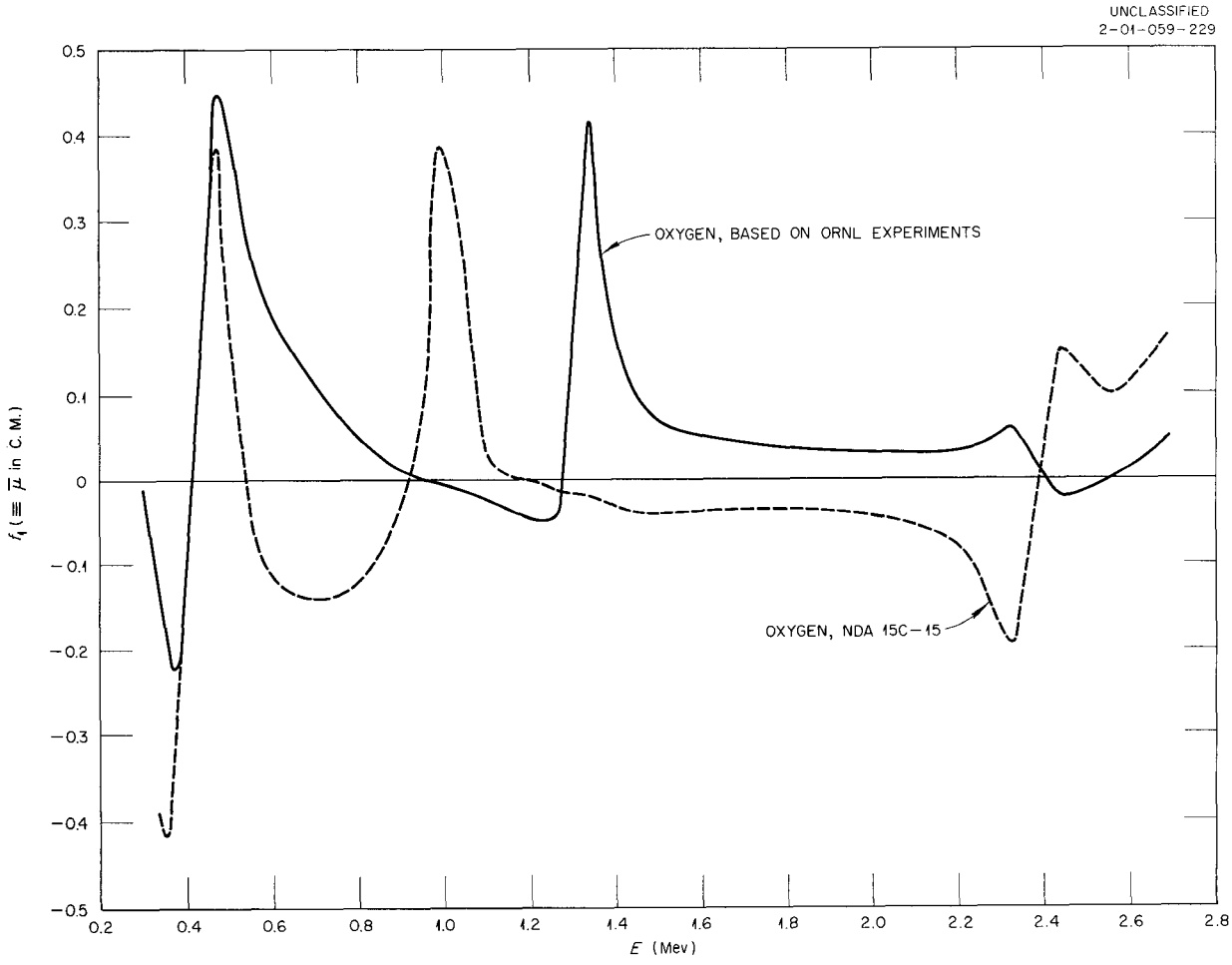

Fig. 8.12.1. Average Cosine in the Center-of-Mass System for Neutron Scattering from Oxygen.

8.13. AGE OF FISSION NEUTRONS IN DIPHENYL AND IN OIL

J. H. Marable

The neutron ages to slowing down past 1.45 ev from fission have been calculated on the Oracle Monte Carlo age program[1] for diphenyl ($C_{12}H_{10}$) and for a hydrocarbon oil (essentially CH_2). The compositions of the compounds and the results of the calculations follow:

	Diphenyl	Oil
Density (g/cm^3)	0.982	0.882
Carbon-to-hydrogen atomic ratio	1.2	0.5696
Oxygen-to-hydrogen atomic ratio		0.00246
Age (cm^2)	47.51 ±0.5	22.75 ±0.2

A number of errors were found in the code and were corrected. As a check on the corrected program, three simple test cases, which were analytically calculable, were run. The results of the Oracle calculations were about 2% lower than those from the analytical calculations, although the standard deviations were only about 1%. These results are insufficient to lead to a definite conclusion concerning a possible bias on the error analysis. By using the uncorrected code, a calculation of the age in graphite was erroneous. It has not been recalculated.

[1]R. R. Coveyou, *Appl. Nuclear Phys. Ann. Rep. Sept. 10, 1956*, ORNL-2081, p 144.

Part 9

SHIELDING RESEARCH

9.1. STUDY OF A THIN LEAD-BORON-WATER SHIELD

E. B. Johnson K. M. Henry
J. D. Kington

A series of experiments has been carried out at the Bulk Shielding Facility to determine the configuration of a lead-boron-water shield which would vary the neutron-to-gamma-ray ratio of the radiation which leaks from the reactor. This information was especially needed for the design of the new Tower Shielding Reactor II (see Sec. 3.1). The problem was to study the secondary gamma-ray production in the lead and to delineate methods of reducing it.

Two ways to reduce secondary gamma rays were to introduce water between reactor and lead and to introduce layers of boral (boron carbide in aluminum). The configurations tried and the results of the measurements are shown in Figs. 9.1.1 and 9.1.2, respectively. It is seen that boron carbide next to the lead has little effect, indicating that capture gamma rays produced in the following water are most important. This is confirmed by the strong effect of increasing the water layer between the reactor and lead, which reduces the neutron flux in and following the lead, and therefore must reduce the capture gamma-ray production rate.

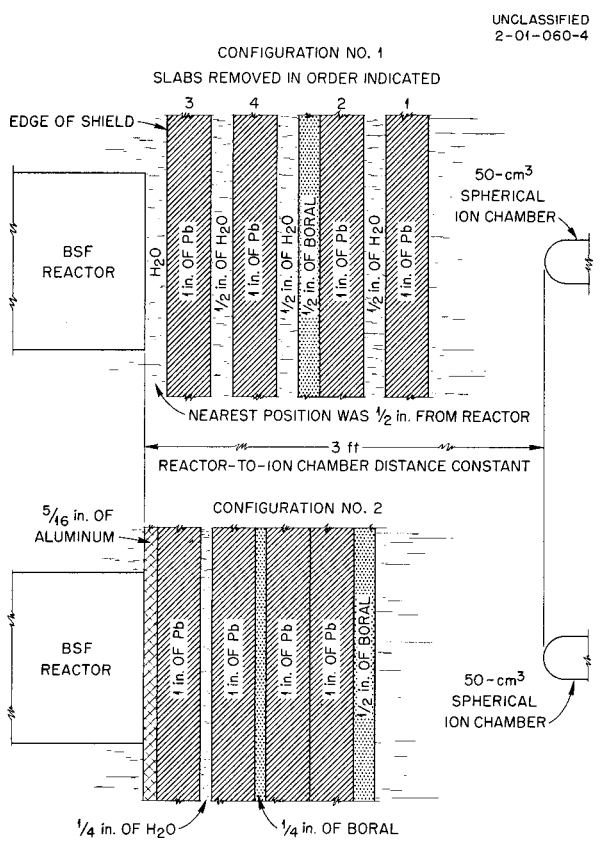

Fig. 9.1.1. Lead-Water Configurations Tested at the BSF.

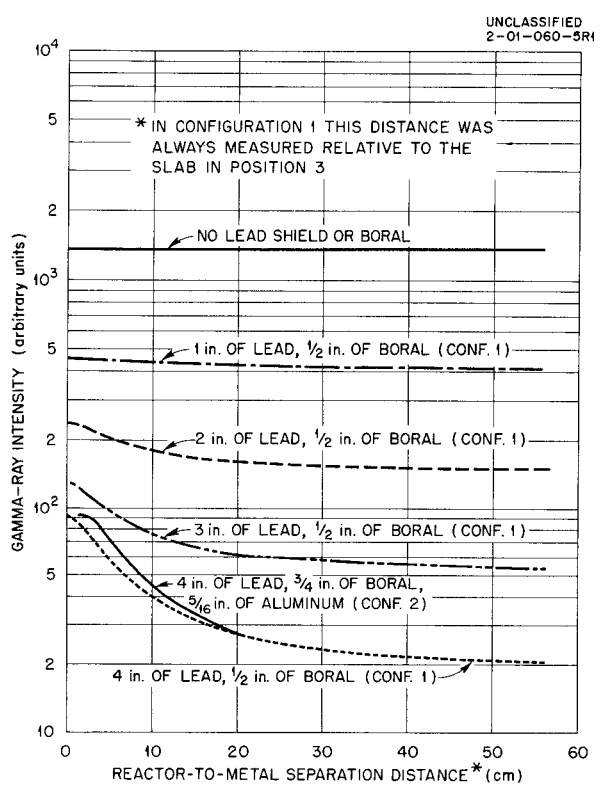

Fig. 9.1.2. Gamma-Ray Intensity 3 ft from the BSR as a Function of Reactor-Lead Separation Distance.

9.2. RADIATION ATTENUATION MEASUREMENTS IN PLAIN WATER, BORATED WATER, AND OIL MEDIA IN THE LID TANK SHIELDING FACILITY

D. W. Cady[1] E. A. Warman[2]

The figures given herein represent the first effort to present, in a single, unclassified report, a set of curves for the attenuation of fast neutrons, thermal neutrons, and gamma rays in various media at the Lid Tank Shielding Facility (LTSF) at ORNL. The media investigated were water, borated water, and transformer oil.

As has been frequently reported,[3] the LTSF fission source consists of a 28-in.-dia enriched uranium (20.8% U^{235}) plate which is placed over a hole in the 7-ft-thick concrete shield of the ORNL Graphite Reactor. The plate absorbs thermal neutrons that stream from the reactor and, in turn, emits a fission spectrum of neutrons and gamma rays. The effective power of the source plate is 5.18 w ±5%.

The borated water used in these tests contained 1.34 wt % natural boron and had a density of 1.05 g/cc. The oil was transformer oil, composed of 86.7 wt % carbon and 12.7 wt % hydrogen. Its density was 0.87 g/cc at 20°C.

In order to avoid mixing of the borated water or oil with the plain water in the Lid Tank proper, these materials were contained in a "configuration" tank which was positioned as close to the source as was physically possible. The tank is constructed of mild steel and has dimensions of $65\frac{1}{2} \times 72 \times 71\frac{1}{4}$ in. The production of capture gamma rays in the tank wall near the source was reduced by the insertion of a $\frac{3}{8}$-in.-thick aluminum window in the side of the tank adjacent to the source. A 2-cm gap between the source and the window was filled with air contained in a thin plastic bag.

Thermal-neutron, fast-neutron, and gamma-ray measurements taken in the three media contained in the configuration tank are shown in Figs. 9.2.1, 9.2.2, and 9.2.3, respectively. Before the data for plain water can be compared with previously published measurements,[4,5] which were taken in the Lid Tank proper, the new curves must be shifted 3 cm to the left. Figure 9.2.4 illustrates the agreement obtained between a thermal-neutron traverse in the Lid Tank proper and a traverse in the configuration tank with the latter shifted on the graph a distance of 3 cm to the left.

The previously reported thermal-neutron curves in oil and borated water represent data taken with the instrument response normalized to gold foil fluxes in plain water. This normalizing procedure is not particularly valid, as is indicated by a comparison of counts-to-flux conversion factors used over a period of time. For example, the current conversion factor used with a $12\frac{1}{2}$-in. BF_3 counter in plain water, obtained by normalizing

[1]On assignment from Wright Air Development Center, Dayton, Ohio.

[2]On assignment from Pratt & Whitney Aircraft, East Hartford, Conn.

[3]See, for example, D. R. Otis, *Appl. Nuclear Phys. Ann. Rep. Sept. 10, 1956*, ORNL-2081, p 163.

[4]D. R. Otis and J. R. Smolen, ORNL CF-57-2-8 (Feb. 8, 1957) (classified).

[5]R. W. Peelle *et al.*, ORNL-2221, p 332 (classified).

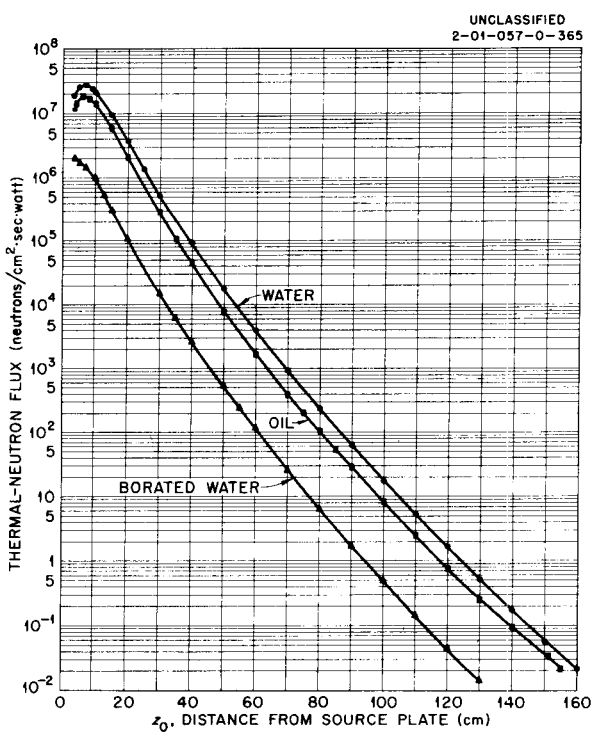

Fig. 9.2.1. Thermal-Neutron Fluxes in Water, Borated Water, and Oil in the Configuration Tank.

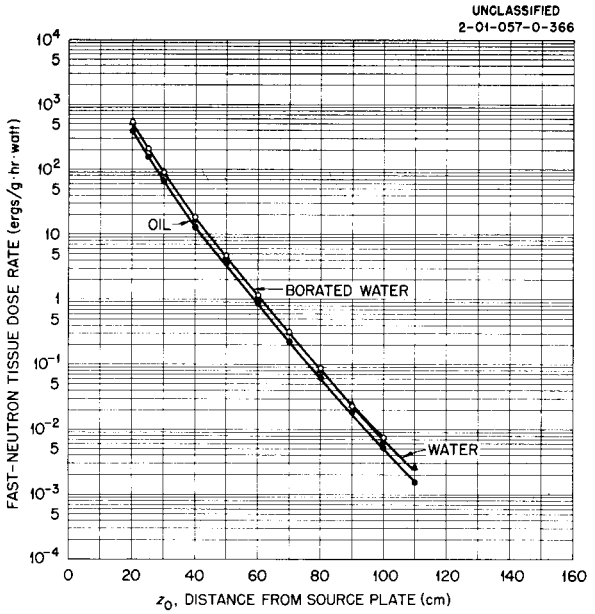

Fig. 9.2.2. Fast-Neutron Tissue Dose Rates in Water, Borated Water, and Oil in the Configuration Tank.

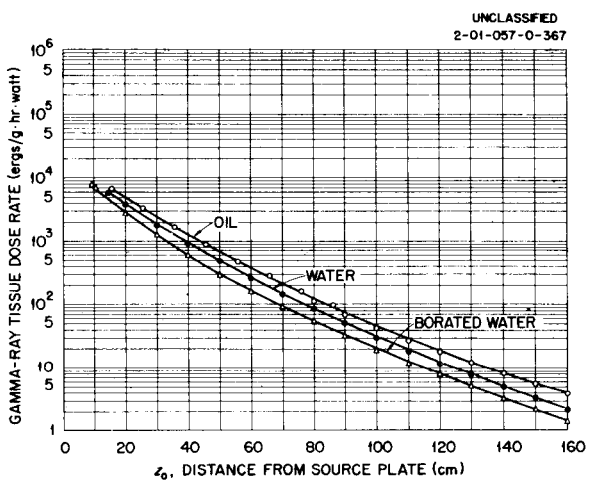

Fig. 9.2.3. Gamma-Ray Tissue Dose Rate Traverses in Water, Borated Water, and Oil in the Configuration Tank.

to the data taken with gold foil in plain water, is 1.66×10^{-3}. Previously, this same factor would have been used for this counter for all media. The newly determined conversion factor for borated water is 9.78×10^{-4}, a change of about 41% in the conversion factor. Similarly, the conversion factors for the 8-in. BF_3 counter, the

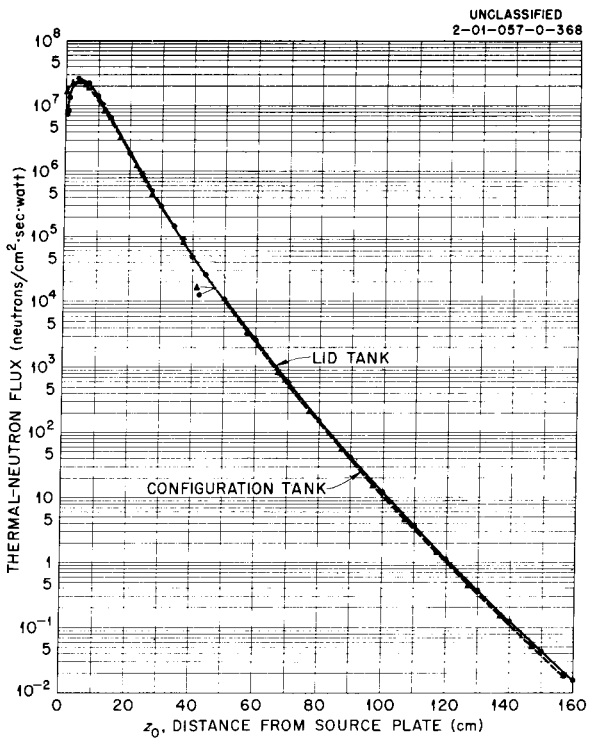

Fig. 9.2.4. Thermal-Neutron Fluxes in Water in the Lid Tank and in the Configuration Tank.

3-in. fission chamber, and the ½-in. fission chamber are reduced by 26, 37, and 16%, respectively. There are corresponding changes in the oil medium.

The data plots presented here are approximately 5% higher than earlier plots owing to the replacement of the old ⅛-in.-thick boral shutter on the source plate by a ¼-in.-thick shutter. Lid Tank data are obtained by determining the difference between the shutter-open and shutter-closed measurements. The old ⅛-in. shutter did not completely shield the source plate from the reactor thermal flux; therefore, even with the shutter closed, there was fissioning in the source plate. When the shutter-closed readings are subtracted from the shutter-open readings, a small percentage of the source plate power is eliminated as background. Thus increasing the shutter thickness essentially increases the *effective* source plate power. This increase is small enough to fall within the uncertainty in source plate power (±5%). A more exact determination of the new effective source plate power will be made at a later date.

Thermal-neutron measurements in water are now being corrected for the flux depression that results from the presence of the gold foils and for self-absorption and "self-shielding" in the foils. These corrections were not made on previously reported curves.[6,7]

Although it is commonly assumed that the flux depression for "thin" foils is negligible, calculations of the flux depression caused by 2-mil-thick, 1-cm^2 gold foils in water, oil, and borated water were made. Several methods of calculation were attempted,[8,9] each producing a different result. The figures reported here are based on a method suggested by W. R. Burrus.[9] The preliminary values computed are 8.5% for water, 5.9% for oil, and 5.0% for borated water. Little flux depression is normally expected in borated water, but the amount of boration in the LTSF water is so slight, 1.34 wt %, that the above figure is reasonable. It should be noted here that cadmium-difference flux measurements in borated water are of dubious validity. The cadmium ratio is so small, about 1.5:1, that the errors inherent in taking the difference between two large, nearly equal, values are considerable.

The self-absorption correction is a correction to the measured activity of the foil after exposure. Since the foil cannot be infinitely thin, there will be scattering and absorption of the radiation in the activated foil itself. Hence the true activity of the foil, or counting rate, will be reduced by some factor which is dependent on the foil thickness. The dependence of the self-absorption on the foil thickness can be roughly calculated by assuming an exponential absorption and an absorption coefficient independent of the depth in which the particles are emitted.[10] Based on the assumption that one-half the thickness of the foil contributed to the self-absorption, calculation yields a self-absorption factor for a 2-mil-thick gold foil of approximately 1%.

If a foil is quite thick, enough neutrons will be absorbed so that the nuclei in the center of the foil will "see" a lower thermal-neutron flux than can be seen by those at the surface. If the ratio of the absorption to the scattering for the foil is large, the "self-protection," or "self-shielding," can be calculated because the incident flux suffers an exponential decrease in the foil.[8] For a 2-mil-thick gold foil this calculation yields a "self-protection" factor of 1.5%.

Figure 9.2.5 shows the effect upon the configuration tank water curve when the 11% correction

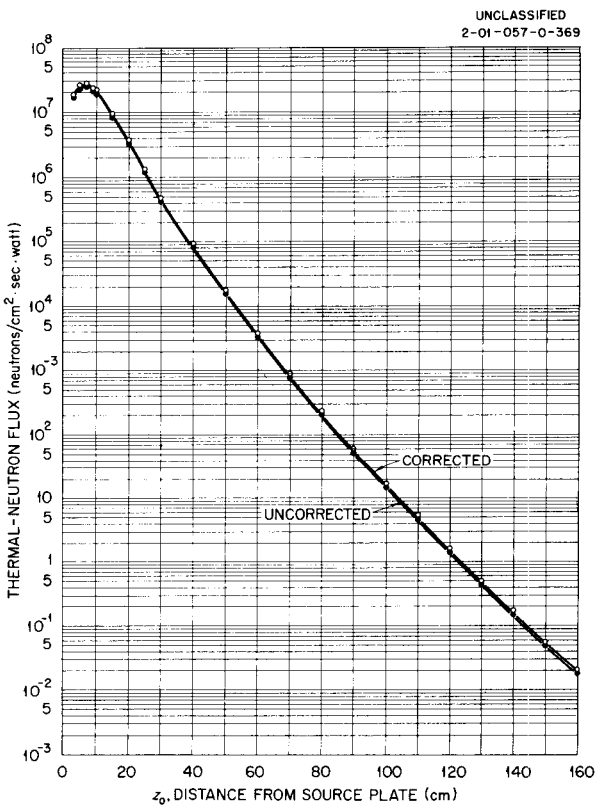

Fig. 9.2.5. Thermal-Neutron Fluxes in Water in the Configuration Tank: Comparison of Uncorrected Measurements with Those Corrected for Flux Depression, Self-Absorption, and Self-Shielding.

[6] W. Zobel *et al.*, ORNL-2340, p 285 (classified).

[7] G. T. Chapman *et al.*, ORNL-1896, p 194 (classified).

[8] D. J. Hughes, *Pile Neutron Research*, Addison-Wesley, Cambridge, 1953.

[9] W. R. Burrus, USAF, Wright Air Development Center, Dayton, Ohio, private communication.

[10] R. Aronson *et al.*, *Penetration of Neutrons from a Point Isotropic Fission Source in Water*, NYO-6267 (Sept. 22, 1954).

due to flux depression, self-absorption, and self-shielding is considered. Both curves shown in Fig. 9.2.5 already contain the 5% correction due to the change in thickness of the boral shutter. Therefore the difference between the two curves is due only to this 11% correction.

[11] E. P. Blizard and T. A. Welton, ORNL-1133, Part 2 (classified).

There have been efforts to theoretically predict the attenuation of gamma rays and neutrons in water.[10-12] The data presented here will be of value to any future work on this problem. It should be noted that no attempt has been made to predict attenuation in the oil or borated water media.

[12] D. R. Otis, *Neutron and Gamma-Ray Attenuation for a Fission Source in Water — Comparison of Theory with LTSF Measurements*, ORNL CF-57-3-48 (March 12, 1957).

9.3. ATTENUATION OF FAST NEUTRONS FROM A FISSION SOURCE BY WATER: COMPARISON OF EXPERIMENT WITH THEORY

D. R. Otis[1]

Since the shielding problem in its simplest terms devolves into a calculation of the attenuation kernel, several computations have been performed to establish values of a kernel for various media. The first value for an attenuation kernel for the fast-neutron dose rate from an isotropic point fission source in water was determined by Blizard and Welton,[2] who based their calculation on some of the early experimental data obtained at the Lid Tank Shielding Facility (LTSF). At that time the LTSF fission source was the old source plate (SP-1), the power of which was estimated to be 6 w, with a neutron leakage factor of 0.6 (resulting in an effective power of 3.6 w). The results of this calculation were lower than those obtained in a similar calculation[2] based on measurements with the Bulk Shielding Reactor (BSR) (a factor of 2.5 to 1.7 at distances from the source ranging from 40 to 110 cm), but it was felt that the differences could be attributed to the difficulty in defining the leakage from the BSR as well as to the uncertainty in power calibration of the two sources. The subsequent BSR calibration confirmed the assumed value, but the LTSF power calibration had to be deferred until a new source plate could be installed. The results based on the LTSF data were also lower by a factor of 4 than those obtained in a calculation performed later by Aronson *et al.*[3] with the use of the "moments" method. At the time, this discrepancy could not be resolved, but measurements with the new LTSF source plate (SP-2, see Sec. 9.2 and ref 4) have allowed some of the differences to be explained. In addition, a new calculation based entirely on experimental data obtained with the new source plate has resulted in agreement with the moments-method calculation. A comparison of all the calculations is presented below.

Recalculation of Point Kernel for SP-1

The accurate source strength calibration for the new source plate[4] allowed a re-estimation of the old source plate power by a comparison of data taken with the old and new sources. A revised "effective power" of 1.7 w (where "effective power" includes the neutron leakage factor) was thus obtained[5] in a calculation based upon the power for SP-2 and a comparison of the relative thermal-neutron flux levels for SP-1 and SP-2. (Thermal-neutron flux data were used rather than fast-neutron dose rate data because the former are, in general, more reliable.) In addition to the revision in power for SP-1, re-examination of the earlier dose rate measurements has resulted in different values from those used by Blizard and Welton[2] (see Table 9.3.1) in their calculation.

Table 9.3.1. Comparison of LTSF Fast-Neutron Dose Rates Used in Calculations for Old Source Plate (SP-1)

z, Distance from SP-1 (cm)	Fast-Neutron Dose Rate (ergs/g·hr)	
	Used in Present Calculation	Used in Blizard-Welton Calculation
40	2.23×10^{1}	1.04×10^{1}
60	1.49×10^{0}	8.09×10^{-1}
80	1.23×10^{-1}	7.35×10^{-2}
100	1.21×10^{-2}	7.63×10^{-3}
110	3.91×10^{-3}	2.56×10^{-3}

Since both these factors would have affected the calculation of the point kernel for SP-1, a new calculation was performed with the use of the revised values for the power and the dose rates. An analytical approximation for transforming from

[1]On assignment from Convair, San Diego.

[2]E. P. Blizard and T. A. Welton, ORNL-1133 (classified).

[3]R. Aronson *et al.*, *Penetration of Neutrons from a Point Isotropic Fission Source in Water*, NYO-6267 (Sept. 22, 1954).

[4]D. R. Otis, *Appl. Nuclear Phys. Ann. Rep. Sept. 10, 1956*, ORNL-2081, p 163.

[5]By comparison with the new source plate, the power of the old source plate (SP-1) has been established to be 1.7 w with an estimated error of ±11%; see J. Smolen, *Appl. Nuclear Phys. Ann. Rep. Sept. 10, 1956*, ORNL-2081, p 164.

a disk to a point source was used.[6] The results are shown in Fig. 9.3.1 and seem to be in good agreement with the moments-method solution obtained by Aronson *et al.*[3] The difference in slope can probably be ascribed to the old LTSF source plate being far from an ideal thin-disk shape, as was assumed in the transformation to a point source.

[6] E. P. Blizard, "Nuclear Radiation Shielding," *Nuclear Engineering Handbook* (ed. by H. Etherington), McGraw-Hill, New York (in press).

Calculation of Point Kernel for SP-2

The calculation described above was repeated with the use of preliminary fast-neutron data obtained with the new source plate (SP-2). The source strength was taken to be 1.62×10^{11}

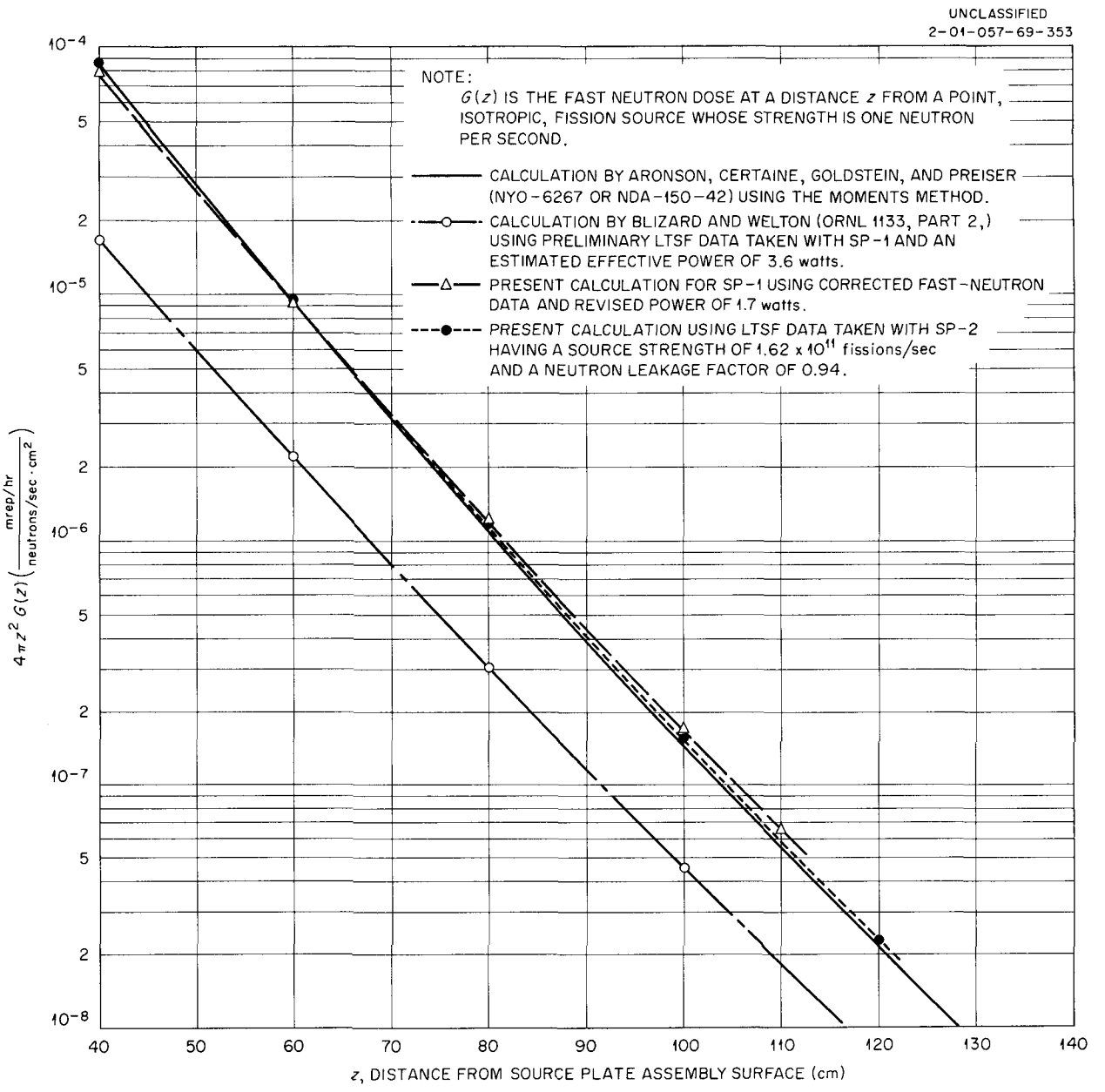

Fig. 9.3.1. Fast-Neutron Dose Rate Attenuation for a Fission Source in Water: Comparison of Kernel Theory with Experiment.

fissions/sec (uniformly distributed over the source plate) with a neutron leakage factor of 0.94 (ref 4). The results of this calculation (Fig. 9.3.1) show somewhat better agreement with the moments-method calculation than was the case for the calculation based on SP-1 data. The better agreement can be ascribed to the ideal thin-disk shape being more nearly approached in the design of SP-2.

Comparison of Calculated and Experimental Dose Rate for SP-2

A calculation was also made of the fast-neutron dose rate in the LTSF water along the SP-2 axis with the use of the point kernel obtained by Aronson *et al.*[3] This calculation involved no analytical approximations to the geometrical transformation but was simply a numerical integration over the source plate surface (assuming a uniform source strength). The results are compared with the experimental measurements in Table 9.3.2. Agreement between theory and experiment is within 12% in the 40- to 120-cm range.

Table 9.3.2. Comparison of Experimental and Calculated Fast-Neutron Dose Rates for New Source Plate (SP-2)

z, Distance from SP-2 (cm)	Fast-Neutron Dose Rate (ergs/g·hr)		Ratio of Experimental to Calculated
	Calculated	Experimental	
5	2.47×10^4	1.95×10^4	0.79
20	1.16×10^3	1.70×10^3	1.46
40	5.79×10^1	6.10×10^1	1.05
60	3.79×10^0	4.25×10^0	1.12
80	3.19×10^{-1}	3.35×10^{-1}	1.05
100	2.83×10^{-2}	3.05×10^{-2}	1.08
120	3.11×10^{-3}	3.30×10^{-3}	1.06

9.4. EFFECTIVE REMOVAL CROSS SECTION OF TUNGSTEN

J. M. Miller

During a recent series of Lid Tank Shielding Facility experiments employing Hevimet, it became convenient to measure the effective removal cross section of tungsten. Hevimet is an alloy of 90 wt % tungsten, 6 wt % nickel, and 4 wt % copper with a density of 16.9 to 17.2 g/cm^3. The sample was fabricated from 11 × 7 × 1 in. blocks glued together to form two slabs 56 × 55 × 2 in., giving a total thickness of 4 in. Each slab was clad with ¼-in.-thick aluminum on each side.

The Hevimet was placed in a medium of plain water at the source plate end of a steel configuration tank, which in turn was placed in the Lid Tank. (There was a 2.1-cm-thick air gap between the source plate and a ⅜-in.-thick aluminum window in the configuration tank.) Thermal-neutron flux measurements were made on the axis of the source plate in the water beyond the material, the results of which are given in Fig. 9.4.1 along with similar measurements made in the water with the tungsten removed. The measurements were made with a 12½-in. BF_3 counter, a 3-in. fission chamber, and a ½-in. fission chamber.

The effective removal cross section of the tungsten was calculated from these measurements by use of a previously published formula.[1] The resulting value was 3.13 ± 0.25 barns as compared with an earlier value[2] of 2.51 ± 0.55 barns. While the agreement between the two results is adequate, it is believed that the latest measurement is more accurate. The value of the mass attenuation coefficient of tungsten ($\Sigma R/\rho$ = 0.0102 ± 0.0008 cm^2/g) calculated from these measurements agreed very well with the value of 0.0105 cm^2/g which is obtained from the curve of Σ/ρ vs A given by Chapman and Storrs.[3]

[1] E. P. Blizard, *Procedure for Obtaining Effective Removal Cross Sections from Lid Tank Data*, ORNL CF-54-6-164 (June 22, 1954).

[2] G. T. Chapman and C. L. Storrs, *Effective Neutron Removal Cross Sections for Shielding*, ORNL-1843 (Sept. 19, 1955).

[3] *Ibid.*, Fig. 3, p 26.

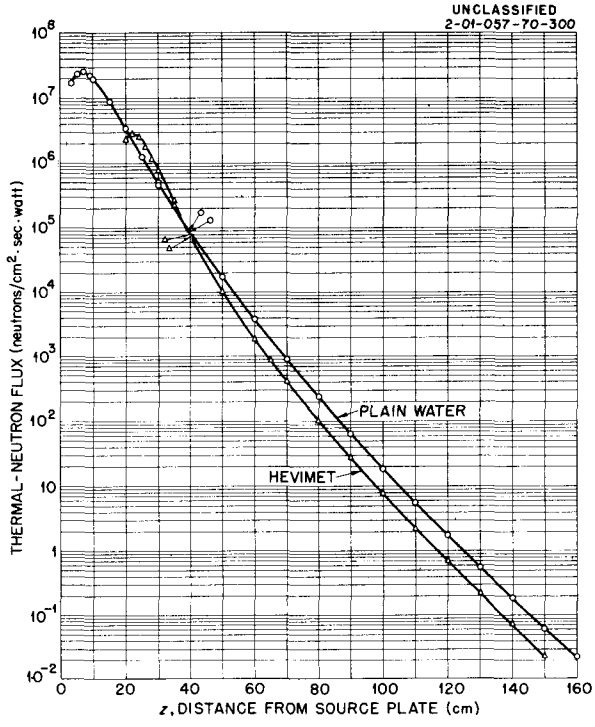

Fig. 9.4.1. Thermal-Neutron Flux Measurements in Water Behind 4 in. of Hevimet.

9.5. GAMMA-RAY AND THERMAL-NEUTRON MEASUREMENTS IN AIR AT VARIOUS DISTANCES FROM THE TOWER SHIELDING REACTOR

F. N. Watson R. M. Davis[1]
W. R. Champion[2]

As a part of the continuing study of the air capture, scattering, and attenuation of reactor radiations, measurements have been made of the gamma-ray dose rate and thermal-neutron flux in air at various distances from the reactor at the Tower Shielding Facility (TSF).

At this facility the reactor, which is a swimming pool reactor contained in a 12-ft-dia water tank, can be hoisted to heights (h) as high as 200 ft above the ground. The position of the reactor within its tank can be varied so that the thickness of the water (ρ) between the reactor face and the tank wall can be altered. In addition, the angle (θ) between the reactor beam and the detector-reactor tank axis can be varied. In the experiment reported here both gamma-ray and thermal-neutron measurements were made with detectors attached to one of the legs of the TSF structure (the structure consists of four 315-ft-high towers arranged in a 100 × 200 ft rectangle) while the reactor tank was positioned at various distances from the leg. In addition, thermal-neutron measurements were made in the air along a line normal to the front face of the reactor. The relative responses of various thermal-neutron detectors used in the experiments were also determined.

Gamma-Ray Dose Rate Measurements

A number of gamma-ray dose rate measurements were made as a function of the distance between the reactor and an unshielded detector on the TSF leg. The effect of the leg on the measured dose rates is assumed to be negligible. Figure 9.5.1 presents these data as a function of separation distance for ρ = 45 cm and for θ = 0, 92, and 270 deg. At θ = 92 deg the reactor is facing the detector. Figure 9.5.2 presents the gamma-ray dose rate at the TSF leg as a function of ρ for a fixed separation distance of 100 ft.

Examination of the data in Fig. 9.5.1 indicates that the direct-beam dose rate (θ = 92 deg) follows the inverse-distance-squared law to a close approximation. The dose rate with the beam of radiation pointed directly away from the detector (θ = 270 deg) decreases more rapidly than the inverse-distance law but much more slowly than the inverse-distance-squared law. As was expected, the dose rate as a function of distance with the beam of radiation directed at 90 deg from the detector (θ = 0 deg) falls somewhere between the other two curves.

Thermal-Neutron Flux Measurements

Thermal-neutron flux measurements were made at distances of 25 and 50 ft as a function of θ for several values of ρ in the range 16 to 90 cm. These measurements were accomplished by mounting a bare BF_3 chamber on the TSF leg and positioning the reactor tank at the desired separation distance. No cadmium-covered detector measurements were made; so the flux reported is governed by the boron $1/v$ cross section. The results of these measurements for the 25-ft separation distance are shown in Figs. 9.5.3 and 9.5.4. It is interesting to note that these curves are almost identical in shape. The reason for this is not immediately obvious. A plot of the data for the 50-ft separation distance (Fig. 9.5.5) shows curves with the same shapes, although the slopes of the curves vary more slowly than do the slopes of the curves for the 25-ft separation distance. It is felt that this is an indication that the ratio of direct-to-scattered flux is changing, with the scattered component becoming more predominant.

Measurements were also taken from which a profile of the thermal-neutron flux in the TSR tank water and in the air normal to the front face of the reactor could be established. Bare and cadmium-covered gold foils, previously calibrated with the ORNL standard pile, were exposed at various distances from the reactor, and the thermal-neutron flux as a function of distance from the reactor was determined. The results are shown in Fig. 9.5.6, where the relative position of the reactor tank wall is indicated. The flux in water at various distances from the Bulk Shielding Reactor (BSR) is also plotted for comparison.[3]

[1] On assignment from The Glenn L. Martin Co.

[2] On assignment from Lockheed Aircraft Corp.

[3] H. E. Hungerford, *Bulk Shielding Facility Water Data Work Sheet*, ORNL CF-52-2-37 (Feb. 1, 1952).

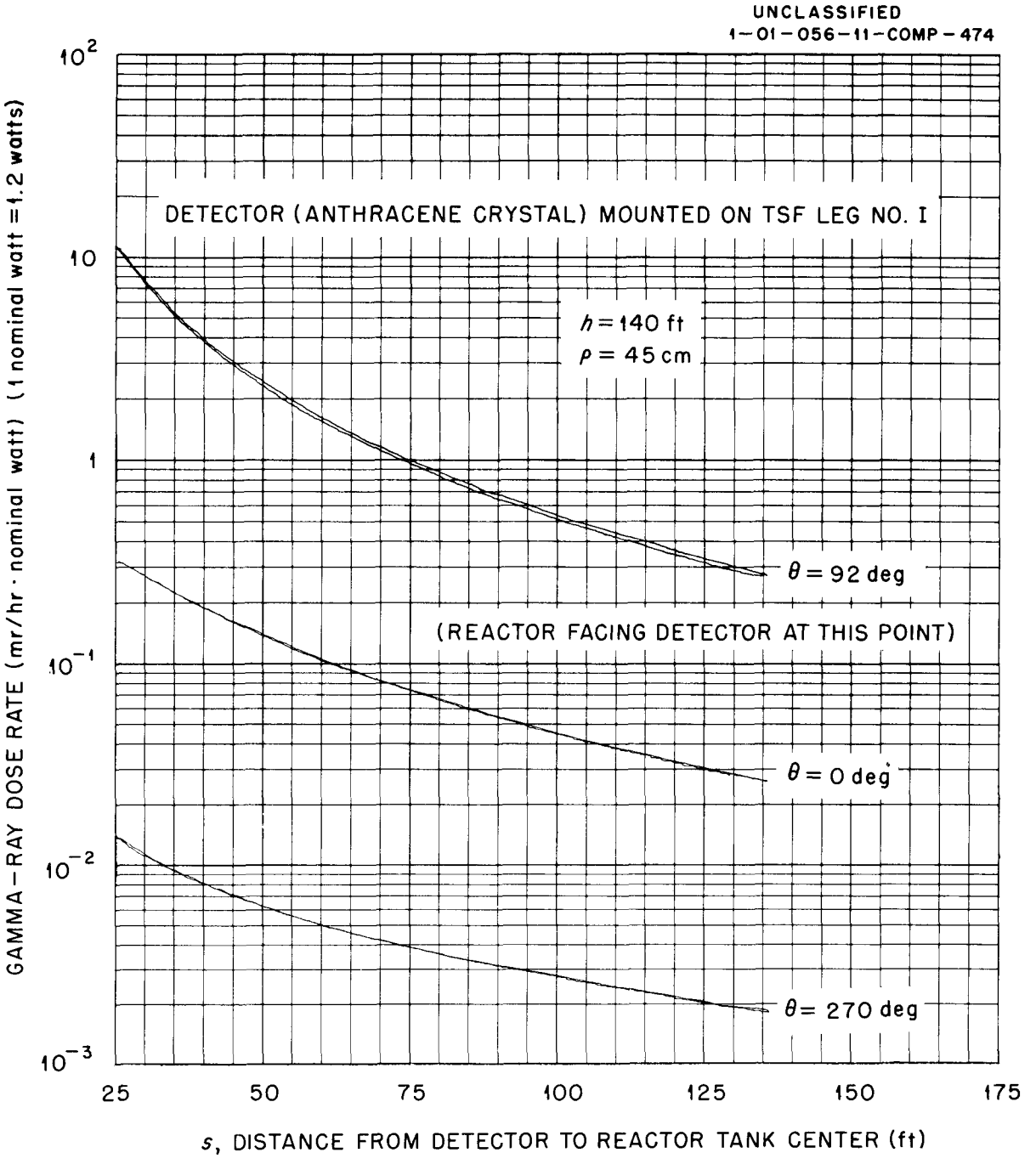

Fig. 9.5.1. Gamma-Ray Dose Rate in Air as a Function of the Reactor-Detector Separation Distance for Various Values of θ.

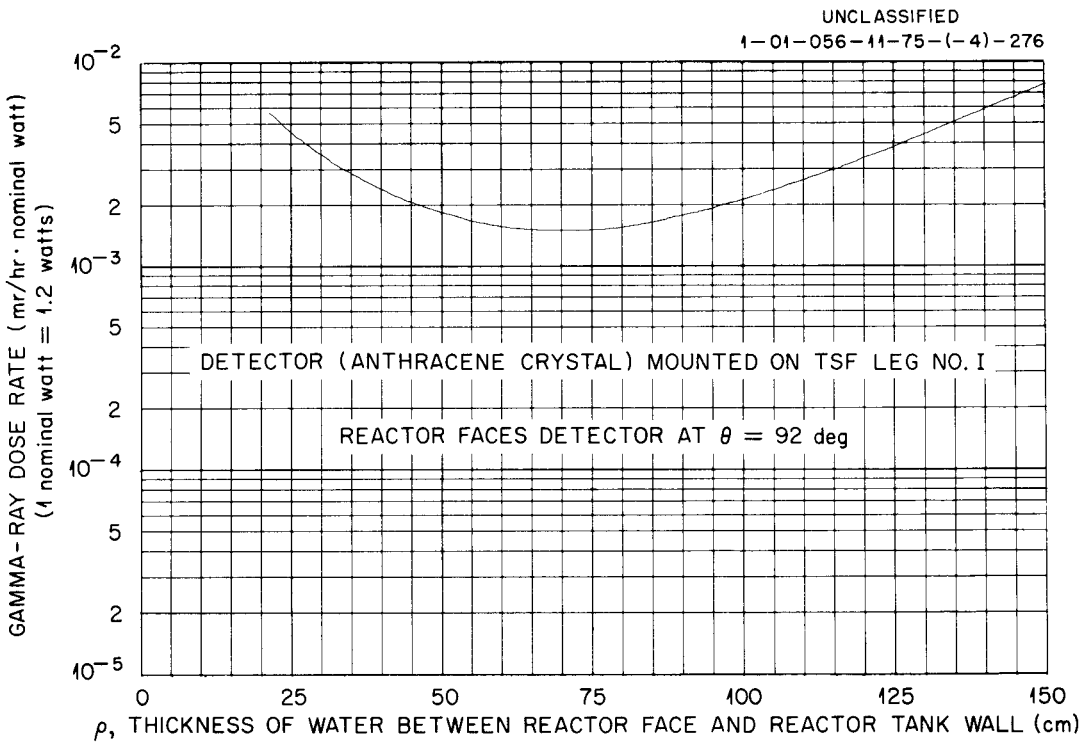

Fig. 9.5.2. Gamma-Ray Dose Rate in Air at a Point 100 ft from the Center of the Reactor Tank as a Function of ρ for $\theta = 270$ deg.

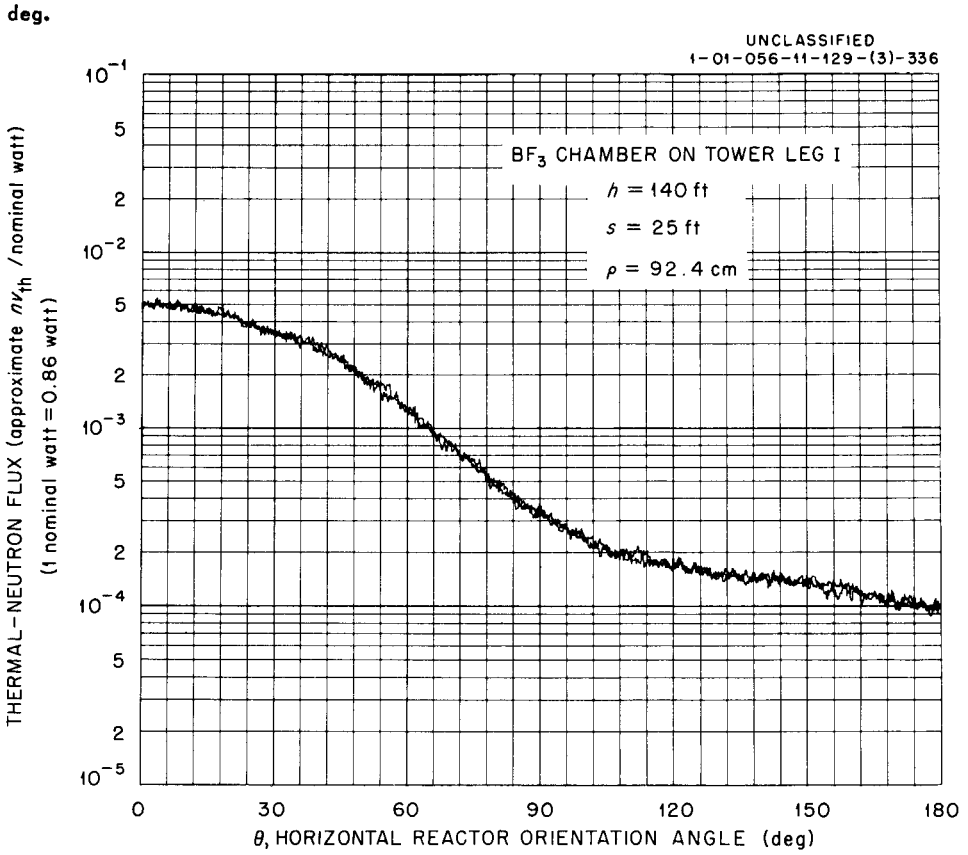

Fig. 9.5.3. Thermal-Neutron Flux in Air at a Point 25 ft from the Center of the Reactor Tank as a Function of θ for $\rho = 92.4$ cm.

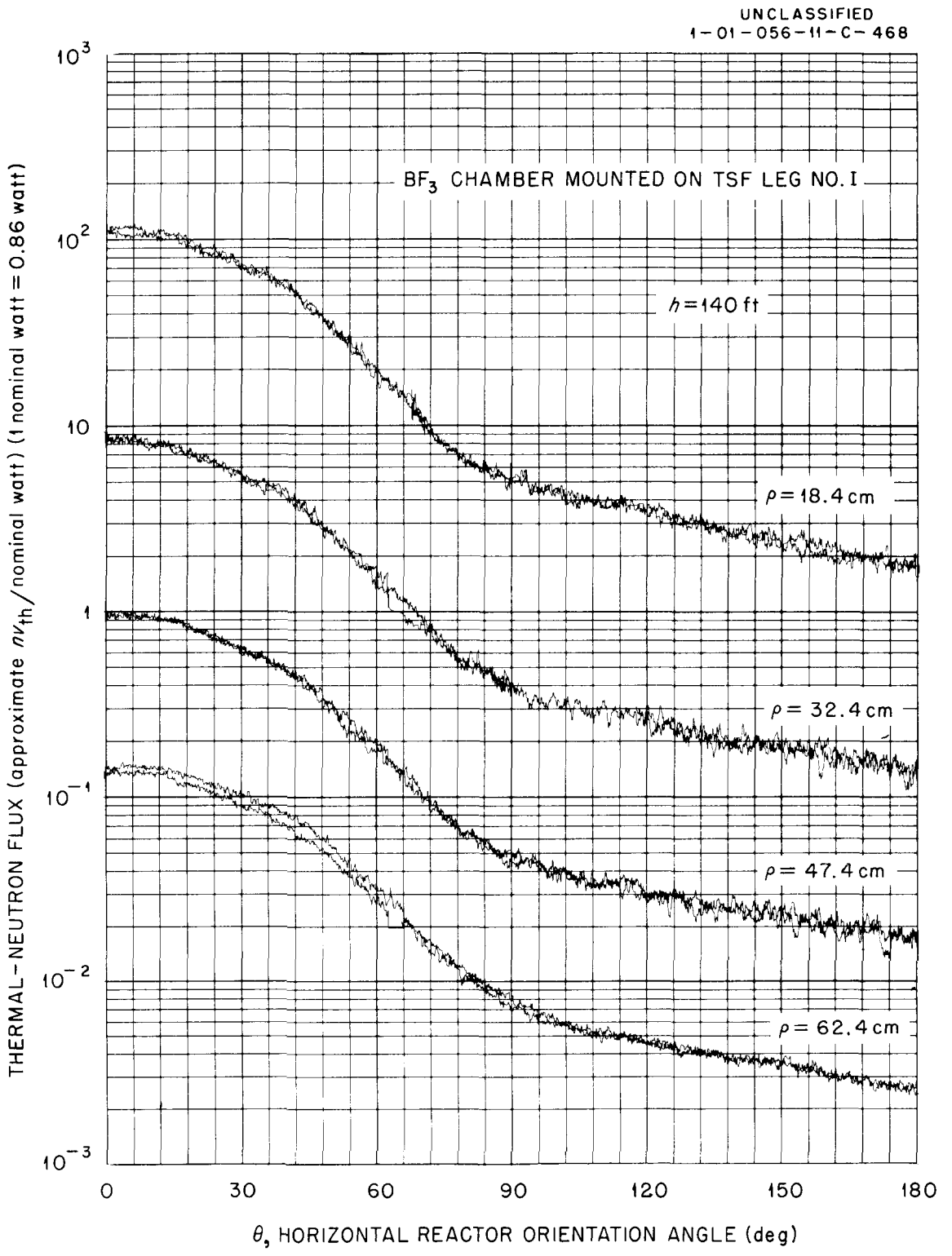

Fig. 9.5.4. Thermal-Neutron Flux in Air at a Point 25 ft from the Center of the Reactor Tank as a Function of θ for ρ = 18.4, 32.4, 47.4, and 62.4 cm.

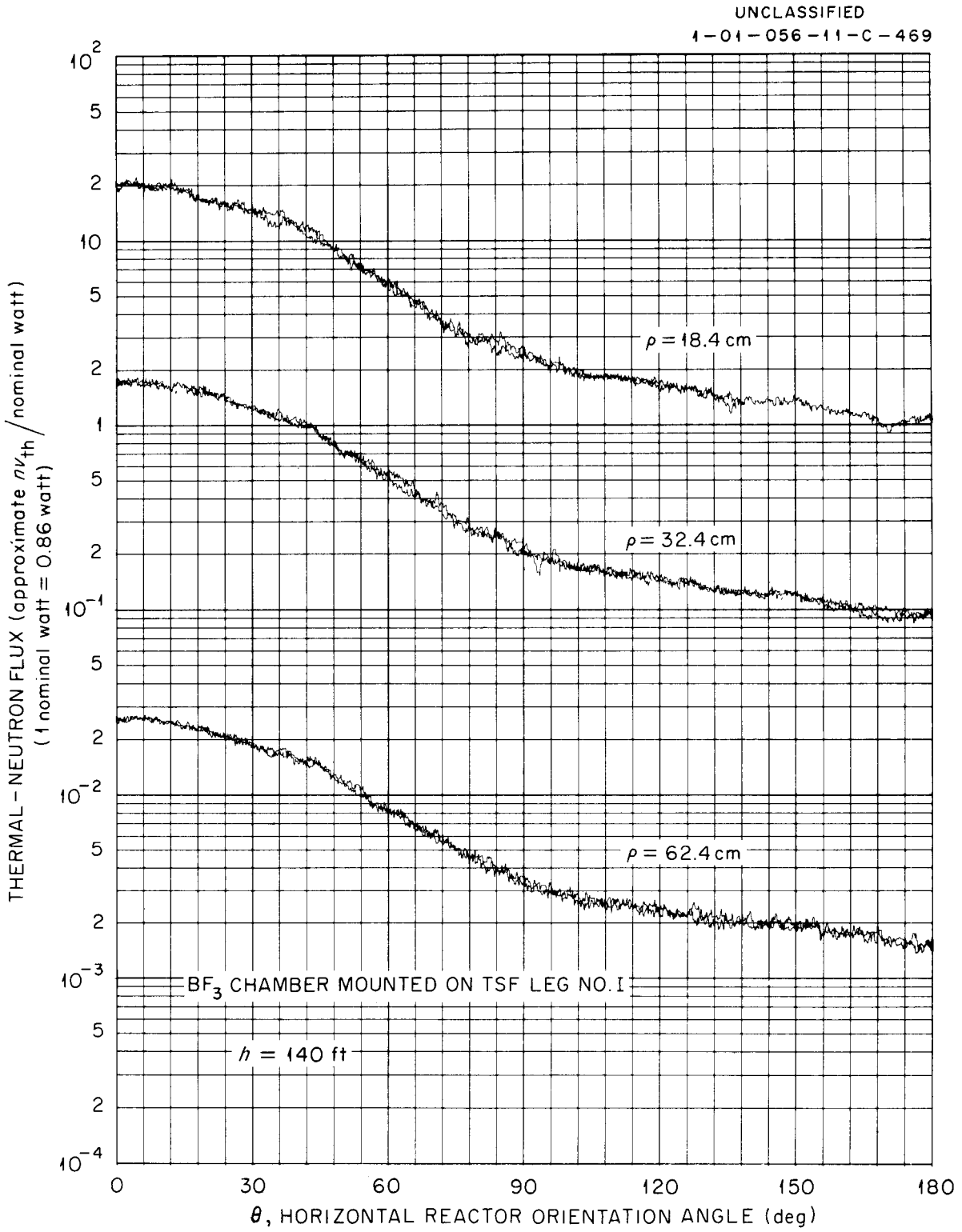

Fig. 9.5.5. Thermal-Neutron Flux in Air at a Point 50 ft from the Center of the Reactor Tank as a Function of θ for ρ = 18.4, 32.4, and 62.4 cm.

From the reactor face to within 5 cm of the tank wall the agreement between the TSR and BSR data is within 10%. Immediately outside the tank wall the thermal-neutron flux is approximately 7% of that predicted from the BSR curve.

The responses of the two thermal-neutron detectors used in these experiments were compared with the response of a third type of detector in another series of measurements. These measurements were made with the reactor-detector center line 6 ft above ground level. The results are plotted as a function of the reactor-detector separation distance, s, in Fig. 9.5.7. It is to be noted that these data follow an inverse-distance-squared relationship if the effective position of the source is considered to be at a point, inside the reactor, 3 cm from the front face. Some of the discrepancy in the results for the different detectors can be attributed to the lack of cadmium-difference data for the fission chamber and the BF_3 counter. The fission chamber may indicate a high flux, because it was designed for use in water and is backed up by a thick plastic block that returns, to the sensitive portion of the counter, both the thermal and the fast neutrons slowed down in the block.

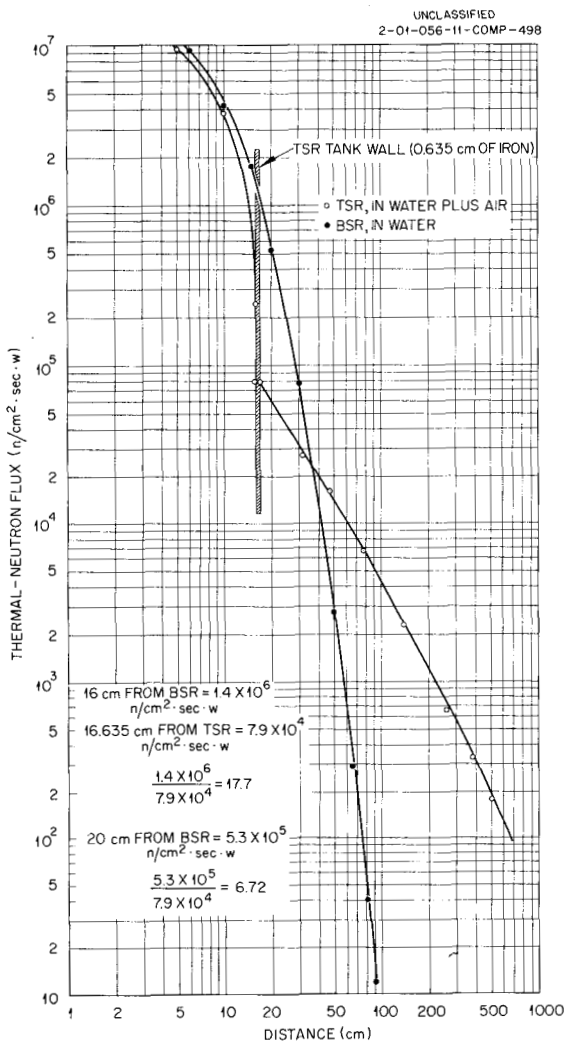

Fig. 9.5.6. Thermal-Neutron Flux as a Function of Distances from the TSR and the BSR.

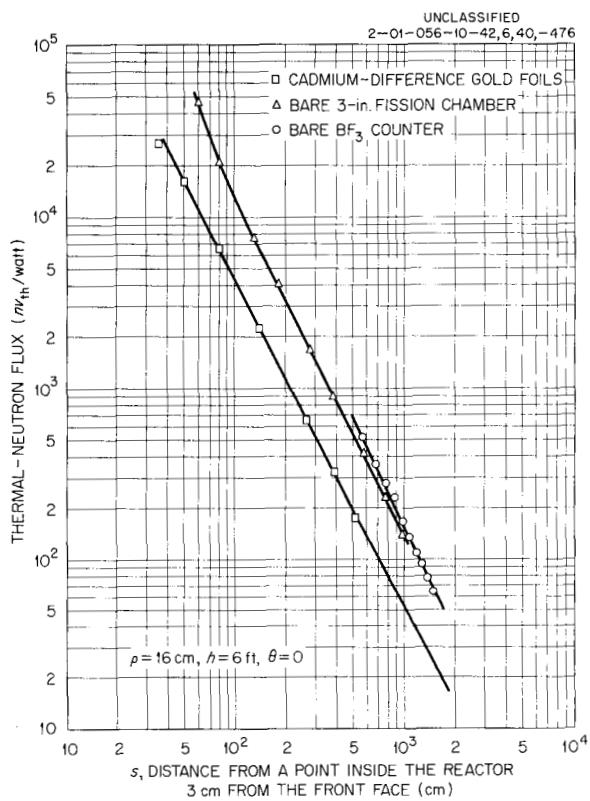

Fig. 9.5.7. Comparison of Response of Various Thermal-Neutron Detectors in Air to Radiation from the TSR.

9.6. STUDY OF AIR AND GROUND SCATTERING OF FAST NEUTRONS AT THE TOWER SHIELDING FACILITY

M. J. Welch
R. M. Davis[1]
W. J. McCool[2]
C. R. Fink[1]

An experiment designed for obtaining information on air and ground scattering of fast neutrons was performed at the Tower Shielding Facility (a brief description of the TSF is given in Sec. 9.5). A highly collimated beam of neutrons was obtained for the experiment by placing one of two air-filled cylindrical aluminum pipes (8- and 15-in. ID) adjacent to the reactor in the reactor tank. Fast-neutron dose rate measurements were made with an unshielded detector at a distance of 64 ft from the reactor tank while both the direction of the beam and the height above the ground were varied.

The geometry for the measurements is shown in Fig. 9.6.1*a*. The angle ϕ is the orientation angle of the collimator axis in the vertical plane, and θ is the corresponding angle in the horizontal plane.

[1]On assignment from The Glenn L. Martin Co.

[2]On assignment from Pratt & Whitney Aircraft.

UNCLASSIFIED
2-01-056-13+14-D-482

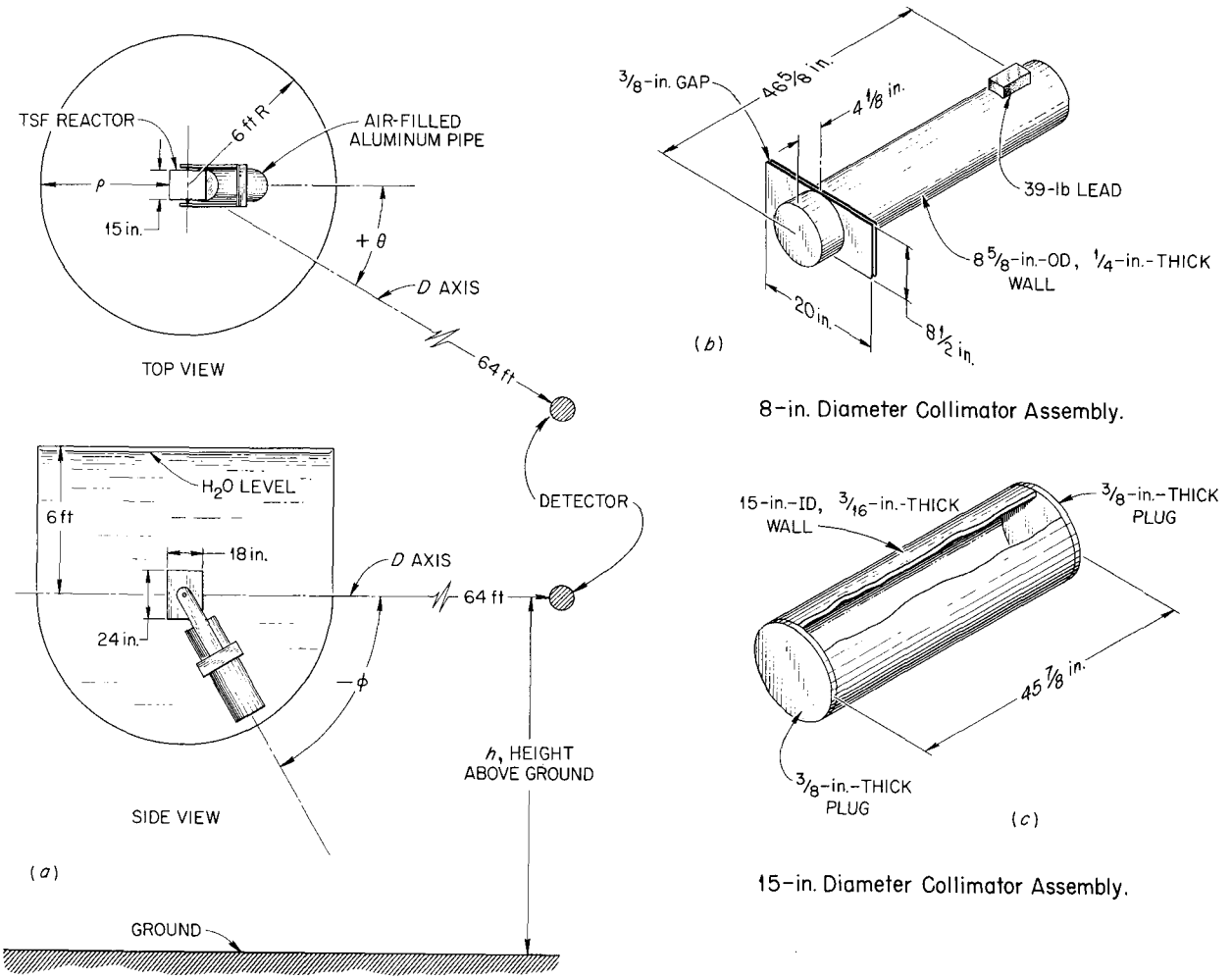

Fig. 9.6.1. Collimator Geometry in the TSR Tank.

At ϕ = 0 deg and θ = 0 deg the collimator is directed at the detector. The collimator assemblies are shown in Figs. 9.6.1*b* and 9.6.1*c*.

The asymmetries in the reactor and the tank wall cause the source strength to vary with ϕ and θ. This variation was determined by placing the detector in the direct beam 64 ft from the reactor center for different values of θ and ϕ. The results (Figs. 9.6.2, 9.6.3, and 9.6.4) must be used to normalize all data taken from the TSF variplotter. In addition, the background (2×10^{-7} mrep/hr·w) must be subtracted from all the variplotter data. This is especially important for the 8-in.-dia collimator measurements since the intensity is lower by a factor of approximately 10 than the intensity for the 15-in.-dia collimator measurements.

Fast-neutron dose rate measurements at ϕ = 0 deg as a function of the horizontal angle θ of the collimator are shown in Figs. 9.6.5 through 9.6.7. The measurements shown in Figs. 9.6.5 and 9.6.6 consist of the direct-beam and the air-scattered contributions, since they were taken at an altitude

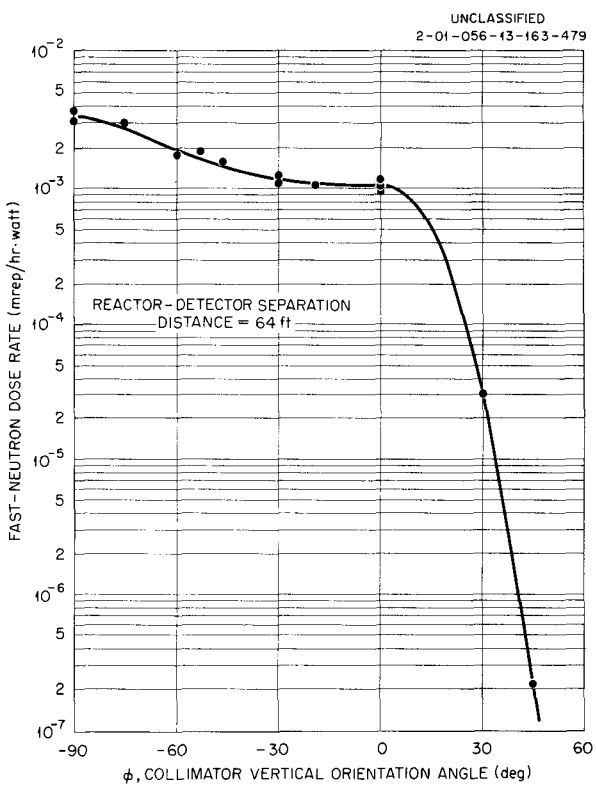

Fig. 9.6.2. Peak Fast-Neutron Intensity as a Function of ϕ for 8-in.-dia Collimator (θ = 0 deg).

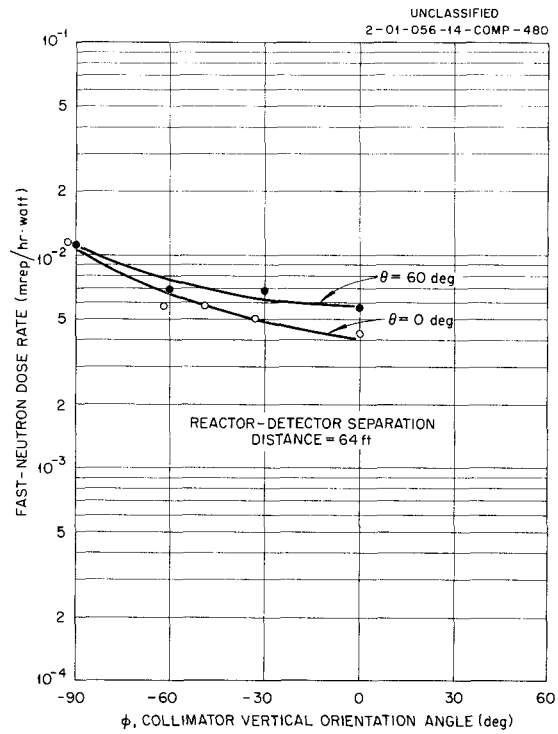

Fig. 9.6.3. Peak Fast-Neutron Intensity as a Function of ϕ for 15-in.-dia Collimator (θ = 0 and 60 deg).

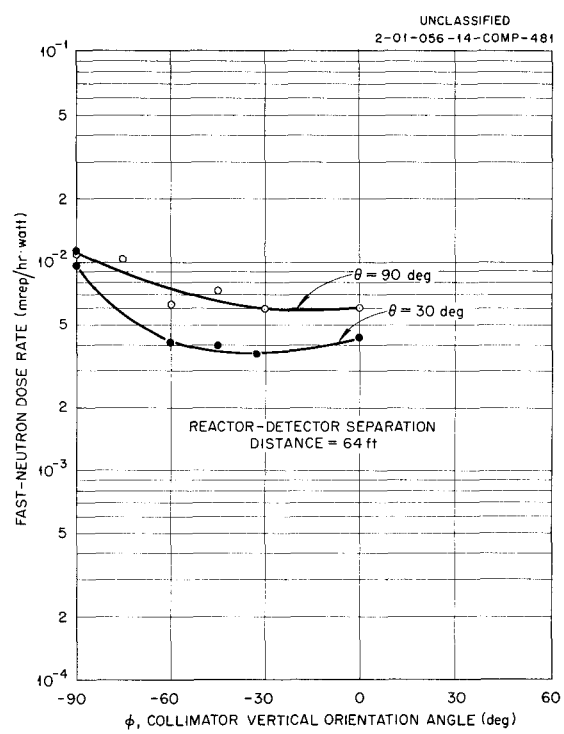

Fig. 9.6.4. Peak Fast-Neutron Intensity as a Function of ϕ for 15-in.-dia Collimator (θ = 30 and 90 deg).

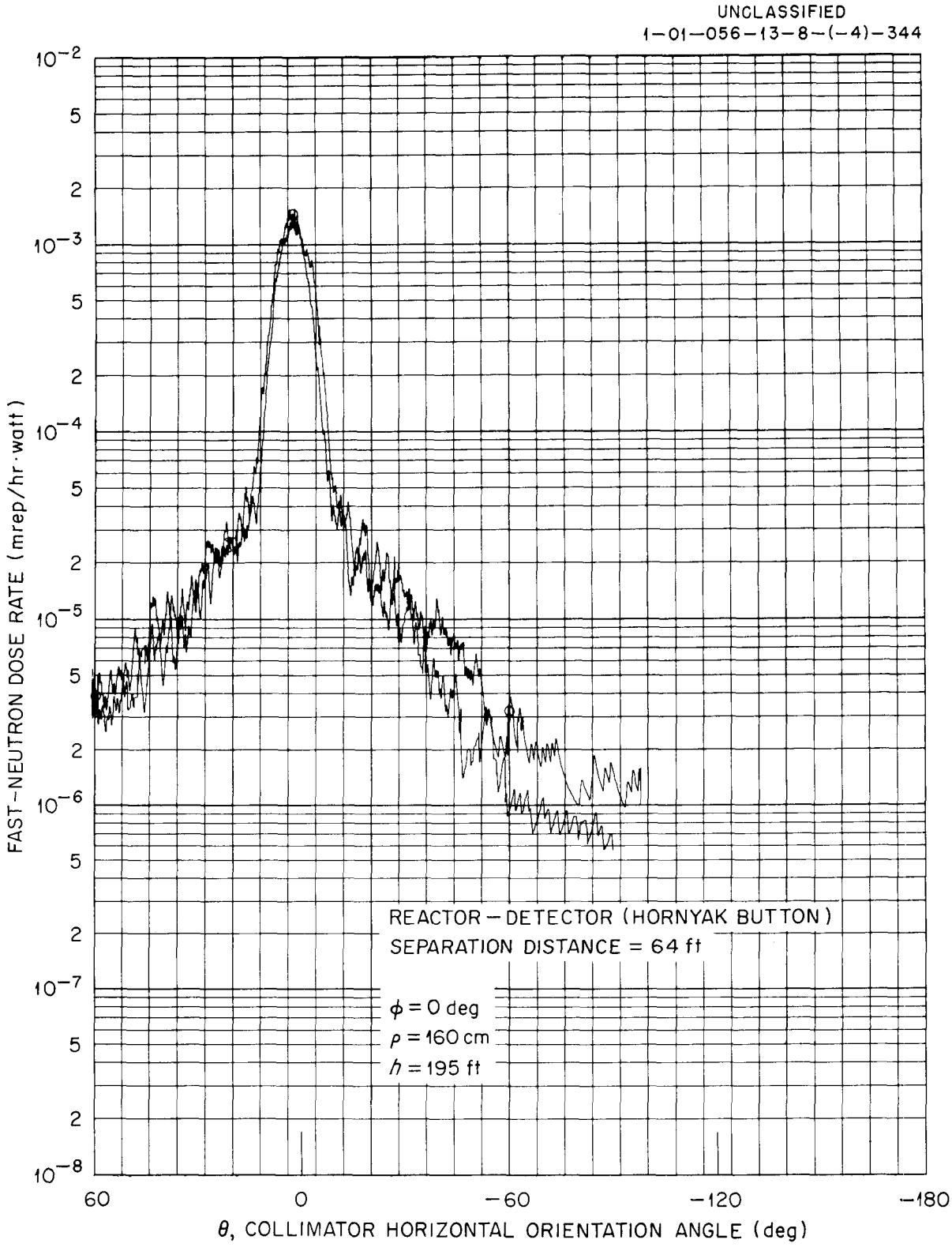

Fig. 9.6.5. Fast-Neutron Dose Rate in Air as a Function of θ for 8-in.-dia Collimator (h = 195 ft).

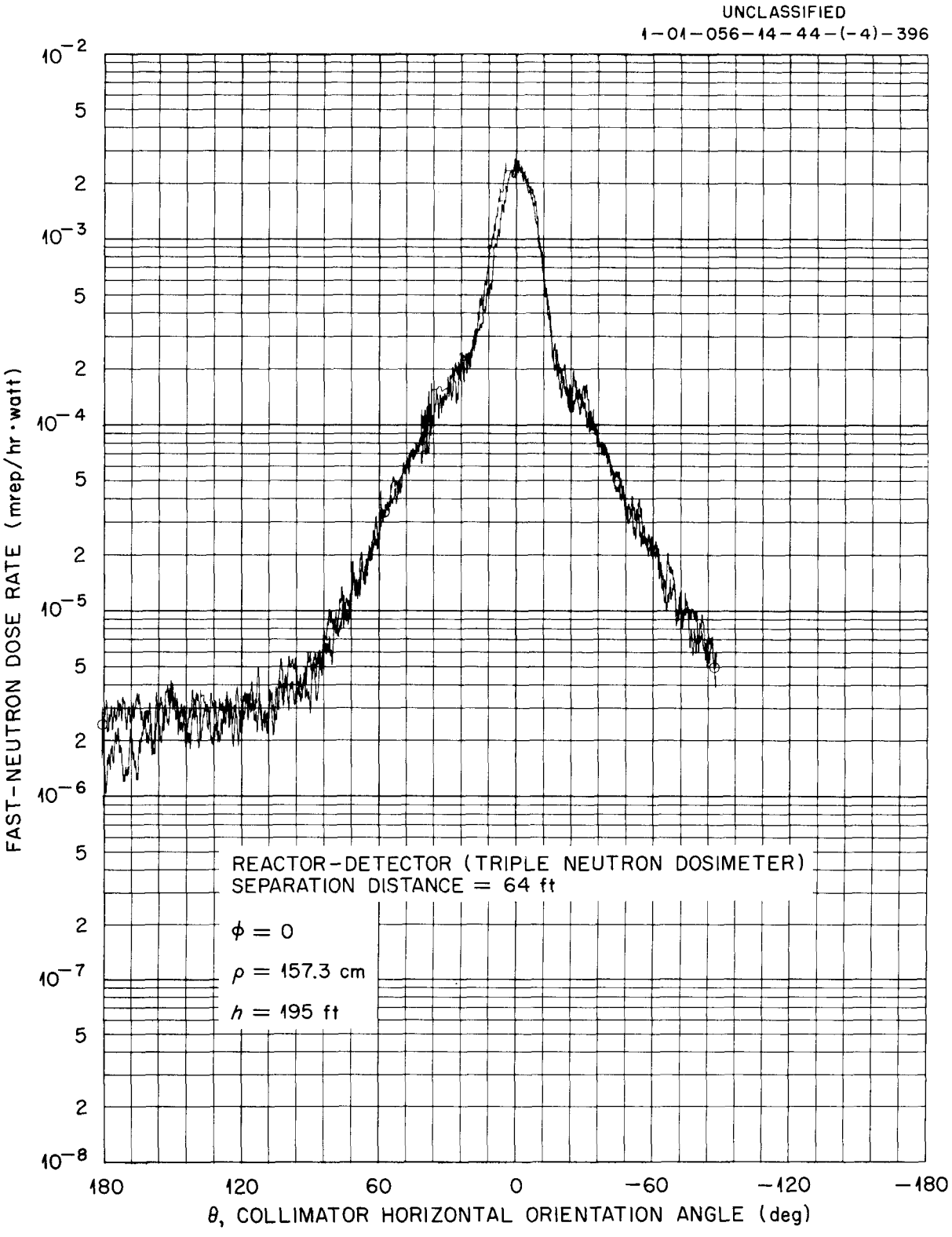

Fig. 9.6.6. Fast-Neutron Dose Rate in Air as a Function of θ for 15-in.-dia Collimator (h = 195 ft).

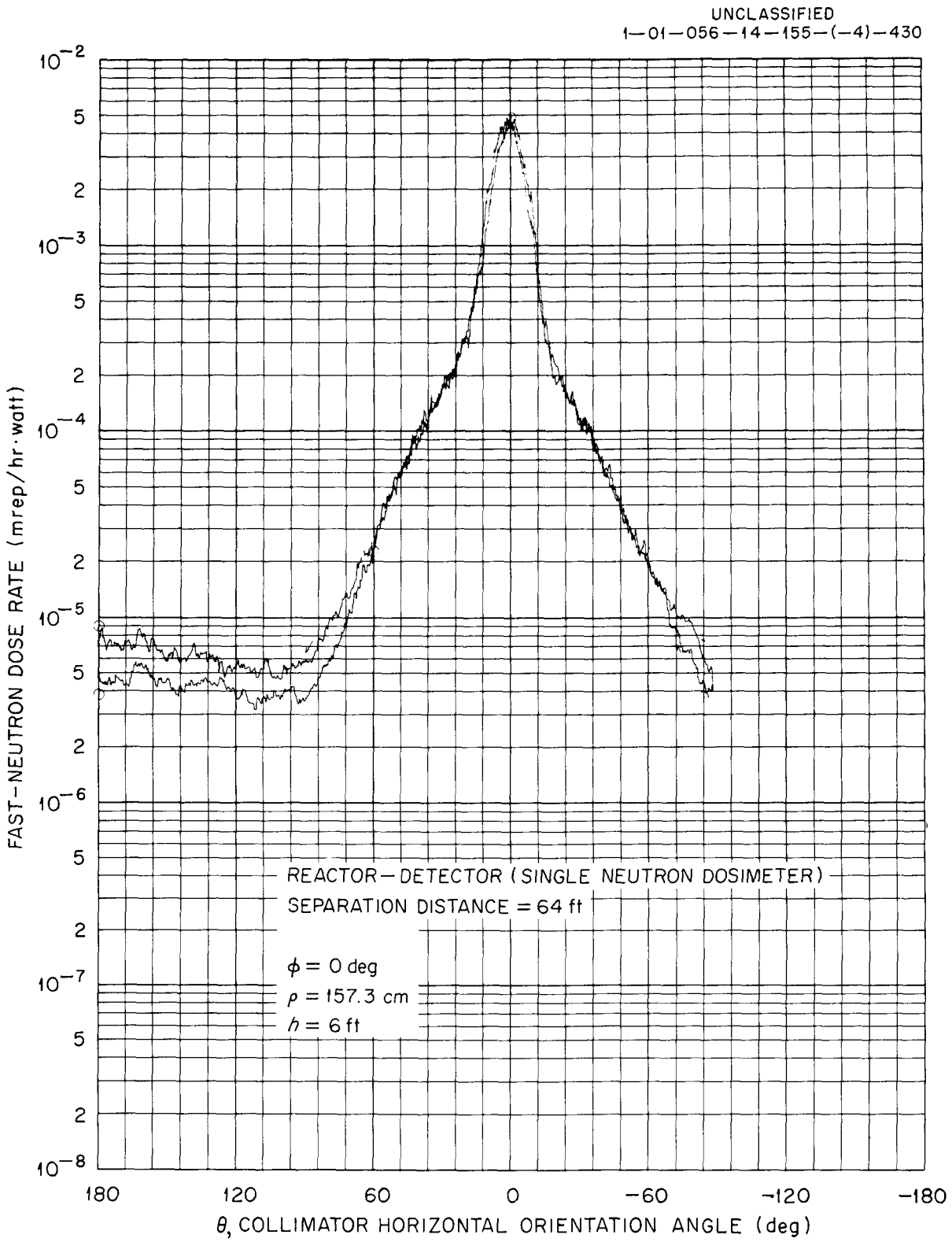

Fig. 9.6.7. Fast-Neutron Dose Rate in Partially Shielded Detector as a Function of θ for 15-in.-dia Collimator (h = 6 ft).

of 195 ft, where the ground-scattered component was assumed to be negligible. (This is probably true only for $\phi = 0$ deg.) The data shown in Fig. 9.6.7 were taken with a detector encased in a shield which was penetrated by a collimator in the direct-beam direction. In this case some contribution from the scattered component was removed.

The direct-beam portion of each of the above θ traverses (that is, the portion in the vicinity of $\theta = 0$ deg) can be fitted by an equation of the form

$$D_\theta = D_{\theta=0} \cos^n \theta ,$$

where $D_{\theta=0}$ is the peak intensity of the beam and D_θ is the intensity at a given angle θ. The cosine power n was found to be approximately 181, 185, and 186 for the 8-in.-dia collimator at angles of θ equivalent to 50, 25, and 10% of the peak intensity, respectively. The fit of the 15-in.-dia collimator to this cosine function was not so good, since the power n was found to vary from 56 to 63 at 50 and 25% of the peak beam intensity.

A plot of the 15-in.-dia collimator data corrected for the change in source strength mentioned above is shown in Fig. 9.6.8, along with the measured data. In order to determine the total neutron dose leaving the collimator, the corrected curve was resolved into the direct-beam and air-scattered components between $\theta = 0$ and 30 deg by extrapolating the curve from the point where $\theta = 30$ deg back to where $\theta = 0$ deg and assuming that the extrapolated curve represents the air-scattered component. The direct-beam contribution was then determined by subtraction. By integrating the area under the direct-beam curve, the total neutron dose leaving the collimator was determined as follows:

$$D_T = 2\pi l^2 \int_0^{\pi/2} D_\theta \sin\theta \, d\theta ,$$

where l is the separation distance. The values of D_T determined for the 15-in. collimator for $l = 15$, 30, and 64 ft were 1.32×10^3, 1.16×10^3, and 1.26×10^3 mrep·cm^2/hr·w, respectively.

Fast-neutron dose rate measurements as a function of altitude were made for various values of ϕ and θ (Figs. 9.6.9 through 9.6.16). These traverses show a maximum intensity of dose rate at an altitude of between 20 and 40 ft. The intensity decreases as higher altitudes are approached

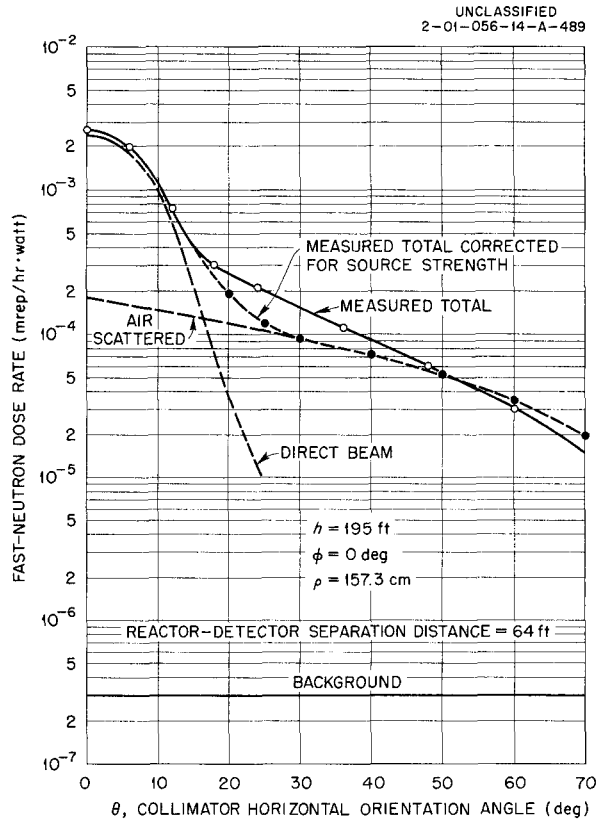

Fig. 9.6.8. Fast-Neutron Dose Rate in Air as a Function of θ for 15-in.-dia Collimator (h = 195 ft).

because of decreasing ground scattering, which overrides the small increase in air scattering. The ground-scattering effects are seen at higher altitudes for greater negative values of ϕ.

Measurements as a function of ϕ were taken at altitudes of 12.5, 25, and 195 ft (Figs. 9.6.17 through 9.6.22). The background (that is, the dose rate with the collimator removed from the tank) has been subtracted from the results plotted in Figs. 9.6.21 and 9.6.22, and corrections have been made for the variations in source strength caused by the asymmetry in the reactor tank. The traverses with the 8-in.-dia collimator were taken with the reactor tank centered over the concrete pad to one side of the pool. With the exception of the data shown in Fig. 9.6.16, the large collimator traverses were taken with the reactor tank centered over the pool.

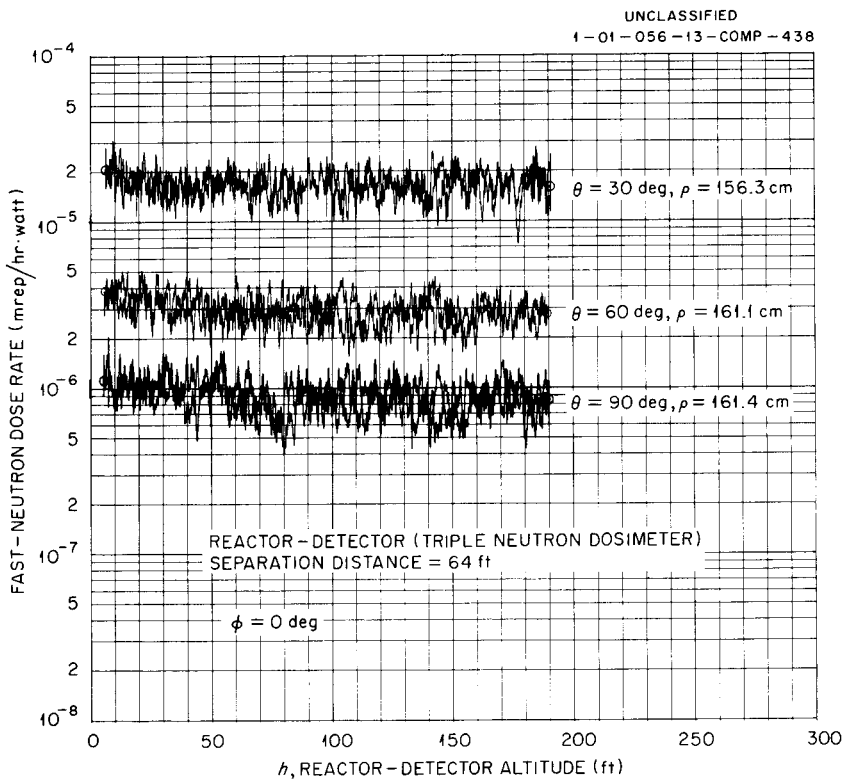

Fig. 9.6.9. Fast-Neutron Dose Rate in Air as a Function of Altitude for 8-in.-dia Collimator ($\theta = 30$, 60, and 90 deg; $\phi = 0$).

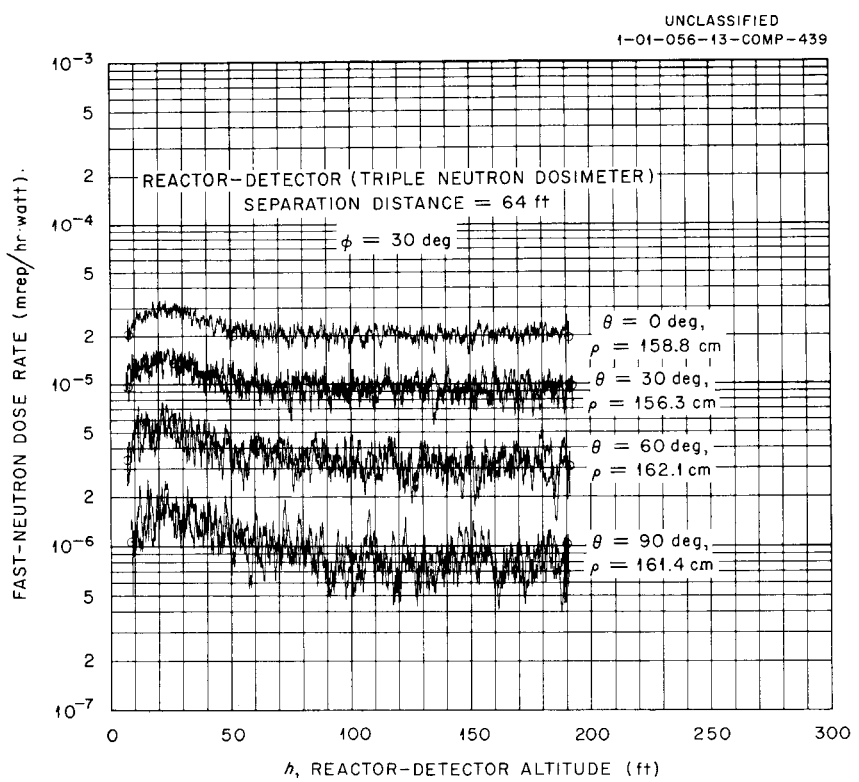

Fig. 9.6.10. Fast-Neutron Dose Rate in Air as a Function of Altitude for 8-in.-dia Collimator ($\theta = 0$, 30, 60, and 90 deg; $\phi = 30$ deg).

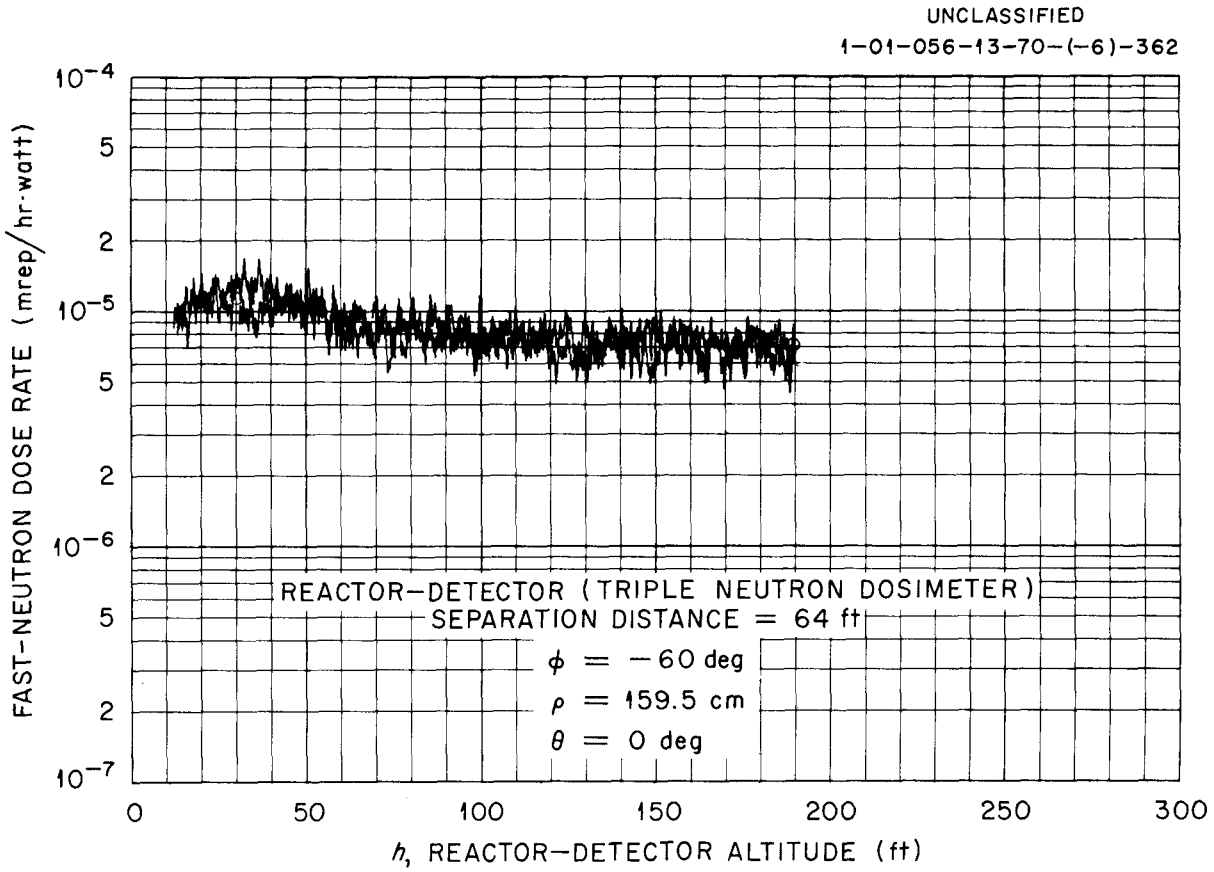

Fig. 9.6.11. Fast-Neutron Dose Rate in Air as a Function of Altitude for 8-in.-dia Collimator ($\theta = 0$; $\phi = -60$ deg).

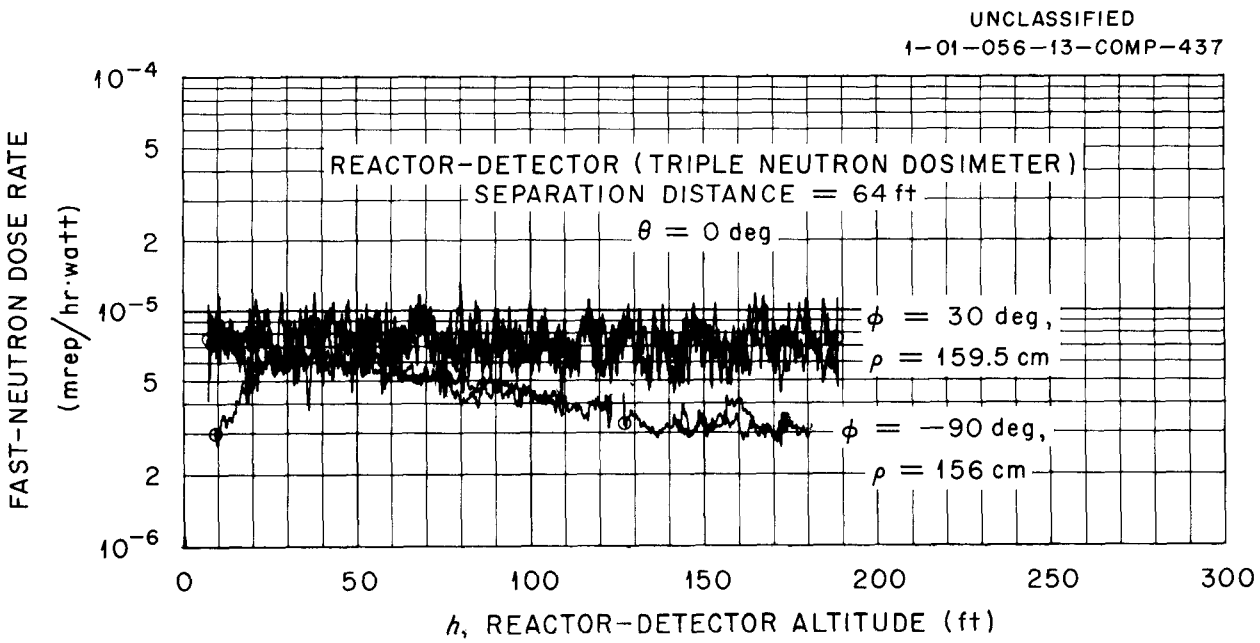

Fig. 9.6.12. Fast-Neutron Dose Rate in Air as a Function of Altitude for 8-in.-dia Collimator ($\theta = 0$; $\phi = +30$ and -90 deg).

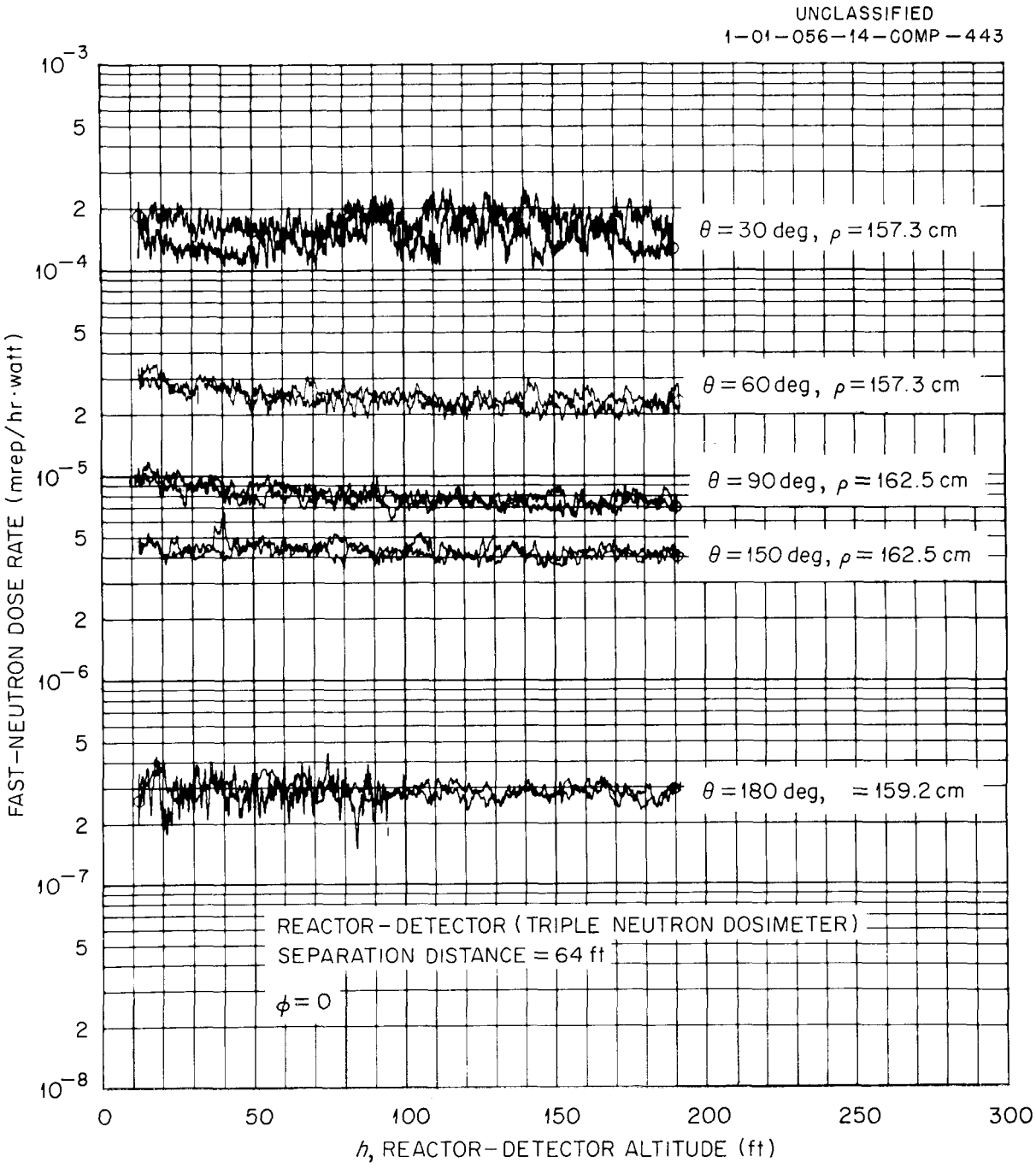

Fig. 9.6.13. Fast-Neutron Dose Rate in Air as a Function of Altitude for 15-in.-dia Collimator ($\phi = 0$; $\theta = 30$, 60, 90, 150, and 180 deg).

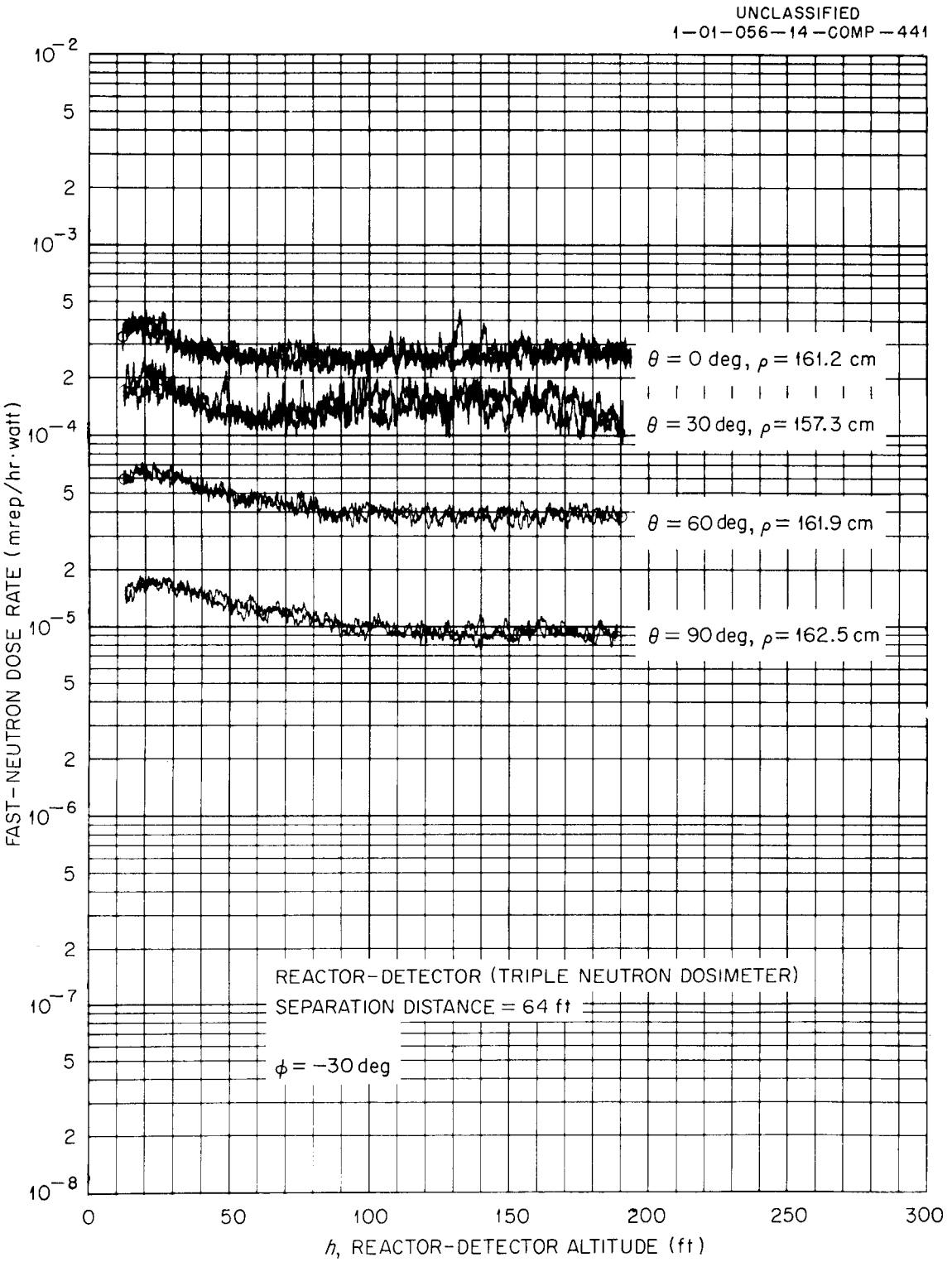

Fig. 9.6.14. Fast-Neutron Dose Rate in Air as a Function of Altitude for 15-in.-dia Collimator (ϕ = −30 deg; θ = 0, 30, 60, and 90 deg).

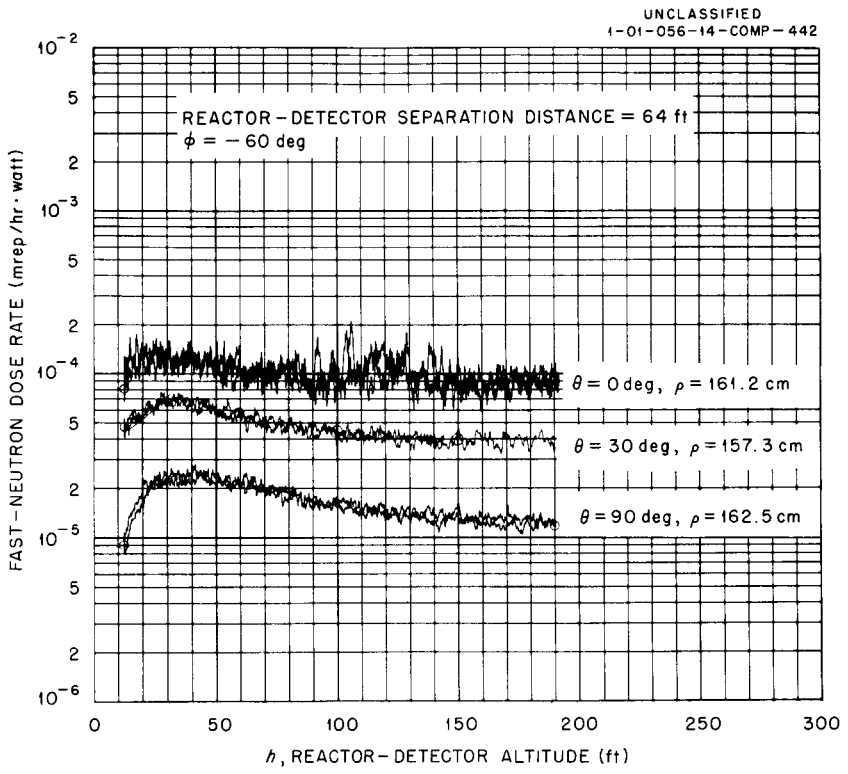

Fig. 9.6.15. Fast-Neutron Dose Rate in Air as a Function of Altitude for 15-in.-dia Collimator (ϕ = −60 deg; θ = 0, 30, and 90 deg).

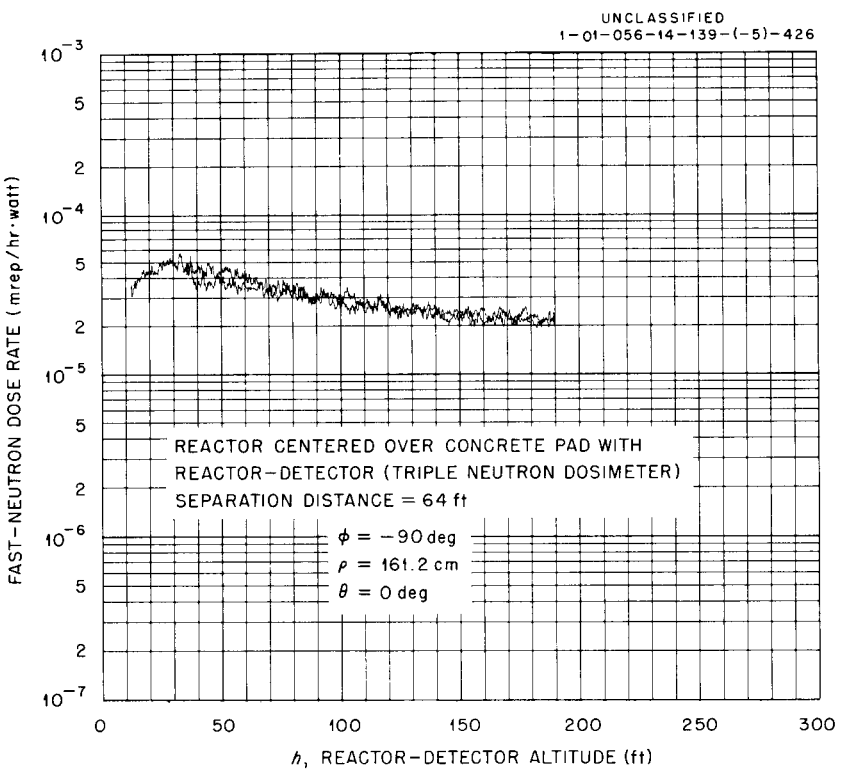

Fig. 9.6.16. Fast-Neutron Dose Rate in Air as a Function of Altitude for 15-in.-dia Collimator (ϕ = −90 deg; θ = 0 deg).

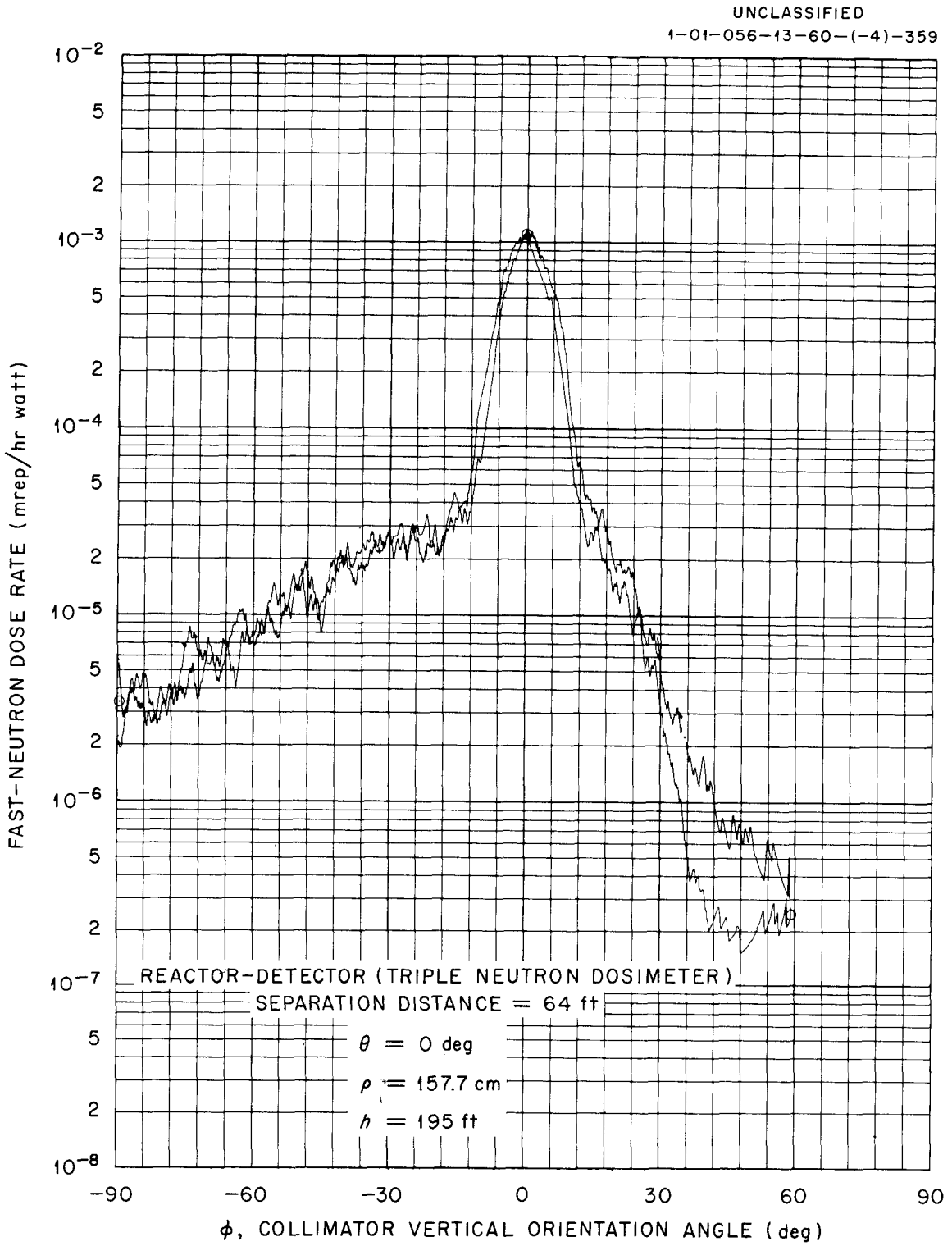

Fig. 9.6.17. Fast-Neutron Dose Rate in Air as a Function of ϕ for 8-in.-dia Collimator (θ = 0 deg).

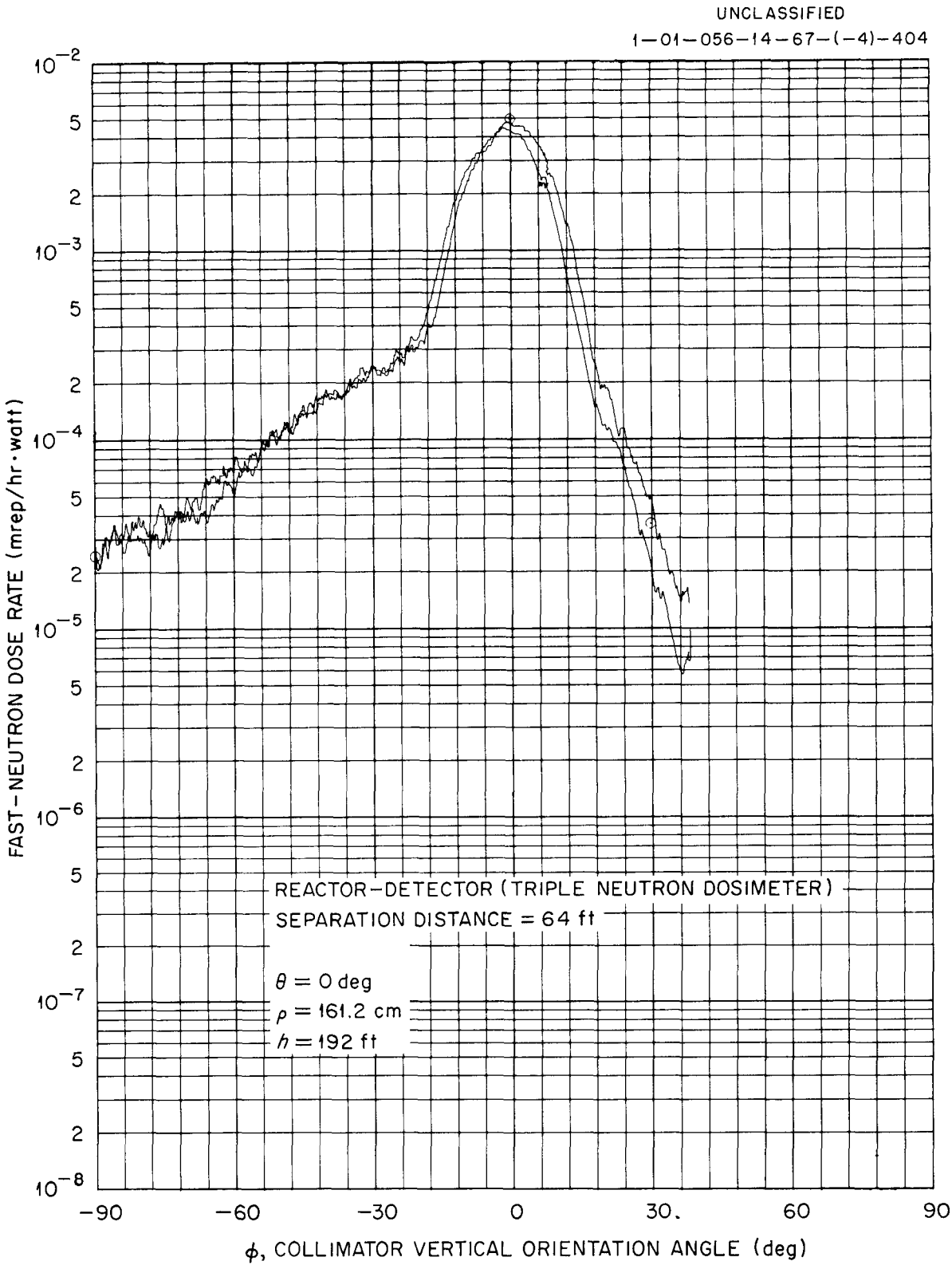

Fig. 9.6.18. Fast-Neutron Dose Rate in Air as a Function of ϕ for 15-in.-dia Collimator ($\theta = 0$ deg).

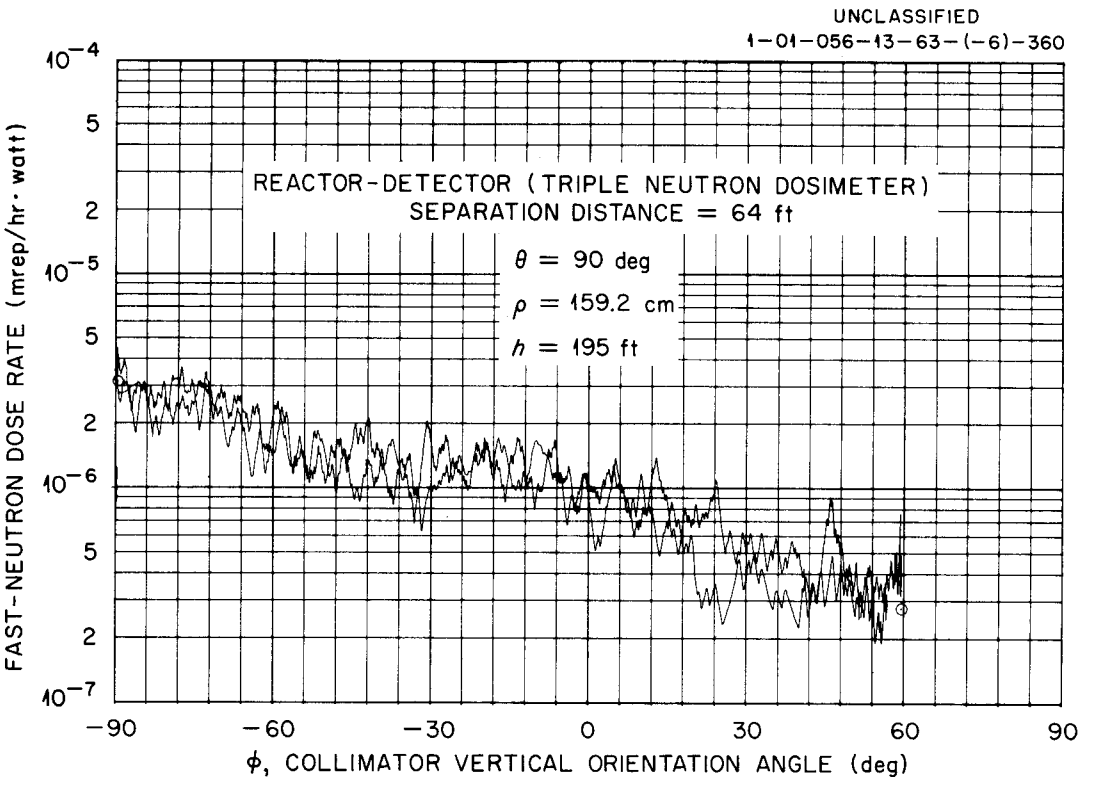

Fig. 9.6.19. Fast-Neutron Dose Rate in Air as a Function of ϕ for 8-in.-dia Collimator ($\theta = 90$ deg).

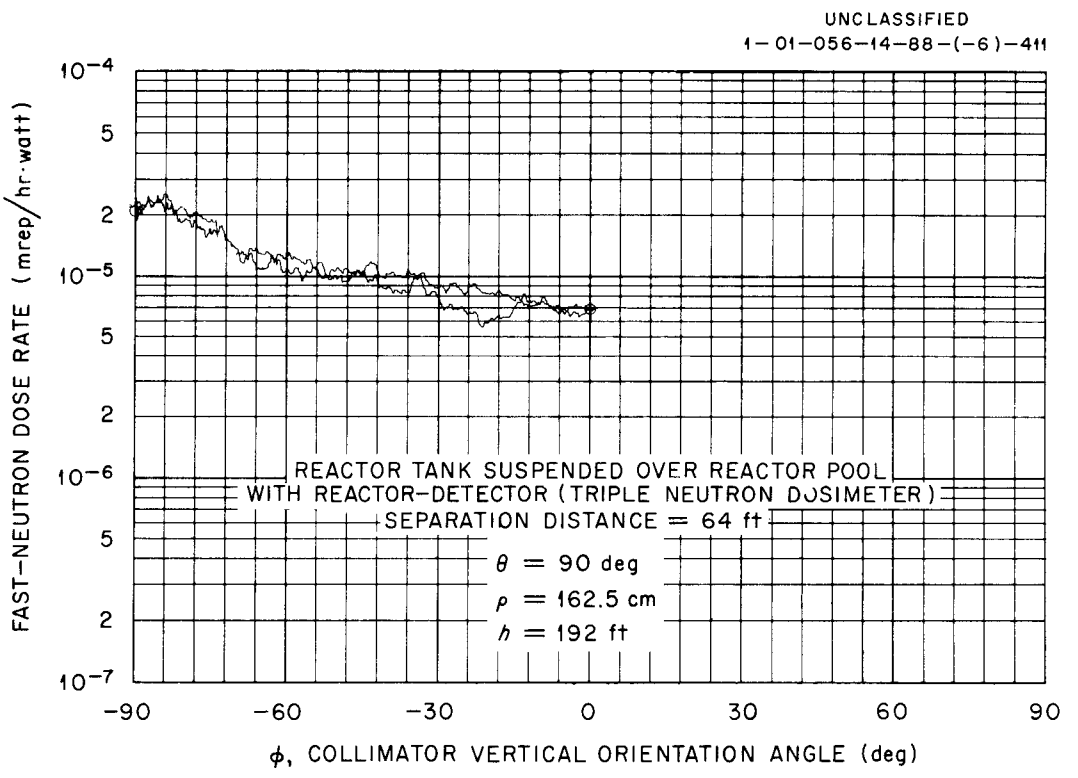

Fig. 9.6.20. Fast-Neutron Dose Rate in Air as a Function of ϕ for 15-in.-dia Collimator ($\theta = 90$ deg).

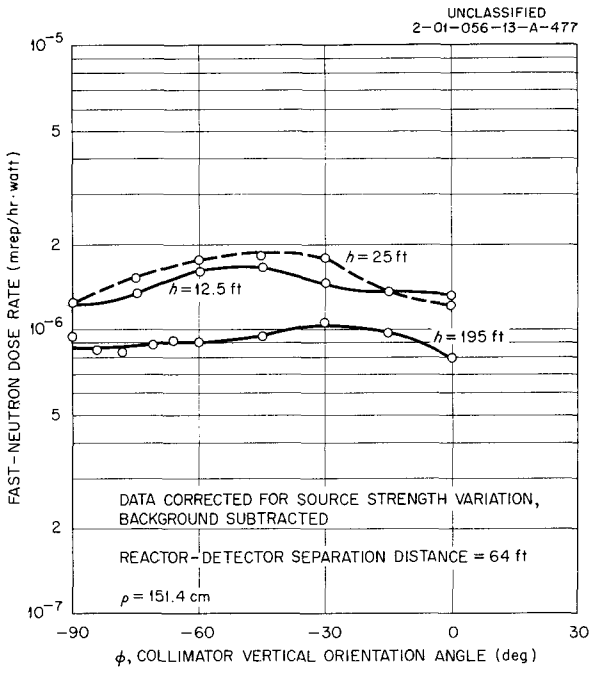

Fig. 9.6.21. *Fast-Neutron Dose Rate in Air as a Function of ϕ for 8-in.-dia Collimator (θ = 90 deg; h = 12.5, 25, and 195 ft).*

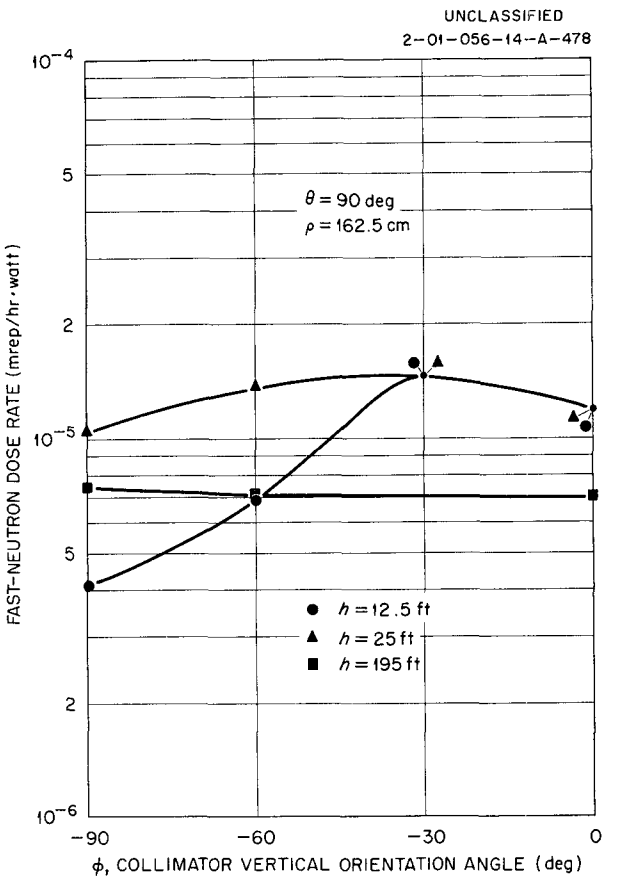

Fig. 9.6.22. Fast-Neutron Dose Rate in Air as a Function of ϕ for 15-in.-dia Collimator (θ = 90 deg; h = 12.5, 25, and 195 ft).

9.7. DETERMINATION OF GAMMA-RAY DOSE RATES AND SPECTRA FROM SOIL AND CONCRETE SAMPLES AFTER IRRADIATION AT THE TOWER SHIELDING FACILITY

F. J. Muckenthaler
J. L. Hull
W. R. Champion[1]
V. R. Cain

Four samples of concrete and one sample of soil were irradiated at the Tower Shielding Facility (TSF) for determining the amount of activation and which components were responsible for the activation. The soil sample was contained in a wooden box 3 × 3 × 1 ft, and the concrete samples were of the same size. The concrete samples consisted of one of plain concrete, one of barytes concrete, and one of each type containing an admixture of 1% boron. They were exposed, in the geometry shown in Fig. 9.7.1, for 20 hr to the radiation from the Tower Shielding Reactor (TSR) operating at a power of 400 kw. The reactor had only 13.7 cm of water and ½ in. of boral as a shield, and the fast-neutron dose rate measured on top of the soil sample was 0.986 erg/g·hr·w. The dose rate measured on top of one of the concrete samples (No. 325) was 0.725 erg/g·hr·w. A $\cos^4 \theta$ angular distribution was used to calculate the dose rates at the other sample positions, and the result was also 0.725 erg/g·hr·w. The unborated samples (Nos. 237 and 321) were placed next to the reactor to minimize any effect of the boron on the other samples (Nos. 296 and 325), and all the samples were surrounded with concrete blocks to simulate the conditions of the facility.

The arrangement shown in Fig. 9.7.2 was used in measuring the gamma-ray intensity from the irradiated samples. Figures 9.7.3 to 9.7.7 show the gamma-ray intensity from the various blocks as a function of the horizontal distance from the center of the block. A good estimate for the background in these runs would be approximately 15 counts/min, as indicated in Fig. 9.7.7. The dose rates for these curves can be calculated by multiplying the count rate by the tissue dose rate factor, 2.3×10^{-4} erg/g·count.

Figure 9.7.8 shows the gamma-ray dose rate measurements at a point directly above the blocks as a function of time after shutdown. Because all

[1]On assignment from Lockheed Aircraft Corp.

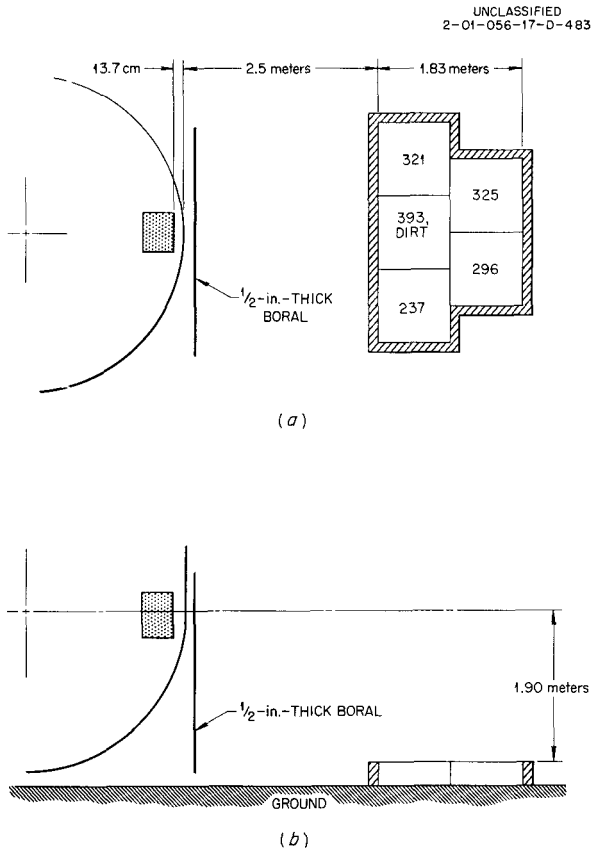

Fig. 9.7.1. Geometry for Irradiation of Concrete and Soil Samples. (*a*) Top view; (*b*) side view.

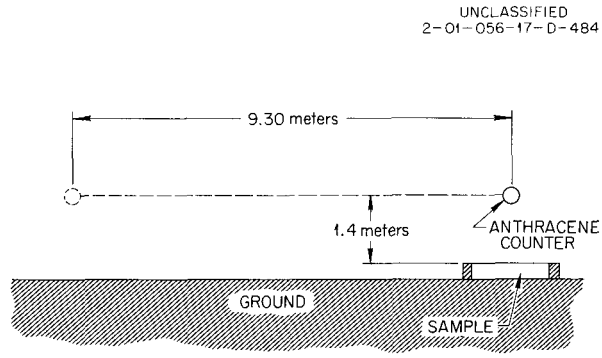

Fig. 9.7.2. Geometry for Measurement of Gamma-Ray Intensity from Irradiated Concrete and Soil Samples.

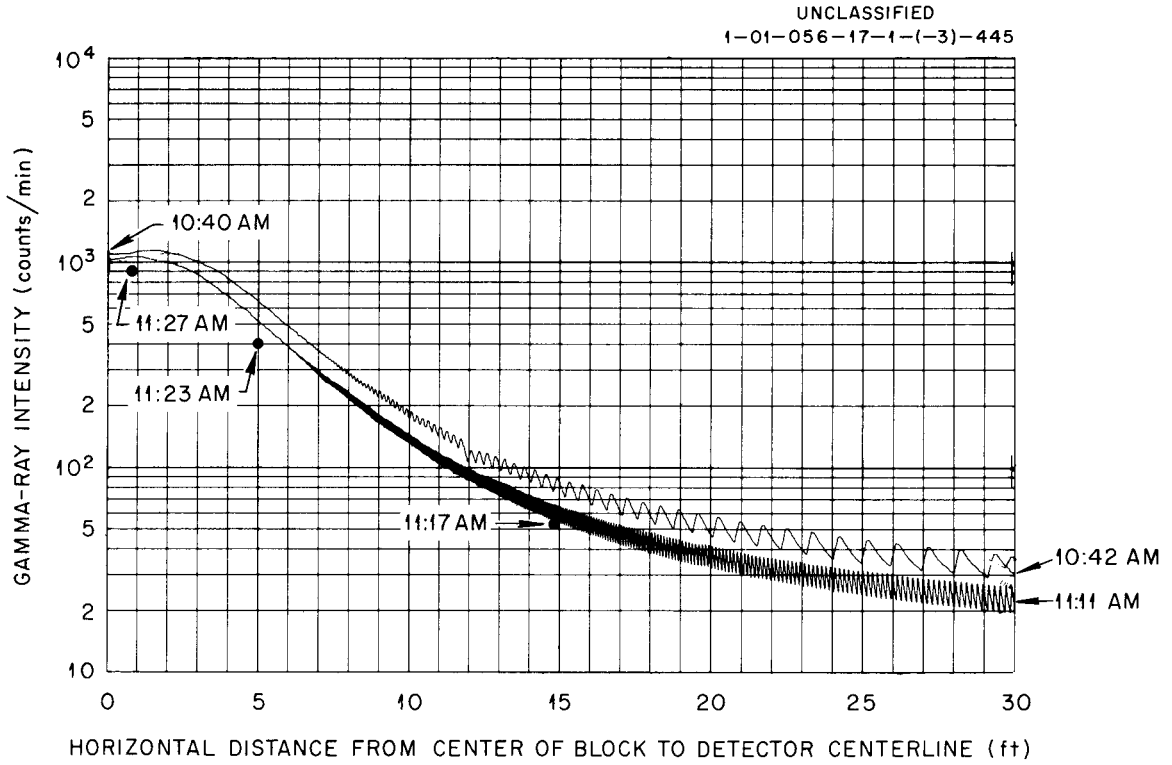

Fig. 9.7.3. Gamma-Ray Intensity as a Function of Distance from Barytes Concrete (Unborated) Sample No. 237.

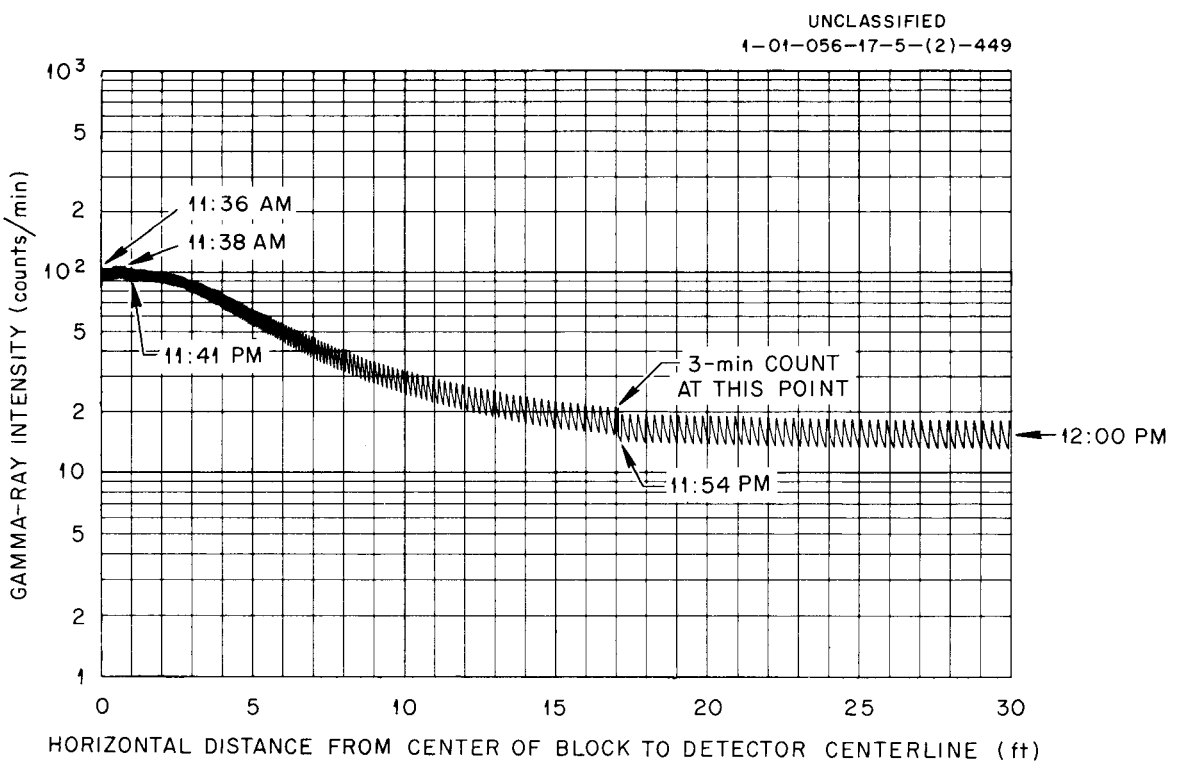

Fig. 9.7.4. Gamma-Ray Intensity as a Function of Distance from Borated Barytes Concrete Sample No. 296.

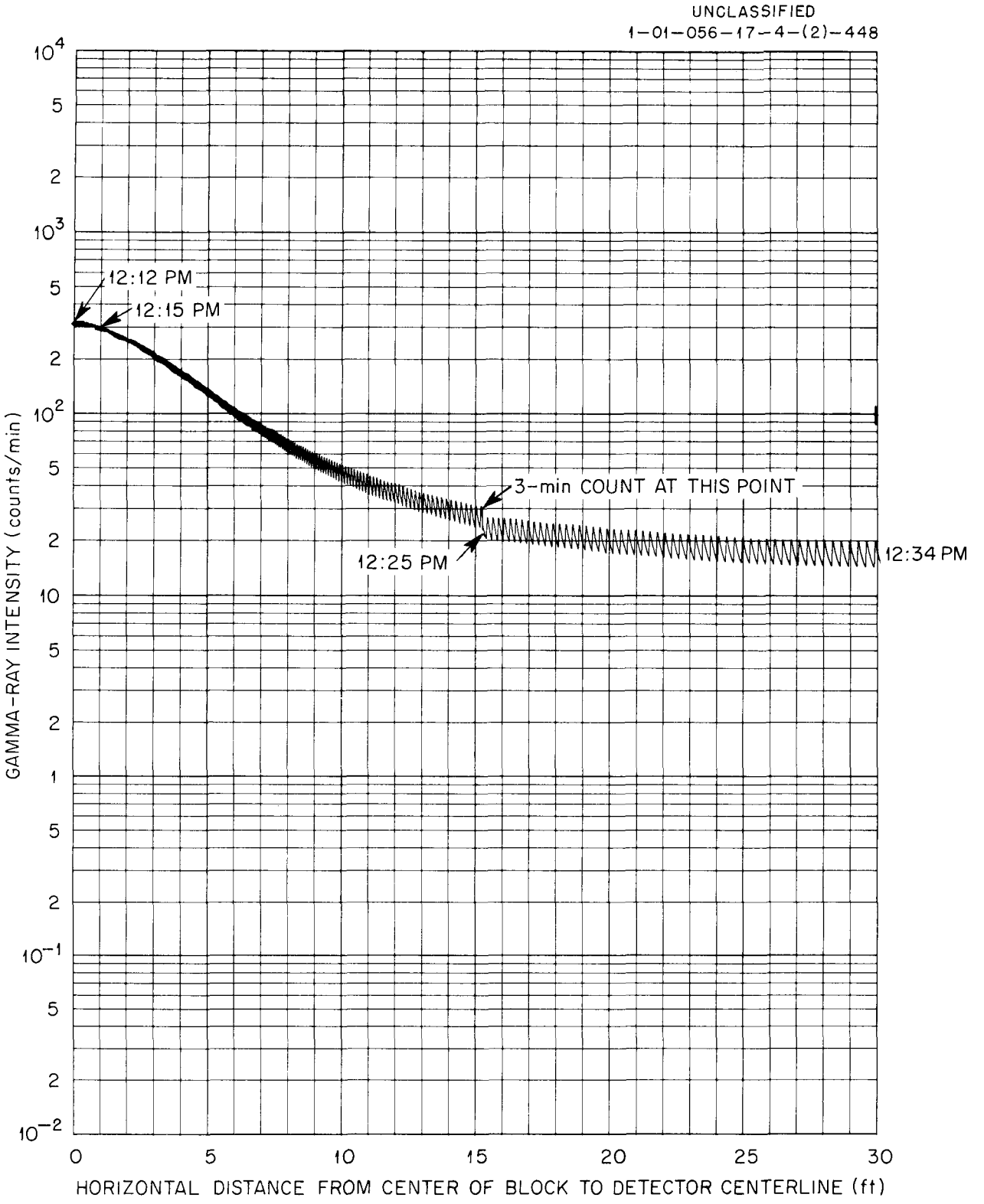

Fig. 9.7.5. Gamma-Ray Intensity as a Function of Distance from Soil Sample No. 393.

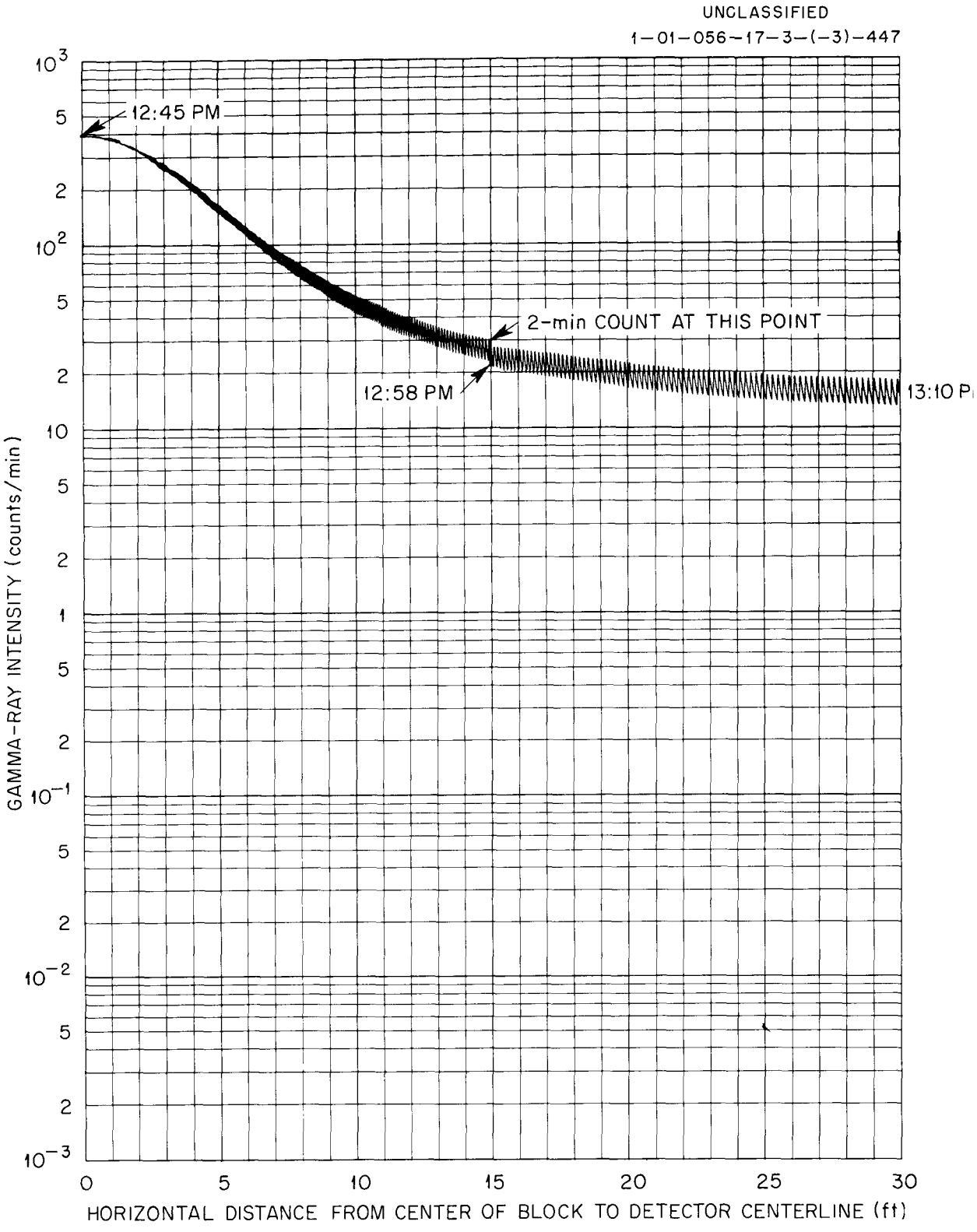

Fig. 9.7.6. Gamma-Ray Intensity as a Function of Distance from Plain Concrete (Unborated) Sample No. 321.

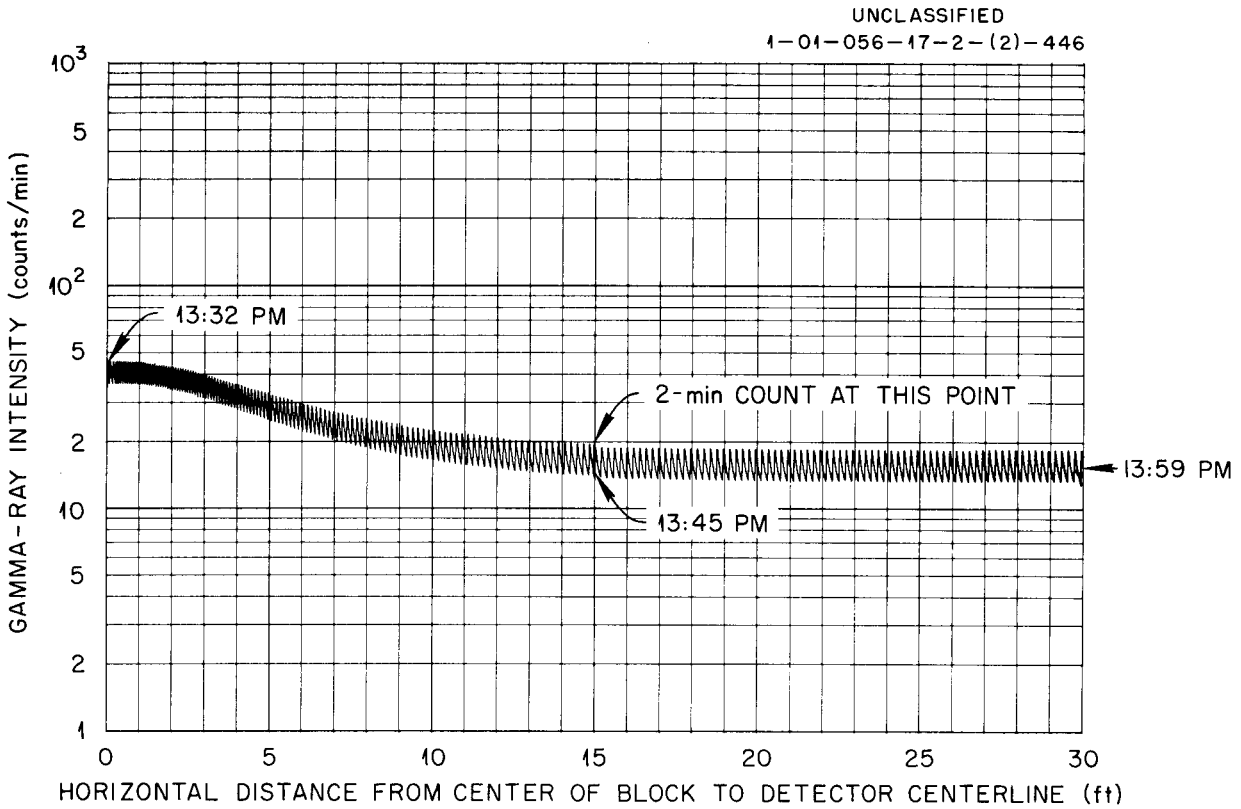

Fig. 9.7.7. Gamma-Ray Intensity as a Function of Distance from Borated Plain Concrete Sample No. 325.

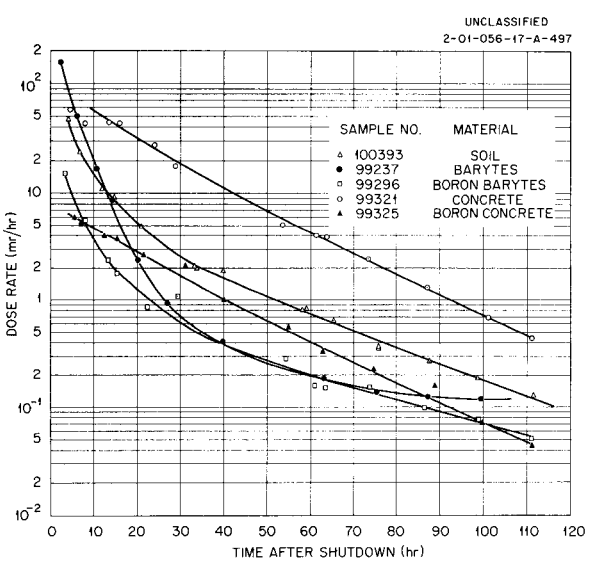

Fig. 9.7.8. Gamma-Ray Dose Rates Directly Above Irradiated Samples as a Function of Time After Shutdown.

the samples did not have the same rate of decay, it is possible to make comparisons only at a specific time after irradiation. For the barytes concrete and soil samples a large part of the gamma-ray dose rate 4 hr after shutdown was due to a thermal (n,γ) reaction in Mn^{55}. Between 24 and 100 hr after shutdown the main contribution was from the same reaction in Na^{23}. For the plain concrete samples the gamma-ray dose rate throughout the first 100 hr after irradiation was also due to the thermal (n,γ) reaction in Na^{23}. The higher neutron dose rate at the soil sample was not considered in these comparisons.

Samples from these blocks were also irradiated in the ORNL Graphite Reactor for longer periods (approximately 80 hr) in order to study the rate of gamma-ray decay over an extended period of time. Owing to a very long half life, estimated at several hundred days, this analysis is not complete, but it is hoped that the final results will enable the contribution from each element to be calculated.

It should be mentioned, however, that this long half life appears only in the barytes concrete and soil samples.

A 3 by 3 in. NaI crystal and a 20-channel analyzer were used to measure a pulse-height spectrum of the gamma rays from the irradiated samples of plain concrete containing boron. A Zn^{65} gamma-ray source was used for calibration of the detector. The geometry for this measurement is shown in Fig. 9.7.9; the gamma-ray intensity from the sample determined the separation distance between the crystal and sample. The resulting pulse-height spectrum (Fig. 9.7.10) again indicated that, for energies above 1 Mev, the thermal (n,γ) reaction in Na^{23} is the main contributor to the gamma-ray dose rate >24 hr after shutdown.

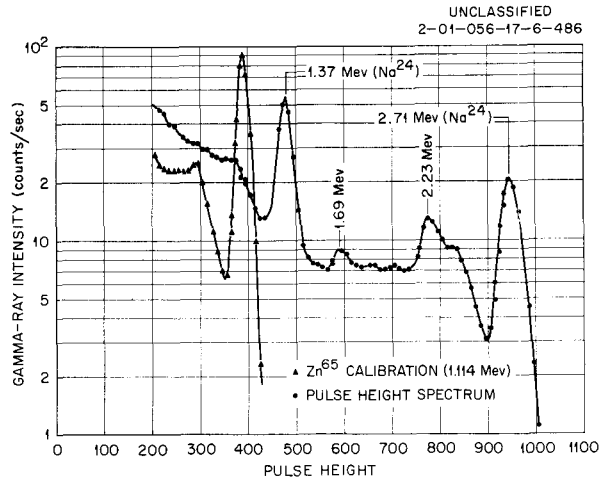

Fig. 9.7.10. Typical Spectrum of Gamma Rays from an Irradiated Concrete Sample 28 hr After Shutdown (Borated Concrete Sample No. 325).

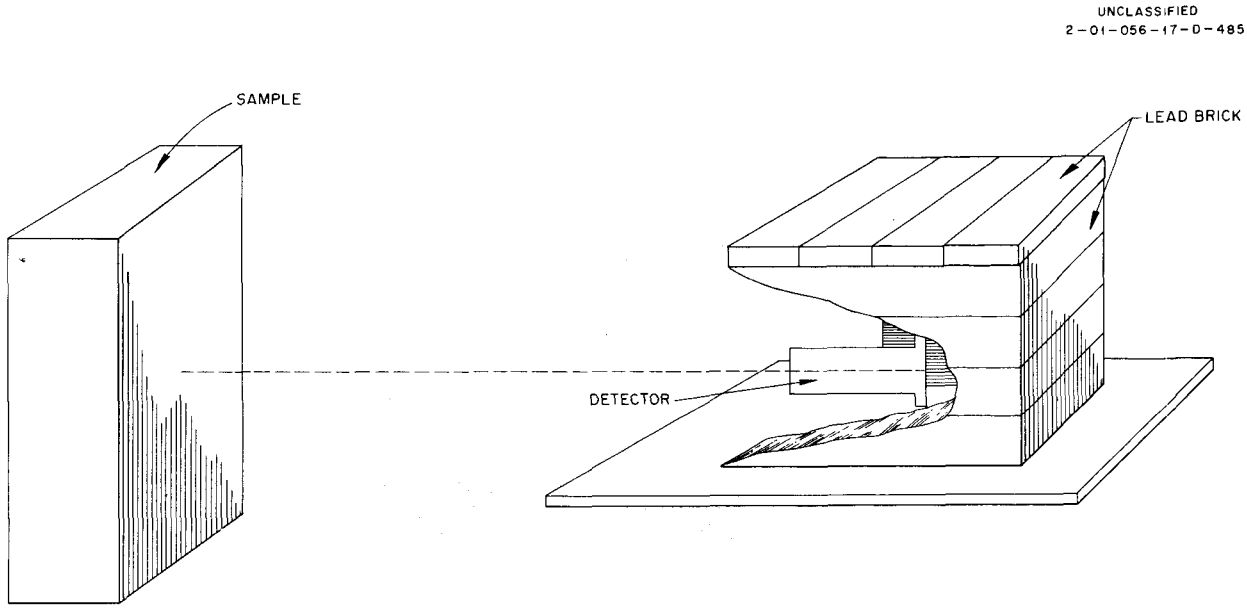

Fig. 9.7.9. Geometry for Measurement of Gamma-Ray Spectra of Irradiated Concrete and Soil Samples.

9.8. SUMMARY OF MONTE CARLO CALCULATIONS OF GAMMA-RAY PENETRATION IN VARIOUS MULTIREGION SHIELDS WITH SLAB GEOMETRY

S. Auslender[1] A. T. Futterer[1]

Partial results of a Monte Carlo calculation of the gamma-ray penetration of lead and water slab shields were reported previously.[2] The information obtained directly from the calculation, which was coded for computation on the Oracle, included dose rate, energy flux, and energy deposition. Dose rate and energy buildup factors, as well as heating in the shield, were obtainable from the results. For these first calculations total composite slab thicknesses of 1 and 2 mean free paths (mfp) were used. The initial energy of the gamma rays was considered to be either 1 or 3 Mev, and the angles of incidence of the gamma rays were assumed to be 0, 60, 70.5, or 75.5 deg.

Since the first calculations were reported, similar calculations have been carried out for other two-region lead and water shields, and the entire series has been designated as the DO2C55 series. In addition, the gamma-ray penetration of other types of shields has been determined with the same machine code. Since inclusion of the results of all the calculations in this report would be impractical, only a summary of the various types of problems is presented here; the detailed results will be reported elsewhere.[3] The summary (Table 9.8.1) designates the materials, thicknesses, gamma-ray energies, and angles of incidence investigated. Two studies were carried out to determine the penetration of Cs^{137} and Co^{60} gamma rays through slabs of polyethylene and lead and were designated as CE137 and COB60 series, respectively. The primary purpose of these calculations was to establish the validity of the calculational method by comparing calculated results with results obtained in an experiment. The particular experiment chosen was performed by the National Bureau of Standards.[4] The two types of results were in good agreement.

Another calculation, designated the FAB series, was performed to determine the effect of the extent of lamination in a shield consisting of a total of 16 cm of water and 4 cm of lead. The materials were subdivided and alternated (2 to 16 regions) to mock up the progression toward a homogeneous shield.

An extensive study of shields consisting of 7, 14, and 21 cm of water was designated as AB series for shields with a 0.1-in.-thick lead backing and as AO series for shields without the lead backing. Calculations were performed for seven gamma-ray energies and seven incident angles. Initial histories ranged in number from 1000 to 2500 for incident angles less than 60 deg. For greater angles the number of histories ranged from 400 to 800 to avoid excessive machine time. In all cases a doubling technique was used, which tends to maintain an even population throughout the shield, to allow statistics to be obtained near the final boundary without the excessively large initial histories which would have otherwise been required. The transmitted and reflected energy spectra from this study have been stored in a systematic order on magnetic tape and are available for calculations. The energy spectra give the fraction of the incident energy which may be expected within each of 120 energy-solid angle intervals (that is, 10 energy by 12 angular intervals) for both the reflected and the transmitted energy of each of the 294 cases.

Another set of problems, the B series, was a study of thick lead-and-water shields. The energy spectra for this series were also stored systematically on magnetic tape. The low number of initial histories combined with the large thickness of the shields resulted in poor statistics for the energy spectra information despite the doubling technique.

---

[1] On assignment from Pratt & Whitney Aircraft.

[2] S. Auslender, *Appl. Nuclear Phys. Ann. Rep. Sept. 10, 1956*, ORNL-2081, p 180.

[3] S. Auslender, *Compilations of Monte Carlo Calculations of Gamma-Ray Penetration in Multiregion Shields with Slab Geometry*, ORNL-2310 (to be published).

[4] F. S. Kirn, R. J. Kennedy, and H. O. Wyckoff, *Radiology* 63, 94–104 (1954).

Table 9.8.1. Summary of Monte Carlo Calculations of Gamma-Ray Penetration in Multiregion Shields with Slab Geometry

Series	Shield	Gamma-Ray Energy (Mev)	θ, Angle of Gamma-Ray Incidence (deg)
CE137 (for Cs^{137})[a]	0, 2, 5, 9, or 14 in. of polyethylene + 0, 0.25, or 0.5 in. of Pb	0.661	0
COB60 (for Co^{60})	0, 2, 5, 9, or 14 in. of polyethylene + 0, 0.25, or 0.5 in. of Pb	1.25	0
FAB[b]	16 cm of H_2O + 4 cm of Pb Two sections of 8 cm of H_2O + 2 cm of Pb Four sections of 4 cm of H_2O + 1 cm of Pb Eight sections of 2 cm of H_2O + 0.5 cm of Pb 4 cm of Pb + 16 cm of H_2O Two sections of 2 cm of Pb + 8 cm of H_2O Four sections of 1 cm of Pb + 4 cm of H_2O Eight sections of 0.5 cm of Pb + 2 cm of H_2O	1.0, 3.0, 8.0	0
DO2C55	1 mfp of Pb 0.75 mfp of Pb + 0.25 mfp of H_2O 0.5 mfp of Pb + 0.5 mfp of H_2O 0.25 mfp of Pb + 0.75 mfp of H_2O [c]	1.0, 3.0	0, 60, 70.5, 75.5 (sec θ = 1, 2, 3, 4)
	1 mfp of H_2O 0.75 mfp of H_2O + 0.25 mfp of Pb 0.5 mfp of H_2O + 0.5 mfp of Pb 0.25 mfp of H_2O + 0.75 mfp of Pb	1.0, 3.0	0, 60, 70.5, 75.5 (sec θ = 1, 2, 3, 4)
	2 mfp of Pb 1.5 mfp of Pb + 0.5 mfp of H_2O 1 mfp of Pb + 1 mfp of H_2O 0.5 mfp of Pb + 1.5 mfp of H_2O	1.0	0, 60, 70.5, 75.5 (sec θ = 1, 2, 3, 4)
	2 mfp of H_2O 1.5 mfp of H_2O + 0.5 mfp of Pb 1.0 mfp of H_2O + 1.0 mfp of Pb 0.5 mfp of H_2O + 1.5 mfp of Pb [c]	1.0	0, 60, 70.5, 75.5 (sec θ = 1, 2, 3, 4)
	8 mfp of Pb 6 mfp of Pb + 2 mfp of H_2O 4 mfp of Pb + 4 mfp of H_2O 2 mfp of Pb + 6 mfp of H_2O	3.0	0, 60, 70.5 (sec θ = 1, 2, 3)
AO	7, 14, or 21 cm of H_2O	0.5, 1.0, 2.0, 3.0, 4.0, 6.0, 8.0	0, 20, 40, 60, 70, 80, 85
AB	7, 14, or 21 cm of H_2O + 0.1 in. of Pb	0.5, 1.0, 2.0, 3.0, 4.0, 6.0, 8.0	0, 20, 40, 60, 70, 80, 85
B[d]	10 or 20 in. of H_2O	1.0, 2.23, 2.70, 4.0, 6.814, 9.0	0, 60, 70
	40 in. of H_2O	1.0, 2.70, 6.814, 9.0	0, 60, 70
	2 in. of Pb + 0, 10, or 20 in. of H_2O	1.0, 2.70, 4.0, 6.814, 9.0	0, 60, 70
		2.23	0, 60

Table 9.8.1 (continued)

Series	Shield	Gamma-Ray Energy (Mev)	θ, Angle of Gamma-Ray Incidence (deg)
B[d]	2 in. of Pb + 40 in. of H_2O	1.0, 2.70, 6.814, 9.0	0, 60, 70
	4 in. of Pb + 0, 10, or 20 in. of H_2O	1.0	0
		2.23, 4.0, 6.814, 9.0	0, 60
		2.70	0, 60, 70
	4 in. of Pb + 40 in. of H_2O	1.0	0
		2.7	0, 60, 70
		6.814, 9.0	0, 60
	6 in. of Pb + 0, 10, or 20 in. of H_2O	2.70	0, 60, 70
		4.0	0
		6.814, 9.0	0, 60
	6 in. of Pb + 40 in. of H_2O	2.70	0, 60, 70
		6.814, 9.0	0, 60
Undesignated[e]	11.58 cm of Pb + 35.81 cm of H_2O	1.0, 3.0, 6.0	0, 60

[a]"CE" rather than "Cs" is used because no "s" is available on the machine.

[b]Constant total shield thickness with layers consecutively subdivided and alternated to mock up progression from a two-region shield to a homogeneous shield.

[c]Reported previously; see S. Auslender, *Appl. Nuclear Phys. Ann. Rep. Sept. 10, 1956*, ORNL-2081, p 180.

[d]This series had a maximum of 800 histories and a minimum of 400; a doubling technique was used to improve statistics. Even so, the statistics are poor for the thickest slabs at slant penetrations as far as energy spectral data are concerned.

[e]Reported previously; see S. Auslender, *Appl. Nuclear Phys. Ann. Rep. Sept. 10, 1956*, ORNL-2081, p 184; see also S. Auslender, *A Monte Carlo Study of the Gamma-Ray Energy Flux Dose Rate, and Buildup Factors in a Lead-Water Slab Shield of Finite Thickness*, ORNL-2194 (Jan. 10, 1957).

9.9. MONTE CARLO CALCULATION OF GAMMA-RAY PENETRATION OF LEAD-WATER SHIELDS

L. A. Bowman[1] D. K. Trubey

The DO2C55 series mentioned in Sec. 9.8 has been continued, and problems have now been computed for all combinations of the following parameters: slab thicknesses of 1, 2, 4, and 6 mean free paths, consisting of eight varying percentages of lead preceding or following water; initial gamma-ray energies of 1, 3, 6, and 10 Mev; and angles of incidence of 0, 60, 70.5, and 75.5 deg from the normal. A total of 512 problems have now been computed in this series. The results include information on heating, dose rates, and energy fluxes throughout the slabs; energy and angular distributions reflected back by the slabs; and energy and angular distributions transmitted through the slabs.

The data from all these problems are now being analyzed. Typical plots are shown in Figs. 9.9.1 through 9.9.4, which represent the heating caused by 3-Mev incident gamma rays in slabs 4 mean free paths thick. Note that the heating in Figs. 9.9.3 and 9.9.4 is reduced by a factor of 2 for ease in plotting.

[1]On assignment from U. S. Air Force.

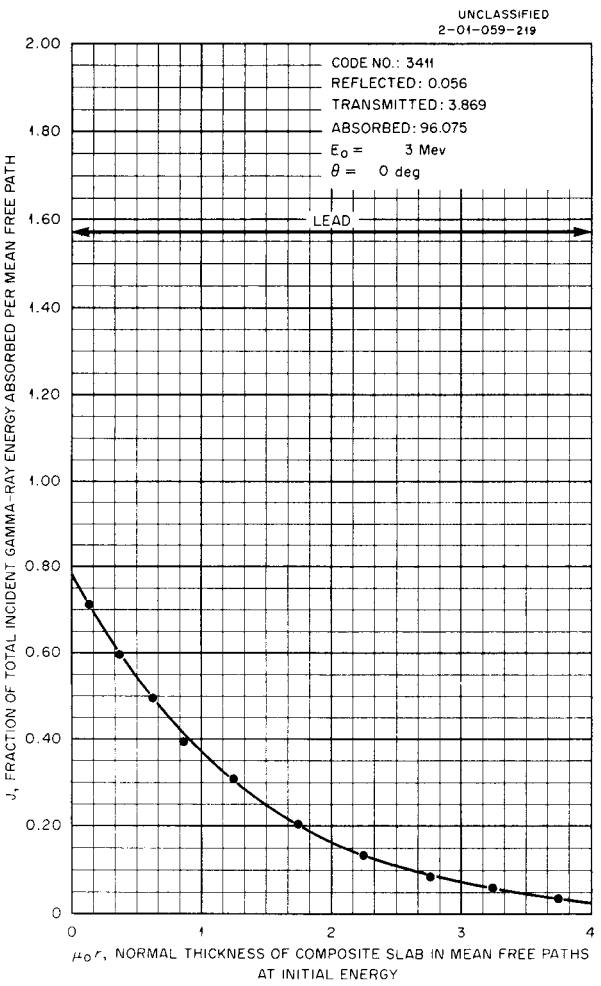

Fig. 9.9.1. Energy Absorption in a Lead Shield as a Function of the Shield Thickness: 3-Mev Gamma Rays Normally Incident.

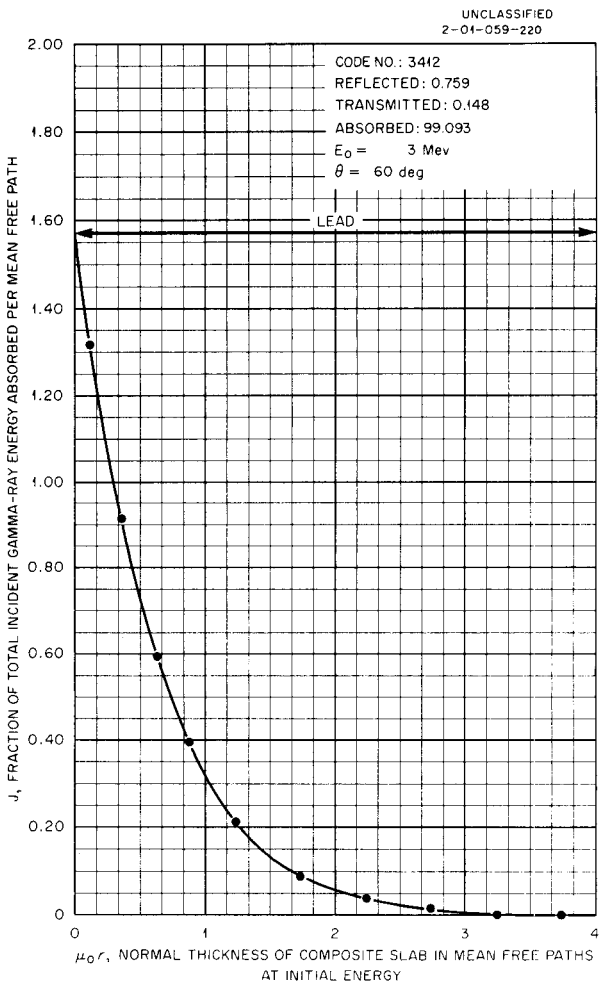

Fig. 9.9.2. Energy Absorption in a Lead Shield as a Function of the Shield Thickness: 3-Mev Gamma Rays Incident at 60 deg.

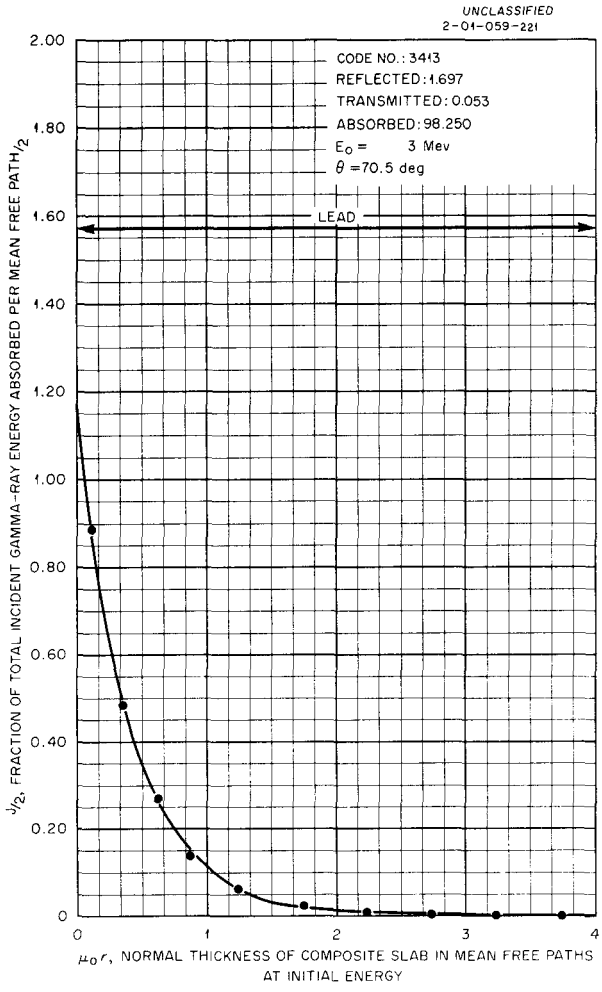

Fig. 9.9.3. Energy Absorption in a Lead Shield as a Function of the Shield Thickness: 3-Mev Gamma Rays Incident at 70.5 deg.

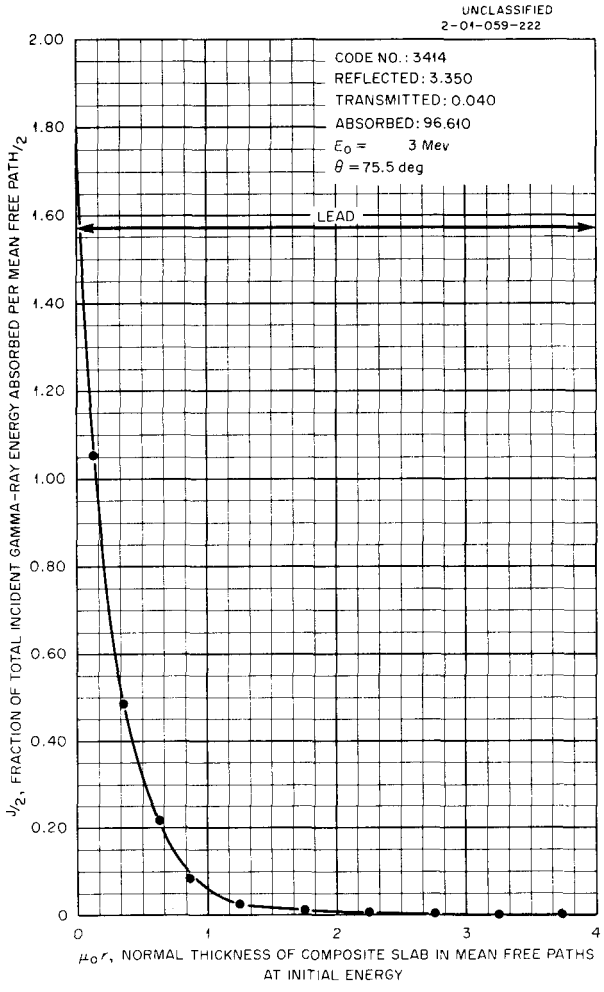

Fig. 9.9.4. Energy Absorption in a Lead Shield as a Function of the Shield Thickness: 3-Mev Gamma Rays Incident at 75.5 deg.

9.10. MONTE CARLO CALCULATION OF GAMMA-RAY PENETRATION OF ALUMINUM SLABS

D. K. Trubey

A Monte Carlo calculation of the energy spectrum and angular distribution of gamma rays which penetrate 3-, 6-, and 9-in.-thick aluminum slabs has been carried out with the Oracle code discussed in Sec. 9.8. For this calculation the gamma rays were assumed to be normally incident upon the slabs and to have initial energies of 0.662 Mev (the energy of Cs^{137} gamma rays).

The energy balance for the three slabs, that is, the fraction of energy reflected, absorbed, or transmitted, is given in Table 9.10.1. The fraction transmitted is further broken down into the uncollided and collided fractions. The transmitted collided-energy fraction is then subdivided into 10 energy groups which are transmitted through 12 angular sectors as shown in Table 9.10.2. Since the incident energy is normal to the slab, there is no dependence on an azimuthal angle. The distribution of the transmitted collided-energy fraction into the various energy groups and angular sectors obtained from the calculation is presented in Tables 9.10.3 through 9.10.5. The total collided energy transmitted per unit solid angle for the three slabs is shown in the histograms in Figs. 9.10.1, 9.10.2, and 9.10.3.

An attempt has been made to fit the histogram plots with analytical expressions. If the distribution is represented by

$$\phi(\theta) = A \cos^b \theta$$

and the energy in each sector is $\phi(i, i+1)$, where $i = 1, 2, \ldots, 13$, then

$$(1) \qquad 2\pi A \int_{\mu_{i+1}}^{\mu_i} \mu^b d\mu = \phi(i, i+1)$$

and

$$(2) \qquad 2\pi A \int_0^1 \mu^b d\mu = N ,$$

where $\mu = \cos\theta$ and N = the total energy transmitted collided. Equation 2 reduces to

$$(3) \qquad \frac{2\pi A}{b+1} = N$$

Table 9.10.2. Angular Sectors and Energy Groups for Transmitted Collided Energy

Angular Sector, S	θ, Polar Angle* (deg)	Energy Group, E	Energy Range (Mev)
1	0–5	1	0–0.03
2	5–10	2	0.03–0.05
3	10–15	3	0.05–0.07
4	15–20	4	0.07–0.09
5	20–25	5	0.09–0.19
6	25–30	6	0.19–0.29
7	30–35	7	0.29–0.39
8	35–40	8	0.39–0.49
9	40–45	9	0.49–0.59
10	50–60	10	0.59–0.662
11	60–70		
12	70–90		

*Angle with the normal.

Table 9.10.1. Fractions of Incident Energy Reflected, Absorbed, and Transmitted

Slab Thickness (in.)	Energy Fraction			
	Reflected	Absorbed	Transmitted	
			Uncollided	Collided
3	0.0477	0.540	0.213	0.199
6	0.0498	0.802	0.0457	0.102
9	0.0483	0.909	0.00977	0.0329

Table 9.10.3. Fraction of Incident Energy Transmitted (Collided) in Energy Group E and Sector S for 3-in.-Thick Aluminum Slab

S	Fraction of Incident Energy										
	$E = 1$	$E = 2$	$E = 3$	$E = 4$	$E = 5$	$E = 6$	$E = 7$	$E = 8$	$E = 9$	$E = 10$	Total
1	0	0	0	0	0.0001268	0.00004886	0	0.00008103	0	0.002545	0.002802
2	0	0	0.00004422	0.0001214	0.0005534	0.0002395	0.0002185	0.0002553	0.0003704	0.007583	0.009386
3	0	0	0.00005692	0.0001443	0.0007589	0.0006092	0.0004436	0.0003113	0.0008273	0.01141	0.01456
4	0	0	0.00008955	0.0002400	0.0009322	0.001012	0.0009466	0.0007345	0.001046	0.01344	0.01844
5	0	0	0.0001136	0.0002382	0.001167	0.0009087	0.0002115	0.001380	0.001411	0.01181	0.01724
6	0	0	0.0001244	0.00018110	0.0009606	0.001033	0.001344	0.001136	0.01356	0.001181	0.01952
7	0	0	0.0001645	0.0002012	0.001573	0.001028	0.0009510	0.001722	0.01308	0.0004495	0.01917
8	0	0	0.0001836	0.0004086	0.001685	0.001071	0.001019	0.001518	0.01319	0	0.01908
9	0	0.00001872	0.0002882	0.0005362	0.003537	0.003130	0.002531	0.01222	0.007077	0	0.02934
10	0	0.000008793	0.0003237	0.0006943	0.003529	0.002386	0.002794	0.01414	0.0008499	0	0.02473
11	0	0.00001838	0.0002007	0.0044540	0.002870	0.001584	0.005738	0.003876	0	0	0.01473
12	0	0.00001828	0.0002145	0.0005365	0.003065	0.001385	0.003609	0.001155	0	0	0.009983
Total	0	0.00006417	0.001804	0.003747	0.0207590	0.014365	0.019807	0.03854	0.05141	0.04842	0.19898

Table 9.10.4. Fraction of Incident Energy Transmitted (Collided) in Energy Group E and Sector S for 6-in.-Thick Aluminum Slab

S	Fraction of Incident Energy										
	$E = 1$	$E = 2$	$E = 3$	$E = 4$	$E = 5$	$E = 6$	$E = 7$	$E = 8$	$E = 9$	$E = 10$	Total
1	0	0	0.00004386	0	0.0001805	0	0.0001698	0	0.00006487	0.001164	0.001623
2	0	0	0	0.00009864	0.0002970	0	0.0002733	0.0004263	0.0001370	0.002511	0.003752
3	0	0	0.00004889	0.00001509	0.0004989	0.0003587	0.0001356	0.0003558	0.0006073	0.005327	0.007347
4	0	0	0.00002740	0.00003203	0.0007486	0.0006221	0.0002833	0.0005175	0.0008115	0.005891	0.008934
5	0	0.00004552	0.00006332	0.0001901	0.0004834	0.0008475	0.0005601	0.001407	0.0003428	0.005755	0.009695
6	0	0.00001986	0.0001945	0.0002363	0.0003369	0.0006139	0.0009168	0.0005214	0.006614	0.0009825	0.01044
7	0	0	0.0001201	0.0002634	0.001028	0.0002668	0.001813	0.0007509	0.008405	0	0.01265
8	0	0.00001183	0.0001232	0.0003411	0.001845	0.001374	0.0007652	0.001347	0.005172	0	0.01098
9	0	0.00004562	0.0003138	0.0006895	0.001695	0.001313	0.001417	0.005916	0.002624	0	0.01401
10	0	0.000005982	0.0002887	0.0002954	0.002164	0.001961	0.001914	0.003420	0.0004832	0	0.01054
11	0	0.000010710	0.00007994	0.0002982	0.001628	0.0008028	0.001932	0.002165	0	0	0.006917
12	0	0	0.0003549	0.0002493	0.001207	0.001075	0.001813	0.0004993	0	0	0.005198
Total	0	0.0001396	0.001659	0.002711	0.01212	0.009243	0.01199	0.01734	0.02526	0.21691	0.10208

Table 9.10.5. Fraction of Incident Energy Transmitted (Collided) in Energy Group E and Sector S for 9-in.-Thick Aluminum Slab

S	Fraction of Incident Energy										
	$E = 1$	$E = 2$	$E = 3$	$E = 4$	$E = 5$	$E = 6$	$E = 7$	$E = 8$	$E = 9$	$E = 10$	Total
1	0	0	0	0.00001919	0.00001206	0	0.00001067	0.00009016	0	0.0005113	0.0006434
2	0	0	0.000002177	0	0.0001452	0.00002060	0.00003799	0	0.00002669	0.001168	0.001400
3	0	0	0.00001126	0.00004094	0.0001060	0.00001336	0.00002675	0.00005468	0.0004522	0.001172	0.001877
4	0	0	0.00003177	0.00003686	0.0001807	0.0002683	0.00002514	0.0006556	0.0003300	0.001517	0.003045
5	0	0	0.00007779	0.00023096	0.0002761	0.0002738	0.0002246	0.0002301	0.0006285	0.001189	0.003131
6	0	0	0.00002119	0.0001118	0.0004371	0.0001221	0.0004751	0.0008794	0.001685	0.0001525	0.003885
7	0	0.000001519	0.000009835	0.00002760	0.0003723	0.0003694	0.0001137	0.0001820	0.001323	0.0002243	0.002623
8	0	0.00001083	0.00002665	0.00004738	0.0006920	0.0007257	0.0001406	0.0002184	0.001169	0	0.003031
9	0	0	0.0001301	0.0001344	0.0006778	0.0008160	0.0003914	0.0009388	0.002061	0	0.005149
10	0	0.000003086	0.0001184	0.0001807	0.0011319	0.0006917	0.0007707	0.001425	0.0001359	0	0.004457
11	0	0.00001308	0.00009961	0.0001479	0.0004565	0.0002915	0.0007973	0.0003005	0	0	0.002106
12	0	0.000000630	0.00003136	0.00008799	0.0005692	0.0006130	0.0002602	0.00003278	0	0	0.001595
Total	0	0.00002914	0.0005602	0.0010658	0.005057	0.004206	0.003274	0.005007	0.007811	0.005934	0.3294

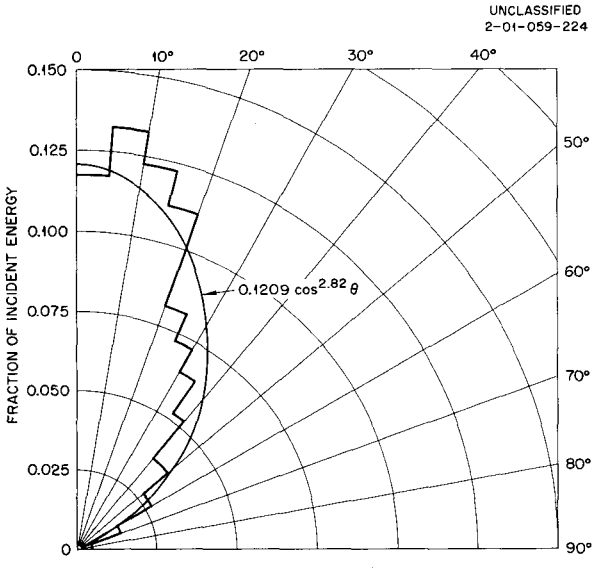

Fig. 9.10.1. Fraction of Incident Energy Transmitted (Collided) per Unit Solid Angle: 0.662-Mev Gamma Rays Normally Incident on a 3-in.-Thick Aluminum Slab.

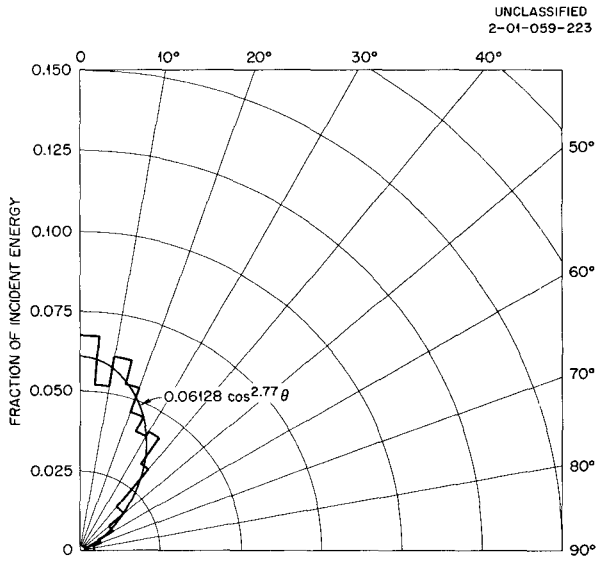

Fig. 9.10.2. Fraction of Incident Energy Transmitted (Collided) per Unit Solid Angle: 0.662-Mev Gamma Rays Normally Incident on a 6-in.-Thick Aluminum Slab.

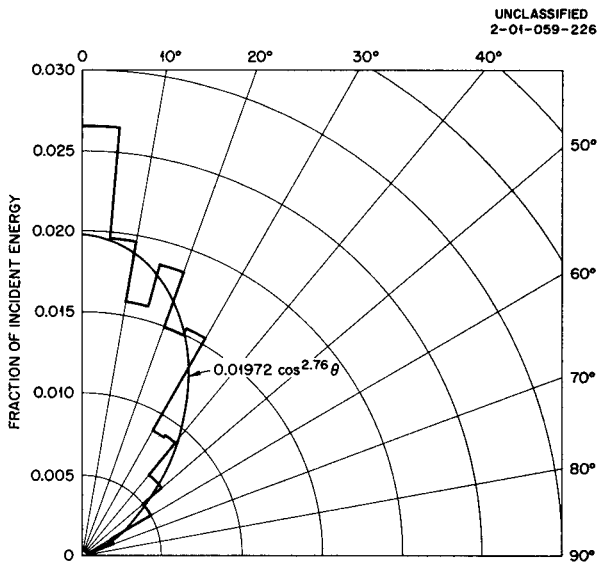

Fig. 9.10.3. Fraction of Incident Energy Transmitted (Collided) per Unit Solid Angle: 0.662-Mev Gamma Rays Normally Incident on a 9-in.-Thick Aluminum Slab.

and Eq. 1 reduces to

$$N\left(\mu_i^{b+1} - \mu_{i+1}^{b+1}\right) = \phi(i, i+1) \tag{4}$$

or

$$\mu_{i+1}^{b+1} = \mu_i^{b+1} - \frac{\phi(i, i+1)}{N}$$

for $\mu_1 = 1$, $\mu_{13} = 0$; therefore

$$\mu_j^{b+1} = 1 - \sum_{i=1}^{j-1} \frac{\phi(i, i+1)}{N}, \quad \text{for } j \neq 1, 13 . \tag{5}$$

Equation 5 may then be used to get 11 estimates of b. It was found that b did not vary greatly, and so an average was used to determine A from Eq. 3. The resulting equations, $\phi = A \cos^b \theta$, are also shown in Figs. 9.10.1 through 9.10.3 and indicate no change in the angular distribution with slab thickness.

9.11. MONTE CARLO CALCULATION OF THE ENERGY AND ANGULAR DISTRIBUTION OF AIR-SCATTERED NEUTRONS FROM A MONOENERGETIC SOURCE

C. D. Zerby

The calculation of the energy and the angular distribution of air-scattered neutrons by the Monte Carlo method[1] was completed. The problem was idealized to have the source and a point detector, with the geometry shown in Fig. 9.11.1, suspended in an infinite body of air. The source was located on an absorbing sphere of diameter D_0, where the axis of symmetry of the radiation leaving the sphere had an angle θ_0 with respect to the source-detector axis. The distribution of source radiation about the symmetry axis was taken as $[(J + 1)/2] \cos^J \theta$ per unit solid angle. The values of D_0, θ_0, J, and the separation distance g were assigned arbitrarily. In particular, D_0 was assigned the value 0 ft, which resulted in a point source, and 12 ft; J was assigned a value of infinity to give a monodirectional beam; and g was considered to be 64 ft. The values of the density of the air and the amount of moisture in the air were allowed to vary.

The cross sections used for oxygen, nitrogen, and hydrogen were taken from BNL-325.[2] The scattering was considered to be isotropic in the center-of-mass system.

The Monte Carlo method used for this computation differed from the straight analog procedure in that a process of statistical estimation was incorporated. This amounted to summing the probabilities that a neutron would pass through the detector after each of its collisions. The distribution of collisions after the first collision was generated by using standard Monte Carlo methods. The contribution of first-scattered particles to the detector response was calculated systematically in order to approximate a numerical solution.

In order to test this statistical calculation against numerical solutions, the code was altered to duplicate the one-velocity transport equation for an isotropic point source in an infinite, homogeneous medium. The scattering was taken to be isotropic in the laboratory system, and test problems were run for several source-detector separation distances. The results of these test problems are shown in Fig. 9.11.2 and are compared with the numerical solutions given by Case, de Hoffmann, and Placzek.[3] In one set of problems a ratio of the macroscopic scattering cross section to the total macroscopic cross section of 1.0 was used, while in the other set a ratio of 0.9 was used. In

[1] C. D. Zerby, *Appl. Nuclear Phys. Ann. Rep. Sept. 10, 1956*, ORNL-2081, p 180.

[2] D. J. Hughes and J. A. Harvey, *Neutron Cross Sections*, BNL-325 (July 1, 1955).

[3] K. M. Case, F. de Hoffmann, and K. M. Placzek, *Introduction to the Theory of Neutron Diffusion*, vol. 1, U. S. Government Printing Office, Washington, 1953.

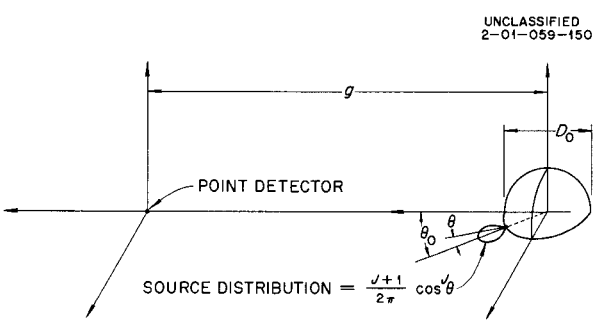

Fig. 9.11.1. Geometry Used for Neutron Air-scattering Problem.

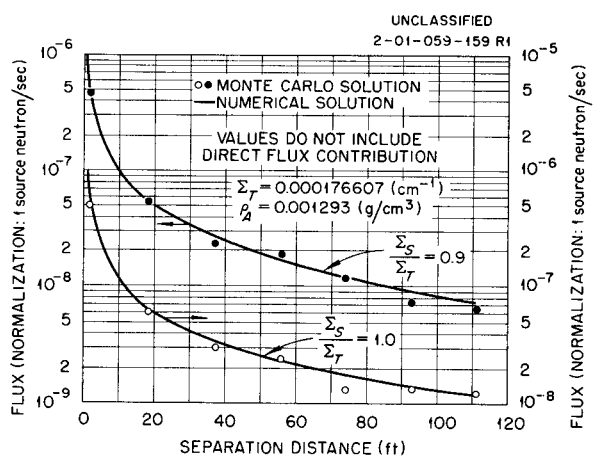

Fig. 9.11.2. Comparison of Numerical and Monte Carlo Solutions of the One-Velocity Boltzmann Equation for an Isotropic Point Source of 1-Mev Neutrons in Infinite Air (Scattering Taken as Isotropic in the Laboratory System; Density of the Air = 0.001293 g/cm^3).

both cases only that portion of the flux which was contributed by particles that had made one or more collisions is presented. In almost every case the error between the statistically determined values and the numerically determined values is less than 10% out to separation distances of 0.6 mean free path. This is of particular interest since the error indicates the error that may be expected when a problem is calculated by using energy degradation and isotropic scattering in the center-of-mass system.

A set of problems was then calculated for a source-detector separation distance of 64 ft. These calculations included energy degradation and isotropic scattering in the center-of-mass system. In every case the source was taken as a line beam of monoenergetic neutrons. For one set of problems the diameter of the absorbing sphere was considered to be zero; that is, the source was a point source. In the other set the diameter of the sphere on which the point source was located was considered to be 12 ft. The source energies included in the calculation were 0.55, 1.2, 2, 3, and 5 Mev. For the point source, θ_0 was considered to be 2, 15, 30, 60, 90, 135, and 180 deg. For the point source on the 12-ft-dia sphere θ_0 was considered to be 15, 90, 135, and 180 deg. The results of these calculations included the energy and angular distribution of the neutrons at the detector.

The energy flux at the detector for a source energy of 3 Mev is shown in Fig. 9.11.3. In this figure the flux values do not include the direct flux. The lower curve shows the marked depression in the energy flux caused by the absorbing sphere shielding the detector. It is to be noted that at $\theta_0 = 180$ deg the scattered energy flux for the point source was 0.2324×10^{-8} when normalized to a unit energy source. The results of the calculation showed that the single-scattering contribution for the point source was only 0.1217×10^{-8}. This is to be compared with the value of 0.915×10^{-9} for the sources on the absorbing sphere.

Figure 9.11.4 shows the fractional contribution to the scattered energy flux by neutrons which have scattered one, two, and three times. This set of data was obtained from the 3-Mev point source cases shown in Fig. 9.11.3.

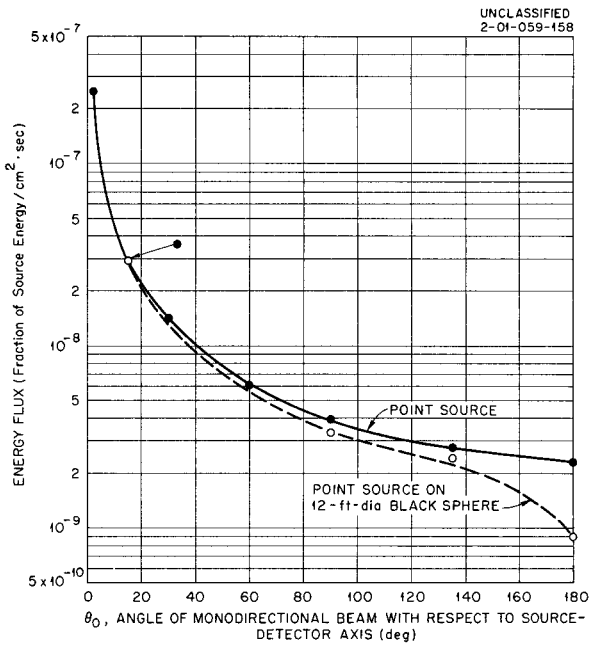

Fig. 9.11.3. Energy Flux of Air-scattered Neutrons from a Monodirectional Beam of 3-Mev Neutrons at a Source-Detector Separation Distance of 64 ft (Density of the Air = 0.001250 g/cm^3).

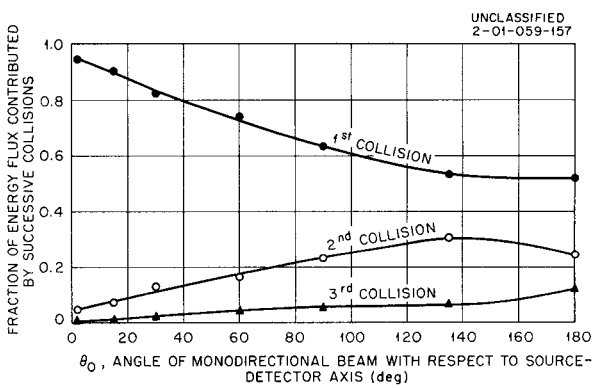

Fig. 9.11.4. Fraction of Energy Flux of Air-scattered Neutrons from a Point, Monodirectional Beam of 3-Mev Neutrons Contributed by Successive Collisions at a Source-Detector Separation Distance of 64 ft (Density of the Air = 0.001250 g/cm^3).

9.12. ANALYSIS OF MONTE CARLO CALCULATION OF AIR-SCATTERED NEUTRONS FROM A MONOENERGETIC SOURCE

J. Hilgeman[1] F. L. Keller
C. D. Zerby

Analysis of the results of the calculations presented in Sec. 9.11 shows that the total air-scattered flux, ϕ, at a detector placed a distance g from a source from which a 1-neutron/sec line beam of initial energy E_0 leaves at an angle θ_0 may be represented by the relation

$$\phi = \frac{\Sigma_s(E_0)}{4\pi g} \frac{\pi - \theta_0}{\sin \theta_0},$$

where $\Sigma_s(E_0)$ is the macroscopic scattering cross section of air at the initial energy, E_0. This is the same relation that is obtained from an analytical calculation of the single-scattered flux from a line beam under the assumption that the scattering is isotropic in the laboratory system and that there is no material attenuation. It was also found that the total air-scattered dose rate, D, at the detector may be represented by

$$D = \frac{C(E_0)}{1.2} \frac{\Sigma_s(E_0)}{4\pi g} \frac{\pi - \theta_0}{\sin \theta_0},$$

where $C(E_0)$ is the flux-to-dose rate conversion factor at the initial energy, E_0. Of course, the angular distribution and energy spectra of the neutrons which arrive at the detector differ considerably from the results obtained from single-scattering calculations which assume isotropic scattering in the laboratory system and neglect attenuation and energy degradation. The discrepancy naturally increases with increasing θ_0. Representative plots of angular distributions and energy spectra at the detector will be included in a topical report.[2]

[1] On assignment from the U.S. Air Force.

[2] J. Hilgeman, F. L. Keller, and C. D. Zerby, *Monte Carlo Calculations of Fluxes and Dose Rates Resulting from Neutrons Multiply Scattered in Air*, ORNL-2375 (to be published).

9.13. CALCULATION OF AIR-SCATTERED NEUTRON DOSE RATES AROUND A CYLINDRICALLY SYMMETRIC SOURCE

C. A. Goetz[1]

A code has been written for the Oracle with which the neutron dose rate around a cylindrically symmetric source can be calculated. The detector is located a distance g from the source and at an angle ψ with respect to the axis of symmetry of the source distribution. The geometry for the calculation is illustrated in Fig. 9.13.1. In this figure α is the angle between a particular neutron direction, $\vec{\Omega}$, and the axis of symmetry of the source; and θ_0 is the angle between $\vec{\Omega}$ and the source-detector axis. The angle ϕ is the azimuthal angle between the axis of symmetry of the source and $\vec{\Omega}$, as measured from the source-detector axis.

UNCLASSIFIED
2-01-060-24

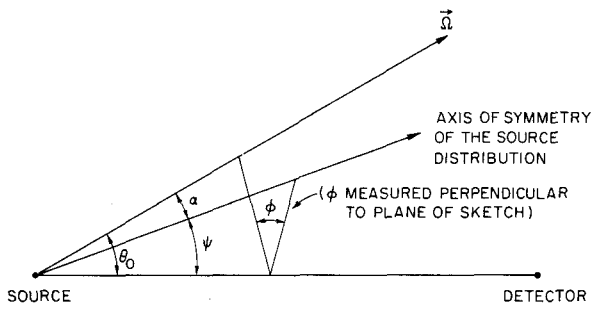

Fig. 9.13.1. Geometry for Calculation of Air-scattered Neutron Dose Rates Around a Cylindrically Symmetric Source.

The air-scattered neutron dose rates obtained in the Monte Carlo calculation discussed in Secs. 9.11 and 9.12 are used in this calculation. These dose rates are denoted as $P(g, E_0, \theta_0)$, which can be represented by

$$P(g, E, \theta) = \frac{A(E_0)}{g} \frac{\pi_0 - \theta_0}{\sin \theta_0} ,$$

where

$A(E_0) = C(E_0)\, \Sigma_s(E_0)/4.8\pi$,

$\Sigma_s(E_0)$ = macroscopic scattering cross section of air at the initial energy, E_0, cm^{-1},

$C(E_0)$ = neutron flux-to-dose conversion factor at the initial energy, E_0, (mr/hr)/(neutrons/cm^2·sec).

Hence, if the energy spectrum of the neutrons which leave the source is not strongly dependent upon the angle α, then the following average may be defined:

$$\bar{A} = \frac{\int A(E_0)\, N(E_0)\, dE_0}{\int N(E_0)\, dE_0} ,$$

where $N(E_0)$ is the energy distribution of the source neutrons. Actually, $A(E_0)$ is fairly consistent for fast neutrons so that the value of $\bar{A}$ is not extremely sensitive to the shape of $N(E_0)$.

If a source strength, $S(\alpha)$, is defined such that $S(\alpha)\, d\Omega$ is the number of neutrons per second which leave in the element of solid angle $d\Omega$ about $\vec{\Omega}$, then the air-scattered neutron dose rate at the detector, $D(\psi, g)$, may be expressed as:

$$D(\psi, g) = \int_{\theta=0}^{\pi} \int_{\phi=0}^{2\pi} S(\alpha)\, \bar{P}(g, \theta_0) \sin \theta_0\, d\theta_0\, d\phi ,$$

where

$$\bar{P}(g, \theta_0) = \frac{\bar{A}}{g} \frac{\pi - \theta_0}{\sin \theta_0}$$

and

$$\cos \alpha = \cos \theta \cos \psi + \sin \theta \sin \psi \cos \phi .$$

Thus

$$D(\psi, g) = \frac{\bar{A}}{g} \int_{\theta=0}^{\pi} (\pi - \theta_0) \int_{\phi=0}^{2\pi} S[\alpha(\theta, \psi, \phi)]\, d\phi\, d\theta .$$

The source strength, $S(\alpha)$, is entered into the machine in tabular form, and the machine then carries out this double integration for any specified value of ψ.

[1]On assignment from Pratt & Whitney Aircraft.

9.14. MONTE CARLO CALCULATION OF AIR-SCATTERED GAMMA RAYS

R. E. Lynch[1] W. P. Johnson[1]
J. W. Benoit[1] C. D. Zerby

A Monte Carlo calculation of air-scattered gamma rays has recently been completed. The purpose of the calculation was to provide detailed information about the angular distribution and energy spectrum of multiply scattered gamma rays at various positions in the air. For general utility, the problem was idealized to have a point monodirectional, monoenergetic source in an infinite body of air, and a series of calculations were carried out in which the following parameters were varied: the energy of the gamma rays leaving the source; the angle between the beam of gamma rays and the source-detector axis; and the distance between the source and the detector. The particular initial conditions selected for computations were beam angles of 1, 15, 30, 60, 90, 135, and 180 deg; source energies of 0.6, 1, 2, 4, 7, and 12 Mev; and source-detector separation distances of 5, 10, 20, 40, 65, and 100 ft. All the problems were completed for an air density of 0.00125 g/cc, but the results can be transformed to apply to other air densities by use of a transformation which has been described elsewhere.[2]

The detailed results of the calculation which include fluxes, tissue dose rates, angular distributions, and energy spectra will appear in tabular form in a forthcoming report.[3] The tissue dose rates are plotted in Figs. 9.14.1 through 9.14.6.

[1] Wright Air Development Center.

[2] C. D. Zerby, *Radiation Flux Transformation as a Function of Density of an Infinite Medium with Anisotropic Point Sources*, ORNL-2100 (Oct. 9, 1956).

[3] R. E. Lynch *et al.*, *A Monte Carlo Calculation of Air-Scattered Gamma Rays*, ORNL-2292 (to be published).

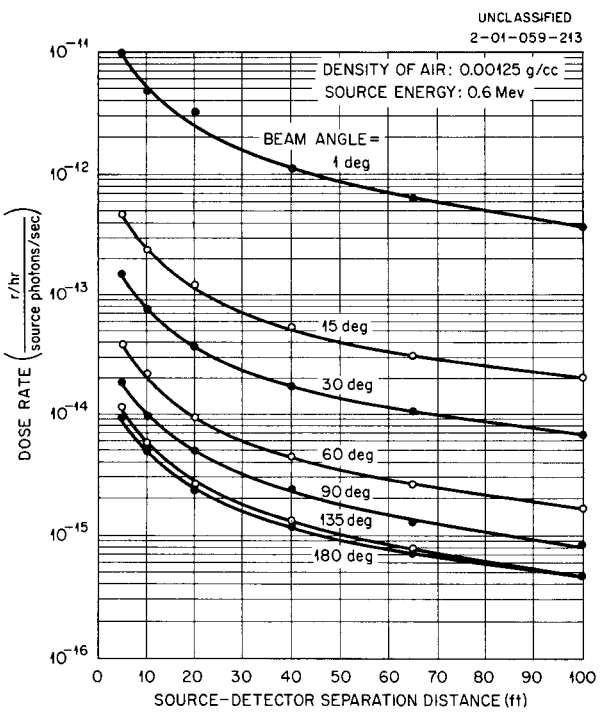

Fig. 9.14.1. Gamma-Ray Dose Rates in Air as a Function of the Source-Detector Separation Distance: Source Energy = 0.6 Mev.

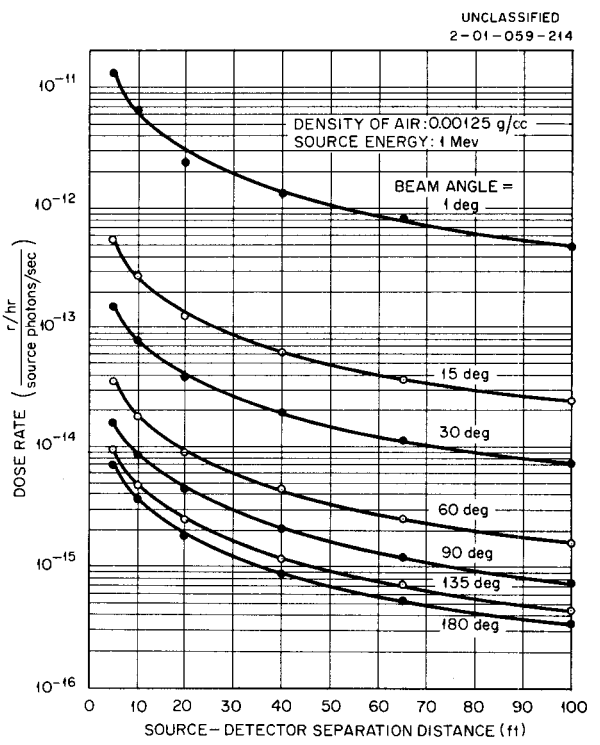

Fig. 9.14.2. Gamma-Ray Dose Rates in Air as a Function of the Source-Detector Separation Distance: Source Energy = 1 Mev.

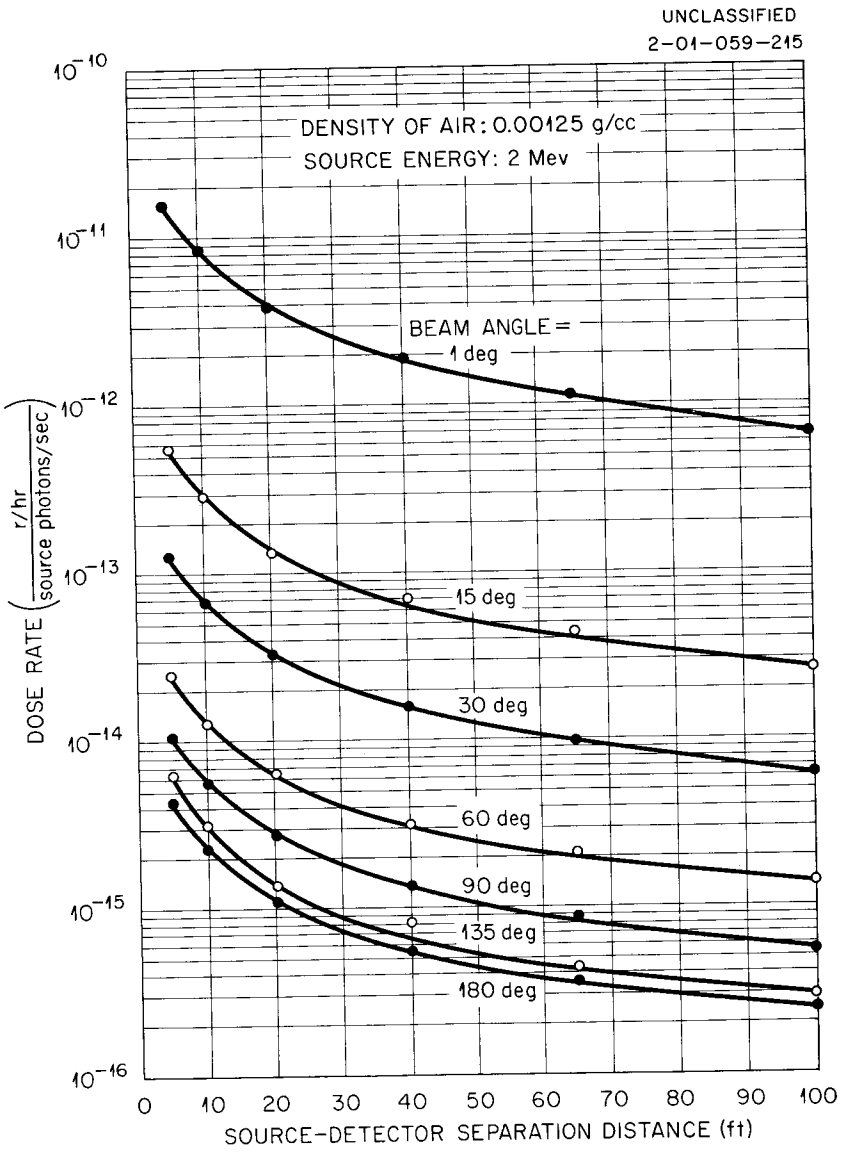

Fig. 9.14.3. Gamma-Ray Dose Rates in Air as a Function of Source-Detector Separation Distance: Source Energy = 2 Mev.

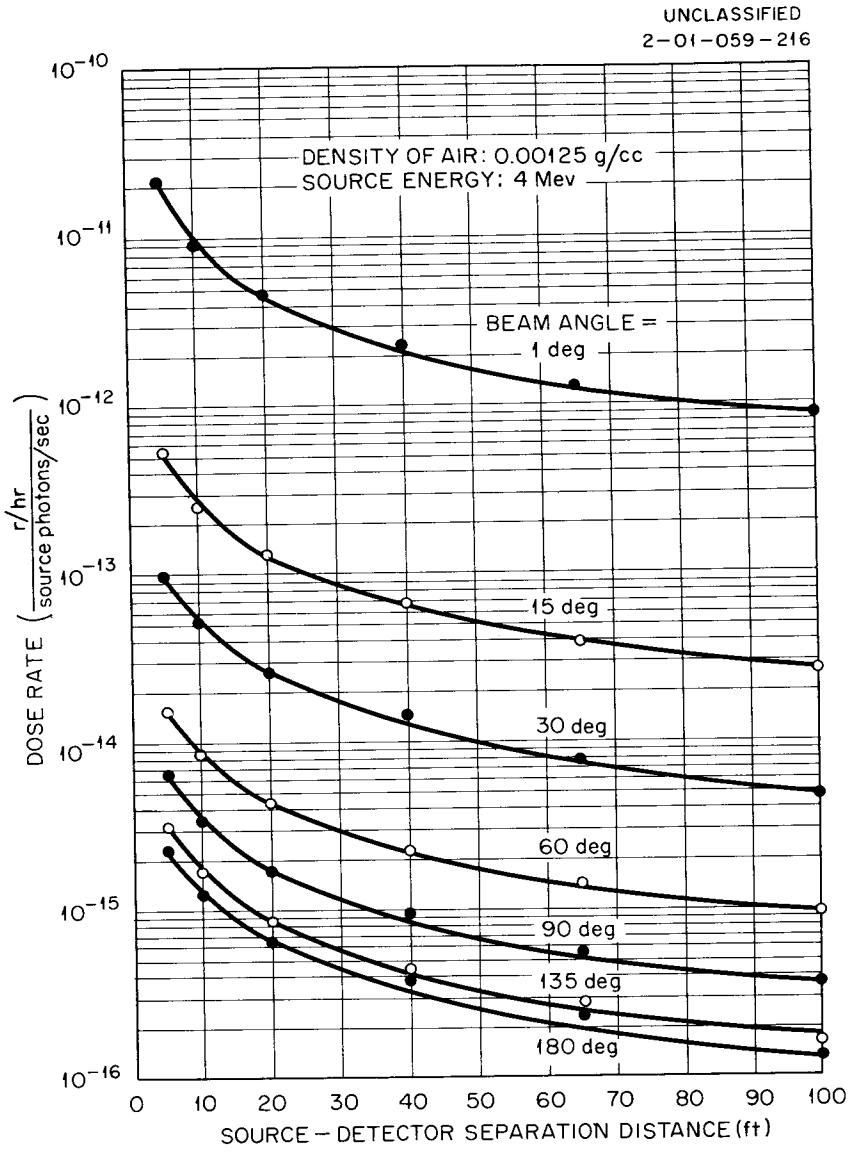

Fig. 9.14.4. Gamma-Ray Dose Rates in Air as a Function of the Source-Detector Separation Distance: Source Energy = 4 Mev.

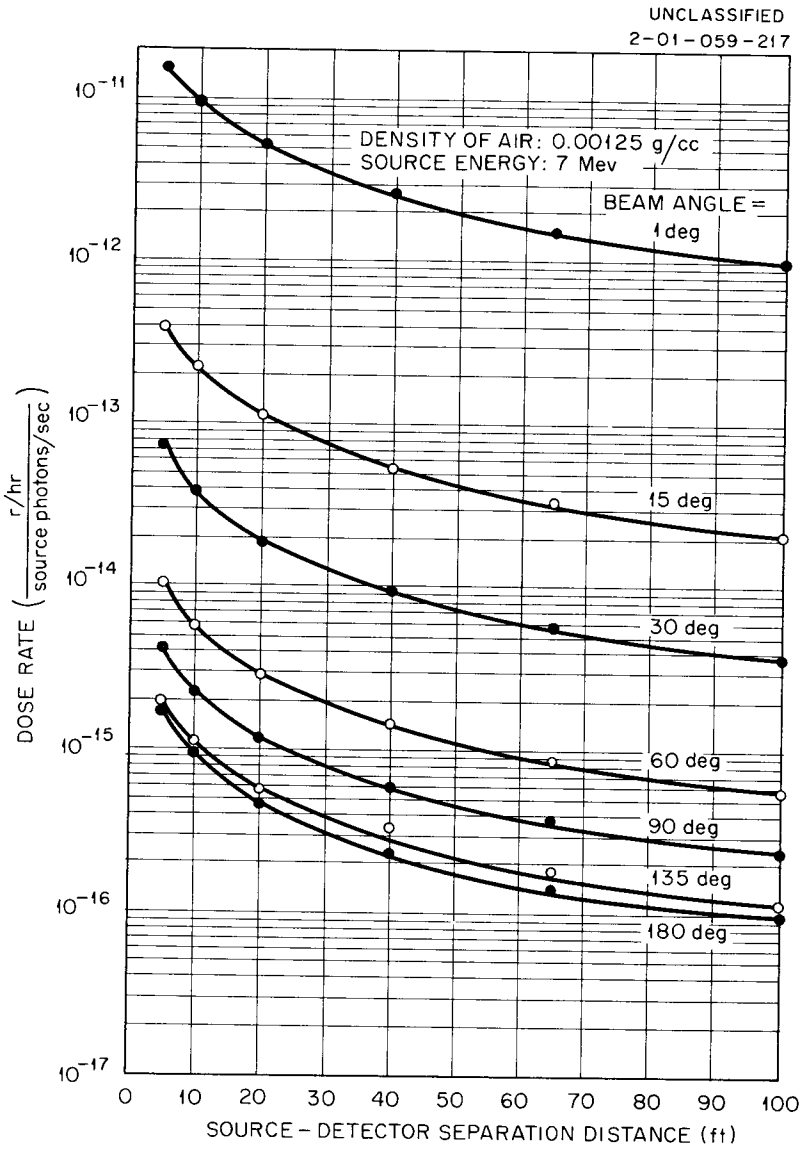

Fig. 9.14.5. Gamma-Ray Dose Rates in Air as a Function of the Source-Detector Separation Distance: Source Energy = 7 Mev.

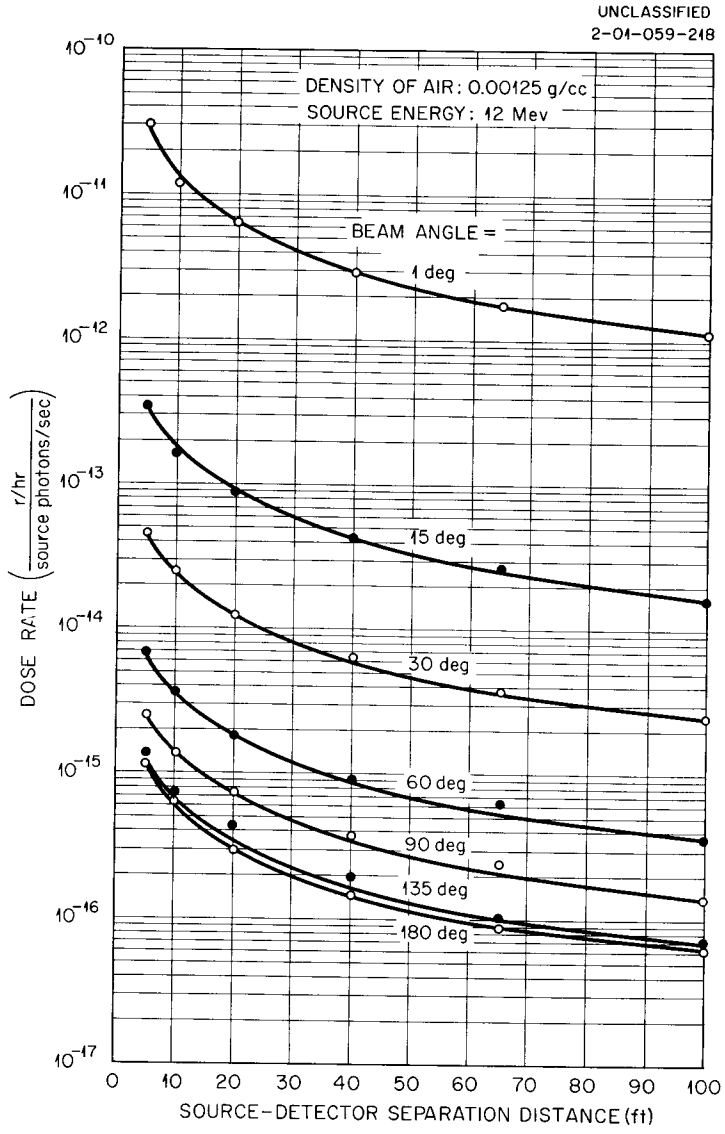

Fig. 9.14.6. Gamma-Ray Dose Rates in Air as a Function of the Source-Detector Separation Distance: Source Energy = 12 Mev.

Part 10

RADIATION DETECTOR DEVELOPMENT

10.1. TOTAL-ABSORPTION GAMMA-RAY SPECTROSCOPY

G. T. Chapman T. A. Love

The possibility of using very large sodium iodide thallium-activated crystals for gamma-ray spectral measurements is being investigated at the Bulk Shielding Facility (BSF). These so-called "total-absorption" crystals potentially may facilitate the interpretation of complex gamma-ray spectra with the possible simplification of "unscrambling" techniques (see Sec. 6.1) required in analyzing data for continuous spectra. Basically, the response of the crystal-photomultiplier system to monoenergetic gamma rays may be represented by a Gaussian distribution about the incident gamma-ray energy with a lower energy "tail" consisting of the distribution of pulses from gamma rays scattered and escaping from the crystal. The spectrum from a source with a continuous energy distribution consists of the sum of such distributions. With small crystals this tail is very prominent, and the ratio of the area under the full-energy peak to the area under the total distribution curve becomes small at high energy. For example, at 4.5 Mev a 1.7-in.-dia by 2-in.-long crystal would be expected to have a peak-to-total ratio of about 0.17, whereas a crystal as large as 5 in. in diameter and 9 in. in length would have a ratio of about 0.62 (ref 1). The large total-absorption crystal is expected to de-emphasize the tail because of the increased probability that the gamma ray will lose all its energy in the crystal.

Currently, the peak-to-total ratio is increased by use of multicrystal spectrometers.[2] These spectrometers unfortunately have complicated electronics and low efficiencies which require time-consuming operations. The total-absorption crystal, with its greater sensitivity, should simplify spectral measurements through the possible elimination of the complicated two-speed coincidence and pulse-height analysis system required with such spectrometers.

The NaI(Tl) crystal investigated at the BSF during the last year is shown in Figs. 10.1.1 and 10.1.2. The crystal is about $9\frac{3}{8}$ in. in diameter at the large end, 2 in. in diameter at the truncated end of the cone, and approximately $9\frac{3}{8}$ in. in length. The geometry of the crystal, which was covered on the surface with a packed aluminum oxide reflector except at the large end, was dictated by the geometry of the ingots obtained in manufacture. It was canned by the vendor[3] in a shock-mounted cast aluminum housing with a $\frac{1}{2}$-in.-thick glass window for covering the large end of the crystal. Normally the gamma rays enter the crystal through a 0.040-in. thickness of aluminum at the truncated end of the cone. The well shown in Fig. 10.1.1 was not initially in the crystal and was added as a result of some of the tests described below. Three 5-in.-dia photomultiplier tubes were used to observe the light pulses in the crystal.

In order to investigate the response of the crystal, 0.662-Mev (Cs^{137}) to 2.76-Mev (Na^{24}) gamma rays were collimated onto the 2-in.-dia truncated end, and the pulse-height distributions were obtained with multichannel pulse-height analyzers. During the tests with 0.66-Mev gamma rays it was observed that the gain of the photomultiplier tubes had to be matched closely, as indicated in the full-energy peak distributions shown in Figs. 10.1.3 and 10.1.4. Figure 10.1.3 shows the results with the three photomultiplier tubes misaligned so that the peak channel for any tube differed from the other tubes by about five channel widths. Figure 10.1.4 shows the gains adjusted so that the peak channels for all three tubes matched within one channel width. With the photomultiplier tubes adjusted for equal gain, the resolution, that is, the full percentage width at half-maximum, was reduced from 16.1% to 12.5%. The two figures also show the similarity to a Gaussian distribution of the form

$$Y(E) = Y(E_0) \exp - \frac{4 \ln (2)}{R^2} \left(\frac{E - E_0}{E_0} \right)^2 ,$$

[1] M. J. Berger and J. Doggett, *J. Research Natl. Bur. Standards* **56**, 335 (1956).

[2] T. A. Love, R. W. Peelle, and F. C. Maienschein, *Electronic Instrumentation for a Multiple-Crystal Gamma-Ray Scintillation Spectrometer*, ORNL-1929 (Oct. 25, 1955).

[3] Harshaw Chemical Co., Cleveland, Ohio.

UNCLASSIFIED
2-01-058-0-203

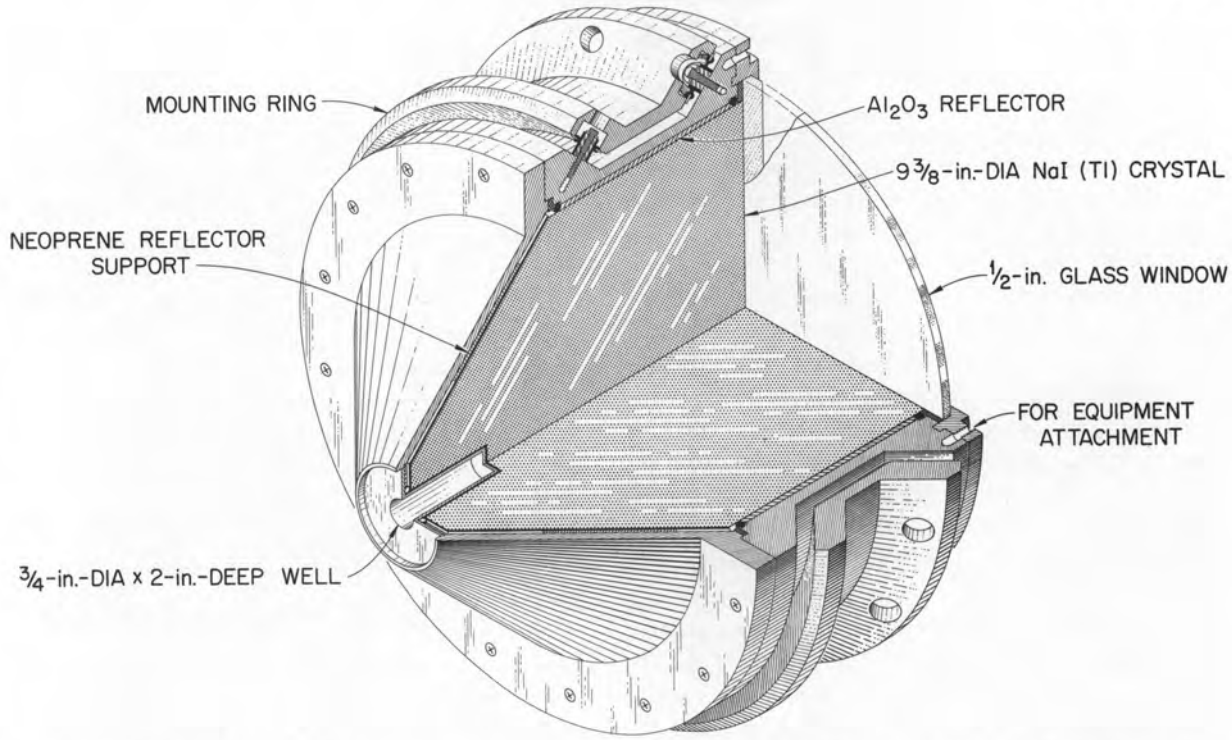

Fig. 10.1.1. Sketch of $9\frac{3}{8}$-in.-dia NaI(Tl) Gamma-Ray Spectrometer Crystal Showing Cast Aluminum Housing and $\frac{3}{4}$-in.-dia by 2-in.-deep Well in Truncated End.

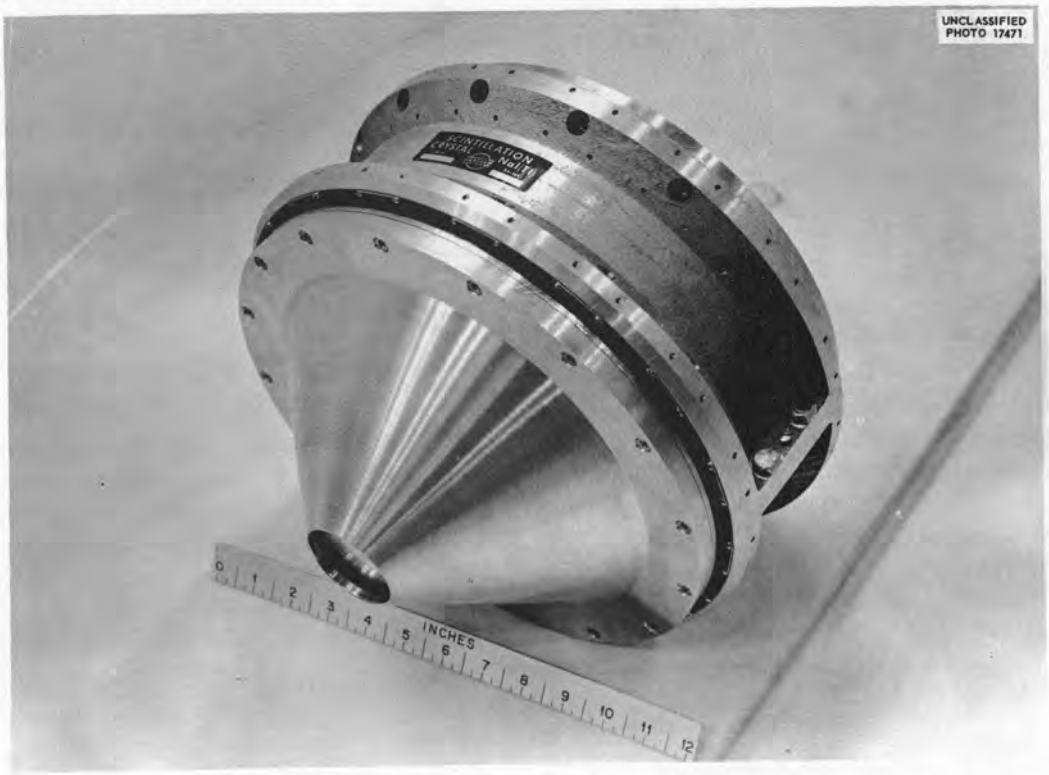

Fig. 10.1.2. Photograph of the $9\frac{3}{8}$-in.-dia Aluminum-canned NaI(Tl) Crystal. (Note: The gamma rays will normally enter the crystal through the small truncated end of the cone.)

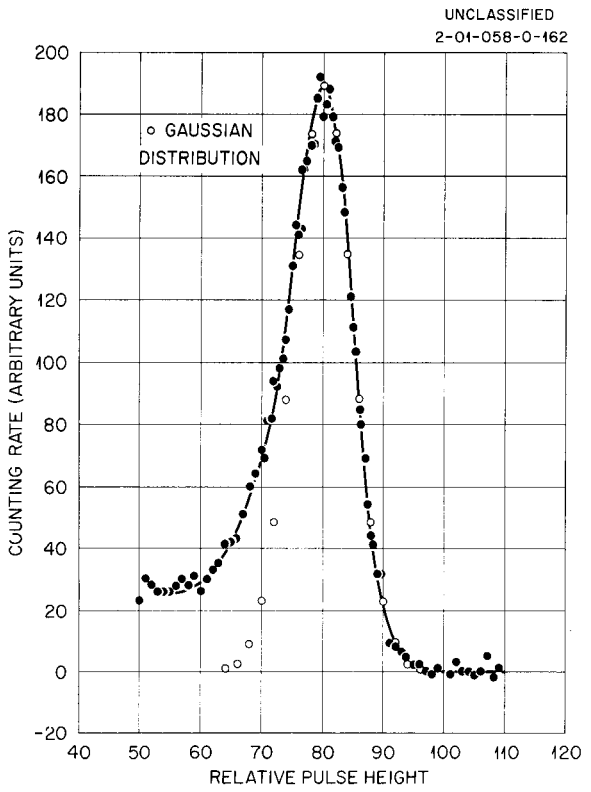

Fig. 10.1.3. Response of the 9 3/8-in.-dia Crystal to 0.662-Mev Cs^{137} Gamma Rays with the Phototube Gains Misaligned by Five Channel Widths (Resolution = 16.1%). The open circles show a Gaussian distribution fitted to the upper edge of the peak; compare with Fig. 10.1.4.

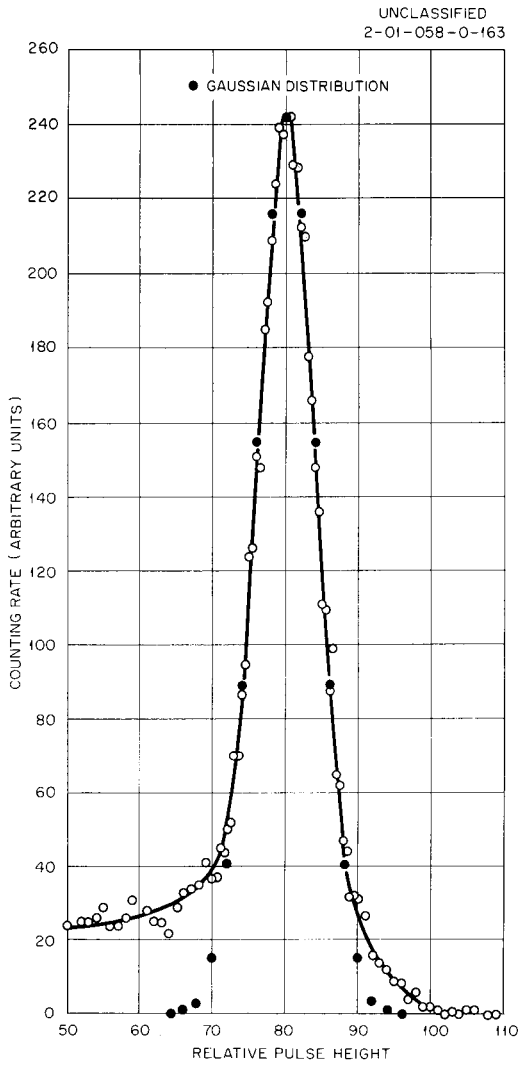

Fig. 10.1.4. Response of the 9 3/8-in.-dia Crystal to 0.662-Mev Cs^{137} Gamma Rays with the Phototube Gains Aligned to Within One Channel Width (Resolution = 12.5%). The closed circles show a Gaussian distribution fitted to the upper edge of the peak; compare with Fig. 10.1.3.

where

$Y(E)$ = count rate per channel (arbitrary units),

R = full percentage width at half-maximum,

E_0 = channel number of peak channel,

E = channel number.

The calculated distribution was fitted roughly to the high-energy side of the peak.

When gamma rays with energy greater than 1.6 Mev were collimated onto the 2-in.-dia flat face of the crystal, a noticeable distortion was observed on the low-energy side of the full-energy peak. This distortion is seen in Fig. 10.1.5, which shows the response to the 2.76-Mev gamma rays from Na^{24}. It was postulated that the distortion was due to the interaction of the gamma rays near the surface of the crystal and to subsequent escape of the scattered gamma rays from the small-diameter region of the cone.

Subsequently, the gamma rays were collimated into the crystal through a collimator perpendicular to the side surface of the cone. Data were taken in this manner along a traverse up the side of the cone, and, as the large-diameter end was approached, the pulse-height distribution became more nearly comparable to an expected Gaussian distribution. As shown in Fig. 10.1.6, the distortion was resolved into a small peak at the base

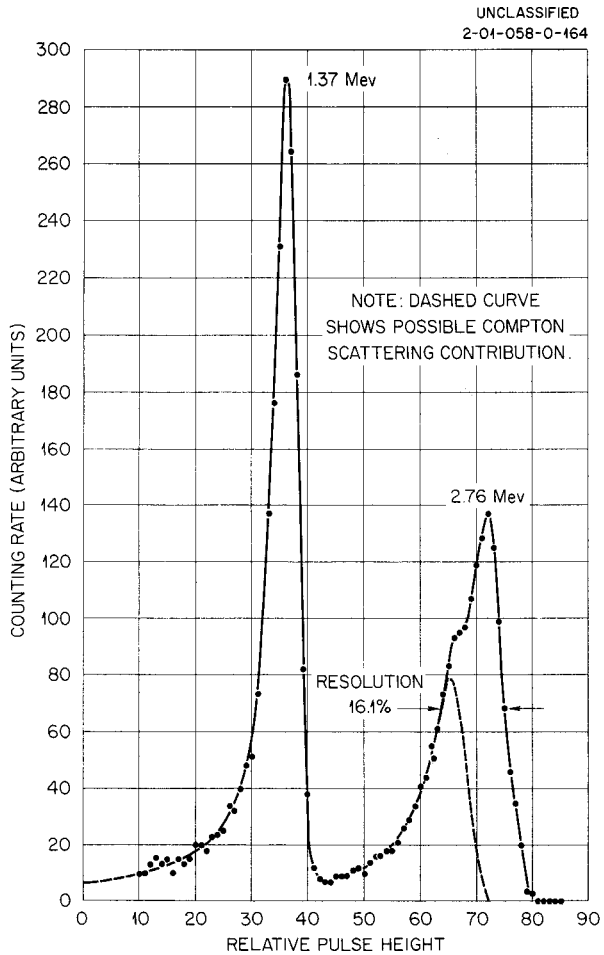

Fig. 10.1.5. Response of the $9\frac{3}{8}$-in.-dia Crystal to 2.76- and 1.37-Mev Na^{24} Gamma Rays Collimated into the Truncated End of the Crystal. The distortion on the 2.76-Mev peak was postulated to be the result of multiple interactions in the small-diameter region of the cone.

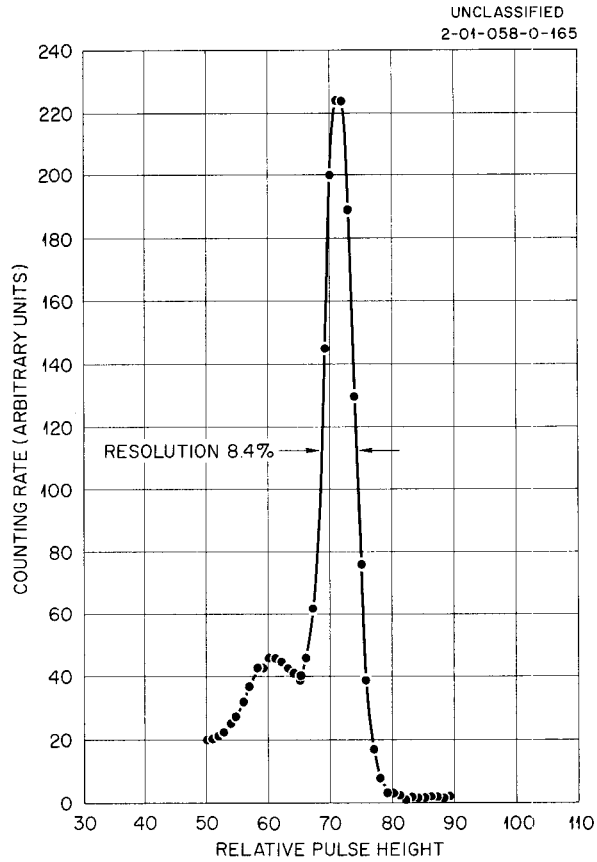

Fig. 10.1.6. Response of the $9\frac{3}{8}$-in.-dia Crystal to 2.76-Mev Na^{24} Gamma Rays Collimated into the Side of the Cone 5 in. from the Truncated End. The distortion noted in Fig. 10.1.5 has been resolved into the small peak at a relative pulse height of 60.

of the 2.76-Mev full-energy peak, and the resolution was improved by a factor of 2. The data taken along the traverse mentioned above indicated that the percentage resolution did not change uniformly with distance along the cone. This, along with the satisfactory results at the large end of the cone, indicated that there was possibly a non-homogeneous region in the cone. In addition, those gamma-ray interactions taking place predominantly in the small-diameter region of the cone with the subsequent escape of the scattered radiation apparently gave rise to distortions. For these reasons, the crystal was returned to the vendor for drilling a $\frac{3}{4}$-in.-dia by 2-in.-deep well, as shown in Fig. 10.1.1.

Upon the return of the crystal to ORNL, it was again investigated by gamma rays being collimated into the bottom of the well. Lead collimators smaller in diameter than the well were used to assure that the gamma-ray beam would at all times shine only on the bottom of the well.

Figure 10.1.7 shows the response of the crystal with the well to 0.662-Mev gamma rays from a small Cs^{137} source. The shape of the distribution is satisfactory, but the percentage resolution has been increased from 12.5% (obtained without the well) to 15.7%. The photofraction, that is, the ratio of the peak area to the total area, was found to be 0.87. The distributions for gamma rays of other energies are shown in Figs. 10.1.8

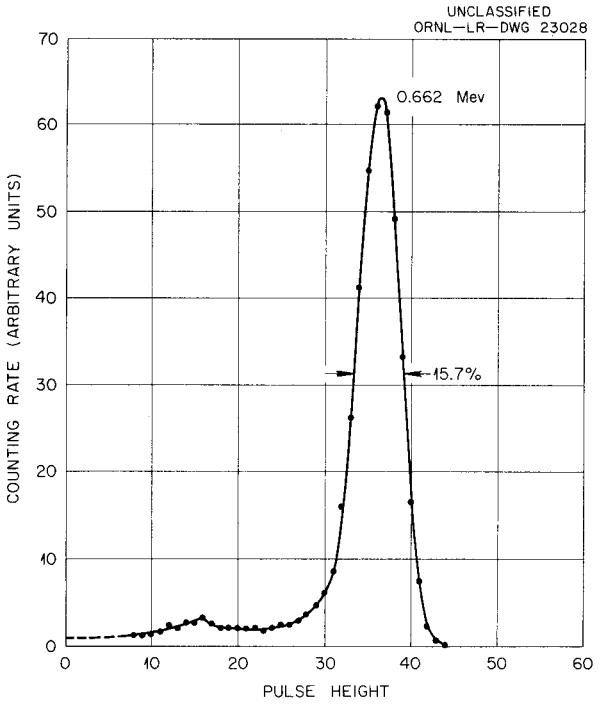

Fig. 10.1.7. Response of the 9 3/8-in.-dia Crystal to 0.662-Mev Cs^{137} Gamma Rays Collimated into the Bottom of the Well. The ratio of peak area to total area is 0.87.

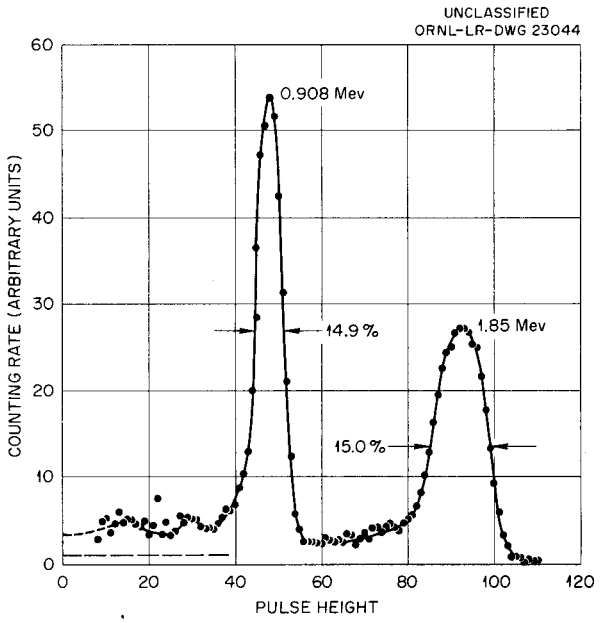

Fig. 10.1.8. Response of the 9 3/8-in.-dia Crystal to Y^{88} Gamma Rays Collimated into the Bottom of the Well. The ratio of the peak area to the total area is 0.74 for the 0.908-Mev gamma ray and 0.70 for the 1.85-Mev gamma ray.

and 10.1.9, with the resulting photofractions indicated in Table 10.1.1 and plotted as a function of gamma-ray energy in Fig. 10.1.10. The shapes of the distributions obtained with the well are improved compared with the shapes obtained without the well. However, the nearly constant percentage resolution is as yet unexplained.

Figure 10.1.10 also shows a comparison of the photofractions obtained with the well in the crystal to those calculated by Berger and Doggett,[1] who used a Monte Carlo technique for a 5-in.-dia by 9-in.-long cylindrical crystal. The measured photofractions agree to within about 3.5% with the calculated values. Probably the comparison is realistic even though the calculations were for a 5-in.-dia crystal and the measurements were made with a 9 3/8-in.-dia crystal, since in both cases the gamma rays were in the energy region <3 Mev and were introduced in a narrow beam along the axis of the crystal. The radial energy loss is low for crystals as large as 5 in. in diameter.

As a basis for comparison with existing spectrometers, Table 10.1.2 shows the measured photofractions for the total-absorption spectrometer and

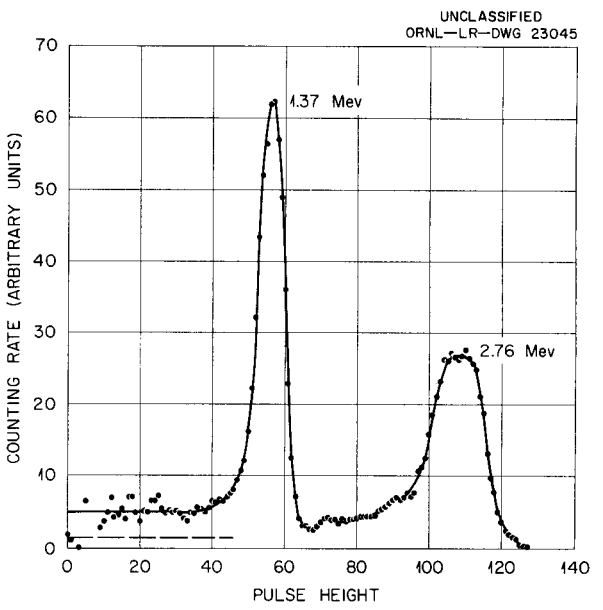

Fig. 10.1.9. Response of the 9 3/8-in.-dia Crystal to Na^{24} Gamma Rays Collimated into the Bottom of the Well. The ratio of the peak area to the total area is 0.73 for the 1.37-Mev gamma ray and 0.67 for the 2.76-Mev gamma ray.

those measured with multicrystal spectrometers.[4] The values for the multicrystal spectrometers were obtained from a rough fit to data taken by Peelle, Love, and Zobel.[5] On the basis of the measured photofractions only, the pair spectrometer is by far better than the other two over the energy region investigated, but the total-absorption spectrometer is better than the Compton spectrometer over the energy range up to 3 Mev.

This work is being continued, and preparations are being made to place seven 3-in.-dia photomultiplier tubes (DuMont 6363) on the crystal. Workers using these tubes have reported resolutions comparable to those obtained with 2-in.-dia tubes, whereas tubes 5 in. in diameter or larger are seldom capable of giving completely satisfactory results, probably because of a nonuniform photocathode surface and inefficient electron focusing within the tube.

An auxiliary program to the investigation of the total-absorption crystals will be an experimental study of collimators. In reactor spectral measurements it is essential to use collimators to reduce the intensity of background radiation incident on

[4] F. C. Maienschein, *Multiple-Crystal Gamma-Ray Spectrometer*, ORNL-1142 (July 3, 1952).

[5] W. Zobel, private communication.

Table 10.1.1. Percentage Resolutions and Photofractions Obtained with the Total-Absorption Spectrometer for Gamma Rays of Various Energies

Gamma-Ray Energy (Mev)	Resolution (%)	Photofraction
0.662	15.7	0.87
0.903	14.9	0.74
1.37	14.8	0.73
1.85	15.0	0.70
2.76	15.7	0.67

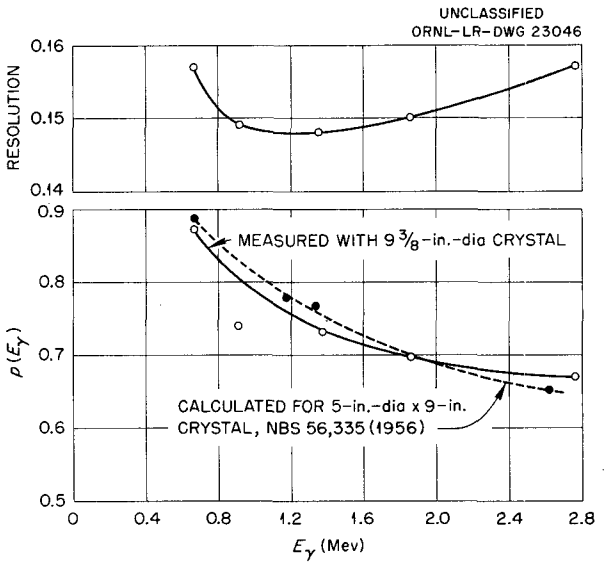

Fig. 10.1.10. Percentage Resolution and Ratio of Peak Area to Total Area, $p(E_\gamma)$, for 9 3/8-in.-dia Crystal as a Function of the Energy of Gamma Rays Collimated into the Well.

Table 10.1.2. Photofractions Obtained with Several Spectrometers for Gamma Rays of Various Energies

Gamma-Ray Energy (Mev)	Photofractions		
	Total-Absorption Spectrometer	Pair Spectrometer	Compton Spectrometer
0.662	0.87		0.81
0.903	0.74		0.76
1.37	0.73	0.99	0.67
1.85	0.69	0.94	0.57
2.76	0.67	0.84	0.38

the crystals, to allow an unobstructed path for radiation through the necessarily thick shield surrounding the spectrometer, and to define the direction of the incident radiation. Currently, for the multiple-crystal spectrometer, the material of the collimators is considered to be opaque to the radiations incident on the spectrometer; and little consideration is given to the scattering from the wall of the collimator, because the small crystal is not likely to detect radiation scattered through any significant angle. The total-absorption crystal, however, presents a very large area to the collimator and consequently is more sensitive to radiations scattered out of the direct beam. Such degraded radiations from scattering could introduce important modifications in the resulting pulse-height distributions observed with the total-absorption spectrometer.

10.2. FAST-NEUTRON SPECTROMETER DEVELOPMENT

R. B. Murray J. J. Manning

This report presents a summary of work carried out in the past year on the development of $Li^6I(Eu)$ as a single-crystal scintillation spectrometer for fast neutrons. A report on the initial phase of this program was given previously,[1] at which time an investigation had been made of the scintillation response of various crystals of $Li^6I(Eu)$ to monoenergetic fast neutrons. It was found that the fast-neutron response of a crystal operating at room temperature was unsatisfactory in that the pulse-height spectrum showed a broad and poorly defined fast-neutron peak. When the crystals were cooled to about −140°C, however, the fast-neutron peak was observed to become sharper and to assume a nearly Gaussian shape.

This program has continued with a further investigation of the apparatus and techniques necessary for operation of a scintillation counter at very low temperatures. Pulse-height spectra from crystals operating at the liquid-nitrogen point (−196°C) have been recorded for neutrons from the (d,d), (d,t), and $Be^9(d,n)B^{10}$ reactions, from a Po-Be source, and from U^{235} fission. The scintillation response of various crystals of LiI(Eu) to gamma rays also has been studied in an effort to provide a means of monitoring the gamma-ray contribution to an observed pulse-height spectrum. The results of these experiments and the techniques employed are discussed below.

Scintillation Response of LiI(Eu) to Charged Particles

The broad and "rectangular" band appearance of the fast-neutron peak observed at room temperature has been tentatively ascribed to a difference in the scintillation efficiency of LiI(Eu) to alpha particles and tritons. It is known, for example, that the scintillation efficiency of NaI(Tl) to alpha particles is substantially lower than that for other light charged particles. The sharper fast-neutron peak in LiI(Eu) at low temperatures might then be due to an increasing scintillation efficiency to alpha particles with decreasing temperature. In order to obtain some experimental information on this subject, an experiment was carried out in which an LiI(Eu) crystal was simultaneously excited by 1.12-Mev gamma rays from Zn^{65}, by alpha particles from U^{233}, and by the alpha-triton pair resulting from slow-neutron capture. The peaks observed in the pulse-height spectrum resulting from these three modes of excitation were followed as a function of temperature from room temperature to the liquid-nitrogen point. The results of the experiment are shown in Fig. 10.2.1, in which the pulse heights of the three peaks are normalized to the same value at room temperature. It is seen that the scintillation efficiency of the crystal to alpha particles increases much more rapidly with decreasing temperature than it does to gamma rays or the alpha-triton pair. The results of this experiment are thus consistent with the proposed explanation of the improved fast-neutron response at low temperatures.

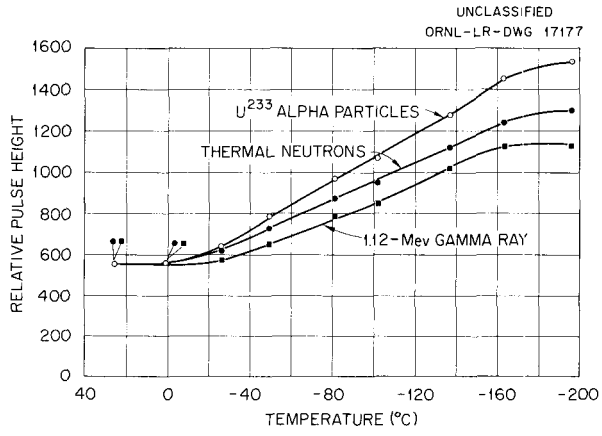

Fig. 10.2.1. Relative Pulse Height as a Function of Temperature for Normal LiI(Eu) Crystal.

Experimental Apparatus

The initial experiments on the scintillation properties of LiI(Eu) at low temperatures were carried out with an apparatus in which the crystal was cooled by a flow of dry nitrogen gas which had been circulated through a liquid-nitrogen heat exchanger. This apparatus required frequent attention and rather large quantities of both gaseous and liquid nitrogen. Accordingly, it was replaced by a device in which the crystal is cooled directly by liquid nitrogen (see Fig. 10.2.2).

[1] R. B. Murray, *Appl. Nuclear Phys. Ann. Rep. Sept. 10, 1956*, ORNL-2081, p 191.

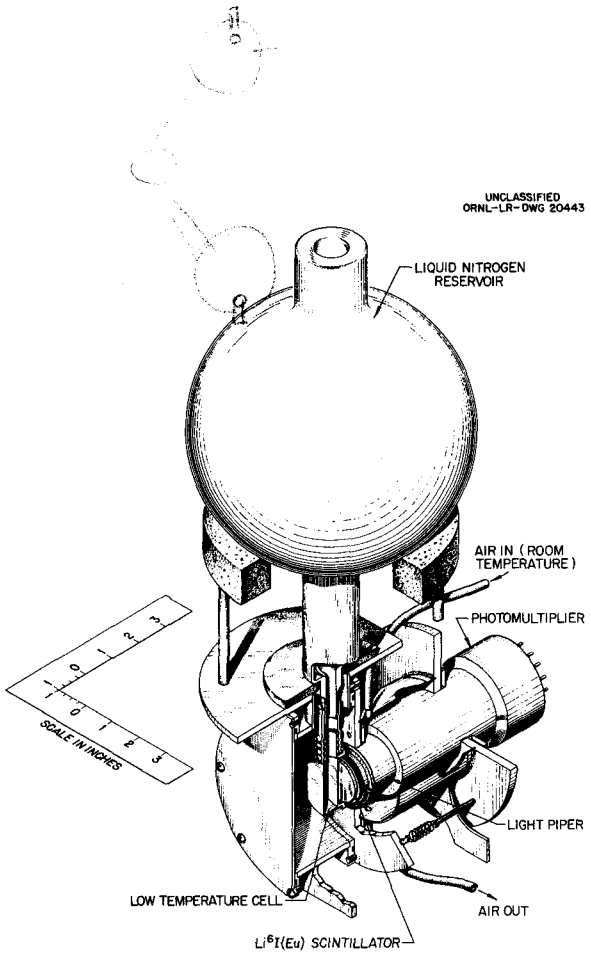

Fig. 10.2.2. Low-Temperature Scintillation Spectrometer.

Since conventional photomultipliers fail to function below about −140°C, this apparatus was designed so that the temperature of the photocathode would be maintained well above that of the crystal. In the apparatus shown in Fig. 10.2.2, the LiI(Eu) crystal (whose dimensions are typically 35 mm in diameter and 2 mm in thickness) is mounted on a polished Lucite light piper about $1\frac{1}{4}$ in. long. The light piper is optically coupled to the photomultiplier by DC-200 silicone grease; a flow of compressed air around the photomultiplier and light piper maintains the photocathode surface near room temperature. The "cold" end of the light piper is provided with a flange and is threaded so that the crystal may be sealed from the atmosphere by a thin-wall brass cap which seats on a rubber O-ring against the flange. This cap is part of the liquid-nitrogen system and communicates directly with the liquid-nitrogen reservoir.

It has been necessary to mount the crystal directly on the light piper without the use of an optical grease, since the various greases normally used solidify upon cooling and may break either the optical seal or the crystal or both. In the case of thin LiI(Eu) crystals mounted on Lucite, it was found that the room-temperature resolution (for slow neutrons) of a crystal mounted dry is very little different from that of the same crystal mounted with an optical grease. The reverse face of the crystal is normally covered with a thin aluminum foil reflector. A good LiI(Eu) crystal mounted in this manner, in conjunction with a selected photomultiplier, will normally give a slow-neutron peak of 6% resolution.

The liquid-nitrogen reservoir shown in Fig. 10.2.2 is a glass Dewar vessel and requires filling about every 4 hr. The Dewar vessel is connected to the liquid-nitrogen cell adjoining the crystal by a short length of rubber hose.

Some of the crystals used in this work were grown at ORNL, and others were obtained from Harshaw Chemical Company. Crystals from these two sources proved to be about equally satisfactory. The difficulty encountered in obtaining *good* crystals of $Li^6I(Eu)$ remains as one of the main disadvantages of this technique. It is hoped that improved crystal-growing technology will result in a more uniform product.

Photomultipliers 2 in. in diameter were used throughout this study; best results were obtained with selected DuMont 6292 and RCA 6342 tubes. The photomultiplier pulses were fed to an A-1D preamplifier and amplifier. Since the rise time of LiI(Eu) pulses is slightly less than 2 μsec, it was necessary to use a 4-μsec delay-line clipping in the A-1D amplifier. The amplified 4-μsec pulses were then fed to an Atomic model 520 20-channel analyzer. Since 4-μsec pulses were being analyzed, it was necessary to restrict the over-all counting rate to a few thousand counts per second to avoid an appreciable overlapping of pulses.

Neutron Spectra

The spectrum of neutrons from various sources has been recorded with the apparatus shown in Fig. 10.2.2. Neutrons from nuclear reactions were obtained by accelerating deuterons in the ORNL 625-kev Cockcroft-Walton accelerator. The pulse-height spectrum from 2.92-Mev neutrons from the (d,d) reaction is shown in Fig. 10.2.3. For comparison, Fig. 10.2.4 shows the pulse-height spectrum from the same crystal at room temperature. The counts observed in Fig. 10.2.3 between the fast-neutron peak and the slow-neutron peak are

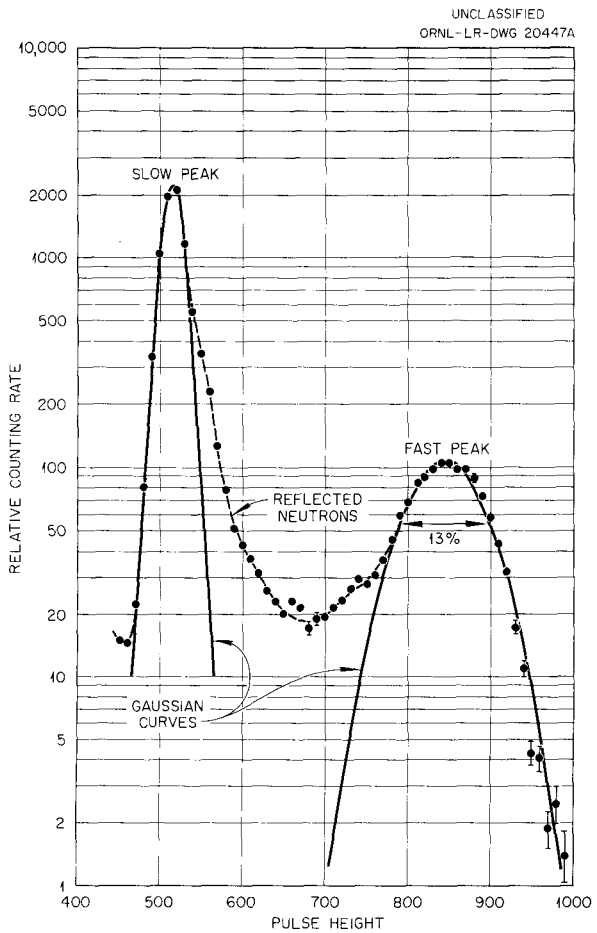

Fig. 10.2.3. Scintillation Response of $Li^6I(Eu)$ Crystal at −196°C to 2.92-Mev Neutrons.

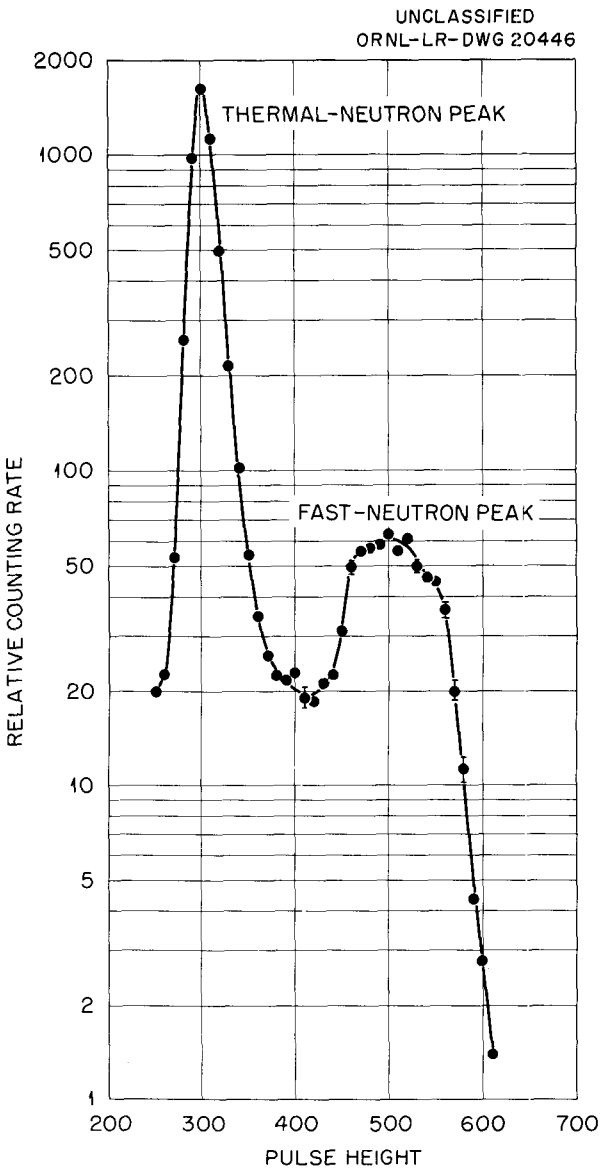

Fig. 10.2.4. Scintillation Response of $Li^6I(Eu)$ Crystal at Room Temperature to 2.92-Mev Neutrons.

attributed to neutrons scattered to the crystal by the surrounding apparatus. Probably the most offensive piece of apparatus in this respect is the Lucite light piper, which is immediately adjacent to the crystal and which contains hydrogen. The light piper also is primarily responsible for the large slow-neutron peak which is always observed in a fast-neutron experiment. The counts due to these degraded neutrons constitute, of course, a background in the form of a low-energy "tail," which must be taken into account in a measurement of a continuous spectrum. This point will be discussed later.

The spectrum from 14.3-Mev neutrons from the (d,t) reaction is shown in Fig. 10.2.5. The very large continuous background observed here is due to the competing nuclear reactions $Li^6(n,dn)He^4$ and $Li^6(n,p)He^6$, which are excited by neutrons of such high energy, to Li^6 elastic recoils, and to degraded neutrons scattered to the crystal. It may be pointed out, however, that these competing reactions need be considered only for neutrons with an energy of approximately 8 Mev or greater, since the Q value of the (n,α) reaction is high. In a fission-like spectrum, then, this effect will give rise to a very small background.

The $Be^9(d,n)B^{10}$ reaction (E_d = 550 kev) provides a source of five groups of monoenergetic neutrons. The energies of the various neutron

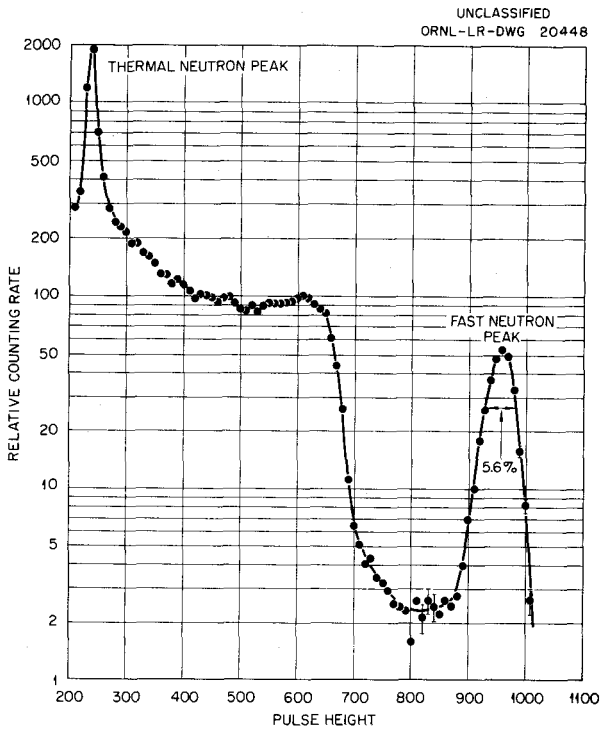

Fig. 10.2.5. Scintillation Response of $Li^6I(Eu)$ Crystal at −196°C to 14.3-Mev Neutrons.

groups are predictable from the known level structure of the B^{10} nucleus. The pulse-height spectrum resulting from bombardment of an $Li^6I(Eu)$ crystal at −196°C by $Be^9(d,n)B^{10}$ neutrons is shown in Fig. 10.2.6. The calculated energies of the neutron groups are indicated by arrows. The neutron energy scale at the top of Fig. 10.2.6 is determined by a plot of pulse height vs neutron energy (see Fig. 10.2.7). The groups at 2.90 and 4.51 Mev are weak and occur alongside the more intense 2.52- and 3.84-Mev peaks. It should be noted that the ordinate of Fig. 10.2.6 is the relative counting rate and has not been corrected for the energy dependence of the $Li^6(n,\alpha)H^3$ cross section. Since the (n,α) cross section decreases with increasing energy, this correction has the effect of multiplying the ordinate in Fig. 10.2.6 by a factor which increases with energy.

The relative number of neutrons expected in the various groups shown in Fig. 10.2.6 can be estimated from previous measurements of neutron spectra and angular distributions at other laboratories. These measurements have generally been carried out with nuclear emulsion techniques,

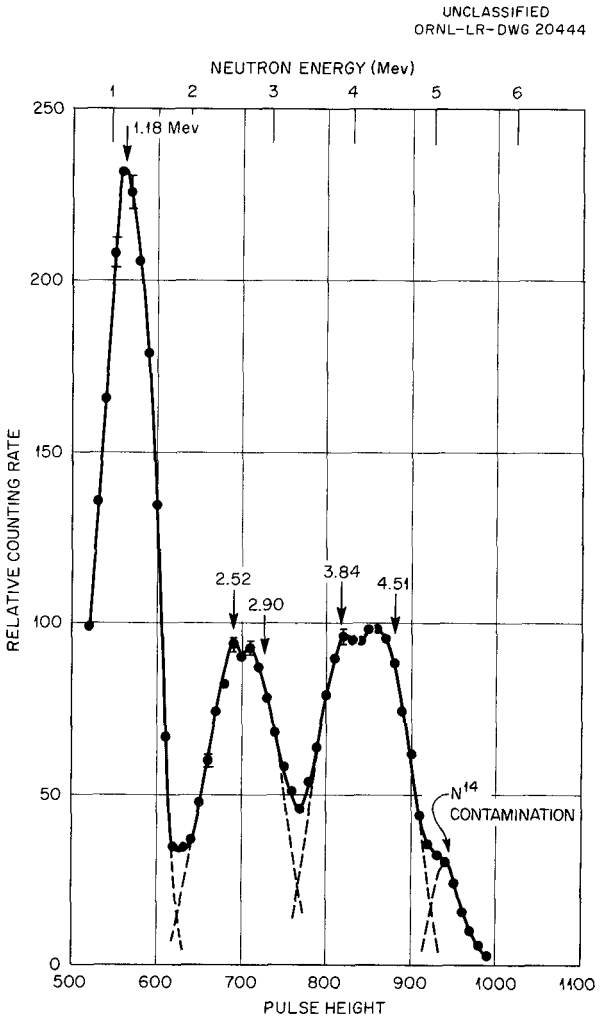

Fig. 10.2.6. Scintillation Response of $Li^6I(Eu)$ Crystal at −196°C to $Be^9(d,n)B^{10}$ Neutrons. Thermal-neutron peak and approximate correction for reflected neutrons have been subtracted.

which permit better resolution than $Li^6I(Eu)$ in this energy region. In order to compare the $Li^6I(Eu)$ data with previous measurements, the areas of the neutron peaks in Fig. 10.2.6 were determined numerically (lumping together the pair at 2.52 and 2.90 Mev, and the pair at 3.84 and 4.51 Mev) and were corrected for the $Li^6(n,\alpha)H^3$ cross section. The resulting relative intensities compared favorably with the estimated values, that is, within the uncertainty of calculating peak areas from published papers.

The spectrum of neutrons from a Po-Be source is a continuous distribution in energy up to about

11 Mev. Because of the widespread use of Po-Be sources, it has been of considerable interest in the past to measure this spectrum. Results of recent measurements with proton recoil techniques may be found in the literature.[2-4] Although no two spectra are exactly alike, they are qualitatively similar. The spectrum of neutrons from a 1-curie Po-Be source was recorded with an $Li^6I(Eu)$ crystal by means of the low-temperature apparatus of Fig. 10.2.2. The pulse-height spectrum was corrected for spurious counts arising from neutrons reflected to the crystal and from competing nuclear reactions. This correction amounted to about 50% of the counts at 1.5 Mev, 20% at 3 Mev, and was negligible above 5.5 Mev. The resulting spectrum, after correction was made for the $Li^6(n,\alpha)H^3$ cross section, is given in Fig. 10.2.8. The standard deviation shown on some of the points represents counting statistics only. The data shown here were recorded with a 20-channel analyzer in a period of about 5 hr. The neutron spectrum presented in Fig. 10.2.8 is quite similar to the spectra previously reported.[2-4]

As a further check on the applicability of the $Li^6I(Eu)$ technique to the measurement of fission-like spectra, an experiment was carried out to

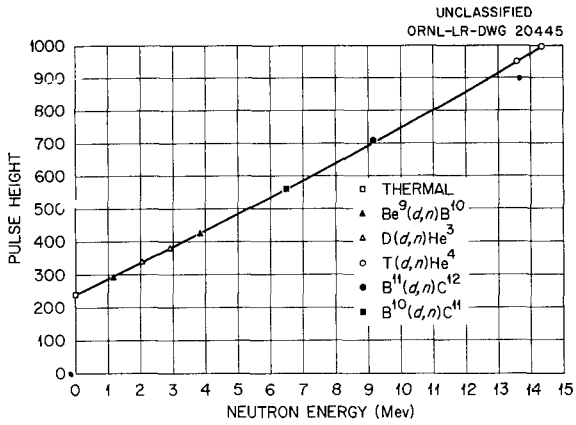

Fig. 10.2.7. Pulse Height as a Function of Neutron Energy for $Li^6I(Eu)$ Crystal at −196°C.

[2] B. G. Whitmore and W. B. Baker, *Phys. Rev.* **78**, 799 (1950).

[3] R. G. Cochran and K. M. Henry, *Rev. Sci. Instr.* **26**, 757 (1955).

[4] R. J. Breen, M. R. Hertz, and D. U. Wright, Jr., *The Spectrum of Polonium-Beryllium Neutron Sources*, MLM-1054 (June 13, 1955).

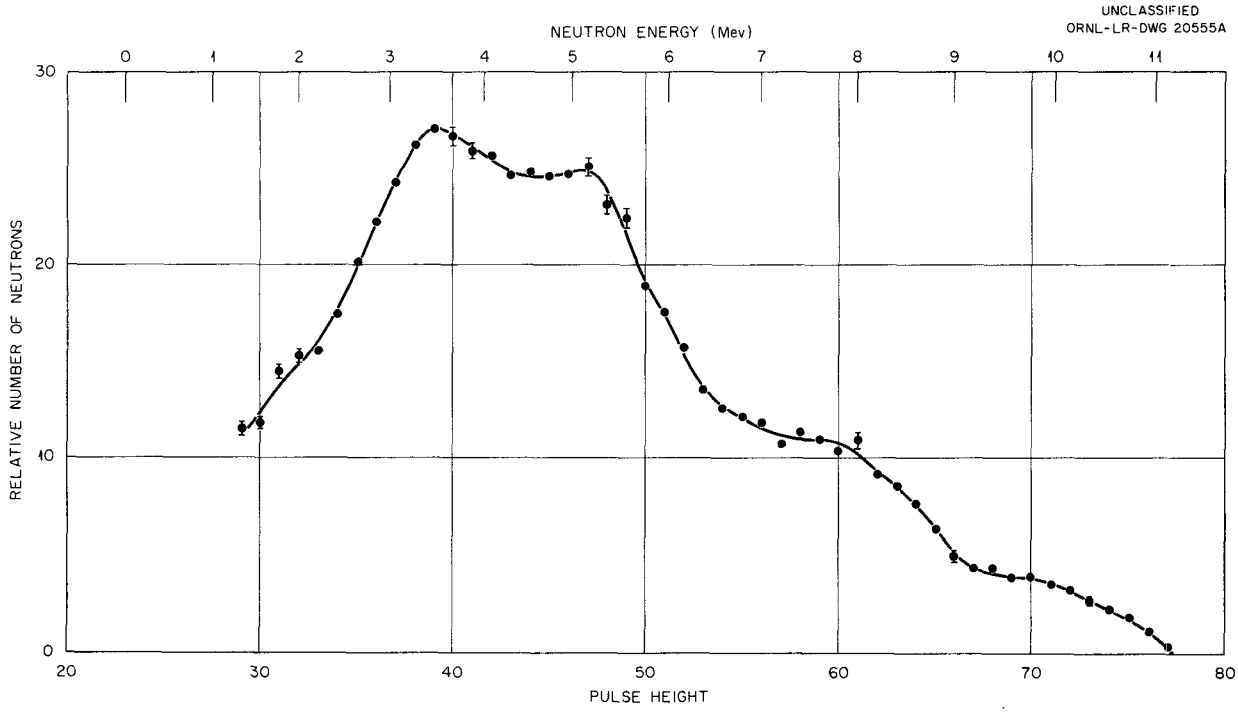

Fig. 10.2.8. Spectrum of Neutrons from a Po-Be Source Detected by an $Li^6I(Eu)$ Crystal.

measure the spectrum of neutrons from U^{235} fission. The 2.5-Mev Van de Graaff accelerator was used as the source of neutrons so that the fission source and the detector would be far away from floors, walls, concrete shields, etc., a condition difficult to realize with local reactors. Protons were accelerated to an energy above the threshold of the (p,t) reaction, producing low-energy (~200 kev) neutrons in a forward cone. These neutrons initiated fission events in a $\frac{5}{8}$-in.-thick by 1-in.-dia U^{235} slug. The $Li^6I(Eu)$ detector, in the apparatus of Fig. 10.2.2, was placed outside the cone of threshold neutrons and was 3 in. from the fission source. The pulse-height spectrum was corrected for scattered neutrons and for the $Li^6(n,\alpha)H^3$ cross section. The scattered-neutron correction amounted to 15% at 1.5 Mev, 5% at 3 Mev, and was negligible above 4 Mev. The resulting fission neutron spectrum is presented in Fig. 10.2.9. These data were recorded on a 100-channel analyzer in about 6 hr. For comparison, the U^{235} fission spectrum as measured by photographic plates at Los Alamos[5] is also shown. The two sets of data are normalized in a completely arbitrary manner. The standard deviation on the $Li^6I(Eu)$ points represents counting statistics only. An additional uncertainty in these data (and in the spectra discussed above) is introduced because of probable errors in the $Li^6(n,\alpha)H^3$ cross section of 11 to 18% and because no cross-section data are available between 6.5 and 14 Mev. The cross section in this region was taken from a smooth curve joining the data below 6.5 Mev with the one point at 14 Mev. The parallel curves in Fig. 10.2.9 represent bounds of ±11% to ±18% on a smooth curve drawn through the $Li^6I(Eu)$ data points. The two sets of data in Fig. 10.2.9 really should not be compared directly, as the thick source used in the $Li^6I(Eu)$ experiment is expected to modify the spectrum. Within the uncertainties mentioned above, however, the two sets of data seem to be in reasonable agreement.

[5] L. Cranberg *et al.*, *Phys. Rev.* **103**, 662 (1956).

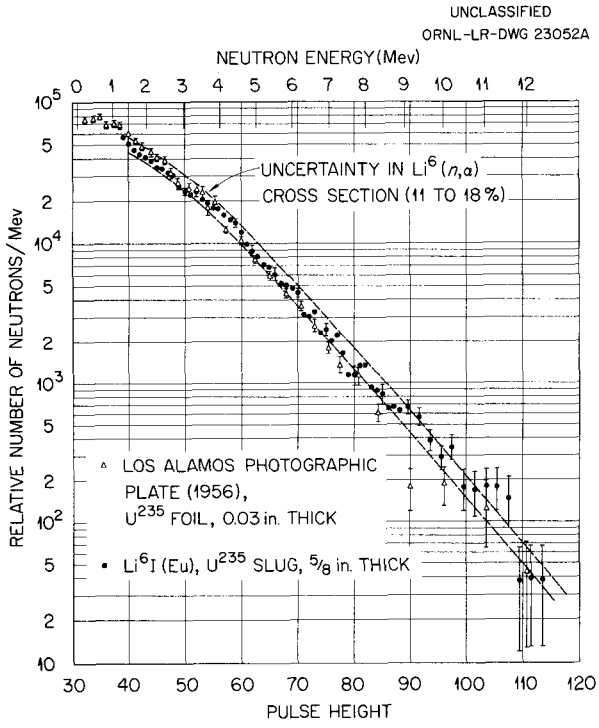

Fig. 10.2.9. Measurement of U^{235} Fission Neutron Spectrum with an $Li^6I(Eu)$ Crystal; Comparison with Measurement at Los Alamos with Photographic Plates.

Background and Gamma-Ray Corrections

The corrections referred to above were primarily necessitated by neutrons being reflected to the crystal and were estimated from a number of pulse-height spectra similar to the spectrum shown in Fig. 10.2.3. An idea of the shape and size of the low-energy tail was obtained from Fig. 10.2.10, which shows the expected background associated with 1000 counts at energy E_0. In addition to the experimental information of Fig. 10.2.10, it was possible to obtain a rough idea of the expected background by the use of a Monte Carlo calculation, previously set up (by C. D. Zerby) to obtain the spectrum and dose of neutrons reflected from slabs. The low-energy tail predicted by this calculation agreed reasonably well with the curves in Fig. 10.2.10. It should be pointed out that the corrections due to reflected neutrons are still rather uncertain; more definitive experimental information is needed to verify them. Even so, the Po-Be spectrum shown in Fig. 10.2.8, the relative intensities of the groups in Fig. 10.2.6, and the fission spectrum in Fig. 10.2.9 are in reasonable agreement with previous measurements.

Two additional points may be made concerning the low-energy tail. First, this effect would be minimized if it were possible to eliminate the Lucite light piper. A device is now being constructed in which the $Li^6I(Eu)$ crystal is mounted inside a cylindrical, thin-walled aluminum sleeve whose interior wall is highly polished and which slips over the photomultiplier. Preliminary results

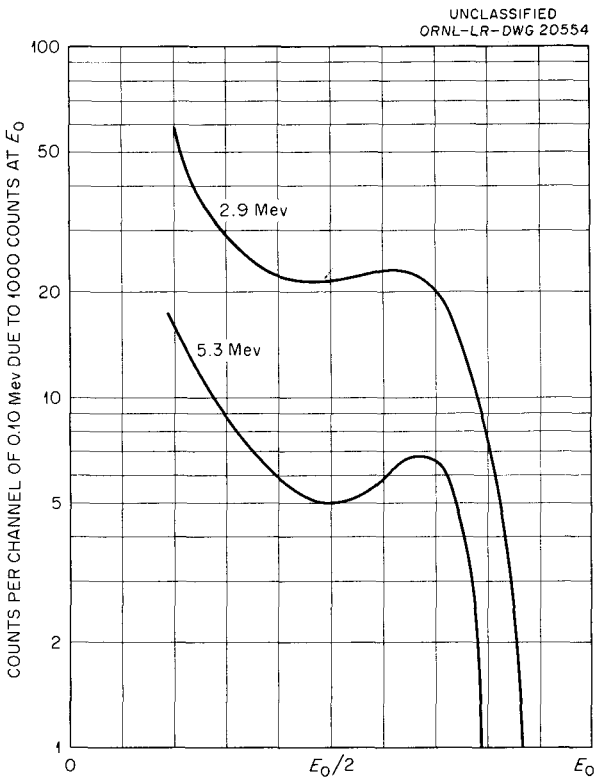

Fig. 10.2.10. Neutron Background Associated with $Li^6I(Eu)$ Detector for Various Source Energies.

indicate that this may be a feasible technique, in which case the low-energy tail and the slow-neutron peak should be substantially reduced. Second, a fission-like neutron spectrum falls off very rapidly with energy above 1 or 2 Mev, so that there are relatively few fast neutrons to give rise to a low-energy tail. (As indicated above, the correction to Fig. 10.2.9 at 1.5 Mev was only 15%.) In this respect the Po-Be spectrum is most disagreeable, since its peak occurs between 3 and 5 Mev, providing a large background at lower energies.

It was believed that the gamma-ray background which inevitably accompanies neutron sources and which is expected to be large in the case of an operating reactor could be minimized by the following means:

(1) The thermal peak in a properly activated crystal occurs at a gamma-ray equivalent pulse height of about 4.8 Mev, and therefore the large Q value of the (n,α) reaction would provide a built-in bias to discriminate against gamma-ray-induced pulses up to almost 5 Mev.

(2) With the use of thin crystals (~2 or 3 mm) the probability that a high-energy gamma ray (say, 8 Mev) will deposit its full energy in the crystal would be very small.

(3) With the use of an auxiliary crystal of $Li^7I(Eu)$ as a gamma-ray monitor, the $Li^7I(Eu)$ pulse-height spectrum could be subtracted from that recorded with $Li^6I(Eu)$, which should eliminate the gamma-ray counts from the neutron spectrum.

In order to determine the validity of these points, several experiments were carried out with gamma rays. The crystals chosen were an $Li^7I(Eu)$ crystal (99.9% Li^7) grown at ORNL and a normal LiI(Eu) crystal (7.4% Li^6) supplied by Harshaw and were slightly over 2 mm thick. (In practice, of course, an enriched Li^6 crystal is used for the neutron spectrum.) The first question considered was whether the pulse-height response of these two arbitrarily selected crystals would be sufficiently similar so that the gamma-ray spectra could be superimposed. The pulse-height spectrum of Zn^{65} gamma rays on the two crystals was recorded; the amplifier gain was adjusted so that the peaks fell at the same pulse height. The results, shown in Fig. 10.2.11, indicate that the spectra are essentially identical.

The spectrum of gamma rays from the Po-Be source (primarily the 4.43-Mev gamma ray from C^{12}) is shown in Fig. 10.2.12. The distinguishable gamma-ray peak in the $Li^7(Eu)$ spectrum is the two-escape peak from the 4.43-Mev gamma ray. It should be noted that the small thermal-neutron peak in the Li^7 spectrum does *not* occur at the same pulse height as that from the Li^6 spectrum; the gamma-ray calibration for the two crystals, however, is still the same. This reflects the fact that the relative scintillation efficiency of a given crystal to neutrons and gamma rays is a function of activator content. An $Li^7I(Eu)$ monitor must then be intercalibrated with an $Li^6I(Eu)$ crystal with *gamma rays*.

The $B^{11}(p,\gamma)C^{12}$ reaction, excited by protons from the Cockcroft-Walton accelerator, produces gamma rays at 16 Mev and an 11.6 + 4.43-Mev cascade; the 16-Mev gamma is weak with respect to the cascade. The spectrum of these gamma rays on the two crystals is shown in Fig. 10.2.13. Again, the spectra can be well superimposed. The number of counts above 600 pulse-height units was completely negligible, despite the presence of the

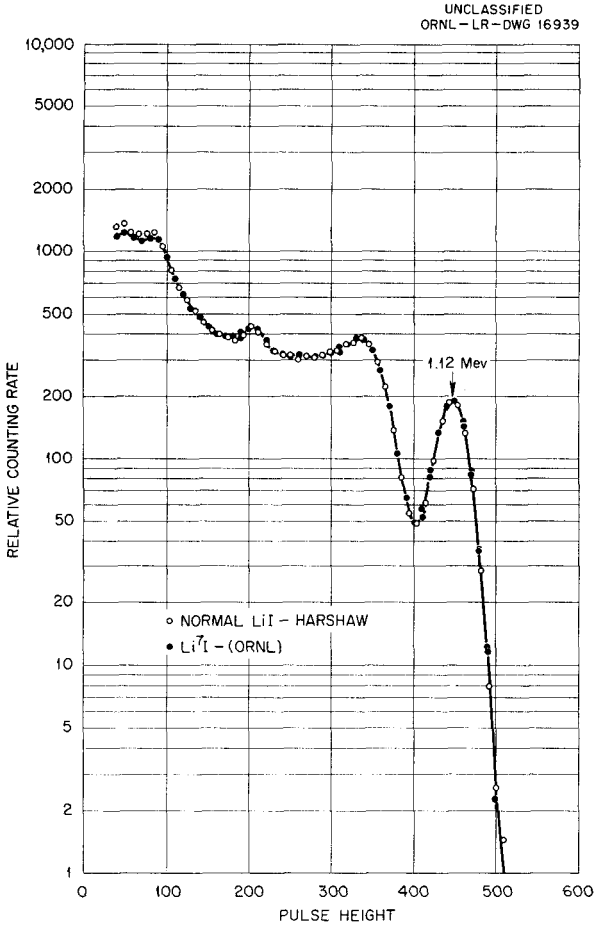

Fig. 10.2.11. Response of LiI(Eu) and Li^7I(Eu) Crystals to Gamma Rays from Zn^{65}.

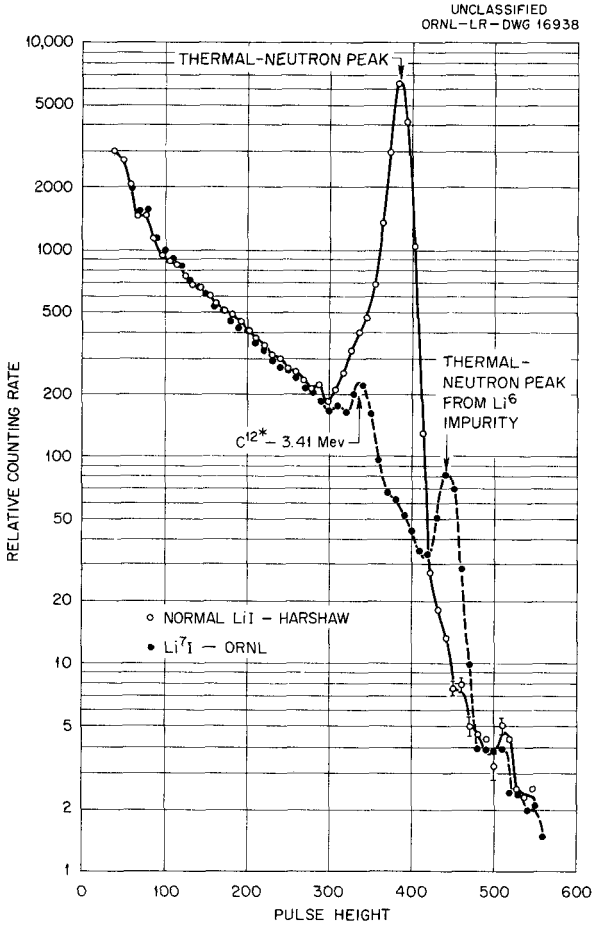

Fig. 10.2.12. Response of LiI(Eu) and Li^7I(Eu) to Neutrons and Gamma Rays from Po-Be.

11.6-Mev gamma ray. This fact is taken as evidence in support of point (2) above; namely, that very few high-energy gamma-ray pulses will be observed with crystals of the order of 2- to 3-mm thickness. It may be noted in Fig. 10.2.13 that the gamma-ray counts become negligible above about 6 Mev equivalent pulse height. This indicates that the gamma contribution to an observed neutron spectrum may be expected to be very small above a neutron energy of 1 or 2 Mev.

The gamma-ray background in the fission experiment was monitored with an auxiliary crystal of Li^7I(Eu). At a neutron energy of 1.5 Mev the gamma-ray counting rate was 10^{-3} times the neutron counting rate. Similarly, the gamma-ray background was negligible in the Po-Be spectrum.

The conclusion from the experiments described seems to be that a gamma-ray background can be tolerated and monitored under reasonable circumstances; of course, a situation in which the counter is completely swamped by gamma rays cannot be tolerated. What this means in terms of a reactor surrounded by a neutron shield remains to be seen.

Summary

The experiments described above indicate that $Li^6I(Eu)$ offers considerable promise as an instrument suitable for measuring fission-like neutron spectra above an energy of approximately 1.5 Mev. Its principal features as a fast-neutron spectrometer are a relatively high detection efficiency and moderate resolution. It now seems appropriate to consider application of the $Li^6I(Eu)$ technique to experiments in shielding and fission physics.

There is obviously room for improvement in the apparatus described in this report. As was mentioned, it is hoped that the Lucite light piper can be eliminated. It would be most desirable to surround the crystal with a slow-neutron absorbing material to cut down on the counts in the slow-neutron peak.

Finally, the relatively few $Li^6(n,\alpha)H^3$ cross-section points in the energy region of interest lead to considerable uncertainty in the detector efficiency. It is hoped that the use of experimental techniques described here will permit a remeasurement of the (n,α) cross section in more detail.

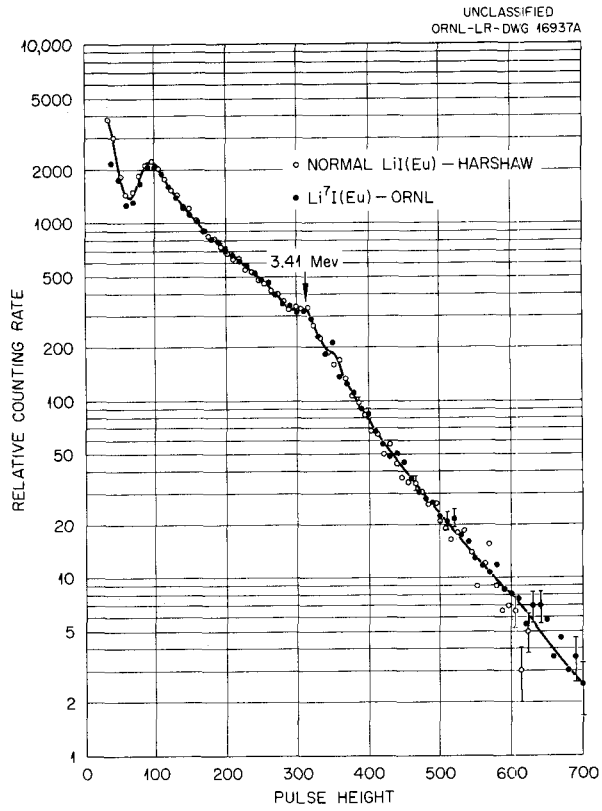

Fig. 10.2.13. Response of LiI(Eu) and $Li^7I(Eu)$ to Gamma Rays from the $B^{11}(p,\gamma)C^{12}$ Reaction.

10.3. PULSE-AMPLITUDE-INDEPENDENT TIMING CIRCUITS FOR DRIVING AN INTERMEDIATE-SPEED COINCIDENCE UNIT FROM THE OUTPUT OF A DOUBLE-LINE PULSE AMPLIFIER[1]

R. W. Peelle T. A. Love

All time-coincidence problems which arise in nuclear spectroscopy require that some element of the electronic apparatus associated with each detector observe the signal from that detector and produce a timing pulse. To the remainder of the circuit this pulse is the sole representation of the time of occurrence of each physical event. The precision attainable in the timing pulse depends upon the rise time and uniformity of the pulse from the detector and upon the characteristics of any pulse amplifiers placed between the detector and the timing circuit. In general, the slower the rise time of the detector and amplifier, the less precise the timing signal may be. The precision of the timing circuit, in turn, influences the attainable resolving time and the random coincidence rate which must be tolerated in a given experiment.

A method is discussed for improving the attainable timing precision by using the output from standard linear amplifiers. The method depends upon the characteristics of pulses from amplifiers with pulses shaped by two successive delay lines, wherein the pulse is shaped mainly by the successive action of two shorted delay lines of the same length, isolated from one another in the amplifier circuit. Some of the usual coincidence methods are summarized, and the design and properties of the method being introduced are discussed.

Coincidence Timing Systems for Nuclear Spectroscopy

Various problems in nuclear spectroscopy require that some small preselected fraction of the pulses from an energy-sensitive detector be analyzed according to pulse height. This fraction must frequently be chosen on the basis of time coincidence with pulses of preset heights in one or more auxiliary detectors. Such a requirement is used for all gamma-ray spectral measurements employing the multiple-crystal scintillation spectrometers previously described by the authors.[2] The necessary pulse-height analysis requires a single-channel differential pulse-height analyzer in the signal line from each of the auxiliary detectors and a multichannel pulse-height analyzer on the signal line from a main detector. If NaI(Tl) scintillation crystals or certain types of proportional counters are used, there is a strongly pulse-height-dependent time lag between the release of energy in the detector and the appearance of an output pulse from the corresponding single-channel analyzer. Therefore, it is impossible to use the output of the single-channel analyzer as a precise timing signal for determining coincidences between the physical events in the detector. If such a single-speed (single coincidence circuit) system is used with NaI(Tl) scintillation detectors, only the most favorable conditions allow resolving times of less than 0.5 μsec, and more typically a 1.0-μsec resolving time would be required. Usually two-speed coincidence systems are employed.

Two-speed coincidence systems help to meet the combined time and pulse-height analysis problems by employing partially separate circuit elements for the two functions. Figure 10.3.1 shows the block diagram of a two-speed (fast and slow) coincidence system which might be adjusted to give the optimum resolving time possible, with high efficiency, with the use of NaI scintillation detectors. Entirely separate signal channels are used for the timing and pulse-height requirements. The slow linear amplifier measures the total amount of charge collected at the photomultiplier, while the fast (wide-bandpass) amplifiers sense the rate of light output. Since the important phosphoresence of NaI(Tl) has a decay time of about 0.25 μsec, the linear amplifier "sees" a slowly rising pulse at its input, while the fast amplifier sees a pulse whose maximum is near in time to the physical occurrence of the event. If the energies of the gamma rays being detected are not too low, a

[1]The authors are indebted to E. Fairstein of the Instrumentation and Controls Division, who cooperated with them in discovering methods of approach for this problem.

[2]F. C. Maienschein, *Multiple-Crystal Gamma-Ray Spectrometer*, ORNL-1142 (April 14, 1952); T. A. Love, R. W. Peelle, and F. C. Maienschein, *Electronic Instrumentation for a Multiple-Crystal Gamma-Ray Scintillation Spectrometer*, ORNL-1929 (Oct. 25, 1955).

system of the type shown in Fig. 10.3.1 is capable of using coincidence resolving times as short as 10 to 20 mμsec with counting efficiencies greater than 95%.

Since the fast amplifiers required for the fast-slow system of Fig. 10.3.1 are expensive, tend to react badly to overload pulses, and generally complicate the operation and maintenance of the equipment, a more simple two-speed system has become popular with those who do not require minimum resolving time. Figure 10.3.2 illustrates another two-speed system, which will be called an "intermediate-slow" system. The distinguishing feature of such systems is that the timing signal used to announce the occurrence of each pulse to the faster leg of the coincidence system is here obtained from the output of the slow linear pulse amplifier. The difficulties of obtaining a timing signal from a slow pulse, and the consequent loss of attainable resolving time, may be compensated for by the elimination of the need for wide-bandpass amplifiers.

Two phenomena, usually called "walk" and "jitter," are important in considering the time lag

UNCLASSIFIED
2-01-058-0-340

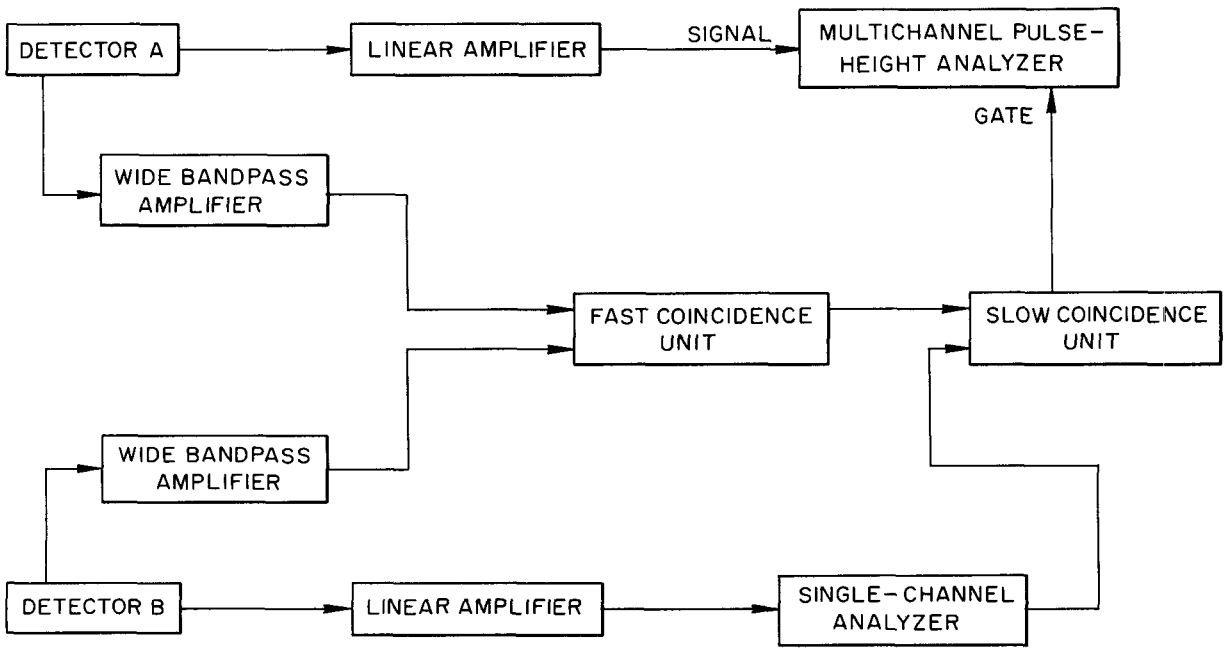

Fig. 10.3.1. Block Diagram for a Typical Two-Speed Coincidence Circuit Employing "Fast" and "Slow" Coincidence Circuits as Used to Gate a Multichannel Analyzer. "Fast" and "slow" refer to the pulse rise times within the two coincidence circuits. The fast circuit allows coincidence resolving times on the order of 10^{-8} sec, while the slow circuit might use about 2 μsec. In the unit shown, a completely independent fast-signal channel is employed to determine the time coincidence. The rise time at the output of the wide-band amplifiers is sufficiently sharp for the threshold device built into the fast coincidence circuit to adequately determine the pulse timing. In principle, the fast circuit can be made to trigger on the first few electrons emitted from the photocathode of the photomultiplier. As is usual in two-speed circuitry, the slow coincidence circuit mixes signals from the pulse-height analyzers and the fast circuit to assure that the coincident pulses have pulse heights in the preset range. A twofold circuit is illustrated here, but additional channels may be added which are similar to the one associated with detector B.

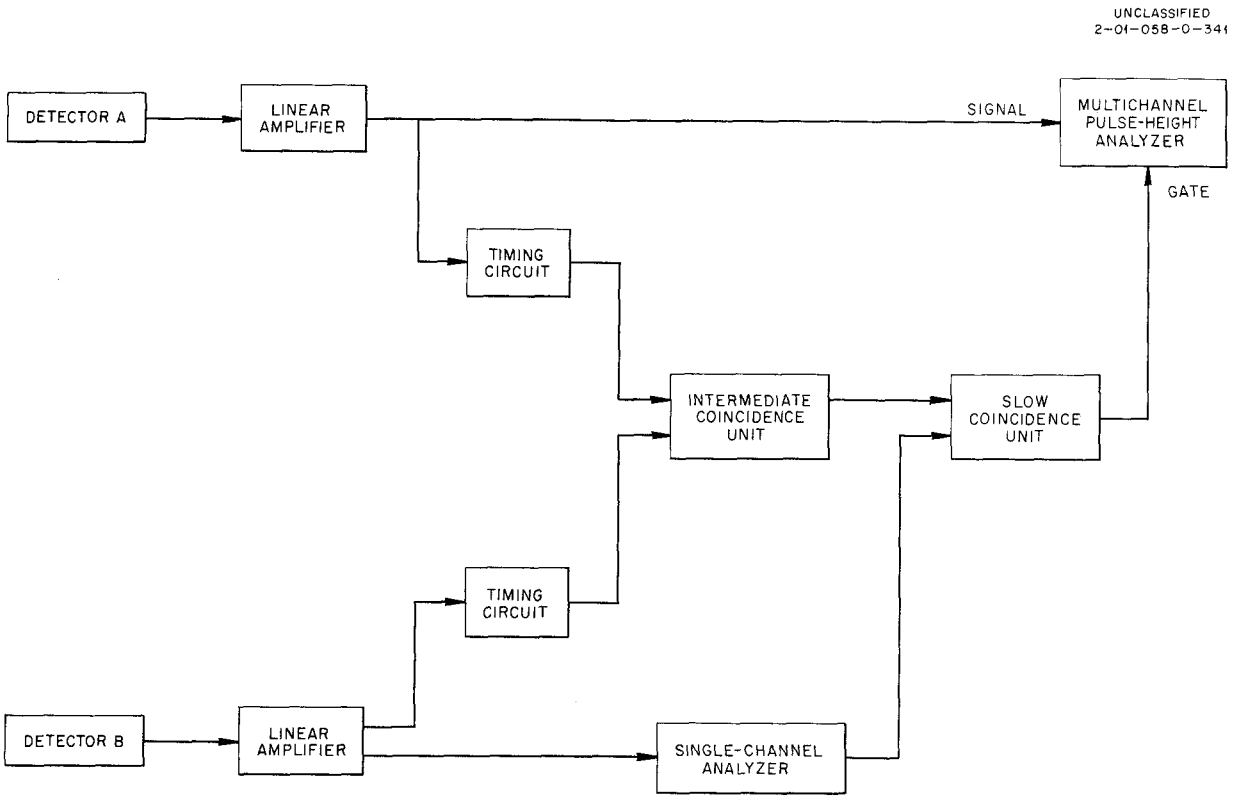

Fig. 10.3.2. Block Diagram of a Typical Intermediate-Speed–Slow-Speed Coincidence System for Use in Gating a Multichannel Analyzer. In this case the timing circuits which gate the intermediate coincidence circuit obtain their input signals from the output of the slow linear amplifiers. Usually these timing circuits contain threshold devices which observe the time at which the amplifier output crosses a voltage level just above, or in the upper reaches of, the noise level. The pulse-amplitude-independent timing circuits described in this paper replace the simple threshold timing circuits.

between the detected event and the output of the timing circuit of Fig. 10.3.2. The magnitude of these effects, which are more serious here than in the true fast-slow systems, limits the usable resolving time of the system of Fig. 10.3.2. "Jitter," which refers to statistical fluctuations in this time lag that occur for a given pulse height, is generally caused by random noise or by fluctuations in the amplifier output-pulse shape caused by detector statistics. "Walk," which refers to any systematic pulse-height dependence of the time lag, limits the coincidence resolving time in the usual intermediate-slow system.

Figure 10.3.3 illustrates the cause of walk in the usual timing circuits. These circuits yield an output signal when the amplifier output pulse crosses a preset threshold level V_T. This threshold is adjusted to the lowest level consistent with the detection of noise, and may usually be set lower than the lower limit of the range of the pulse-height analyzer V_L. The two pulses shown correspond to the limits, V_L and V_U, of the analyzer pulse-height range, and the walk between these pulse heights is the interval ΔT between the times that these two pulses cross the threshold level V_T. In the case of sodium iodide detectors the total rise time of the pulses is almost 1 μsec, and so the walk will be this large unless the threshold level V_T can be set well below V_L. In the intermediate-slow system[2] the section of the "intermediate" coincidence circuit corresponding to the multichannel analyzer required a 0.3-μsec coincidence gate with V_T = 1.5 v, V_L = 4.5 v, and V_U = 45 v. Since more restricted ranges of pulse

heights were employed on the auxiliary signal channels, the corresponding walk was smaller and the required coincidence gates were as narrow as 0.05 μsec. (The coincidence circuit employed allows for different lengths of rectangular-shaped pulses for each of its inputs.)

Figure 10.3.3 also illustrates the circumstance which allows a reduction in walk from timing circuits of the type required for Fig. 10.3.2. The pulse shapes shown are supposed to be taken from the output of a double-line amplifier such as the DD-2 amplifier.[3] It is to be noted that both the small and large pulses cross the base line at the same time. The lag from the beginning of the pulse to this crossover is approximately equal to the time delay of the pulse-clipping delay lines in the amplifier, plus an allowance for finite rise time which is approximately equal to the time required for the pulse to reach half its maximum amplitude. These times are fixed by delay-cable characteristics, phosphor light-output decay time, and amplifier rise time, and are therefore *nearly independent* of pulse height if no part of the amplifier circuitry is saturated.

The remainder of this section is devoted to a description of "crossover pickoff" timing circuits capable of giving output pulses at the illustrated crossover point.

[3]E. Fairstein, *Rev. Sci. Instr.* 27, 475 (1956).

UNCLASSIFIED
2-01-058-0-342

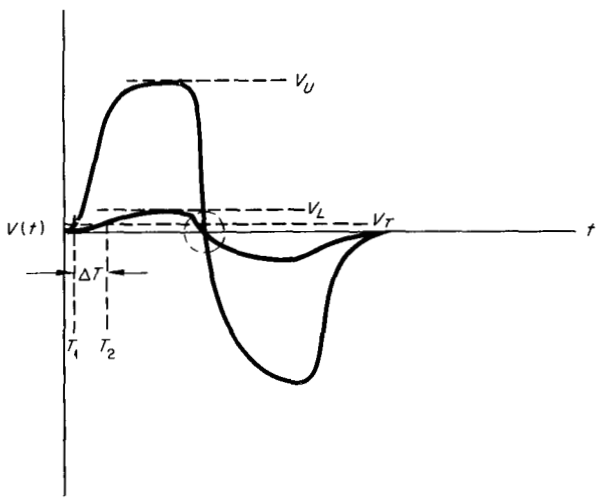

Fig. 10.3.3. Illustration of the "Walk" Phenomenon for Pulses from a Double-Delay-Line Pulse Amplifier. Two pulses are shown with heights V_L and V_U corresponding to the lowest and highest channels of the multichannel analyzer used. V_T represents the voltage threshold of a conventional pulse-timing circuit. T_1 and T_2 are the time lags at which the conventional timing circuit would yield output pulses. The walk over the important range of pulse amplitude is here ΔT. The circled point on the time axis is where all non-overload pulses cross the base line. The typical delay between the occurrence of the event and this pulse crossover is 1.6 μsec with a sodium iodide detector if the amplifier uses about 1.3-μsec clipping lines.

General Design of Crossover Pickoff Timing Circuits

In the paragraphs which follow, some of the general requirements for the design of antiwalk timing devices which use the pulse crossover of a double-line amplifier are discussed, and the methods of approach which have thus far been used in the design are indicated.[4]

Since the circuits are to be designed to eliminate walk, they should be capable of reducing the limits of this shift to about 5 to 15 mμsec for pulses with amplitudes between the upper and lower levels illustrated in Fig. 10.3.3. As will be discussed later, jitter in the position of the crossover point tends to preclude benefit from any further lessening of the walk. The circuits must fail to fire on pulses smaller than some noise threshold, and the optimum condition is for this threshold (V_T) to coincide with lower level (V_L) of the range of pulses to be analyzed. While in most cases the desired noise threshold is in the region between 2 and 5 v, it should be possible to adjust the circuit to a higher threshold provided that the lower level of the analyzer range is also raised. The circuit must be free of bias shifts which change the position of the timed pulse at the highest count rates to be used. Jitter caused by the pile-up of pulses in the amplifier cannot be avoided, but that caused by the voltage distortion persisting after propagation of a pulse in the timing circuit must be eliminated by a reduction in the time required for recovery.

[4]E. Fairstein and T. A. Love, "A Pulse Crossover Pickoff Gate for Use with a Medium-Speed Coincidence Circuit," *Instrumentation and Controls Ann. Prog. Rep. 1957* (in press).

The utilization of the hysteresis voltage in a Schmidt trigger circuit has been proposed as the basic element of an antiwalk timing circuit. A basic trigger circuit is illustrated schematically in Fig. 10.3.4. The voltage difference V_H is the hysteresis of this circuit, and its magnitude depends upon the tube characteristics, the size of the pulse applied to the grid of the second tube from the plate of the first tube, and the potentials on the tube electrodes. This hysteresis voltage is approximately as stable as the other characteristics of the trigger circuit. The desired antiwalk device may be constructed by setting the hysteresis voltage equal to the desired noise threshold and adjusting the input bias until a pulse of height V_H will just trigger the circuit. Under these conditions the circuit will reset just as the input signal crosses the base line. The trailing edge of the output signal is then used to provide the timing pulse. With this circuit the level V_L of Fig. 10.3.3 may be set equal to V_T of Fig. 10.3.4*b*.

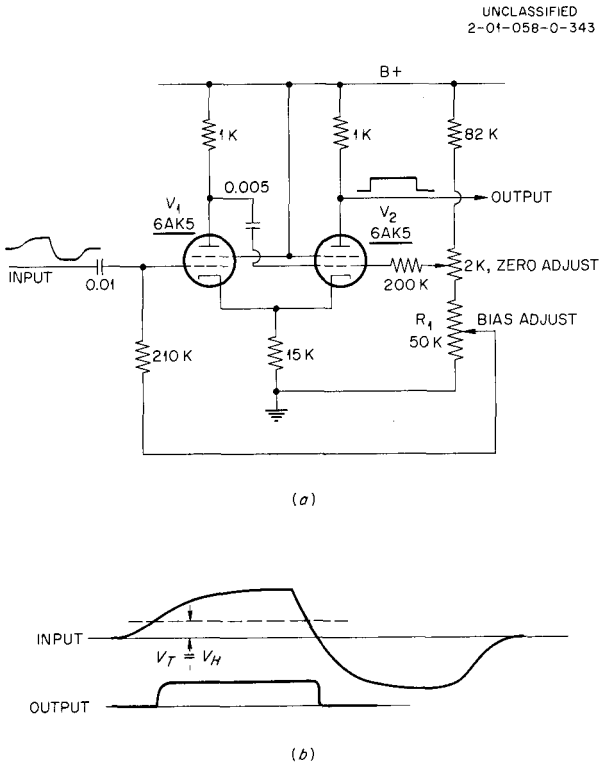

Fig. 10.3.4. Use of a Basic Schmidt Trigger Circuit as a Pulse-Crossover Pickoff Device. (*a*) Schematic drawing of the circuit. All pulses above a voltage threshold V_T trigger the feedback network which rapidly transfers plate current from V_2 to V_1. The circuit resets on the negative-going back edge of the input pulse, but not until this input pulse reaches a level $V_T - V_H$. V_H is known as the hysteresis voltage of the circuit. The text describes how this circuit must be modified to produce a useful timing circuit. (*b*) Input and output pulses of the circuit on the same time scale. It is assumed that the voltage threshold has been set equal to the hysteresis voltage. Note that the output recovers to its initial level at the pulse-crossover time. The next stage of the timing circuit must be designed to give an output pulse at the time of this negative transient.

Fairstein has designed[4] a conventional Schmidt trigger circuit with a novel pulse-limiting device at the input, which satisfies all the criteria of the above paragraph. The authors are developing a similar circuit which avoids limiting the input pulses, at the expense of additional active elements. An additional nonessential advantage of the second hysteresis device is that it may be used as an integral discriminator, although it must be realized that the antiwalk feature depends on a proper matching of hysteresis and discriminator voltages. The design of this circuit, which has not yet been thoroughly tested, is discussed later (see "The Bootstrap-Schmidt Hysteresis Antiwalk Circuit").

The authors have also used the independently designed crossover-pickoff antiwalk device described later (see "A Bias-Transfer Timing Circuit"). It yields an output on the negative-going part of the input pulse from a double-line amplifier and is normally biased so that noise pulses cannot trigger the circuit. With the occurrence of a sufficiently large pulse, the bias is temporarily altered so that the circuit triggers at the pulse crossover point.

While these circuits are typically capable of reducing walk in an intermediate-coincidence system by about 20 times, jitter is usually made more serious (see "Performance of the Bias-Transfer Circuit").

A Bias-Transfer Timing Circuit

The timing device which has been used with the multiple-crystal gamma-ray spectrometer during the past year (see, e.g., Sec 6.2) was adopted in order to allow reduction of random backgrounds by shortening the coincidence-circuit resolving times. Figure 10.3.5 shows the complete schematic of the

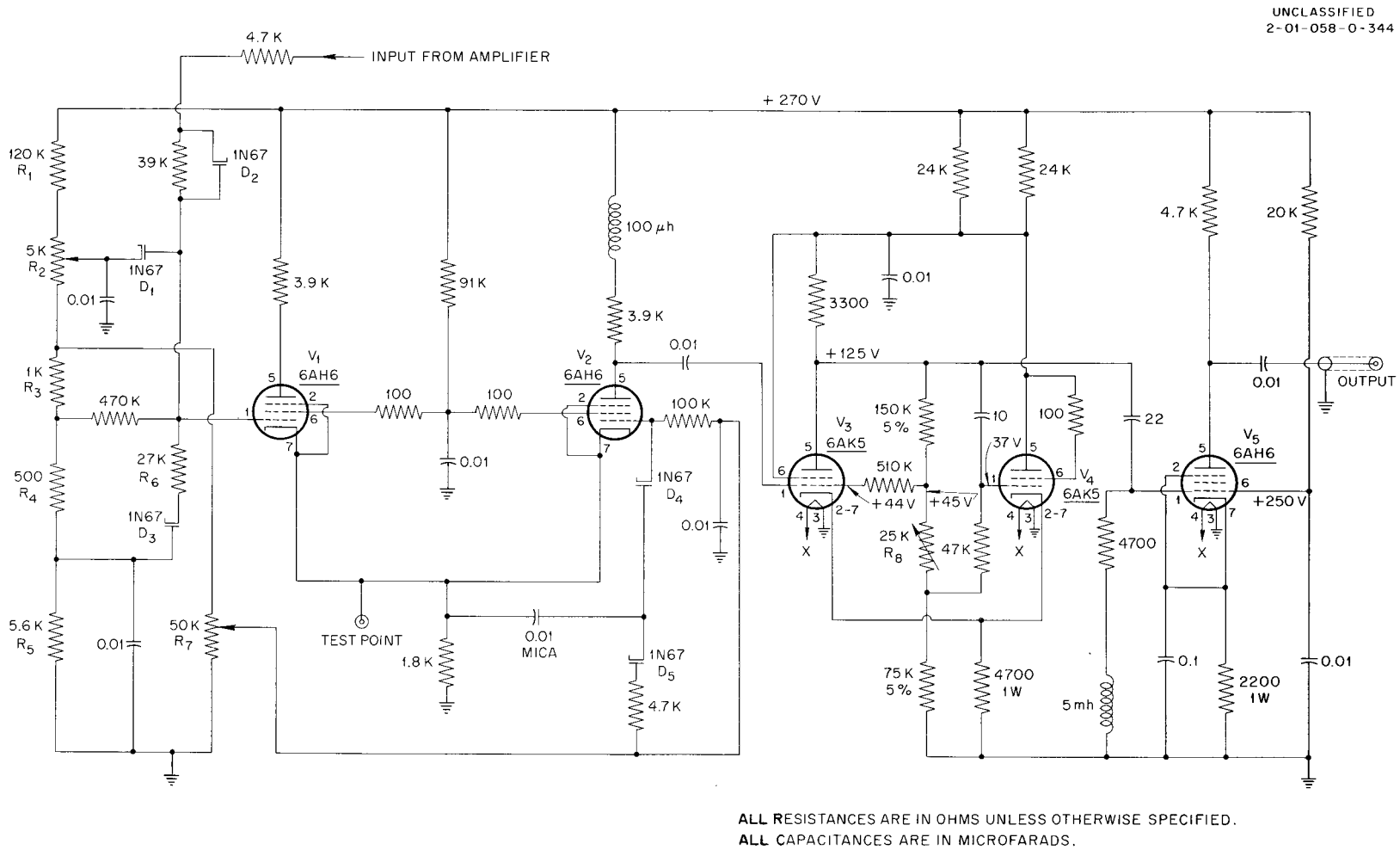

Fig. 10.3.5. Circuit Schematic Drawing of a Bias-Transfer Pulse-Height-Independent Timing Circuit. This unit has been mounted on the chassis of a DD-2 double-delay-line amplifier. The input of this circuit is d-c–coupled from the amplifier output, and the output of the timing circuit is fed to the coincidence circuit which has an input impedance of 1000 ohms.

timing circuit presently in use. The first stage, based on two 6AH6 vacuum tubes, is a difference amplifier designed to yield an output pulse at the instant that the double-line amplifier pulse crosses the base line. The set of 6AK5 tubes (V_3 and V_4) forms a trigger-circuit pulse shaper adjusted to fire when the negative output from the difference amplifier reaches the 5-v level. The output 6AH6 tube is designed to feed a 20- to 30-v, ½-μsec-wide negative spike into a 1000-ohm load at the input of the coincidence circuit. Except for the bias adjustment resistor, R_8, the last two stages are identical to the corresponding stages of the integral discriminator (PHS) circuit on the standard A-1 amplifier designed by Bell and Jordan.[5] The remainder of the discussion is confined to the two-tube difference amplifier at the input of the timing circuit.

The left side, V_1, of the modified difference amplifier is normally conducting, so that a negative pulse of sufficient magnitude applied to its grid will yield a negative output from the plate of V_2. The positive phase of the input signal from the double-line amplifier is limited by the diode D_1 when the d-c level at its plate reaches the level preadjusted by the potentiometer R_2. The 39K resistor in series with the signal prevents serious loading of the amplifier on the positive swing and aids the clipping action. The negative-going phase of the input pulse, if of sufficient magnitude, switches plate current from V_1 to V_2, yielding a negative output pulse to the shaper circuit. The diode, D_2, across the 39K resistor prevents the negative-going pulse from being unduly slowed by the parasitic capacity on the grid of V_1. Care is taken to d-c–couple the signal from the amplifier in order to avoid bias shifts in the grid circuit of the 6AH6 tube. The diode D_3 and resistor R_6 are not essential to the logic of the circuit but are required at high counting rates to avoid serious d-c shifts in the bias-resistor stick, $R_1 \ldots R_5$. Current through D_3 on the negative phase of the input pulse tends to balance the current through D_1 in the positive phase, keeping the grid bias on the input tubes reasonably constant.

It is necessary to clip the input positive pulse close to the lowest level desired for the pulse-height analysis, so that the grid of V_1 sees a constant pulse height for all inputs in the region where walk is to be avoided. A typical level V_C for this clipping is 5 v, and the circuit seems not to work well for V_C below about 4 v. This level is such that grid current is not drawn in V_1 during the positive pulse. The positive input signal drives the common cathode and feeds some charge through diode D_4 onto the parasitic capacity at the grid of V_2. The resulting voltage increment, approximately V_c, decays with a time constant of a little less than 1 μsec and so is largely gone when the input pulse recovers from its negative swing. The diode D_5 provides a discharge path for the parasitic capacity on the plate of D_4.

If the potentiometer R_7 is adjusted so that when the grid of V_1 lies at its no-signal level, the addition of V_c to the bias on V_2 would produce sufficient plate current in V_2 to fire the trigger circuit, the circuit should give an output at the crossover time of any amplifier pulse which has an amplitude larger than V_c. A number of corrections to this simple explanation arise from the decay of the stretched pulse on the grid of V_2, the slowing of the fall of the input pulse by the input network, the nonideal characteristics of the various diodes, the less-than-unity gain of V_1 on the positive-going phase of the input pulse, and the variations in the firing time of the circuit V_3–V_4 with the character of the signal from V_2.

The adjustment procedure for this circuit depends upon whether the noise threshold or the lower level of the nonwalk region is more important. In the first case R_7 is adjusted first, but in the latter case R_2 is adjusted first. Optimum adjustment of the other resistor is accomplished by educated trial and error. The circuit functions in a trouble-free manner for large pulses; the difficulties always occur for pulses near the threshold. (For discussion of circuit performance see "Performance of the Bias-Transfer Circuit," below.)

The Bootstrap-Schmidt Hysteresis Antiwalk Circuit

Figure 10.3.6 shows the complete diagram of an experimental timing circuit which utilizes the hysteresis effect of a modified Schmidt trigger circuit. As explained above (see "General Design of Crossover Pickoff Timing Circuits"), the operation of this unit depends upon the input bias

[5] W. H. Jordan and P. R. Bell, *Instruction for Use of Al Amplifier and Preamplifier*, Mon P-323 (revised Feb. 15, 1949).

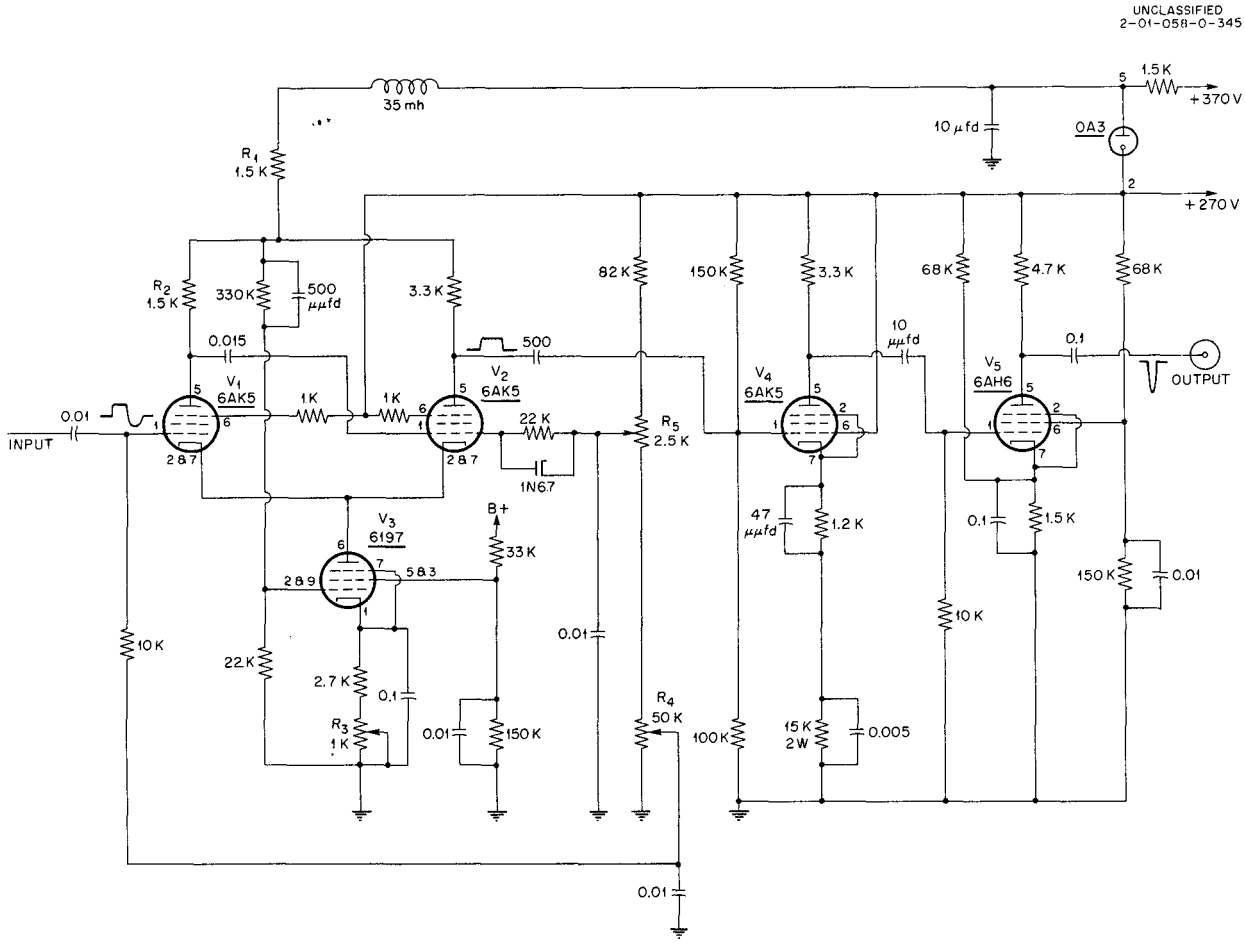

Fig. 10.3.6. Circuit Schematic Drawing of a Bootstrap-Hysteresis Pulse-Height-Independent Timing Circuit. The first three tubes form the novel trigger circuit which signals the pulse-crossover point. The circuit acts as a timing circuit if the bias adjustment R_4 is set so that V_T equals V_H, as in Fig. 10.3.4. The unit may act as an integral pulse-height discriminator for pulses higher than $\frac{1}{2}V_H$ by setting V_T at the desired level, provided that the zero adjustment R_5 has been properly set. This circuit obtains its input signal from the DD-2 amplifier on which it is mounted and feeds its output into a 1000-ohm load at the input of the coincidence circuit.

being set so that a pulse having a height just equal to the hysteresis voltage will barely fire the trigger circuit. The output tubes V_4 and V_5 comprise a pulse-forming network which is designed to yield a negative output about 25 v in height with a fast rise time (~ 0.1 μsec) and a width at the base of about 0.5 μsec, into a 1000-ohm resistance, at the time at which the trailing edge of the positive pulse from the bootstrap-Schmidt circuit goes negative. This output circuitry will not be discussed further here, although it is important that the time and shape of the output pulse should not depend upon counting rate or the magnitude of the input pulse.

The bootstrap-Schmidt circuit shown in Fig. 10.3.6 resembles the simple trigger circuit in Fig. 10.3.4, but it differs in that the common cathode resistor has been replaced by a bootstrap pentode, V_3. The function of this pentode resembles that of a constant current tube, but the grid senses the current in a common plate resistor, R_1. In this manner the pentode in the cathode circuit acts to hold constant the total plate current in the two 6AK5 tubes. This type of modification is necessary if the input signal is not to be limited. After the circuit has flipped on the rising transient of the input pulse, the constant-plate-current tube prevents the input 6AK5 tube from drawing grid

current on large input pulses, and on the negative transient which leads to the crossover point, the bootstrap feature allows the cathode of the 6AK5 tube to follow the input pulse accurately. In other respects, this circuit seems to operate much like an ordinary Schmidt trigger circuit. The circuit illustrated in Fig. 10.3.5 has been partially tested, but the design needs some further revision. The trailing edge of the positive pulse from the trigger stage is very fast, requiring only about 20 mμsec to reach the base line. The walk of this transient is less than 10 mμsec for the entire range of input signals from the hysteresis level, where the circuit first triggers, to 90 v. The hysteresis level has been successfully adjusted from 2.5 to 18 v by the values of R_2 and R_3 being changed appropriately. There is adequate immunity to count-rate shifts for rates up to 5×10^4 counts/sec. The linearity as an integral discriminator and the drift rate have not yet been studied. The walk is most serious for pulses larger than 50 v, suggesting that some redesign is required for optimum performance, since the most difficult region might be expected to lie near the triggering level.

Performance of the Bias-Transfer Circuit

Four types of evidence are deemed important in the evaluation of the performance of the bias-transfer circuit: extent of walk and jitter, dependence upon count rate, and drift rate. These items are discussed in the paragraphs below.

Four copies of the bias-transfer circuit have been used by the authors, three of which have been adjusted to give minimum attainable walk in the region of amplifier output pulses between 5 v and overload. The corresponding amplifiers are clipped with 1.3-μsec decay lines. With a noise-counting threshold between 1.5 and 2.0 v it has always been possible to reduce the walk to the extent that the corresponding rectangular pulse in the coincidence circuit would lie within ±5 mμsec of its position with large pulses. This measurement is performed with 60 counts/sec test pulses by observing the position of the rectangular pulse on an externally triggered oscilloscope, while adjusting the "coarse gain" switch on the amplifier. The assumption is made that the pulse shape is independent of this switch, an assumption not fully verifiable. One bias-transfer circuit has been operated with the noise-counting threshold at about 5.5 v and the lower edge of the usable analyzer range at about 16 v. This circuit has operated less satisfactorily, although this may be attributed to the fact that the input pulses were shaped with shorter (~~1.5~~ 0.75 μsec) clipping lines. Walk in this circuit measures less than ±10 mμsec.

The effect of high count rates has been observed by superimposing high random rates from natural sources upon the 60 counts/sec test pulses used for visual observation. At count rates over 10^4 counts/sec, the jitter caused by pulse pile-up becomes important enough to make observations more difficult, but walks of less than 10 mμsec are observed when count rates of about 10^5 counts/sec of 50-v pulses are introduced.

No systematic record of drift rate has been maintained. However, each circuit has been checked about twice a week during the past nine months. Minor readjustments have been required about once in three weeks for each circuit. Need for more than trivial adjustment is much less frequent.

For intermediate-speed timing circuits which sense the pulse-crossover point, jitter has been found to dominate the choice of coincidence resolving time. Jitter originates because the position of the crossover point depends upon the pulse shape. A signal of constant amplitude and frequency from a test pulse generator has a jitter of <3 mμsec. Some of the possible causes for pulse-shape fluctuations are listed below:

1. Random noise may be superimposed upon the pulses, especially in applications using high-gain amplifier systems.
2. At high count rates, pile-up may occur, in which small pulses may be superimposed upon those of the size being analyzed. This causes jitter much like that from random noise.
3. Detector and photomultiplier statistical variations generate fluctuations in pulse shape.

Noise is seldom important for scintillation detectors, although it makes a contribution in the case of the spiral fission chamber used by the authors. Pile-up pulses, if not generated simultaneously, produce a single output which does not fall at the time appropriate for either of the physical events responsible for the pulses. However, a small pile-up pulse will produce a small displacement in the timing pulse for a much larger pulse of interest. This behavior differs markedly from that of a simple threshold pulse-timing circuit in which the timing pulse will be correctly located

for the first of two interfering pulses, provided that the first pulse exceeds the threshold level before the arrival of the second pulse. This difference of behavior may be an advantage or a disadvantage.

If it is assumed that the linear pulse amplifier precisely reproduces the pulse shape from a scintillation detector, it should be possible to estimate the amount of jitter which might be observed for a given absorbed energy. This may be done if the jitter is considered to arise from the same statistical origin as the energy spread observed with a monoenergetic gamma-ray source and the scintillation detector. This implies that the transit-time spread of electron traversing the photomultiplier is ignored. Depending upon tube type and operating conditions, this spread is of the order of 5 to 10 mμsec.

The effect of time jitter may also be measured in at least two ways. One method involves the measurement of a fixed coincidence rate with varying coincidence resolving time, the signal delays being carefully adjusted for optimum coincidence efficiency. In this measurement the effect of jitter is seen in a lower apparent coincidence rate for short resolving times. The second method requires the use of a time analyzer such as that described in Sec 10.5. For twofold coincidence work, a time analyzer allows a differential time spectrum of the interval between the timing pulses from the two detectors. Figure 10.3.7 shows a typical time distribution obtained by using bias-transfer timing circuits and NaI(Tl) scintillation detectors. The curve was obtained by using a positron source, which gives rise to annihilation quanta useful for generating true coincidences. Figure 10.3.7 indicates that for this case, which involved little question of walk, the differential jitter distribution is accurately represented by a normal, or Gaussian, distribution.

If a sufficiently small-sized pair of NaI crystals is used to assure a reasonable number of pulses at energies lower than the 511-kev quanta, the time analysis method may be used to study jitter as a function of energy absorbed in each scintillation. Figure 10.3.8 shows three such distributions obtained for absorbed energies of about 100, 300, and 511 kev. The results clearly indicate that jitter may be expected to increase for lower absorbed energies.

The variation of the width of the jitter distribution as a function of amplifier rise time has also been studied by using coincidences from 500-kev absorbed energy in each of the two detectors. With the rise time for scintillation pulses, from the

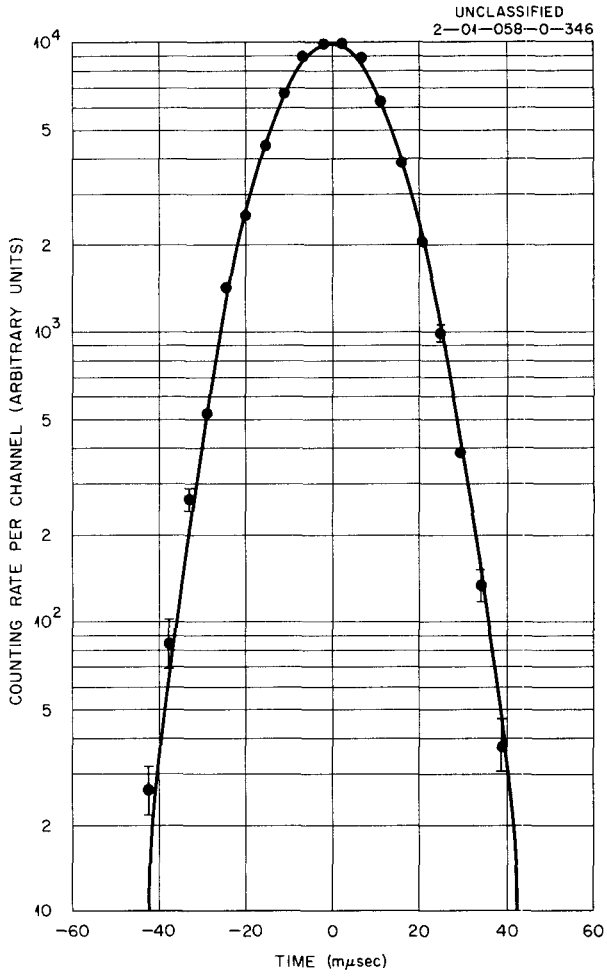

Fig. 10.3.7. Differential Jitter Distribution Observed with Bias-Transfer Timing Circuits. The solid points were experimentally obtained by using gamma rays of 250- to 350-kev energy absorbed in each of two sodium iodide crystals. One RCA-type 6655 and one Dumont-type 6291 photomultiplier tube were used. The time analyzer is described elsewhere in this report (see Sec 10.5). Typical statistical errors are shown. "Zero" time and the ordinate position have been set arbitrarily. The solid line is a fitted normal distribution with a standard deviation of 11.8 mμsec. The fit is considered to be excellent. This figure indicates that a coincidence resolving time of 35 mμsec would have a 99.5% counting efficiency at this energy.

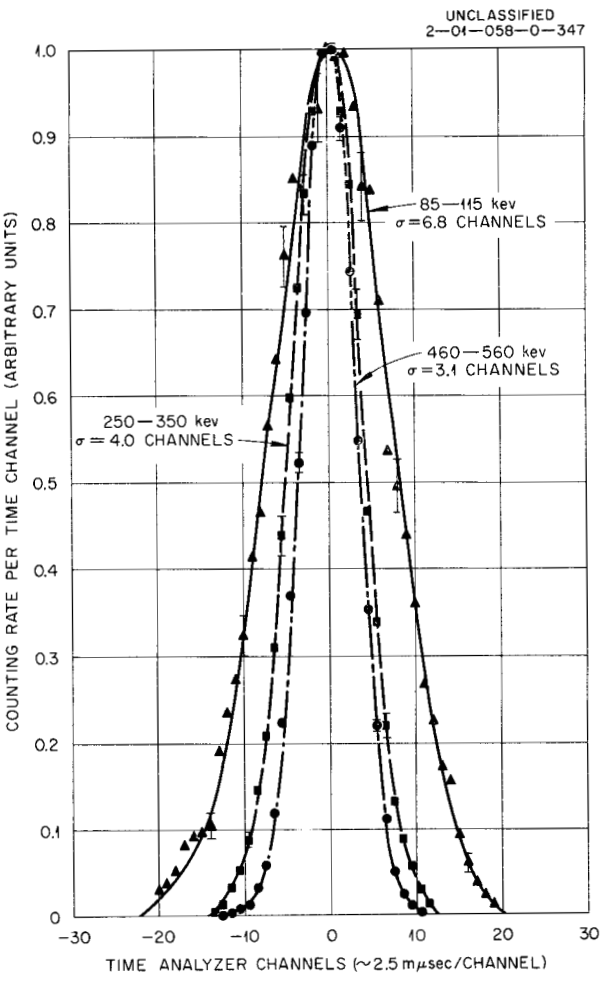

Fig. 10.3.8. Energy Dependence of Jitter with NaI(Tl) Scintillation Crystals. Differential jitter distributions are shown on an arbitrary scale. These distributions were obtained with time analyzer channels 2.48 ± 0.05 mμsec in width. An Na^{22} source was placed between two 1-in.-dia sodium iodide scintillation crystals, one placed on an RCA-type 6655 photomultiplier tube, and the other on a DuMont-type 6291 tube. Single-channel analyzers on each branch of the circuitry were set on the energy ranges shown. Although the lines have been drawn to follow the experimental points, the curves may be fit with normal distributions having the standard deviations shown. The standard deviation of the approximately 300-kev data differs from that of Fig. 10.3.7 because the amplifier rise times were shortened between the two runs. Typical standard deviations are shown. For these data, the pulses from the detector required about 0.22 μsec to reach half their maximum amplitude.

start of each pulse up to one-half its maximum height, measured to be about 0.4 μsec, the standard deviation of the corresponding jitter distribution was 9.4 mμsec. With the time for the pulse to reach half height shortened to 0.14 μsec, the standard deviation of the jitter became 6.5 mμsec. This shows clearly that the rise time affects the jitter distribution, but the details of the mechanism are not apparent. Some of the increase in jitter as the pulse is slowed may arise because the sharpness of pulses inside the timing circuit is affected; that is, some of the jitter might arise from uncertainties in the pulse-shaping stage (V_3 and V_4 in Fig. 10.3.5).

Summary

Circuits have been designed which take advantage of the pulse-height independence of the time at which the output signal from a double-line amplifier crosses the base line. These circuits materially reduce the resolving times necessary for the high-efficiency operation of two-speed coincidence systems without wide-bandpass amplifiers, and display drift and count-rate characteristics which allow their wide and consistent use.

10.4. NEW ION CHAMBERS FOR GAMMA-RAY DOSE MEASUREMENTS

J. D. Kington R. K. Abele

Two ion chambers of the graphite-wall type have been designed and tested. One is a 50-cm^3 spherical ion chamber which is an improved version of the old 50-cm^3 standard ion chamber.[1] The other is a high-level ion chamber designed for measuring gamma-ray energy deposition in graphite in a high-intensity field such as would be encountered in a radiation damage facility.

The new 50-cm^3 spherical chamber (Fig. 10.4.1) was designed with the same diameter electrodes (high voltage and collector) as those used in the old design. Spherical design was chosen in an attempt to obtain a more uniform directional response. The materials of construction are essentially the same as those previously used. Materials of low thermal-neutron cross section (graphite and magnesium) are used in the sensitive end of the detector. The waterproof housing is of Lucite for water equivalence, and part of this can be removed for air calibration. Signal insulation is polystyrene, chosen for radiation damage considerations, and polyethylene, which is used in the available coaxial cable, but fluorothene is used for high-voltage insulation. Here hydrogenous materials were avoided because this material is exposed to the collecting volume of the chamber, and these chambers may be operated in a neutron flux of appreciable magnitude. In addition, all air volumes were eliminated around the coaxial signal lead except at the connectors. The volume at the connector is several inches behind the sensitive volume, but it could be eliminated for special applications.

The second gamma-ray ion chamber (Fig. 10.4.2) has an active volume of 4 cm^3. The materials are essentially the same as those of the 50-cm^3 chamber described above. One difference is that the waterproof case is made of polystyrene because of radiation damage considerations. This is a chamber for use in high-level radiation fields (up to 3×10^5 $ergs \cdot g^{-1} \cdot sec^{-1}$). The 4-$cm^3$ volume is the result of a compromise between the desired sensitivity and problems associated with small size. The smaller volume increases the percentage contribution of the ion-collection volumes which are located outside the chamber proper. In addition, ruggedness is sacrificed in an extremely small chamber of graphite. A spherical configuration was not used for this chamber, since structural reliability would have been sacrificed.

One of the first experiments with these chambers was conducted in an attempt to ascertain the degree of ion collection as a function of the radiation field and the chamber voltage. Both chambers were tested next to the Bulk Shielding Reactor at various appropriate power levels up to 200 kw, with the results shown in Fig. 10.4.3. The currents were measured with (1) a Beckman

[1] L. H. Ballweg and J. L. Meem, *A Standard Gamma Ray Ionization Chamber for Shielding Measurements*, ORNL-1028 (July 9, 1951).

UNCLASSIFIED
2-01-058-0-300

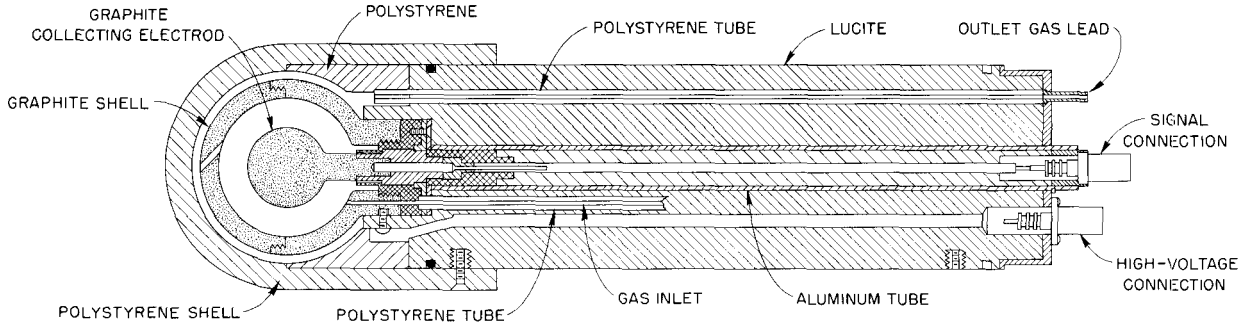

Fig. 10.4.1. A 50-cm^3 Spherical Gamma-Ray Ion Chamber.

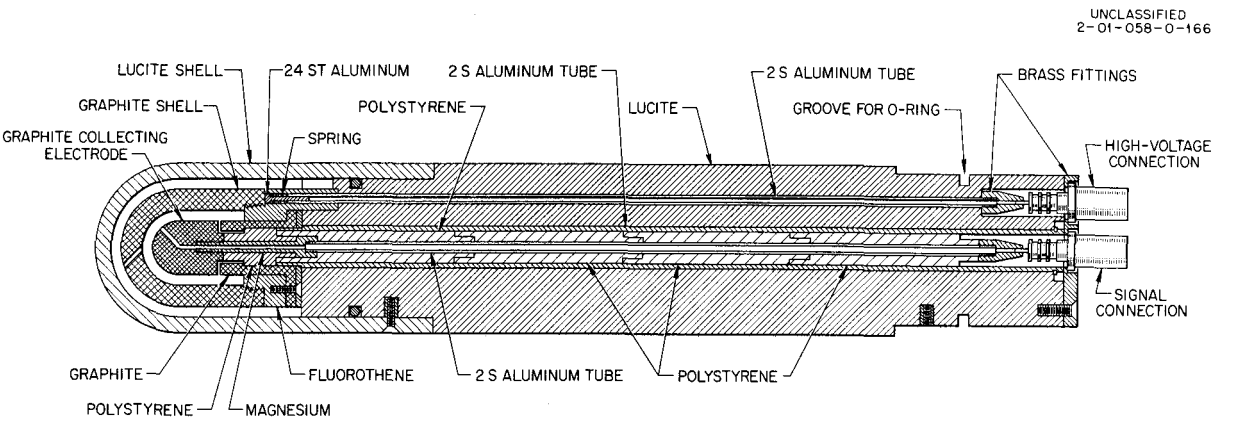

Fig. 10.4.2. A High-Level Gamma-Ray Ion Chamber.

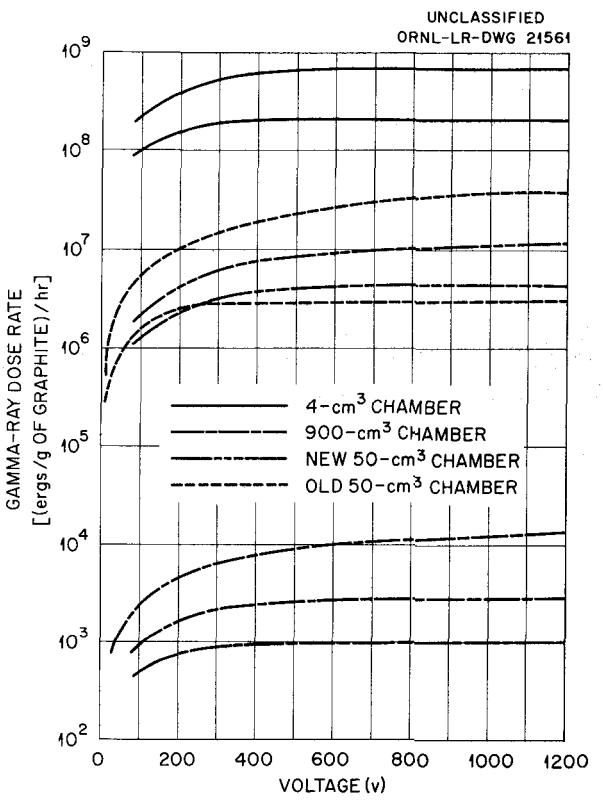

Fig. 10.4.3. Saturation Properties of Several Gamma-Ray Ion Chambers: Ion Current as a Function of Collection Voltage.

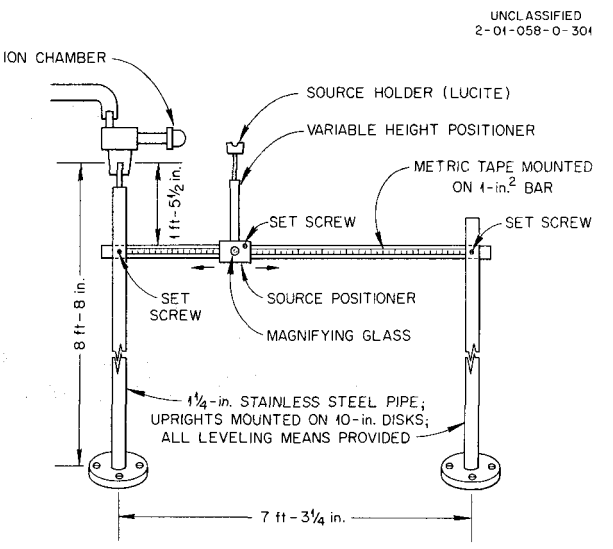

Fig. 10.4.4. Apparatus for Testing or Calibrating Gamma-Ray Ion Chambers.

micromicroammeter, (2) an electrometer and galvanometer, and/or (3) a current chopper feeding a Berkeley Universal timer and printer.

In another experiment a new apparatus (see Fig. 10.4.4), which was built for testing and calibrating the ion chambers in either air or water as a function of the angular incidence of the radiation, was used. A source at the end of a rod can be revolved about a point on the locating bar just under the center of detection of the ion chamber. The angular response of the 50-cm^3 spherical chamber to a source of Co^{60} gamma rays 54 cm from the center of detection in water is compared to the response of the 50-cm^3 standard chamber in Fig. 10.4.5. The nose of the counter points toward 0 deg. A similar comparison of the responses of the two counters in air is given in Fig. 10.4.6. The tests indicate that the two chambers are similar with respect to angular

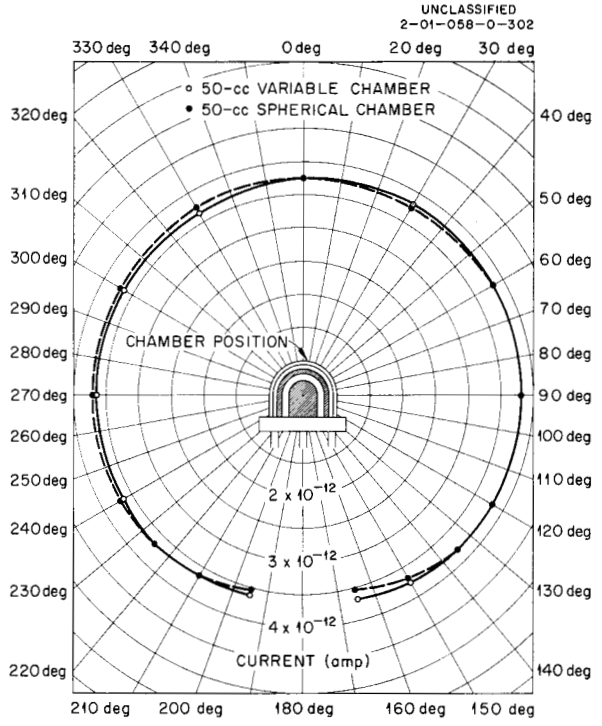

Fig. 10.4.5. Response of 50-cm^3 Gamma-Ray Ion Chambers in Water as a Function of the Angular Incidence of Radiation: Co^{60} Source (1 r/hr at 1 meter) Positioned 54 cm from Geometrical Center of Chamber.

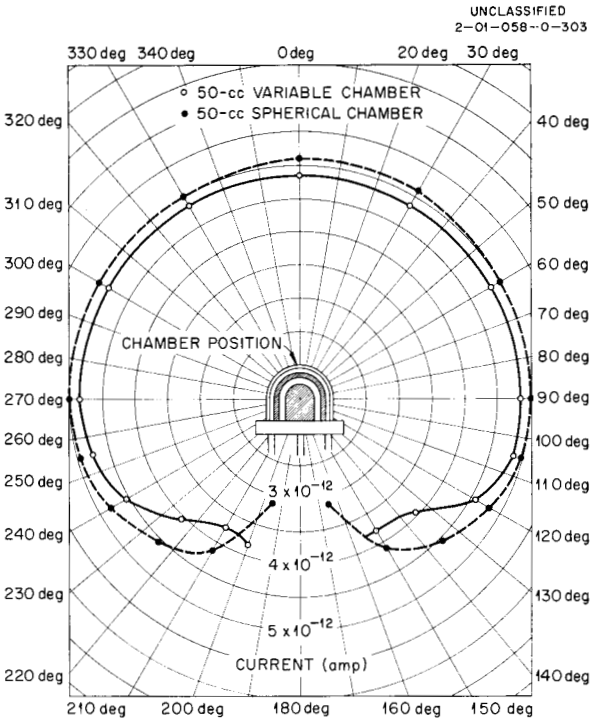

Fig. 10.4.6. Response of 50-cm^3 Gamma-Ray Ion Chambers in Air as a Function of the Angular Incidence of Radiation: Co^{60} Source (0.165 r/hr at 1 meter) Positioned 54 cm from Geometrical Center of Chamber.

response, saturation characteristics, and sensitivity. No marked improvement was noted in the new design, and either would be satisfactory for shielding work.

Because of its relatively low sensitivity, a large (3.85-cm-dia) Co^{60} gamma-ray source with a source strength of 1 curie was used to test the response of the 4-cm^3 ion chamber in air. A plot of the resulting air attenuation curve failed to follow the usual $1/r^2$ pattern at distances greater than 40 cm. There is a possibility that ion collection was occurring in regions other than the supposed sensitive volume (e.g., the connecting cable). Studies are under way to investigate this effect further.

10.5. A SIMPLE TIME-TO-PULSE-HEIGHT CONVERTER FOR THE ANALYSIS OF TIME DIFFERENCES IN THE MILLIMICROSECOND RANGE

R. W. Peelle F. C. Maienschein
T. A. Love

Frequently there is experimental interest in the time distribution of pulses from a nuclear particle detector with respect to some set of timing pulses. In the case of fast-neutron time-of-flight spectroscopy, for instance, the detection of each fast neutron is timed with respect to the previous beam pulse from the accelerator which produced the neutron. If the particles to be observed are the photon decays from a nuclear isomeric state, timing pulses must be obtained from a detector which observes the nuclear transition that feeds the isomeric state. In this case the timing pulses themselves occur randomly in time, and a maximum of one delayed observation can be made for each timing pulse. Even with prompt coincidences, time analysis may be used to study the circuitry associated with a set of detectors by obtaining the distribution of pulses from one detector signal channel relative to those in the other. Such a procedure may be desirable to predict details of coincidence circuit performance.

The multichannel time analyzers required for these problems are frequently constructed[1] by combining an existing multichannel pulse-height analyzer with an auxiliary circuit designed to convert each measured time interval into a proportional pulse height. This method is appropriate when the time intervals are of the order of microseconds or less, or for longer intervals when only a single delayed event occurs for each timing pulse.

The time-to-pulse-height converter circuit described is of the type described above. It is based upon the linear sweep circuit of a standard laboratory oscilloscope and is intended to be used with a multichannel pulse-height analyzer to form a multichannel time analyzer. The method is economical only for cases when time analysis is needed temporarily, since for a permanent installation the cost of an oscilloscope is greater than that of an independent converter unit.

In this instrument, triggering pulses (T) from one signal channel initiate the linear sweep of an oscilloscope, while pulses from the other channel (S) stop this sweep. The resulting output pulse from the sweep generator circuit has a magnitude linearly related to the time interval between the pulses from channels T and S.

Description of the Method

Figure 10.5.1 shows the block diagram of the complete system in use at the present time. The majority of the indicated components are not unique. The oscilloscope triggering signal is derived from one nuclear detector channel (T), and the elapsed time is measured until the next signal appears in the stop channel (S), provided that this time interval is smaller than the range of the analyzer. Since the signal channels are symmetrical, the roles of the detectors may be interchanged without penalty. However, if it is desired to have true coincidences generate pulses which fall in channels other than channel zero, the signal in channel S must be electrically delayed. The system illustrated includes provision for pulse-height analysis in both signal channels; events are recorded only if they produce pulses whose heights are within preset ranges. The components are shown in Fig. 10.5.1 and are discussed below.

The detector, amplifier, and single-channel analyzer sections of the circuit involve equipment generally used in fast- or intermediate-speed coincidence work. Fission chamber and sodium iodide scintillation detectors have been used by the authors[2] in a two-speed system similar to that used by others. The occurrence of the physical event is signaled by a timing pulse which enters the higher-speed channel of the coincidence circuit, but all pulses are finally rejected which do not have the correct height as determined by the single-channel analyzer in the slow branch of the

[1] R. L. Chase and W. A. Higinbotham, *Rev. Sci. Instr.* 28, 448 (1957); J. H. Neiler *et al.*, *Phys. Semiann. Prog. Rep. Sept. 10, 1955*, ORNL-1975, p 66.

[2] F. C. Maienschein, *Multiple-Crystal Gamma-Ray Spectrometer*, ORNL-1142 (July 3, 1952); T. A. Love, R. W. Peelle, and F. C. Maienschein, *Electronic Instrumentation for a Multiple-Crystal Gamma-Ray Scintillation Spectrometer*, ORNL-1929 (Oct. 25, 1955); T. A. Love, R. W. Peelle, and W. Zobel, *Appl. Nuclear Phys. Ann. Rep. Sept. 10, 1956*, ORNL-2081, p 208.

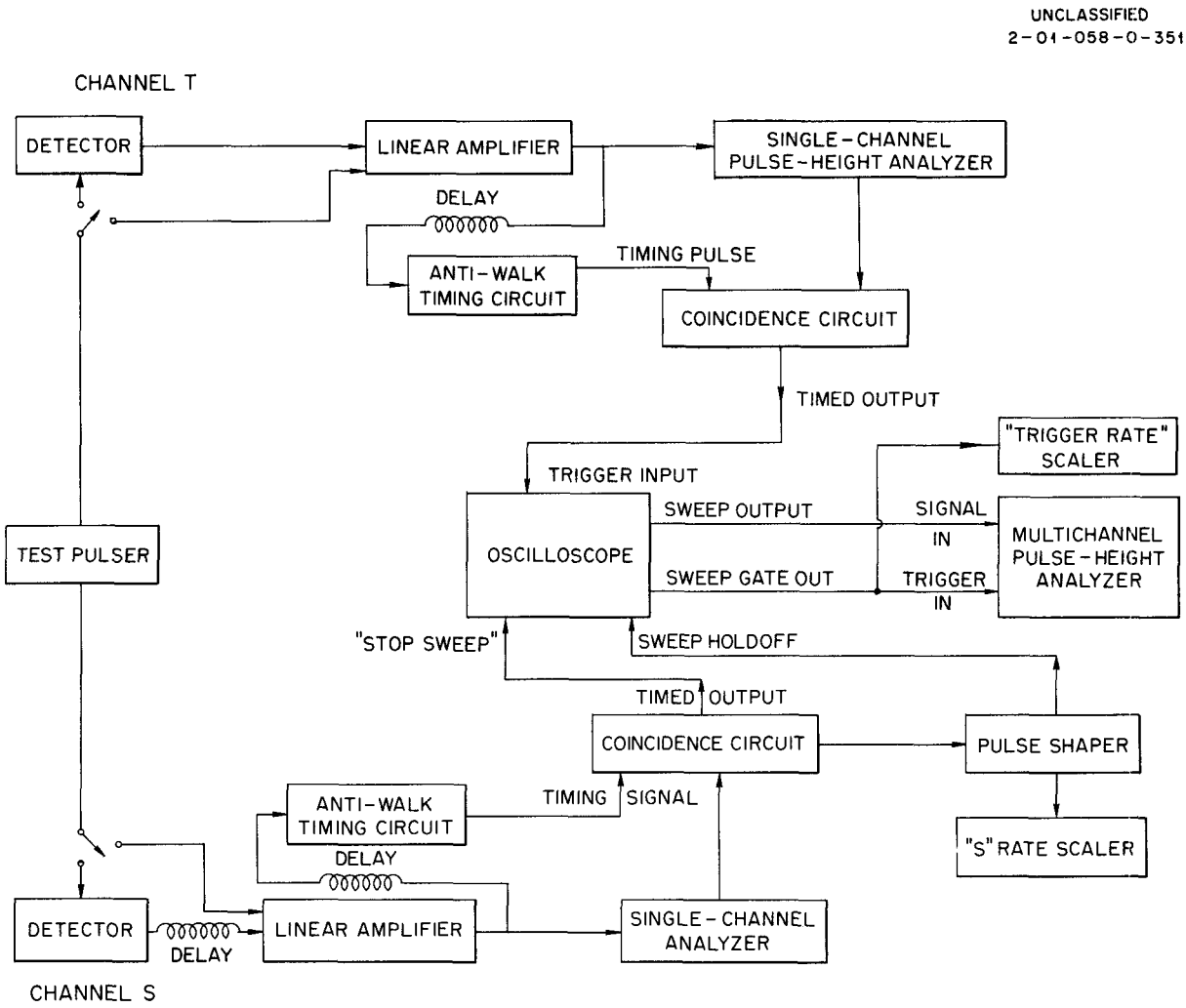

Fig. 10.5.1. Time Analyzer Block Diagram. The detectors used have been NaI(Tl) scintillation detectors and fission chambers. The diagram assumes the pulse preamplifiers to be a part of each detector. The amplifiers shown are of the double-delay-line differentiated type described by Fairstein (ref 3). The antiwalk timing circuits are described in Sec 10.3. The single-channel analyzers and coincidence circuits are described in ORNL-1929 (ref 2). The oscilloscope used was a Tektronix type-545, and the multichannel pulse-height analyzer was of the Argonne type (ref 4).

circuitry. In the illustrated case, the timing signal is obtained from an antiwalk timing circuit (described in Sec 10.3) placed at the output of a DD2 double-delay-line amplifier.[3] For most users, each timing signal would more naturally be obtained from the output of the fast amplifier whose input senses the current signal at a detector. It is in any case necessary to adjust the signal delays between the timing pulse and the single-channel analyzer output pulse so that these pulses are coincident for all acceptable amplifier output pulse heights.

Only one unusual requirement is placed upon the coincidence circuits shown in Fig. 10.5.1. The output pulse must have the sharpest practical rise time and must bear a fixed time relation to the timing-pulse input. This is necessary in the system described because the outputs of the coincidence circuits actually start and stop the sweep circuit. The authors used the intermediate-speed

[3]E. Fairstein, *Rev. Sci. Instr.* 27, 475 (1956).

coincidence circuit described in ORNL-1929[2] by removing the delay-line clipper from one input channel and applying to the corresponding coincidence diode a small fraction of the output pulse from the single-channel analyzer. A coincidence produces a 12-v positive pulse in this circuit, and a fast pulse alone produces less than 2 v. The first 10 v of the rise of the coincidence output pulse requires less than 80 mμsec. A variety of coincidence output pulse shapes are acceptable in this method, especially on channel T, which triggers the oscilloscope, with the only requirement that sweep triggering be reliable and without serious time drift. The coincidence pulse characteristics needed for the S channel depend on the oscilloscope used, but those described above were adequate for the unit used by the authors.

A Tektronix type-545 oscilloscope is being used by the authors, with only minor internal modification. The d-c trigger input was d-c coupled to the output of the T channel coincidence circuit. These choices were made in order to avoid possible shifts associated with changing count rate, but are not thought important. The circuit additions and modifications necessary to allow precise stopping of the sweep generator are shown in Fig. 10.5.2. The d-c coupling from the coincidence circuit is quite desirable in this instance. Sweeps which are initiated by the T channel but not stopped by any pulse in the S channel continue to rise until stopped by the built-in provisions of the oscilloscope. The sweep length control was adjusted to yield a 7-cm horizontal deflection, which corresponds to the maximum sweep output pulse height of about 100 v desired to avoid overloading of the pulse-height analyzer input circuitry. With some oscilloscopes it may prove difficult to obtain a sufficiently low-voltage sweep output signal. Although the Tektronix type-545 oscilloscope is equipped with a cathode follower output designed for external sampling of the sweep, the sweep signal for the analyzer is taken directly from the sweep output (pin 1, V80). The sweep gate output, which furnishes with each sweep a rectangular pulse having the same duration, is used to trigger the multichannel analyzer and to allow a counter record of the total number of sweeps in a given experiment.

An Argonne-type analyzer having 256 channels[4] is used by the authors, but in principle the choice is almost arbitrary. However, three aspects of the pulse shape presented to the analyzer may cause difficulties for some of the analysis systems in use. If a "fast sweep" is being utilized, corresponding to a small number of millimicroseconds per analyzer channel, the total rise time of the input pulses may be a fraction of a microsecond. Furthermore, there is always a positive or negative slope on the pulse, that is, it is always triangular in shape. Both these features may tax the speed of the input circuits of the pulse analyzer used. In the case of the Argonne analyzer the internal stretched pulse responds to the 150-v/μsec input pulses with a gain not seriously less than that for the usual slower pulses, though with some loss of linearity for pulses over 50 v. In cases of low time resolution, where the linear sweep signals may be many microseconds long, the analysis of the resulting input pulse may be inconsistent with the internal time sequencing of the analyzer. No such difficulty is experienced with the Argonne-type units, and in other known cases the trouble can be removed by the addition of appropriate delays.

Performance Characteristics

The time–to–pulse-height converter described has been utilized with time resolutions between 2.1 mμsec and 1.1 μsec per channel with the 256-channel analyzer. Longer intervals per channel have not thus far been attempted, but presumably no additional difficulties are involved. Attempts to obtain much shorter time channels by using a sharper ramp signal are not feasible with the analyzer used, since the 150-v/μsec triangular signal nearly saturates the input circuits. Improved resolution could be obtained, however, by increasing the conversion gain of the analyzer so that each channel would correspond to a smaller voltage interval at the input.

Figure 10.5.3 presents typical results showing application of the circuit to gamma-ray coincidences. The peak in Fig. 10.5.3 occurs in the

[4] R. W. Schumann and J. P. McMahon, *Rev. Sci. Instr.* 27, 675 (1956).

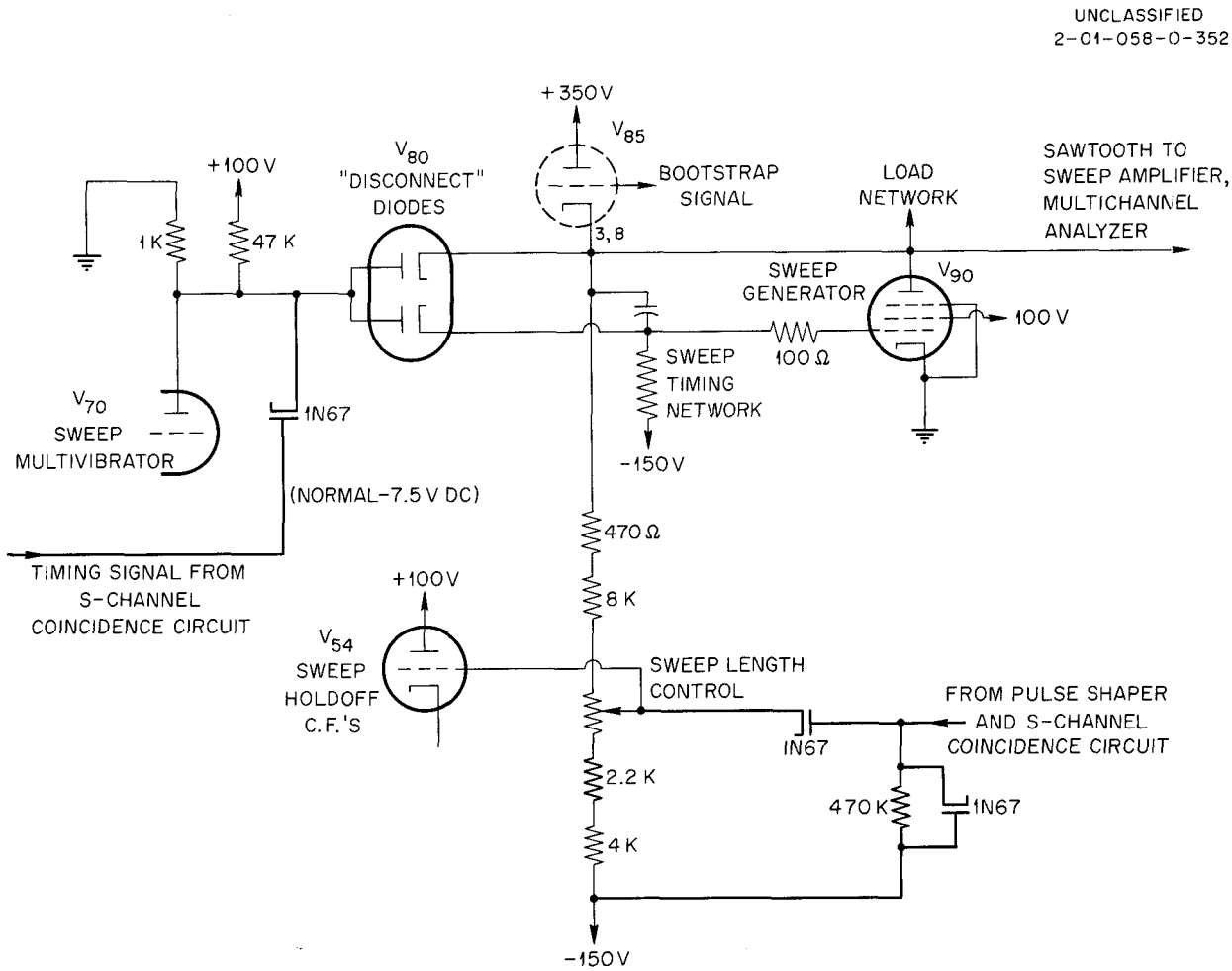

Fig. 10.5.2. Suggested Modifications to the Tektronix Type-545 Oscilloscope to Allow for Stopping the Sweep with Pulses from the *S* Channel. The heavy lines represent parts added to the circuit; no parts have been removed. In this oscilloscope the sweep control multivibrator (V70), after being flipped by a pulse from the trigger input, starts and maintains the sweep by applying a negative pulse to the plates of the disconnect diodes (V80) in order to stop current flow from V80 through the sweep timing resistor. During the sweep the level at the plates of V80 is maintained at about −7.5 v. To stop the sweep, the control multivibrator may be reset, lifting this potential to just above ground. This resetting action is normally actuated when the sweep output raises the voltage into the sweep holdoff cathode followers (V54) up to a given level. Circuit delays in the sweep holdoff system are designed to prevent the sweep from being triggered again until the entire sweep generator system has recovered. For time-to-pulse-height conversion the tasks of resetting the sweep control multivibrator and initiating the sweep holdoff action are met by a slow 1-μsec-long 10-v positive pulse from the pulse shaper driven by the *S*-channel coincidence circuit. However, this action is not sufficiently rapid to provide the precise timing needed. The fast low-source-impedance d-c-coupled positive pulse from the *S*-channel coincidence circuit is therefore applied directly to the plates of the disconnect diodes, cutting off the sweep which would again rise if the control multivibrator were not reset by the slower pulse described above.

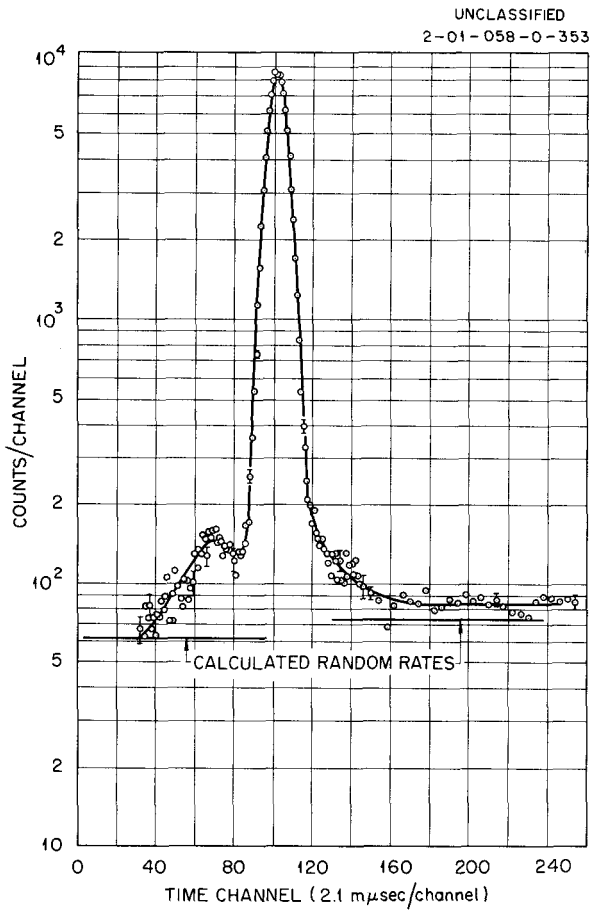

Fig. 10.5.3. Time Analysis of Gamma-Ray Coincidences from a Co^{60} Source. Sodium iodide scintillation crystals (2 by 2 in.) placed on RCA-6655 photomultiplier tubes viewed an approximately 0.1-mc Co^{60} source from the distance of about 30 cm. Single-channel analyzers on each signal line were adjusted to accept pulses corresponding to absorbed energies greater than 0.5 Mev. About 1700 pulses/sec corresponded to the accepted energy range in each crystal. About 10^4 sec was required to accumulate these data. Sample statistical errors are shown on some of the plotted points. Channels have been combined in the regions above channel 150. The approximate calculated random coincidence rates are shown, based upon the calibrated average channel width of about 2.1 mμsec per channel for channels less than 140, and the average width of about 2.4 mμsec per channel in the higher-numbered channels. This figure illustrates the spreading of the prompt coincidence peak caused by jitter, the background caused by random coincidences, and additional backgrounds which are presumed to be accounted for by pulse pile-up, etc.

channels which correspond to a zero time interval between the events in the detectors of the T and S channels. The width of this peak is a manifestation of "walk" and "jitter" of the timing pulse with respect to the physical events in the detector. "Walk" is defined as systematic variation in this time delay associated with changes in pulse height from the detector, while "jitter" refers to statistical variations of delay for a given pulse height. The use of conventional fast timing techniques or of the antiwalk devices described elsewhere (see Sec 10.3) can reduce walk to a value of 5 to 10 mμsec for the 5- to 100-v range of pulse heights usually important in pulse-height analysis. Jitter, however, can be more difficult to eliminate. Jitter can originate from the superposition of noise upon the signal from the detector or from fluctuations in the shape of the detector output pulse arising, say, from photomultiplier statistics. The extent of the jitter is a function of the type of timing circuit and is relatively severe with the antiwalk circuit used. At points on the abscissa of Fig. 10.5.3 far from the prompt-coincidence peak, the recorded events can no longer correspond to walk and do not seem to arise from the unavoidable jitter. These events, which interfere with any experiment attempting to measure time-delayed coincidences, can come from at least three sources:

1. random coincidences between pulses in the T and S channels which have no natural correlation, events which cannot be avoided by circuit changes;
2. true electric noise coincidences, which can arise if single noise events trigger both channels, at different times within the range of the analyzer;
3. pile-up pulses in either of the signal channels, which can cause logical malfunction of the apparatus.

The last effect mentioned can be produced in a manner very similar to the jitter production by random noise, except that in this case the pulses are large and can cause events to be recorded far from the prompt coincidence peak. The last two sources seem to be important in the equipment described here, though they are likely to be less serious in a corresponding modification of one of the more conventional "fast-slow" coincidence systems.

No count-rate shifts have been observed at the small count rates which have been necessary to minimize the random backgrounds. A shift as small as 5 mμsec in the position of the prompt coincidence peak could have been observed had it been present during a run which had a measured counting rate of a few thousand counts per second.

The drift with time of the channel number corresponding to the prompt coincidence peak has been observed by measuring this position before and after each of a number of data runs, some of which lasted as long as one day. Such checks were made during both high- and low-resolution runs. With the instrument operating at a resolution of about 3 mμsec per channel, no drifts of more than 1.5 channels have been observed for the case where the prompt coincidence peak falls at a pulse height of about 30 v. Even at very low time resolutions of 20 to 40 mμsec per channel, daily drifts of about 0.5 to 1.0 channel can be expected from analyzer and oscilloscope drifts. In the case of the high-resolution runs, the observed drift is much less than that which is to be expected with the use of slow-speed circuitry.

Two time-calibration curves are shown in Fig. 10.5.4 corresponding to linear sweep rates of 150 and 15 v/μsec. These data were obtained by cross calibration against a Tektronix type-180 oscilloscope sweep calibrator. The linearity of such curves is heavily involved with the acceptability to the analyzer of the pulse shape from the time sweep generator and with the linearity of the oscilloscope sweep output as a function of time between trigger and stop pulses.

The analyzer circuit has been applied to measurements of fission-associated radiation (see, for example, Sec 6.2) and has also been applied to measurements of two isomeric states in Ta^{181}. The isotope Hf^{181} beta decays[5] to excited states of Ta^{181}, including a level in the neighborhood of 600 kev, which is known to decay with a half life in the neighborhood of 20 μsec.[6] In the photon cascade to the ground state of Ta^{181}, there is a 0.482-kev state with a half life of about 10^{-8} sec.[7] Both these periods have been measured with the described time analyzers. Figure 10.5.5 shows the measurement of the longer period, which yields the tentative result of $T_{1/2} = 18.1 \pm 0.7$ μsec. The short-period measurement shown in Fig. 10.5.6 has not been fully analyzed to take the jitter into account, but it appears to correspond to a half life of 10.2 ± 0.5 mμsec for the 480-kev level. These measurements are in the range of the best published values, and pending final analysis appear to be approximately as precise. The results for the tantalum isomers indicate that this time analyzer may properly be used to measure unknown decay lifetimes.

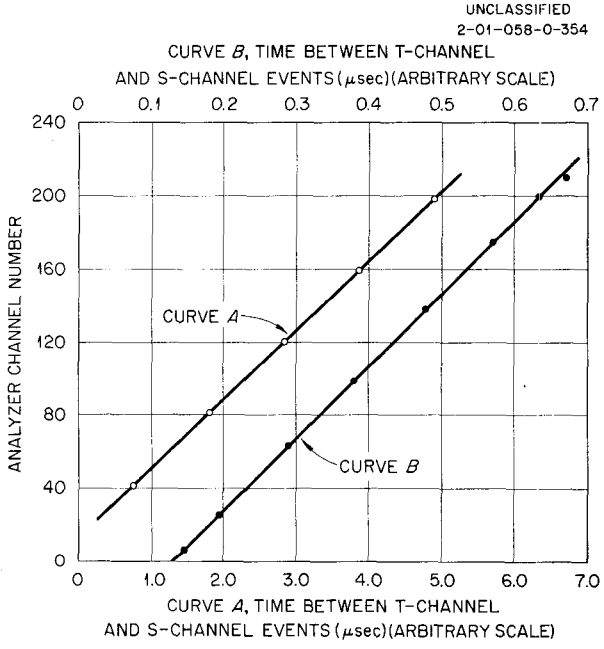

Fig. 10.5.4. Typical Time Calibration Data for a Multichannel Time Analyzer Using the Described Converter Circuit. Two curves are shown as straight lines passing through the data, one for the 1-μsec/cm oscilloscope sweep and the other for the 0.1-μsec/cm sweep. The appropriate sweep of a Tektronix type-517 oscilloscope was calibrated using a Tektronix type-180 time-mark generator. The length of the type-545 oscilloscope sweep was then measured as a function of pulse height observed with the multichannel analyzer. Delay cables were inserted into the *S*-channel signal line to produce different length delays. A comparison of the resulting curves produced the calibration plots shown above. For each point, estimated standard deviations in both pulse height and time are about 0.3% of the corresponding full-scale readings.

[5] For a discussion of the Hf^{181} decay scheme see F. Boehm and P. Marmier, *Phys. Rev.* 103, 342 (1956).

[6] D. E. Bunyan *et al.*, *Proc. Phys. Soc. (London)* 61, 300 (1948); S. H. Vegors, Jr., and P. Axel, *Phys. Rev.* 101, 1067 (1956).

[7] W. C. Barber, *Phys. Rev.* 80, 332 (1950); E. E. Berlovich, *Izvest. Akad. Nauk S.S.S.R. Ser. Fiz.* 19, 343 (1955).

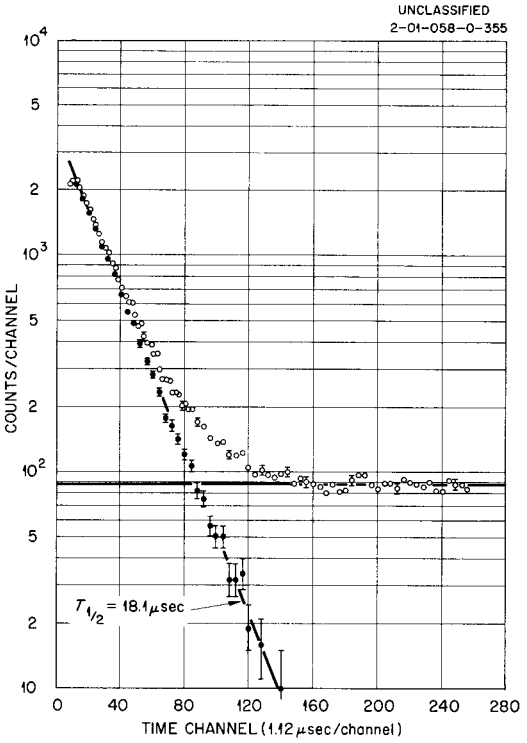

Fig. 10.5.5. Half-Life Determination of the Approximately 20-μsec Ta^{181} Isomer. The measured points correspond to delays between beta particles of energy greater than 80 kev and gamma rays of energy greater than 100 kev; the beta particles arise from the decay of Hf^{181}, and the gamma rays arise from the resulting photon cascade in Ta^{181}. The beta-particle detector was a 0.027-in.-thick by 1-in.-dia NaI(Tl) crystal, and the gamma-ray detector was a 2 × 2 in. cylindrical NaI(Tl) crystal. The Hf^{181} source was placed between these detectors, which were arranged coaxially with minimum spacing. A 1-mil-thick aluminum foil separated the source from the beta-particle detector. The entire assembly was placed within an 8-in.-thick lead shield. The beta-particle detector measured about 30 counts/sec, and the gamma-ray detector about 62 counts/sec. This curve was obtained in about 15 hr when a time channel width of 1.12 ± 0.02 μsec was used. The time corresponding to prompt coincidences is located at about channel −10. The horizontal line at 88 counts/channel is the average background observed for channels greater than 140. The open circles are experimental, with data from adjacent channels combined. Sample statistical errors are shown on some of the points. The solid circles indicate the data after subtraction of the indicated background. Four channels have been combined for each point. The oblique line corresponds to a half life of 18.1 μsec. Errors in the half life have not been fully evaluated, but the estimated standard deviation is ±4%.

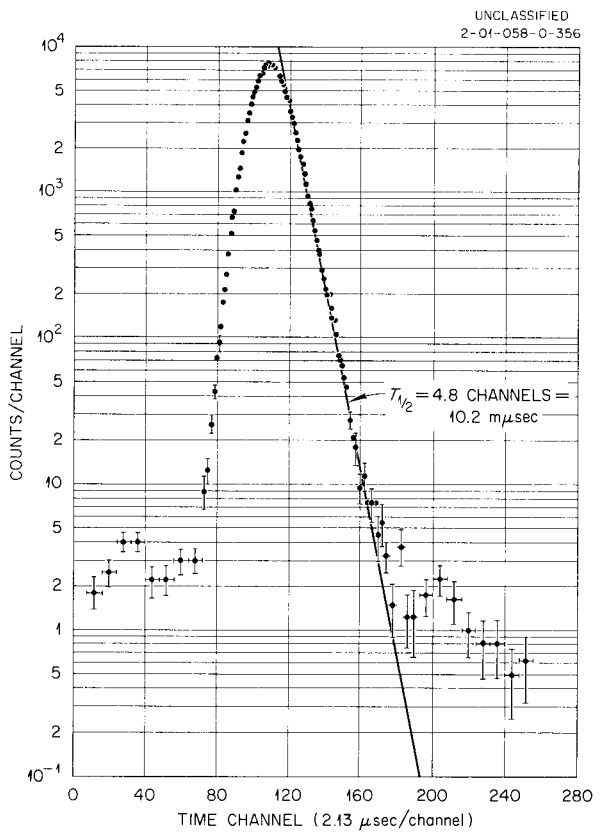

Fig. 10.5.6. Half-Life Determination for the 478-kev Level of Ta^{181}. This excited state is fed by a 133-kev gamma ray and a 136-kev gamma ray. Sodium iodide crystals (2 by 2 in.) placed on RCA-6655 photomultipliers were positioned as closely as possible on either side of the Hf^{181} source. The assembly was shielded by 8 in. of lead. The single-channel analyzer connected to the detector observing the 130-kev transitions had a counting rate of about 44 counts/sec, while that viewing the 480-kev line had only 27 counts/sec. This curve was obtained in about 21 hr, with the best available time resolution of 2.13 ± 0.02 mμsec used per channel. Sample statistical errors are shown on some of the points, and the horizontal ranges are indicated where more than two channels have been combined to improve statistical errors. The calculated random rate which is expected on either side of the peak is about 0.2 count/channel, much smaller than that observed. The straight line shown is for a half life of 10.2 mμsec, not necessarily a best fit to the data with background subtracted. The shape of the left side of the peak is evidence of jitter. A best value from these data cannot be given for the half life until the curve has been corrected for jitter, but an estimated standard deviation to the quoted value is ±5%.

10.6. DEVELOPMENT OF THE HORNYAK BUTTON AS A FAST-NEUTRON DOSIMETER

F. J. Muckenthaler

It was reported previously[1] that the Hurst-type fast-neutron dosimeters which are commonly used for fast-neutron dose measurements at the ORNL shielding facilities are limited by several features and that efforts were being devoted toward the development of a new dosimeter using a Hornyak button[2] as the detector. (The Hornyak button consists of a homogeneous mixture of fine Lucite and ZnS powder.) At that time the response of various Hornyak buttons to fast neutrons from a Po-Be source and from the Tower Shielding Reactor and Bulk Shielding Reactor had been examined. In addition, some preliminary tests had been performed in which the response of the button to monoenergetic neutrons produced by the ORNL 5.5-Mev Van de Graaff generator was compared directly with the response of the Hurst-type dosimeter. This dosimeter serves as a good basis for a comparison because the neutron dose rate it measures is approximately the dose rate absorbed in tissue.

Further tests now have been performed to compare various Hornyak buttons with the Hurst-type dosimeter. For these tests monoenergetic neutrons produced by a tritium gas target bombarded with protons from the Van de Graaff were used as the source. In order to ensure that both detectors had an incident neutron flux of the same energy, they were placed in the same horizontal plane, each located at an angle of 15 deg from the generator beam with their centers of detection the same distance from the target. The counting time for each run was based on a predetermined beam current, since this is necessary for the calculation of the neutron flux for each energy interval. The ratio of the dosimeter response to that of the Hornyak button was then plotted as a function of the neutron energy.

In the earlier tests[1] it was shown that the ratio of the dose rates from the two detectors varied considerably from unity only at neutron energies below about 1 Mev. Since this was the energy region of interest during this experiment, the range of neutron energies measured by each button was kept below about 2.2 Mev, which reduced the experimental time on each button and permitted a larger number of buttons to be tested.

It was necessary to keep the over-all gain of the dosimeter constant for each run for a comparative evaluation of the results. Since the dosimeter response to gamma rays is a linear function of gain and bias, the dosimeter was placed in a 2-r/hr Co^{60} gamma-ray field and the gain of the A-1 amplifier was adjusted until 25 counts/min were observed for a predetermined high voltage and a pulse-height selector reading of 6 v. A precision pulser was used to check and adjust the electronic gain for the dosimeter prior to each measurement at different neutron energies. The Hornyak buttons were also biased to give 25 counts/min at a pulse-height reading of 6 v when placed in a 2-r/hr gamma-ray field. For convenience only, the electronic gain was kept constant and the high voltage on the photomultiplier was changed to give this bias. With the gamma-ray source removed, the two detectors were then calibrated against a Po-Be source of known intensity.

The Hornyak buttons used in this series of tests contained ZnS particles of 25-μ diameter or of 3- to 5-μ diameter. The lowest concentration of the ZnS used in the buttons containing 25-μ-dia particles was 50 parts by weight to 70 parts of Lucite, since earlier data for lower concentrations indicated that when the amount of ZnS was increased to 50 parts and the thickness of the button was decreased to 20 mils the relative response to low-energy neutrons increased. The concentrations of ZnS used in the buttons containing 3- to 5-μ-dia particles varied from 0.4 to 50 parts by weight for 70 parts of Lucite and various button thicknesses. The minimum button thickness tested was about 20 mils.

The ratios of the dose-rate response of the dosimeter to the response of various Hornyak buttons containing the 25-μ-dia ZnS particles are shown in Figs. 10.6.1 through 10.6.4. For ZnS concentrations of 100 and 150 parts the low-energy response increased as the button thickness was decreased. For a concentration of 250 parts, however, the response in the low-energy region decreased. This reversal can be attributed to

[1] F. J. Muckenthaler, *Appl. Nuclear Phys. Ann. Rep. Sept. 10, 1956*, ORNL-2081, p 199.

[2] W. F. Hornyak, *Rev. Sci. Instr.* **23**, 264 (1952).

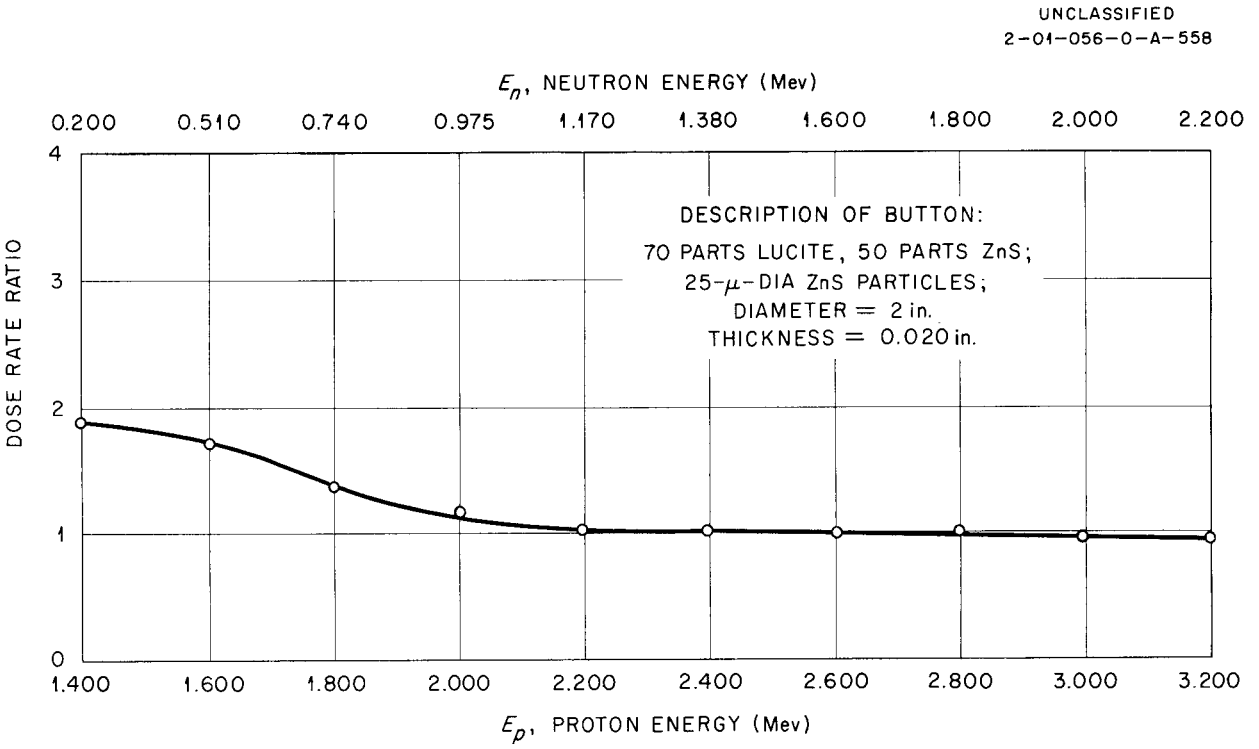

Fig. 10.6.1. Ratio of the Dose-Rate Response of the Dosimeter to the Response of the Hornyak Button to Neutrons from the (p,t) Reaction (Van de Graaff Generator).

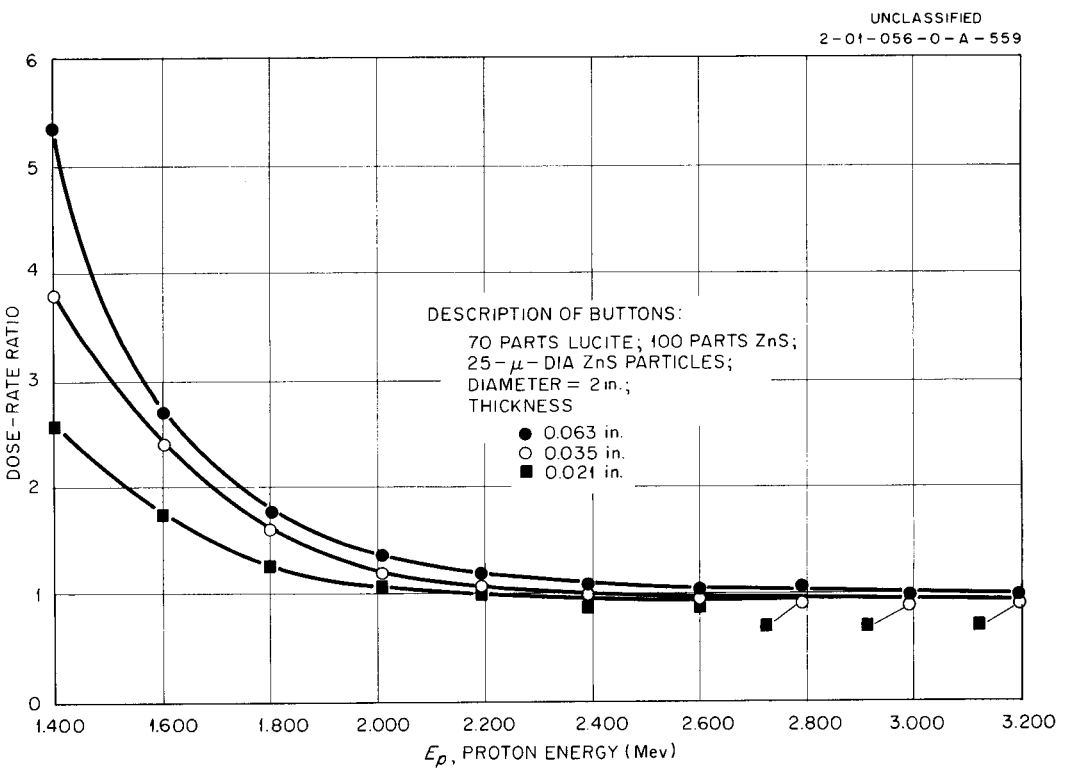

Fig. 10.6.2. Ratio of the Dose-Rate Response of the Dosimeter to the Response of Various Hornyak Buttons to Neutrons from the (p,t) Reaction (Van de Graaff Generator).

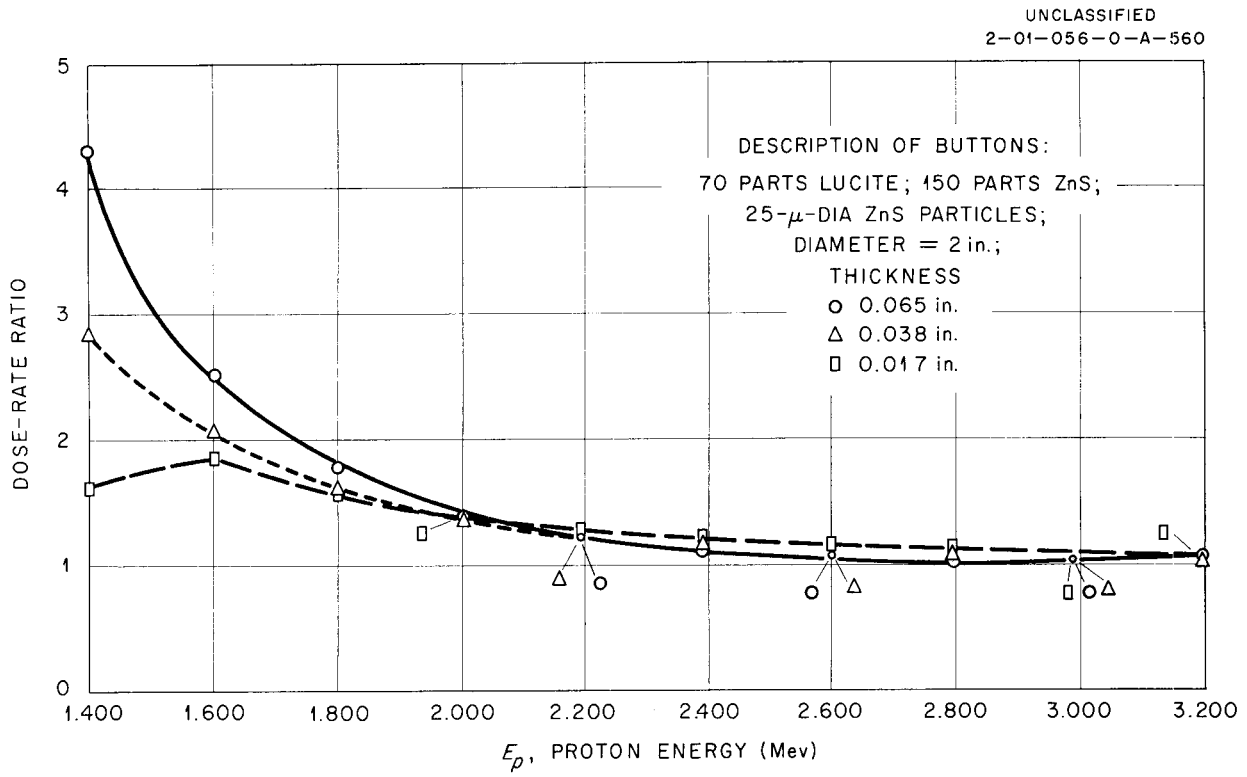

Fig. 10.6.3. Ratio of the Dose-Rate Response of the Dosimeter to the Response of Various Hornyak Buttons to Neutrons from the (p,t) Reaction (Van de Graaff Generator).

cracks in the Lucite-ZnS crystal, resulting from difficulty in machining a crystal with large concentrations of ZnS. A summary of the best response obtained with buttons of each concentration of 25-μ-dia ZnS particles is given in Fig. 10.6.5. There appears to be little difference between the buttons with 50 and 100 parts of ZnS, but above this concentration the dose-rate ratio stays above unity even at neutron energies of 2 Mev. This appears to confirm the earlier observation[1] that the optimum ZnS concentration for maximum low-energy response is between 50 and 100 parts by weight to 70 parts of Lucite.

The results of tests with buttons containing 3- to 5-μ-dia ZnS particles are shown in Figs. 10.6.6 through 10.6.10. For ZnS concentrations of 20, 50, and 100 parts, the low-energy response increased as the button thickness was decreased. Changing the thickness of the button appeared to have no effect for ZnS concentrations of 0.4 to 5 parts. A summary of the data (Fig. 10.6.11) shows that for concentrations of 0.4 to 4 parts by weight, the dose-rate ratio is approximately 1 at the low neutron energies and less than 1 for slightly higher energies. As the ZnS concentration was increased, the low-energy response decreased.

In conjunction with the above measurements, other data were obtained for comparing some of the buttons with the dosimeter for measurements beyond several reactor shield configurations at the Tower Shielding Facility. For these tests the detectors were placed in air 64 ft from the reactor tank. The reactor was positioned along the tank-detector axis 60 cm from the tank wall to give a hardened direct beam. Other measurements were made with the reactor in a position 90 deg from the detector-tank axis and 20 cm from the tank wall. This arrangement resulted in a neutron spectrum at the counter that had a large low-energy air-scattered component. Comparisons of the response of the two detectors indicate a trend similar to that which was found with monoenergetic neutrons. For the air-scattered spectrum the buttons containing 25-μ-dia particles gave dose-rate readings that

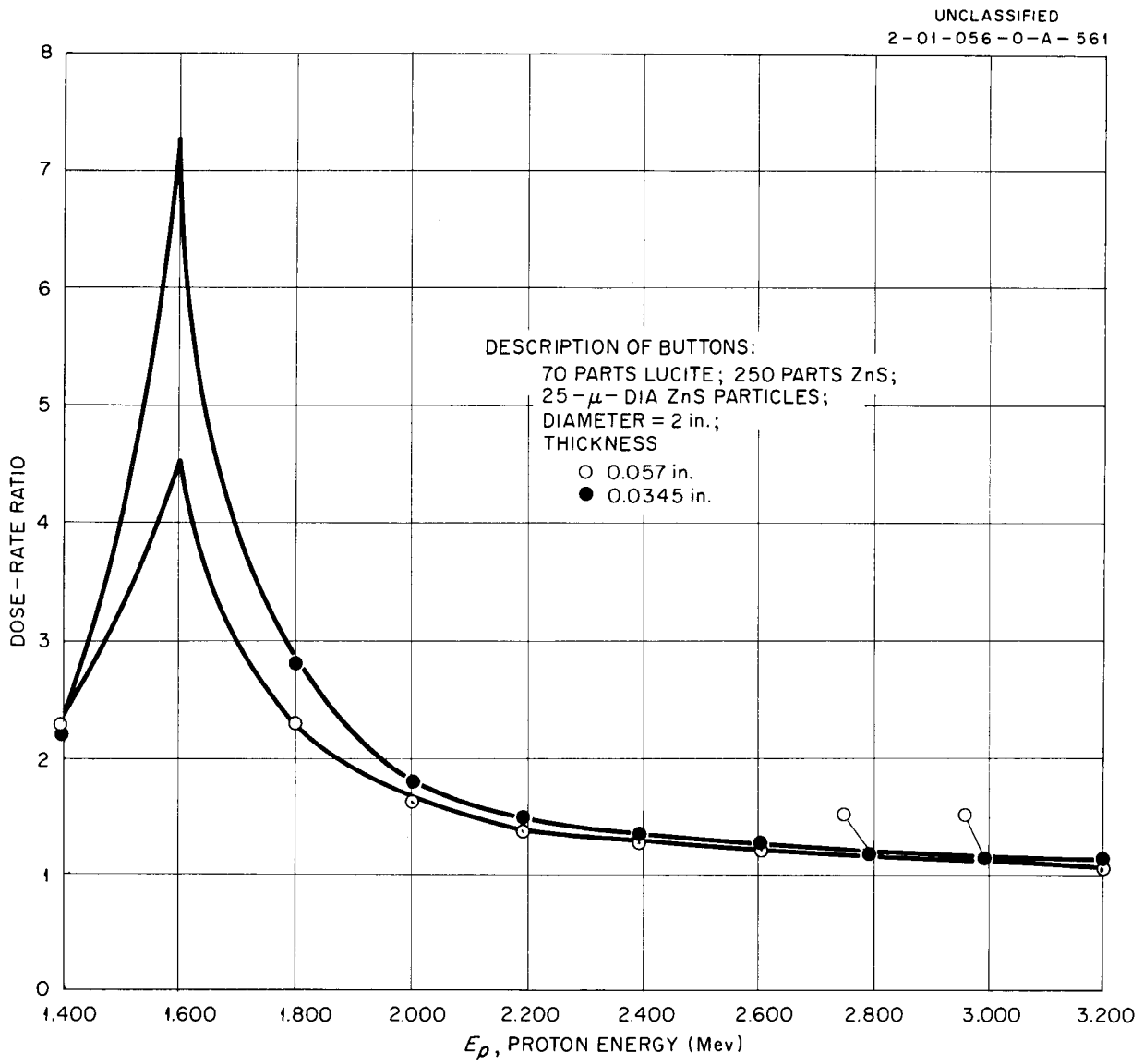

Fig. 10.6.4. Ratio of the Dose-Rate Response of the Dosimeter to the Response of Various Hornyak Buttons to Neutrons from the (p,t) Reaction (Van de Graaff Generator).

were lower than those given by the dosimeter by about 10%. For the hard direct beam the dose rates observed were almost equal. Lack of sufficient measurements with the buttons containing 3- to 5-μ-dia particles prevents a comparison to be made of their response to that of the dosimeter at this time; however, there is an indication that these buttons give higher dose-rate readings than the dosimeter for the particular spectra checked.

In the past, neutron dose-rate measurements were made with the dosimeter biased for gamma-ray fields greater than the normal 2 r/hr. In order to take such data, the bias levels on the integrator were changed. (The discriminator tubes in the integrator biased at 6 and 10 v require pulses of 6 and 10 v, respectively, before they will conduct. Conduction is necessary before the integrator will record the input pulse. Changing the two 6-v and one 10-v bias levels to 14 v prevents the recording of any pulses below 14 v. For the integrator used in the above measurements, the number of 14-v bias levels would then be changed from one to

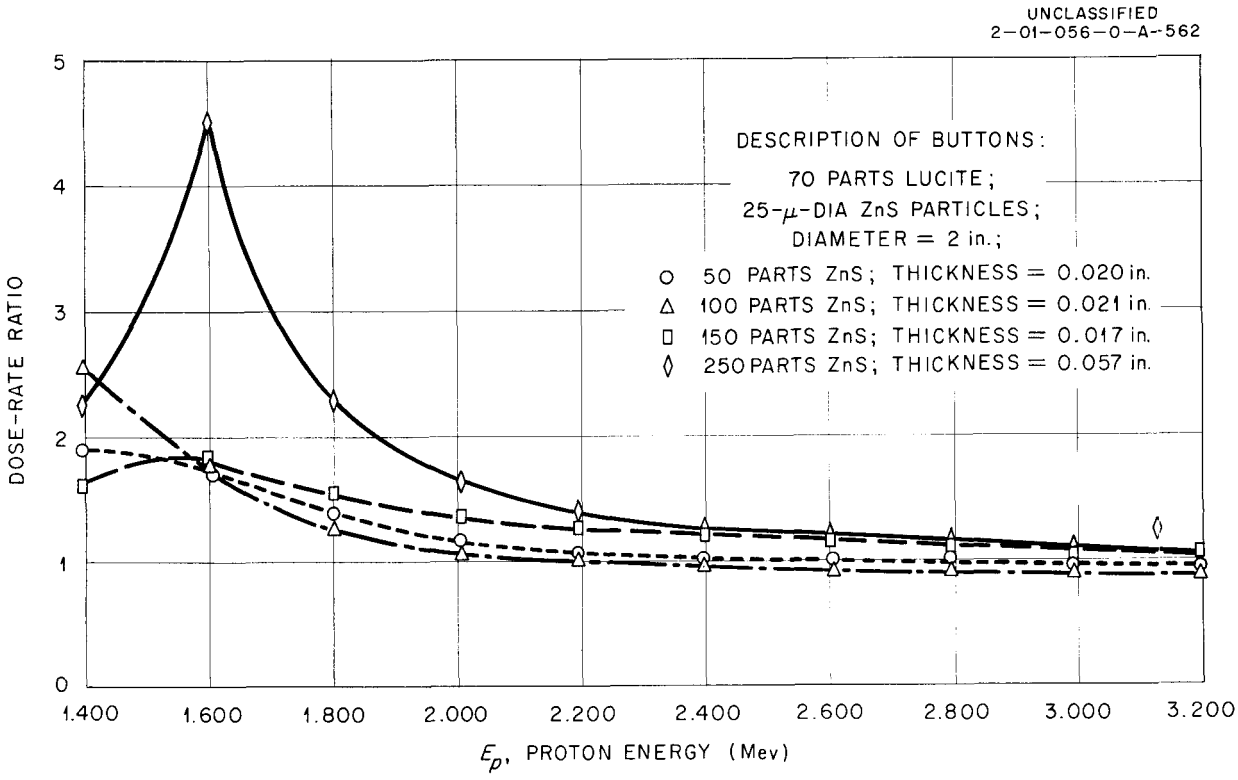

Fig. 10.6.5. Ratio of the Dose-Rate Response of the Dosimeter to the Response of Various Hornyak Buttons to Neutrons from the (p,t) Reaction (Van de Graaff Generator).

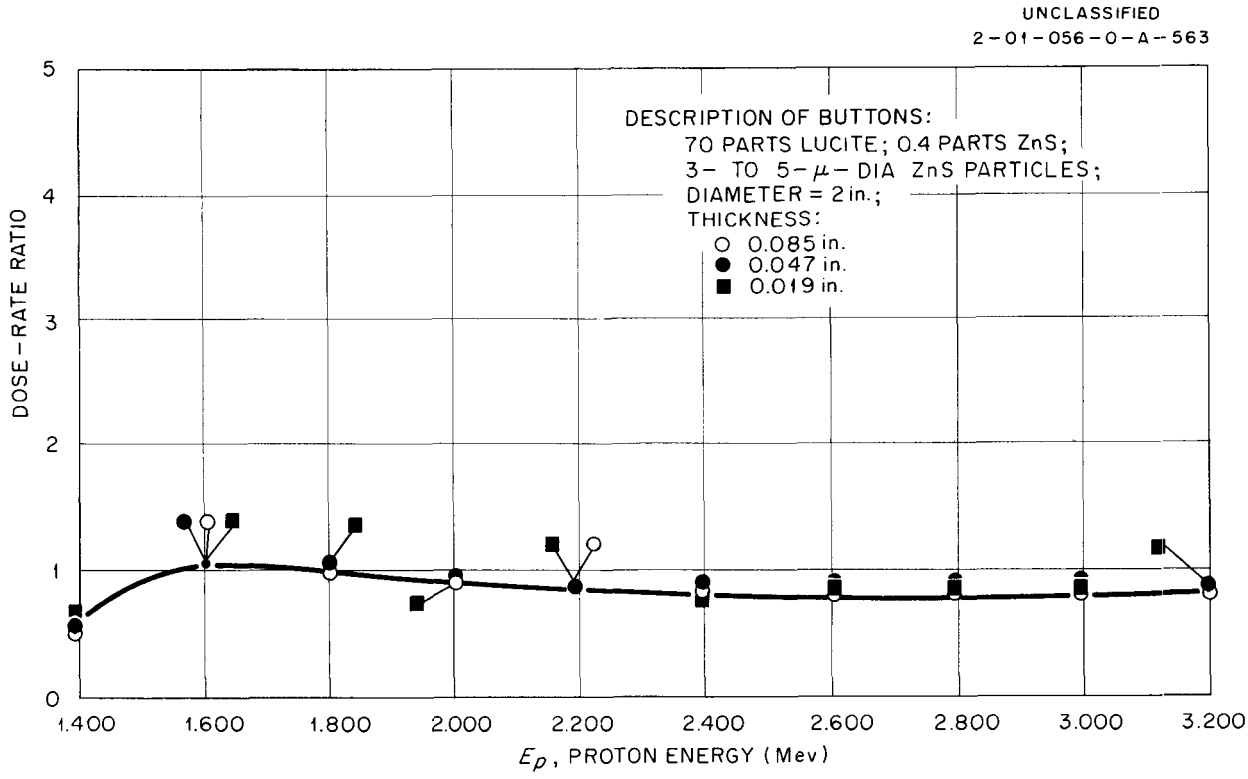

Fig. 10.6.6. Ratio of the Dose-Rate Response of the Dosimeter to the Response of Various Hornyak Buttons to Neutrons from the (p,t) Reaction (Van de Graaff Generator).

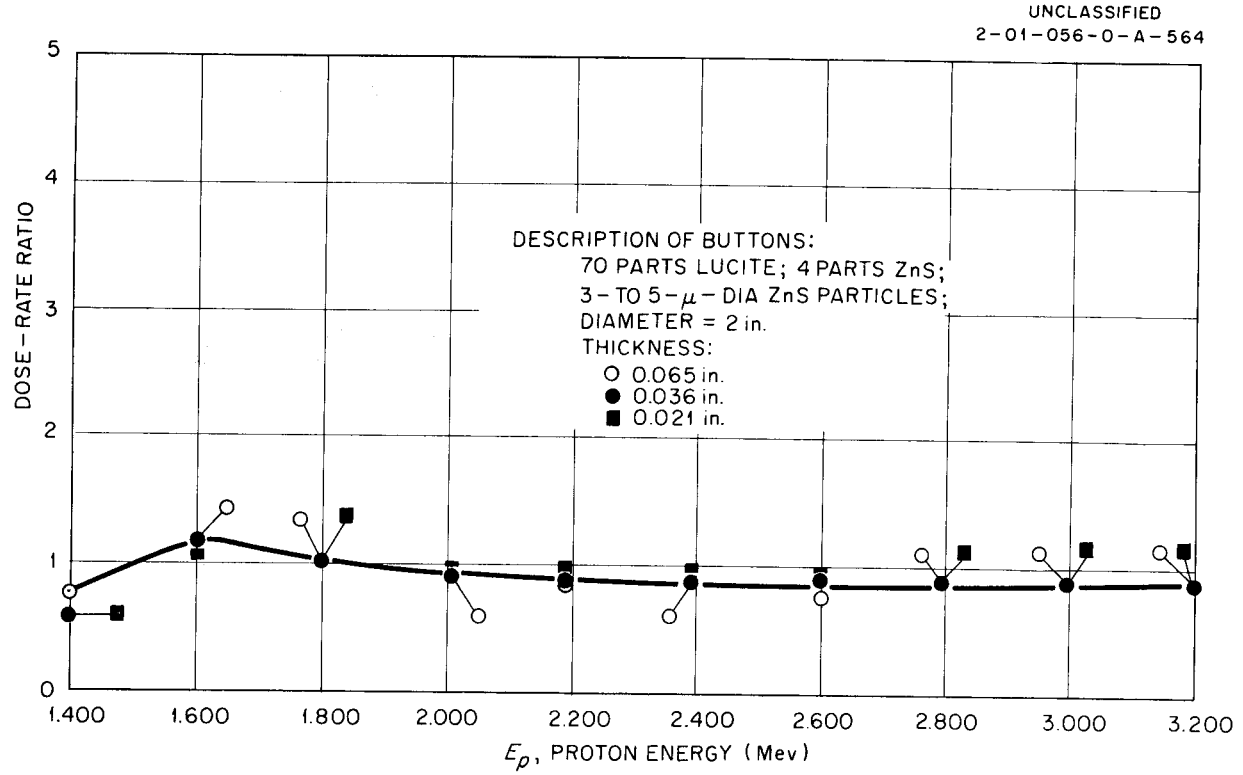

Fig. 10.6.7. Ratio of the Dose-Rate Response of the Dosimeter to the Response of Various Hornyak Buttons to Neutrons from the (p,t) Reaction (Van de Graaff Generator).

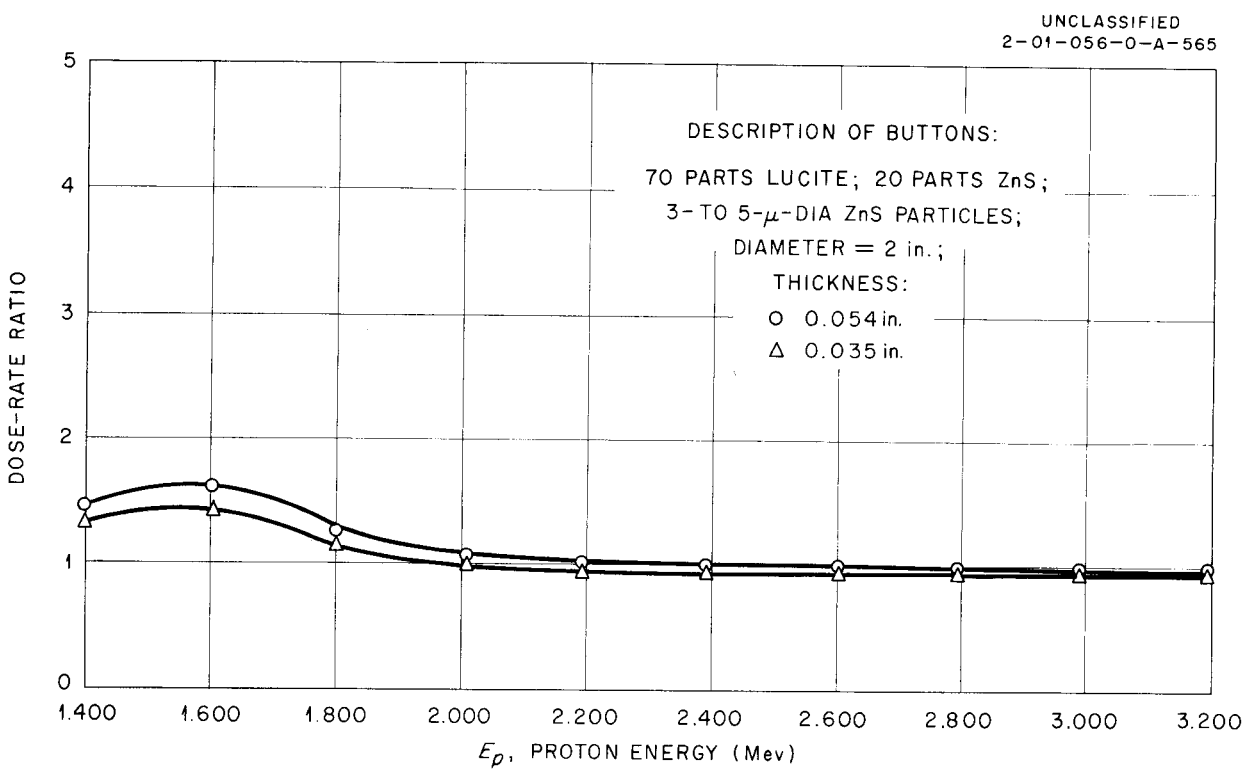

Fig. 10.6.8. Ratio of the Dose-Rate Response of the Dosimeter to the Response of Various Hornyak Buttons to Neutrons from the (p,t) Reaction (Van de Graaff Generator).

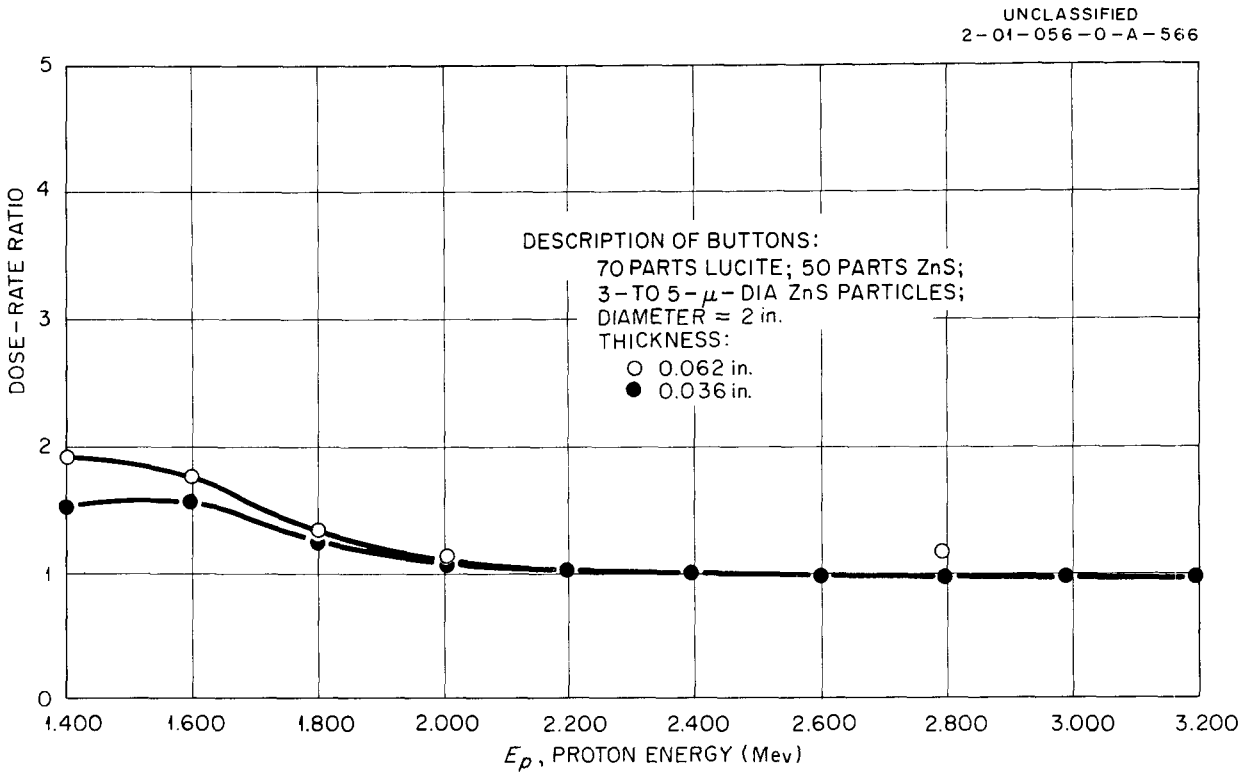

Fig. 10.6.9. Ratio of the Dose-Rate Response of the Dosimeter to the Response of Various Hornyak Buttons to Neutrons from the (p,t) Reaction (Van de Graaff Generator).

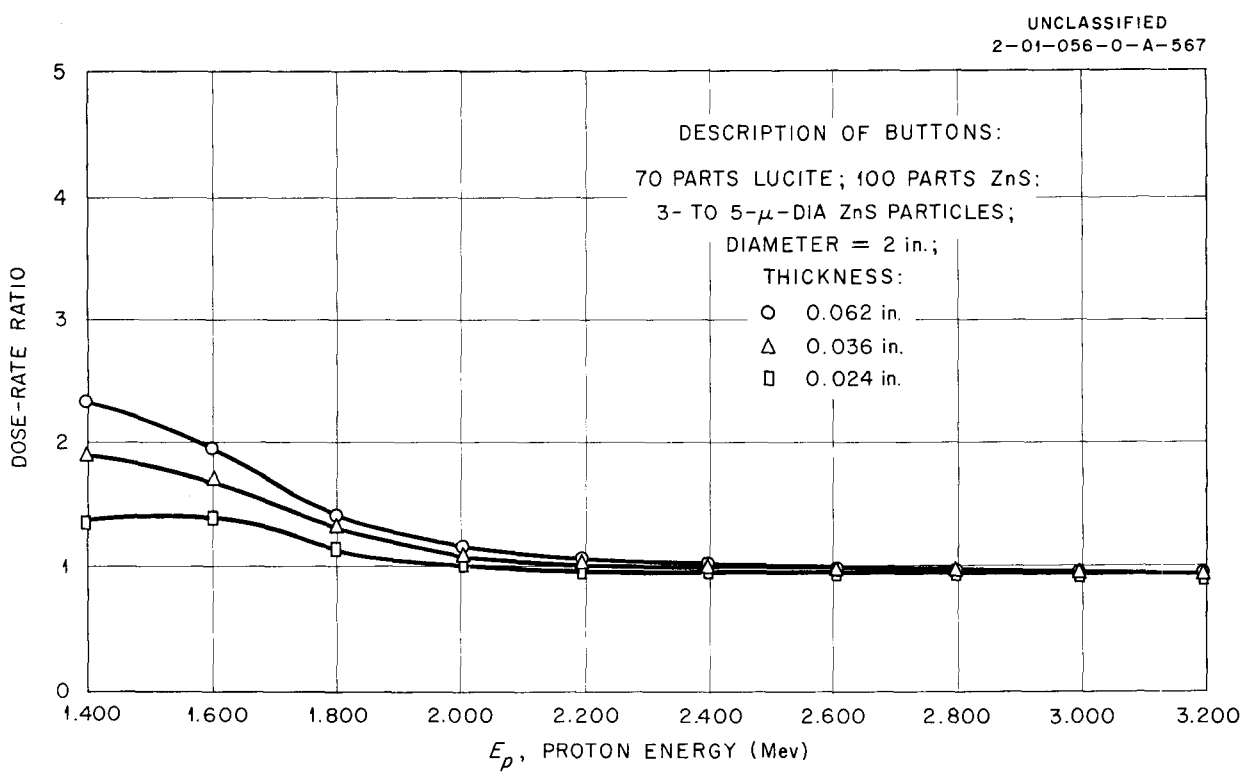

Fig. 10.6.10. Ratio of the Dose-Rate Response of the Dosimeter to the Response of Various Hornyak Buttons to Neutrons from the (p,t) Reaction (Van de Graaff Generator).

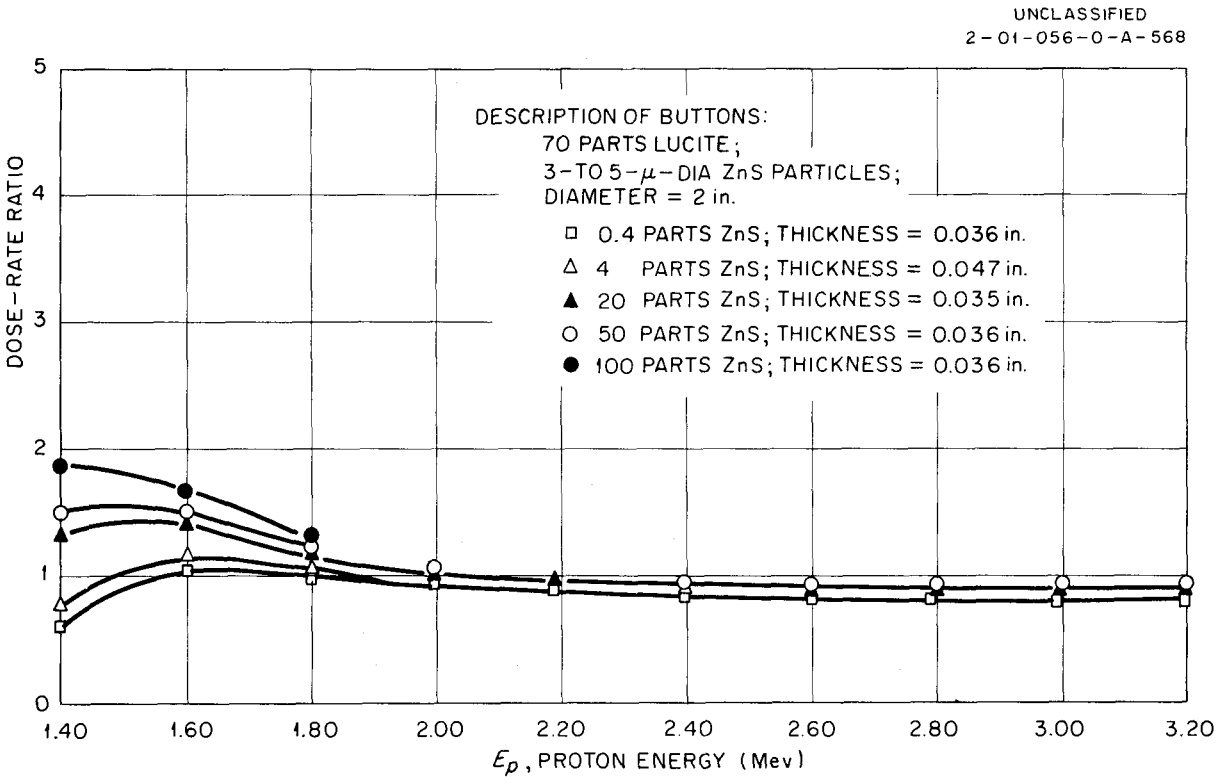

Fig. 10.6.11. Ratio of the Dose-Rate Response of the Dosimeter to the Response of Various Hornyak Buttons to Neutrons from the (*p,t*) Reaction (Van de Graaff Generator).

four. The loss or increase in the dose rate measured would then depend on the hardness of the neutron spectrum. For a 2-r/hr gamma-ray field, the electronic gain of the dosimeter is adjusted to give approximately 25 counts/min from gamma rays for a bias of 6 v. Increasing the gamma-ray field from 2 to 20 r/hr does not change the slope of the count rate vs pulse-height curve for gamma rays obtained with the dosimeter but does increase the number of 14-v pulses observed. Thus upping the bias level to 14 v permits an increase in the gamma-ray field in which the neutron dose is to be measured, even though the counting rate due to gamma rays is held to approximately 25 counts/min. Details of such an integrator are given in the literature.[3]) For example, to make measurements in a 20-r/hr gamma-ray field, the 6- and 10-v bias levels were set at 14 v. It was not known at that time how much difference this would make in the measured dose, since the spectrum being measured may vary considerably. In order to indicate the error that might be encountered, a check has been made with monoenergetic neutrons. For this comparison, the dosimeter was first biased for a 2-r/hr field and compared with the Hornyak button, also biased for a 2-r/hr field. The neutron energy was varied between 0.2 and 4.4 Mev. The 6- and 10-v bias levels on the integrator were then set for 14 v, giving a total of four levels at that bias. The dosimeter was again calibrated with a Po-Be source, and the measurements were repeated. The ratio of the two dose rates is plotted in Fig. 10.6.12. For the lowest neutron energies the ratio of the dosimeter response is nearly 10. The two dose rates agree at about 1.5 Mev. The difference in the actual dose rate measured in a 2-r/hr field and that measured with a change in the integrator bias levels for a 20-r/hr field then depends upon the hardness of the neutron spectrum involved.

[3]F. M. Glass and G. S. Hurst, *Rev. Sci. Instr.* **23**, 67 (1952).

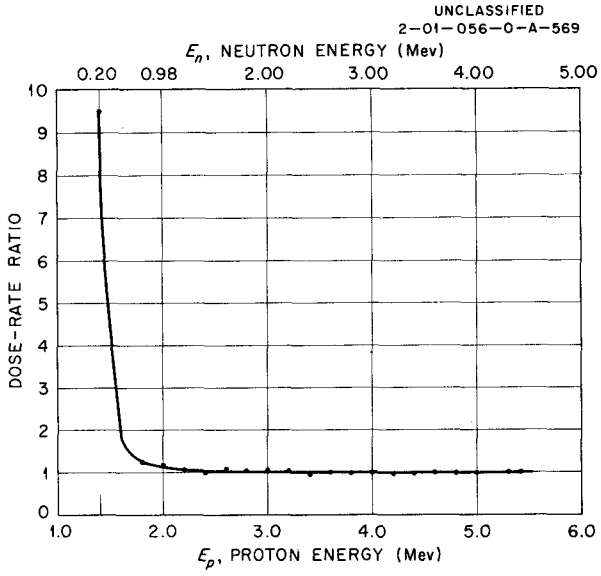

Fig. 10.6.12. Ratio of the Response of the Hurst-Type Dosimeter to 0.2- to 4.4-Mev Neutrons in 2- and 20-r/hr Gamma-Ray Fields.

10.7. AUTOMATIC COUNT-TIME CLOCK FOR USE WITH SLOW PULSE ANALYZERS

T. A. Love F. C. Maienschein R. W. Peelle

The 256-channel pulse-height analyzer[1] designed at the Argonne National Laboratory has a dead time per pulse which varies with pulse height between about 20 and 150 μsec. A number of other available analyzers have comparable or larger dead times. With the Argonne type of analyzer, for a typical pulse-height spectrum, the rather low counting rate of 10^3 sec^{-1} results in a counting loss of about 10% for which the measured counting rates must be corrected. For counting rates of this magnitude it is not even possible to subtract background spectra without making a correction to the elapsed counting time. The magnitude of the counting losses leads to the desirability of measuring the time during which the analyzer is open to receive a count. Such a measured "on-time" would be independent of spectral shape and counting rate. At the request of the Applied Nuclear Physics Division, an instrument has been designed and constructed (by T. M. Emmer and N. Hill, Instrumentation and Controls Division) to measure this "on-time." A similar device has subsequently been reported by Travis *et al.*[2]

In the Argonne type of analyzer, when an input pulse has been accepted for storage, a gate circuit at the input prevents additional pulses from entering the circuit during the quantization and storage of the accepted pulse. In the on-time clock, a 1-mc crystal-controlled oscillator is turned off during the intervals when the analyzer input is "closed" for the analysis of a pulse. Each oscillator pulse generated during the on-time is fed into a decade counting circuit and represents 1 μsec of on-time. The sum of all such pulses during a data accumulation period equals the total time during which the analyzer was open to receive a count. The circuit presently used allows a preset on-time for any integral number of seconds up to 10^4.

This clock circuit has the accuracy of the crystal-controlled oscillator and is usually used in preference to a 60-cps timing clock, which may have greater frequency errors over short intervals. The circuit does not take into account any dead-time error (comparable to the width of the input pulse) caused by pulse pile-up. In future models of the clock circuit, the oscillator frequency may be reduced by one or two orders of magnitude. Reductions in this frequency must be limited to ensure that the statistical errors in the on-time measurement are well below those in the count measurement.

[1] R. W. Schumann and J. P. McMahon, *Rev. Sci. Instr.* 27, 675 (1956).

[2] C. M. Travis *et al.*, *Gate-On Timer*, NARF-57-34T (Aug. 15, 1957).

Part 11

SPUTTERING PRODUCED BY IONS WITH ENERGIES ABOVE 50 kev

11.1. SPUTTERING PRODUCED BY IONS WITH ENERGIES ABOVE 50 kev

D. T. Goldman A. Simon

Previous theoretical treatments of the problem of sputtering have been limited to the region below a few kilovolts[1] and have been primarily concerned with determining the threshold for sputtering. However, low-energy ions have a mean free path of only a few atomic layers, and the phenomenon involves a complicated analysis of surface interactions. As the energy of the bombarding ion increases, a simplifying feature emerges: the range of the incident particle increases greatly ($\cong 10^{-4}$ cm for a 500-kev deuteron incident on a copper target), while the knock-on particles maintain an approximately constant mean free path ($\cong 10^{-7}$ cm). Hence only a small portion of the initial track length of the incident particle produces knock-ons which can re-emerge from the surface. The displacement rate is nearly constant over this region, thus enabling relatively simple solutions of the diffusion problem for emission to be obtained.

The number of primary particles produced per unit volume in the solid is given by

$$q = \frac{I}{A} \frac{\mathbb{1}(R)}{\lambda_i(E)} , \tag{1}$$

where

I = particle flux of the incident beam,

A = cross-sectional area of the beam,

R = range of the incident ions,

λ_i = mean free path for the production of a primary particle,

$\mathbb{1}$ = a unit step function equal to unity for penetrations up to R and zero thereafter,

E = energy at penetration depth R.

If it is assumed that the knock-ons which emerge from the surface originate from a depth which is small compared with R, Eq. 1 takes the form

$$q \cong \frac{I}{A\lambda_i(E_i)} , \tag{2}$$

where E_i is the incident energy.

The sputtering ratio R, defined as the ratio of the total current of sputtered atoms divided by the incident current, is

$$R = \frac{\gamma}{\lambda_i \cos \psi} , \tag{3}$$

where γ = the proportionality factor between the current J and the source (i.e., $J = \gamma q$) and ψ = the angle that the beam makes with the normal to the surface.

The mean free path for the production of primary particles can be determined from the Rutherford scattering cross section.[2] The cross section for the production of a primary particle, σ_d, is found to be

$$\sigma_d = 4\pi a_0^2 \frac{M_1 M_2}{(M_1 + M_2)^2} \frac{z_1^2 z_2^2}{E_d E} R_y^2 , \tag{4}$$

where

$R_y = e^2/2a_0$
$= 13.6$ ev,

$a_0 = \hbar^2/me^2$
$=$ radius of first Bohr orbit
$= 0.529 \times 10^{-8}$ cm,

M_1 = mass of incident particle,

M_2 = mass of target particle,

z_1 = charge of incident particle,

z_2 = charge of target particle,

E = energy of incident particle,

E_d = binding energy of a target particle in the lattice.

The mean free path then is

$$\lambda_i = \frac{1}{n_0 \sigma_d} , \tag{5}$$

where n_0 is the particle density in the material.

[1] D. E. Harrison, Jr., *Phys. Rev.* 102, 1473 (1956).

[2] F. Seitz and J. S. Koehler, *Solid State Physics* (ed. by F. Seitz and D. Turnbull), vol 2, p 305, Academic Press, New York, 1956.

For the example of a beam of 500-kev deuterons striking a copper target (E_d = 25 ev),

$$\lambda_i = 0.858 \times 10^{-4} \text{ cm} .$$

The average energy transferred to each primary knock-on particle is

$$\bar{T}_d = E_d \ln \frac{T_m}{E_d} , \quad \text{for } T_m \gg E_d ,$$

where

$$T_m = \left[4M_1M_2/(M_1 + M_2)^2\right] E ,$$

the maximum energy that can be transferred. For the example considered here,

$$\bar{T}_d = 247.6 \text{ ev} .$$

Since the average energy of the primary knock-ons is so low, any successive scattering of these primary particles can be considered as hard sphere collisions with a cross section $\sigma = \pi\mathcal{R}^2$, where $\mathcal{R}$ is a solution of

$$\frac{z_2^2 e^2 e^{-\mathcal{R}/a'}}{\mathcal{R}} = \bar{T}_d ,$$

where a' is the screening constant set equal to $a_0/z_2^{1/3}$. The mean free path of the primary particle is now

$$(6) \qquad \lambda = \frac{1}{\pi\mathcal{R}^2 n_0} .$$

For the example considered here the value of λ is 7.44×10^{-8} cm.

As the primary particles diffuse through the medium, they will collide with lattice ions, producing still more displaced atoms. The average number of all knock-on particles, $\bar{\nu}$, produced is[2]

$$(7) \quad \bar{\nu} = \left[0.107 + 0.561 \ln\left(\frac{T_m}{E_d} + 1\right)\right] \frac{(T_m/E_d) + 1}{T_m/E_d} .$$

For this example, $\bar{\nu}$ = 7.895.

The source term is now replaced by an effective source, $\bar{\nu}q$, and the diffusion of these particles through the material[3] is computed. To keep the average number of collisions of the effective source particles equal to the average of the actual secondaries, λ_s is set equal to λ_a, where λ_a is the mean free path for an absorptive collision. Then the current diffusing from the surface of the material is

$$(8) \qquad J = \frac{q\bar{\nu}}{\sqrt{3}} \lambda(0.294) .$$

For the example chosen here

$$\gamma = \frac{7.895}{\sqrt{3}} \lambda_s(0.294) .$$

As an alternative means of calculating the return current, only the uncollided flux has been considered. This method would give a valid result if $\Sigma_a \gg \Sigma_s$ but should give a lower limit for the current in this case. Since the primary directions are actually peaked at right angles to the path of the incident particles, the effects of a $\sin^2 \theta$ distribution of primary particles about the incident direction have also been considered. The results indicate that the uncollided flux estimate is very close to the diffusion theory solution and that an anisotropic distribution of primary particles changes the values very little.

The general expression for the sputtering ratio is obtained by substituting Eqs. 4 through 8 into Eq. 3, which yields

$$(9) \quad R = \left[0.107 + 0.561 \ln\left(\frac{T_m}{E_d} + 1\right)\right] \frac{T_m + E_d}{T_m} \frac{1}{\cos\psi} 4\pi a_0^2 \frac{M_1M_2}{(M_1 + M_2)^2} \frac{z_1^2 z_2^2}{E_d} \frac{R_y^2}{E} \frac{1}{\pi\mathcal{R}^2} .$$

For the illustrative example considered here, that is, 500-kev deuterons striking a copper target, $\mathcal{R} = 2.324 \times 10^{-3}$.

[3] S. Glasstone and M. C. Edlund, *The Elements of Nuclear Reactor Theory*, p 90 ff, Van Nostrand, New York, 1952.

The numerical values obtained from Eq. 9 are probably trustworthy only in their order of magnitude. The dependence on energy, incident angle, and mass ratio may be more reliable. From Eq. 9 this dependence is

$$R \sim \frac{\ln E}{E} \frac{\mu}{(1+\mu)^2} \frac{1}{\cos \psi}, \tag{10}$$

where $\mu = M_1/M_2$.